LOAN DOCUMENT

AD-A269 275

DTIC ACCESSION NUMBER

PHOTOGRAPH THIS SHEET

LEVEL

1

INVENTORY

WL-TR-93-2091

DOCUMENT IDENTIFICATION

Aug 93

DISTRIBUTION STATEMENT A
Approved for public release
Distribution Unlimited

DISTRIBUTION STATEMENT

HANDLE WITH CARE

ACCESSION FOR
NTIS GRA&I ☑
DTIC TRAC ☐
UNANNOUNCED ☐
JUSTIFICATION

BY

DISTRIBUTION/

AVAILABILITY CODES

DISTRIBUTION	AVAILABILITY AND/OR SPECIAL	
A-1		

DISTRIBUTION STAMP

DTIC
ELECTE
SEP 3 1993
S C D

DATE ACCESSIONED

DTIC QUALITY INSPECTED 5

DATE RETURNED

93 9 01 059

DATE RECEIVED IN DTIC

93-20529

REGISTERED OR CERTIFIED NUMBER

PHOTOGRAPH THIS SHEET AND RETURN TO DTIC-FDAC

DTIC FORM 70A JUN 90

DOCUMENT PROCESSING SHEET

PREVIOUS EDITIONS MAY BE USED UNTIL STOCK IS EXHAUSTED.

LOAN DOCUMENT

WL-TR-93-2091

INVESTIGATIONS IN THE FLUID DYNAMICS OF SCRAMJET INLETS

DR. PHILIP SULLIVAN ET AL.
UNIVERSITY OF TORONTO
INSTITUTE FOR AEROSPACE STUDIES
4925 DUFFERIN STREET
DOWNSVILLE, ONT CANADA M3H 5T6

DR. SANNU MOLDER ET AL.,
RYERSON POLYTECHNICAL INSTITUTE
DEPARTMENT OF MECHANICAL ENGINEERING
350 VICTORIA STREET
TORONTO ONT, CANADA M5B 2K3

AUGUST 1993

Final Report for the Period September 1987 to March 1993

Aero Propulsion and Power Directorate
Wright Laboratory
Air Force Materiel Command
Wright-Patterson AFB, Ohio 45433-7251

NOTICE

When Government drawings, specifications, or other data are used for any purpose other than in connection with a definitely Government-related procurement, the United States Government incurs no responsibility or any obligation whatsoever. The fact that the government may have formulated or in any way supplied the said drawings, specifications, or other data, is not to be regarded by implication, or otherwise in any manner construed, as licensing the holder, or any other person or corporation; or as conveying any rights or permission to manufacture, use, or sell any patented invention that may in any way be related thereto.

This report is releasable to the National Technical Information Service (NTIS). At NTIS, it will be available to the general public, including foreign nations.

This technical report has been reviewed and is approved for publication.

DEAN P. PETTERS, CAPT, USAF
DESIGN & TEST MANAGER
ANALYSIS & APPLICATIONS BRANCH

DR. WILLIAM C. BURSON, JR, BRANCH CHIEF
PROPULSION DEVELOPMENT BRANCH
ADVANCED PROPULSION DIVISION

ROBERT E. HENDERSON, DIVISION CHIEF
ADVANCED PROPULSION DIVISION
AERO PROPULSION & POWER DIRECTORATE

If your address has changed, if you wish to be removed from our mailing list, or if the addressee is no longer employed by your organization please notify WL/POPA , WPAFB, OH 45433-7650 to help us maintain a current mailing list.

Copies of this report should not be returned unless return is required by security considerations, contractual obligations, or notice on a specific document.

REPORT DOCUMENTATION PAGE

Form Approved
OMB No. 0704-0188

1. AGENCY USE ONLY (Leave blank)	2. REPORT DATE	3. REPORT TYPE AND DATES COVERED
	AUG 1993	FINAL

4. TITLE AND SUBTITLE INVESTIGATIONS IN THE FLUID DYNAMICS OF SCRAMJET INLETS

5. FUNDING NUMBERS
C F33615-87-C-2748
PE 61102
PR ILIR
TA P7
WU 07

6. AUTHOR(S)
S. MOLDEN, P. A. SULLIVAN ET AL

7. PERFORMING ORGANIZATION NAME(S) AND ADDRESS(ES)
RYERSON POLYTECHNICAL INSTITUTE
UNIVERSITY OF TORONTO INSTITUTE FOR AEROSPACE STUDIES
4925 DUFFERIN ST AND 350 VICTORIA ST
DOWNSVILLE, ONT CA M3H5T6 AND TORONTO ONT,CA M5B 2K3

8. PERFORMING ORGANIZATION REPORT NUMBER

9. SPONSORING / MONITORING AGENCY NAME(S) AND ADDRESS(ES)
AEROPROPULSION AND POWER DIRECTORATE
WRIGHT LABORATORY
AIR FORCE MATERIEL COMMAND
WRIGHT PATTERSON AFB OH 45433-7650

10. SPONSORING / MONITORING AGENCY REPORT NUMBER
WL-TR-93-2091

11. SUPPLEMENTARY NOTES

12a. DISTRIBUTION / AVAILABILITY STATEMENT
APPROVED FOR PUBLIC RELEASE; DISTRIBUTION IS UNLIMITED.

12b. DISTRIBUTION CODE

13. ABSTRACT *(Maximum 200 words)*

Research on projects related to the hypersonic fluid mechanics of scramjet inlets is described. Four experimental tasks were performed which used a hypersonic gun tunnel to generate flows having stagnation enthalpies up to 1400K, Mach numbers of about 8.3, and Reynolds numbers for a typical model in the range of 5 to 15 million. The first project investigated the interaction of a shock wave with a laminar boundary layer in the neighborhood of a convex corner. The second project dealt with flow established in a two-dimensional inlet consisting of a forebody-cowl combination. The third project investigated flow in a circular duct having a length to diameter ratio of about 10. The fourth project detailed the effects on inlet performance of using three distinctly different inlet geometries: axisymmetric internal flow, two-dimensional internal flow, and axisymmetric external flow.

14. SUBJECT TERMS	15. NUMBER OF PAGES
INLETS, HYPERSONIC TECHNOLOGY, LIQUIED FUELLED RAMJET ENGINES	458
	16. PRICE CODE

17. SECURITY CLASSIFICATION OF REPORT	18. SECURITY CLASSIFICATION OF THIS PAGE	19. SECURITY CLASSIFICATION OF ABSTRACT	20. LIMITATION OF ABSTRACT
UNCLASSIFIED	UNCLASSIFIED	UNCLASSIFIED	UL

GENERAL INSTRUCTIONS FOR COMPLETING SF 298

The Report Documentation Page (RDP) is used in announcing and cataloging reports. It is important that this information be consistent with the rest of the report, particularly the cover and title page. Instructions for filling in each block of the form follow. It is important to ***stay within the lines*** to meet ***optical scanning requirements***.

Block 1. Agency Use Only *(Leave blank)*.

Block 2. Report Date. Full publication date including day, month, and year, if available (e.g. 1 Jan 88). Must cite at least the year.

Block 3. Type of Report and Dates Covered. State whether report is interim, final, etc. If applicable, enter inclusive report dates (e.g. 10 Jun 87 - 30 Jun 88).

Block 4. Title and Subtitle. A title is taken from the part of the report that provides the most meaningful and complete information. When a report is prepared in more than one volume, repeat the primary title, add volume number, and include subtitle for the specific volume. On classified documents enter the title classification in parentheses.

Block 5. Funding Numbers. To include contract and grant numbers; may include program element number(s), project number(s), task number(s), and work unit number(s). Use the following labels:

C	- Contract	**PR**	- Project
G	- Grant	**TA**	- Task
PE	- Program Element	**WU**	- Work Unit Accession No.

Block 6. Author(s). Name(s) of person(s) responsible for writing the report, performing the research, or credited with the content of the report. If editor or compiler, this should follow the name(s).

Block 7. Performing Organization Name(s) and Address(es). Self-explanatory.

Block 8. Performing Organization Report Number. Enter the unique alphanumeric report number(s) assigned by the organization performing the report.

Block 9. Sponsoring/Monitoring Agency Name(s) and Address(es). Self-explanatory.

Block 10. Sponsoring/Monitoring Agency Report Number. *(If known)*

Block 11. Supplementary Notes. Enter information not included elsewhere such as: Prepared in cooperation with...; Trans. of...; To be published in.... When a report is revised, include a statement whether the new report supersedes or supplements the older report.

Block 12a. Distribution/Availability Statement. Denotes public availability or limitations. Cite any availability to the public. Enter additional limitations or special markings in all capitals (e.g. NOFORN, REL, ITAR).

- **DOD** - See DoDD 5230.24, "Distribution Statements on Technical Documents."
- **DOE** - See authorities.
- **NASA** - See Handbook NHB 2200.2.
- **NTIS** - Leave blank.

Block 12b. Distribution Code.

- **DOD** - Leave blank.
- **DOE** - Enter DOE distribution categories from the Standard Distribution for Unclassified Scientific and Technical Reports.
- **NASA** - Leave blank.
- **NTIS** - Leave blank.

Block 13. Abstract. Include a brief *(Maximum 200 words)* factual summary of the most significant information contained in the report.

Block 14. Subject Terms. Keywords or phrases identifying major subjects in the report.

Block 15. Number of Pages. Enter the total number of pages.

Block 16. Price Code. Enter appropriate price code *(NTIS only)*.

Blocks 17. - 19. Security Classifications. Self-explanatory. Enter U.S. Security Classification in accordance with U.S. Security Regulations (i.e., UNCLASSIFIED). If form contains classified information, stamp classification on the top and bottom of the page.

Block 20. Limitation of Abstract. This block must be completed to assign a limitation to the abstract. Enter either UL (unlimited) or SAR (same as report). An entry in this block is necessary if the abstract is to be limited. If blank, the abstract is assumed to be unlimited.

RYERSON POLYTECHNICAL INSTITUTE
Department
of
Mechanical Engineering

UNIVERSITY OF TORONTO
Institute
for
Aerospace Studies

Toronto, Canada

INVESTIGATIONS IN THE FLUID DYNAMICS OF SCRAMJET INLETS

Section Authors

Ryerson	Toronto
S. Molder	P. A. Sullivan
R. J. McGregor	J. P. Sislian
T. W. Paisley	J. J. Gottlieb
S. C. Weston	R. J. Hawboldt
R. J. Rogers	R. L. Deschambault
	C. P. T. Groth
	D. W. Hawken
	Z.-D. He
	L.-W. Chen
	K. A. Gordon

United States Air Force Contract No: F33615-87-C-2748
Johns Hopkins University Applied Physics Laboratory Contract No: APL 602235-0

July 1992

The wayfarer
Perceiving the pathway to truth
Was struck with astonishment.
It was thickly grown with weeds.
"Ha," he said,
"I see that none has passed here
In a long time."
Later he saw that each weed
Was a singular knife.
"Well," he mumbled at last,
"Doubtless there are other roads."

by Stephen Crane

Acknowledgements

The Project was made possible only as a result of the active support and encouragement of many people. Dr. F. S. Billig and Dr. E. T. Curran of the United States Air Force Aerospace Propulsion Laboratory arranged contracts from their respective agencies, and this in turn enabled grants to be obtained from two Canadian sources. These were the Natural Sciences and Engineering Research Council of Canada's Shared Equipment and Facilities Program (Grant SEF 8703), and the Province of Ontario's University Research Incentive Fund (Grant TO 4-013). The Canadian Government's National Research Council donated the gun tunnel on which the project was based. Additional financial support was provided by Viatec Resource Systems of Toronto, Pratt and Whitney (Canada), Mississauga, and by the two institutions performing the work. Of the many individuals who provided assistance and encouragement we must mention Dr. R. C. Tennyson, Director of the University of Toronto's Institute for Aerospace Studies, Prof. R. Guerriere, Director of Ryerson Polytechnical Institute's Office of Research and Innovation, and Dr. W. E. White, Dean of the latter institution's Faculty of Engineering and Applied Science. Professors H. A. Stassen and P. J. Short of the Ryerson Polytechnical Institute provided technical guidance for the piston development project. The contract was monitored by M. E. White of JHU/APL, and by Lts. R. Clausen, W. Smith and Capt. D. Petters of the USAF. Technical advice was provided by F. S. Billig, D. Van Wie, M. E. White, G. P. Corpening, and M. V. Thompson, all of JHU/APL. Finally, Mr. J. E. Shepherd and Mr. L. D. Secord of Viatec Resources played key roles in securing and administering the contracts.

Abstract

Research on projects related to the hypersonic fluid mechanics of scramjet inlets is described. Four were experimental and used a hypersonic gun tunnel to generate flows having stagnation enthalpies up to 1400K, Mach numbers of about 8.3, and Reynolds numbers for a typical model in the range 5 to 15 million. The first project investigated the interaction of a shock wave with a laminar boundary layer in the neighbourhood of a convex corner. This flow shares features with other hypersonic interactions such as that generated by an externally generated shock wave impinging on a flat plate boundary layer flow. However in the convex corner case, as the incident shock wave is moved towards the corner, separation is suppressed and the flow remains attached even when incidence occurs a significant distance downstream. In all cases the pressure far downstream approaches the ideal or cancellation value corresponding to a single incident shock but, even when the flow remains attached, many boundary layer thicknesses are required to achieve this value. The second project dealt with flow establishment in a two-dimensional inlet consisting of a forebody-cowl combination. The effect on inlet flow starting of Reynolds number, cowl angle of attack, inlet contraction ratio and initial tunnel plenum pressure were determined. It was found that impulsive flow starting in the gun tunnel facilitates the starting of inlets with contraction ratios far exceeding the quasi-steady Kantrovitz criterion. Inlet starting is facilitated also by a lower contraction ratio, a thinner forebody boundary layer and a lower initial plenum pressure. The third project investigated flow in a circular duct having a length to diameter ratio of ten. Measurements of wall static pressure, and of instream pitot and static pressures were obtained to allow reconstruction of the internal flow. The purpose of the fourth experimental project was to discover the effects on inlet performance of using three distinctly different inlet geometries: one having axisymmetric internal flow, another, two-dimensional internal flow, and a third, axisymmetric external flow. The shapes of these inlets were designed so that the inviscid flows in all inlets would be the same. This ensured that effects of geometric differences were confined solely to the boundary layer. In all cases inlet performance was determined by wall static pressures. For the axisymmetric internal flow inlet, drag was also measured. Predicted and experimental pressures agreed to 3 to 4%, and drag measurements to 5%. Inviscid theory predicts highest efficiency for the internal axisymmetric inlet, and a viscous correction makes them theoretically equally efficient. Experimental results show that the axisymmetric inlets have the same performance and that the two-dimensional inlet is inferior. The report also describes the calibration of the gun tunnel used in the experiments, and three supporting numerical projects. The first of these is a finite difference code for predicting tunnel performance, the second is a code for predicting the details of inlet starting processes, and the third is development of an improved gun tunnel piston. An overview in the Introduction provides summaries of each project.

Table of Contents

Notation — Section 2

Roman

C_g	specific heat of heat flux gage
D	exit diameter of nozzle
D_p	diameter of static pressure probes
e	internal energy of test gas
h	enthalpy of test gas
k_g	thermal conductivity of heat flux gage
M	Mach number, M_∞ = test section free stream Mach number
p	static pressure
p_p	pitot pressure
p_o	stagnation pressure
p_∞	free stream static pressure
Pr	Prandtl number
q	heat flux per unit area
R	gas constant in perfect gas law
Re	Reynolds number
R_g	nose radius of stagnation point heat transfer model
R_o	resistance of heat flux gage
s	distance from cone-cylinder junction locating pressure taps in static pressure probes
T	temperature
t	time
V	speed of gas flow

x	axial distance along test section from nozzle exit plane; also distance in from surface in heat flux gage

Greek

γ	specific heat ratio of test gas
θ	$T-T_0$, temperature rise in heat flux gage
μ	viscosity of test gas
ρ	density of test gas

Subscripts

d	downstream of de-excitation shock
e	gas properties at edge of stagnation point boundary layer
fr	vibrationally frozen
p	pitot
s	surface of heat flux gage
tr	translational internal energy
u	upstream of de-excitation shock
v	vibrational internal energy
w	gas properties at wall for stagnation point boundary layer
0	stagnation conditions
1	initial conditions in driver
2	conditions after first shock at nozzle end of barrel before reflection
4	initial charge conditions in barrel
5	conditions after first shock reflection at nozzle end of barrel
∞	free stream conditions in test section

Notation — Section 3

Roman

C	Chapman-Rubensin parameter
L	length
M	Mach number
p	pressure
Re	Reynolds number
T	temperature
t_o	offset time
W	model width
x	distance from leading edge
z	transverse distance from centerline

Greek

α	convex corner angle
δ_o	boundary layer thickness
θ	shock generator angle
χ	viscous interaction parameter = $M_\infty^3 C^{1/2}/Re_x^{1/2}$

Subscripts

c	convex corner
d	downstream of interaction
fp	flat plate value
i	shock impingement
p	plateau

u	unit
x	distance from leading edge
0	stagnation conditions
1	initial charge conditions in barrel
∞	free stream in test section

Notation — Section 4

Roman

A	area
A_2/A_3	contraction (area) ratio
H	cowl height
H_t	total enthalpy
h	static enthalpy
I_{sp}	specific impulse
i	incident shock
LE	leading edge
L	cowl length
L_c	diffuser length
M	Mach number
m	mass flow
P	static pressure
P_t	total pressure
P_3/P_2	compression or pressure ratio

R	0.2870
r_c	cowl leading edge radius
r	reflected shock
Re	Reynolds number
s	entropy
T	temperature
T_t	total temperature
tran	boundary layer transition
V	velocity
X	linear distance downstream from cowl leading edge
X_c	forebody length to cowl entry

Greek

α	cowl angle
δ	boundary layer thickness
δ^*	displacement thickness
η_{pt}	total pressure recovery
η_{ke}	kinetic energy efficiency
η_{th}	thermodynamic efficiency
η_{el}	polytropic efficiency
η_{Kd}	Kd efficiency
η_x	energy efficiency
γ	specific heat ratio
ρ	density
θ	momentum thickness

Subscripts

1	forebody leading edge plane
2	cowl entry plane
3	cowl exit plane
t	total condition
inf	freestream condition
fs	freestream condition
TS	test section

Notation — Section 5

Roman

D	duct diameter
L	duct length
M	Mach number
p	static pressure
P	total (isentropic recompression) pressure
Re	Reynolds number
x	axial distance along duct
y	distance along a radius from duct wall

Greek

α	pitch angle of duct relative to nozzle axis
θ	momentum thickness of wall boundary layer

Subscripts

bl	boundary layer
ch	barrel charge pressure

p	pitot
w	values at wall
0	reservoir or total conditions corresponding to freestream
1	instream static probe
∞	funnel freestream conditions

Notation — Section 6

Roman

A	area
A_3/A_1	area ratio
C_p	specific heat at constant pressure
C_v	specific heat at constant volume
f	force on fluid in inlet
H_t	total enthalpy
h	static enthalpy
I_{sp}	specific impulse
M	Mach number
m	mass flow
p	static pressure
Pt	total pressure
Q	heat flow to fluid in inlet
r	radial distance from Mach 1 radial to a point on the streamline where the Mach number is M
S	distance along the Prandtl-Meyer streamline measured from the sonic point

s	entropy
T	temperature
T_t	total temperature
u	velocity component
V	velocity
x, y	Cartesian coordinate measured from entry tip of intake
X, Y	coordinates of Prandtl-Meyer compression fan focal point

Greek

α	contraction ratio (A_1/A_3)
π	compression ratio (p_3/p_1)
γ	specific heat ratio
ρ	density
τ	heat loss parameter
ν	Prandtl-Meyer turning angle
Φ	angular coordinate in Prandtl-Meyer flow measure from M = 1
μ	Mach angle
θ	coordinate angle
θ_s	shock angle
δ_2	flow deflection through conical shock
η_{pt}	total pressure recovery
η_{el}	polytropic efficiency
η_{th}	thermodynamic efficiency
η_{ke}	kinetic energy efficiency
η_{Kd}	Kd efficiency
η_x	energy efficiency

Subscripts

0	freestream condition
1	inlet entry plane
2	end of inlet isentropic compression
3	inlet exit plane
t	total condition
r	in radial direction
θ	in θ-direction
n	normal

Notation — Section 7

Roman

a	sound speed
A	cross-sectional area of duct
A	source term column vector
b	antidiffusive flux ratio
c_s	species mass fraction
C_p	specific heat at constant pressure
D_h	hydraulic diameter
e	total specific internal energy
e_{tr}	translational-rotational energy of mixture
e_v	vibrational energy
e	eigenvectors of homogeneous flux vector Jacobian
f	Darcy-Weisbach friction factor

F_p	frictional force acting on the piston
F_{wall}	equivalent wall boundary-layer viscous body force
F_{loss}	equivalent pressure-loss body force
F	homogeneous flux vector
h	total specific energy
H	nonequilibrium flow homogeneous flux column vector
I	identity matrix
J	Jacobian of homogeneous flux vector
k	thermal conductivity
L	reference length
L_p	piston length
m_p	piston mass
M	Mach number
$\mathcal{M}$	molecular weight
N	number of species in mixture
Nu	Nusselt number
p	pressure
Pr	Prandtl number
Q_{wall}	wall heat transfer ratio
Q_{zero}	rate of change of mixture zero-point energy
Q	nonequilibrium flow source term column vector
r	duct radius
r_p	piston radius
R	specific gas constant
R	Reynolds number

R_p	piston Reynolds number
$\mathcal{R}$	universal gas constant
S	source term column vector
t	time
T	temperature
u	velocity
U	solution column vector
V_p	piston velocity
W	nonequilibrium flow solution column vector
x	axial position coordinate

Greek

α	elemental wave strength
γ	specific heat ratio
θ	time-stepping control parameter
λ	eigenvalues of homogeneous flux vector Jacobian
Λ	comprssibility correction factor
μ	dynamic viscosity
ν	local CFL number for gas dynamic subsystem
ρ	flow density
σ	piston skirt porosity
ϕ	flux limiter
ω	local CFL number for thermodynamic subsystem

Subscripts and Superscripts

i	index of spatial node of computational mesh
k	characteristic field index

n	index of time step
s	species index

Notation — Section 8

Roman

A	four-by-four influence matrix in Eqs. (8.67) and (8.68)
C	characteristic velocity of propagation (sound speed)
E	gas energy per unit volume
f	actual flux crossing a cell boundary
F	approximate flux crossing a cell boundary
h	interface flux term defined by Eq. (8.27)
i	index number for a cell
I	four-by-four identity matrix
J	Jacobian defined by Eq. (8.430
L	matrix defined by Eq. (8.52)
N	number of intervals or cells
P	gas pressure
S	source term
t	time, normalized time
Q	limiter term defined by Eqs. (8.30) and (8.79)
R	four-by-four matrix defined by Eq. (8.48)
X	distance in x-direction
Y	distance in y-direction
U	flow in the X-direction

V	flow in the Y-direction
W	weights for fluxes defined by Eq. (8.52)

Greek

α	projection in the difference of U across an interface onto the m^{th} eigenvector
β	time-step size divided by cell width ($\Delta t/\Delta x$)
δ	small real number ranging from 0.01 to 0.15
Δ	difference between two values of a variable
ε	gas specific energy (per unit mass)
Φ	modified interface flux defined by Eqs. (8.26) and (8.78)
γ	ratio of specific heats of a gas
η	computational grid coordinate for Y
λ	Jacobian of the interface flux
θ	compression parameter
ρ	gas density
σ	sign of a scalar valued Jacobian
Ω	defined in EQ. (8.48)
ω	compression parameter
ξ	computational grid coordinate for X

Subscripts

i	index number for a cell in direction x
k	index number for a cell in direction y
n	index number of a time step
T	indicates the transpose of a matrix

1.0 Introduction

1.1 Preamble

This report describes research undertaken to support the development of scramjet engine inlets for hypersonic air breathing flight vehicles. It was an international effort involving financial support from various United States and Canadian agencies. The primary motivation for the work was provided by contracts from the United States Air Force (USAF) and the Johns Hopkins University Applied Physics Laboratory (JHU), which specified two phases. In the first phase, four topics were investigated:

(i) experimental measurements of shock-boundary layer interactions in the vicinity of a convex corner,

(ii) inlet starting limits in impulsive hypersonic facilities,

(iii) hypersonic flow development in long ducts,

(iv) experimental determination of the efficiencies of three generic hypersonic inlets.

Owing to financial limitations, the second phase was not implemented.

The program arose from discussions between Dr. F. S. Billig of The Johns Hopkins University and Prof. S. Molder of Ryerson Polytechnical Institute in the spring of 1986, at which time the project tasks were formulated. The idea of using the Canadian National Research Council's (NRC) hypersonic gun tunnel to perform the work was explored by Billig and Molder on a visit to Mr. L. Ohman of NRC in 1986. This facility, which had been built in the late 1950's, was at that time in storage. Lack of adequate space prevented the installation of the tunnel at Ryerson. Consultations with the Director of the University of Toronto's Institute for Aerospace Studies (UTIAS), Dr. J. H. de Leeuw, and with Dr. I. I. Glass of the same institute led to an invitation for the University of Toronto's participation. In the meanwhile Billig had obtained a promise of support from both The Johns Hopkins University and the United States Air Force. The newly appointed Director of UTIAS, Dr. R. C. Tennyson, agreed to University of Toronto's participation and the project was started with Molder as Project Director.

Since the financial support from JHU and the USAF was earmarked for the specific tasks listed above, additional funding was required for tunnel refurbishment and for certain supporting projects. A Shared

Equipment and Facilities Grant was awarded to Ryerson by Canada's Natural Science and Engineering Research Council (NSERC) with Molder as Principal Investigator. Another major grant in support of the related work was obtained from the Ontario Government's University Research Incentive Fund with Dr. J. P. Sislian and Molder as principal investigators. Both of these grants required the active participation of an industrial partner. Viatec Resource Systems of Toronto was invited to participate and its chairman, Mr. J. E. Shepherd, later played a key role in securing both grants. The NSERC award required a concomitant demonstration of industrial interest through a cash donation to the project by an industrial concern. This was obtained by Dr. Tennyson from Pratt and Whitney Canada Ltd.

Both the financial arrangements and the condition of the facility presented a special challenge. The Canadian funds for tunnel refurbishment could not be released until the USAF and JHU contracts were in place. The tunnel had to be transported to the UTIAS site, reassembled and recertified, equipped with a modern instrumentation and data acquisition system, and then calibrated. Thus progress towards the goals set in the USAF and JHU contracts was paced by the refurbishment and especially by the calibration activities. In this respect, although NRC had expended considerable effort in the development of the facility, detailed documentation of test section flow properties was not available.

A key feature of the overall effort was the incorporation of the supporting projects. In addition to describing the results obtained for the four tasks specified by USAF and JHU, the present report also reviews the work completed on tunnel calibration and progress on three of these projects. One is a numerical simulation of the gun tunnel operation, the second is development of a code which can predict inlet starting processes and the third is development of improved strength-to-weight ratio pistons.

1.2 Overview of Projects

1.2.1 Tunnel Development and Calibration

A gun tunnel obtains the high pressures and temperatures required to generate hypersonic flow by using compressed air impulsively released from a reservoir or driver to accelerate a piston along a barrel. The piston compresses and heats the test gas, which then flows through a convergent-divergent nozzle into an

open jet test section. The concept provides an inexpensive method of achieving moderately hypersonic Mach numbers and a modest range of Reynolds numbers. Running times achieved in this way can be 20 milliseconds and longer. When these facilities were first developed over three decades ago it was anticipated that they could achieve high stagnation enthalpies, but for a variety of reasons only moderate values have been obtained; hence they have proven mainly useful for investigating fluid mechanical effects.

The present section describes the facility, discusses briefly some development problems encountered during refurbishment, and then reviews the calibration results. The principal results of this calibration are as follows. In the current configuration mean barrel end stagnation pressures of about 26.5 MPa (3,800 psi) are obtained but the compression and heating process induced by the piston motion is not uniform, so that the effective stagnation pressure variation during a run lasting 25 milliseconds can be as much as a total of 20%. However, the flow in the nozzle and test section is believed to be quasisteady because the pitot pressures measured in the test section have histories closely similar in form to that of the barrel pressures; furthermore the ratio of pitot to barrel pressure remains effectively constant during a run.

The method chosen to infer stagnation enthalpy histories is based on measurement of stagnation point heat transfer rates in the tunnel test section. This is a well known approach; platinum-film-on-glass heat flux gages are used, and estimates of the heat flux are obtained by solution of the equations for heat conduction in the glass. In the present case these solutions are obtained numerically. Results obtained thus far suggest that the method can resolve in detail the stagnation temperature history. However the computed values are significantly higher than those predicted by the simulation. This discrepancy is thought to arise from uncertainties in the thermal properties of the commercial heat flux gages used in the tests performed to date.

The role of vibrational nonequilibrium effects in the tunnel nozzle is discussed with particular reference to the possibility that a vibrational de-excitation shock reported by others might significantly affect test section Mach number. The numerical simulation, which does not consider this phenomenon, implies that the thermodynamics of the nozzle flow may be treated as ideal with a specific heat ratio of 1.4. It is inferred from measurements of test section static and pitot pressures that, for the tunnel nozzle currently installed, the postulated de-excitation phenomenon has no significant effect.

The contoured nozzle originally developed for the tunnel has an exit diameter of 217 mm and supplies an inviscid core having a diameter of about 140 mm. The flow is uniform and free of Mach number gradients. The Mach number is about 8.3, and unit Reynolds numbers can be set between 2.3×10^7/m and 4.5×10^7/m.

In general the facility produces repeatable high quality test data, and thus can play a useful role in the continued development of hypersonic fluid mechanics.

1.2.2 Shock-Boundary Layer Interactions at a Convex Corner

Many candidate scramjet inlet geometries rely on the use of an oblique shock wave to turn a hypersonic boundary layer around a convex corner in such a way that it does not significantly disrupt the main flow by large-scale separation or other interactions. Although interactions between shock waves and hypersonic boundary layers have been investigated extensively in the last thirty years, this particular configuration has not. At the commencement of the present project only one experimental paper was available to us; the data was obtained at upstream Mach numbers = 1.8 and 2.5.

The project commenced with a review of the literature on experimental techniques used to study this type of flow. As a result it was decided that, in a first investigation, it would be appropriate to use surface pressure measurements combined with schlieren photography on a planar model. Although surface heat transfer measurements were considered because of their ability to accurately detect incipient separation, their interpretation to ascertain other flow field features is difficult; in contrast pressure measurements can be readily related to gross features observed in schlieren flow visualizations such as separation bubbles and shock waves. Also, to avoid the edge effects associated with planar models, axisymmetric models were considered; however their use was rejected owing to the difficulty and cost of obtaining geometry changes and to the high visibility available for planar models. The test program finally specified called for an exploratory phase to develop a suitable model configuration and obtain some preliminary results. In the final phase a refined geometry was to be used.

The exploratory phase commenced with a simple flat plate model in order to select a model size as large as possible and a pressure tap geometry having adequate response. Previous research on interactions had suggested that, for this geometry, the boundary layer should be laminar. However it is also known that in this type of facility, transition depends to a considerable extent on the flow noise, with smaller tunnels having a tendency to reduce the transition Reynolds number. The present flat plate tests indicated that the boundary layer was laminar but very close to transition.

The transitional character of the boundary layer was confirmed in the next stage of the exploratory phase, which was to obtain data on the interaction of the boundary layer with a shock wave generated externally by an inclined flat plate mounted above the model. It was intended that this data would provide one of two references or baselines for interpreting the convex corner data.

The second baseline data was the interaction of a boundary layer with a convex expansion corner. In this case pressure measurements downstream of the corner were obtained for the two corner angles to be used in the interaction tests. Since this involved the generation of static pressures well below that in the tunnel free stream, it was considered important to establish if a region of interference-free downstream boundary layer growth could be established.

For the two convex corner angles tested, 5° and 10°, the shock generator plate was mounted so that the incoming shock would intersect the boundary at various points upstream and downstream of the corner. In all cases the pressure rise far downstream of the corner approached the ideal or cancellation value corresponding to a single oblique shock, but the details of the process depended critically on the location of the shock wave relative to the corner. With the shock impingement point far enough upstream of the corner a plateau pressure characteristic of a separation bubble was formed, but this was always less than the value for a flat plate interaction corresponding to the same overall pressure rise. For both corners separation was suppressed by moving the shock to within a few boundary layer thicknesses upstream of the corner, but even in this case, although the pressure increase was monotonic, it required many boundary layer thicknesses to reach the ideal value. When the shock wave impinged downstream of the corner, evidence of an initial expansion process occurred in some cases. In only one case was evidence of separation

downstream of the corner observed. In no case were we able to obtain complete uncoupling of the basic corner expansion flow and shock-boundary layer interactions.

The final part of the exploratory phase was to test for edge effects by cutting the width of the exploratory model and examining its effects on centerline pressure distributions. This established that edge effects were not influencing the data.

As a result of these tests a model geometry for the final test phase was chosen mainly to reduce transitional effects. However at the time of writing the tests remain to be completed.

1.2.3 Hypersonic Inlet Flow Starting in the Gun Tunnel

As an aid to the design of oblique shock inlet models to be tested in the gun tunnel, experiments have been performed to explore the limits of impulsive starting in the facility. A simple model was used for these tests; basically it consisted of two flat plates, the lower aligned parallel to the tunnel stream, and the upper mounted at an angle of attack. To form an inlet these were enclosed between end-plates which contained windows for flow visualization. It was tested under different conditions of Reynolds number, area ratio, and contraction rate or cowl angle, with a fixed Mach number and total temperature. It has been found that:

(a) impulsive flow in the gun tunnel permits the starting of inlets with contraction ratios far exceeding the limits imposed by the quasi-steady Kantrovitz criterion,

(b) impulsive inlet starting is facilitated by a lower contraction ratio, a lower initial plenum pressure, and a lower Reynolds number based on the boundary layer displacement thickness on the lower plate at the cowl entry station,

(c) the amount of gain depends on the flow Reynolds number, the cowl angle and the initial plenum pressure in the gun tunnel's plenum chamber,

(d) inlet starting is facilitated also by decreasing cowl angle as long as this angle remains above a certain minimum (here 6°), below which viscous effects cause a reversal in this trend,

(e) for all Reynolds numbers, a rectangular duct will unstart if the boundary layer displacement thickness at entry exceeds 40% of the capture height,

(f) viscous effects cause large variations from the theoretical values of compression,

(g) shock-boundary layer interactions occur independently of each other at the conditions tested,

(h) maximum compression oblique shock inlets are obtained with cowl angles greater than 10 degrees.

Finally it is noted that, although cowl-plate combinations were not specifically designed as inlets, some respectable performance was obtained at cowl angles below 10 degrees.

1.2.4 An Experimental Study of Hypersonic Flow Development in a Duct

Hypersonic inlets can incorporate passages or ducts having widths or diameters which are small compared to their length. This project was a preliminary investigation into hypersonic flow in such a duct. For simplicity of interpretation, a circular duct having a length to diameter ratio of 10:1 was used. A major disadvantage of this geometry is difficulty in visualizing the internal flow, so that a key objective of the present work was to assess the feasibility of reconstructing the flow from measurements of wall static pressures together with instream static and pitot pressures.

Boundary layer type pitot probes and cone-cylinder static pressure probes were manufactured and tested in the tunnel freestream. The main difficulty in using such probes in the present facility is obtaining adequate response in the short test-time available. The responses of the boundary layer pitot probes were compared with that obtained from a fast response pitot probe built for tunnel calibration. The pressures recorded by several static probe geometries were compared with the freestream value computed from the calibration pitot data, and a geometry which gave best response was selected.

Surveys were obtained at ten stations in a 76.2 mm (3 ins.) diameter duct having a sharp leading edge at a freestream Mach number = 8.33 and a Reynolds number of 29.5×10^6/m. Schlieren photographs of the duct entrance show that the model started properly, and the surveys suggest that an interior leading edge shock wave develops into a Mach disc at about two duct diameters downstream of the entrance. This is followed by a shock-boundary layer interaction at the wall about six diameters from the entrance. At this point the wall-static pressure reaches a peak of just under twice the freestream value and then decays before rising again just upstream of the duct exit. The instream static pressure measurements encountered two

difficulties. Unsteadiness indicative of oscillatory shock wave motion during the tunnel run occurred at some locations, and a probe interference effect as observed by disturbance of the wall static pressures occurred at others.

Subsequently, measurements of wall static pressure were obtained from a 50.4 mm (2 in.) diameter duct. The main purpose of these measurements was to observe the effect of cutting the duct on the flow upstream. This showed that, except when the exit was located near the shock-boundary layer interaction, shortening the duct did not alter upstream pressure. This allows schlieren photography at the duct exit to be used to assist reconstruction of the internal wave structure, and the use of static probes which do not interfere with the flow.

1.2.5 A Comparison of Three Hypersonic Air Inlets

The purpose of this study was to investigate the performance of three hypersonic air inlets both theoretically and experimentally so as to assess their relative merits as manifested in inviscid and viscous losses and as influenced by external versus internal flow and axisymmetric versus two-dimensional geometry. Three geometrically different hypersonic air inlets were designed to operate at Mach 8.33 and a Reynolds number of 23 to 44×10^6/m. The inlets were designed to have the same mass flow and compression ratio and to all produce an exit flow which is uniform, irrotational and aligned in the freestream direction. The three different inlet geometries are characterized by (a) conically and axially symmetric flow with total internal compression — the Busemann Inlet, (b) planarly symmetric flow with total internal compression — the Prandtl-Meyer Inlet, and (c) an axisymmetric combined external/internal flow — the Oswatitsch Inlet. Novel theoretical approaches were used for establishing the required shape of each inlet. In each case flow starting and gross features were confirmed by schlieren photography, as well as by PNS calculations. The design methods and boundary layer correction were verified by surface static pressure measurements, and inlet performance was assessed from throat static pressures and inlet drag measurements.

It was found that all three inlets started and maintained steady flow throughout the tunnel run; predicted flow structures and topography were confirmed by schlieren photographs; design surface pressures and predicted performance agreed to within 7% of measured values. Measured values of Busemann inlet drag agreed to within 7% of the theory and efficiency calculated from the static pressure came to within 8% of the prediction.

It has been demonstrated that the gun tunnel is a convenient, precise, reliable and inexpensive tool for testing hypersonic air inlets. The double diaphragm technique of gun tunnel operation allows the replication of stagnation conditions to better than 1%. This, in turn, permits the relocation of transducers amongst many pressure taps and the interpretation of their data as if it came from a single tunnel run.

1.2.6 Numerical Predictions of Gun Tunnel Performance

A numerical flow analysis has been developed to simulate the operation of the present tunnel and similar facilities. It has been used as an adjunct to the task of calibration and to suggest methods of performance improvement. It is based on the equations of one-dimensional unsteady flow and uses semi-empirical corrections for fluid losses and for piston friction. A key feature is the investigation of real gas effects by the incorporation of ideal or polytropic, real equilibrium and real nonequilibrium gas models. The nonequilibrium model uses a five species, four temperature gas model suitable for vibration and dissociation in air. Solutions of the equations are obtained by finite-difference techniques and use total variation-diminishing schemes including approximate Riemann solvers.

When this code is used to simulate typical gun tunnel conditions it gives very close agreement with measured barrel end stagnation pressure histories, but the predicted stagnation temperature histories are somewhat lower than those inferred from preliminary stagnation temperature measurements. As noted above this is currently thought to be associated with uncertainties in the thermal properties of the heat flux gages used in the experiments. The calculations also support the notion that, in spite of the

significant variation of stagnation pressure and temperature that occurs during the tunnel run time, the flow in the test section may be assumed quasisteady.

The most significant thermodynamic nonequilibrium phenomenon that occurs is vibrational de-excitation of the test gas, air, as it expands in the nozzle. The principal constituent, nitrogen, freezes virtually at the stagnation temperature, thus confirming the conclusion reached during calibration, namely that the nozzle flow may be treated as completely frozen in vibration and thus calorically perfect with a specific heat ratio of 1.4.

The peak stagnation temperature appears to be limited to about 1400K for this facility in its current configuration. However, modest preheating of the test gas before it is compressed can give significant increases. This could be implemented without making major changes in the configuration of the facility.

1.2.7 Two Dimensional Unsteady Hypersonic Flow Predictions

The long term aim of this project is to develop a numerical code to predict the starting processes in the scramjet inlets being tested in the current program. At the time of writing we have developed a code which will compute planar and axially symmetric inviscid flows in multiply connected domains. It solves the Euler equations for calorically and thermally perfect gas flow, transformed from a physical domain having curved boundaries to a computational domain subdivided into square cells. Algebraic stretching functions control the physical distribution of the grid lines. Both explicit and implicit total-variation-diminishing (TVD) algorithms are used to solve the transformed conservation equations. The code computes the approximate solution of a Riemann problem as one stage in the solution procedure. The algorithm of Roe is used as the Riemann problem solver and is implemented so as to compute first-order-accurate fluxes on a rectangular grid. A second-order-accurate flux-limited correction is added to the first-order-accurate flux. Use of the flux limiter to reduce the accuracy towards first order near steep transitions prevents development of oscillations typical of conventional second-order-accurate calculations. The code has been implemented on the CRAY X-MP/24 at the Ontario Centre for Large Scale Computation, at the University of Toronto. A number of test problems have been solved using

both explicit and implicit time-stepping and good results have been obtained. These test problems include one of the inlet configurations tested in the tunnel.

1.2.8 Gun Tunnel Piston Development

Early gun tunnel performance predictions have not been realized, mainly because of limitations on driver and driven tube pressures as imposed by maximum design strength of the piston. Our present piston design has been arrived at experimentally by testing a series of configurations during the period from the 1960's to the present. This design is successful insofar as each piston generally endures more than 100 runs. So, for the present operating conditions there is little incentive to seek a different design or piston material.

However in an attempt to improve gun tunnel performance one must attempt to design a piston with a higher strength-to-weight ratio. The important piston parameter is the strength-to-weight ratio, which, when improved, will lead to the attainment of higher temperatures and pressures in the gun tunnel.

Obviously our present design has not had the benefits of either modern structural analysis methods or the latest developments in high strength-to-weight ratio materials. Consequently a URIF-sponsored project was started with three phases:

(1) Apply Finite Element Analysis to the present design in an attempt to identify its weaknesses.

(2) Using present materials and present tunnel operating conditions, design a better piston. Test this improved design.

(3) Using analysis and design approaches confirmed above, as well as new materials technology, design pistons for enhanced tunnel performance.

The first phase was to verify the analysis, the second phase was to verify the design, and the third phase was to implement both.

Analysis completed so far has predicted the highest stresses in exactly the locations where fatigue cracks appear on the present piston. An improved design has been completed but not tested. Application to advanced materials or enhanced tunnel conditions has not been started.

The gun tunnel is sometimes compared with combustion or piston driven shock tunnels, and it loses out to both on the basis of being able to produce high thermodynamic stagnation conditions. However, because of the presence of the piston, the gun tunnel attains test times which are an order of magnitude longer than those in the shock tunnels. Also, the amount of test gas is precisely known; there is no mixing at the "interface"; the tunnel shuts off when the piston arrives at the throat; 80 to 90% of the driver gas pressure remains in the driver; driver gas or primary diaphragm particles do not pass into the test section. These are very desirable features which are unique to the gun tunnel and which place it in a complementary rather than competitive position in the family of aerodynamic impulse facilities.

2.0 Tunnel Development, Operation and Calibration

P. A. Sullivan, R. L. Deschambault, R. J. Hawboldt and K. A. Gordon

2.1 Introduction

As noted in Section 1, the focus of the programme is a hypersonic gun tunnel designed and built in the late 1950's by the Canadian Government's National Aeronautical Establishment (NAE) at Ottawa (Ref. 2.1) and which had been in storage since 1972. In general, simulation of hypersonic flight in a wind tunnel requires that the test section flow conditions match Mach number, Reynolds number and stagnation enthalpy and, possibly, other parameters. This is a difficult task and, in practise, it is only feasible to obtain partial simulation. Gun tunnels were developed over three decades ago as a way to cheaply achieve moderate Mach numbers (Refs. 2.2-2.5). While they have a limited capability for examination of Reynolds number effects, they cannot match either the Reynolds number or the stagnation enthalpy corresponding to typical flight conditions.

Now even in facilities designed to achieve only Mach number simulation, the working fluid must usually be heated prior to acceleration in the convergent-divergent nozzle in order to avoid liquefaction. As shown in Figure 2.1, a gun tunnel is basically a blow-down facility in which the working fluid is compressed and heated by the motion of a piston in a barrel under the action of high pressure gas released from a reservoir. Although the mass of working fluid that is heated in this way is relatively small, because impulsively started hypersonic flows usually achieve steady state rapidly, a usable test period is achieved in the short time available. Typically, for the present conditions, flow starting time around models is about 1 ms, and available running time is about 10-20 ms. The cost of building and operating such a tunnel is much less than that of the equivalent steady state facility.

Two major disadvantages of this type of tunnel are: (i) problems of data retrieval, and (ii) difficulty in the determination of test-section flow conditions, particularly stagnation enthalpy. When first developed, data from transducers was recorded in analog form by photographing traces displayed

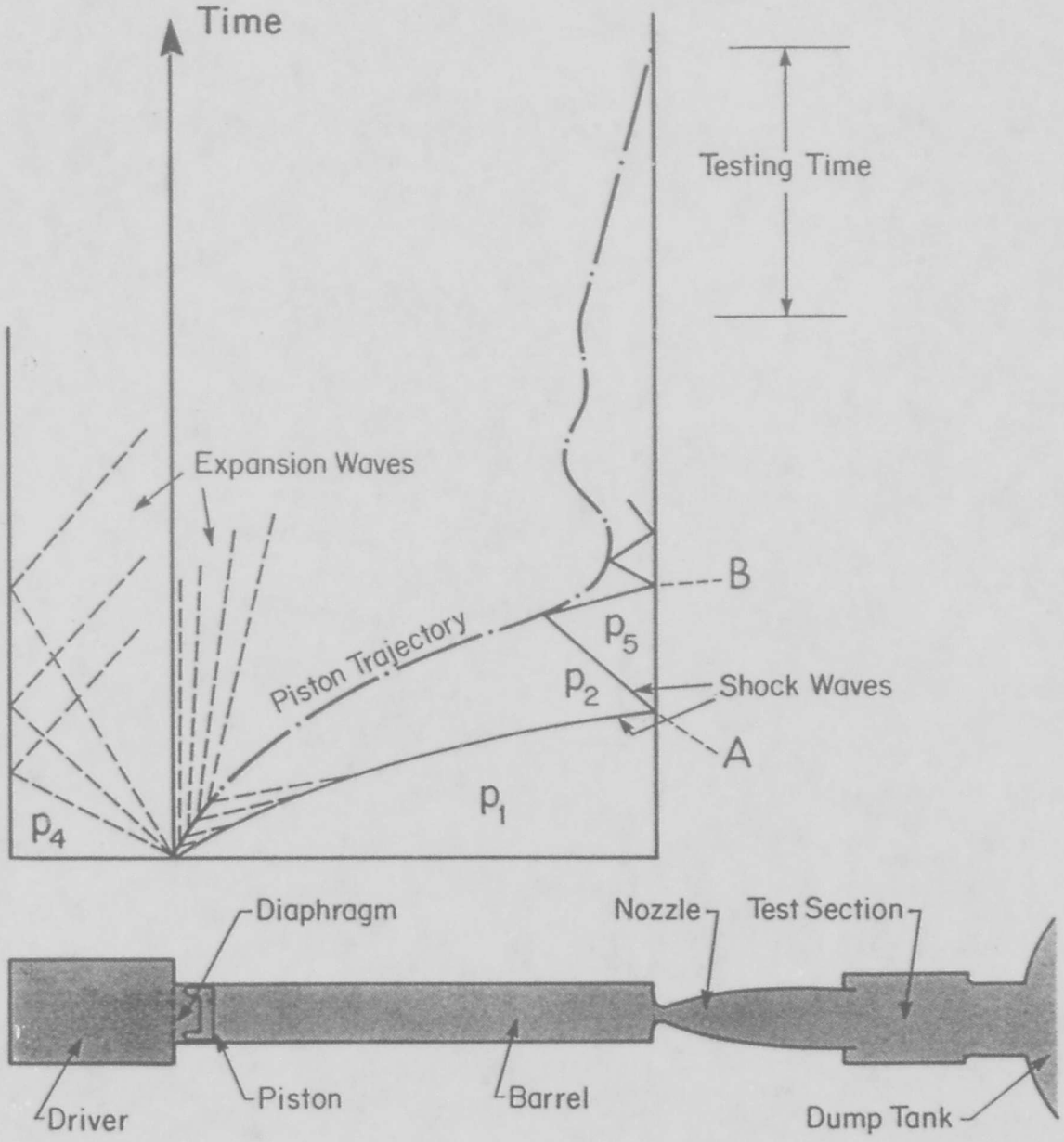

Figure 2.1 Principle of operation of gun tunnel, including major components and wave diagram for processes in the driver and barrel.

on drift-prone vacuum-tube oscilloscopes. As is shown below, the advent of microprocessor-based digital data acquisition systems has largely eliminated the first problem. The numerical code simulating tunnel operation described in Section 7 of this report has also provided useful insights into the second problem.

The following sections describe the facility, its principle of operation, the instrumentation and data acquisition system. Development problems encountered and resolved are outlined, and the work undertaken to calibrate the test section flow is then reviewed. Finally, options for development of the facility are discussed.

2.2 Description of the Tunnel and Its Operation

Figure 2.2, taken from the original assembly drawing, depicts the major components of the tunnel, and Table 2.1 gives the principal dimensions. Air is stored in a reservoir (1), called the driver. The driver is connected to the barrel (4) through an isolating valve (2) and a double diaphragm assembly or breech (3). The barrel is, in turn, connected by the nozzle breech (5) to a convergent-divergent nozzle (6) which delivers the flow to an open-jet test section (7). The test section is connected by a short receiving duct or diffuser (8) to a dump tank (9). An impact-plate is mounted in the tank interior so that debris from any broken pistons or test models does not strike its walls. The tank also includes a large relief diaphragm designed to rupture if, as a result of a piston failure or other incident, the pressure rises significantly above atmospheric. This diaphragm is made from thin mylar and is supported on the evacuated side by a plate containing a large number of small holes. Figures 2.3 to 2.5 are photographs of the refurbished facility.

Preparation of the tunnel for firing requires installation of diaphragms, placing a piston in the barrel just downstream of the diaphragms, and inserting a plug in the nozzle throat. The diaphragms are installed on either side of an 101 mm diameter x 184 mm long intermediate chamber, shown in Figure 2.5, which is part of the diaphragm breech, and the piston is placed in the barrel just downstream of this chamber. The nozzle throat plug allows the test section to be evacuated when the

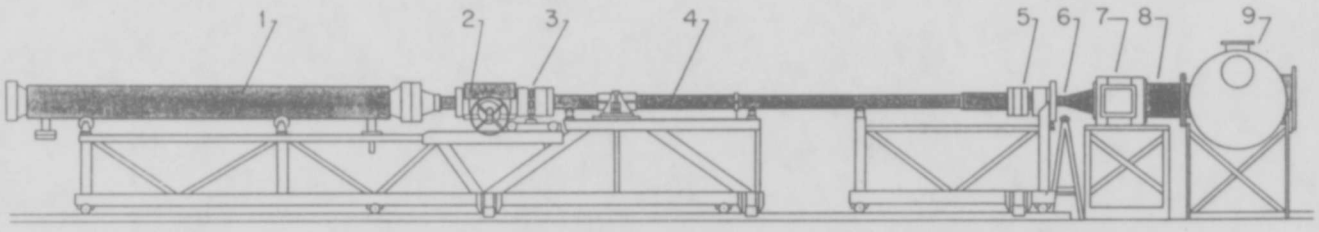

Figure 2.2 Diagram of major elements of hypersonic gun tunnel as developed by NAE. The components are: (1) driver, (2) isolating valve, (3) double diaphragm breech assembly, (4) barrel, (5) nozzle breech, (6) convergent-divergent nozzle, (7) open-jet test section, (8) diffuser, (9) dump tank.

barrel is charged with the test gas. Gated buttress thread systems enable both diaphragm and nozzle breeches to be closed rapidly, and hydraulically pressurized annular pistons load the breech sealing surfaces.

Table 2.1: Principal Dimensions of Tunnel

Driver		
	Interior Dimensions:	305 mm dia x 5.2 m
	Charge Pressure:	20.5 MPa
Barrel		
	Interior Dimensions:	76.2 mm dia x 6.1 m
	Charge Pressure:	1.45 atm to 8 atm (145-800 kPa)
Nozzle		
	Contoured	1.52 m long
	Throat diameter:	12.7 mm
	Exit plane diameter:	217 mm
Test Section		
	Open jet	610 mm x 635 mm section
	Length:	610 mm
Dump Tank		1.22 m dia x 2.44 m
Typical Operating Conditions		
	Stagnation (reservoir) pressure:	25.5 MPa
	Stagnation temperature	800-1300K
	Free stream Mach number	8.3
	Free stream unit Reynolds number	(20-40) x 10^6/m
	Usable test time	8-40 ms

Once assembled, the test section and dump tank are evacuated to about 50 Pa, and the test gas, usually air, is loaded into the barrel. Currently, barrel charge pressures p_1 are between 145 and 800 kPa. Air is bled from the driver into the diaphragm breech intermediate chamber to a pressure of 10 MPa, and then into the small volume between the intermediate chamber and the isolating valve to the full driver pressure of 20 MPa. Thus each diaphragm is loaded to a pressure differential of about 10 MPa, and the pressure across the isolating valve is equalized, so that it can then be opened.

A run is initiated by raising or lowering the pressure in the intermediate chamber, that is, between the two diaphragms. Their thickness is chosen so that they can withstand 10 MPa, but not the full

Figure 2.3 View of tunnel taken from the data acquisition computer station. The tunnel driver (1 in Figure 2.2) is in the background, and the barrel (4) can be clearly seen. The research assistant is operating the data acquisition computer.

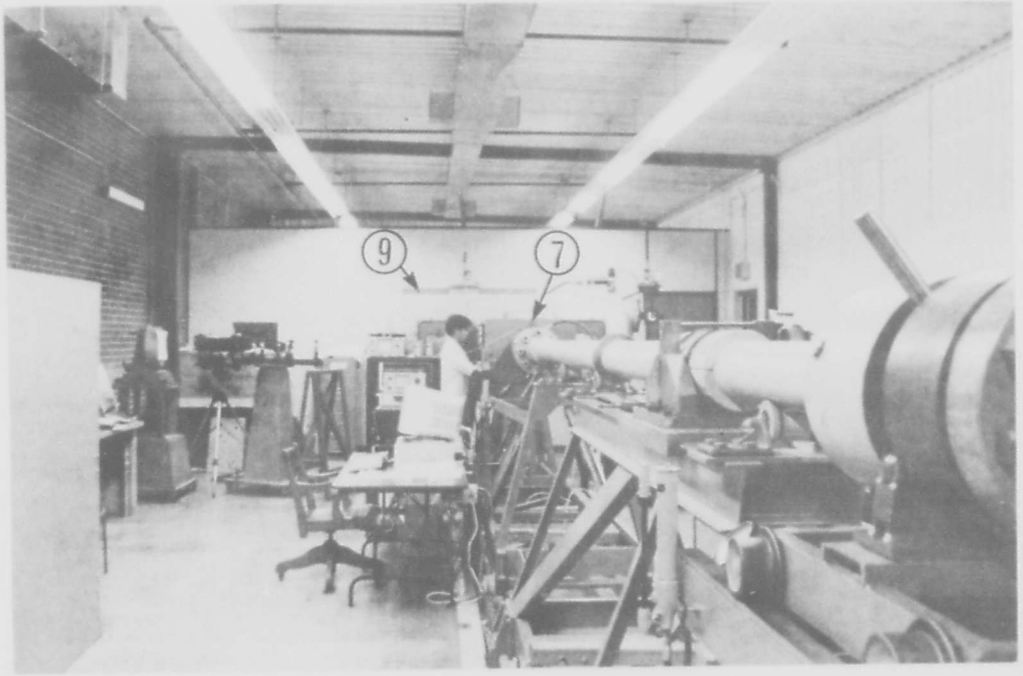

Figure 2.4 View of tunnel from diaphragm station. The test section (7) and dump tank (9) can be seen in the background, and a research assistant is installing a model.

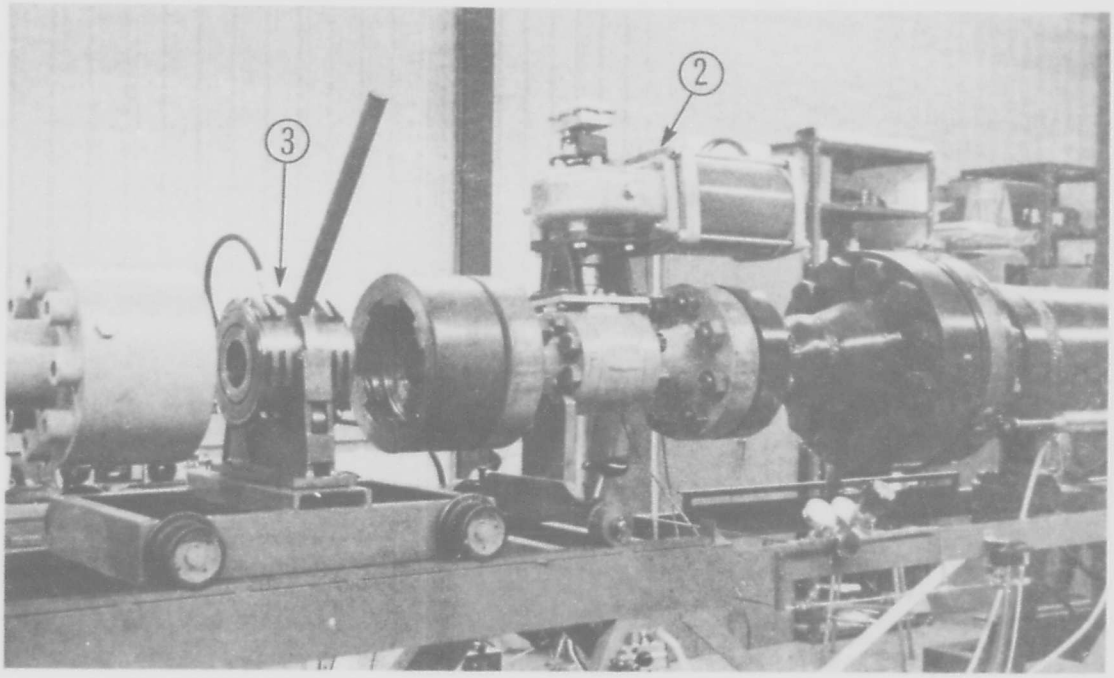

Figure 2.5 Tunnel double-diaphragm breech (3) and driver isolating valve (2). The original hand-operated gate valve has been replaced by a remotely actuated ball valve.

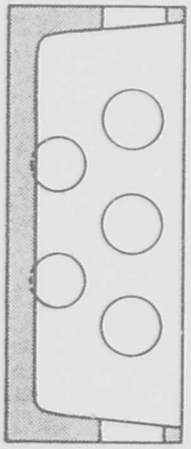

Figure 2.6 Cross-section of current piston geometry.

driver pressure. Thus they rupture, and the piston is propelled along the barrel, compressing and heating the working fluid. The nozzle throat plug geometry and material are chosen so that the pressures generated by the piston motion expel the plug through the throat and into the test section, and so that the aerodynamic forces to which it is subjected cause it to fly to one side of the test section thereby avoiding impact with a model.

A pressure transducer located at the nozzle end of the barrel is used to detect the arrival of the first shock wave generated by the piston motion, and thus to provide a trigger for the data acquisition system, and for a schlieren flow visualization system light source.

2.3 Facility Refurbishment

The original NAE compressor used soap and water lubrication in order to avoid contamination of the driver air with combustible oils, and an attendant risk of explosion. The replacement compressor, a 15 kW air-cooled Hamworthy 4TH-A35, delivers 9.2 *l*/sec of free air at 20 MPa. It uses oil lubrication, and relies on filtration to remove any suspended oil. In selecting the filter system we chose units designed to give breathable quality air and, as a safety measure, installed two such units in series. The driver was recertified as a pressure vessel; this involved removal of some interior corrosion, ultrasound testing to check wall thickness, and coating of the interior with epoxy paint to eliminate the possibility of further corrosion. The original 101.6 mm bore isolating gate valve, (2) in Figure 2.2, required 25 turns of a 700 mm diameter wheel to open or close. It also leaked, and required extensive maintenance. We replaced it with the 76.2 mm bore pneumatically operated ball valve shown in Figure 2.5; this requires only a quarter turn to open and close. The replacement test section vacuum pump is a Leybold Model S100C, 3.75 kW rotary vane mechanical unit having a displacement of 36 *l*/sec and capable of achieving a pressure of 1.3 Pa. Apart from cleaning and appropriate painting, none of the other tunnel components required significant servicing. However we had to build and install a new control console. It features both safety interlocks and automatic

sequencing of a number of operations associated with tunnel firing, including closing of the driver isolating valve immediately after a run.

2.4 Instrumentation and Data Acquisition

Currently flow visualization is achieved with a standard schlieren system based on 229 mm diameter, 1.83 m focal length front-silvered mirrors. We have two light sources; one is a standard camera flash unit having a light pulse duration of about 250 μsec, and the second is a four-spark argon atmosphere unit. The use of an argon atmosphere for the sparks gives the 6 joule light pulses a duration of about 750 ns. When used with a delay sequencer capable of 1 μsec resolution, this enables us to obtain as many as four schlieren images on one negative in any given run.

As noted in Section 2.1, the major facility improvement is the use of a digital data acquisition system. The key elements of the system are transient recorders and a minicomputer for data storage. Currently we have ten Pacific Model 9830 recorders, each capable of sampling with 12 bit resolution at a maximum rate of 1 MHz, and storing a maximum of 64 Kwords. The data retrieval computer has 640 Kb of internal memory, a 340 Mb hard drive for storage of data, and a colour monitor for simultaneous display of up to 6 transducer histories.

Our instrumentation includes 16 piezo-resistive pressure transducers having various pressure ranges, an accelerometer and a load cell. We also acquired commercially manufactured platinum-film-on-glass heat flux gages for heat transfer measurements. However, as discussed below, these have proven to be unsuitable for the present work, and we have developed our own capability of manufacturing such gages.

2.5 Current Operational Status

Initial operation involved resolving several development problems, two of which are worth noting here. The most serious problem was caused by a leak of hydraulic oil past a diaphragm breech sealing piston into the barrel. This led to combustion in the test gas, and the combustion products

then ablated the stainless steel nozzle throat from its nominal diameter of 12.7 mm to about 20 mm. To reduce the possibility of a similar occurrence, the carbon-based oil originally specified for the hydraulics was replaced with a silicone-based equivalent, and the design of the sealing piston assembly that leaked was modified. The nozzle throat was also modified to take a replaceable insert.

A second major difficulty was frequent failure of the pistons. For our initial runs we adopted the design evolved by NAE on a trial-and-error basis (Ref. 2.1), a section of which is shown in Figure 2.6. It is basically a 5.08 mm thick disc with a 30.5 mm long internally tapered trailing skirt; it is machined from a solid bar of 7075T6 aluminum, and lightening holes are drilled in the skirt. Initially these pistons would last no more than three runs, so that we explored the possibility of developing more robust designs. However, we found that, while NAE design specified a clearance fit of about 0.051 mm (0.002 ins), there is a slight narrowing in the barrel about 1 m from the diaphragm breech. Reduction of the piston diameter by 0.026 mm (0.001 in) has solved the problem; they now last over 150 runs before being discarded. It appears that, except for extreme operating conditions, piston failure occurs by toppling, because the outer surface of the skirt becomes increasingly tapered. In fact, prior to every run, we check piston condition by first visually inspecting it for cracks, and then by listening to the sounds it makes as it is propelled down the length of the barrel by an air jet. The onset of unacceptable tapering causes a characteristic clinking sound during its motion. At the highest enthalpy condition used to date, corresponding to p_1 = 145 kPa, failure appears as cracks at the disc-skirt junction. For this condition, development of an improved design is desirable.

The diaphragms originally specified for the tunnel were made from 1.27 mm thick cold-rolled steel and used hand-scribed rupture grooves, and these have proved to be entirely satisfactory. However, we have changed the material for the nozzle throat plugs from nylon to lexan, since the latter does not create debris in the test section by shattering on impact.

The use of an oil-lubricated air compressor has not presented any operational problems. We opened the driver once to inspect for oil accumulation. None was observed, and furthermore, periodic analyses of samples of driver air have indicated the presence of only trace amounts of

hydrocarbons and other contaminants. However, one difficulty was carbon build-up on the high pressure stage valves of the compressor. These had to be cleaned at 100 hrs. instead of the expected 1,000 hr. interval. We believe that this problem occurs because this type of compressor is designed to run for extended periods, so that driver topping-up now includes 20 minute warm-up and cool-down periods, during which the compressor operates unloaded.

Since March of 1989 the tunnel has operated without incident, and nearly two thousand runs have been accumulated. The compressor is able to charge the driver to the current operating pressure of 20.5 MPa in about two hours, and to top it up in about 10 minutes from the 18.5 MPa that remains immediately after a run. The vacuum pump can evacuate the test section and dump tank to the required 50 Pa (0.375 torr) in less than 25 minutes. The usual work required to make changes to test models, set up the data acquisition system, and prepare the tunnel, implies that our maximum firing rate is about once per hour.

2.6 Calibration

2.6.1 General Comments

Key questions arising in the use of facilities of this type are:

(i) How uniform and repeatable are the effective reservoir or stagnation conditions in the gas compressed and heated by the piston?

(ii) What are these reservoir conditions, in particular pressure and enthalpy?

(iii) What are the thermodynamic processes in the nozzle?

(iv) What are the test-section flow properties?

Our current assessment of these questions for the present tunnel is described below.

2.6.2 Barrel Pressures

Figure 2.7 gives the details of the initial stages of the barrel pressure history at the nozzle station. The abrupt pressure rise associated with the arrival and reflection of the first shock wave generated by the

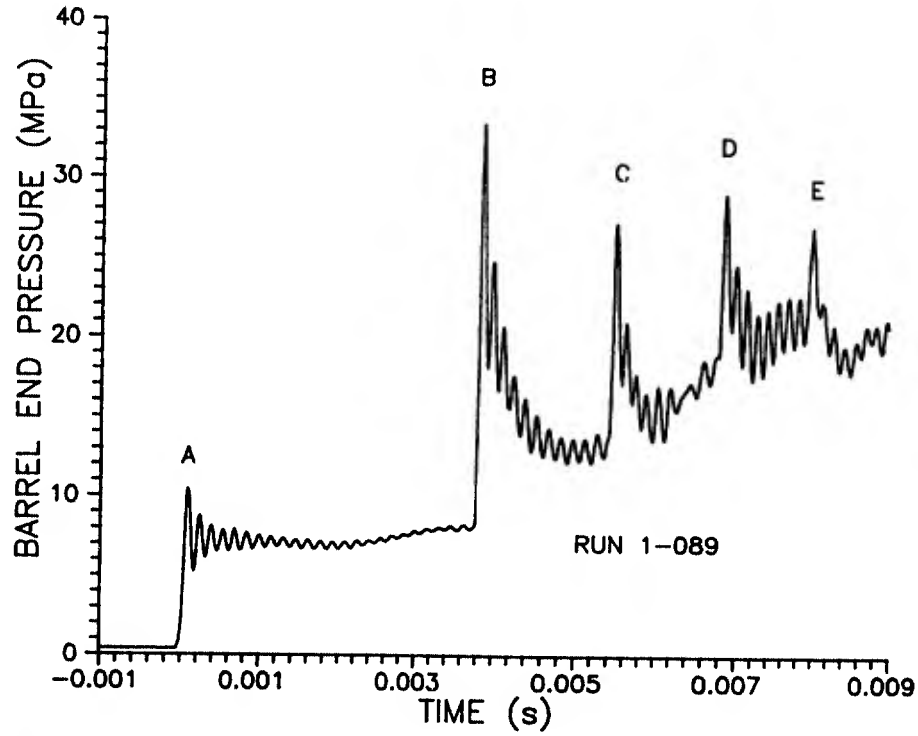

Figure 2.7 A typical barrel pressure history in the first 9 milliseconds.

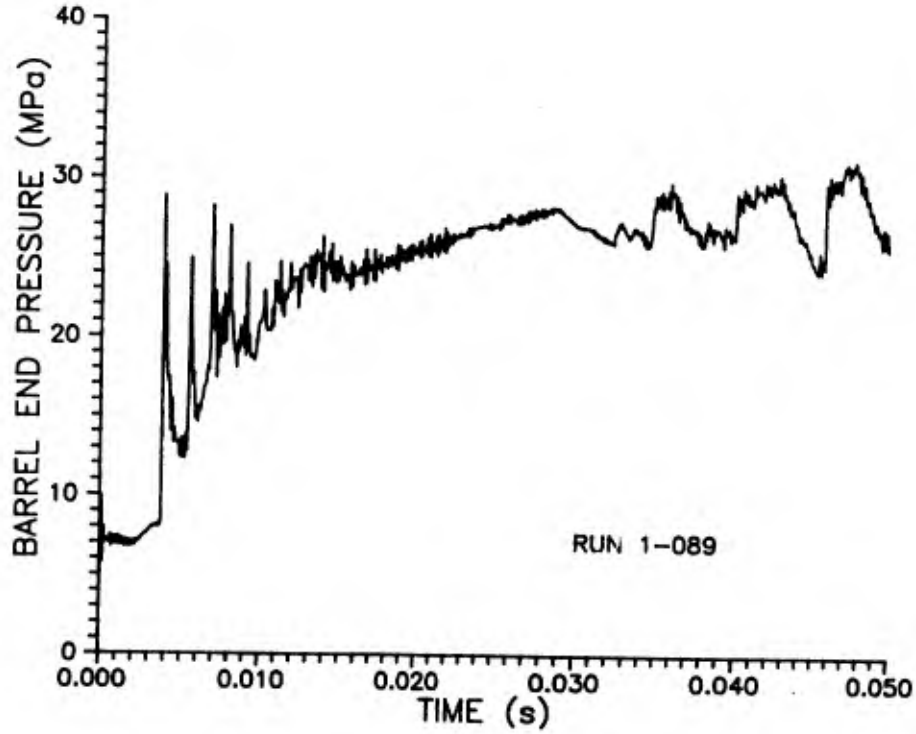

Figure 2.8 A representative barrel pressure history for p_t = 400 kPa. This may be compared with the history for a second run at the same nominal conditions given in Figure 2.9.

piston motion can be clearly seen (A), as can subsequent jumps (B, C, D, E) associated with a sequence of shock reflections between decelerating piston and barrel end. In this and all subsequent discussion the time origin corresponds to the event "A" in Figures 2.1 and 2.7. The damped oscillation just after the arrival of the first shock is believed to be an acoustic resonance caused by the geometry of the barrel pressure transducer mount. To protect it from damage by debris, this transducer is mounted with its 5.54 mm diameter sensing face in a cavity connected to the barrel by a 1.02 mm dia × 12.7 mm long pressure tap. Increasing the tap diameter to 2.04 mm reduced this frequency from 8.33 kHz to 6.57 kHz.

Figures 2.8 and 2.9 give two representative barrel pressure histories from successive tunnel runs encompassing the period used as testing time. Figure 2.9 also includes pitot and static pressure histories taken during the same run, with the static pressures being obtained from a flat plate, as described in Section 3. The structure of the barrel pressure histories is very repeatable from run to run, although during the period used for testing, which is between about 12 ms and 32 ms after the first pressure rise (A in Figure 2.7), there is significant variation. Typically, for seven successive runs, when averaged over the nominal test period, the mean value of the final barrel pressure p_0 was 26.51 MPa (3842 psi) with the standard deviation for variation between runs being 1.3%. When this was corrected for slight variations in driver charge pressure p_4, the standard deviation was reduced to 0.6%. However, in any given run, the total variation within the designated test period is about 20% of the mean. This seems larger than desirable, but Figure 2.9 shows that both pitot and static pressure histories have very similar structure and, as discussed below, analysis of these histories suggests that the test section flow response is quasisteady.

2.6.3 Stagnation Enthalpy

Of the parameters required for interpretation of gun tunnel data, the stagnation enthalpy, the enthalpy of the heated and compressed test gas, is perhaps the most difficult to determine. When these facilities were first developed, direct measurement of the enthalpy or temperature T_0 of the

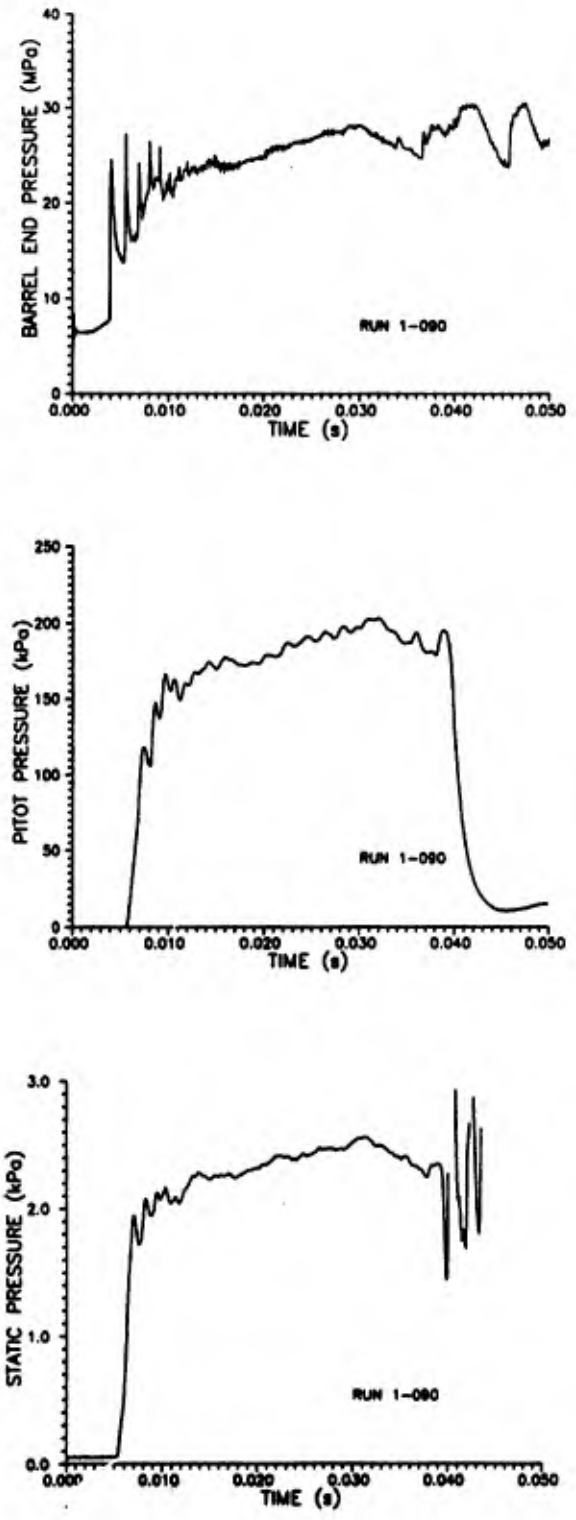

Figure 2.9 Barrel, pitot, and static pressure histories all taken during the same run. In each case t = 0 corresponds to the arrival of the first shock at the barrel pressure transducer.

compressed gas was extremely difficult, and various methods for inferring a temperature from other measurements were used. The measurements used for this purpose included test section velocities (Ref. 2.6), barrel pressure histories and running times (Ref. 2.7), and stagnation point heat transfer rates. Of these, stagnation point heat transfer rates appear to have been accepted as the most reliable basis for estimating stagnation enthalpy (Refs. 2.8 and 2.9).

Techniques based on spectroscopic concepts might seem suited to the task. Thus, an attempt was made to measure the temperature of the gas in the stagnation region of a blunt body mounted in the test section of a gun tunnel by using a technique known as the sodium line reversal method (Ref. 2.10). However this method follows the vibrational temperature of the gas so that, since significant vibrational nonequilibrium phenomena can occur in the nozzle (Refs. 2.11, 2.12) the temperature it measures can differ significantly from either the reservoir stagnation temperature, or the local translational temperature, and large corrections may be required. We considered the possibility of exploiting recent developments in spectroscopy to measure the temperature directly in the barrel. Since the gas is believed to be optically thick, it follows that direct spectral analysis of the radiation is subject to considerable uncertainty about the representative nature of temperatures thus determined. That is, the temperatures inferred may be those in the thermal boundary layer generated by the barrel walls. One possibility is to observe selected electronic state transitions excited by a laser beam transmitted through the compressed gas. This offers the possibility of specifying unambiguously the region being observed (Ref. 2.13), but the cost and labor involved have prevented it from being part of the present effort.

The more recent literature indicates that stagnation point heat transfer measurements continue to be the method of choice for estimating T_0 for facilities of the present type (Ref. 2.14). However, interpretation of these measurements is based on assumptions and calibration factors that cannot be easily verified in any particular laboratory. A potentially attractive alternative is to observe the growth and convection of a wave generated by a short duration electrical spark discharged in the test section (Ref. 2.6). If the disturbance can be shown to be acoustic, then both the flow and sound speeds can be measured in terms of quantities readily traceable to length and time standards. We have attempted

to develop this technique using a suitable spark source and the four pulse schlieren light source. However, this exploratory work indicated that required equipment developments placed it beyond the scope of the present effort. Consequently we decided to use three ways of estimating T_0. In addition to heat transfer measurements, these are: approximate calculations using barrel pressure histories as proposed by Lemke (Ref. 2.7), and predictions described in Section 7. The results available to date from these sources are discussed below.

Two of the calculations proposed by Lemke use the barrel pressure measured in the period after the reflection of the first shock wave, that is, in the interval between A and B in Figures 2.1 and 2.7. The data and the simulations suggest that this may be assumed sensibly constant, and is denoted as p_5. The first calculation, called here *reflected shock*, assumes that to attain p_5, the fluid originally at the nozzle end of the barrel is compressed by two shocks: by the first shock wave generated by the piston motion to the intermediate pressure p_2 in Figure 2.1, and then by the reflection of the first shock at the barrel end to p_5. It is then assumed to be compressed isentropically to the final measured barrel pressure p_0 and temperature T_0. The second calculation, called here *piston face*, assumes that, because piston acceleration is relatively smooth, the fluid originally near the diaphragm end of the barrel is compressed isentropically to p_2, then by a single shock to p_5, and finally isentropically to p_0 and T_0. To make these calculations Lemke assumed that the compression and heating is in thermodynamic equilibrium, so that a Mollier chart or tabulated data can be used and both computations are straightforward. Note that, because isentropic compression to p_2 causes less heating than shock compression to the same pressure, the two methods provide an estimate of the degree of non-uniformity of the overall heating process. The results of these calculations are given in Figure 2.10.

Figures 2.11 and 2.12 give, for p_1 = 400 and 200 kPa respectively, predictions of stagnation temperature histories obtained from the simulation. Figure 2.11 also includes preliminary estimates obtained from stagnation point heat transfer measurements obtained in two tunnel runs. These measurements and their interpretation are described in Section 2.8. The simulation results shown in Figures 2.11 and 2.12 correspond to the most realistic of the three gas models used in these

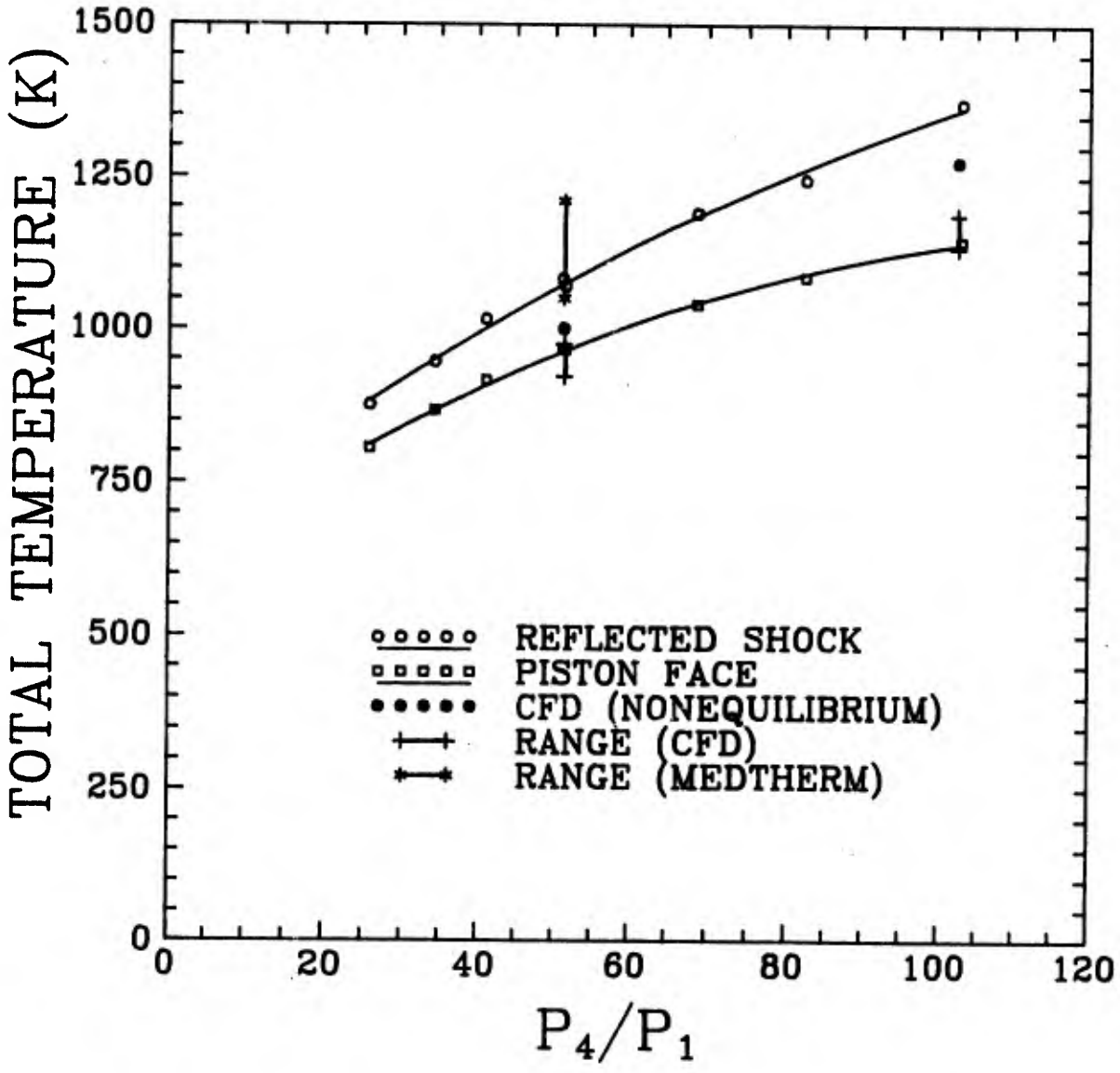

Figure 2.10 Estimates of stagnation temperature T_o, obtained by approximate methods, compared with CFD predictions, and with preliminary stagnation enthalpy measurements.

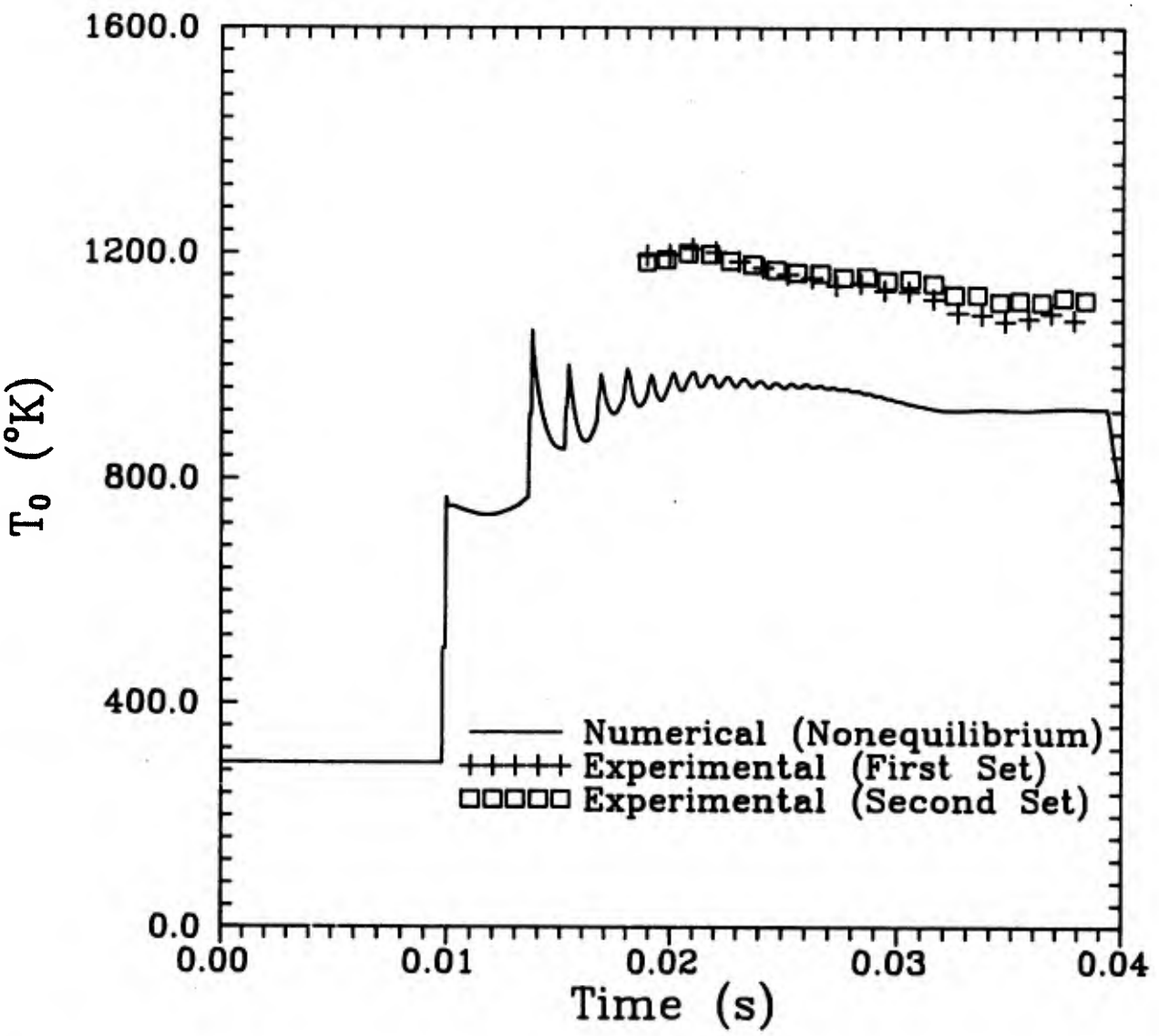

Figure 2.11 Stagnation temperature history for barrel charge pressure p_i = 400 kPa as obtained from simulation together with estimates based on stagnation point heat transfer measurements obtained from two runs.

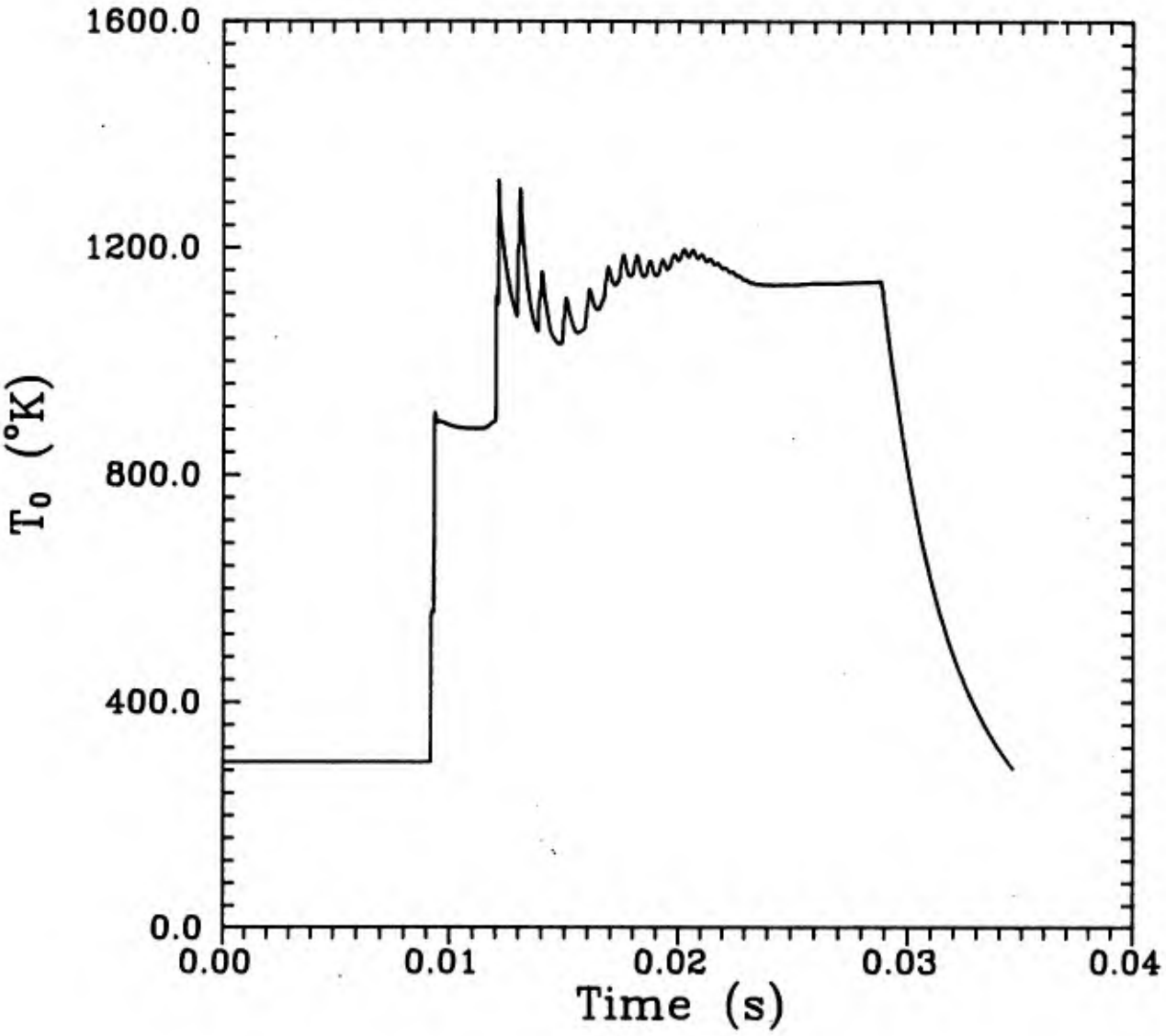

Figure 2.12 Predicted stagnation temperature history for p_1 = 200 kPa.

calculations, and include estimates of the effect of heat loss to the barrel walls during the compression process. For both p_1, T_0 is predicted to decrease abruptly soon after the compression process appears to be complete and then remain essentially constant until the cessation of the run. This behaviour is believed to be caused by the nonuniform heating of the gas as it is compressed. The temperature range in this sudden decrease is included in Figure 2.10. They suggest that the degree of nonuniform heating is significantly less than indicated by the approximate calculations of Lemke (Ref. 2.7). The estimates based on heat transfer measurements are significantly higher than the simulation predictions. As discussed in Section 2.8, this is believed to be associated with uncertainties in the thermal properties of the heat flux gauges. However their histories agree qualitatively with the predictions, and they tend to confirm the predicted decay in T_0.

2.6.4 Test Section Pitot Profiles

Measurement of free stream pitot pressures provides the most convenient way of assessing the quality of the test section flow. For the present work they have been used to assess the steadiness and uniformity of the test section flow and to infer flow conditions. The latter include static pressure, Mach and Reynolds numbers of the free stream.

Now as Figures 2.8 and 2.9 show, the barrel pressure has a distinct and highly repeatable structure, but is not constant in the usable test time. However, Figure 2.9 suggests that both free stream pitot and static pressures, p_p and p_∞ respectively, have a history that is very similar in structure to that of the barrel pressures. Figure 2.13, which is a superposition of pitot histories for p_1 = 145, 200, and 400 kPa tends to confirm this. It also shows that the principal effect of increasing p_1 is to increase run time. Furthermore the pitot and static histories show a well-defined delay time which is repeatable from run to run and which varies slightly with p_1. This delay time, t_s, is about 1.3 msec, and is associated with the time required for a pressure pulse to traverse the nozzle. Thus it seems reasonable to assume that the flow in the test section is quasisteady. To check this hypothesis, the history of the ratio $p_p\,(t+t_s)/P_O(t)$ was calculated for three representative p_1, with t_s

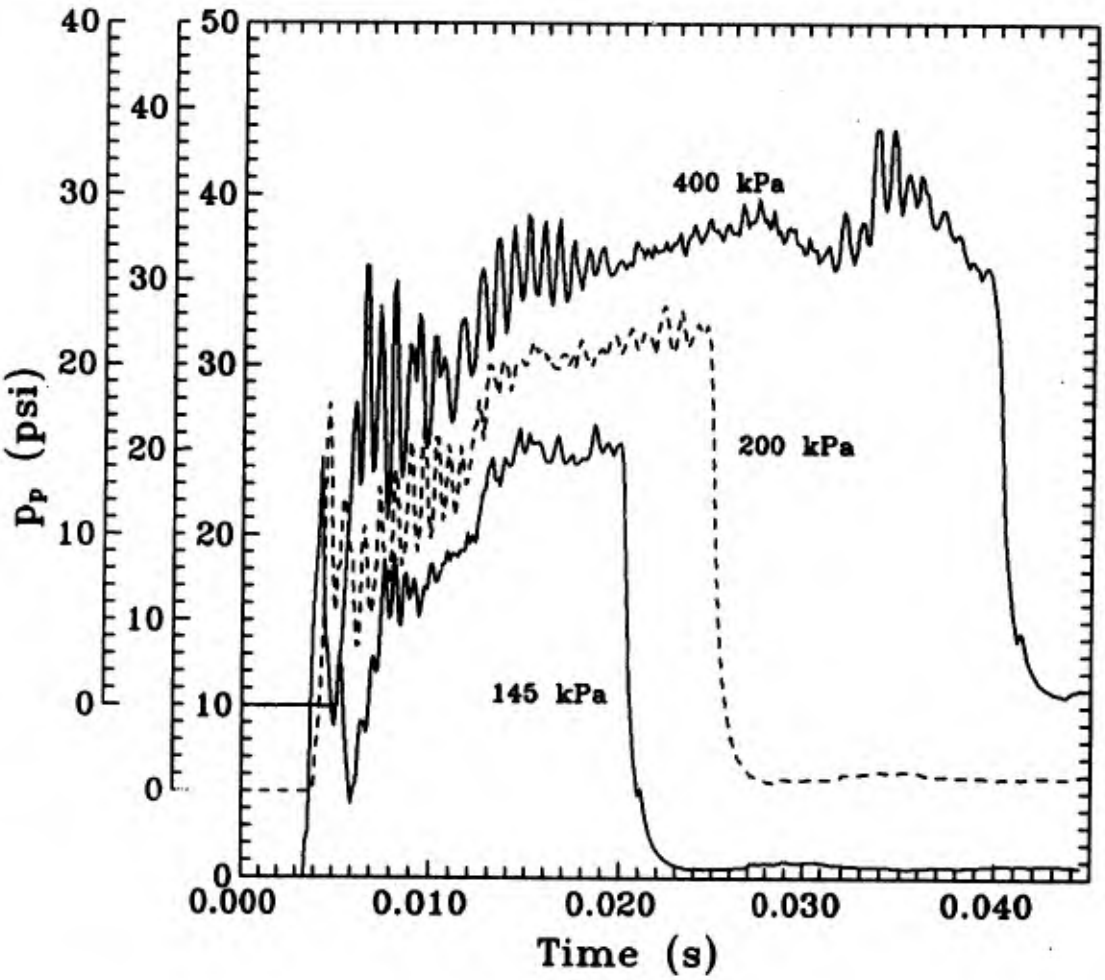

Figure 2.13 Typical pitot traces for p_1 = 145, 200 and 400 kPa.

chosen by visually aligning features of the barrel and pitot traces (Ref. 2.15). The results are shown in Figure 2.14 and indicate that, to within experimental error, the ratio remains constant. The validity of t_s assumed for these calculations was checked by computing averages for the intervals marked in Figure 2.14 and then adjusting t_s to minimize mean square errors. It was found that ascertaining t_s by visually aligning features is adequate. As a result, in all the subsequent calculations it is assumed that the flow is quasisteady.

Figures 2.15 to 2.18 give the detailed test section pitot surveys for two values of p_1 used in the present work. In general they are shown to be highly repeatable with some evidence of fine structure. However in all three cases the flow exhibits a high degree of uniformity in both axial and radial directions, and negligible gradients in the flow direction.

These results also suggest that p_p/P_o is virtually independent of barrel charge pressure p_1. Now the above data required about 80 tunnel runs to obtain, with the test period extending over several months (Ref. 2.15). Some of the scatter is believed to be caused by drift in pressure transducer calibrations. Consequently a special test was undertaken to confirm the observation. Since the pitot rake used in these tests can take measurements at four positions in any given run, with the rake fixed in one position, runs were made in quick succession for three values of p_1. The results are given in Figure 2.19. They show clearly that p_p/P_o is independent of p_1. Furthermore they tend to confirm the existence of some small but repeatable structure within the nozzle flow.

2.6.5 Thermodynamics of the Nozzle Flows

Determination of test section flow properties such as Mach number M_∞ requires a knowledge of the thermodynamics of the nozzle flows. For the present type of facility, pitot pressure measurements have usually been used to calculate M_∞, because they are insensitive to flow alignment, and because their interpretation has usually been thought to be straightforward (Refs.2.16 and 2.17). That is to say, it has usually been assumed that, if dissociation does not occur, the flow in the nozzle is calorically perfect or at least isentropic. However Boudreau (Ref. 2.17) has recently suggested that

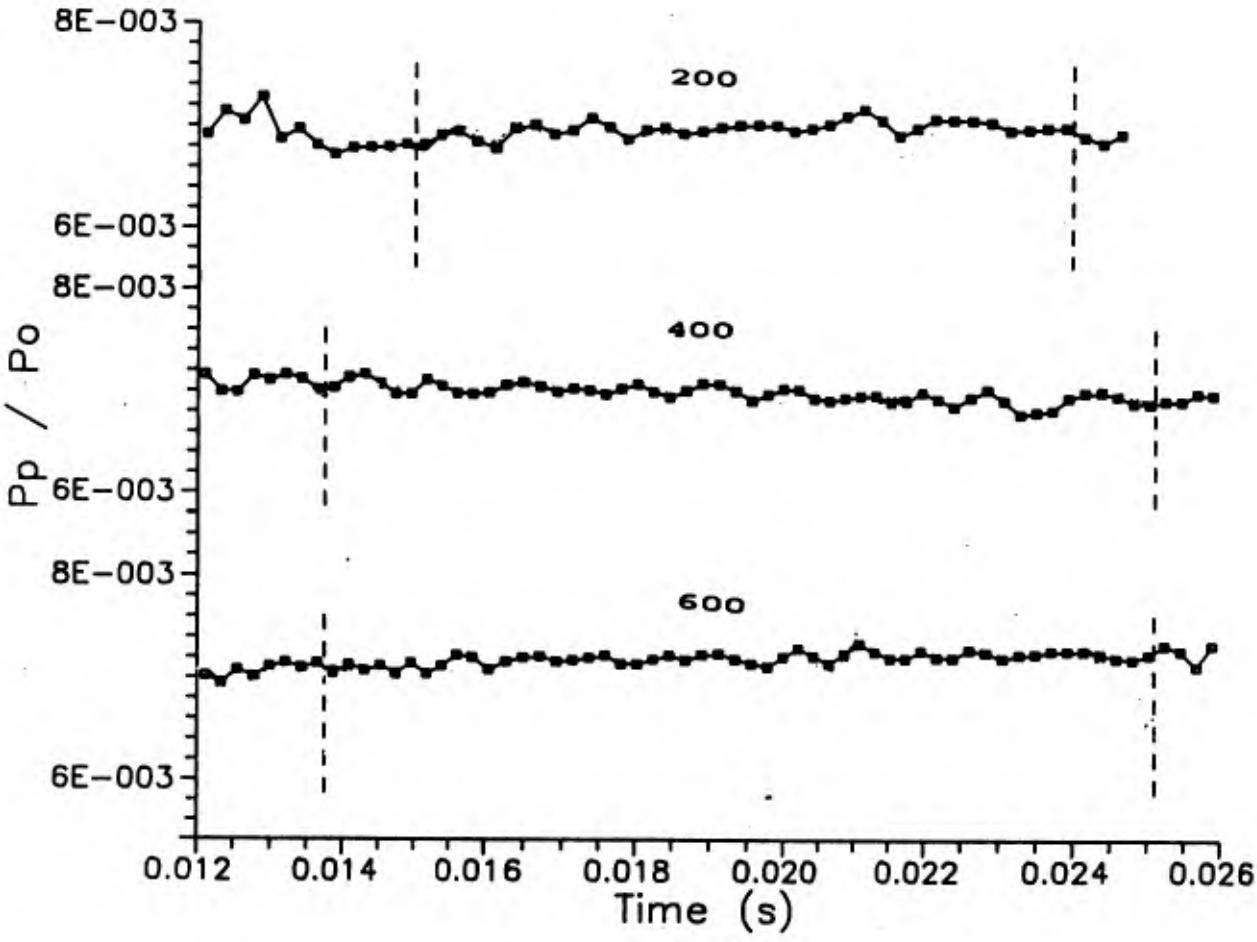

Figure 2.14 History of ratio of pitot to barrel pressure $p_p(t+t_s)/P_o(t)$ for barrel charge pressure p_1 = 200, 400 and 600 kPa. The intervals used to obtain an overall average are also marked.

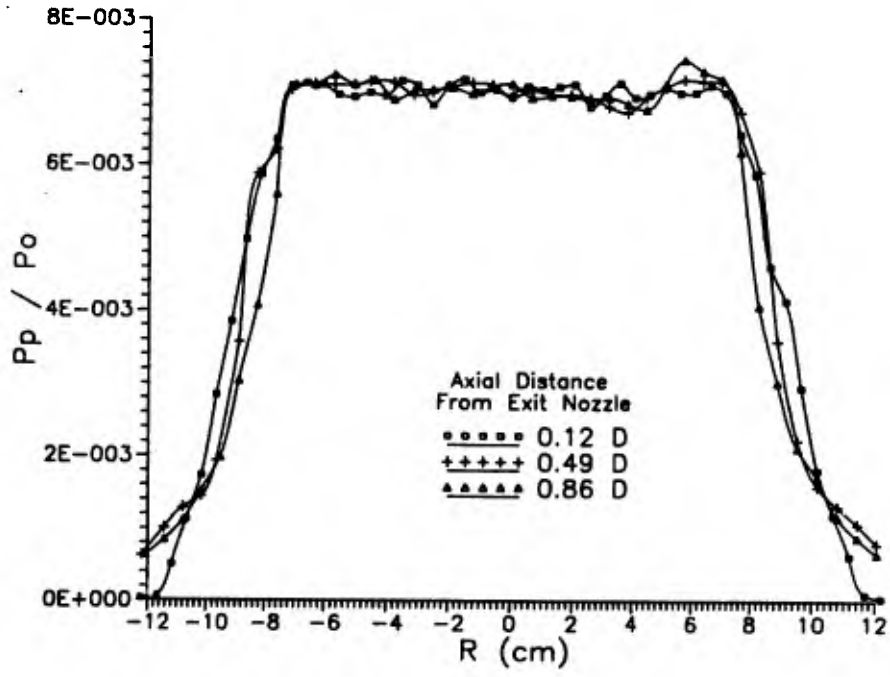

Figure 2.15 Surveys of test section pitot to barrel pressure ratios p_p/P_o for p_1 = 200 kPa along a horizontal plane through the nozzle axis for three axial distances from the nozzle exit plane. The line joining each data point has been drawn to allow easy identification of data, and axial distance from the nozzle exit plane is expressed as a fraction of its exit plane diameter = 217 mm.

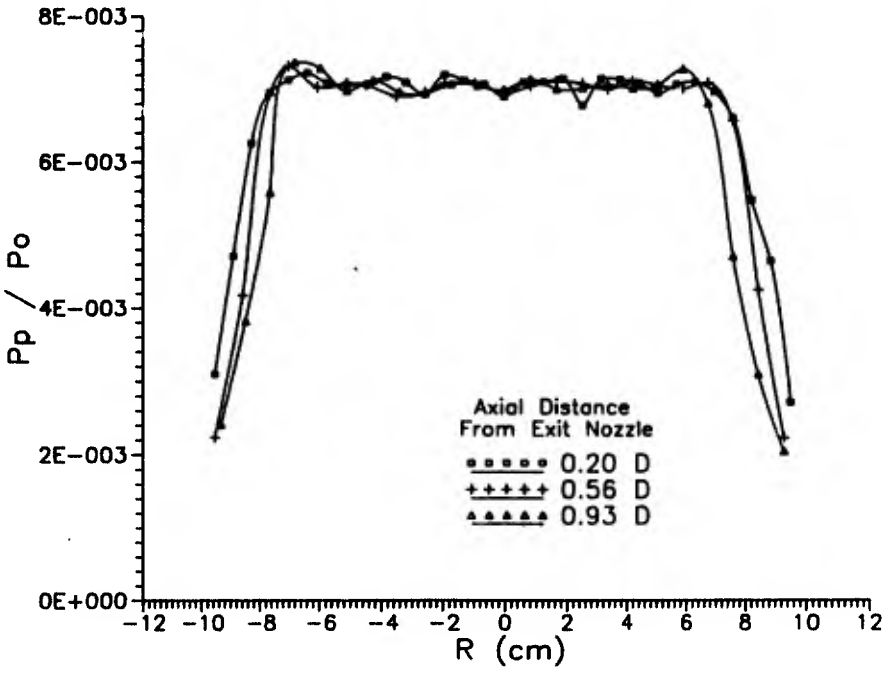

Figure 2.16 Surveys of p_p/P_o for p_1 = 200 kPa along a vertical plane through the nozzle axis.

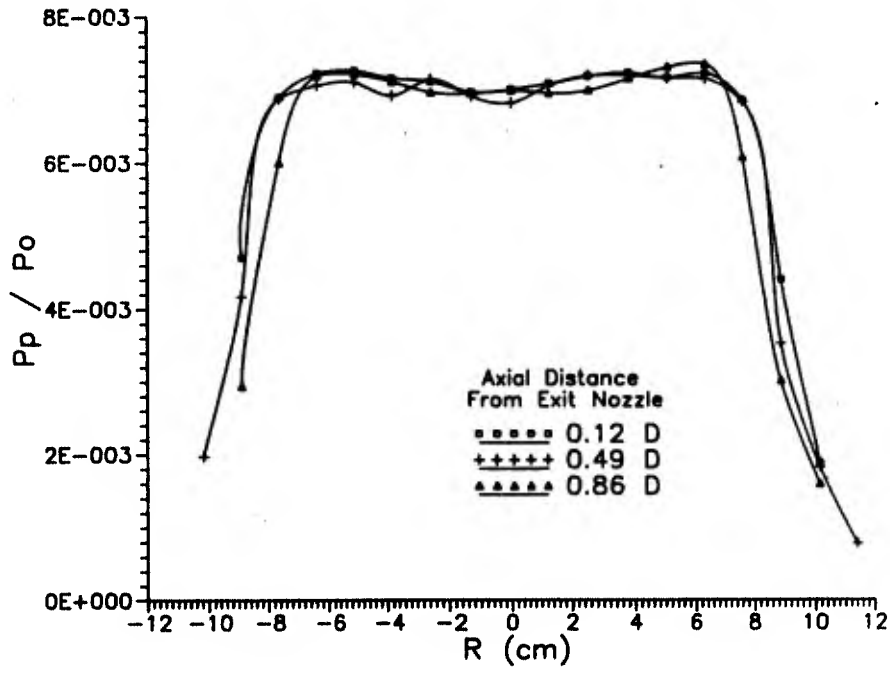

Figure 2.17 Horizontal surveys of p_p/p_o for p_1 = 400 kPa.

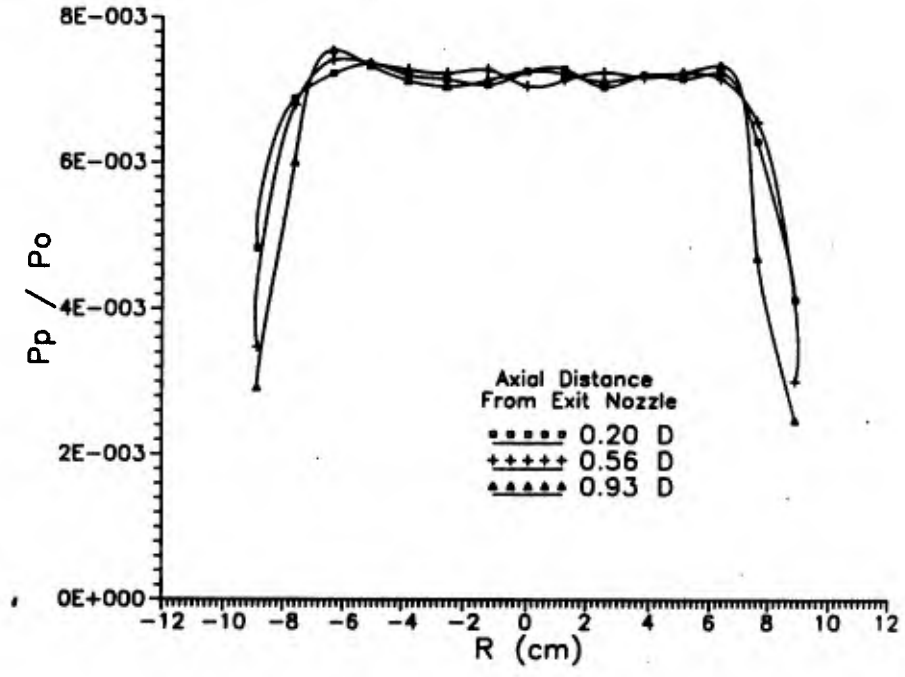

Figure 2.18 Vertical surveys of p_p/p_o for p_1 = 400 kPa.

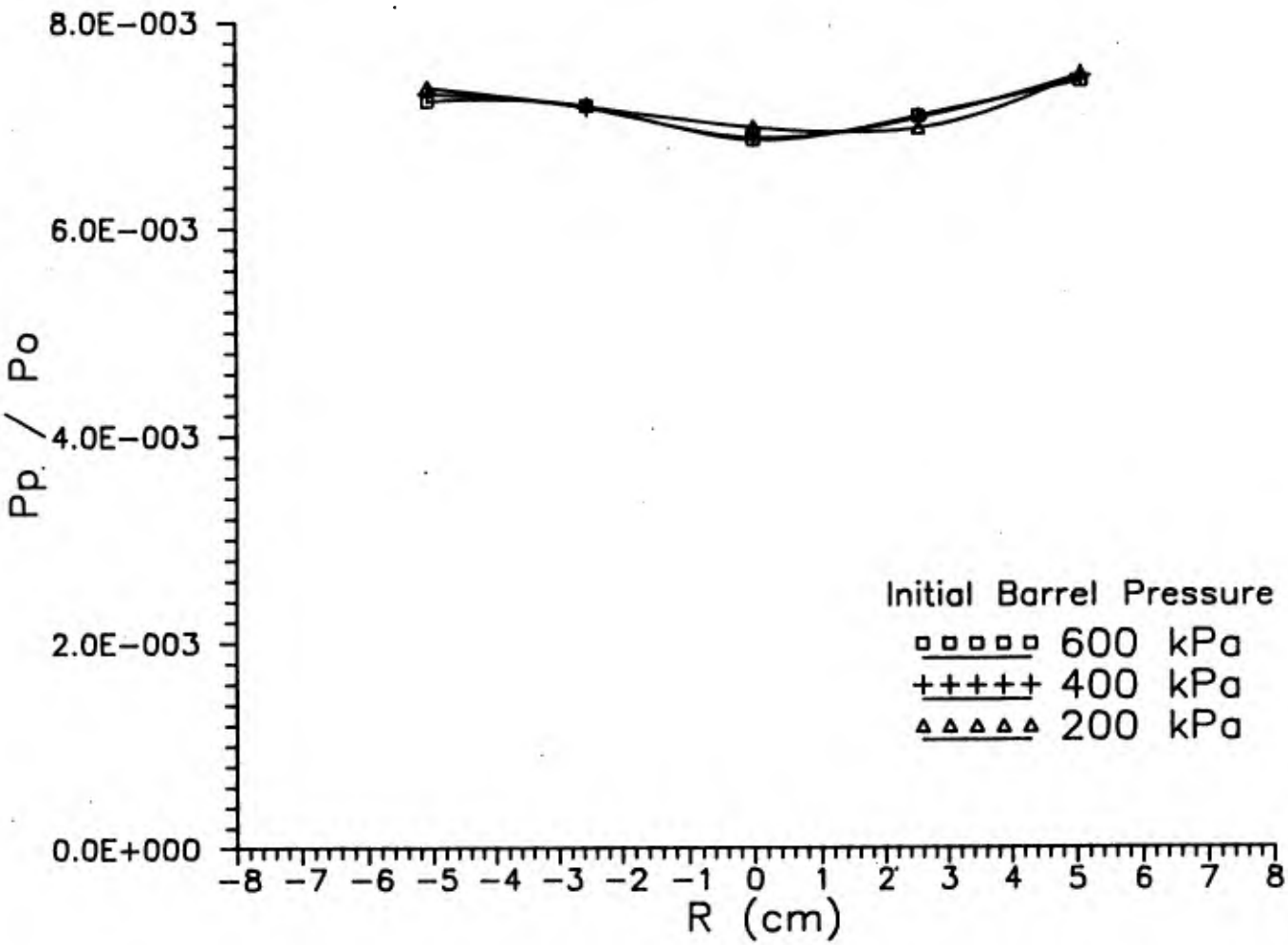

Figure 2.19 **Effect of barrel charge pressure p_1 on pitot pressure ratio p_p/P_o.**

nonequilibrium phenomena in the nozzle flow can introduce significant errors in such an approach at $M_\infty = 8$ and above, and that pitot pressure measurements are insensitive to the processes involved.

The dominant nonequilibrium phenomenon that occurs at the reservoir conditions generated by the present tunnel is vibrational relaxation of the principal diatomic constituents of air, O_2 and N_2. This has been long known (Ref. 2.11); typically the flow freezes vibrationally when it becomes moderately supersonic. In this case, pitot data has usually been interpreted by assuming that the entire nozzle flow is vibrationally frozen, so that the gas has an effective $\gamma = 1.40$ (Ref. 2.16). However, Boudreau suggests that contaminants, especially water vapor, can cause a sudden vibrational de-excitation, leading to significant increases in p_∞ and reductions in M_∞, but showing negligible change in p_p (Ref. 2.17).

For the present calibration, the potential significance of vibrational nonequilibrium effects was assessed in three ways. The first was the nonequilibrium calculations included in the simulation of in Section 7. These calculations suggest that, for p_1 = 200 and 400 kPa, the dominant species, nitrogen, N_2, freezes in vibration close to T_0, whereas O_2 freezes at substantially below T_0.

For the second calculation we assumed that the Mach number that occurs as a result of vibrational relaxation lies between that for flow in which the gas is, on the one hand, vibrationally frozen at T_0 for the entire nozzle flow, and on the other, in thermodynamic equilibrium. Now, with ρ the density of the gas, at the present reservoir conditions, deviations of the thermal equation of state from the perfect gas law $p = \rho RT$ are not negligible. Typically at T_0 = 1000K and P_0 = 26.5 MPa, $Z \equiv p/(\rho RT) = 1.075$. However, if one does assume a thermally perfect gas the completely frozen calculation is straightforward. The energy equation for the steady flow of a diatomic gas is

$$e_v(T_0) + h_{tr0} = e_v(T_v) + h_{tr} + \frac{1}{2}v^2 \qquad (2.1)$$

where e_v is the internal energy per unit mass in vibration, T_v is the vibrational temperature, $h_{tr} = 7/2\ RT$ is the enthalpy in the absence of vibrational excitation, and V is the fluid speed. If

$T_V = T_0$ then $c_V = 5R/2$ and $\gamma = 1.40$, so that the estimation of Mach number for given pitot or free stream static pressure then reduces to a standard calculation. For the equilibrium calculation we used a large-scale Mollier chart for air; sample calculations using the chart for conditions at which the gas behavior is known to be ideal, gave accuracies to better than 0.5%.

The results of these calculations are given in Figure 2.20. They are based on estimated values of P_0 and p_∞ and, as such, give a slightly low M_∞. The calculations also include an estimate based on the γ corresponding to reservoir conditions, $\gamma = \gamma_0$, and several results for partial freezing obtained by assuming calorically perfect gas flow at $\gamma = \gamma_0$ to M = 2.5, and vibrationally frozen flow thereafter. The most important result is the close agreement between the estimates of M_∞ for the fully frozen and equilibrium models for the values of T_0 of interest here, $900K \leq T_0 \leq 1400K$. However, the partially frozen calculations suggest that, if the vibrational de-excitation phenomenon discussed below does not occur, an equilibrium calculation appears to be slightly more accurate.

The third calculation undertaken to assess the significance of vibrational nonequilibrium phenomena follows the ideas of Boudreau (Ref. 2.17). The vibrational de-excitation is assumed to occur over a very short distance, and thereby to be governed by the equations of a normal shock wave; for a thermally perfect diatomic gas these are, with the subscripts u and d denoting, respectively, properties upstream and downstream of the jump,

Energy:
$$h_{tru} + e_v(T_{fr}) + \frac{1}{2} V_u^2 = h_{trd} + \frac{1}{2} V_d^2 \qquad (2.2)$$

Momentum:
$$p_u + \rho_u V_u^2 = p_d + \rho_d V_d^2 \qquad (2.3)$$

Continuity:
$$\rho_u V_u = \rho_d V_d \qquad (2.4)$$

State:
$$p = \rho RT \qquad (2.5)$$

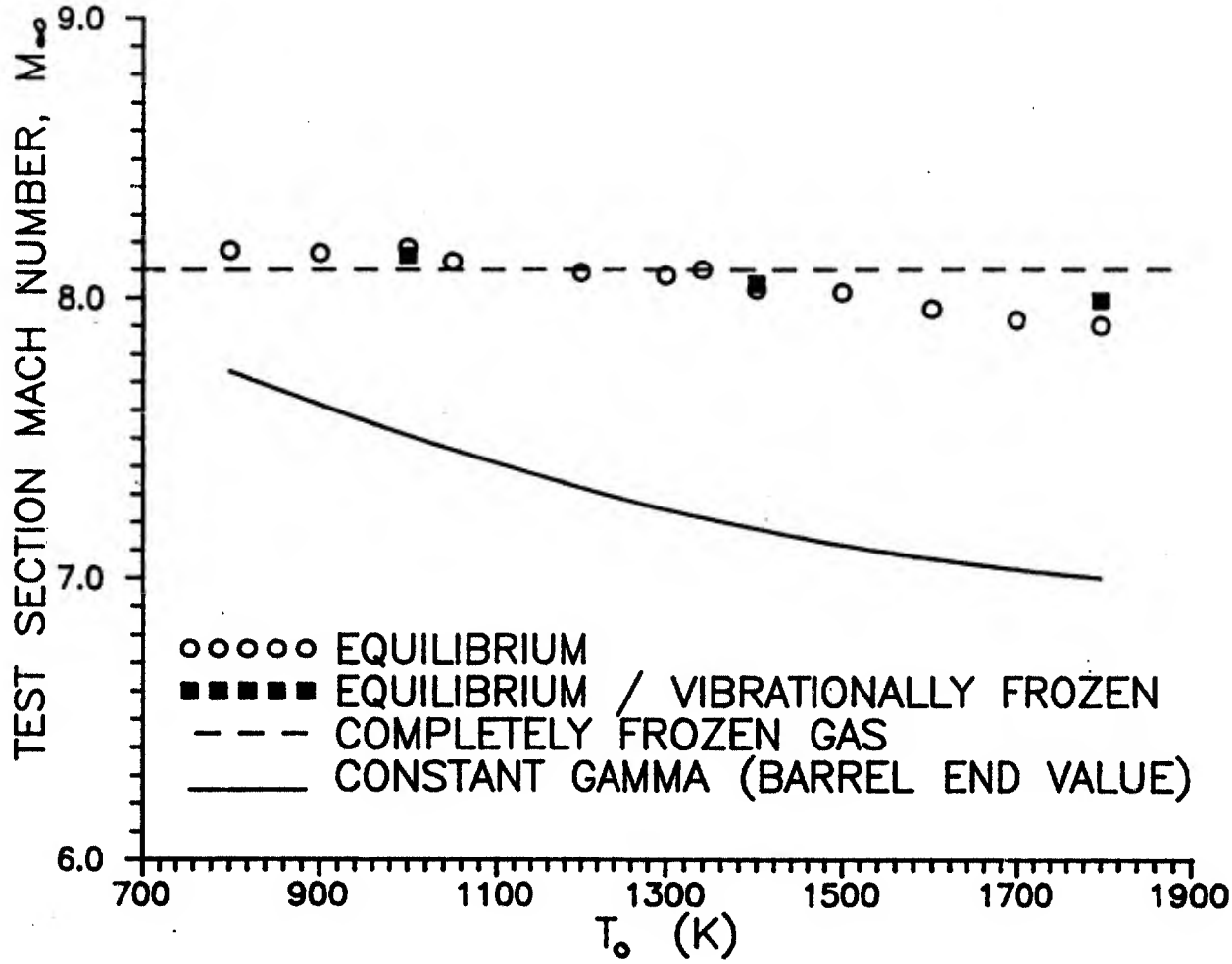

Figure 2.20 **Estimates of test section Mach number based on assumed barrel pressure P_o = 23.44 MPa (3400 psi) and free stream static pressure of 2.206 kPa (0.320 psi).**

Note that the form of the energy equation assumes that all of the energy frozen into vibration, $e_v(T_{fr})$, is released to the flow. These equations can be manipulated into the form

$$\frac{M_d^2\{5 + M_d^2\}}{\{5 + 7M_d^2\}^2} = \frac{M_u^2\{5(E_v + 1) + M_u^2\}}{\{5 + 7M_u^2\}^2} \tag{2.6}$$

where $E_v = [e_v/h_{tru}]$, and M_u is the frozen flow Mach number upstream of the de-excitation zone. For given M_u and E_v this equation is a quadratic in M_d^2; two results are discussed below.

Using $p_p/P_o = 7.07 \times 10^{-3}$ as representative of the data in Figures 2.15-2.19 and the assumption $\gamma = 1.40$ in the Rayleigh pitot formula,

$$\frac{p_p}{P_o} = \left[\frac{(\gamma+1)M_\infty^2}{(\gamma-1)M_\infty^2 + 2}\right]^{\frac{\gamma}{\gamma-1}} \left[\frac{\gamma+1}{2\gamma M_\infty^2 - (\gamma-1)}\right]^{\frac{1}{\gamma-1}} \tag{2.7}$$

gives a test section $M_\infty = 8.33$. The possible effects of vibrational de-excitation according to Eq. (2.6) are assessed by assuming that the de-excitation zone would occur in the section of the nozzle just upstream of the exit plane. Since the geometry there is virtually constant diameter, it is assumed that M_u is 8.33. Assuming that freezing occurs at the barrel stagnation temperature, that is, $T_{vf} = T_o$, for $T_o = 1000K$, $M_d = 8.09$. For $T_{vf} = 850K$, $M_d = 8.22$.

These results suggest that the test section Mach number should be estimated using only test section flow properties. Boudreau (Ref. 2.17) advocates measuring pressures of blunted slender cones for this purpose, however the interpretation of the data so obtained requires a suitable viscous flow code. We used static pressure probes having geometries specified in Refs. 2.18 and 2.19. Basically they are cone-cylinders with the tip of the 5° taper cone being sharp, and the static taps placed at various distances "s" downstream of the cone-cylinder junction. Four probes were used, three having cylinder diameter $D_p = 1.07$ mm, with $s/D_p = 10$, 14.7 and 21.0 respectively and one with $D = 1.65$ mm and $D_p = 16.0$. All used 0.348 mm taps; 4 spaced at 90° for $D_p = 1.07$ mm, and

three spaced at 120° for D_p = 1.65 mm. Figure 2.21 gives a typical static probe history for p_1 = 400 kPa; it does not follow the structure of the barrel pressure history as does the pitot and static records shown in Figure 2.9. However it remains sensibly constant during the running interval identified from the pitot history; which is $0.018 < t < 0.038$ s approximately. Figure 2.22 gives the histories of the ratio of static to pitot pressure p_∞/p_p for the four probes. Each point has been obtained by averaging the records over 0.7 ms subintervals. Included in this plot is the value of p_∞/p_p computed by assuming calorically perfect flow from the barrel, which corresponds to M_∞ = 8.33. Although these histories pass through a minimum corresponding to the peak in p_p at t = 0.030 ms, their overall average is close to the computed value. This strongly suggests that vibrational de-excitation effects do not occur here. Consequently in all subsequent calculations, to estimate M_∞ and other free stream properties, we have used Eq. (2.7) together with γ = 1.40.

2.7 Test Section Flow Conditions

The pitot pressure data described in Section 2.5 indicate that the spatial variations in test section flow properties in the inviscid core are small, and comparable to the scatter in the measurements. Figure 2.23 presents estimates of the test section properties M_∞ and Reynolds number Re_∞ as a function of driver to barrel pressure ratio p_4/p_1. As is to be expected, increasing p_4/p_1 significantly reduces Re_∞ through its effect on T_0. There is also a slight reduction in M_∞; this is consistent with a thickening of the boundary layer on the nozzle wall associated with increasing T_0.

2.8 Stagnation Enthalpy Measurements

2.8.1 Background

As noted above, one of the two methods chosen for direct determination of T_0 is to interpret measurements of stagnation point heat transfer rates q_s obtained on a model mounted in the tunnel test section. The model designed and built for this purpose is a 52.8 mm (2 inch) diameter hemisphere-cylinder with a commercially produced 3.1 mm (1/8") diameter heat flux gage mounted at the

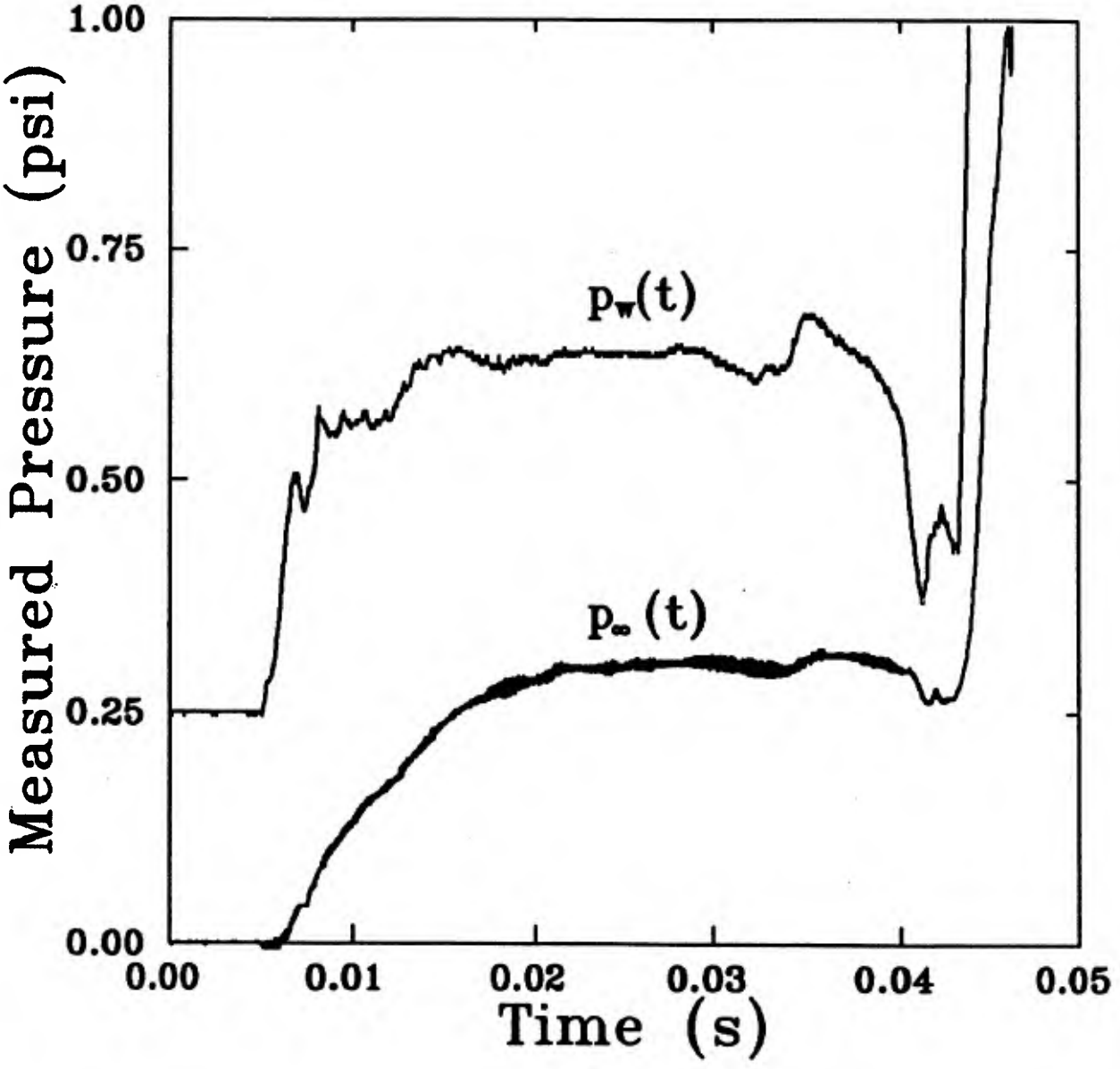

Figure 2.21 Typical in-stream static pressure probe history for p_1 = 400 kPa compared with response of a static wall tap on a model. The wall static trace is offset from zero to separate them.

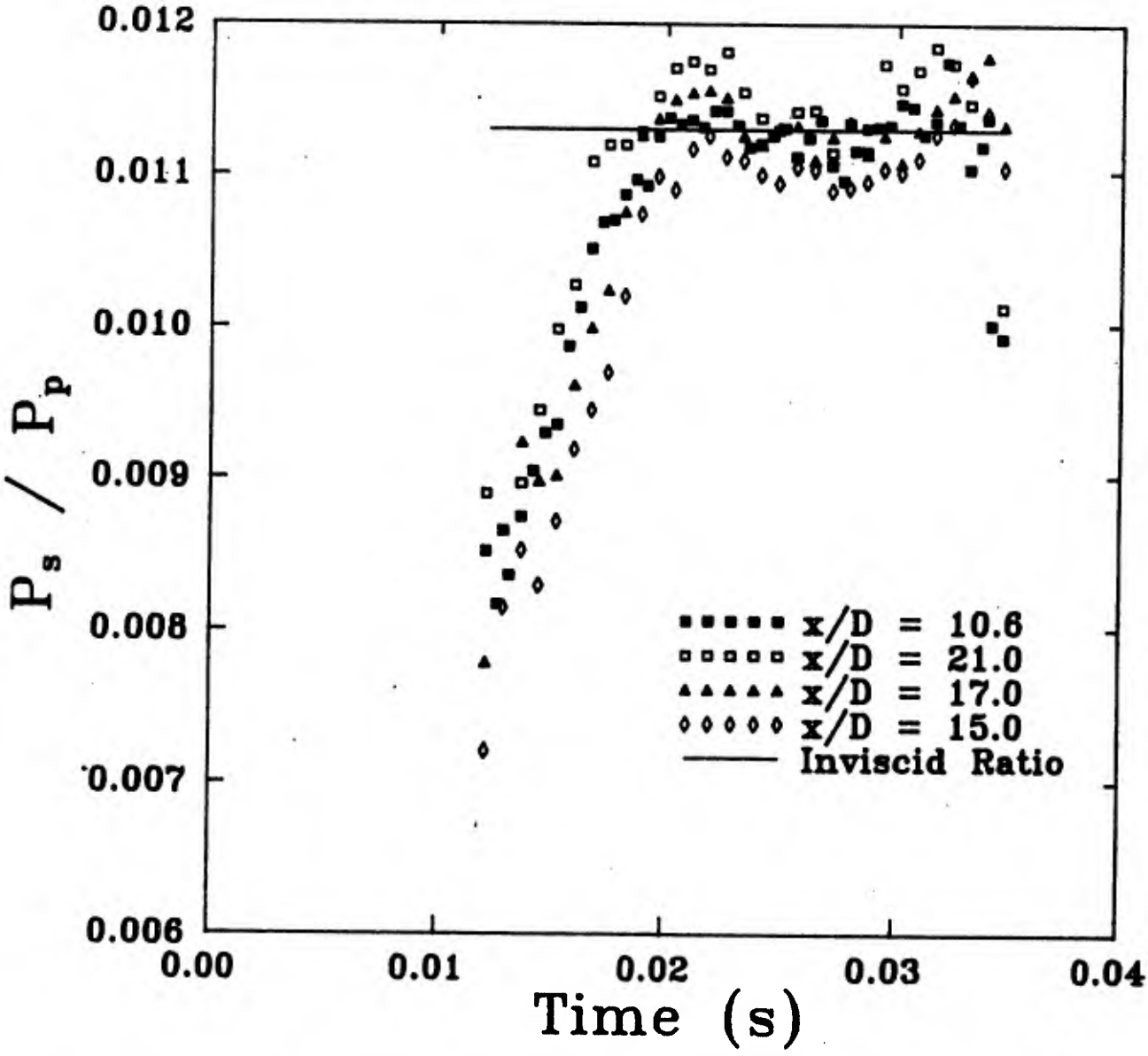

Figure 2.22 Computed histories of the ratio of static to pitot pressure p_s/p_p for the four probes compared with prediction based on isentropic calorically perfect flow at $M_\infty = 8.33$.

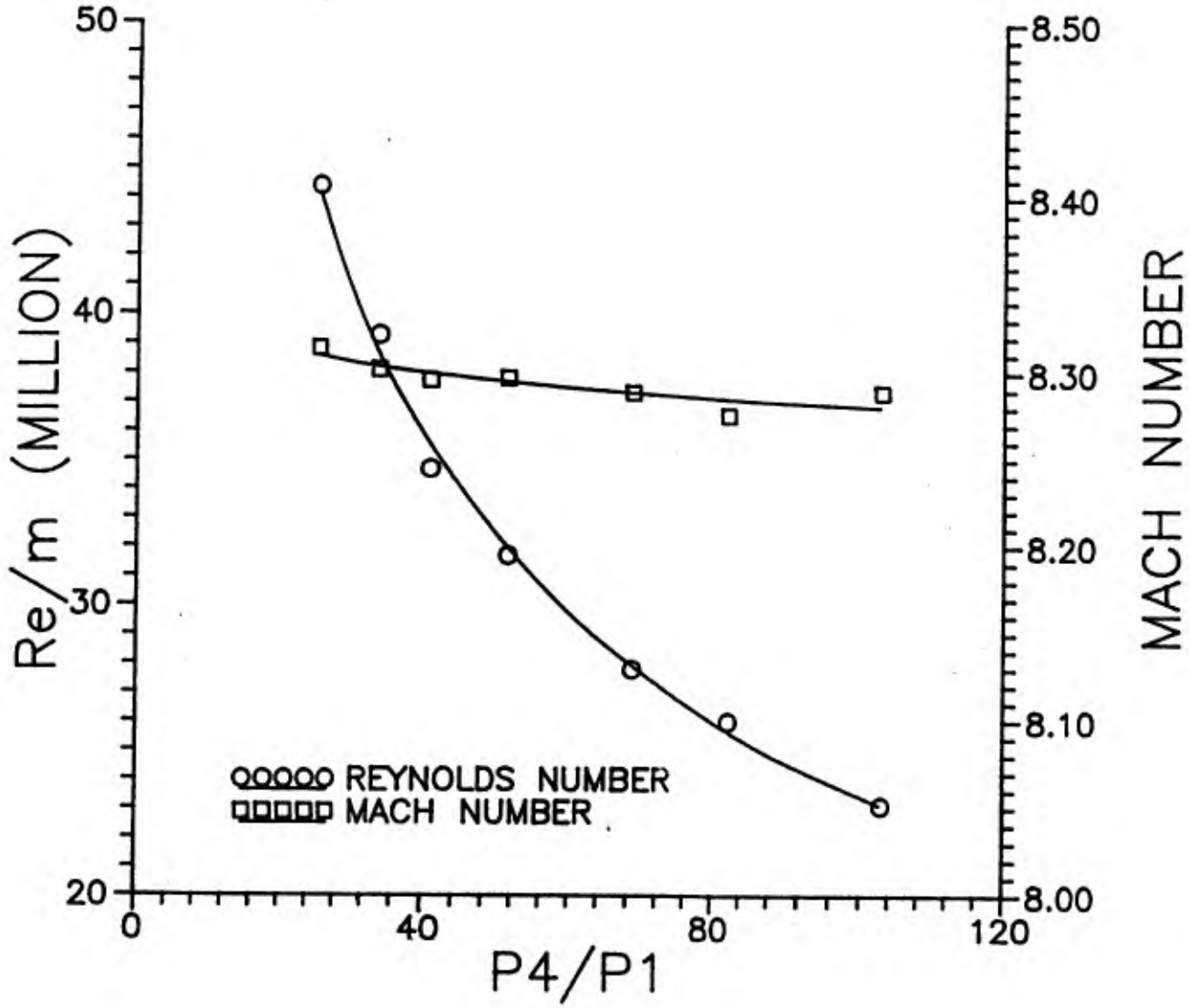

Figure 2.23 Estimates of test section Mach and Reynolds numbers.

stagnation point. This gage operates on the so-called semi-infinite principle (Ref. 2.20); basically it is a block of insulating material on which is mounted a thermometer to measure the history of T_S. Under certain circumstances the heat-conduction process into the block can be assumed one-dimensional, in which case the differential equation governing the process can be solved for the measured $T_S(t)$ to obtain $q_S(t)$ at the surface. Success in the technique depends on using a thermometer to measure T_S in a way which does not significantly affect the heat conduction process.

For short duration hypersonic wind tunnels the one-dimensional heat flux requirement is usually satisfied, the insulator is often a glass, and the surface thermometer is invariably a very thin platinum film resistance gage. Although it has been used for measuring heat transfer rates since 1956 (Ref. 2.21), and although it has been the subject of considerable development, as discussed below, its use is not necessarily straightforward.

When stagnation enthalpies were first determined using this technique thirty years ago the standard approach to interpretation was based on the classical self-similar solutions to the laminar boundary layer equations developed by Fay and Riddel (Ref. 2.22), and an approximate analytical solution for the external inviscid shock layer flow known as the modified Newtonian rule. It seems that, in spite of the successful development of numerical methods for hypersonic blunt-body and boundary layer flows, these approximate solutions are still the accepted basis of interpretation (Refs. 2.14 and 2.23). We use them here.

2.8.2 Typical Measurements

Figure 2.24 gives two voltage histories taken for p_1 = 200 kPa, or p_4/p_1 = 102.5. Since the gage is supplied from a precision constant current source, the voltage is directly proportional to gage resistance. One of the traces shows an abrupt rise at about 6 msec after the start of the records. Now the room-temperature gage resistance, R_O, is checked before and after each run to assess film damage caused by tunnel debris. Measurement of R_O showed that it had increased by about 1%. Abrupt increases such as this were at first observed after several runs, but eventually this phenomenon largely

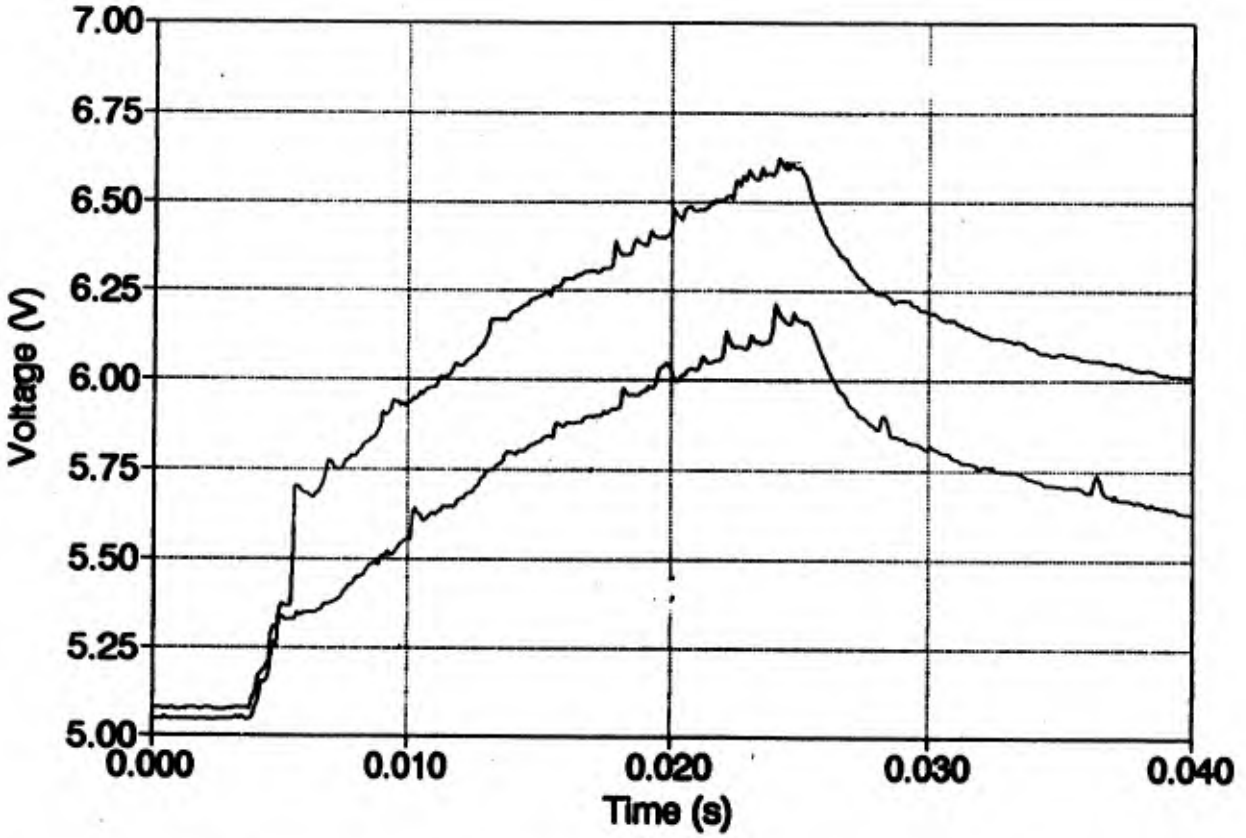

Figure 2.24 Two successive voltage histories from stagnation point heat transfer probe taken during first few runs. Barrel pressure p_1 = 200 kPa.

ceased. Inspection of the gage with a magnifying glass suggested that a transparent protective coating had been applied during manufacture, and that this had been flaking off during the runs and taking parts of the platinum film with it.

Figure 2.25 shows the results of two successive runs for p_1 = 400 kPa taken after the coating appeared to have been completely removed. The traces have been offset slightly to show their structure. In general they show excellent agreement, and the increase in R_0 has settled down to about 0.25% or less per run. This presumably is caused by erosion from tunnel debris, which can pose a severe problem for these gages. It appears that this tunnel is relatively clean.

2.8.3 Determination of Heat Transfer Rate

If the conditions of one-dimensional unsteady heat conduction in a semi-infinite slab are met, then the temperature field T(t,x) in the gage is governed by

$$\rho_g c_g(T) \frac{\partial T}{\partial t} = \frac{\partial}{\partial x}\left\{(k_g(T)) \frac{\partial T}{\partial x}\right\} \tag{2.8}$$

subject to the boundary conditions

$$T(0,x) = T_i = \text{const}, \qquad 0 \le x \le \infty \tag{2.9}$$

$$T(t,0) = T_s(t), \qquad T_s(0) = T_0 \tag{2.10}$$

In these equations, ρ_g, c_g and k_g are, respectively, the density, specific heat and thermal conductivity of the gage material. The aim is to obtain

$$q_s(t) = -k_g(T) \left.\frac{\partial T}{\partial x}\right|_{x=0} \tag{2.11}$$

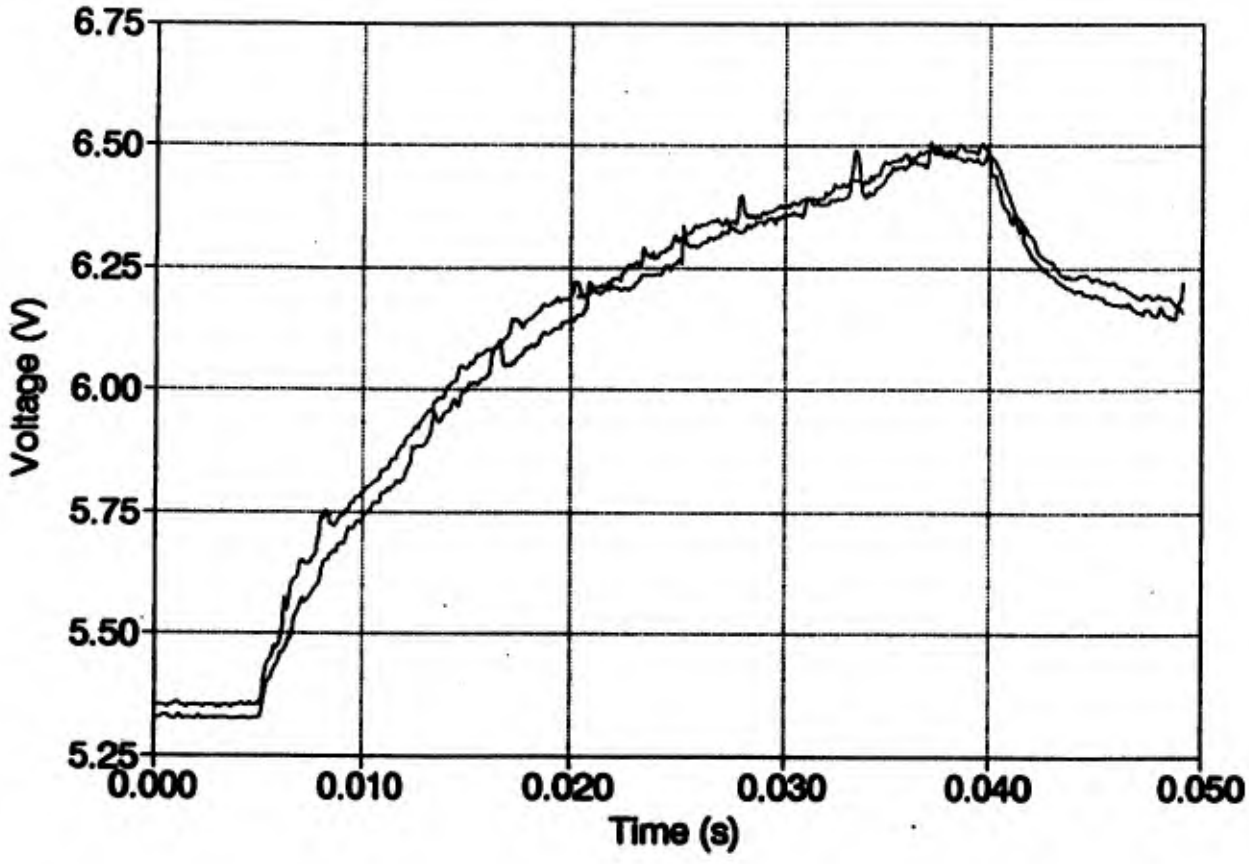

Figure 2.25 Stagnation point heat transfer probe histories obtained at p_1 = 400 kPa after the initial resistance changes appeared to have ceased.

In general, while ρ_g is constant for the ranges of T usually encountered, both c_g and k_g can vary significantly. Solution of these equations have in the past been obtained by a variety of techniques (Ref. 2.20). For the present exercise, in which high accuracy is desirable, it seems appropriate to apply numerical finite difference procedures directly, since these are well developed for heat conduction equations, and are readily adapted to variable thermal properties.

A difficulty with the gage used here is the determination of $c_g(T)$ and $k_g(T)$. For precision measurements the best material appears to be fused quartz, since the properties are well known (Ref. 2.20). For other materials, such as the Pyrex 7740 used in the present gage, the properties are believed to vary sufficiently from sample to sample that individual calibration is required (Ref. 2.20). Unfortunately, although the manufacturer provided a precision calibration of the gage, no information on the thermal properties of the substrate was supplied. Consequently we have used data quoted in the literature (Ref. 2.24) and summarized in Figures 2.26 and 2.27 .

2.8.4 Calculation of Stagnation Enthalpy

As described by Miller (Ref. 2.14) the correlation of Fay and Riddel for laminar stagnation point transfer rates in a one-species gas is

$$q_s = \frac{0.76}{Pr_w^{0.6}} (\rho_e \mu_e)^{0.4} (\rho_w \mu_w)^{0.1} (h_e - h_w) \left(\frac{du_e}{dx}\right)^{1/2} \qquad (2.12)$$

for a sphere, where Pr, ρ, μ and h are, respectively, Prandtl number, density, viscosity and enthalpy of the gas, the subscripts "e" and "w" denote gas properties at the edge of the stagnation point boundary layer and at the wall respectively, and du_e/dx is the velocity gradient of the fluid at the edge of the boundary layer as it accelerates away from the stagnation point. It is assumed that $h_e = h_o$, the stagnation enthalpy of the free stream.

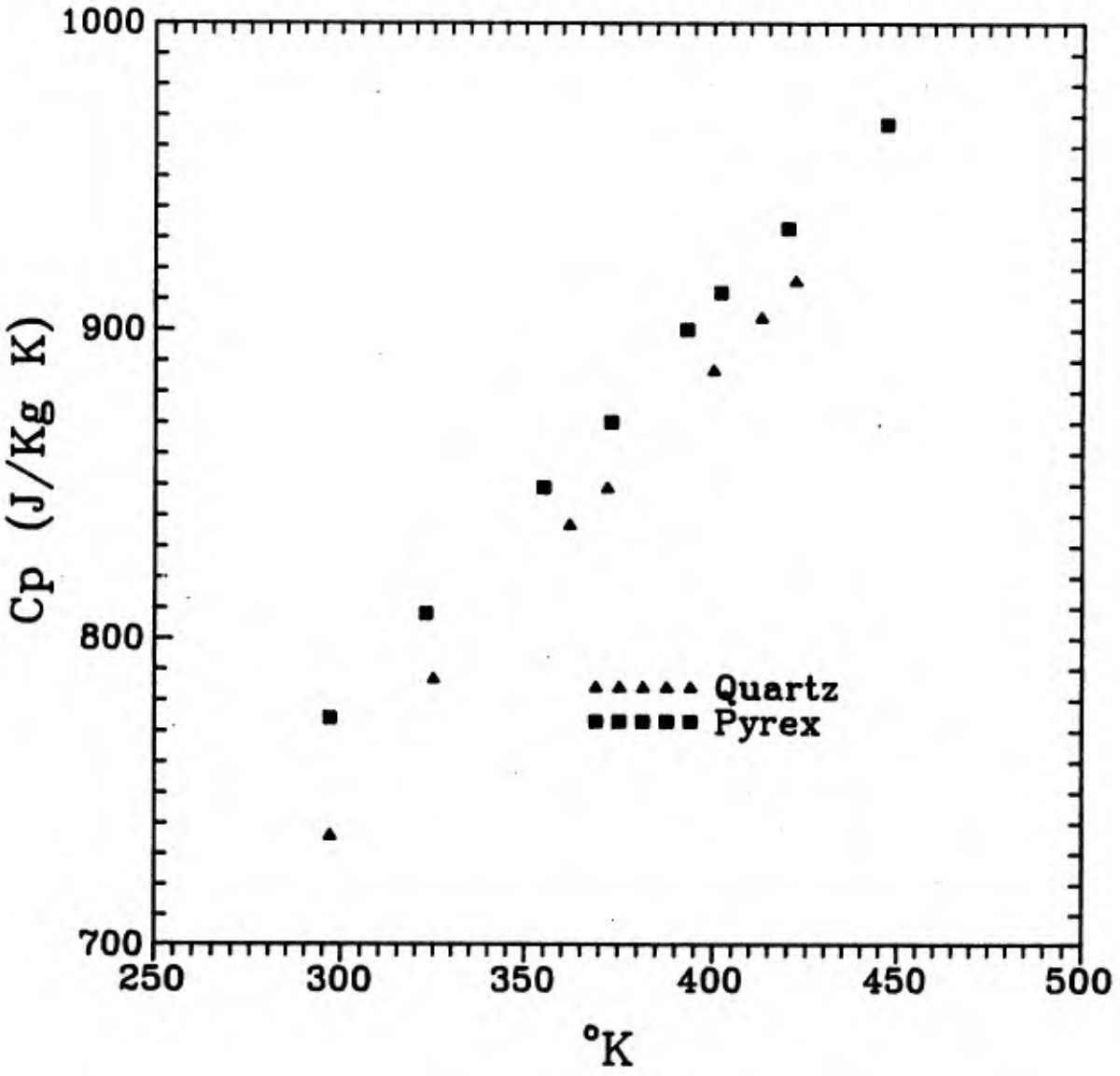

Figure 2.26 Heat capacity of Pyrex 7740 and quartz as reported by Hartunian and Varwig (Ref. 2.24).

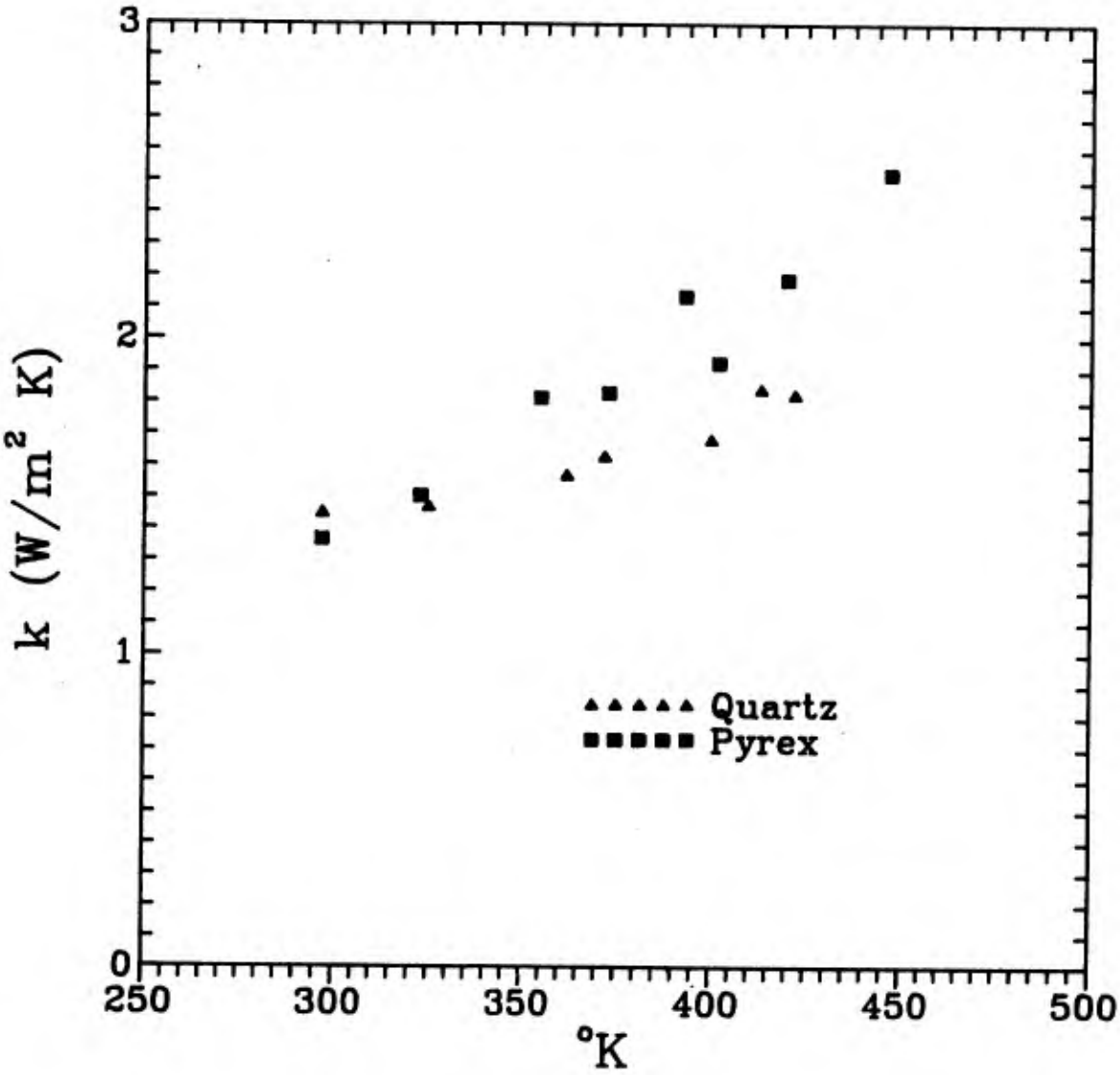

Figure 2.27 Thermal conductivity of Pyrex 7740 and quartz as measured by Hartunian and Varwig.

It is assumed that the gas in the stagnation region is thermally perfect, in which case

$$\rho_w = \frac{p_e}{RT_w}, \quad \rho_e = \frac{p_e}{RT_e} \tag{2.13}$$

and the viscosity is given by Sutherland's law, which for air in SI units is:

$$\mu = 1.462\times10^{-6}\, T^{1.5}/(T + 112) \tag{2.14}$$

The enthalpy is given by

$$\frac{h}{RT} = 3.51715 - 2.5041\times10^{-4}T + 5.5079\times10^{-7}T^2 - 1.7197\times10^{-10}T^3, \tag{2.15}$$

an empirical formula known to be accurate to within 0.1% for 200K < T < 1200K (Ref. 2.14). The term du_e/dx is calculated from

$$\frac{du_e}{dx} = \frac{1}{R_g}(2(p_e - p_\infty)/\rho_e)^{1/2} \tag{2.16}$$

where p_e is assumed equal to the pitot pressure p_p, R_g is the probe radius, and p_∞ is calculated using

$$p_\infty = 0.995\, p_e\left\{\left[1.2\, M_\infty^7\right]\left[6/(7M_\infty^2 - 1)\right]^{2.5}\right\}^{-1} \tag{2.17}$$

This is based on the usual calorically perfect formula for $\gamma = 1.4$, together with a small correction for real gas effects (Ref. 2.14).

Since many of the quantities in the above expressions are functions of the unknown $T_e = T_0$, the equations must be solved iteratively. A programme has been written for this purpose. It also uses tabulated data for Prandtl number (Ref. 2.25).

2.8.5 Implementation

A modified Crank-Nicholson technique was selected to solve Eq. (2.8). The data of Hartunian and Varwig was fitted with linear equations, so that

$$c_g(t) = c_o(1 + A_c\theta) \tag{2.18}$$

$$k_g(t) = k_o(1 + A_k\theta) \tag{2.19}$$

where $\theta = T(t) - T_O$. The reference values T_O, c_O and k_O are usually taken to be those at the laboratory temperature. If τ_E is the duration of the experiment, then a scale length L is defined as

$$L = \{(\tau_E k_o)/(\rho c_o)\}^{1/2} \tag{2.20}$$

Consequently, with

$$t = \tau_E \bar{t}, \quad x = L\bar{x} \tag{2.21}$$

Eqs. (2.8), (2.18) and (2.19) can be written in the form

$$(1 + A_c\theta)\frac{\partial\theta}{\partial\bar{t}} = (1 + A_k\theta)\frac{\partial^2\theta}{\partial\bar{x}^2} + A_k\left(\frac{\partial\theta}{\partial\bar{x}}\right)^2 \tag{2.22}$$

With uniform space and time grids $\Delta\bar{x}$ and $\Delta\bar{t}$ respectively, and with $\theta_j^n = \theta\{(j-1)\Delta x, (n-1)\Delta t\}$ this can be discretized to

$$(1 + A_c\theta_j^*)\left(\frac{\theta_j^{n+1} - \theta_j^n}{\Delta t}\right) = \left(\frac{1 + A_k\theta_j^*}{2\Delta x^2}\right)\left\{\theta_{j-1}^{n+1} - 2\theta_j^{n+1} + \theta_{j+1}^{n+1} + \theta_{j-1}^n - 2\theta_j^n + \theta_{j+1}^n\right\} + \frac{A_k}{4\Delta x^2}\left(\theta_{j+1}^{n+1} - \theta_{j-1}^{n+1}\right)\left(\theta_{j+1}^n - \theta_{j-1}^n\right), \quad j = 2 \text{ to } N-1 \tag{2.23}$$

If θ_j^* is an estimate of $\theta_j^{n+\frac{1}{2}}$ obtained in one of several ways, then Eq. (2.17) is linear and the overall system of equations can be assembled into a tridiagonal matrix for the temperature at the new time level $t^{n+1} = n\Delta t$. Solution then involves a simple marching procedure in time. Two estimates of $\theta_j^{n+\frac{1}{2}}$ were tried:

$$\theta_j^* = \theta_j^n \quad \textit{("lagging coefficients")} \tag{2.24}$$

$$\theta_j^* = \frac{3}{2}\theta_j^n - \frac{1}{2}\theta_j^{n-1} \quad \textit{("extrapolating")} \tag{2.25}$$

The boundary conditions are, with $M = (\bar{x}_{max}/\Delta\bar{x}) + 1$,

$$\theta_1^n = T_s\big((n-1)\Delta t\big) - T_o, \qquad \theta_M^n = 0 \tag{2.26}$$

At any given t, the surface heat flux $q_S(t)$ is calculated using second order backward differences:

$$q_S^n = q(0, t) = -\frac{k_o}{2L\Delta\bar{x}}\big(1 + A_k\theta(0, t)\big)\big(3\theta_1^n - 4\theta_2^n + \theta_3^n\big) \tag{2.27}$$

The algorithm was validated in a variety of ways. Tests for mesh refinement showed that $\bar{x}_{max} = 6$, $\Delta\bar{x} = 0.1$, $\Delta\bar{t} = 0.01$ and setting $\theta_j^* = \theta_j^n$ were adequate. A source term $S(\bar{x}, \bar{t})$ was added to Eq. (2.22) corresponding to a known or specified θ to check for accuracy of the nonlinear solution. Also, it can be shown that if both the gage thermal properties and q_S are constant, then $T_S(t) = Kt^{1/2}$, where $K = 2q_S/(\pi\rho_g c_g k_g)^{1/2}$ (Ref. 2.20). On using this temperature history with $A_C = A_k = 0$, the algorithm achieved the corresponding q_S to an error of less than 0.02% in just three time steps.

Figure 2.28 is a plot of $q_S(t)$ obtained by applying this algorithm to the lower of the two curves in Figure 2.25. While a clear trend is discernible, it is evident that precise interpretation requires smoothing of the temperature histories. Two approaches were tried; one was based on digital filtering

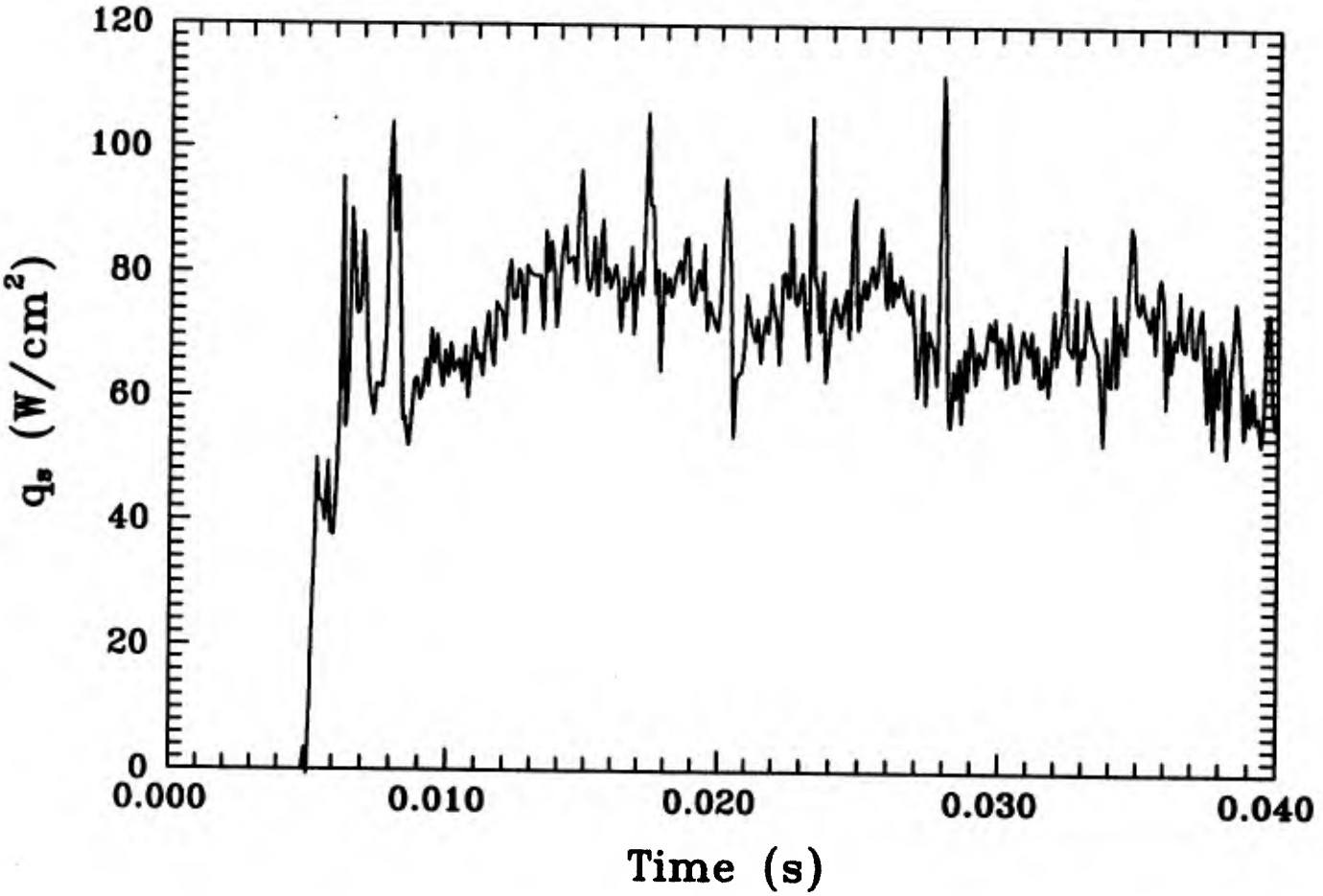

Figure 2.28 Heat flux at surface of gage predicted from lower of two histories in Figure 2.25.

using fast Fourier transform (FFT) techniques, and the second used polynomial fitting. Although the FFT spectrum of the data in Figure 2.28 exhibits a structure which suggests a cut-off frequency suitable for low-pass filtering, annihilation of the FFT components above this frequency followed by application of the inverse transform produced a record containing oscillations which we found difficult to interpret. Consequently for the present development, notwithstanding their well-known limitations, polynomial fitting was used. That is, a polynomial of given order was fitted to the data with the order being selected both by visual inspection of the fit of features judged to be important, and by evidence of convergence in the computed $q_S(t)$. Typically for the data of Figure 2.25, fits for for polynomials of order 7, 8 and 9 gave very similar $q_S(t)$.

An additional test of this procedure was undertaken by applying it to simulated data corresponding to the known solution for a constant heat transfer rate, and for glass having thermal properties independent of temperature. The simulated data for a typical $q_S = 100$ W/cm^2 is shown in Figure 2.29. The smoothed temperature history and the corresponding computed $q_S(t)$ is given in Figure 2.30. This suggests that, except for the neighbourhood of the ends of the fitting interval, polynomial smoothing introduces errors of about ±1%.

2.8.6 Preliminary Results and Discussion

Figure 2.31 gives the smoothed temperature history for the lower of the two curves in Figure 2.24, together with surface heat fluxes computed using the algorithm described in Section 2.8.5. The two q_S histories are for the glass thermal properties held constant at their values corresponding to T_O,and for variable properties. It shows that the variable thermal properties increase the estimate of $q_S(t)$ continuously during the run, with the cumulative error being about 19%. Processing the data for the upper of the two curves in Figure 2.24 produced, as expected, significant discrepancies between the computed $q_S(t)$ at the beginning and end of the test interval. This is shown in Figure 2.32. However, for the interval from t = 0.01 sec to 0.027 secs in Figure 2.24 the agreement between the two sets of data was close; that is, the deviation was less than ±2% of the mean. Hence this data was judged

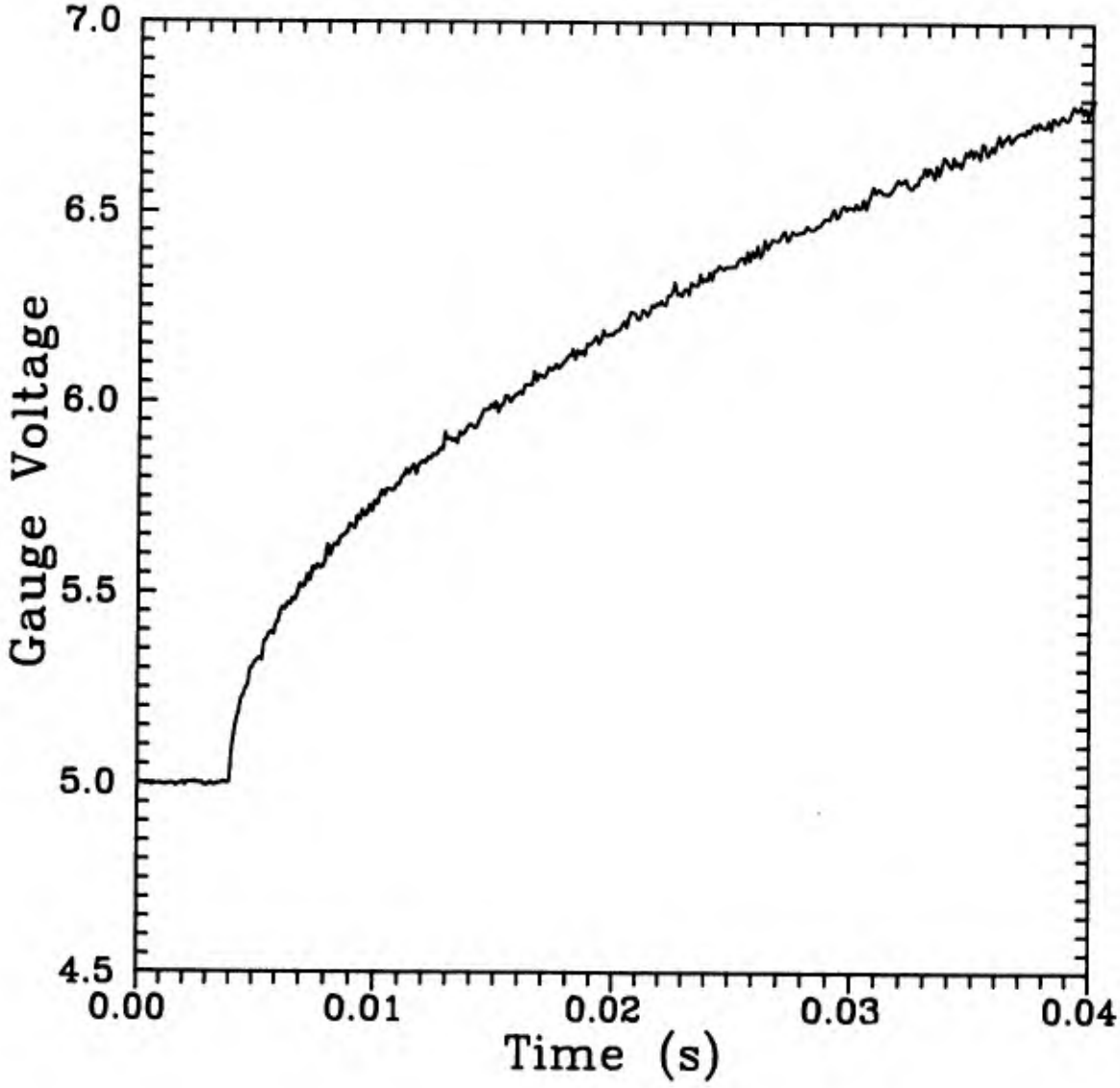

Figure 2.29 Simulated gage voltage data corresponding to a Pyrex 7740 having constant thermal properties at the laboratory temperature $T_o = 22°C$ and a constant heat flux $q_s = 100$ W/cm^2.

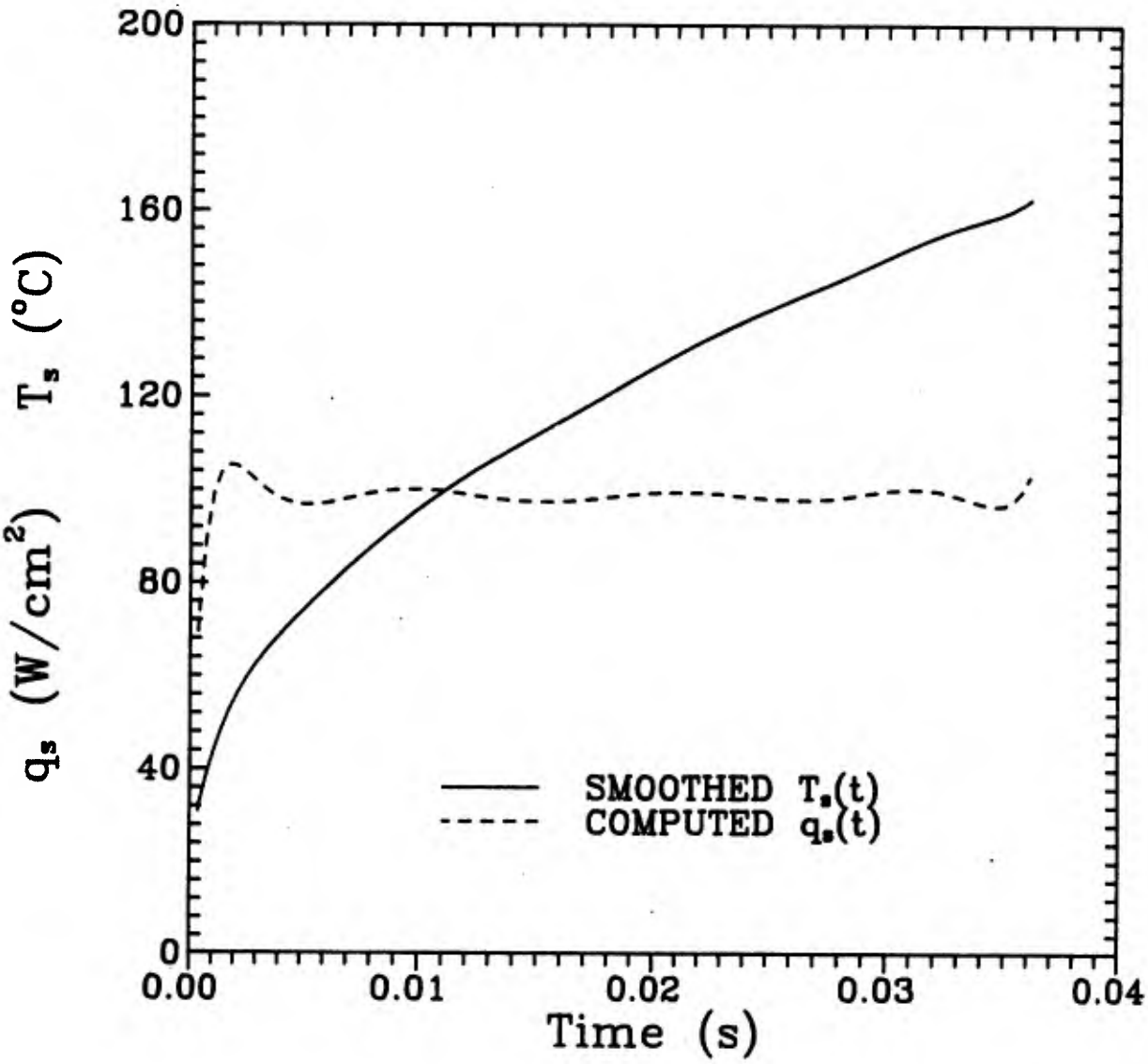

Figure 2.30 Polynomial fit of the simulated data of Figure 2.26, together with computed heat flux.

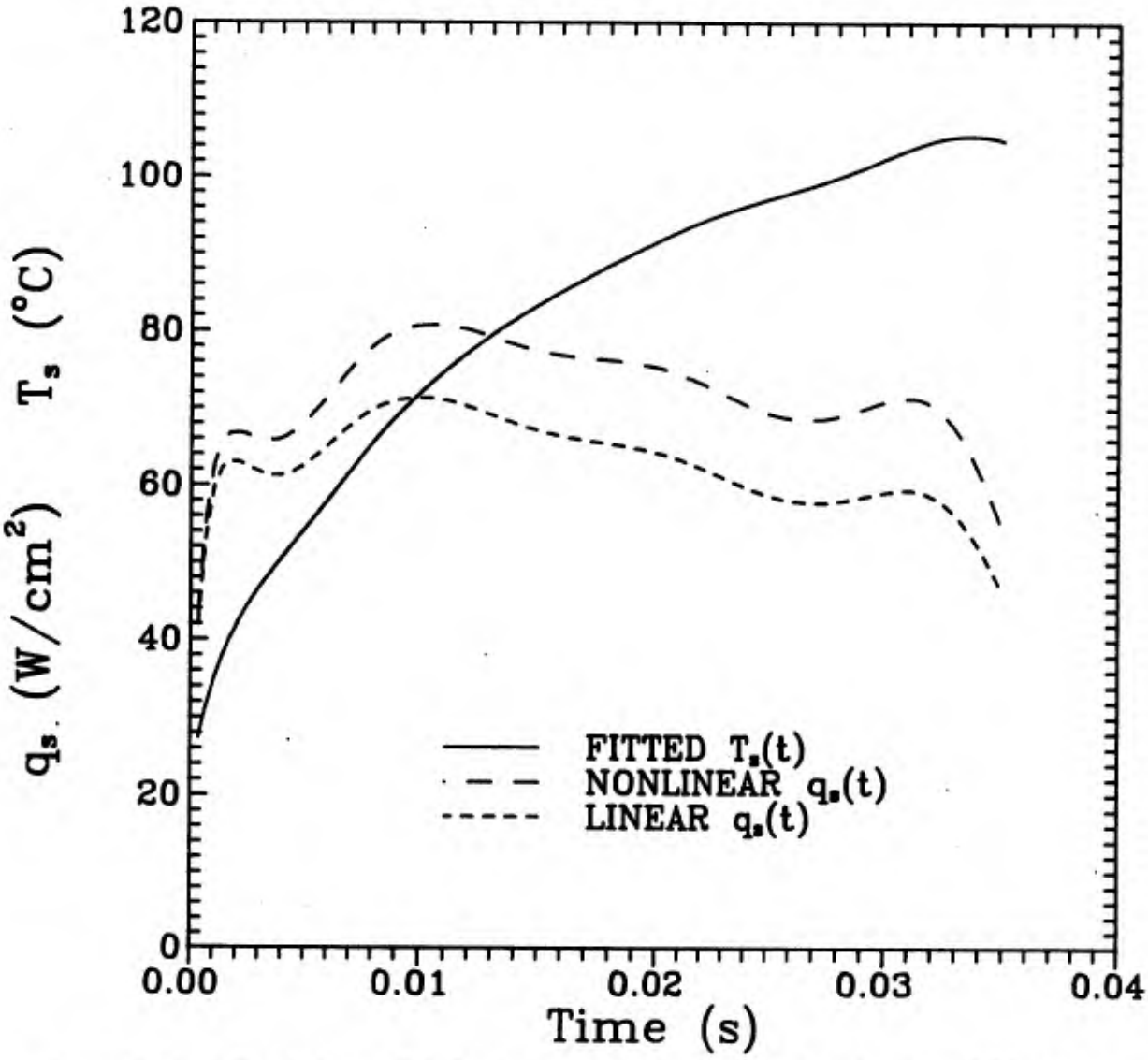

Figure 2.31 Fitted history of Ts for the lower of the two curves given in Figure 2.25 together with computed heat flux. Barrel charge pressure p_1 = 400 kPa.

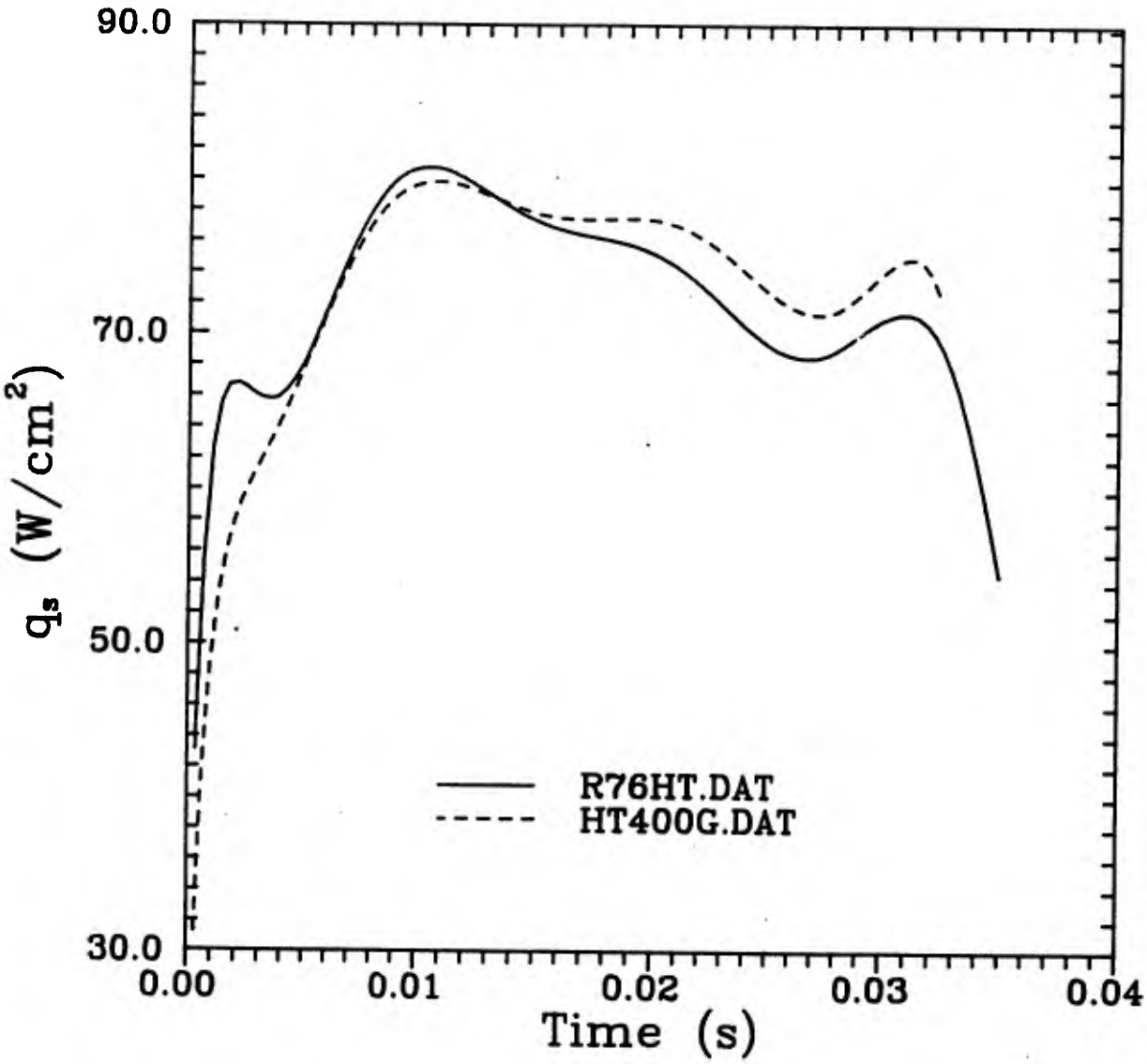

Figure 2.32 Predicted stagnation point heat flux histories for the two gauge temperature histories in Figure 2.25.

reliable enough to allow a computation of the history of T_0. The estimations from the two runs are included in Figure 2.11. Because of the difficulties associated with the data for p_1 = 200 kPa, this was not processed.

As noted in Section 2.6.3, the estimates of T_0 are high relative to the predictions of both the approximate method and the simulations. However they imply that the method can resolve the temperature history. Currently we attribute the discrepancies to the uncertainty in the thermal properties of the Pyrex used in the gauge material.

2.9 Conclusions

Although the gun tunnel concept does not produce a uniformly compressed and heated test gas, both the numerical simulations in Section 7 and the present calibration results indicate that, for most purposes, the flow in the test section may be assumed quasisteady. Consequently digital data acquisition techniques, which were not available when these facilities were first developed, make it relatively easy to compensate for the unsteadiness, and thus to produce repeatable high quality experimental data. Also, for the highest enthalpies generated to date, which correspond to a stagnation temperature of about 1300K, real gas effects including vibrational nonequilibrium effects may be ignored, and the flow in both nozzle and test section treated as if it were thermally and calorically perfect.

The only remaining calibration issue is the history of the stagnation enthalpy. The limited results obtained to date from the heat transfer measurements give stagnation enthalpy histories which are significantly above the numerical predictions, and the reason for this discrepancy is not yet resolved. One possibility currently being pursued is errors in the assumed thermal properties of the Pyrex heat flux gages. Nevertheless they agree qualitatively with the predictions, suggesting that the major source of nonuniformity in the stagnation enthalpy lies in the original compression process rather than in cooling by the barrel walls. With further development, it appears possible that the stagnation point heat transfer technique is capable of resolving in detail the history of the stagnation enthalpy.

The basic facility has proven to be very reliable, cheap to operate and productive. In particular it appears that, except for one high enthalpy test condition, the current piston design — which was evolved on a trial and error basis — is adequate. As many as 150 runs can be obtained before the piston must be replaced.

With regard to tunnel development, aside from the manufacture of nozzles to attain other test section flow conditions and to accommodate larger models, the major desirable improvement is to increase stagnation enthalpy. One approach is to increase the ratio of driver to barrel charge pressure. However, our operating experience indicates that this requires redesign of the piston to obtain higher strength to weight quotients. The analysis of Section 9 suggests that significant improvements in piston design can be readily made. However, to take advantage of this option, major changes to the configuration of the facility may have to be made in order to obtain a useable test-time. A relatively inexpensive alternative suggested by the simulation of Section 7 is to preheat the barrel air, possibly by electrically heating the barrel.

2.10 References

2.1 Meyer, R. F., Campbell, W. F., and Jackson, K. P., "The NAE Hypersonic Gun Tunnel, Part 1: The Compression Heater," National Research Council of Canada, Ottawa, Canada, Aeronautical Report LR-432, Aug. 1965.

2.2 Cox, R. N., and Winter, D. F. T., "The Light Gas Hypersonic Gun Tunnel at ARDE, Fort Halstead, England," AGARD Report No. 139, 1957.

2.3 Bray, K.N.C., Pennelegion, L., and East, R. A., "Performance Studies for the University of Southampton Hypersonic Gun Tunnel," University of Southampton, Southampton, England, Dept. of Aeronautics and Astronautics, Report No. 103, April 1959.

2.4 Stollery, J. L., Maull, D. J., Belcher, B. J., "The Imperial College Hypersonic Gun Tunnel, August 1958-July 1959," *Journal of the Royal Aeronautical Society*, Vol. 64, No. 589, Jan. 1960, pp. 24-32.

2.5 Wittliff, C. E., "A Survey of Existing Hypersonic Ground Test Facilities — North America," Proceedings of AGARD Conference on Aerodynamics of Hypersonic Lifting Vehicles, Bristol, England, April 6-9, 1987, AGARD Report CP-428, Nov. 1987.

2.6 Merritt, G. E., "Velocity Measurements in the University of Southampton Hypersonic Gun Tunnel," University of Southampton, Southampton, England, Dept. of Aeronautics and Astronautics Report No. 172, April 1961.

2.7 Lemke, B., "An Investigation of the Stagnation Condition in the Shock-Compression Heater of a Gun Tunnel," Aeronautical Research Institute of Sweden, Stockholm, Sweden, Report No. 90, Feb. 1962.

2.8 Needham, D. A., "Progress Report on the Imperial College Hypersonic Gun Tunnel," Imperial College of Science and Technology, London, England, Aeronautics Dept. Report No. 118, Aug. 1963.

2.9 Needham, D. A., Elfstrom, G. M., and Stollery, J. L., "Design and Operation of the Imperial College Number 2 Hypersonic Gun Tunnel," Imperial College of Science and Technology, London, England, Aeronautics Dept. Report No. 70-04, May 1970.

2.10 Stollery, J. L., "Stagnation Temperature Measurements in a Hypersonic Gun Tunnel Using the Sodium Line Reversal Method," Imperial College of Science and Technology, London, England, Aeronautics Dept. Report No. 16, Sept. 1960.

2.11 Stollery, J. L., and Smith, J. E., "A Note on the Variation of Vibrational Temperature along a Nozzle," *Journal of Fluid Mechanics*, Vol. 13, Pt. 2, June 1962, pp. 225-236.

2.12 Stollery, J. L., and Park, C., "Computer Solutions to the Problem of Vibrational Relaxation in Hypersonic Nozzle Flows," Imperial College of Science and Technology, London, England, Aeronautics Dept. Report No. 115, Jan. 1963.

2.13 Measures, R. M., Private Communication.

2.14 Miller, C. G., "Comparison of Thin-Film Resistance Heat Transfer Gages with Thin-Skin Transient Calorimeter Gages in Conventional Hypersonic Wind Tunnels," National Aeronautical and Space Administration, Washington, TM 83197, 1981.

2.15 Gordon, K. A., "An Investigation of Local Mach Numbers in Hypersonic Gun Tunnel," University of Toronto, Toronto, Canada, B.A.Sc. Thesis, April 1991.

2.16 ———— "Calspan Hypersonic Shock Tunnel: Description and Capabilities," Calspan Corporation, Advanced Technology Center, Buffalo, New York, Dec. 1984, p. 16.

2.17 Boudreau, A. N., "Characterization of Hypersonic Wind Tunnel Flow Fields for Improved Data Accuracy," Proceedings of AGARD Conference on Aerodynamic Data Accuracy and Quality: Requirements and Capabilities in Wind Tunnel Testing, Naples, Italy, Sept. 28-Oct. 1, 1987, AGARD Report CP-429, July 1988.

2.18 Williams, M. J., "Static Pressure Probes at Mach Number 7.5," Commonwealth of Australia, Aeronautical Research Laboratories, Melbourne, Australia, Note ARL/A 327, 1976.

2.19 Gray, J. D., "Evaluation of Probes for Measuring Static Pressure in Supersonic and Hypersonic Flows," Arnold Engineering Development Center, Arnold Air Force Station, Tennessee, Report AEDC-TR-71-265, 1972.

2.20 Shultz, D. L., and Jones, T. V., "Heat Transfer Measurements in Short-Duration Hypersonic Facilities," AGARDograph No. 165, Feb. 1973.

2.21 Vidal, R. J., "Model Instrumentation Techniques for Heat Transfer and Force Measurements in a Hypersonic Shock Tunnel," Cornell Aeronautical Laboratories, Buffalo, New York, Report AD-917-A-1, 1956.

2.22 Fay, J. A., and Riddel, F. R., "Theory of Stagnation Point Heat Transfer in Dissociated Air," *Journal of the Aeronautical Sciences*, Vol. 25, No. 2, Feb. 1958, pp. 73-85.

2.23 Anderson, J. D., *High Temperature and Hypersonic Gas Dynamics*, McGraw-Hill, New York, 1989, p. 53.

2.24 Hartunian, R. A., and Varwig, R. L., "On Thin-Film Heat-Transfer Measurements in Shock Tubes and Shock Tunnels," *Physics of Fluids*, Vol. 5, No. 2, Feb. 1962, pp. 169-174.

2.25 Hilsenrath, J., et al, "Tables of Thermal Properties of Gases," U.S. National Bureau of Standards, Washington, DC, Nov. 1955.

3.0 Shock Wave-Boundary Layer Interactions at a Convex Corner

R.J. Hawboldt, P.A. Sullivan and J.J. Gottlieb

3.1 Introduction

Interactions between boundary layers and shock waves in hypersonic flows have been the subject of extensive experimental, analytical and numerical investigation (Ref. 3.1-3.6). However, these investigations have been mainly confined to consideration of configurations depicted in Figure 3.1. These include an externally generated shock impinging on a constant pressure boundary layer, the flows generated by forward and backward facing steps, and the interaction at a concave corner. In contrast, the flows generated by the inlets being developed for supersonic combustion ramjets often involve an interaction in the neighbourhood of a convex corner. For many proposed geometries, the first stage of compression uses a forebody which turns the ingested flow away from the free stream direction and, as shown in Figure 3.2, a cowl is used to generate an oblique shock wave which further compresses and turns the flow into a rectangular or annular duct. The inlet geometry is chosen so that, ideally, the flow is turned sufficiently to allow cancellation of this cowl shock at the corner formed by the junction of the forebody and the duct. However, it must also interact with the boundary layer that develops on the forebody, so that success of the concept depends critically on controlling this interaction to allow effective cancellation. We take this to imply that the shock should not cause boundary layer separation or any other large scale modification of the flow field which would interfere significantly with the pressure recovery.

Hence the objective of this study is to obtain experimental data on the shock wave-boundary interaction near a convex corner in order to ascertain the conditions necessary for separation, and to establish the major features of the flow field both for separated and unseparated flows. Questions specifically addressed include:

1) how far from the convex corner must the shock impingement point be to uncouple the interaction and corner-turning processes?

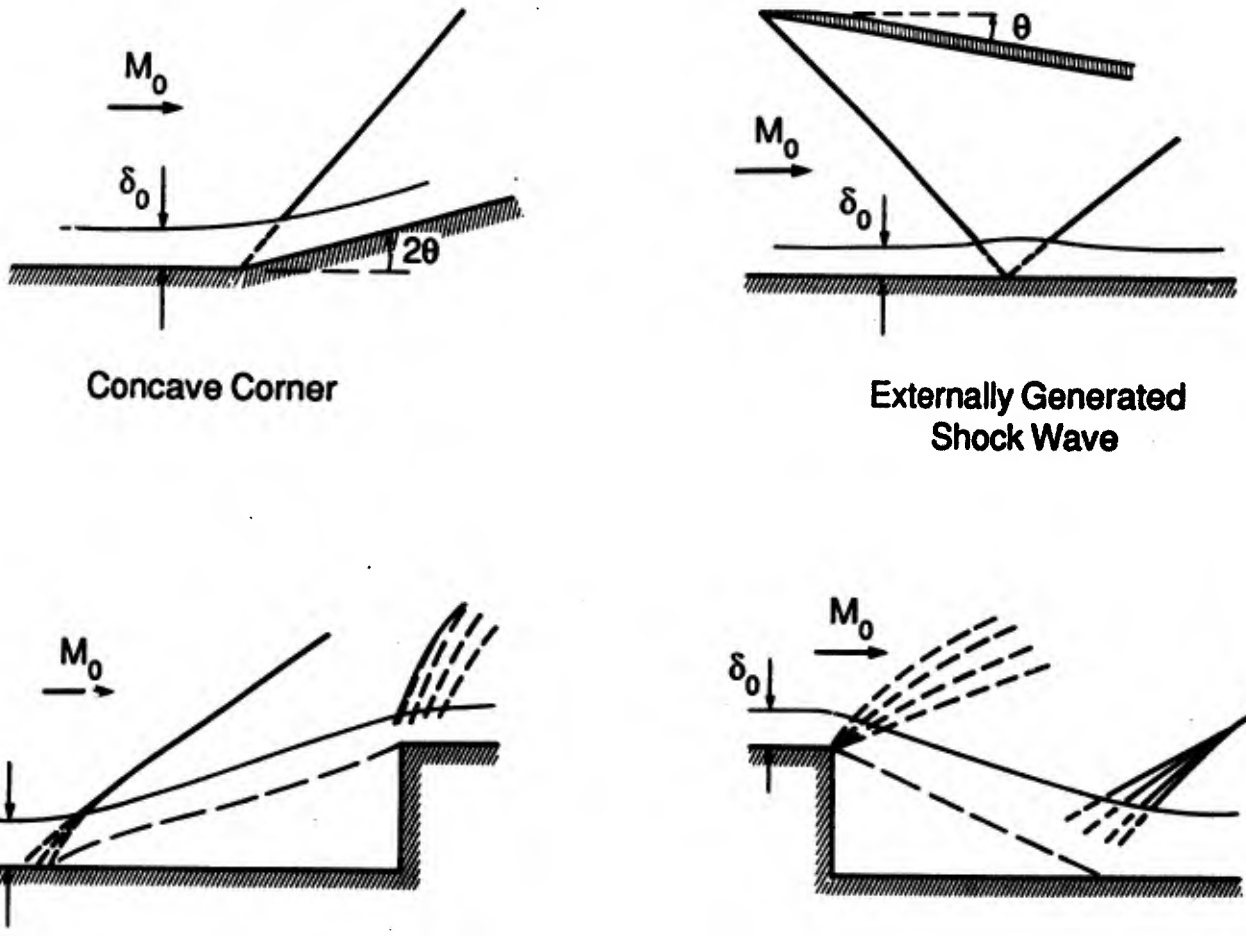

Figure 3.1 Four basic shock wave-boundary layer interactions previously investigated.

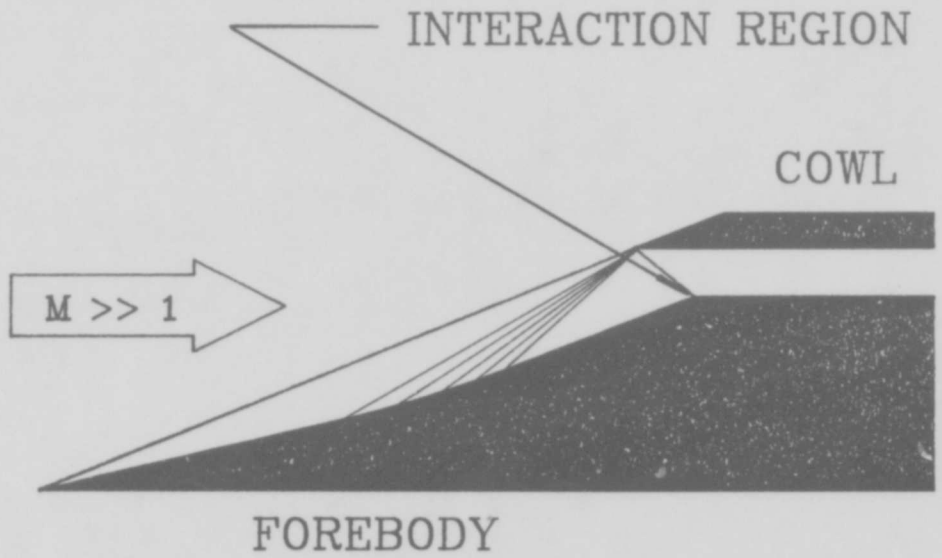

Figure 3.2 Possible scramjet engine inlet configurations showing location of the interaction studied here.

2) what conditions are necessary for incipient separation?

3) what are the important features of the separated flow?

4) what comparisons can be made between this case and those previously investigated?

The program developed to answer these questions contained three components: a literature review, an exploratory test program and a final test program.

The aims of the literature review were to identify existing investigations of convex corner interactions, to survey experimental techniques and, for comparison purposes, to obtain relevant experimental data on the two configurations we believe to be most closely related to the convex corner case. These are the externally generated oblique shock impinging on a flat plate boundary layer and the concave corner interaction. The exploratory program involved using a simplified model with an adjustable geometry and had two objectives. The first was to obtain data for a flat plate interaction; comparisons with existing data obtained in other facilities would then provide a check on the adequacy of our test procedures. The second objective was to obtain a limited amount of data for the convex corner case. It was envisaged that this data would be used to guide both the choice of a final model geometry, and selection and location of instrumentation. Because of the relative simplicity of both implementation and interpretation, surface static pressure measurements and schlieren flow visualization were used to obtain this data. It was initially envisaged that surface heat transfer measurements would also be used in the final test program since, as discussed below, these are believed to be the most sensitive of the indirect methods of detecting incipient separation in short duration hypersonic facilities.

At this juncture we make several comments about the way the program evolved. The first is that, although the contract called for the use of axisymmetric models in order to avoid the well known difficulties planar models present in achieving two-dimensional hypersonic separated flows, a planar model was ultimately used for the following reasons:

1) it is relatively easy to construct and can be modified easily during the course of the experiments,

2) a clear view of the shock wave-boundary layer interaction is possible,

3) we judged an internal axisymmetric model to be inappropriate at this point because it is impossible to use schlieren flow visualization and because of the mechanical complications of making geometry and configuration changes,

4) an external flow axisymmetric model could use schlieren flow visualization but its design is complicated by the limited space available to properly mount pressure transducers and by the difficulty in making configuration changes.

The second comment is that the program involved using a test facility for which no relevant operating experience was available. As a direct result, several problems were encountered. Finally, owing the budgetary limitations, the final test program was not undertaken within the contract period. In spite of this, the preliminary data that has been obtained allows useful conclusions to be made.

The following sections describe the results of our literature review and the exploratory test program. The test results are presented in five parts. The first part describes data from a flat plate boundary layer in the absence of an interaction. Originally intended as part of our test validation procedures, it revealed the operating problems noted above. Second, data obtained for a series of flat-plate shock wave interactions is described. The third and fourth parts present the data for boundary layers flowing over 5 and 10° convex expansion corners, and for shock wave-boundary layer interactions in the neighbourhood of these corners. Finally data on the effect of model width changes is presented to demonstrate that the edges of the model did not affect the flow at its center-line.

3.2 Literature Review

3.2.1 Introduction

The availability of several excellent reviews (Ref. 3.1 - 3.6) of the literature on shock wave-boundary layer interactions has considerably simplified the present task. Green (Ref. 3.1) gives a general discussion of the four basic types of interactions with emphasis on turbulent boundary layers. Hankey (Ref. 3.2) and Adamson & Messiter (Ref. 3.3) deal primarily with the prediction of shock wave-turbulent boundary layer interactions in transonic and supersonic flows. The analytic techniques discussed in these and other

reviews are described in detail by Delery & Marvin (Ref. 3.4), and they outline the advantages and limitations of the various methods. Also included is a discussion of the solution to the time averaged Navier-Stokes equations for turbulent boundary layer interactions.

Holden (Ref. 3.2) reviews experimental shock wave-boundary layer interaction studies and compares some of these experimental results to analytic predictions from solutions of the integral form of the boundary layer equations. Included is a discussion of hypersonic facilities, measurement techniques and the differences between laminar and turbulent interactions. Holden, Delery & Marvin (Ref. 3.4) and Delery (Ref. 3.5) provide fairly complete descriptions of a variety of shock-boundary layer interactions, including the concave corner and externally generated shock cases, and an overview of the experimental data available at that time. Just recently, Hamed (Ref. 3.6) has reviewed the experimental techniques and results for two-dimensional shock wave-boundary layer interactions with particular emphasis on the turbulent regime.

3.2.2 Previous Studies of Shock-Boundary Layer Interactions Near a Convex Corner

The literature search revealed only two investigations of shock wave-boundary layer interactions near a convex corner (Refs. 3.7 and 3.8). Chew (Ref. 3.7) performed experiments in a supersonic blowdown wind tunnel in which an adiabatic turbulent boundary layer developed on the floor of the rectangular test section. The Mach numbers used in this study were 1.8 and 2.5, the corner angle was 6° and the shock generator angles were 4, 6 and 8°. Wall static pressures were measured through the interaction region, and both schlieren photography and surface oil flow visualization were used. Some of Chew's conclusions were:

- the final static pressure downstream of the interaction was insensitive to the shock wave impingement point,
- mutual influence of the incident shock and corner expansion wave on the boundary layer occurs when the shock impinges closer than 3-4 boundary layer thicknesses upstream from the corner; the influence also increases with shock strength,

— mutual influence of the incident shock wave and the expansion fan ceased when the shock impinged a short distance downstream from the corner,

— the separation length decreased when the shock impinged nearer to the expansion corner.

The effects of the sidewalls were felt within the middle one third of the working section, indicating that the interaction region may not have been two-dimensional.

Subsequently, Chew & Squire (Ref. 3.8) obtained pitot and static pressure profiles through the boundary layer, and used Preston tubes to obtain the wall skin friction downstream of the interaction, in order to determine the effect of a sudden compression-expansion disturbance on an adiabatic turbulent boundary layer. The development of the boundary layer downstream of the interaction was computed using two different numerical methods and two viscosity models. The numerical and experimental results were then compared.

Data on the combined effects of a convex corner and an externally generated shock wave on a hypersonic boundary layer have not been located. Chew's results are not directly comparable to the present study because of the large differences in Mach number, boundary layer condition and wall temperature.

3.2.3 Experimental Techniques Used in Boundary Layer Separation Studies

Several experimental techniques are used to detect and measure the effects of shock induced boundary layer separations. Most measure the effect of the separated flow on a solid boundary of the flow field, while others can be used to measure or infer the fluid properties throughout the flow field. The advantages and limitations of the techniques are discussed briefly below.

3.2.3.1 Surface Static Pressure Measurements

When a shock wave interacts with a supersonic boundary layer, the upstream influence that propagates through the subsonic portion of the boundary layer causes the layer to thicken ahead of the incoming shock and the external flow is turned away from the wall, generating a precursor compression wave. When the shock is strong enough to cause separation, the main flow is deflected over a "wedge" of recirculating fluid,

so that the static pressure rises to a plateau just downstream of the separation point and then remains constant until the shock wave intersects the edge of the boundary layer. Downstream of the shock impingement point, the compression occurs as reattachment is approached. "Effective" incipient separation is said to occur when the shock wave is just strong enough to cause three inflection points, or a "kink" in the wall static pressure distribution through the interaction region (see pp. 74 of (Ref. 3.4) for a complete summary). Surface pressure data can also be used to determine incipient separation in another way. A gross property of the separated flow such as the overall length of the separation bubble is inferred together with its dependence on a measure of the strength of the disturbance such as the pressure ratio across an incoming shock. By plotting and extrapolating this data to a zero disturbance, the incipient condition is estimated. Holden (Ref. 3.9) discusses this technique.

Surface static pressure measurements are used most often in shock wave-boundary layer interaction studies because they are relatively easy to obtain, they directly indicate the length scales of the interaction and these results can be easily compared to analytic or numeric predictions. In laminar boundary layers, detection of separation is relatively easy because the plateau and separation lengths are quite long. However, in turbulent boundary layers, the shock wave penetrates deep into the boundary layer and Green (Ref. 3.10) reports that relatively large separation bubbles form before the surface static pressure distribution develops three inflection points. When surface static pressure measurements are used, the flow field properties away from the wall must be inferred. The unsteadiness associated with turbulent boundary layer interactions can be measured with flush-mounted pressure transducers having adequate frequency response. However, because the transducer's sensing surface is relatively large, the spatial resolution may be insufficient to make useful measurements in small wind tunnels. Surface static pressures are the most straightforward and reliable measurements for shock wave-laminar boundary layer interaction experiments.

3.2.3.2 Surface Heat Transfer Measurements

Surface heat transfer is related to the boundary layer wall shear stress and its measurement can be used to detect boundary layer transition and separation. In regions of separated flow, the heat transfer rate

decreases at the separation point and increases dramatically near the reattachment. Needham (Ref. 3.11), in his study of the shock wave-boundary layer interaction at a concave corner, suggests that incipient separation occurs when the corner angle is increased just enough for the cusp in the heat transfer distribution, which is located at the corner, to disappear.

Thin-film resistance gages, thin skin calorimeter gages or miniature thermocouples are generally used to measure surface heat transfer rates. Shultz & Jones (Ref. 3.12) have prepared a comprehensive review of heat transfer measurement in short duration wind tunnels. They, as well as Taylor (Ref. 3.13), describe in detail the construction, calibration and use of platinum thin-film resistance gages; and Miller (Ref. 3.14) compares the thermal properties of the insulating substrate materials normally used in these gages: Pyrex, quartz and Macor.

The use of thin-film heat transfer gages in small short duration wind tunnels, such as the gun tunnel used for the present work, is appropriate for the following reasons:

1) they have very short response times,
2) the film width is small, so that several gages can be painted on a single piece of glass substrate in order to achieve high spatial resolution,
3) construction of the gages can be completed with simple laboratory equipment so that, when the technique has been developed, this method is very flexible and relatively inexpensive,
4) many gages can be installed in the model simultaneously, eliminating the need to disassemble the model in order to move gages to new locations, and reducing the period between runs,
5) surface heat transfer rate is a useful parameter for comparison to analytic and numerical predictions.

The disadvantages of this technique are:

1) extensive computation is required to reduce the experimental data,
2) accurate calibration of the gages may be difficult.

3.2.3.3 Surface Shear Stress Measurements

Surface shear stress can be measured directly with skin friction transducers or indirectly from pressure measurements using either Preston tubes or Stanton tubes. Holden (Ref. 3.2) reports the use of a skin friction transducer to measure the wall shear stress in the region of a shock wave-boundary layer interaction. However, these devices are not commercially available, have large sensing surfaces, thus limiting spatial resolution, and must be able to measure very small shear forces at high frequencies. In the present tunnel, the vibrations during an experiment are very large and data interpretation may be difficult. Devices such as Preston tubes disrupt the flow in the separated regions and introduce errors into the measurement (Ref. 3.2).

3.2.3.4 Flow Visualization Techniques

Surface flow visualization, one of several visualization techniques reviewed by Settles & Teng (Ref. 3.15), is frequently used to detect boundary layer separation, and to measure its extent. A pigment is added to an oil or other fluid of suitable viscosity, and the mixture is then painted on the model surface. The boundary layer shear causes the mixture to flow and accumulate in regions where the shear stress is low. A complete description of this technique is given by Maltby (Ref. 3.16); it has three major deficiencies. First, it is unable to respond to unsteadiness in separated flows. Second, in short duration tunnels, it is difficult to ascertain if the pattern is representative of that occurring during the tunnel run, as opposed to start-up or shut-down. Finally, it may be impossible to find a fluid viscous enough to suspend a pigment, yet light enough to flow under very low shear stresses. Needham (Ref. 3.17) addressed this problem by applying a light dusting of talcum powder on his model surfaces. During the run, most of the powder is blown away, but a faint trace indicating separation and reattachment remains.

Schlieren and shadowgraph photography are relatively simple techniques for qualitative flow field visualization. The density gradients in shock wave-boundary layer interactions are large enough so that the major features are observable using schlieren and shadowgraph and wave diagrams can be constructed. Furthermore these observations can be readily related to surface pressure measurements.

3.2.3.5 Flow Field Measurements

A variety of techniques are suitable for non-intrusive flow field measurements in separated boundary layers and some of these are reviewed by Modarress & Azzazy (Ref. 3.18). These measurements are especially useful in the verification of analytic and numerical solutions because they allow comparison through the entire flow field, not just at solid boundaries. While some of these techniques are expensive and difficult to implement, two methods that have been employed successfully at UTIAS are discussed.

A Mach-Zehnder interferometer has been used for many years with the UTIAS hypervelocity shock tube to determine the flow field density in a wide range of shock wave experiments. Recently, at a hypersonic tunnel at the Australian National University, Gai et al (Ref. 3.19) used Fourier analysis to determine the fringe locations in finite fringe interferograms. The results were digitized and used to construct colour coded interferograms that clearly illustrate the variation in density behind a backward facing step. With surface pressure measurements, the fluid properties throughout the entire flow field can be determined.

Quantitative schlieren systems have been used to measure the density gradient through hypersonic boundary layers. Koziak (Ref. 3.20) developed a laser schlieren system to study the flow of a hypersonic laminar boundary layer around an expansion corner. A laser beam was swept through the boundary layer by a high speed rotating mirror and the resulting beam intensity measured by a photomultiplier. Using the density gradient through the boundary layer, as determined from the photomultiplier output, the fluid properties through the boundary layer were inferred. Of these two techniques, the laser schlieren system is simpler and less expensive to implement.

3.2.3.6 Conclusions of Literature Review

The technique most often used to investigate interactions of the type of interest here is surface or wall static pressure measurement. It is relatively simple to implement and to interpret so that, when combined with schlieren or shadowgraph flow visualization, it can provide much detailed information about the structure of the flow field, particularly when separation has occurred. The major limitation is relative insensitivity to the

onset of separation, especially for turbulent flows. Surface heat transfer measurements are the most sensitive of the indirect methods of detecting incipient separation, however they are much more difficult to both interpret and relate to flow visualizations of the wave structure. Thus it seems that, especially if the details of the separated flow are of interest, static pressure measurements combined with schlieren photography is the appropriate approach to a first investigation of the interaction being studied here.

3.3 Exploratory Test Model and Procedures

Figure 3.3 is a photograph of the model used initially in the exploratory test program as installed in the tunnel test section. This configuration consisted of a 6.00 in. (152 mm) wide by 14.0 in. (357 mm) long flat plate supported by a sting which was bolted to an alignment mechanism attached to the test section floor. A 6 in. (152 mm) by 12.0 in. (305 mm) shock generator was mounted above the plate, and attached by sting and alignment mechanism to the test section roof. To facilitate the task of measurement the model was made to be as large as possible consistent with previous usage with facilities of this type (Ref. 3.17). The shock generator assembly was removed for the basic flat plate tests. For the convex corner tests the flat plate was cut 8.167 in. (207 mm) downstream from its leading edge and the aft end then remounted to form 5° and 10° convex corners. Later, as discussed below, the plate width was reduced to 5.0 in.

Most of the experiments were conducted with a tunnel barrel charge pressure p_1 = 200 kPa. Under these conditions, as discussed in Section 2, the free stream Mach number M_∞ is about 8.3, the total temperature T_0 = 1200 K, and the unit Reynolds number at the boundary layer edge Re_u is about 24×10^6/m. Following the above discussion, data was obtained from wall static pressures and schlieren photography.

The wall static pressures were measured through 0.040 in. (1.57 mm) diameter taps distributed along the chord of the flat plate within 0.438 in. (11.1 mm) of the centerline. The streamwise spacing was 0.500 in. (12.7 mm) near the front and rear of the model, and 0.333 in. (8.46 mm) in the middle section where the

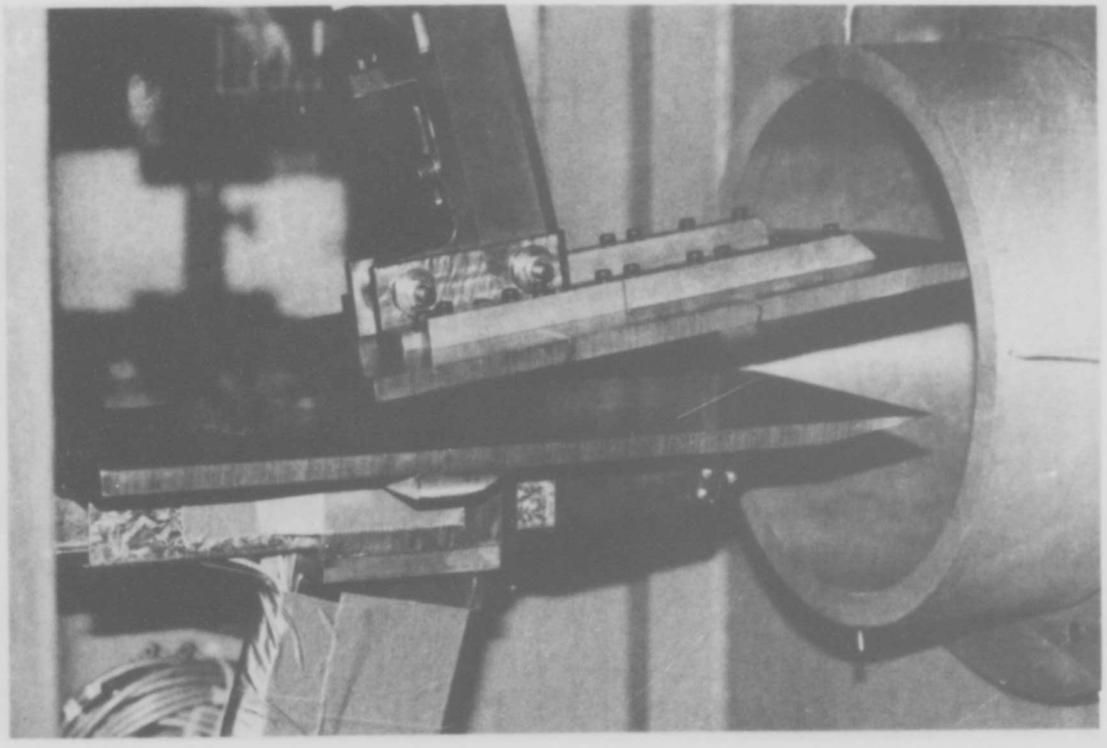

Figure 3.3 Photograph of exploratory model mounted in test section and configured for the flat plate shock interaction.

shock wave-boundary layer interactions occurred. At a distance x = 7.5 in. (190 mm) from the leading edge, eight pressure taps were installed to measure the lateral pressure distribution. Four taps were located on each side of the model between 1.688 in. (42.9 mm) and 2.813 in. (71.4 mm) from the centerline spaced 0.375 in. (9.5 mm) apart. It was impossible to drill lateral pressure taps closer than 1.5 in. (38 mm) to the centerline because of the model-sting connection.

Piezoresistive transducers with proprietary signal conditioners were used to measure pressures, and their outputs were filtered at a cutoff frequency of 20 kHz prior to digitizing at 250 kHz. Calibration of these transducers together with their signal conditioners against a laboratory standard Bourdon tube gage showed that they were highly linear and that their sensitivity was usually stable to within ±0.5% over an extended period. They were subject to offset drift, but this was compensated out during data reduction.

In Section 2 it is noted that, during any given tunnel run, the barrel end or effective reservoir pressure p_o varies by as much as 20% of the mean, and that corresponding quasisteady variations of pitot pressure also occur in the test section. Also the mean p_o can vary by as much as ±2% from run to run. Now in the present tests, as in the test section calibrations, obtaining a complete static pressure distribution required several runs. Consequently, the procedures for data interpretation described in Section 2 to correct for p_o variations were used here. Firstly, the size and geometry of the static pressure taps were chosen so that the transducer response exhibited the characteristic wave-form of the pitot traces. Typical static and pitot traces are shown in Figure 2.9. The pressure p_o and one static pressure chosen as a reference were recorded for every run; this p_o was used normalize all static pressure data. As discussed in Section 2.6.4, t_o was offset in time so that its major features were aligned with those in the static pressure histories. For p_1 = 200 kPa, this time offset was 1.2 ms. The mean static pressure ratios for the run were determined by averaging the normalized static pressure over a 5 ms interval between 18 ms and 23 ms. This interval was chosen because, in some cases, the flow did not stabilize until nearly 18 ms into the run. As an additional check, at selected stations in the interaction region, measurements were repeated.

During the course of the exploratory test program, the schlieren system was modified and upgraded. Two different light sources were tried: a Vivitar camera flash with a light pulse duration of about 250 microsec, and a Pulse Photonics Argon Jet spark light source having a standard duration of about 750

nanosec. Now the argon-spark source can resolve unsteadiness in the flow field because a typical fluid particle in the free stream travels about 1 mm during its spark interval, whereas the same particle travels about 380 mm during the camera flash interval, or about one model length. However the spark location was found to be both difficult to locate and not very repeatable, so that the camera flash pictures were usually much easier to focus, and thus clearer. Also the flash, in effect, produced a time-averaged flow field which, in some cases, made interpretation easier. Hence it was used for most of the schlieren pictures presented here.

A number of surface flow visualization techniques were attempted, but only one was marginally successful. Due to the very low shear stresses and relatively long test section evacuation times, we were unable to find a suitable oil for the oil flow technique, and tried instead the talcum powder technique reported by Needham (Ref. 3.17). If a light dusting of powder was applied to the model surface, a faint image of the boundary layer interaction region could be detected after the run, but accurate measurements of separation length were not possible. Furthermore, it was discovered that the interaction region was greatly extended if too much powder was deposited, so that this technique was used only for diagnostic purposes.

3.4 Experimental Model Development

As noted in Section 3.1, a number of development problems were encountered. They include difficulties in obtaining adequate static pressure response, model blockage effects, and nonuniformities caused by transition of the boundary layer from laminar to turbulent flow. These difficulties and their resolution are described briefly in this section.

3.4.1 Static Pressure Tap Geometry

As originally designed, the exploratory model static pressure taps were connected to the transducers by short lengths of flexible tubing; this was chosen to allow both rapid interchange of taps and transducers and close spacing of taps where necessary. However initial experiments showed that, in order to meet the

response criterion discussed above, the transducers had to be mounted directly in the model close to the pressure taps.

3.4.2 Nozzle Flow Interference by Model

The modifications to the plate-sting connection made to accommodate the new pressure transducer mounting system increased both the bluntness and frontal area of the model, causing the test section flow to become partially "blocked" (Fiore and Law (Ref. 3.21)). A conical compression wave, characteristic of an overexpanded nozzle, was visible in the schlieren photographs; the angle of this wave changed in time indicating that the test section pressure was increasing during the run. Also the apparent strength of the compression wave increased with the degree of obstruction to the nozzle flow.

Because modifications to the sting to reduce both its cross-section and bluntness did not completely eliminate this wave, we decided to verify that the presence of the model in the test section did not change the flow within the volume bounded by the conical compression wave. To this end, a pitot survey was conducted for three cases:

1) with only the pitot rake in the test section, giving negligible blockage effect,

2) with the flat plate located with its leading edge at the nozzle exit plane,

3) with the flat plate leading edge located 50 mm (2 in.) downstream from the nozzle exit.

The results are plotted in Figure 3.4. They show that, while there was variation in pitot pressure ratio spatially, the repeatability from run to run for a given point in the flow field was excellent. For these experiments, the flat plate was levelled with respect to horizontal, but inclined by about 0.5° to the nozzle flow direction and therefore, pitot pressures measured behind the flat plate bow shock were slightly higher. When the bow shock impinged upon the front of a pitot probe, the measured pitot pressures were exceptionally high. Outside the flat plate bow shock, the pitot pressure ratios were nearly identical with and without the model in the test section, indicating that the model's presence had no effect on the flow contained by the conical compression wave.

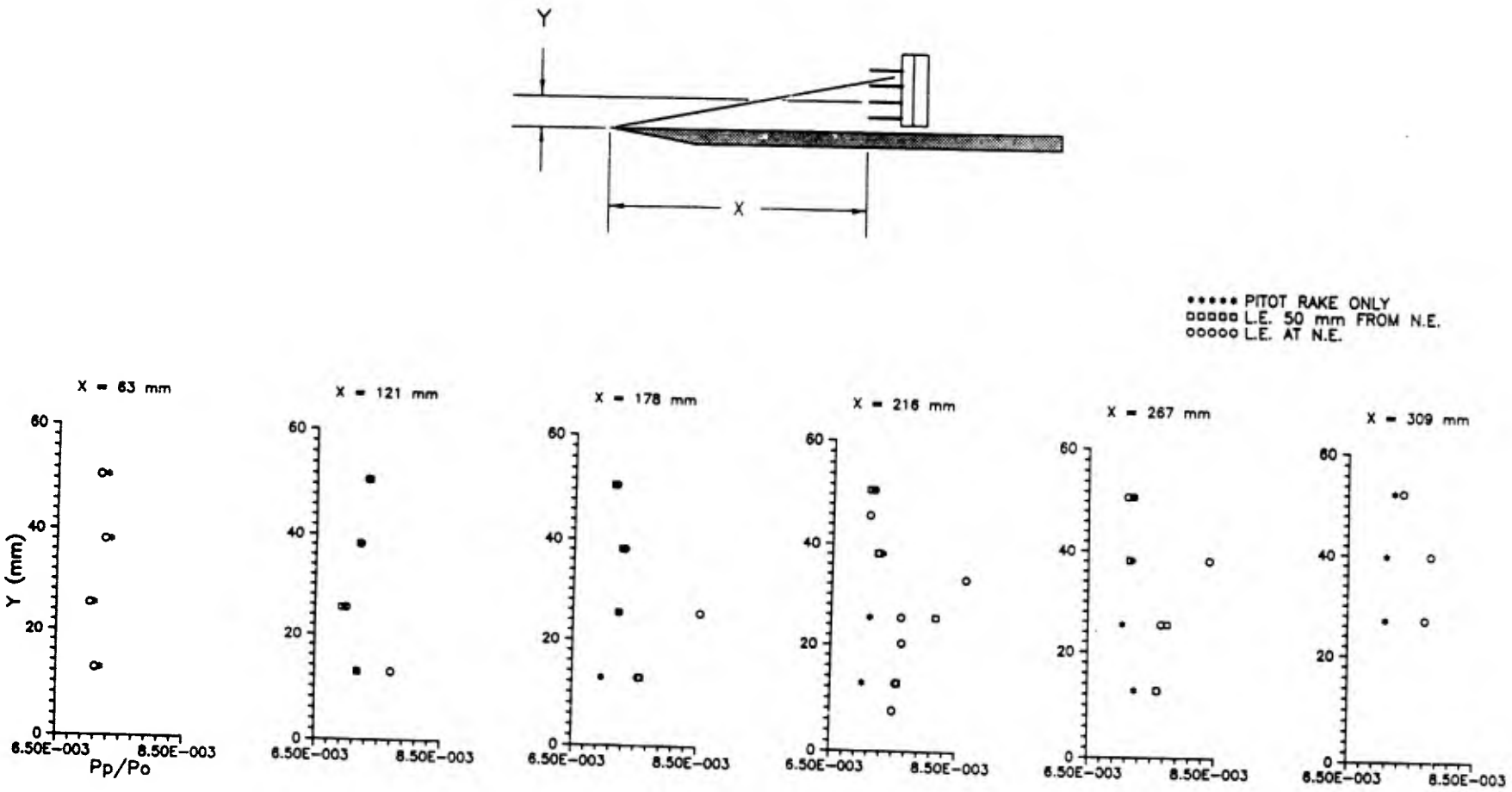

Figure 3.4 Pitot survey along vertical center section of the flow field with and without the flat plate model present.

3.4.3 Study of Edge Effects on the Lateral Pressure Distribution

As a check on the quality of the flow field, using the modified sting configuration, lateral pressure distributions were measured on the plate at x = 7.5 in. (190 mm) from the leading edge. For these tests, $M_\infty = 8.3$ and $Re_u = 24 \times 10^6$/m. The pressures at the plate edges were found to be significantly higher than those nearer the center; furthermore they were increasing in time. Figure 3.5 shows values averaged during the standard interval of 18 to 23 millisec. as a function of transverse distance Z from the centerline.

Two possibilities were considered:

1) high pressure air from the underside of the model was causing flow around the edges to the top surface,
2) the conical compression wave originating at the nozzle exit plane was intersecting and sweeping over the model surface during the run.

To check the first possibility, 1.5 in. (38 mm) skirts extending downward were added to the sides of the flat plate, and the supporting sting was moved rearward. While this markedly improved the uniformity of the lateral static pressure distribution, as shown in Figure 3.5, higher pressures were still observed near the model edges .

Schlieren photographs were used to determine the locus of the intersection of the conical compression wave and the top surface of the model. At the time of the schlieren photograph, which was taken during the averaging interval, the compression wave would have intersected a line through the lateral static pressure taps about 1.9 in. (48 mm) from the centerline. This corresponded to the point where the mean lateral static pressure began to increase towards the model edges, as shown in Figure 3.5.

As a direct result, tests were undertaken to ascertain the effect of model width and flow field conditions on the blockage effect. For these tests, pressure taps were installed 0.375 in. (9.5 mm) apart, at x = 4.00 in. (102 mm) and 8.00 in. (203 mm). The plate width W was reduced progressively from 6 in. (152 mm) to 4.5 in. (114 mm) in 0.75 in. (19 mm) increments. This model was fitted with 1 in. (25 mm) skirts. Two flow field conditions were used for these tests. For condition "A", $p_1 = 200$ kPa and, with the plate aligned to the flow, $M_\infty = 8.3$ and $Re_u = 2.4 \times 10^6$/m. For condition "B", increasing p_1 to 600 kPa and

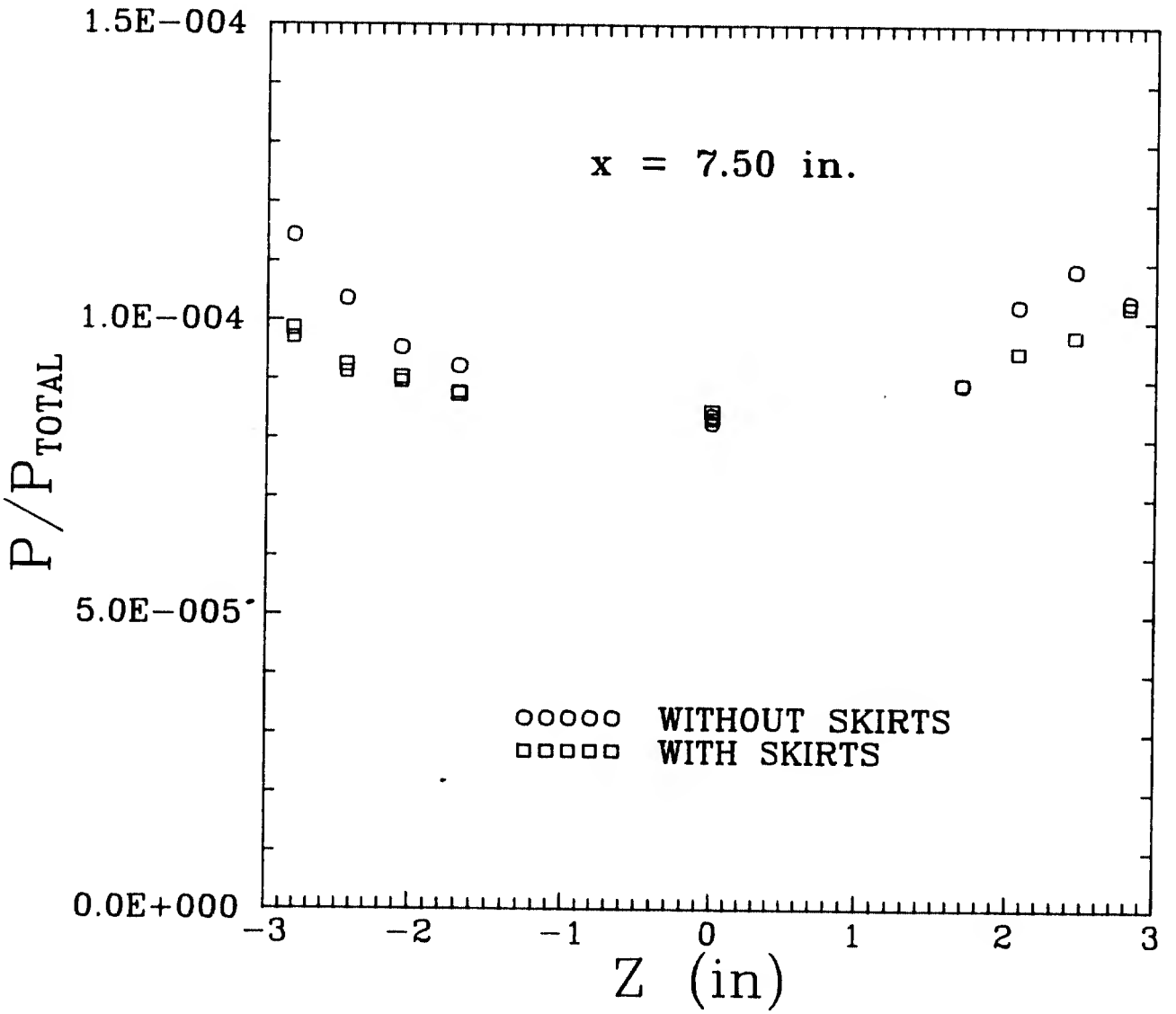

Figure 3.5 Lateral static pressure distribution on flat plate with and without skirts installed.

inclining the flat plate by 4 ° to the flow, the equivalent $M_\infty = 7.3$ and $Re_u = 63 \times 10^6$/m. These conditions represented the limits suitable for boundary layer studies in the present facility.

For flow condition "B", the lateral static pressure distribution is fairly uniform in the neighbourhood of the plate centerline, but trails off at both edges. For W = 6 in., the pressure distributions averaged during the standard interval are plotted in Figure 3.6, and the static pressure ratios in space and time are plotted in Figure 3.7. At x = 4 in., the static pressure is fairly uniform within 2 in. (50 mm) of the model centerline. However, at x = 8 in., the uniform pressure region decreases to 1.5 in. (38 mm) on each side of the centerline. As the width of the plate was reduced from 6.0 in. to 5.25 in. (133 mm) and 4.5 in. (114 mm), the uniform pressure region decreased proportionally while the centerline pressure remains constant.

For flow condition "A", the lateral static pressure distribution is quite different. Figure 3.8 gives the static pressure ratio histories for W = 6 in. At x = 4 in., the pressure distribution is quite uniform in both space and time but the pressure is slightly higher near the model edges. However, at x = 8 in., the static pressure at the edges increases significantly near the end of the run. As shown in Figure 3.9, when the width of the plate is reduced to 5.25 in., the higher static pressures at the model edges during the last half of the run have decreased significantly and the centerline pressure remained unchanged.

Based on these results, the width of the model used for the convex corner interaction experiments used W = 5.0 in. (127 mm), and the 1.5 in. skirts were installed. This combination minimized blockage effects while maintaining an adequate width to preserve two-dimensional flow near the centerline of the model.

3.4.4 Boundary Layer Transition in the Interaction Region

Preliminary estimates of test section flow conditions for this tunnel indicated that the boundary layer generated on the exploratory model should be laminar for flow condition "A". It was decided therefore to investigate laminar interactions, especially since investigations based on static pressure measurements and schlieren photography seem more straightforward than when the boundary layer is turbulent. Schlieren photographs for condition "B" suggest that boundary layer transition occurred between x = 6.6 in. (168 mm) and 9.4 in. (238 mm) (see Figure 3.10). The Reynolds numbers Re_x at these locations are

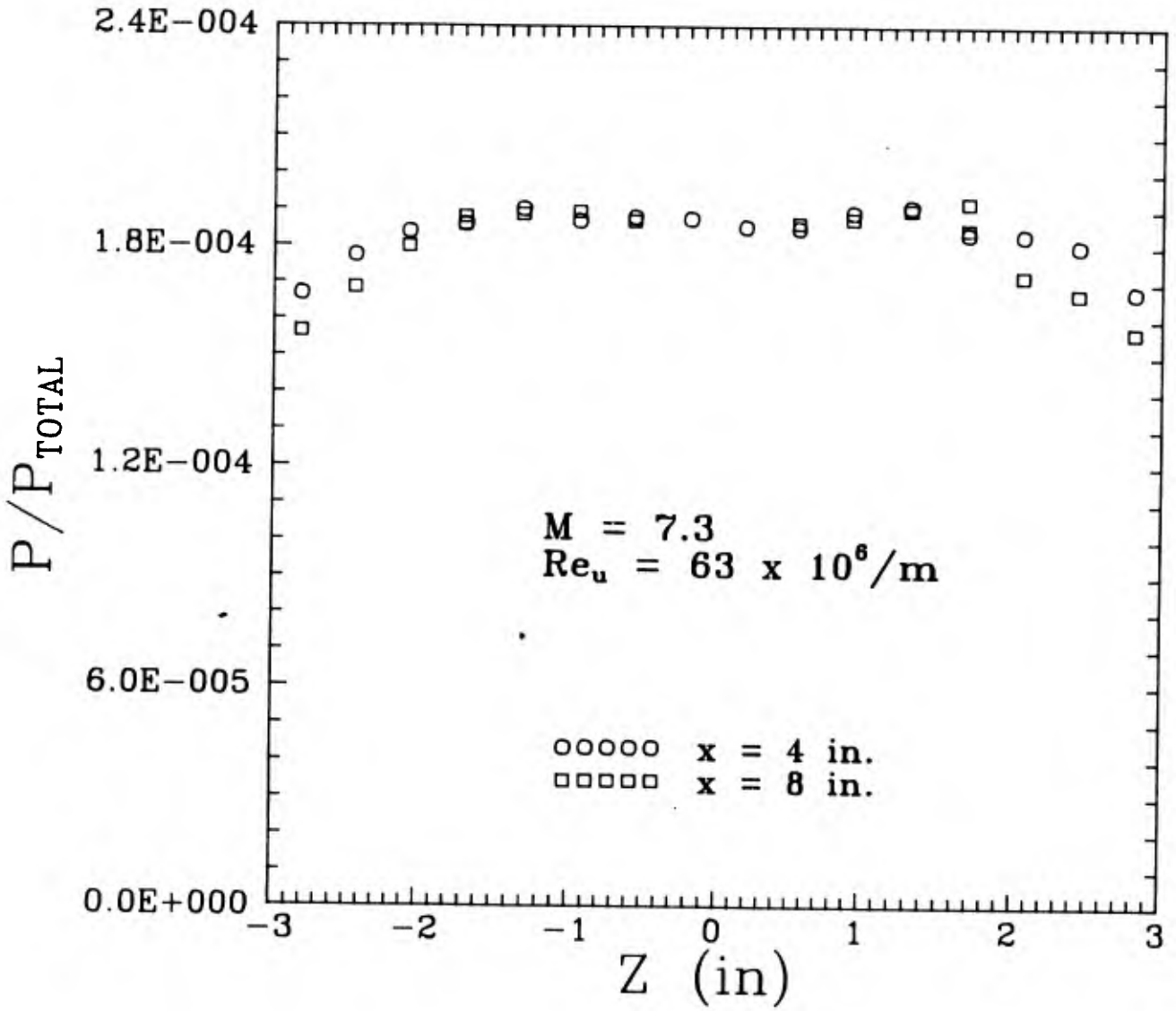

Figure 3.6 Lateral static pressure distribution on flat plate for flow condition "B".

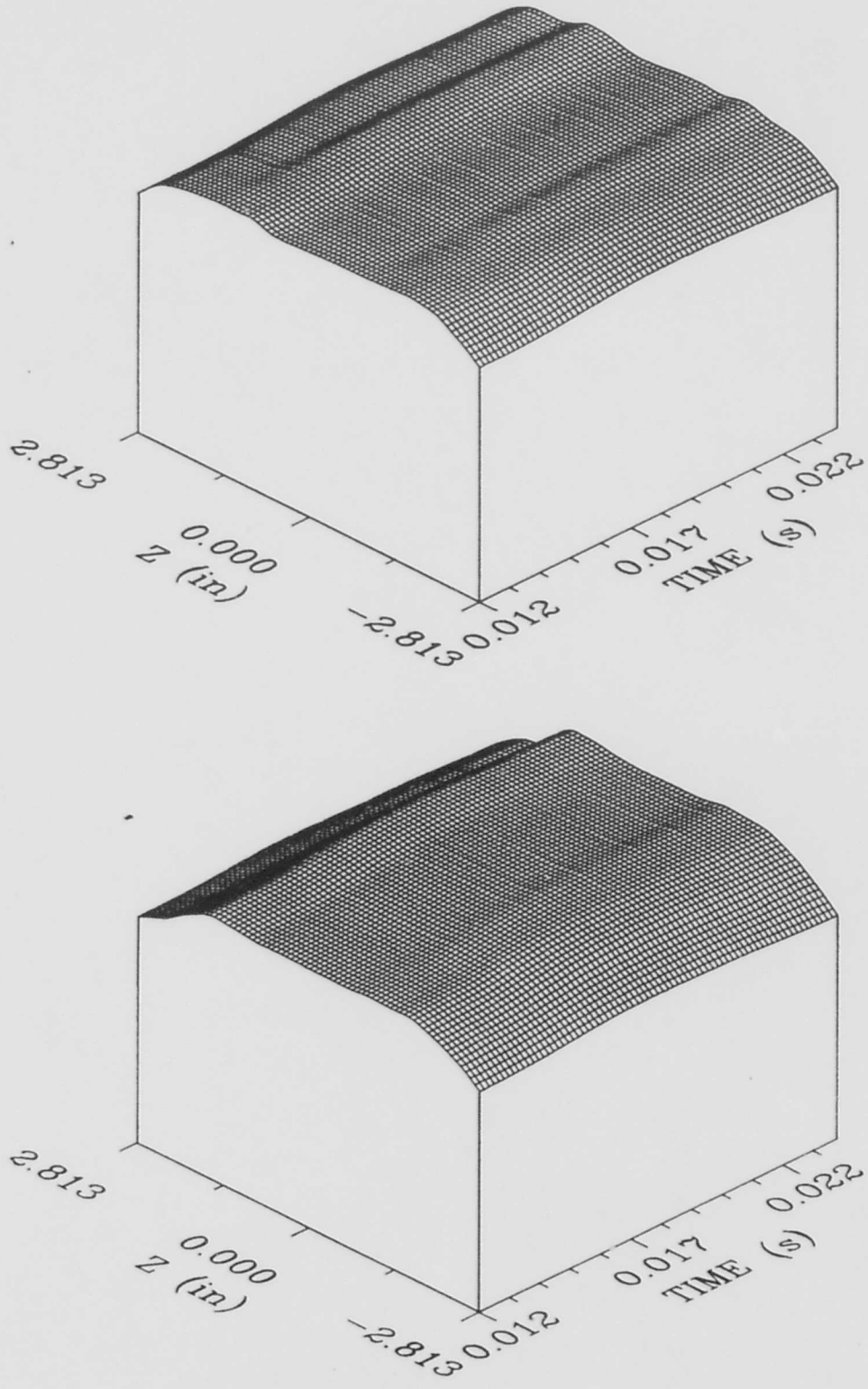

Figure 3.7 Lateral static pressure histories on flat plate measured at x = 4 in. (top) and x = 8 in. (bottom) for flow condition "B" and W = 6 in.

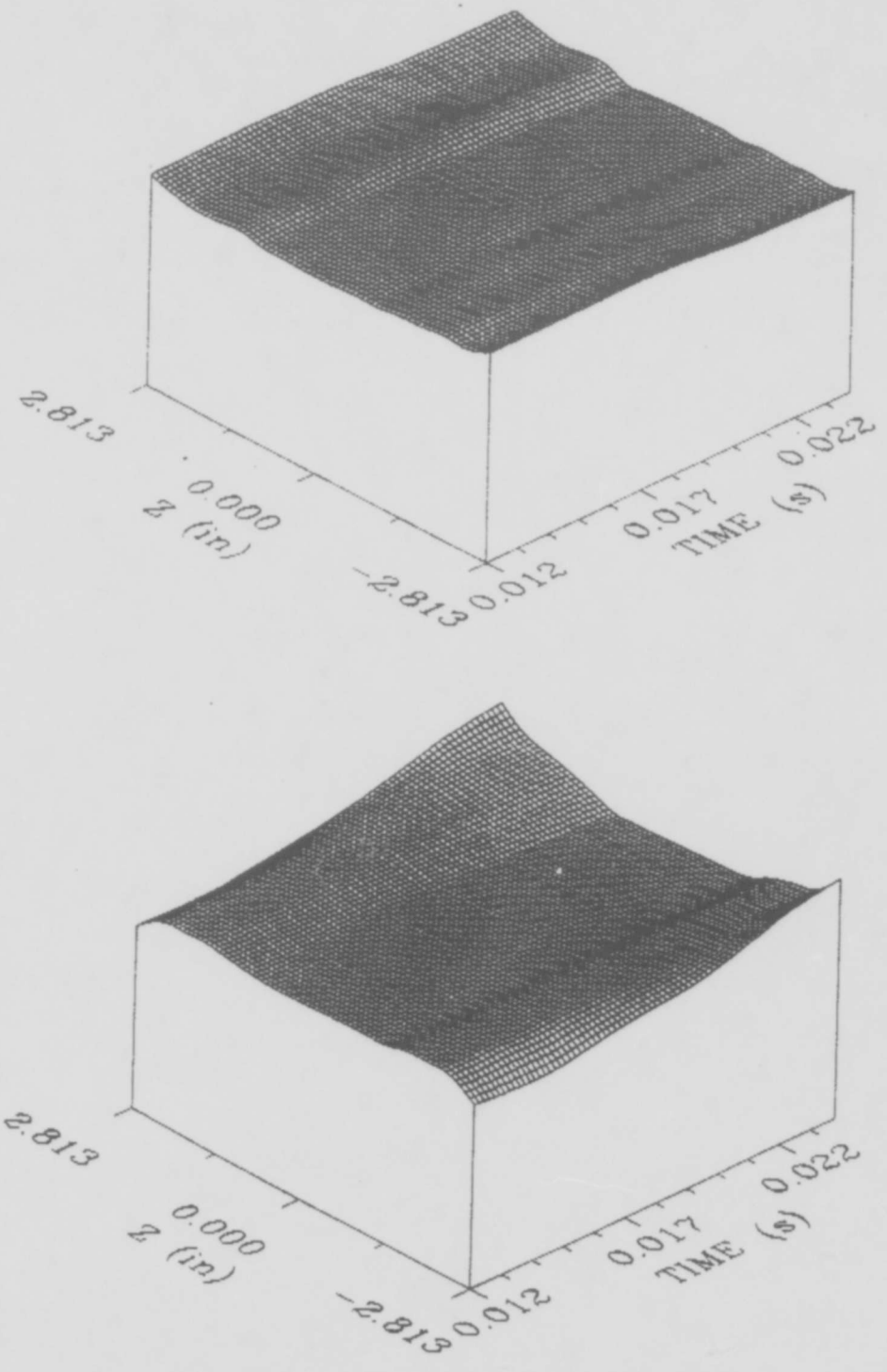

Figure 3.8 Lateral static pressure histories on flat plate measured at x = 4 in. (top) and x = 8 in. (bottom) for flow condition "A" and W = 6 in.

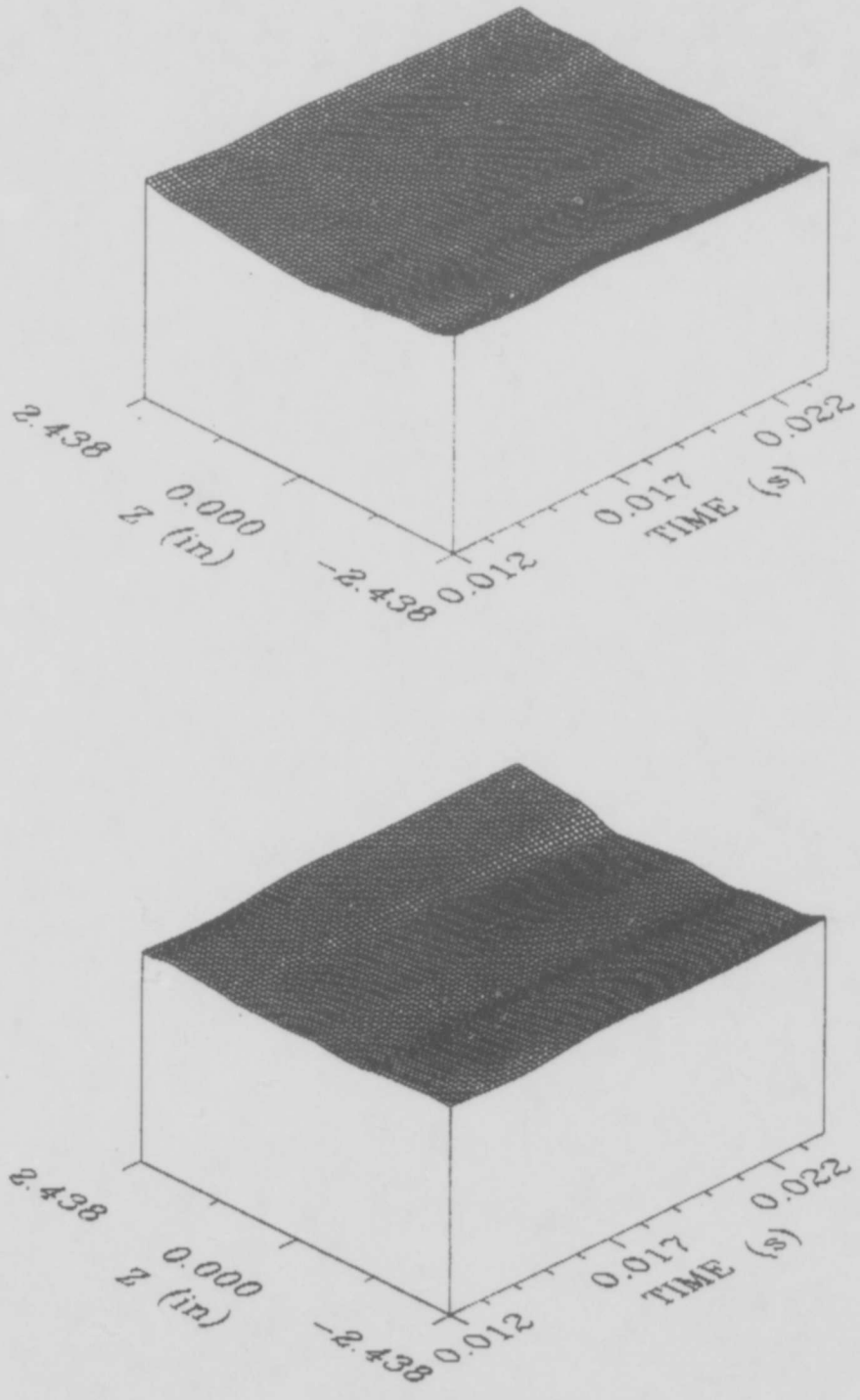

Figure 3.9 Lateral static pressure histories on flat plate measured at x = 4 in. (top) and x = 8 in. (bottom) for flow condition "A" and W = 5.25 in.

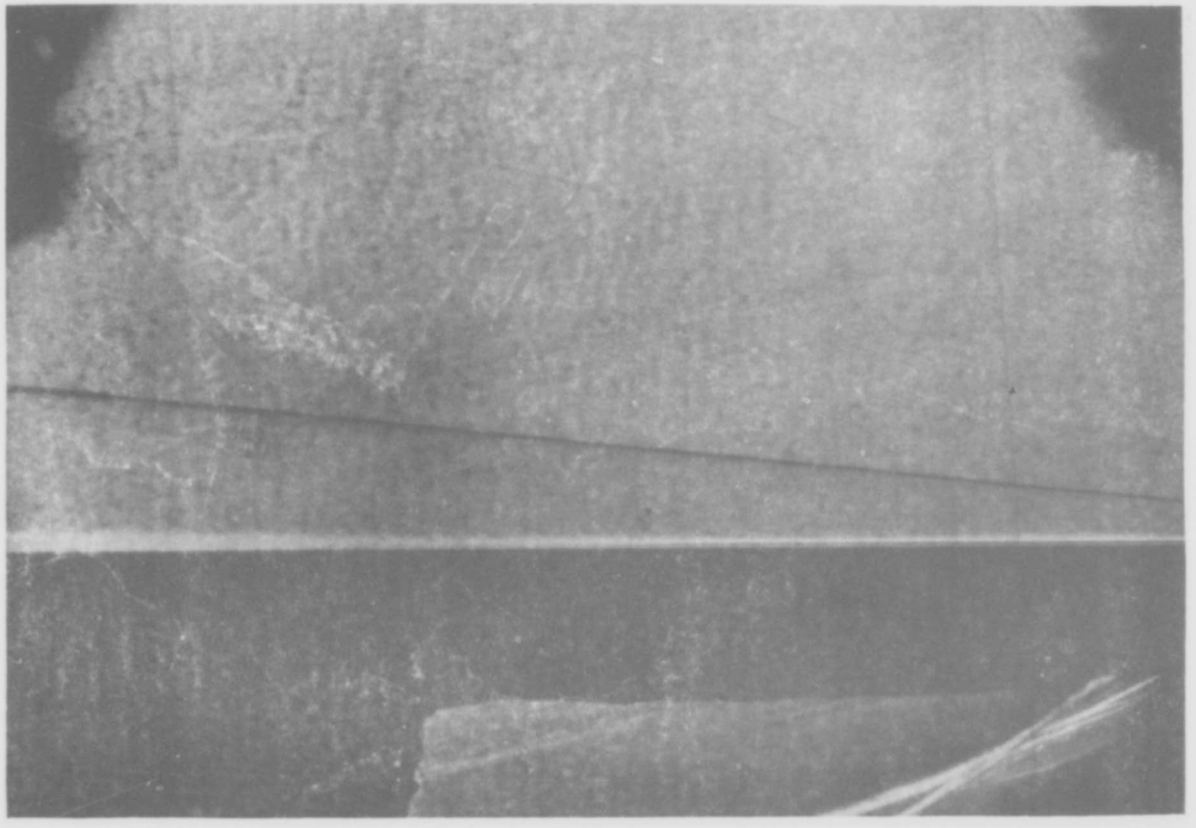

Figure 3.10 Schlieren photograph of flat plate for flow condition "B" showing boundary layer transition.

approximately 10^7 and 1.5×10^7 respectively. These results indicate that a fully turbulent boundary layer that has undergone natural transition is possible in the gun tunnel in its present configuration. However, the working area on a planar two-dimensional model is quite restricted under these conditions and the validity of the two-dimensional assumption is questionable. For flow condition "A" the schlieren photographs indicate that the boundary layer is laminar over the entire length (304.8 mm) of the plate. Using the transition $Re_x = 10^7$, boundary layer transition is not expected on a plate 12 in. long for these flow conditions.

The first series of shock wave-flat plate boundary layer interaction experiments were completed using $p_1 = 400$ kPa, giving $Re_u = 32\times10^6$/m. The incident oblique shock waves were produced by generator angles of 2, 4, 6, 8 and 10° and Re_x at the interaction was about 6.4×10^6. Both surface static pressure measurements and surface flow visualization showed that the separation lengths for these cases were not constant across the width of the model. It was believed that the externally generated shock wave was causing the boundary layer to become transitional during the interaction.

It is well known that the transition Reynolds number in hypersonic wind tunnels decreases as the aerodynamic noise generated by the turbulent boundary layer on the tunnel wall increases, and that smaller tunnels tend to be noisier (Ref. 3.22). Also, a disturbance such as an externally generated shock wave can trigger transition (Ref. 3.23). While the results described above indicate that the flat plate transition Reynolds number is about 10^7, it is uncertain if the transition Re_x is constant over the entire exit area of the nozzle or how it is related to the model size and location with respect to the nozzle exit. In any case, boundary layer transition is an inherently three-dimensional process and unlikely to occur uniformly across the span of a planar model.

The lateral static pressure distribution in the plateau region, plotted in Figure 3.12, indicates that a uniform separated region has not formed. As shown in Figure 3.11, surface flow visualization using talcum powder indicated that the separation length on the left side of the plate (looking downstream) was shorter than on the right side and very irregular (see Figure 3.11). From run to run, the fine details of the separated region on the left side of the plate were not repeatable but the gross features were somewhat consistent. Also, surface static pressures measured through taps on the left side of the centerline indicated a

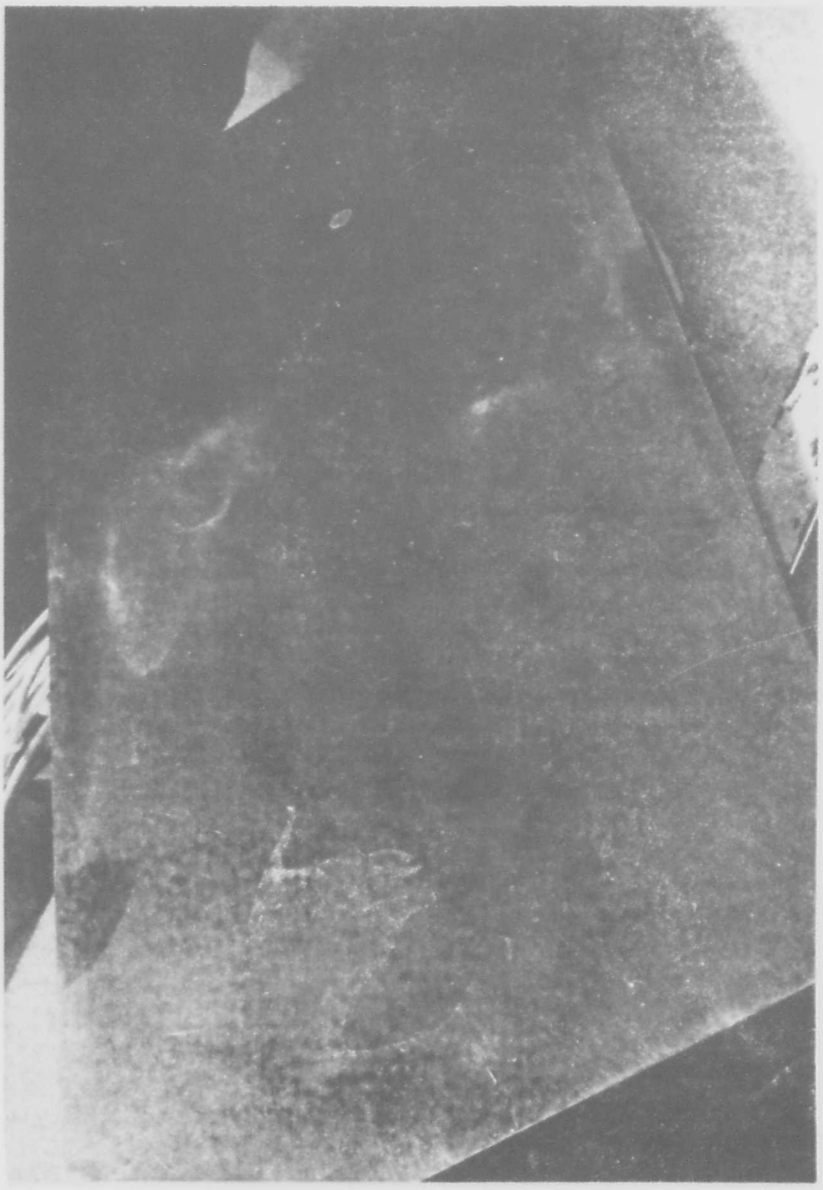

Figure 3.11 Photograph of the talcum powder surface flow visualization obtained during a transitional boundary layer interaction .

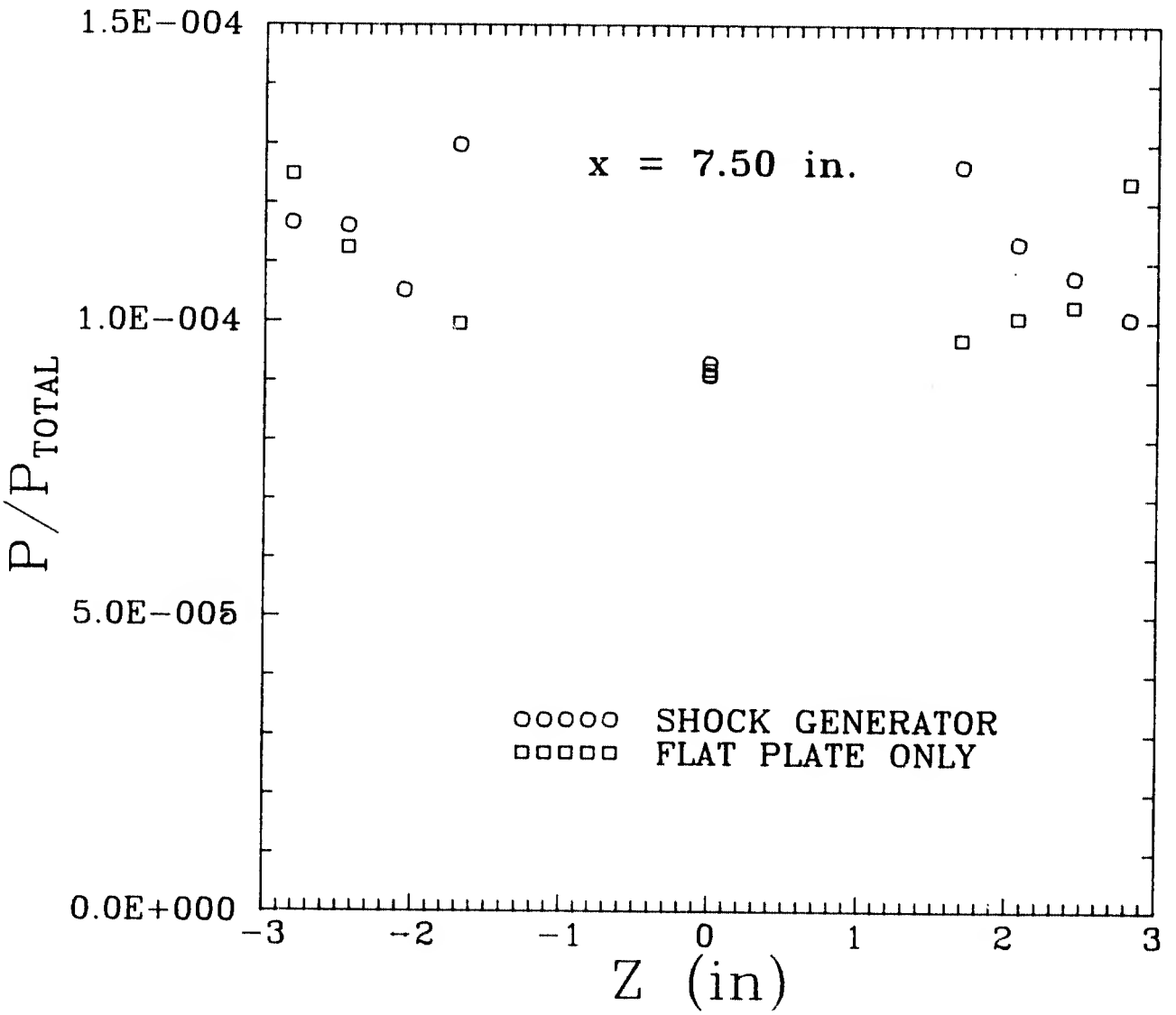

Figure 3.12 Lateral static pressure distribution in the plateau region of a shock wave-flat plate boundary layer interaction.

lower pressure than taps on, or to the right of, the centerline. In schlieren photographs, the separation shock was frequently blurred or two shock waves were visible, indicating that the separation line was not parallel to the axis of the schlieren system.

We believe that the plateau region was not uniform across the width of the plate because of boundary layer transition during the interaction and not due to model edge effects. Chapman et al (Ref. 3.23) reported that the separation length was smaller when transition occurred in the interaction region. While the lower static pressures measured through taps on the left side of center were quite repeatable, the fine details of the surface flow visualization on the left side of the model were not. If the non-uniformity was caused by a model edge effect, it would be expected that the surface flow visualization would be replicated from run to run as well as the static pressure.

Consequently, flow condition "A" was used in all subsequent experiments. In this case the boundary layer in the interaction was still transitional, but the plateau pressure measured on the left side of the model was closer to that measured on the right.

3.5 Results

The results of the experiments described below were obtained after most of the model and experimental procedure development had been completed. However, some modifications to the model and schlieren system were made during the course of these experiments. Because of this and the problems associated with transition in the interaction region, direct comparison of the results from various model configurations must be done with care.

3.5.1 Flat Plate Static Pressure Distribution

The surface static pressure distribution along the chord of the flat plate p_{fp}, in the absence of shock generator or corner, was measured for comparison with subsequent interaction experiments. The plate was 6 in. (152 mm) wide and had been cut at $x = x_c = 8.167$ in. (207 mm), in preparation for the convex corner experiments. The two pieces were carefully butted together, sealed and sanded so that the joint was

smooth. At the hinge line, Re_x was about $5x10^6$, and the viscous interaction parameter χ was about 0.25. The boundary layer thickness at this point δ_0 measured from schlieren photographs, was about 0.09 in. (2.3 mm).

Several runs were required to measure the entire static pressure distribution along the model chord and the measurement repeatability was checked at several locations (see Figure 3.13). A third order polynomial was fitted through the data and the scatter was less than ±2%. The static pressure ratio was not constant along the chord of the plate and this can be attributed to a combination of the following:

- a minor effect due to viscous interaction near the leading edge of the model,
- small variations in local inclination of the model surface to the free stream,
- nozzle blockage effects (discussed earlier), causing the static pressure to rise slightly near the back of the model,
- model edge effects, again, causing the a higher static pressure near the back of the model.

The dominant cause was probably a slight inclination of the rear half of the plate. In spite of careful alignment at the hinge line, the aft section of the plate was not exactly parallel to the forward section. An inclination of about 0.1° would be sufficient to cause the rise in static pressure observed in Figure 3.13.

The static pressure measurements were about 2% higher than inferred from the pitot pressure ratios measured above the plate. This may be due to the difficulty in making accurate static pressure measurements in short duration hypersonic wind tunnels (Rainbird, (Ref. 3.24)). Smaller diameter pressure taps presumably result in more accurate static pressure measurements, however their response to the unsteady pressure in a short duration facility can be very sluggish. To minimize the uncertainty, all surface static pressure measurements from the shock wave-boundary layer interaction experiments were normalized with the flat plate static pressure.

3.5.2 Shock Wave-Flat Plate Boundary Layer Interactions

The flat plate interaction data obtained for technique validation and comparison purposes used four values of shock generator angle θ, with the generator located in each case so that the incoming shock impinged on the

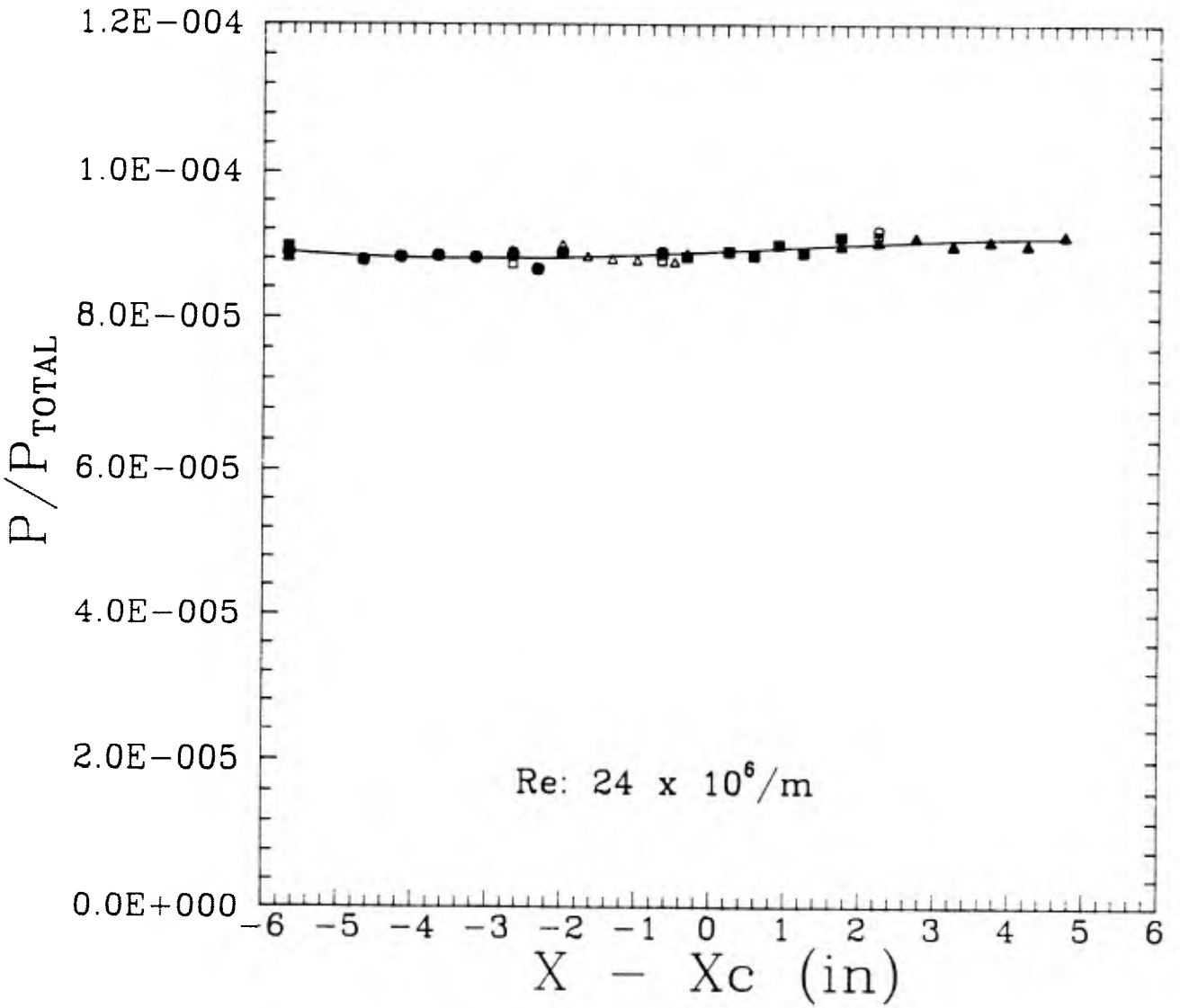

Figure 3.13 Static pressure distribution along the chord of the flat plate model.

boundary layer close to the convex corner hinge line, that is, for x = 8.167 in. The camera flash was used as the schlieren light source. The angle θ was measured prior to each run with an electronic protractor. However, because the generator and flat plate were attached, respectively, to the top and bottom of the test-section owing to wall deformation, their relative positions changed when the test section was evacuated. Consequently θ was determined from the reflected shock pressure ratios and from schlieren photographs. For larger shock generator angles, a slip line, caused by the intersection of the flat plate bow shock and the externally generated shock, was visible in schlieren photographs. The values of θ determined from the pressure ratios and from the schlieren photographs agreed to within 2%.

The static pressure distributions for θ = 2.7, 4.75, 6.6 and 8.5° are plotted in Figures 3.14(a) to 3.14(d) with the experiment numbers given in the legends. These figures also include schlieren flow visualizations enlarged so that their scale corresponds to the horizontal axis of the pressure plot, which is distance downstream relative to the corner hinge-line, $x - x_c$. The pressures have been nondimensionalized by p_{fp} measured at $x = x_c$ in the basic flat plate results of Figure 3.13. In each case, the results from individual tunnel runs have been plotted to indicate the degree of repeatability. In this connection the data in Figure 3.14(d) includes measurements taken both in the presence and absence of surface flow visualization talcum powder. In these figures, a line has been drawn through the data using the schlieren photographs as a guide to locate the important features of the interaction. Based on the pressure measurements and schlieren photographs, we believe this to be the best estimate of the pressure distribution through the interaction for most of the model width. However, in Figure 3.14(d), our best estimate near the separation region bears no resemblance to the data recorded when talcum powder was used, but reflects the observations made using schlieren photographs taken when powder was not used. The measurements showing an exaggerated plateau region evident in run 1-126 (Figure 3.14(d)) have not been used in the construction of the best estimate of the pressure distribution.

The results display the basic features characteristic of this type of interaction; that is, the plateau pressure is essentially independent of θ, and the pressure downstream of the interaction, p_d approaches the ideal reflected shock pressure. However, as stated earlier, the impingement of the shock wave causes the boundary layer to become transitional during the interaction and has resulted in a very uneven separation

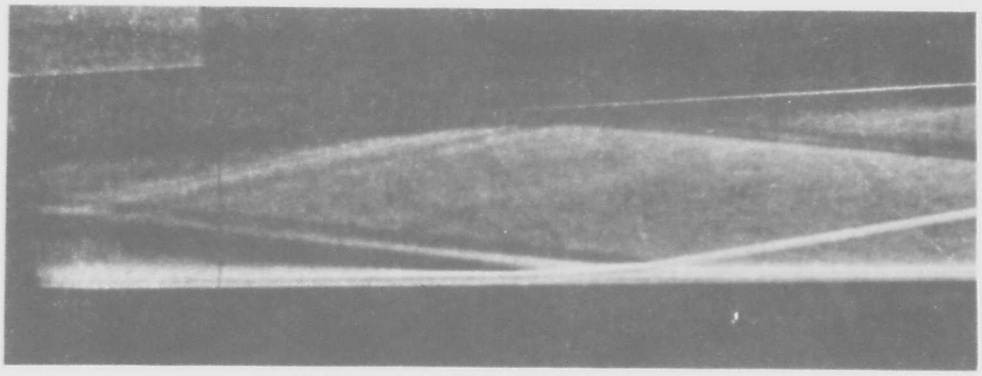

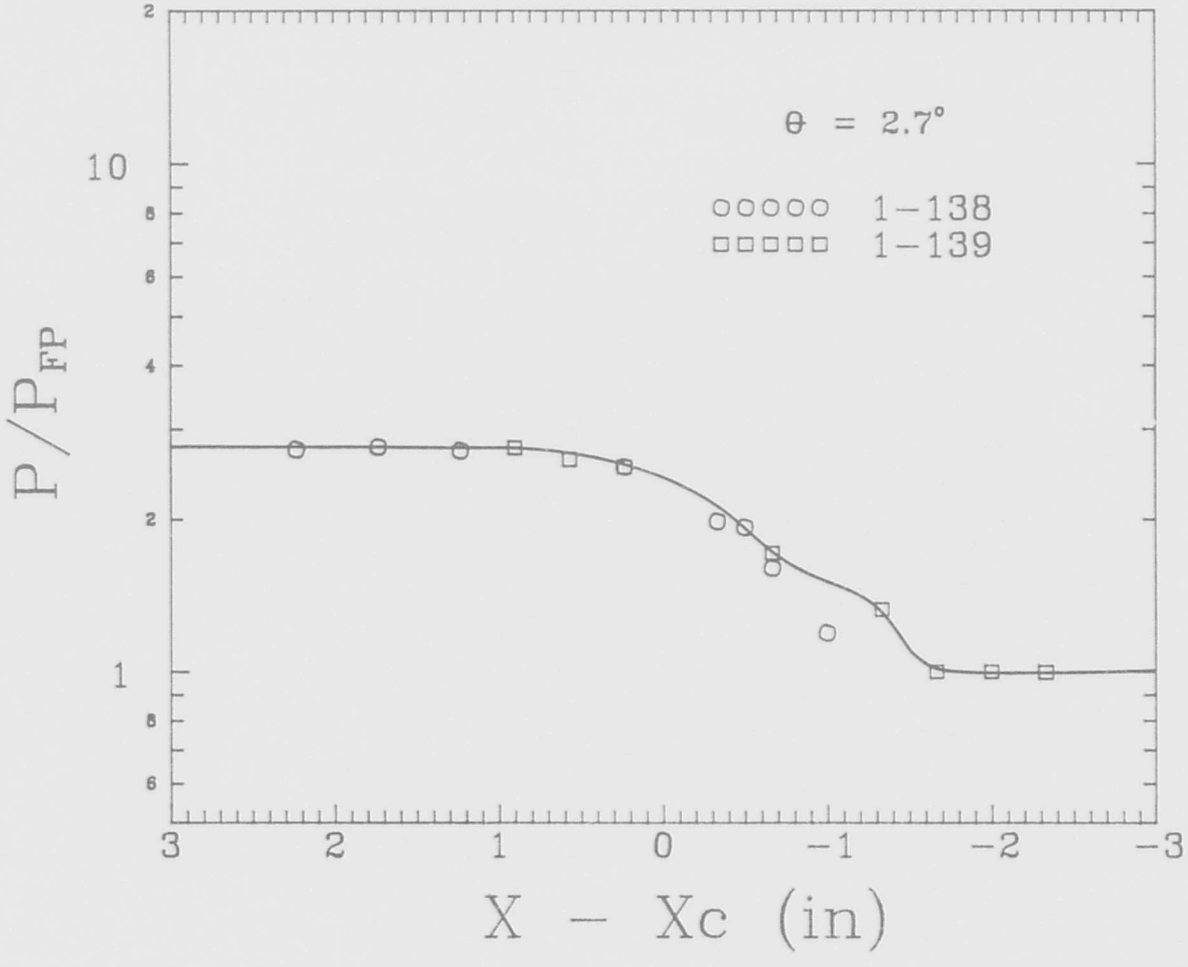

Figure 3.14.a Static pressure distribution and schlieren photograph of a shock wave-flat plate boundary layer interaction for shock generator angle $\theta = 2.7°$, $M_\infty = 8.33$ and $Re_x = 5\times10^6$. The ideal reflected shock pressure ratio is $p_d/p_{fp} = 2.76$.

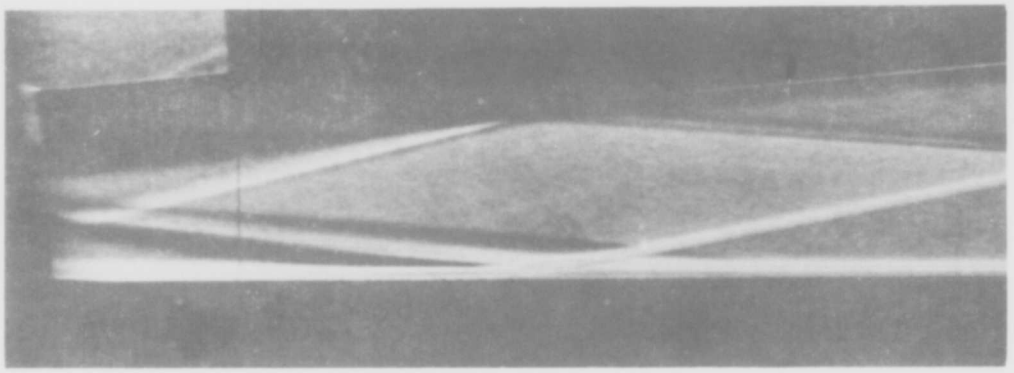

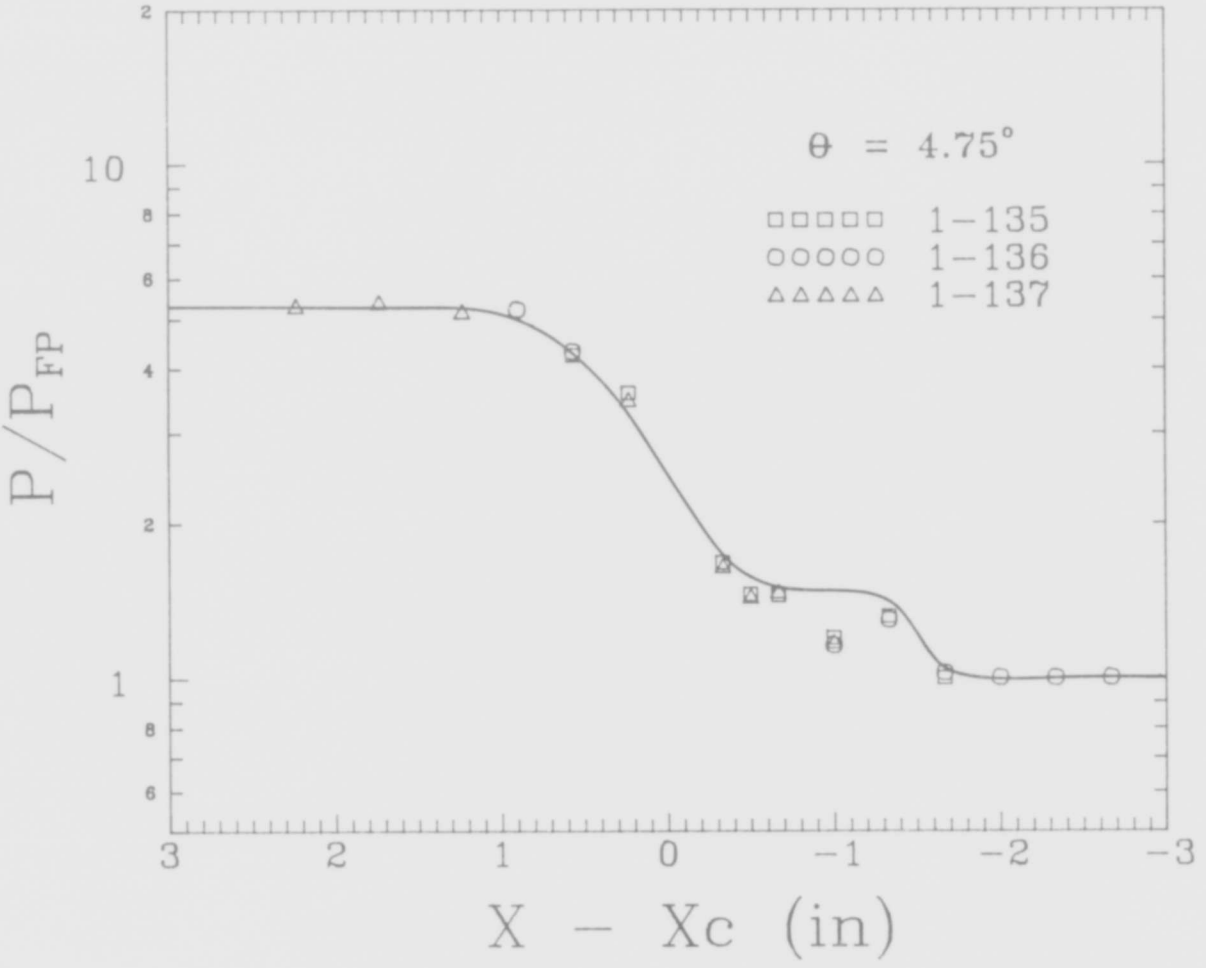

Figure 3.14.b Interaction for $\theta = 4.75°$, $p_d/p_{fp} = 5.35$.

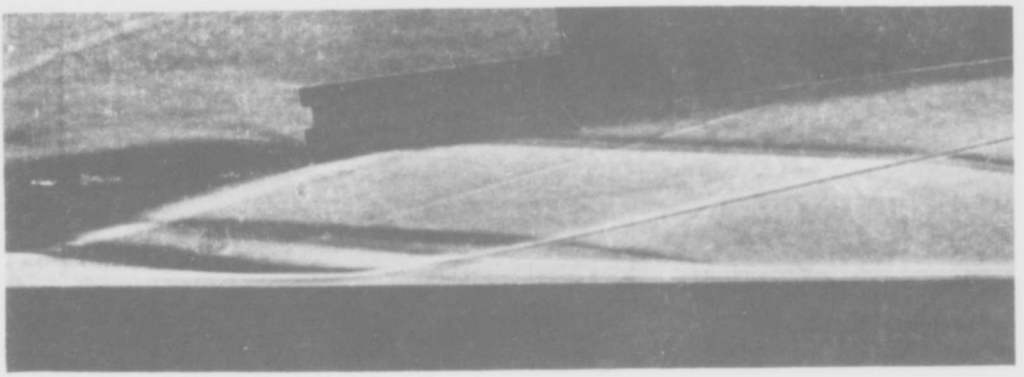

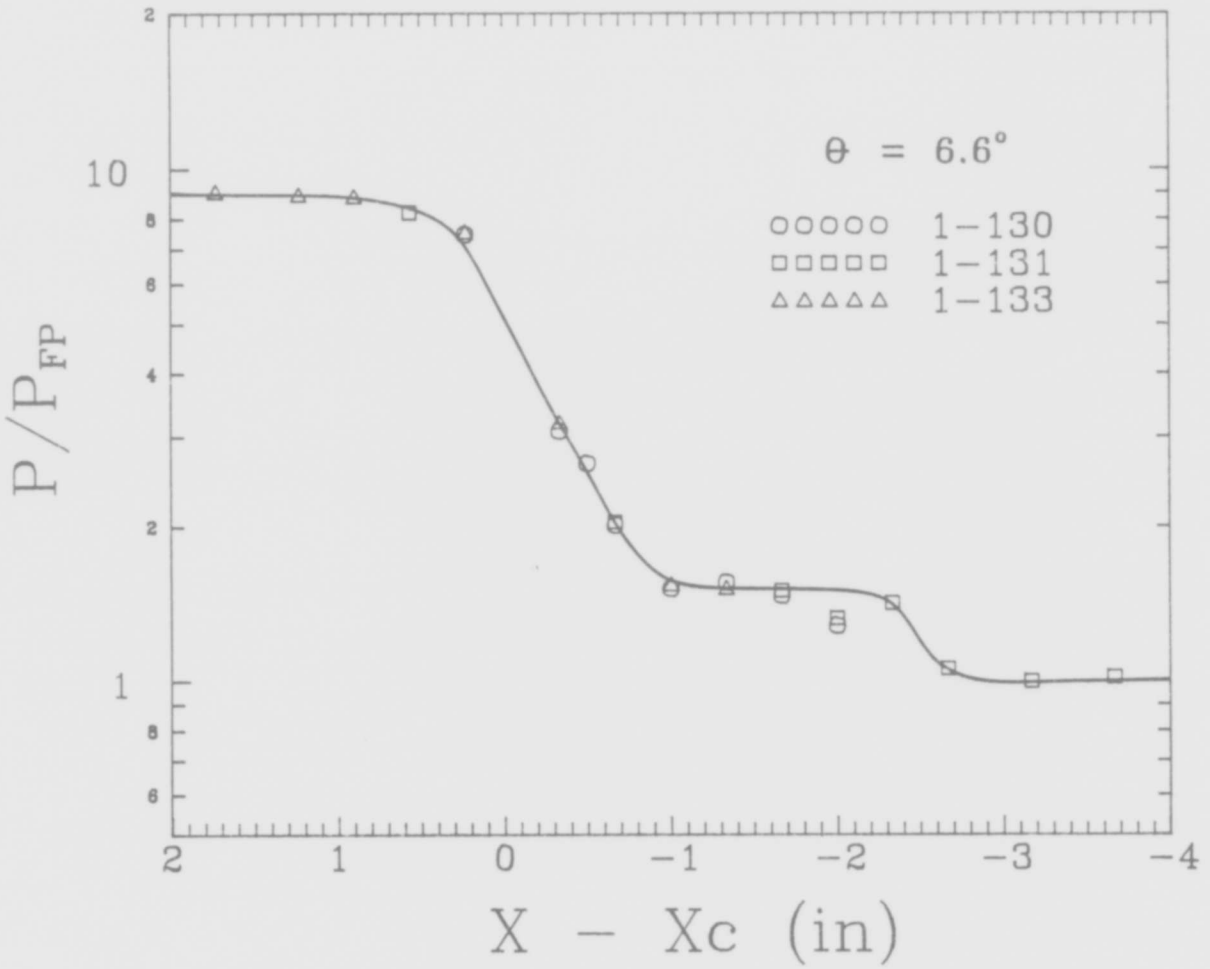

Figure 3.14.c Interaction for $\theta = 6.6°$, $p_d/p_{fp} = 8.98$.

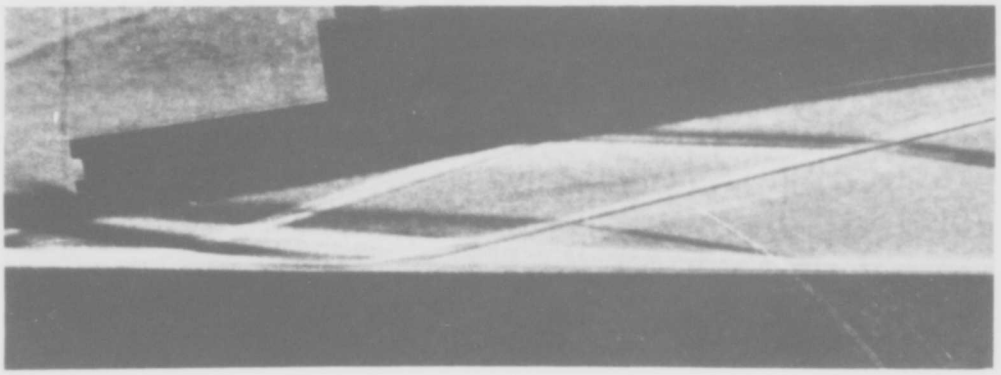

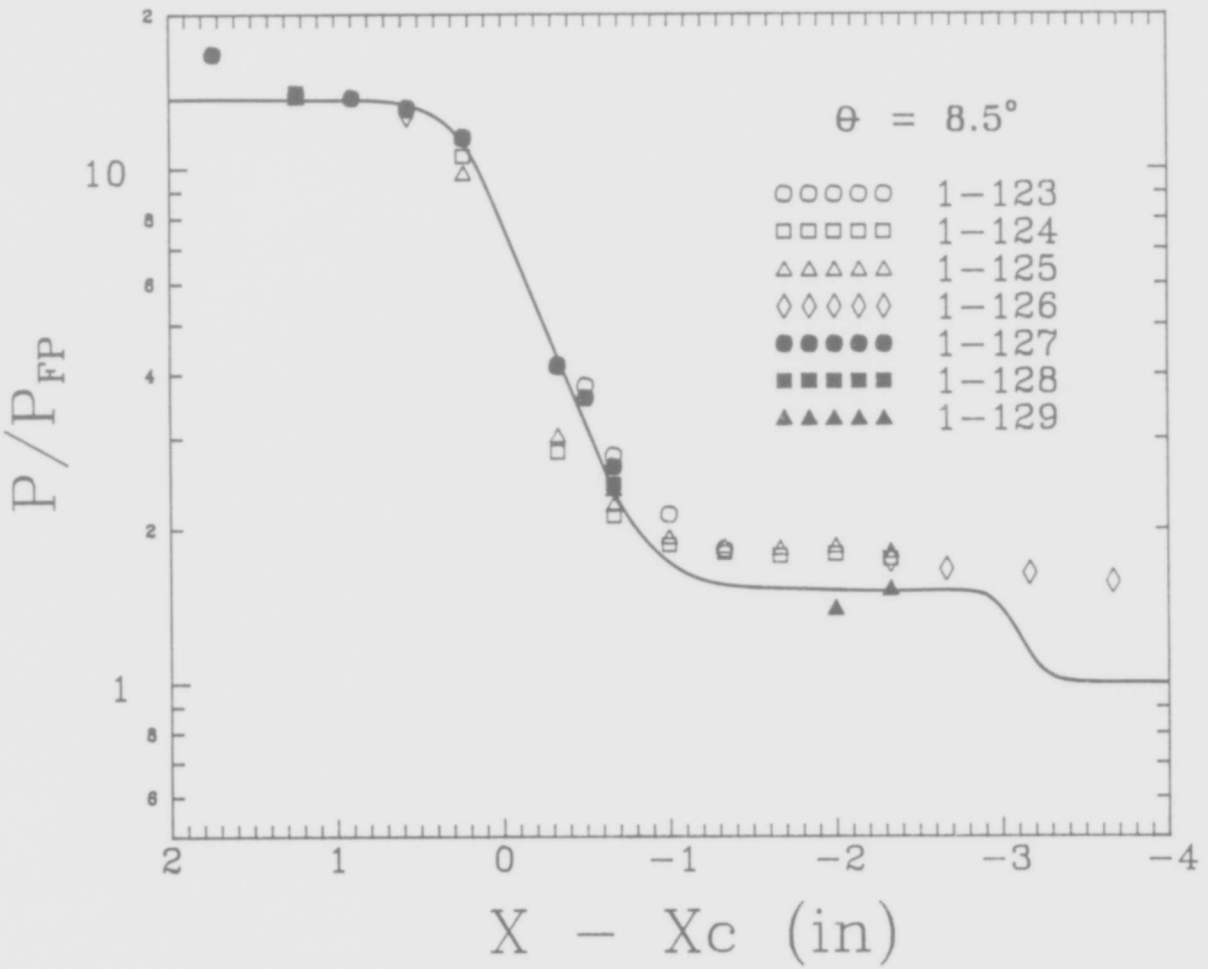

Figure 3.14.d Interaction for $\theta = 8.5°$, $p_d/p_{fp} = 14.3$.

line. Static pressures measured on the left side of the model in the plateau region are less than the corresponding measurements on, and to the right of, the centerline. The plateau pressure predicted by a correlation reported by Needham & Stollery (Ref. 3.25) is about 5% higher than that inferred from Figures 3.14(a) to 3.14(d).

The separation and reattachment points have been estimated from the static pressure data and schlieren photographs. The spatial resolution of the pressure taps was insufficient to capture the features of the free interaction region so that the separation point cannot be determined from static pressure data alone. The separation point was estimated from schlieren photographs by locating the point of intersection of the separation shock and the edge of the deflected boundary layer in the separated region. In some photographs, the separation shock was difficult to locate precisely, either because it was weak or because a double image appeared if the separation line was not parallel to the optical axis. Estimates of the separation and reattachment locations were made by comparing all of the relevant photographs to the plot of pressure data.

The pressure ratios across the flat plate interactions are plotted against the separation and plateau lengths in Figure 3.15. The separation length is taken to be the distance between the separation and reattachment points, and the plateau length is the distance between the separation point and the end of the region of constant pressure. A line has been fitted through this sparse data and, by extrapolating back to a separation length of zero, the pressure rise for incipient separation has been estimated. The shock generator angle θ required for incipient separation, based on the plateau length, is about 1.2°, or a pressure ratio $p_d/p_{fp} = 1.6$. A correlation for laminar boundary layer interactions given by Needham & Stollery (Ref. 3.25) predicts an incipient separation angle of about 2.4 °, or a pressure ratio of 2.5, and Watson et al (Ref. 3.26) predict an angle of about 2.0°, or a pressure ratio of 2.2. However, two points must be considered in this comparison:

1) the boundary layer in this study undergoes transition during the interaction, so that direct comparison to the published correlations may not be appropriate,
2) the data in Figure 3.15 is very sparse, especially near incipient separation, and this simple logarithmic means of prediction may not be very accurate.

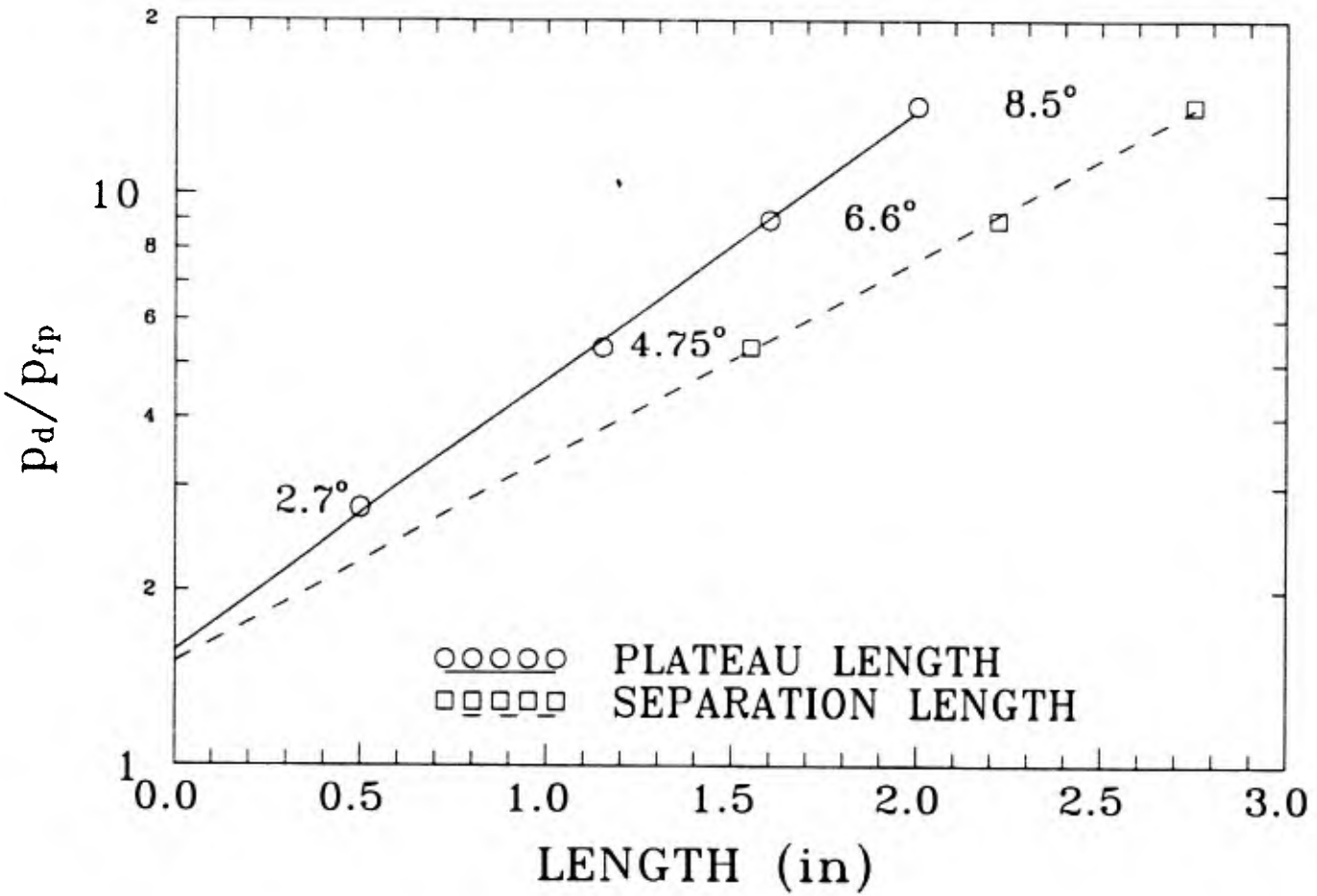

Figure 3.15 Plot of separation and plateau lengths used to estimate the shock generator angle required for incipient separation.

The present results, on their own, are thus of limited value. Nevertheless, because the convex corner experiments are performed with the interaction region in the same location, this data provides a baseline to determine the effect of the convex corner on the shock wave-boundary layer interaction.

3.5.3 Convex Expansion Corner Measurements

Two corner angles, $\alpha = 5°$ and 10° were selected for the convex corner interaction measurements. Because the case in which the incoming shock intersects the boundary layer downstream of the corner is of practical significance, pressure distributions were obtained with the convex corner installed and the shock generator removed. In this case the corner generated an expansion. For $\alpha = 5°$, W = 6 in. (152 mm) whereas for $\alpha = 10°$, W = 5". In both cases, the forward section of the model was aligned to the flow so that $M_\infty = 8.3$ and $Re_u = 24 \times 10^6$/m. The measured surface static pressure distributions are plotted in Figures 3.16 and 3.17, which also include scaled schlieren visualizations. In both cases the downstream pressure corresponding to a centered inviscid Prandtl-Meyer expansion is marked.

For $\alpha = 5°$, the static pressure does not reach a constant value until about 2.75 in. (70 mm), about 30 δ_0, downstream from the corner. This is consistent with an analysis by Sullivan (Ref. 3.27) for this flow. The spatial resolution of the pressure measurement taps near the corner is insufficient to measure any upstream influence of the expansion process. There is, however, a 15% difference between the final static pressure ratio measured downstream from the expansion corner and the predicted inviscid value. At this time, the reasons for this discrepancy are not known. Small changes in α can cause large changes in static pressure downstream of the expansion fan, but in this case, a decrease in α of 0.5° would be required to account for the difference reported here. However, α is within 0.1° of the nominal 5°, and it is unlikely that it changed during the test section evacuation or during the run. Downstream from the expansion, the pressure transducers are operating in the bottom 2% of their range and the resulting resolution of the digital data recorders is about 1.5% of the measured pressure. Based on the results of Rainbird (Ref. 3.24), who reported on the effect of pressure tap diameter on the error in measured static pressure in high speed wind tunnels, the error in these pressure measurements should be small. The histories for pressure taps near the

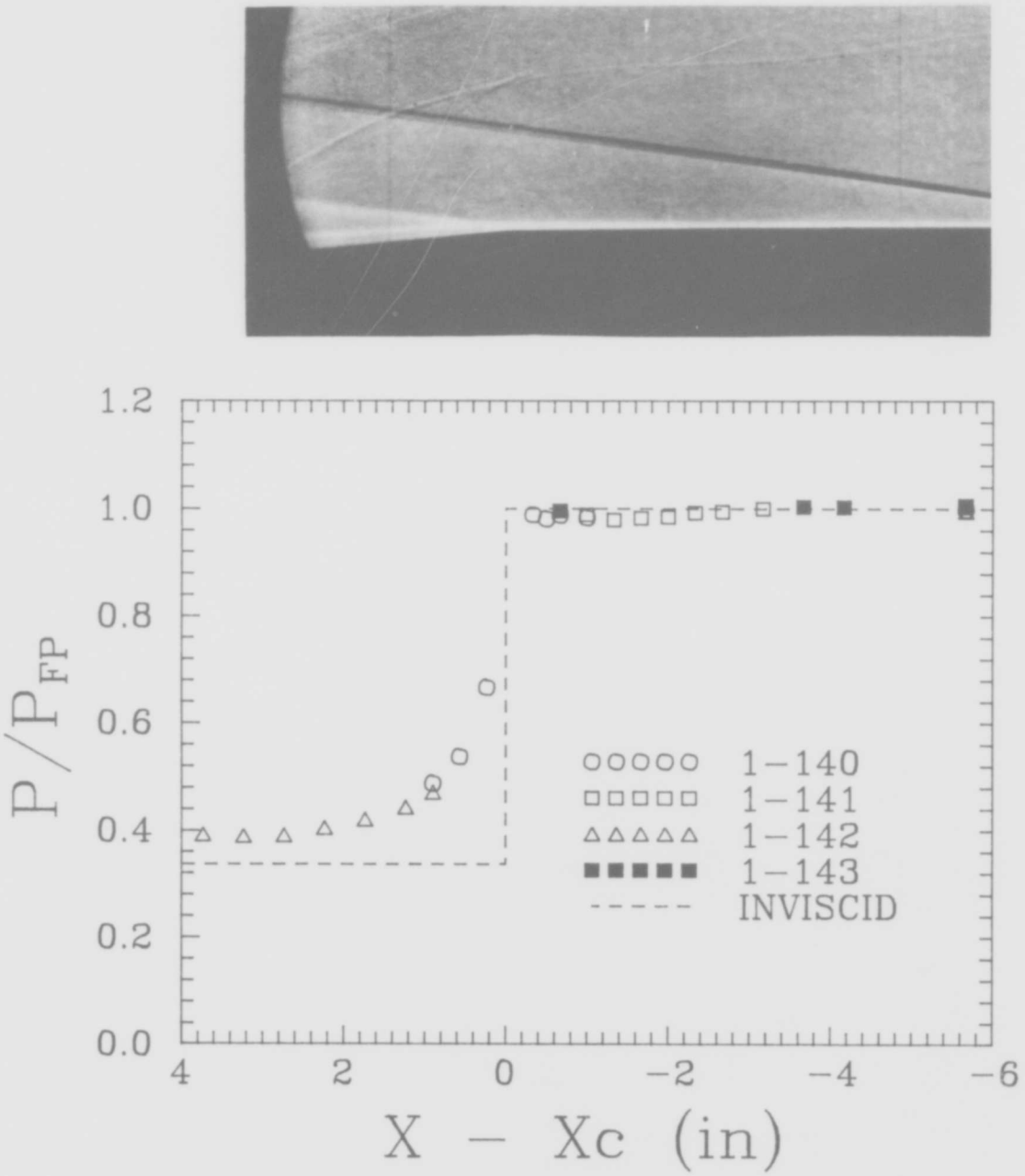

Figure 3.16 Static pressure distribution over a 5 degree convex corner.

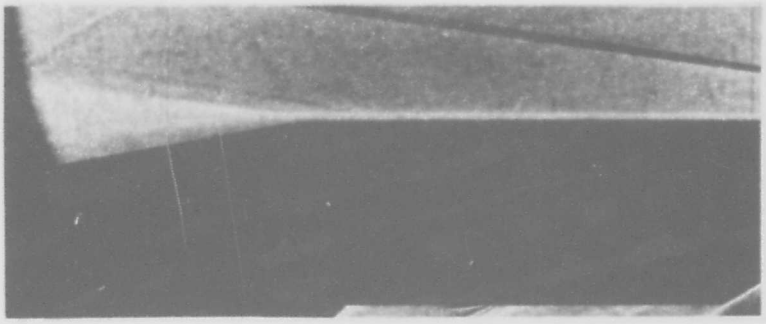

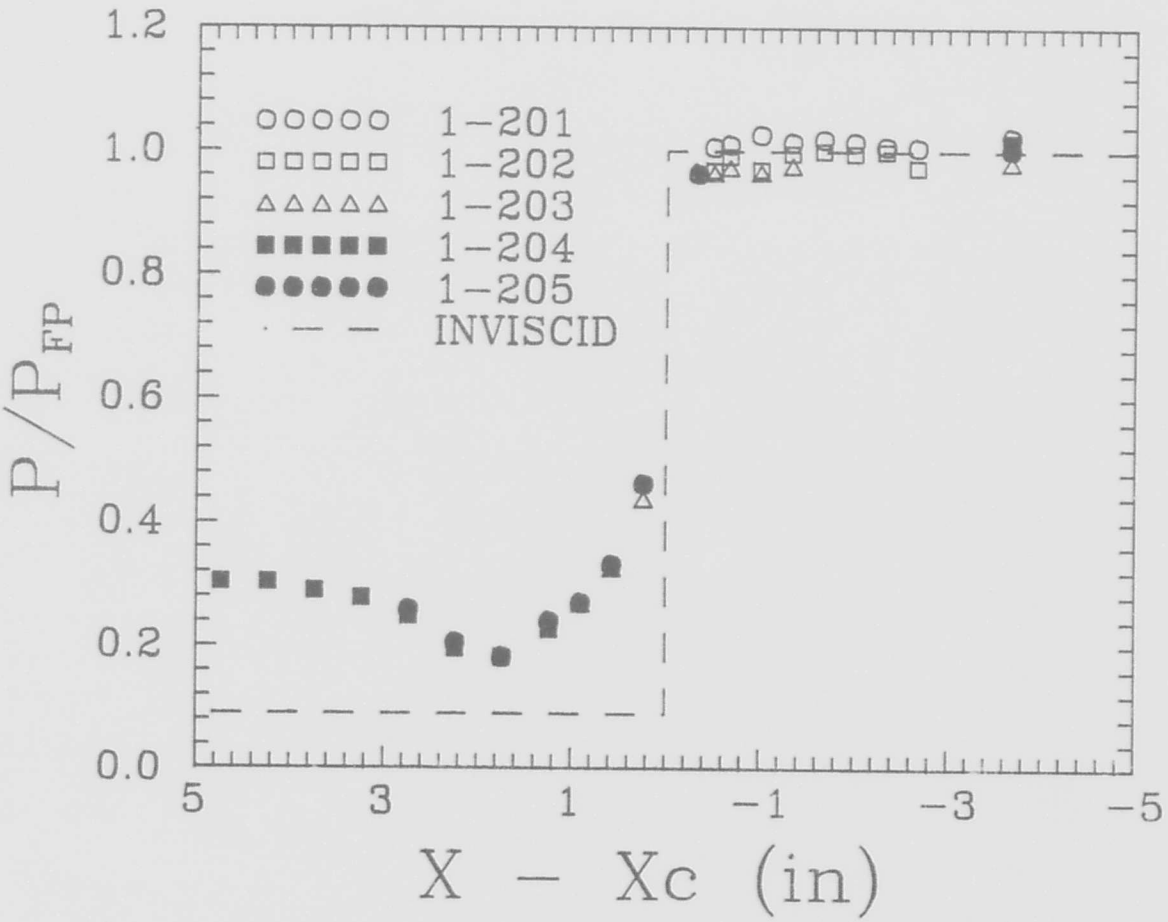

Figure 3.17 Static pressure distribution over a 10 degree convex corner.

downstream end of the model did not indicate the presence of a higher pressure region moving upstream from the back of the plate during the latter part of the run. However, the static pressure in this region is about one third of the free stream static pressure, so that it is possible that incoming flow around the edges of the model downstream from the convex corner have influenced it. Transverse measurements downstream of the corner would be needed to confirm this.

For $\alpha = 10°$, the static pressure histories for the downstream measurement stations show a higher pressure region moving upstream from the back of the model during the course of the run. The magnitude of the mean static pressure ratios plotted in Figure 3.16 reflect how far the high pressure front moves upstream during the run. It appears that if the measured static pressure had reached the inviscid static pressure, the distance required would have been about 3 in. (75 mm), or about 33 δ_0 .

3.5.4 Shock Wave-Boundary Layer Interactions at Convex Corners

For the convex corner interaction experiments, the shock generator was installed so that it was parallel to downstream section of the model to within 0.1°, that is, α approximately equal to θ. The shock wave impingement point was adjusted by translating the generator plate as required vertically and in a streamwise direction.

The centerline surface static pressure distribution was measured for several shock impingement points x_i upstream and downstream of the convex corner. For $\alpha = 5°$, schlieren photographs were taken with the argon-spark light source, while for $\alpha = 10°$ the camera flash was employed. Because, as noted above, the shock generator plate changed both angle and position with respect to the convex corner model during the evacuation of the test section, the geometry of the flow field was verified by measuring the angles of shock waves, slip lines and the edge of the boundary layer in schlieren photographs. The measured static pressures and schlieren photographs were used to construct the best estimate of the static pressure distribution through the region influenced by the externally generated shock wave and the expansion corner. As in the case of the flat plate interaction discussed above, the measured static pressure in the plateau region

was lower on the left side of the model and this was attributed to an uneven separation line caused by boundary layer transition during the interaction. The "best estimates" were used to:

- identify separated regions and separation points,
- measure plateau pressures and plateau lengths,
- determine the important features of the interaction process for the various shock impingement points.

The results of the experiments for $\alpha = 5^\circ$ are plotted in Figures 3.18(a) to 3.18(g) together with scaled schlieren flow visualizations. The externally generated shock wave intersects the edge of the boundary layer between 1.0 in. (25 mm) upstream ($x_i - x_c = -1.0$) and 0.46 in. (12 mm) downstream of the corner ($x_i - x_c$) = +0.46). When the shock impinges well upstream of the corner, the boundary layer is separated and in the separation region, the static pressure distribution is similar to the one shown in Figure 3.14(b) for the flat plate interaction. In this case, the compression and expansion interactions are not completely decoupled and the plateau length is only 60% of the flat plate interaction plateau length. Also, the plateau pressure for the present configuration is slightly lower than the flat plate case. As the shock impingement point moves downstream towards the corner, the separation region begins to disappear. In Figure 3.18(d), a separation shock is not visible and the static pressure distribution and schlieren photograph do not show the characteristics of a boundary layer separation. When the shock wave hits the boundary layer right at the corner, the static pressure rises smoothly through the interaction (Figure 3.18(e)). When the incident shock impinges downstream of the convex corner, the boundary layer edge continues past the corner until acted upon by the shock wave (Figure 3.18(f)), or, at about 4 boundary layer thicknesses downstream from the corner, the beginning of an expansion fan (Figure 3.18(g)). In the second case, the static pressure at the first pressure tap downstream of the corner has fallen to the level measured in the convex corner experiments. It appears that the kink in the static pressure distribution downstream of the corner is not caused by separation, because a separation shock is not visible in the schlieren photograph (see Figure 3.18(g)).

For $\alpha = 10^\circ$, the shock wave intersects the boundary layer edge between 1.2 in. (30 mm or 13 δ_o) upstream and 0.40 in. (10 mm or 4.5 δ_o) downstream of the corner. The results are plotted in

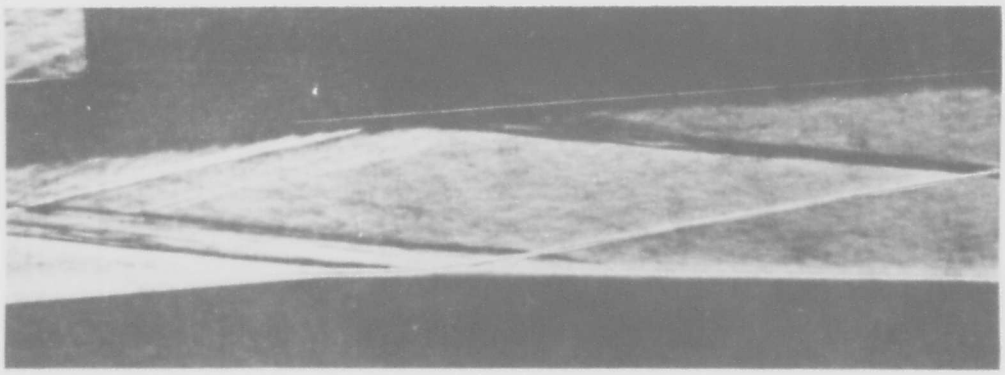

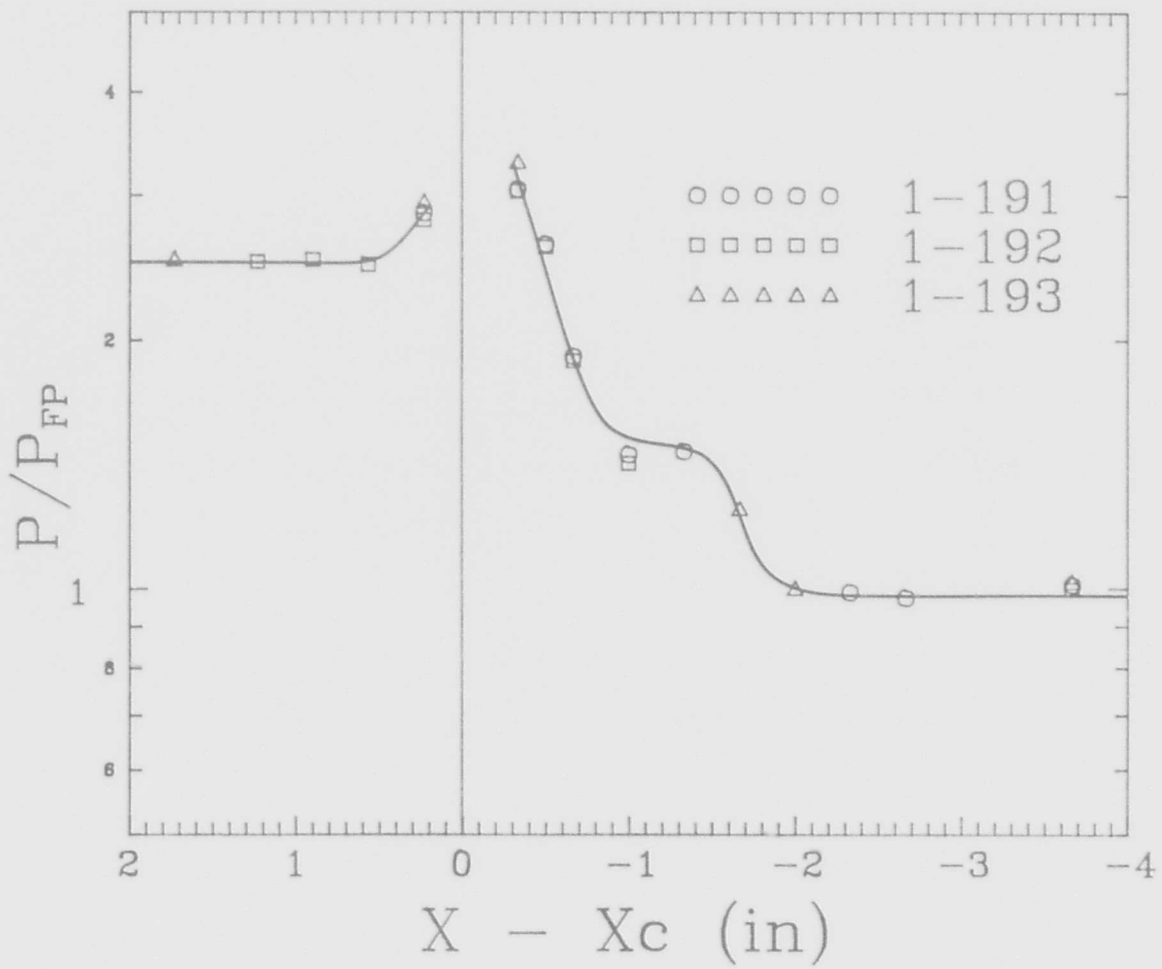

Figure 3.18.a Static pressure distribution and schlieren photograph of a shock wave-boundary layer interaction near a 5 degree convex corner, with $x_i - x_c = -1.0$ in.

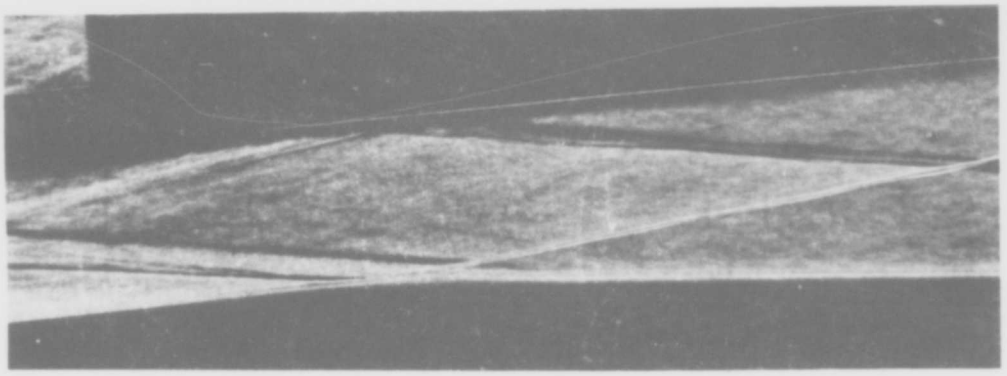

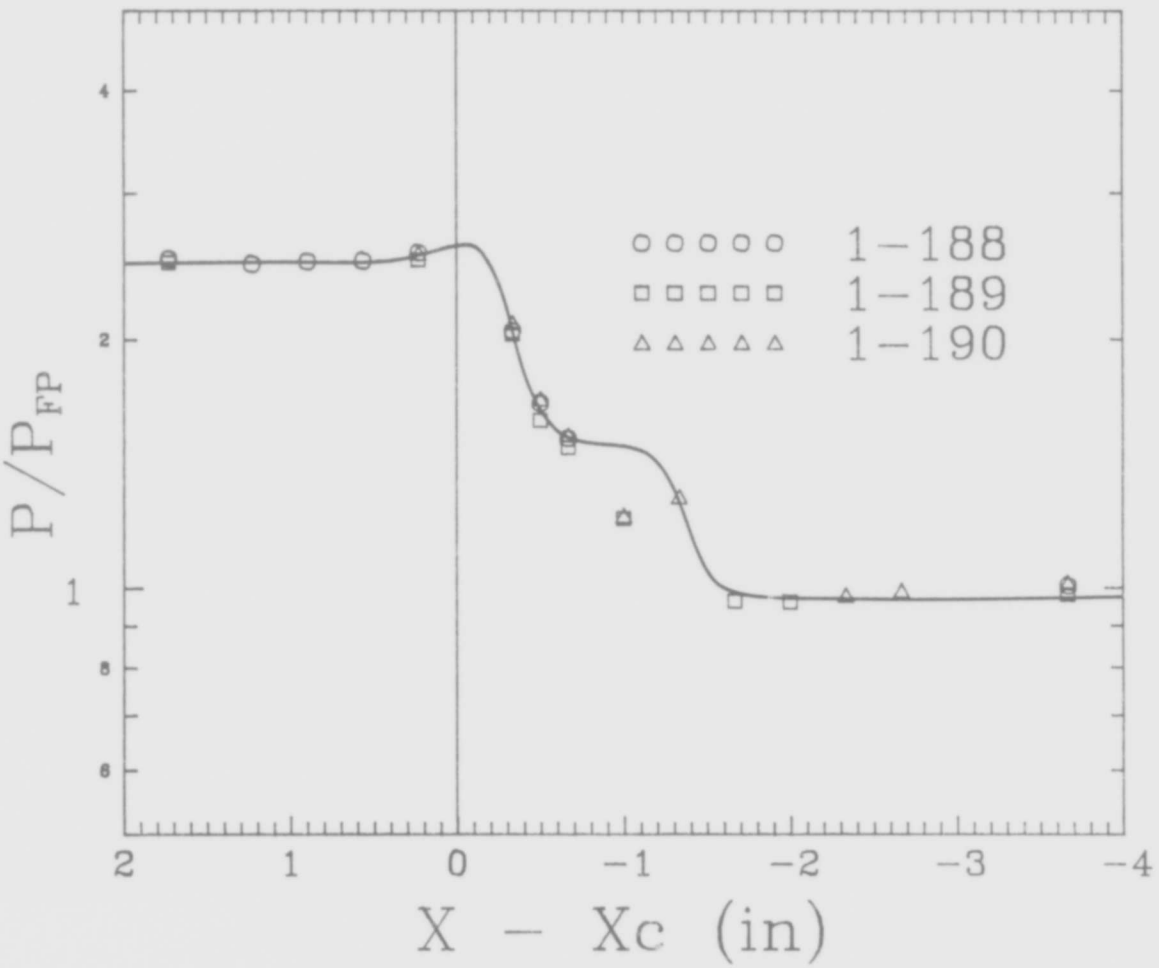

Figure 3.18.b Interaction for $\alpha = 5°$ and $x_i - x_c = -0.65$ in.

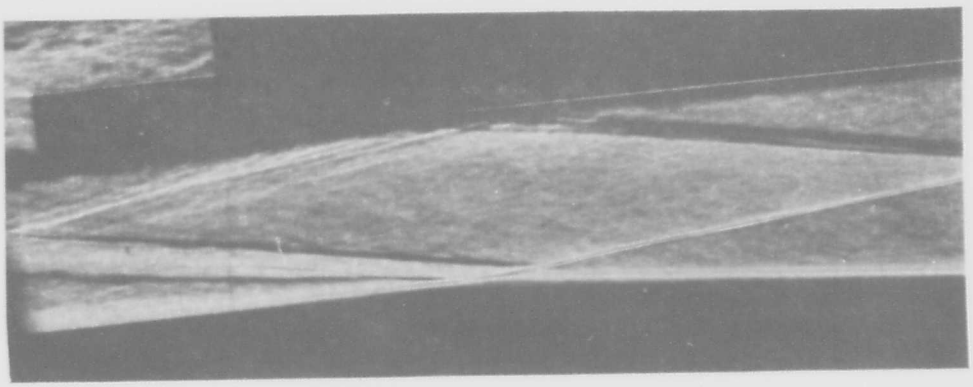

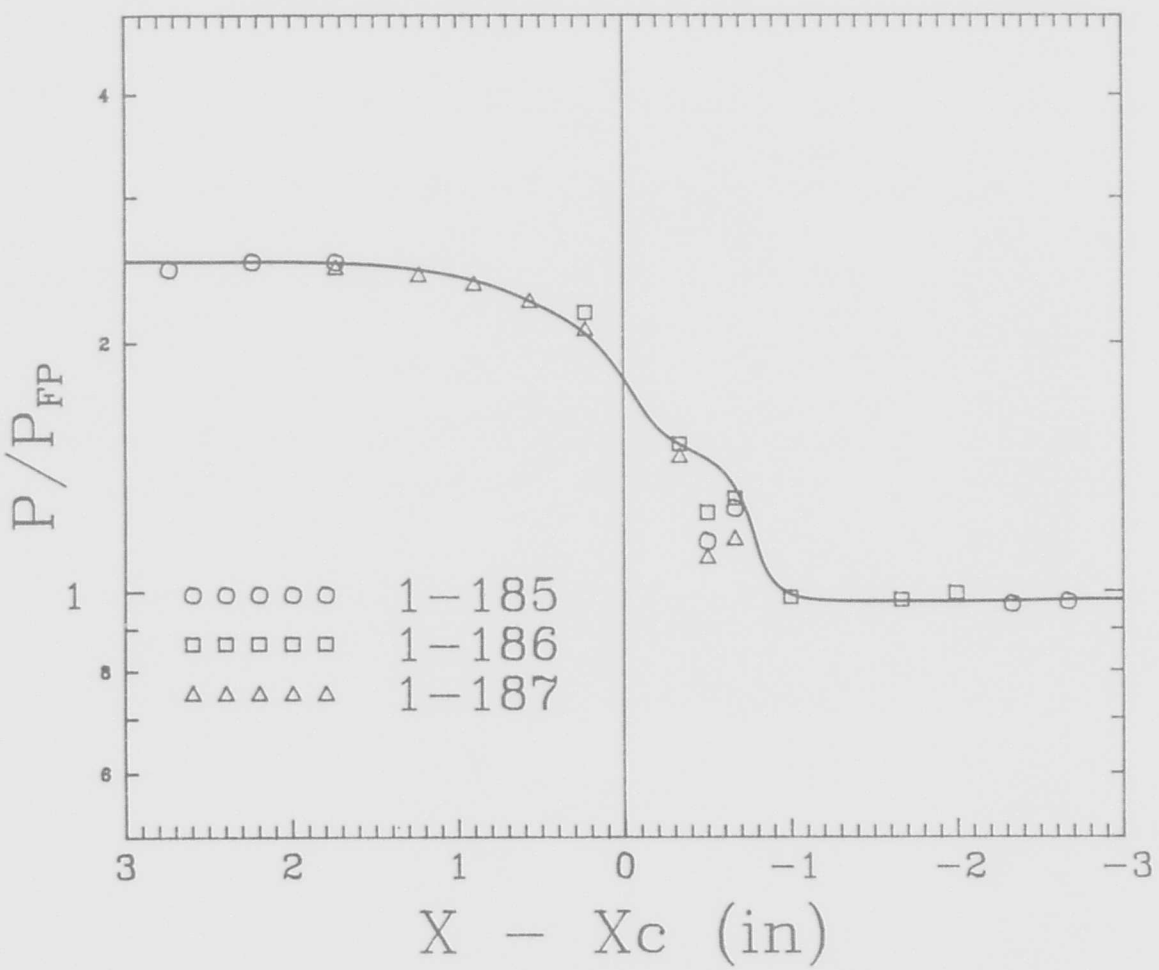

Figure 3.18.c Interaction for $\alpha = 5°$ and $x_i - x_c = -0.46$ in.

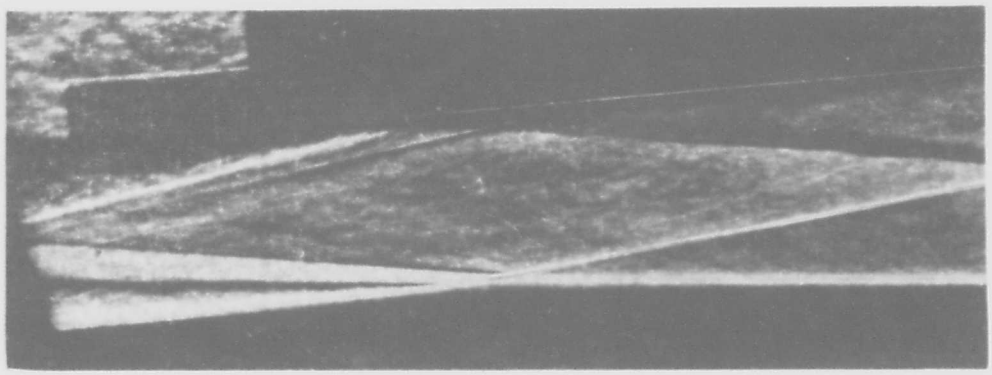

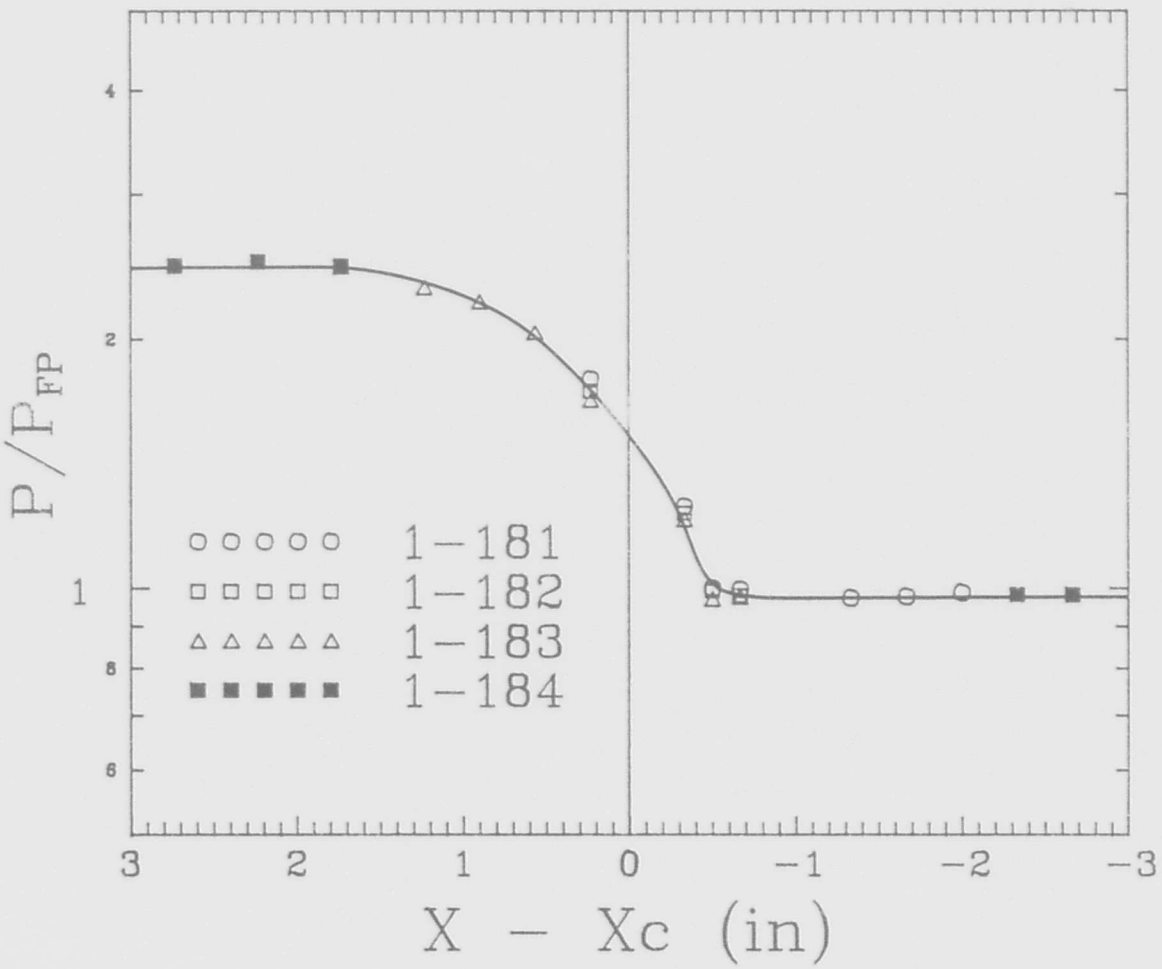

Figure 3.18.d Interaction for $\alpha = 5°$ and $x_i - x_c = -0.12$ in.

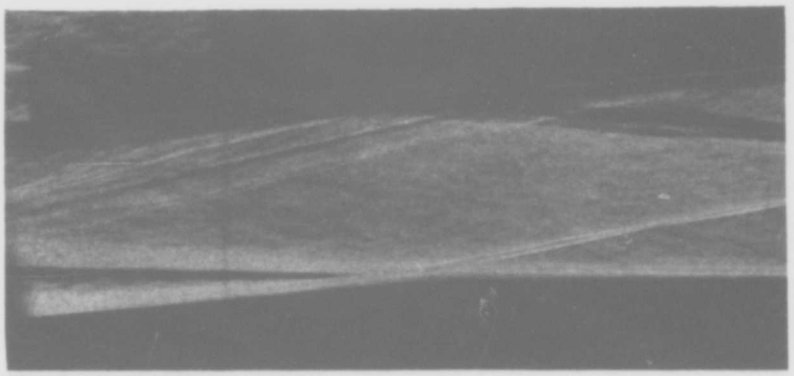

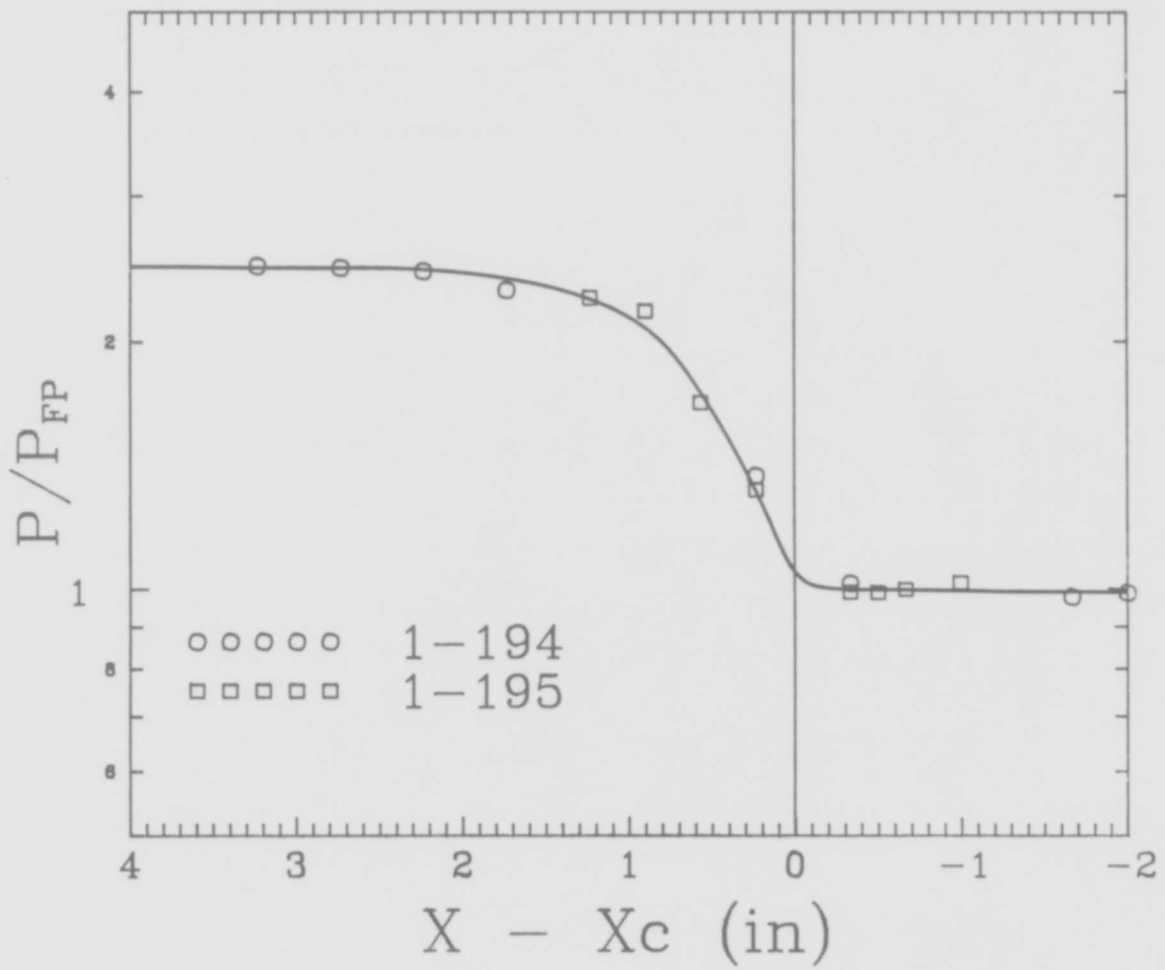

Figure 3.18.c Interaction for $\alpha = 5^{\circ}$ and $x_i - x_c = 0.0$ in.

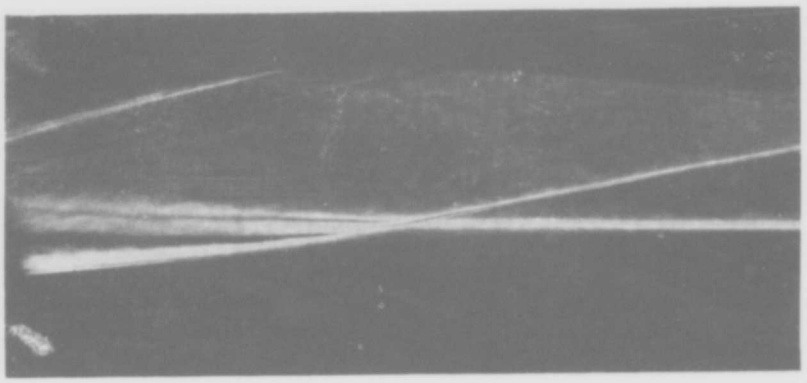

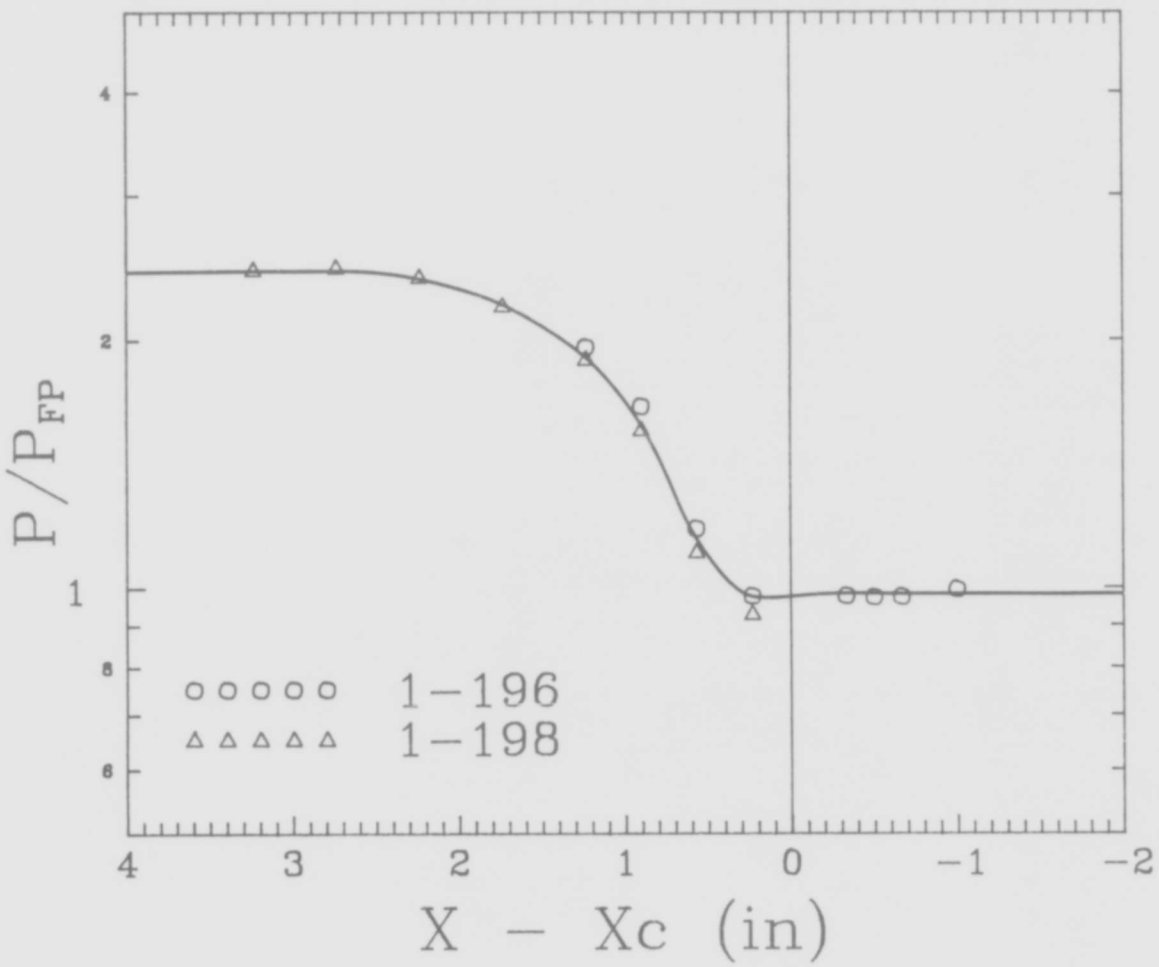

Figure 3.18.f Interaction for $\alpha = 5°$ and $x_i - x_c = +0.25$ in.

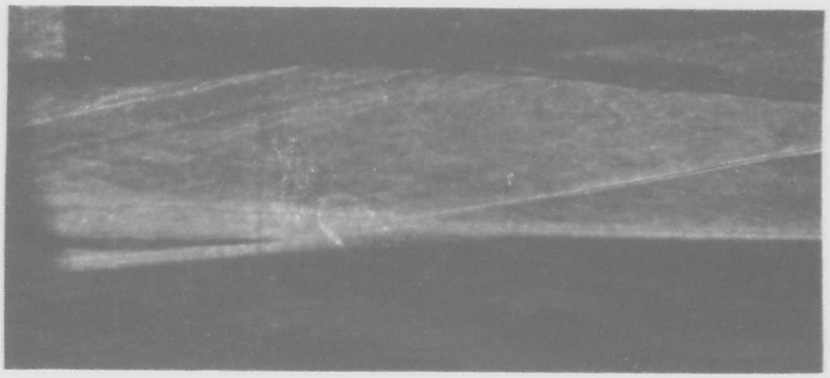

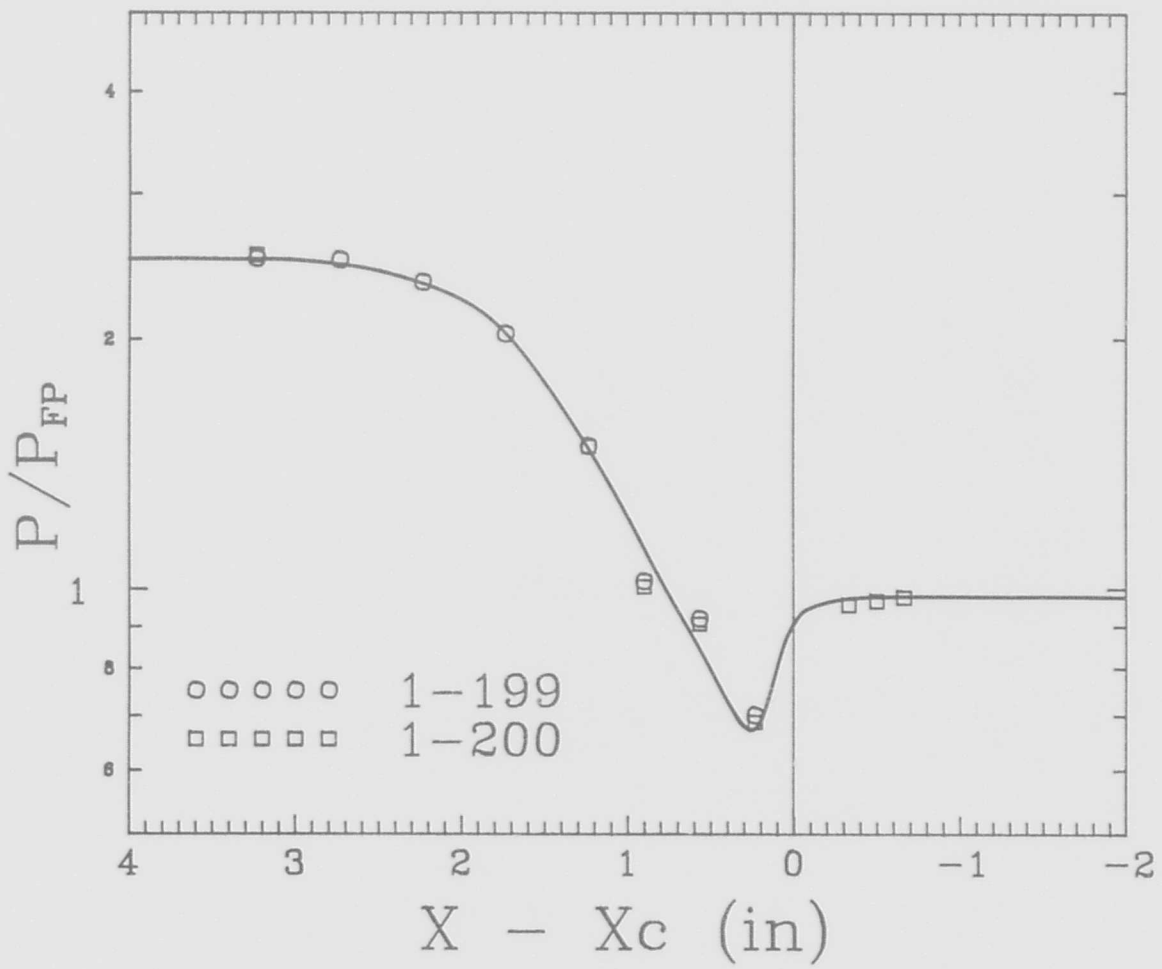

Figure 3.18.g Interaction for $\alpha = 5^{\circ}$ and $x_i - x_c = 0.46$ in.

Figures 3.19(a) to 3.19(g), and are similar to the 5° configuration. The plateau pressure is the same, just slightly lower than the flat plate boundary layer interaction, but the plateau length, as determined from Figure 3.19(a), is about 65% of the value predicted using Figure 3.14 for the flat plate interaction. As the shock impingement point moves downstream towards the convex corner, the plateau length decreases but the plateau pressure remains constant. Figure 3.19(e) shows the shock wave hitting the boundary layer within one boundary layer thickness upstream of the corner; in this case both the static pressure distribution and schlieren photograph indicate the presence of a small separated region. In Figure 3.19(f), the shock impingement point is 0.22 in. (5.6 mm), or about 2.5 boundary layer thicknesses, downstream of the corner and the static pressure appears to be constant across the corner and then rises smoothly. When the shock wave intersects the edge of the boundary layer 0.4 in. (10 mm), or about 4.5 δ_o, downstream of the corner, the static pressure falls slightly, but is well above the corresponding pressure measured using the convex corner alone.

3.5.5 Model Width Experiments

In order to verify that the model width used during the exploratory test program was sufficient, upon completion of the above tests, a series of experiments was completed to check the effect of this width on the shock wave-boundary layer interaction just upstream from the corner. The 10° convex corner-shock generator combination was used with the shock generator adjusted so that $x_i - x_c = -1.1$ in. (28 mm) upstream from the corner, thus provoking separation. The model width W was reduced progressively from 5.0 in. (127 mm) to 4.5 in. (114 mm), 3.75 in. (95 mm), and finally 3.0 in. (76 mm). The results of these experiments are plotted in Figure 3.20. It is evident that W has very little effect on the measured pressure distribution until it is reduced to 3.0 in., at which point, both the plateau pressure and length decrease. The remainder of the static pressure distribution is unaffected by reducing the model width. The length of separation is sensitive to model edge effects (see Ref. 3.28) and W = 5.0 in. is adequate for the present study.

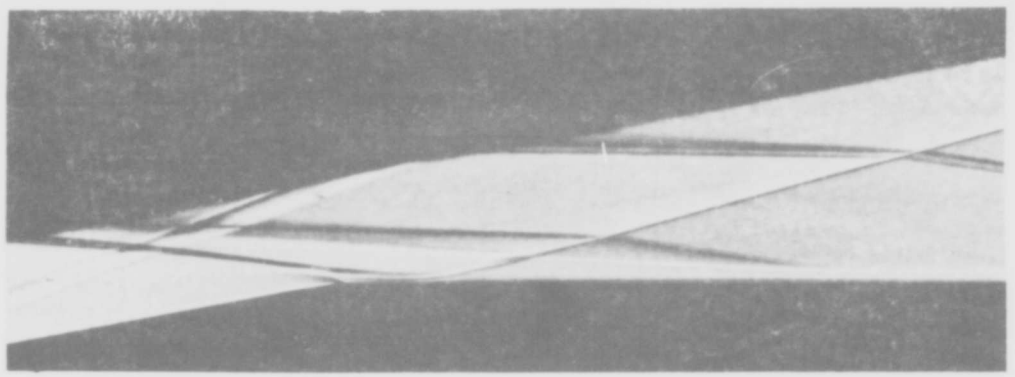

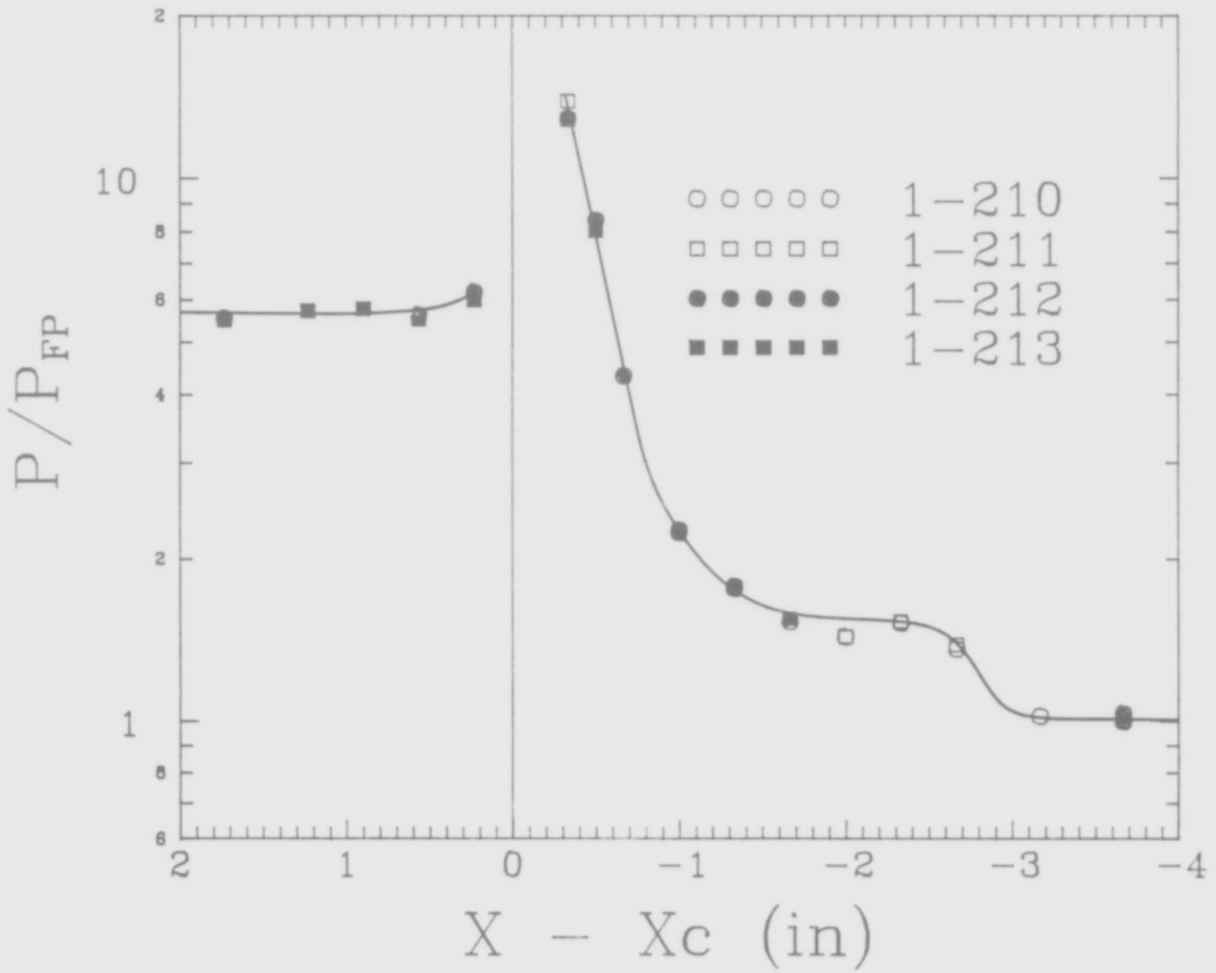

Figure 3.19.a Static pressure distribution and schlieren photograph of a shock wave-boundary layer interaction near a 10 degree convex corner with $x_i - x_c = -1.2$ in.

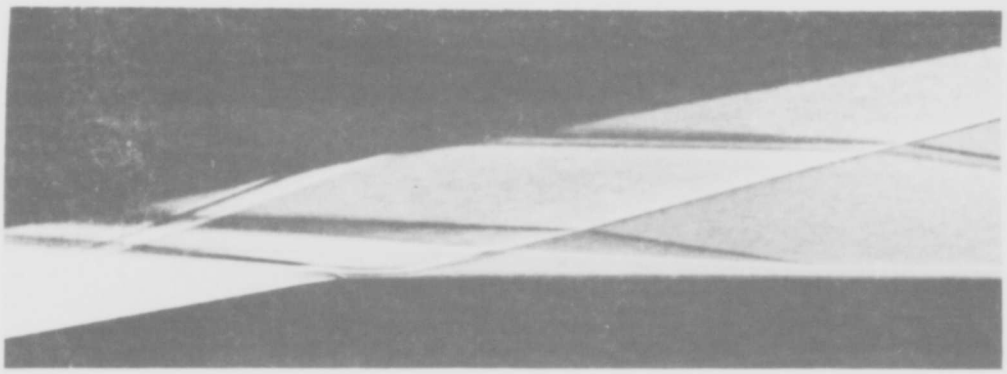

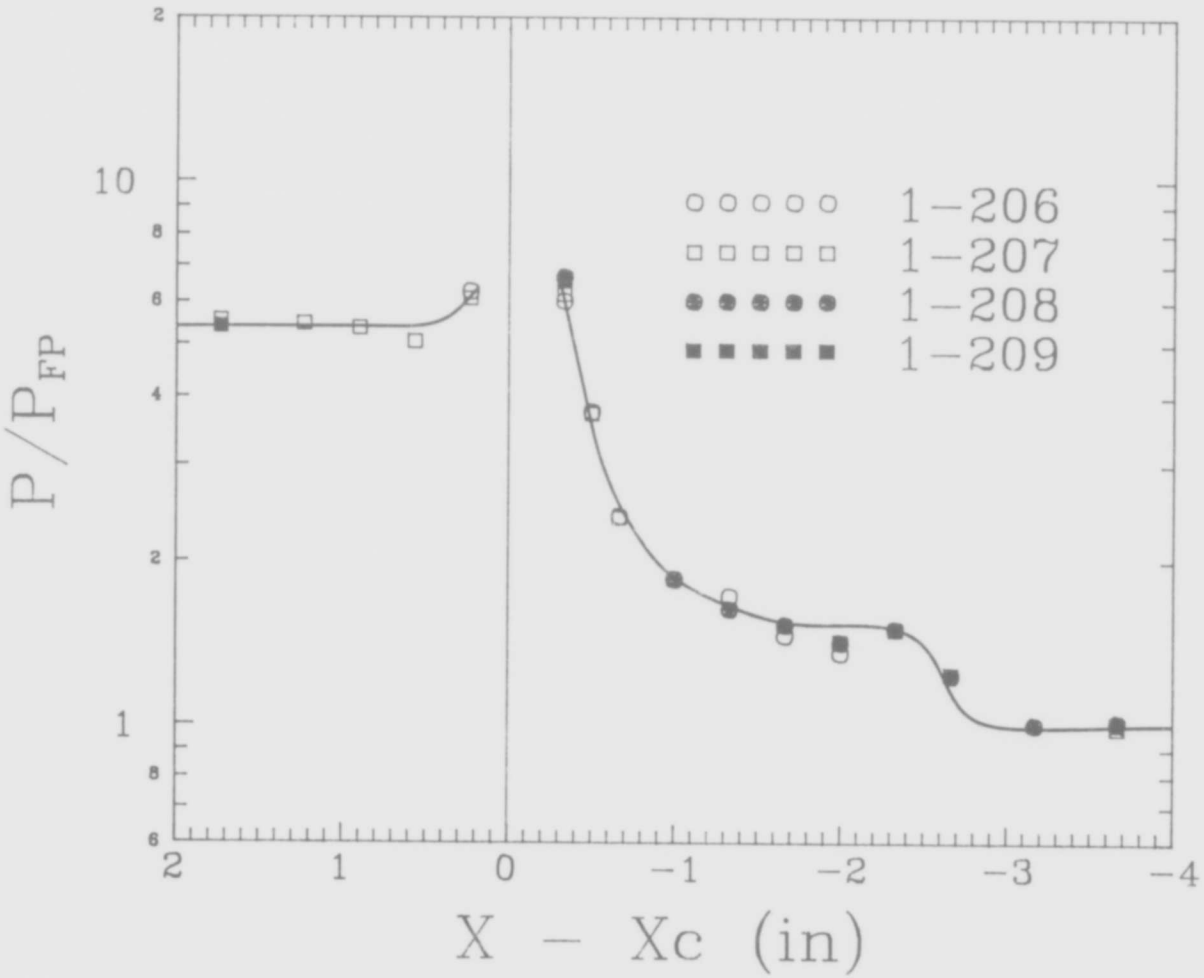

Figure 3.19.b Interaction for $\alpha = 10°$ and $x_i - x_c = -1.0$ in.

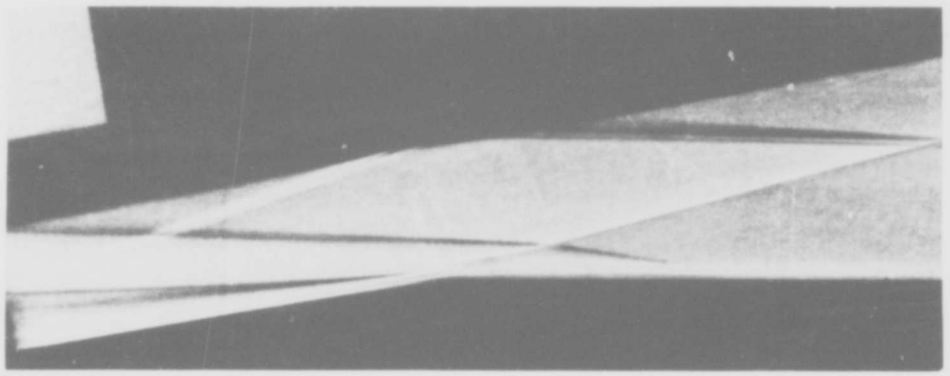

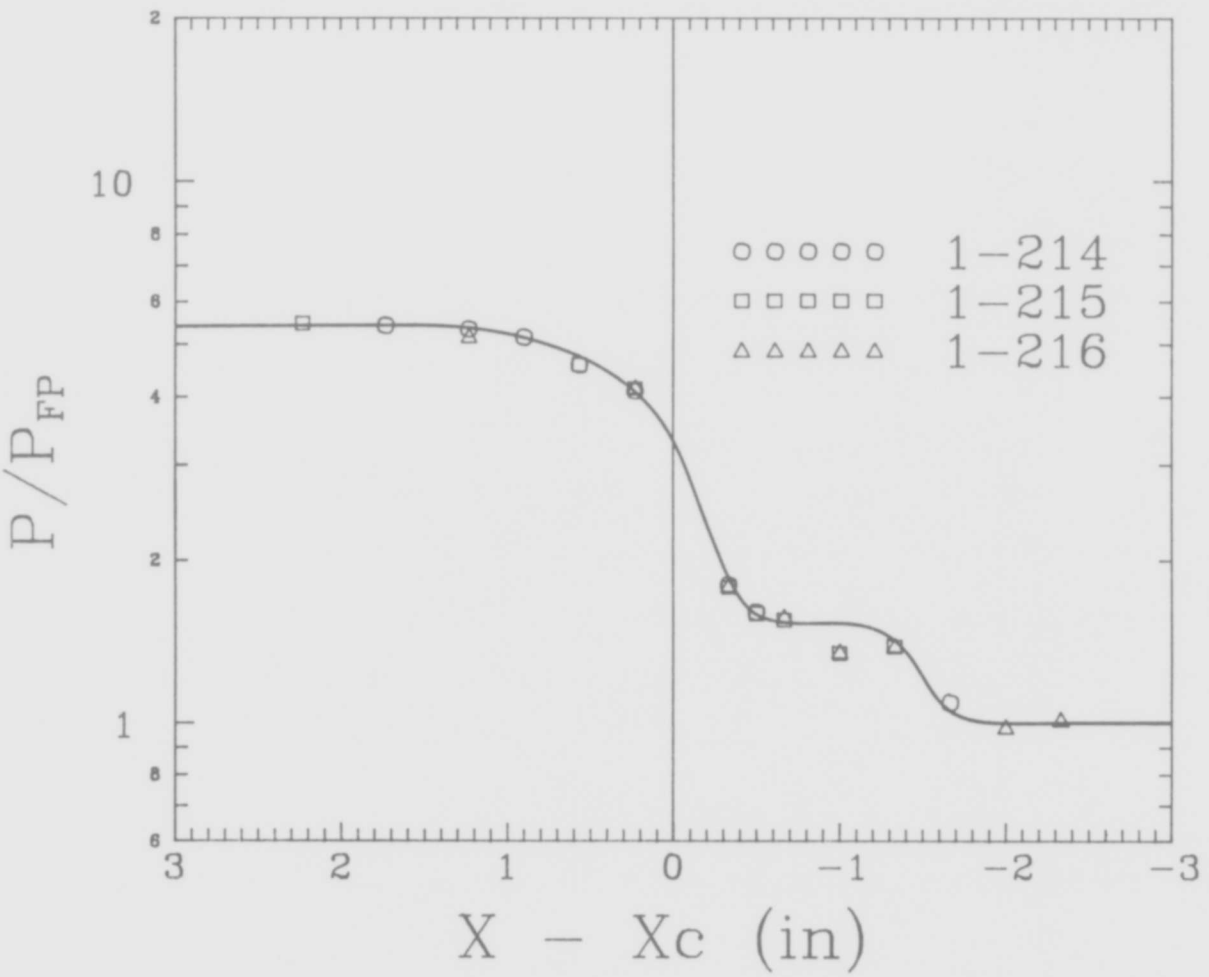

Figure 3.19.c Interaction for $\alpha = 10°$ and $x_i - x_c = -0.50$ in.

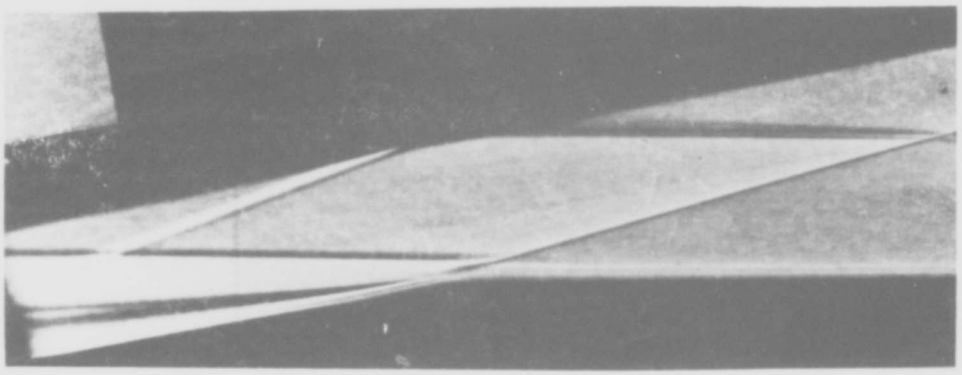

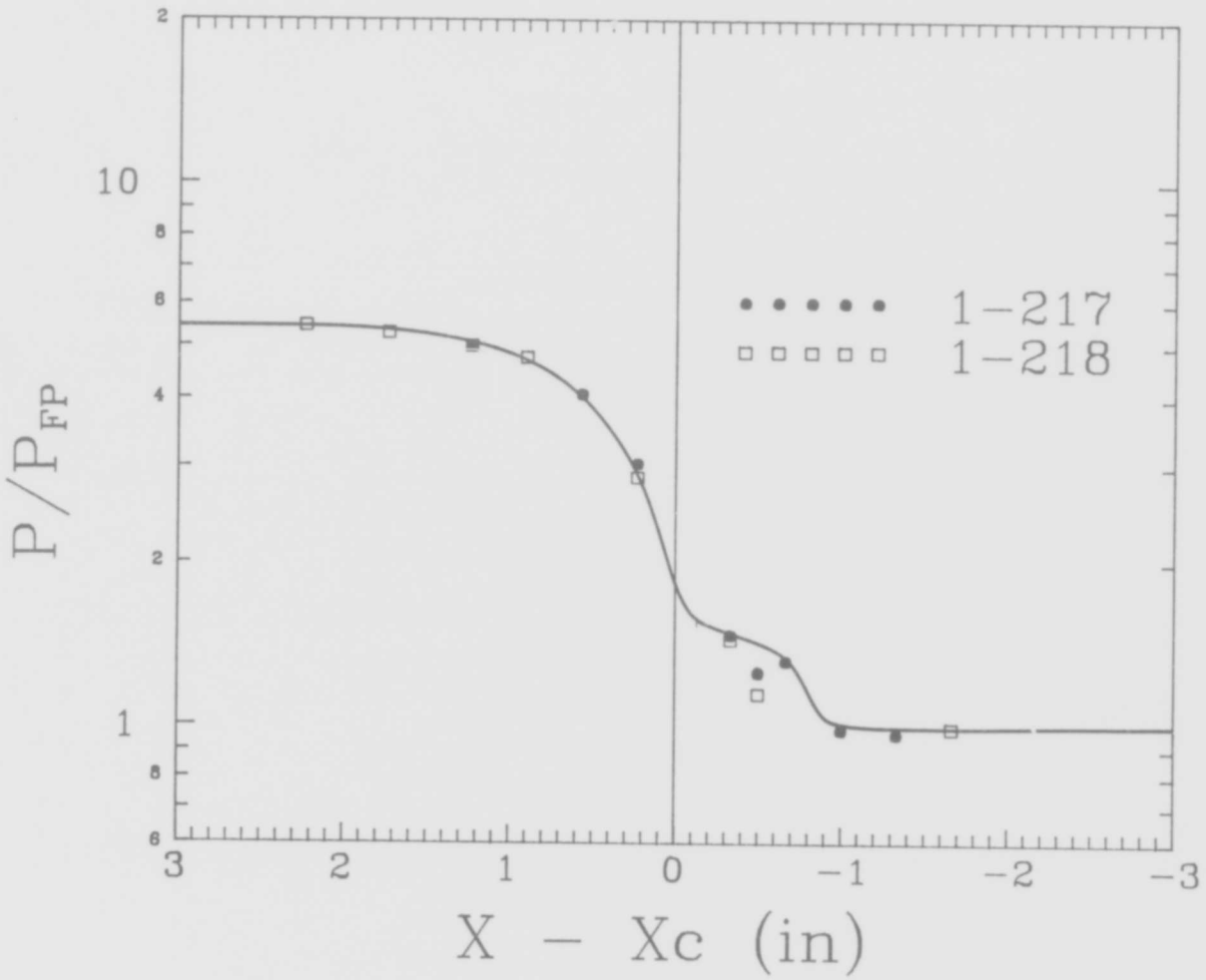

Figure 3.19.d Interaction for $\alpha = 10°$ and $x_i - x_c = -0.25$ in.

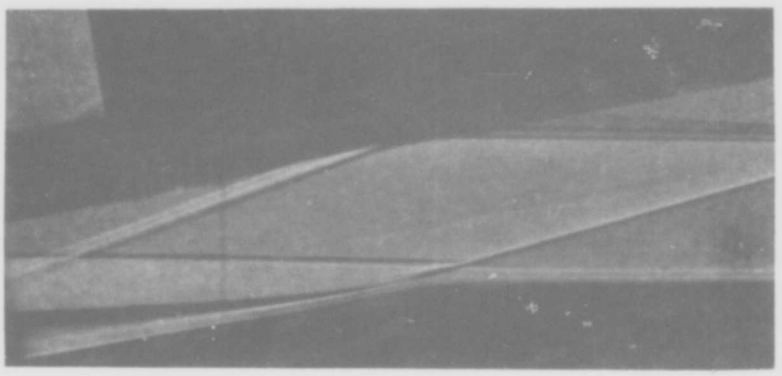

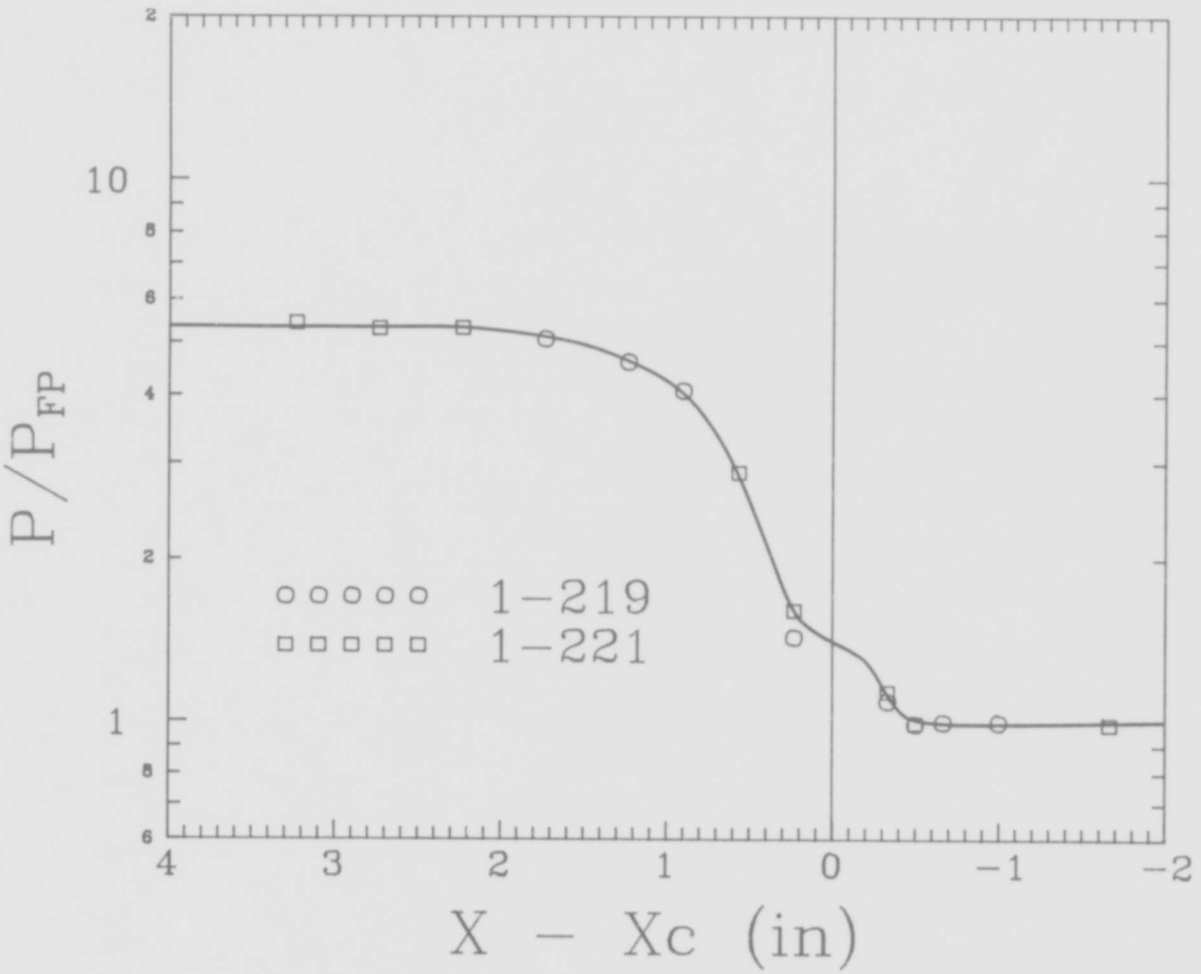

Figure 3.19.e Interaction for $\alpha = 10^{\circ}$ and $x_i - x_c = -0.05$ in.

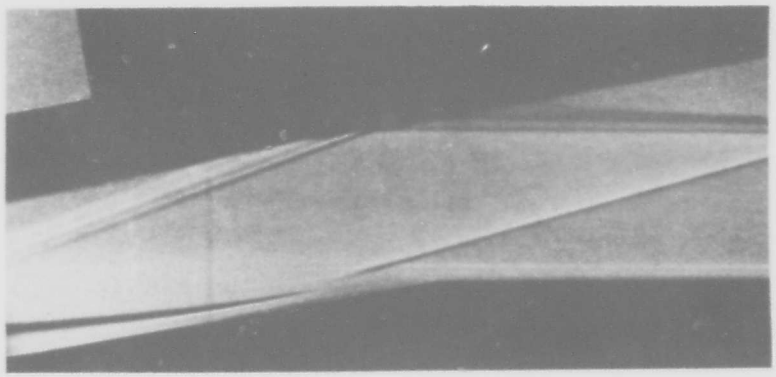

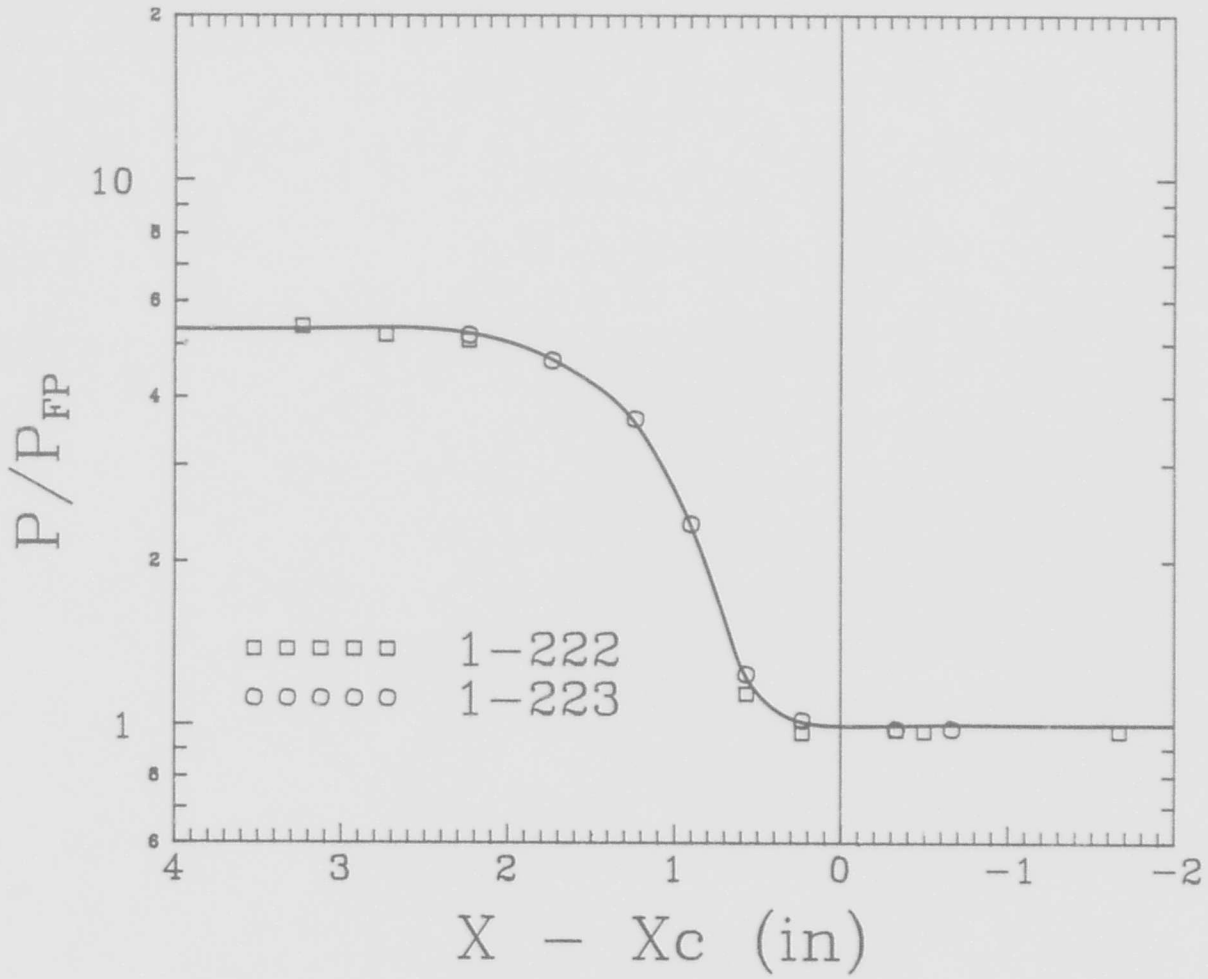

Figure 3.19.f Interaction for $\alpha = 10°$ and $x_i - x_c = +0.28$ in.

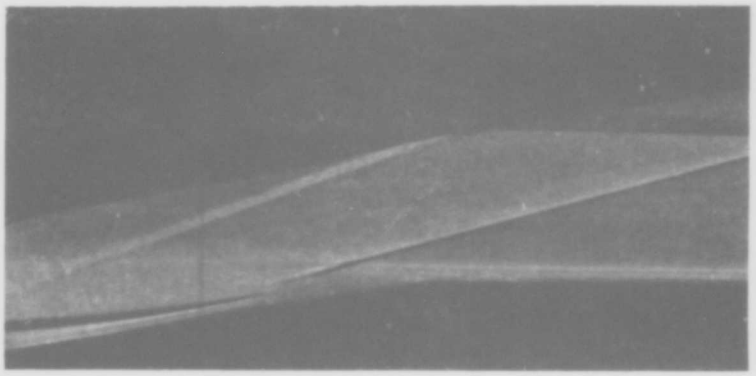

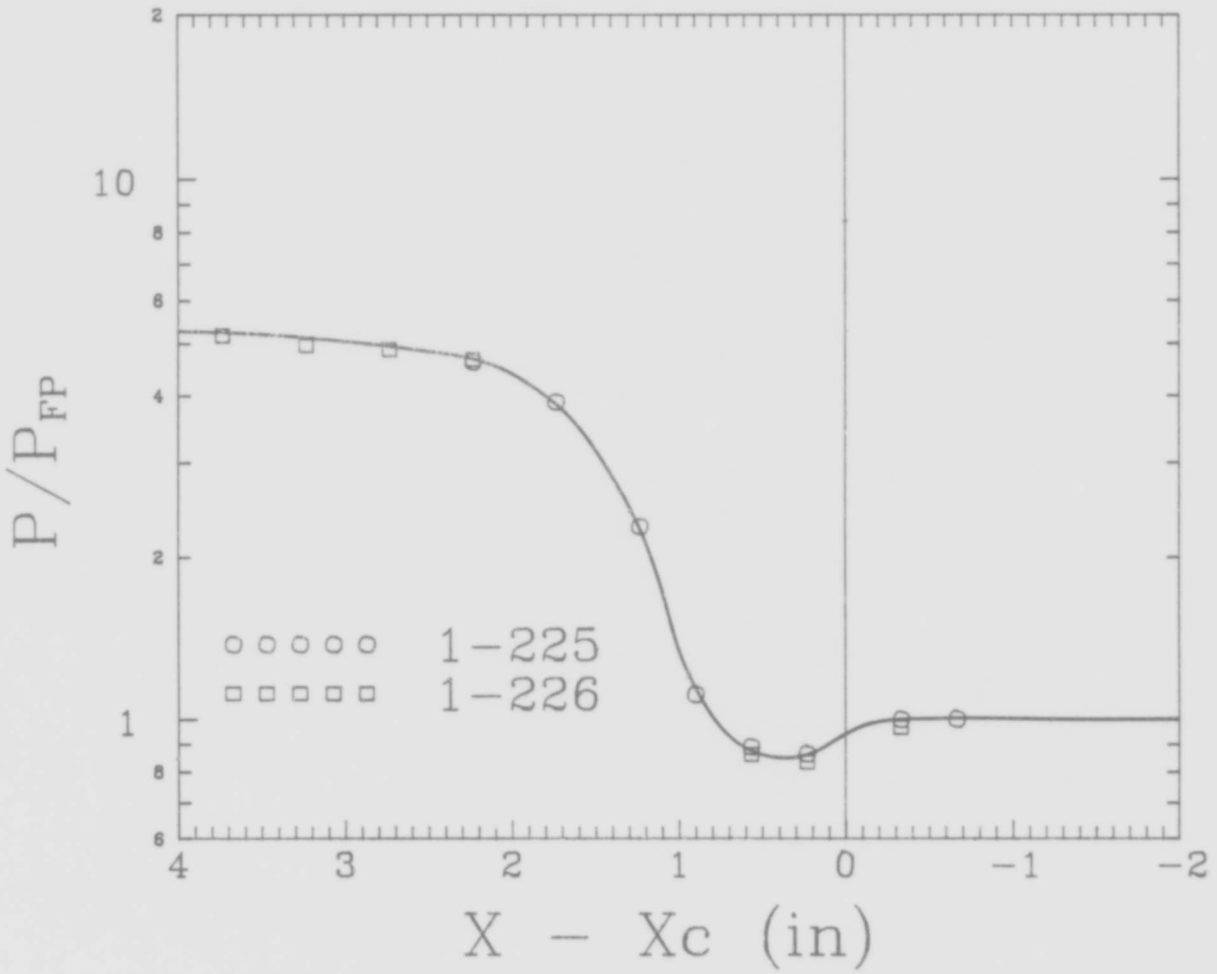

Figure 3.19.g Interaction for $\alpha = 10^{\circ}$ and $x_i - x_c = +0.40$ in.

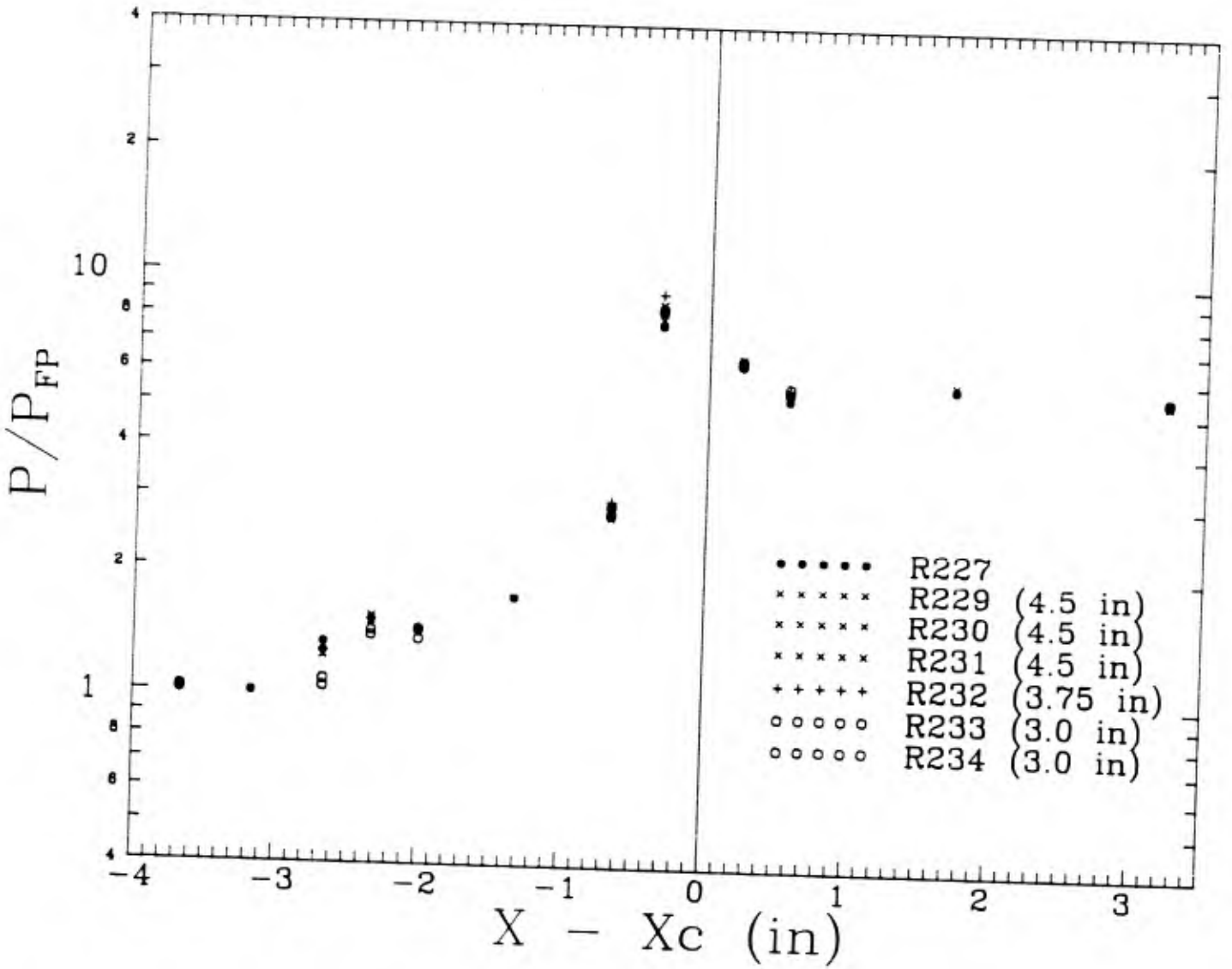

Figure 3.20 Effect on centerline static pressure distribution of reducing the width of the model.

3.6 Discussion and Conclusions

While the flow near the centerline of the exploratory model may have been free of edge effects, the shock wave-boundary layer interactions were not two-dimensional. Boundary layer transition, caused by the disturbance of the incident shock wave, occurred during the interaction and resulted in a separated region that varied in length across the span of the model. Because the location of boundary layer transition within the interaction greatly affects its characteristics, direct quantitative comparison with both previously published results and correlations of the important parameters for laminar and turbulent interactions is thus not possible.

Nevertheless, some tentative conclusions can be made. For example, as in classical interactions, when separation occurs the plateau pressure appears to be independent of the strength of the disturbance. Also, as for the flat plate interaction, the ultimate downstream pressure p_d is independent of the details of the process and is predicted accurately by the basic oblique shock relationships. For $M_\infty = 8.33$ these relationships give $p_d/p_{fp} = 2.55$ for $\alpha = 5°$ and 5.44 for $\alpha = 10°$. However, in contrast to the flat plate interaction, here, both the onset and extent of separation depends critically on the location of shock impingement relative to the corner.

Thus as the shock impingement point, x_i, is moved downstream towards the corner, the plateau and separation lengths decrease. In Figure 3.21, the pressure plateau length L_p is plotted against $x_i - x_c$, with both quantities being normalized with δ_0. For $\alpha = 5°$, boundary layer separation is almost eliminated when the shock impinges within 4 δ_0 of the corner. When x_i is between 7 δ_0 and 12 δ_0 upstream of the corner, L_p seems independent of x_i, but it is only about 60% of the plateau length observed in the flat plate boundary layer interaction. For $\alpha = 10°$, the behavior is a little different. As x_i is moved to about 11 δ_0 upstream from the convex corner, L_p increases to about 65% of the flat plate boundary layer value and becomes constant. It is not known if L_p would have increased to the flat plate levels if the shock interaction had been moved further upstream.

As stated earlier, Needham & Stollery (Ref. 3.25) predict that a pressure ratio p_d/p_{fp} of about 2.5 across an incident shock wave reflection is just sufficient to cause separation of a laminar boundary layer. Now

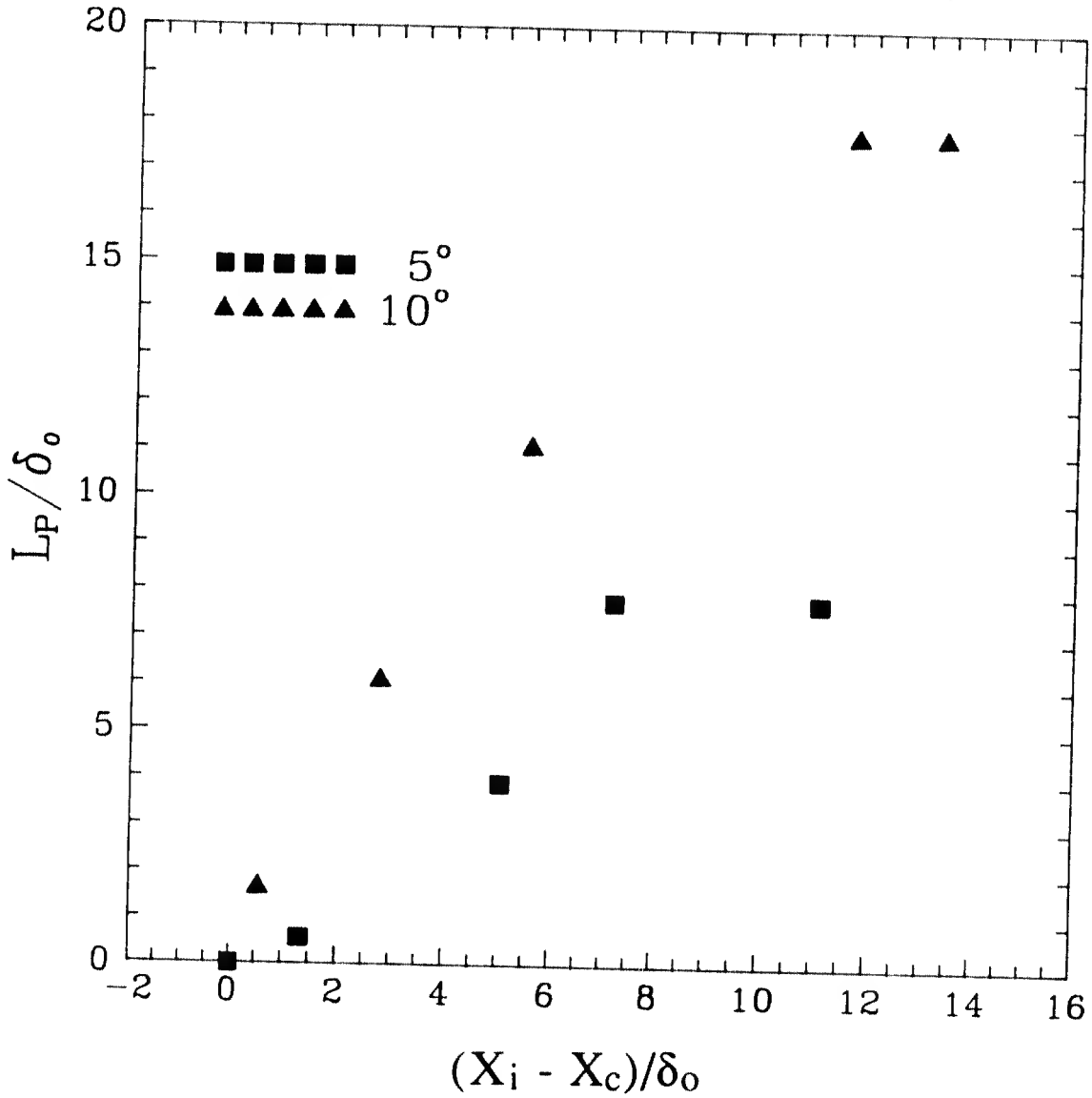

Figure 3.21 Plot of pressure plateau length for shock impingement points upstream of the convex corner.

p_d/p_{fp} for $\alpha = 5^\circ$ is about 2.6. In this case, the formation of a separation bubble is inhibited when the incident shock impinges within about 4 δ_0 upstream of the corner. When the shock impingement point is moved upstream, out of this region, the plateau length rises quickly to a constant value. For $\alpha = 10^\circ$, p_d/p_{fp} is about 5.5 and shock impingement near the corner does not prevent separation. In fact, it seems that there will be a small separated region even if the incident shock wave impinges right at the corner.

Now in hypersonic flows the interactions of a boundary layer with either an incident shock wave or a convex corner expansion wave are relatively long. For example, the length required for the compression caused by an incident shock wave reflection can be the order of 50 boundary layer thicknesses (see Figure 3.13(d) for example), and for a convex corner expansion, approximately 30 boundary layer thicknesses are necessary. Thus, the convex corner interaction in which both processes may occur is very difficult to completely separate on a relatively small model. Consequently, for all of the experiments described above, the compression and expansion processes mutually interacted with the boundary layer or with each other.

Some of the important factors in determining whether boundary layer separation will occur when the shock impinges upstream of the corner are:

- where, with respect to the convex corner, does the large pressure gradient of the compression process occur?
- can the upstream influence of the expansion corner dominate that of the shock wave compression?

The degree to which an incident shock wave or an expansion corner can influence the boundary layer upstream depends largely on the relative thickness of the subsonic portion of the boundary layer. For $\alpha = 5^\circ$, the steep increasing pressure gradient caused by the incident shock wave occurs just downstream of the corner when the shock impingement point is just upstream of the convex corner. When the shock impinges within 4 δ_0, the upstream effect of the expansion corner, to decrease the static pressure, nullifies the increase in pressure upstream of the incident shock wave. When this occurs, separation is prevented or severely curtailed. For $\alpha = 10^\circ$, the upstream influence of the incident shock wave is greater than for the $\alpha = 5^\circ$ case. Figure 3.21 shows that, while the convex corner relieves some of the high pressure in the separated regions upstream from the corner, its influence is not sufficient to eliminate separation.

When the incident shock wave interacts with the boundary layer just downstream of the convex corner, the outer flow is turned by the incident shock wave, with the higher pressures propagating upstream to the corner through the boundary layer. As the shock impingement point is moved further downstream, some expansion occurs but significant upstream propagation still influences the structure. For $\alpha = 5^\circ$, the first static pressure measured downstream from the corner does not fall to the simple convex corner level until the shock impinges about 5 δ_0 thicknesses downstream of the corner. This indicates that the shock impingement point and the convex corner have been separated enough to prevent their mutual interaction with the boundary layer. However, the interaction is not completely decoupled because the shock wave interacts with the corner expansion fan and impinges upon an accelerating boundary layer.

When the incident shock wave impinges within a few boundary layer thicknesses downstream of the corner, the flow is turned by the shock wave without upstream separation and the static pressure rises smoothly through the interaction region over about 20 δ_0 (see Figures 3.18(f) and 3.19(f)). In this configuration, the measured static pressure distribution best approximates the inviscid pressure expected for cancellation of the expansion and reflected shock waves. Therefore, smooth compression and turning of a hypersonic flow is accomplished by ensuring that the incident shock wave impinges within a few boundary layer thicknesses downstream of a convex corner.

If the incident shock wave impinges more than 8 to 10 δ_0 upstream of the convex corner, large separated flow regions are formed. As the shock impingement moves closer to the corner, the separation length decreases, but the nature of the reduction is quite different for $\alpha = 5^\circ$ and 10°. For $\alpha = 10^\circ$, the pressure plateau length decreases continuously to about one boundary layer thickness as the shock impingement point moves to the convex corner. However, for the 5° case, separation is severely restricted if the shock impinges within 4 δ_0 of the convex corner, indicating that the upstream influence of the corner dominated the increasing pressure of the incident shock within this region.

The smoothest, and what appears to be the most compact, compression of hypersonic flow at a convex corner occurs when the shock wave impinges within a few boundary layer thicknesses downstream of the corner. In this configuration, a small separated region may form between the corner and the shock impingement point but does not extend upstream of the corner. The flow is turned by the incident shock

wave and the small separation bubble does not appear to adversely affect the process. Even in this optimum configuration, the order of 20 boundary layer thickness are required to complete compression.

When the shock impingement point is moved further downstream, the flow begins to expand downstream of the corner. Eventually, the upstream influence of the shock wave is insufficient to reach the corner and the flow just downstream of the corner was expanded by a non-centered expansion fan. In this case, the interaction is not as simple as in the case of a flat plate boundary layer because the incident shock wave is interacting with the an accelerating boundary layer.

Listed below are some suggestions for further study of the interactions of a hypersonic boundary layer with an incident shock wave and a convex corner expansion:

1) More detailed surface static pressure measurements are required through the interaction with particular emphasis being placed on the region near the corner. The objectives of this study would be to measure the effect of the convex corner on the pressure gradient imposed on the boundary layer by the incident shock wave and to determine the relative importance of the upstream influence of the convex corner and incident shock wave interactions. The upstream influence indicates the degree to which changes in the boundary layer edge pressure are communicated through the subsonic part of the boundary layer.

2) The present study could be repeated using detailed surface heat transfer measurements to allow accurate measurement of the extent of boundary layer separation and provide more data for comparison to numerical solutions to the Navier-Stokes equations.

3) New nozzles could be manufactured to allow operation at higher and lower Mach number nozzles and thus permit the study of fully laminar and fully turbulent boundary layer interactions. Lowering the driver pressure will also allow reduction of test section Reynolds number with the existing nozzle.

4) A series of experiments could be completed to allow comparison of the results obtained from two-dimensional planar and axisymmetric models for equivalent boundary layer interactions.

5) A quantitative schlieren system or interferometry could be incorporated into the gun tunnel's optical measurement system to allow non-intrusive measurement of the density throughout the entire interaction region. This data would be excellent for verification of numerical predictions of the flow field.

3.7 References

3.1 Green, J.E., "Interactions Between Shock Waves and Turbulent Boundary Layers", Progress in Aerospace Sciences, Vol. 11, 1970, pp. 235-340.

3.2 Hankey, W.L. and Holden, M.S., "Two-Dimensional Shock-Wave Boundary Layer Interactions in High Speed Flows", AGARD-AG-203, June 1975.

3.3 Adamson, T.C. and Messiter, A.F., "Analysis of Two-Dimensional Interactions Between Shock Waves and Boundary Layers", Annual Review of Fluid Mechanics, 1980, pp. 103-138.

3.4 Delery, J. and Marvin, J.G., "Shock-Wave Boundary Layer Interactions", AGARD-AG-280, Feb. 1986.

3.5 Delery, J., "Shock/Shock and Shock-Wave/Boundary-Layer Interactions in Hypersonic Flows", AGARD-FDP-VKI Special Course, Aerothermodynamics of Hypersonic Vehicles, June 1988.

3.6 Hamed, A., "Flow Separation in Shock Wave Boundary Layer Interactions at Hypersonic Speeds", NASA CR 4274, Feb. 1990.

3.7 Chew, Y.T., "Shock Wave and Boundary Layer Interaction in the Presence of an Expansion Corner", Aeronautical Quarterly, Vol. 30, 1979, pp. 506-527.

3.8 Chew, Y.T. and Squire, L.C., "The Boundary Layer Development Downstream of a Shock Interaction at an Expansion Corner", Aeronautical Research Council, R&M No. 3839, 1979.

3.9 Holden, M. S., "Separated Flow Studies at Hypersonic Speeds, Part II: Two-Dimensional Wedge Separated Flow Studies", CAL Report No. AF-1285-A-13(2), Dec. 1964.

3.10 Green, J.W., "Reflection of an Oblique Shock Wave by a Turbulent Boundary Layer", Journal of Fluid Mechanics, Vol. 40, 1970, pp. 81-95.

3.11 Needham, D. A., "A Heat Transfer Criterion for the Detection of Incipient Separation in Hypersonic Flow", AIAA J., Vol. 3, No. 4, April 1965.

3.12 Shultz, D.L. and Jones, T.V., "Heat Transfer Measurements in Short Duration Hypersonic Facilities", AGARD-AG-165, Feb. 1973.

3.13 Taylor, B.W., "Development of Thin Film Heat Transfer Gages for Shock Tube Flows", UTIAS TN 27, June 1959.

3.14 Miller, C.G., "Comparison of Thin-Film Resistance Heat Transfer Gages with Thin Skin Calorimeter Gages in Conventional Hypersonic Wind Tunnels", NASA TN 83167, Dec. 1981.

3.15 Settles, G.S. and Teng, H., "Flow Visualization Methods for Separated Three-Dimensional Shock Wave/Turbulent Boundary Layer Interactions", AIAA J., Vol. 21, No. 3, March, 1983.

3.16 Maltby, R. L., "Flow Visualization in Wind Tunnels Using Indicators", AGARDograph 70, April 1962.

3.17 Needham, D.A., "Progress Report on the Imperial College Hypersonic Gun Tunnel", Imperial College of Science and Technology, Aeronautics Department, Report. 118, 1963.

3.18 Modarress, D. and Azzazy, M., "Modern Experimental Techniques for High Speed Flow Measurements", AIAA Paper No. 88-0420, Jan. 1988.

3.19 Gai, S.L., Reynolds, N.T., Ross, C., Baird, J.P., "Measurements of Heat Transfer in Separated High-Enthalpy Dissociated Laminar Hypersonic Flow Behind a Step", Journal of Fluid Mechanics, Vol. 199, 1989, pp. 541-561.

3.20 Koziak, W. W., "Quantitative Space and Time Resolved Laser Schlieren System for the Study of Hypersonic Flow", Review of Scientific Instruments, Vol. 41, No. 12, Dec. 1970.

3.21 Fiore, A. W., and Law, C. H., "Aerodynamic Calibration of the Aerospace Research Laboratories M = 6 High Reynolds Number Facility", ARL TR 75-0028, Feb. 1975.

3.22 Pate, S. R., and Schueler, C. J., "Radiated Aerodynamic Noise Effects on Boundary Layer Transition in Supersonic and Hypersonic Wind Tunnels", AIAA J., Vol. 7, No. 3, Mar. 1979.

3.23 Chapman, D. R., Kuehn, D. M., and Larson, H. K., "Investigation of Separated Flows in Supersonic and Subsonic Streams with Emphasis on the Effect of Transition", NACA TN 3869, Mar. 1957.

3.24 Rainbird, W. J., "Errors in Measurement of Mean Static Pressure of a Moving Fluid due to Pressure Holes", National Research Council, NRC/NAE Quarterly Report 1967 (3), 1967.

3.25 Needham, D., and Stollery, J. L., "Hypersonic Studies of Incipient Separation and Separated Flow", Aeronautical Research Council, ARC 27 752 Hyp. 539, Jan. 1966.

3.26 Watson, E. C., Murphy, J. D., Rose, W. C., "Investigation of Laminar and Turbulent Boundary Layers Interacting with Externally Generated Shock Waves", NASA TN D-5512, Nov. 1969.

3.27 Sullivan, P.A., "Interaction of a Laminar Boundary Layer and a Corner Expansion Wave", AIAA J., Vol. 8, No. 4, April 1970.

3.28 Rudy, D. H., Thomas, J. L., Kumar, A., Gnoffo, P. A., Chakravarthy, S. R., "A Validation Study of Four Navier-Stokes Codes for High Speed Flows", AIAA Paper No. 89-1838, June 1989.

4.0 Hypersonic Inlet Flow Starting in the Gun Tunnel

R.J. McGregor, S. Molder and T.W. Paisley

4.1 Introduction

The quest for improved economy in placing payloads in low Earth orbit has in the last five years given birth to various hypersonic airplane concepts. The anticipated degree of cost saving is directly related to the airplane's propulsion efficiency and hence to the particular propulsion system(s) chosen for boosting the airplane into orbit. At the same time, it appears that the most cost-effective system requires the longest time and most technology development effort, whereas the least cost-effective system requires no developmental effort since it is already on hand. It has been determined that using the present Shuttle/Orbiter combination costs some $8,000 (Ref. 4.1) to place one kilogram of payload in orbit. However, for the fulfilment of foreseeable space exploration and communication satellite launch needs, this cost must be reduced to about $800.

A possible method of reducing present launch costs is by the use of propulsive engines which use atmospheric oxygen to burn fuel. Such air-breathing engines have the potential for raising the fuel specific impulse (a measure of the fuel's ability to produce engine thrust) from the rocket's 300 seconds up to 1000 to 4000 seconds for the air breathing engine, and mission studies have shown that this order-of-magnitude improvement in propulsive performance results in the desired order of magnitude reduction in launch costs.

Air-breathing engines operating at supersonic and hypersonic speeds ingest air through a converging air intake, and, for useful operation of the engine, the intake must operate stably, predictably, and efficiently through a wide range of flight Mach number and altitude. Efficient operation through a range of Mach number requires some variation in inlet geometry such that the inlet produces a compression ratio of 20 to 50 through the Mach number range of 4 to 25. For these compression ratios, the contraction ratio for a high efficiency inlet must change from 5 to 20 (Ref. 4.2).

Operation of such high contraction ratio inlets presents a problem in that the inlet will not start under steady state conditions. Starting requires that the normal shock in front of the inlet moves downstream

into the inlet (is swallowed) and that a stable supersonic flow is established throughout the converging portion of the inlet. Steady state starting occurs only if the ratio A_2/A_3 is decreased to the classical "Kantrovitz Limit" as shown in Figure 4.1. At this limit, the flow at the downstream opening of the inlet becomes subsonic, and the mass flow throughout the inlet can then increase to such extent that the normal shock is not required to cause spillage but the inlet will accept the freestream flow captured by the entry of the inlet. The normal shock then moves downstream, establishing started supersonic flow in the inlet. However, the small amount of contraction allowed for starting yields poor performance as an inlet, and to obtain reasonable engine performance the inlet's contraction ratio must be increased. This requirement of variable geometry for inlet starting and subsequent operation, however, presents serious problems for operational engine inlets as well as the windtunnel testing of such inlets. In particular, for hypersonic inlet testing in shock and gun tunnels, where steady flow durations are of the order of 10 ms, it becomes difficult to design for extremely rapid and precisely timed motion of inlet components.

Figure 4.1 shows the success attained by various supersonic and hypersonic facilities to start diffusers or inlets (black symbols) and then close the diffusers down to operating area ratios (open symbols) without shock expulsion. The black symbols being generally below the Kantrovitz limit, show that it is easier to start inlets than predicted by the Kantrovitz limit; suggesting that during starting, the flow process does not consist of the motion of a single normal shock as assumed by the Kantrovitz theory. Open symbols indicate that practical diffusers (without boundary layer bleed) can be operated stably at contraction ratios somewhat above the "ISENTROPIC SONIC THROAT AREA RATIO" limit. Figure 4.1 does not represent the state of the art as much as it shows the state of experience insofar that a diffuser design for stable operation can be based on the line "MAXIMUM RUNNING THROAT AREA RATIO". The experimental symbols at M_2=8.33 refer to experimental results obtained in this study as well as other inlet investigations undertaken in the Ryerson/UT gun tunnel facility.

Fortunately, the conditions during the starting of hypersonic impulse tunnels are such that high contraction ratio inlet models placed in the test section will start without the incorporation of variable geometry. As can be seen in Figure 4.1, several impulse facilities, including our own, have attained starting with high contraction inlets (low A_3/A_2). This happy circumstance stems from the fact that, prior

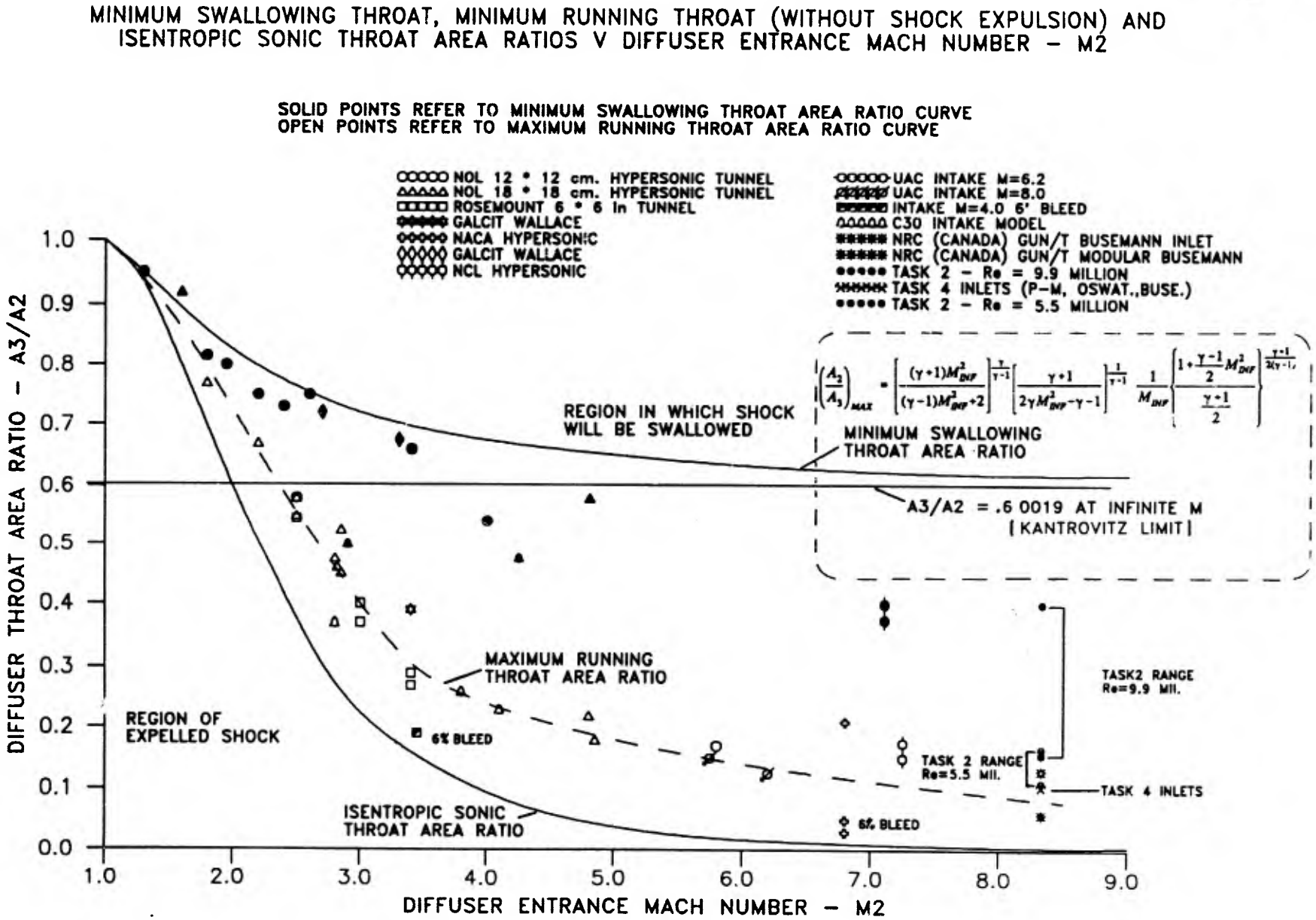

Figure 4.1 Isentropic and the classic Kantrovitz limits to the area ratios of started inlets are shown as a function of the freestream Mach numbers of several steady state and impulsive facilities including the Ryerson/U of T Gun tunnel.

to a tunnel run, the test gas upstream of the throat is blocked from entering the nozzle and the test section by a thin diaphragm or throat plug and the nozzle and test section are evacuated to a low pressure (10-50 Pa). This is done to accelerate the subsequent nozzle starting process; for otherwise, an overly long nozzle start-up transient would eat into the already short testing time. As a consequence of the low initial pressure in the inlet, the non-steady starting flow from the nozzle passes easily into the inlet and the inlet flow starts. Although the details of the inlet starting flow are by no means simple, it is a well-known experimental fact (Ref. 4.3) that inlets with contraction ratios of 10 and even up to 20 have been started in impulsive tunnels. Eliminating the need for inlet geometry variation makes the impulsive wind tunnel eminently suitable for hypersonic inlet testing. It is the purpose of this report to present the results of a systematic study of impulsive starting of a two-dimensional forebody-cowl type inlet, examining on a go-no-go basis, the effects on inlet starting of:

a) tunnel total to initial test section pressure ratio;

b) amount of internal contraction;

c) rate of internal contraction (the cowl angle); and

d) Reynolds number

4.1.1 Theoretical Considerations

In this section, we will discuss the theoretical aspects of flow behaviour in a converging passage placed in a supersonic/hypersonic freestream flow. Considerations will be given to unstarted flow, started flow, and the mechanism involved in each. Discussion of steady and quasi-steady flow relies on the results of compressible, one-dimensional, inviscid, steady flow analysis.

4.1.1.1 The Unstarted Condition

A convergent inlet placed in a steady supersonic freestream is unstarted when a bowshock sits in front of the inlet and, as a direct consequence, the flow inside the inlet is subsonic, (Fig. 4.2a). The mass flow

passing through the inlet determines the location and shape of the bowshock. At the exit, the flow becomes sonic (M_3=1), which serves to isolate the inlet from effects of downstream pressure variations so that the mass flow through the exit plane is given by (Ref. 4.4);

$$\dot{m}_3(M_3=1)=\sqrt{\frac{\gamma}{R}}\frac{Pt_3}{\sqrt{Tt_3}}A_3\,F(1) \tag{4.1}$$

where

$$F(M)=\frac{M}{(1+\frac{\gamma-1}{2}M^2)^{\frac{\gamma+1}{2(\gamma-1)}}} \tag{4.2}$$

so that

$$F(1)=\frac{1}{\left(\frac{\gamma+1}{2}\right)^{\frac{\gamma+1}{2(\gamma-1)}}} \tag{4.3}$$

The freestream mass flow captured by the inlet under these conditions is of course equal to that which passes through the exit so that:

$$\dot{m}_{INF}(M=M_{INF})=\sqrt{\frac{\gamma}{R}}\frac{Pt}{\sqrt{Tt_{INF}}}A_{INF}\,F(M_{INF})=\dot{m}_{INF}(M=1) \tag{4.4}$$

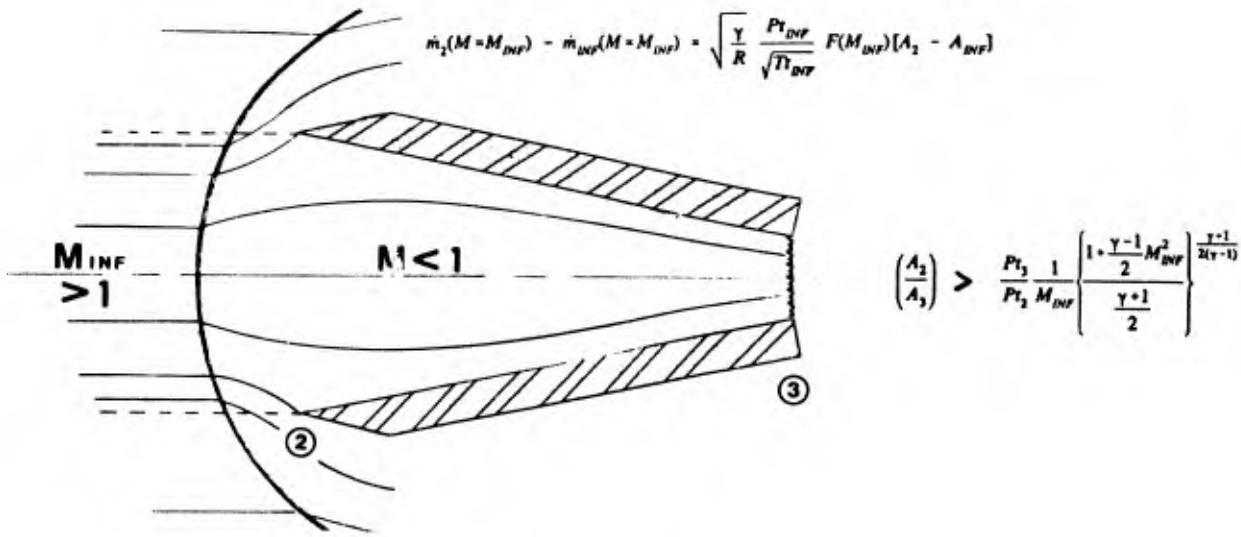

Figure 4.2a Shock and streamline characteristics in a typical unstarted diffuser. Bow shock sits in front of inlet.

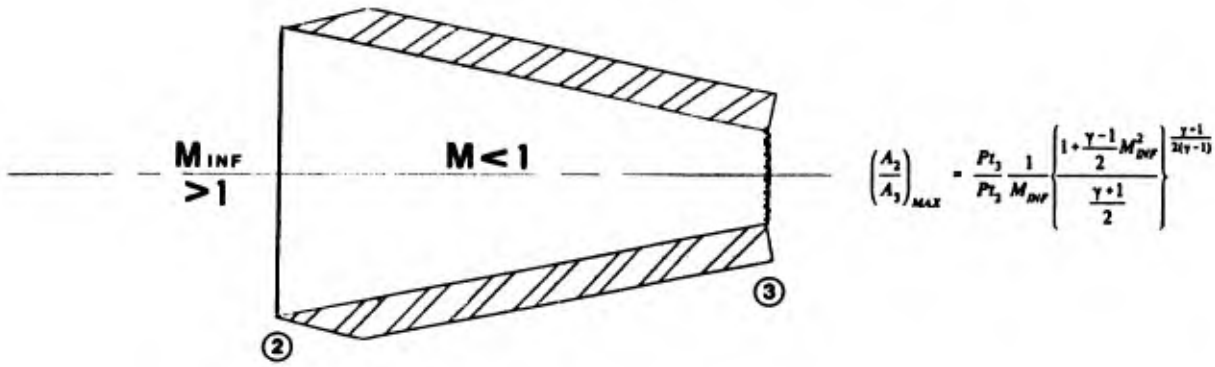

Figure 4.2b Unstarted inlet without flow spillage.

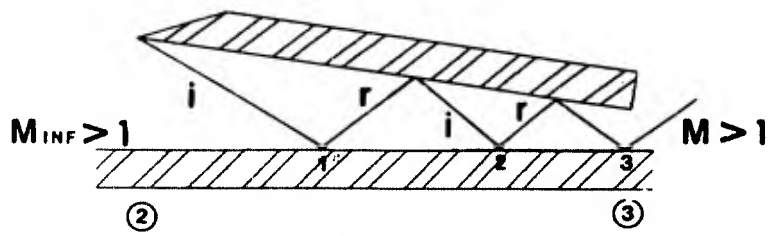

Figure 4.3a Characteristics of a typical started diffuser. Multiple reflected shocks and supersonic exit flow are evident.

The amount of spilled mass flow is then:

$$\dot{m}_2(M=M_{INF}) - \dot{m}_{INF}(M=M_{INF}) = \sqrt{\frac{\gamma}{R}} \frac{Pt_{INF}}{\sqrt{Tt_{INF}}} F(M_{INF})[A_2 - A_{INF}] \tag{4.5}$$

If now A_2 is adjusted (made smaller) such that there is no spillage, i.e. $A_2 = A_{inf}$ then we see that:

$$\sqrt{\frac{\gamma}{R}} \frac{Pt_{INF}}{\sqrt{Tt_{INF}}} A_2 F(M_{INF}) = \sqrt{\frac{\gamma}{R}} \frac{Pt_3}{\sqrt{Tt_3}} A_3 F(1) \tag{4.6}$$

If the flow is adiabatic then $Tt_{inf} = Tt_3$ and;

$$\frac{A_2}{A_3} = \frac{Pt_3 F(1)}{Pt_{INF} F(M_{INF})} \tag{4.7}$$

gives the contraction ratio for the inlet where there is no spillage and the normal shock must then be located at the entrance of the inlet (Fig. 4.2b). Any further decrease in A_2 (or increase in A_3) will cause the exit flow to become subsonic and the shock to move downstream out of the inlet. This shock "swallowing" constitutes the inlet starting process as set forth here on the basis of one-dimensional theory assuming a normal shock, adiabatic flow, isentropic subsonic flow and an invariant freestream at a constant Mach number M_{inf}. The ratio of A_2/A_3 can be written in terms of γ and M_{inf} only if the total pressure ratio can be specified as a function of γ and M_{inf}:

$$\left(\frac{A_2}{A_3}\right)_{MAX} = \frac{Pt_3}{Pt_2}\frac{1}{M_{INF}}\left\{\frac{1+\frac{\gamma-1}{2}M_{INF}^2}{\frac{\gamma+1}{2}}\right\}^{\frac{\gamma+1}{2(\gamma-1)}} \tag{4.8}$$

For the case of a normal shock, the total pressure ratio across the shock is;

$$\frac{Pt_3}{Pt_2} = \left[\frac{(\gamma+1)M_{INF}^2}{(\gamma-1)M_{INF}^2+2}\right]^{\frac{\gamma}{\gamma-1}}\left[\frac{\gamma+1}{2\gamma M_{INF}^2-(\gamma-1)}\right]^{\frac{1}{\gamma-1}} \tag{4.9}$$

so that equation (4.8) becomes

$$\left(\frac{A_2}{A_3}\right)_{MAX} = \left[\frac{(\gamma+1)M_{INF}^2}{(\gamma-1)M_{INF}^2+2}\right]^{\frac{\gamma}{\gamma-1}}\left[\frac{\gamma+1}{2\gamma M_{INF}^2-\gamma-1}\right]^{\frac{1}{\gamma-1}}\frac{1}{M_{INF}}\left\{\frac{1+\frac{\gamma-1}{2}M_{INF}^2}{\frac{\gamma+1}{2}}\right\}^{\frac{\gamma+1}{2(\gamma-1)}} \tag{4.10}$$

This equation gives the "MINIMUM SWALLOWING THROAT AREA RATIO" in Fig. 4.1. It is referred to as the KANTROVITZ CRITERION and the value of A_2/A_3 approaches 0.60019 as M_2 approaches infinity.

This theory was first set forth by Eggink (Ref. 4.5) and later independently by Kantrovitz and Donaldson (Ref. 4.6). It places a very severe restriction on the operation of air inlets, as well as windtunnel diffusers, in that the area ratio required for starting by equation (4.8) is far removed from that required for subsequent efficient engine or windtunnel operation.

4.1.1.2 Started Inlet Flow

A convergent inlet in supersonic flow is started when there exists steady supersonic flow at both entry and exit of the inlet. Such an inlet operates at its design condition, as defined by a contraction and compression ratio, which have been selected to be the values to give best engine performance. Studies have shown (Ref. 4.2) that highest engine performance of a given engine operating at specified flight conditions is obtained at specific values of contraction and compression ratio which do not necessarily correspond to highest efficiency of the inlet as defined by any of the proposed measures (Ref. 4.7, 4.8, 4.9) of efficiency. In supersonic inlets, both a reduction in flow area (contraction) and an increase in pressure (compression) can be obtained by passing the flow through shock waves or compression waves (Figure 4.3a). Although compression waves are generally preferable because flow through compression waves is isentropic, there are many reasons why practical inlets employ a combination of shock waves and compression waves. In all supersonic/hypersonic inlets, the Mach number is reduced. In high compression/contraction inlets, however, it may happen that the Mach number is reduced to one, while the flow area is still being reduced. This results in the formation of a strong shock which moves against the incoming inlet flow to position itself in front of the inlet thus re-establishing the unstarted condition. This type of unstart can also occur if the downstream pressure in the inlet is raised to a level higher than that which is compatible with the given started flow.

4.1.1.3 Inlet Unstart

As introduced in the previous section, inlet unstart occurs when the Mach number tends to one in a converging section of the inlet. This is a serious and dramatic limit on inlet operation, and it provides a boundary for the present study of impulsive inlet starting because there is no point in trying to start an inlet which will not remain started. It should also be noted that for scramjet inlets, unstarting is an unlikely event since exit velocities for scramjet inlets are far from sonic.

Consider first, an all-isentropic inlet. The area ratio between the entry area A_2 at M_2 and the exit area, A_3 at $M_3 = 1$, is (A_3/A_2) isentropic. This "ISENTROPIC SONIC THROAT AREA RATIO" line is plotted against entry Mach number, M_2, in Figure 4.1. This curve represents the limit of contraction for all inlets

(with adiabatic flow). At this condition, any increase in A_2 or decrease in A_3 would lead to inlet unstart. Since real inlets are not isentropic, we expect not to attain the isentropic limit in practice but to be limited at a higher value of A_3/A_2 where M_3 reaches one. For non-isentropic inlets, the maximum contraction ratio is given by:

$$\left(\frac{A_{INF}}{A_3}\right)_{MAX} = \frac{Pt_3}{Pt_{INF}} \cdot \frac{F(1)}{F(M_3)} \tag{4.11}$$

where Pt_3/Pt_2, or ηpt, is the stable, operating, total pressure recovery of the inlet and a commonly applied measure of inlet performance (Ref. 4.9).

It is now of interest to relate some practical inlet designs to the limit imposed by Equation (4.11). The totally isentropic inlet, containing only compression waves and no shocks and no boundary layers, has already been described and its limit of stable operation is given by the isentropic curve labelled "ISENTROPIC SONIC THROAT AREA RATIO" on Figure 4.1. Another inlet design consists of a wedge (or cowl) and a flat wall (Figure 4.3a) which cause a set of n pairs of incident and reflected shockwaves in a narrowing passage. In the particular figure shown n = 3, and after every reflected shock, r, the flow is parallel to the freestream direction. The 3-pair inlet reaches its limiting contraction when the Mach number after the 3rd reflected shock becomes one. The stable operating limits of oblique shock inlets are shown in Figure 4.3b. A reduction of A_3/A_2 below any curve would cause unstart of the inlet defined by that curve. For example at Mach 5, 2 pairs of reflected shocks produce a flow between opposite wedges such that after the final reflected shock, the Mach number is one and the contraction ratio is $A_3/A_2 = 0.1$. Figure 4.3c shows that a wedge of 16.5 degrees is required to produce the two pairs of shocks.

Comparing Figure 4.3b and Figure 4.1 it is seen that the 1-shock pair line in Figure 4.3b and the "MAXIMUM RUNNING THROAT AREA RATIO" curve in Figure 4.1 are in close agreement with one another. This implies that most of the actual diffusers on which Figure 4.1 is based operated with

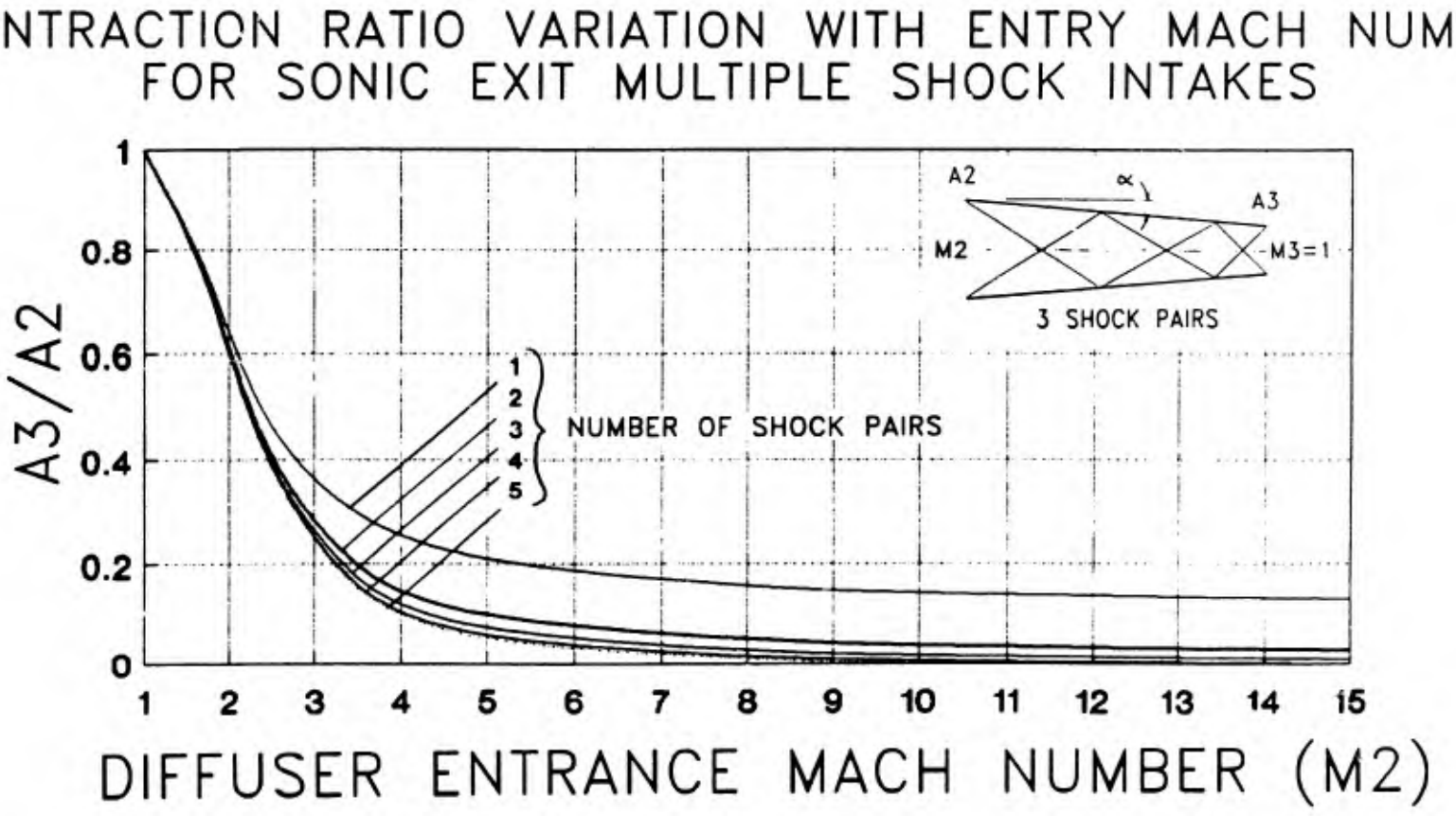

Figure 4.3b Start limiting inlet area ratios for inviscid flow.

COWL ANGLE VARIATION WITH ENTRY MACH NUMBER FOR SONIC EXIT MULTIPLE SHOCK INTAKES

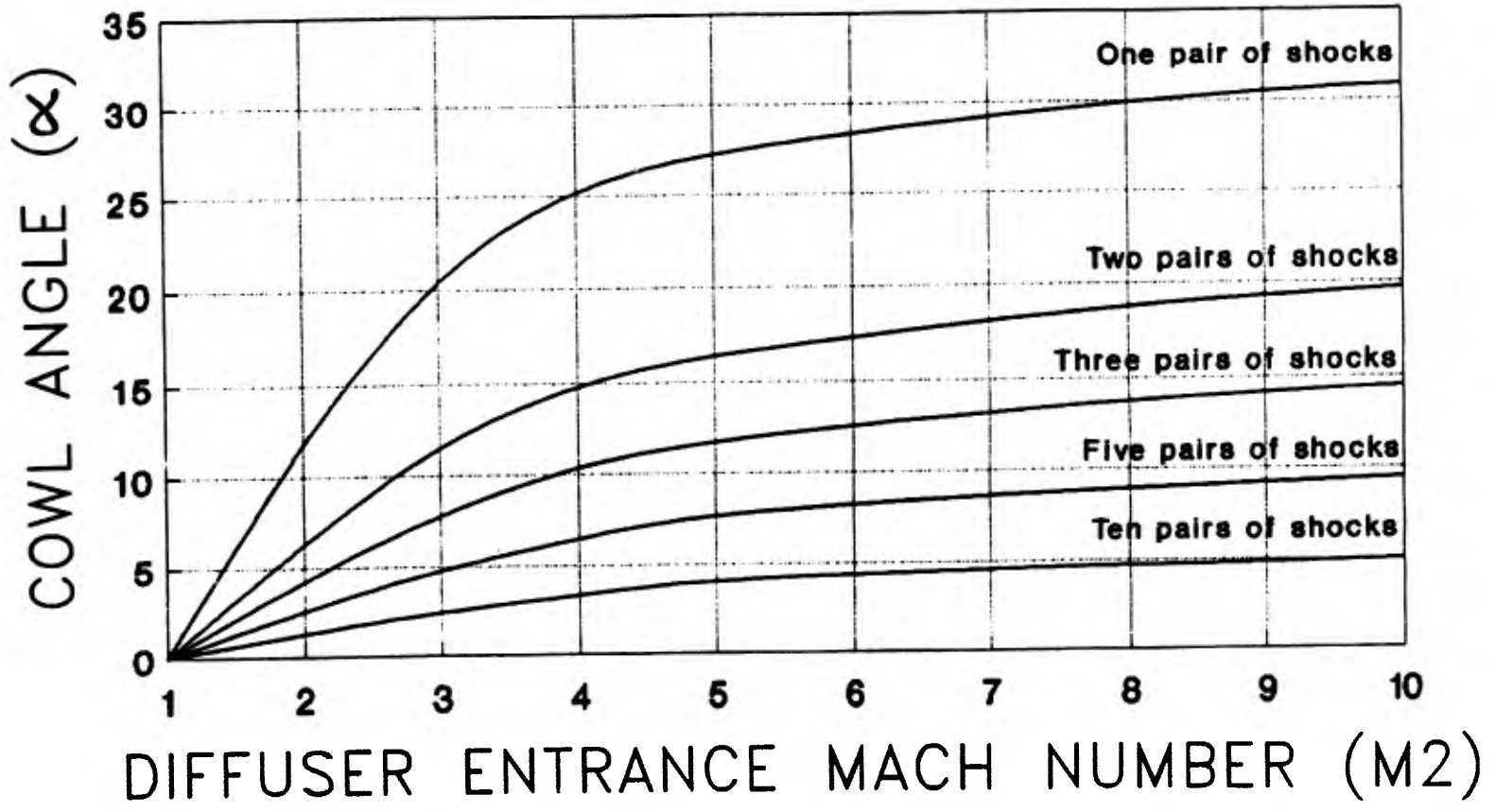

Figure 4.3c Start limiting cowl angle for inviscid multiple shock intakes.

efficiencies (when started) which were close to that obtained by the one-shock pair of reflecting oblique shocks.

There is thus a clear limit to the stable operation of these multiple oblique shock inlets as here posed by inviscid ideal gas oblique shock theory. This limit is overly optimistic when applied to real inlets due to the effects of boundary layers and overly pessimistic due to the ameliorating effects of real gas behaviour. The effect of the boundary layer is to produce a displacement thickness which reduces the effective (inviscid) exit area. This causes sonic exit flow at a geometric A_2/A_3 which is smaller than that predicted by inviscid theory; the result is inlet unstart at a lower contraction ratio. Such boundary layer induced unstarting can be further aggravated if the adverse pressure gradients in the inlet flow are strong enough to separate the boundary layer. In such a case, the flow displacement caused by a separated region may lead to effective flow contraction larger than that caused by boundary layer displacement alone with consequent inlet unstarting. The wall temperature of the inlet surface has a marked effect on both of the above phenomena in that a rising temperature causes a bigger displacement thickness and an earlier boundary layer separation. Stable inlet flow on a cool wall may very well unstart once the inlet wall surface approaches adiabatic wall temperatures as a result of aerodynamic heating. This effect has been observed on hypersonic inlets tested in continuous facilities (Ref. 4.10) where the initially cool model wall has had an opportunity to approach tunnel total temperatures. These tests were done on inlets which were designed to produce subsonic exit Mach numbers aft of a converging throat. Hence, their area ratios were too large to be useful for scramjet applications.

Many cycle calculations have shown that best scramjet engine performance is attained when the inlet brings about a reduction in freestream Mach number by a factor of about 3. Consequently, hypersonic air inlet designs are such that inlet unstart by choking is unlikely since the exit Mach number is well above one. This, of course, does not mean that, under the same conditions, starting is at all likely.

A recent technical note by Azevedo, Lin and Rae (Ref. 4.11) shows results for the more complicated case of Mach reflections between plane wedges. However only one set of reflected shocks is considered so that, to cause a substantial amount of subsonic flow at the exit, the shocks are too strong for such a geometry to be a practical engine inlet.

4.2 Technical Approach

The purpose of this task is to provide data for the design of rectangular inlet models to be tested in the gun tunnel. In particular it is desirable to predict whether a given forebody/cowl combination will or will not start.

Figure 4.4 illustrates the geometric as well as the gasdynamic problem. It is convenient to refer to the plate angle of attack (α), in terms of the primary geometric variables;

$$\sin\alpha = \frac{H_2+H_3}{L} \tag{4.12}$$

Our first analysis assumes that the flow is planarly symmetric so that the width of the plate does not enter the picture. Later analysis will make some attempt to account for the 3-dimensional nature of the flow caused by the viscous influence of the side walls.

It will be assumed that flow starting in the inlet is governed by some combination of the physical and gasdynamic variables forming three primary influences:

a) The nozzle flow starting process. This is determined by Pt, Pb, M_{in}, and nozzle shape.

b) The inlet geometry as specified by the four variables, Xc, H_2, H_3, and Lc.

c) Viscous effects as determined by and wall temperature. It is expected that the viscous effects are especially important when $(H_2 + H_3)/2$ is small.

In our present tests, the following variables are kept constant;

Pt, ρ, V, M_{in}, Re (freestream), L, and rc

This leaves the following variables for study:

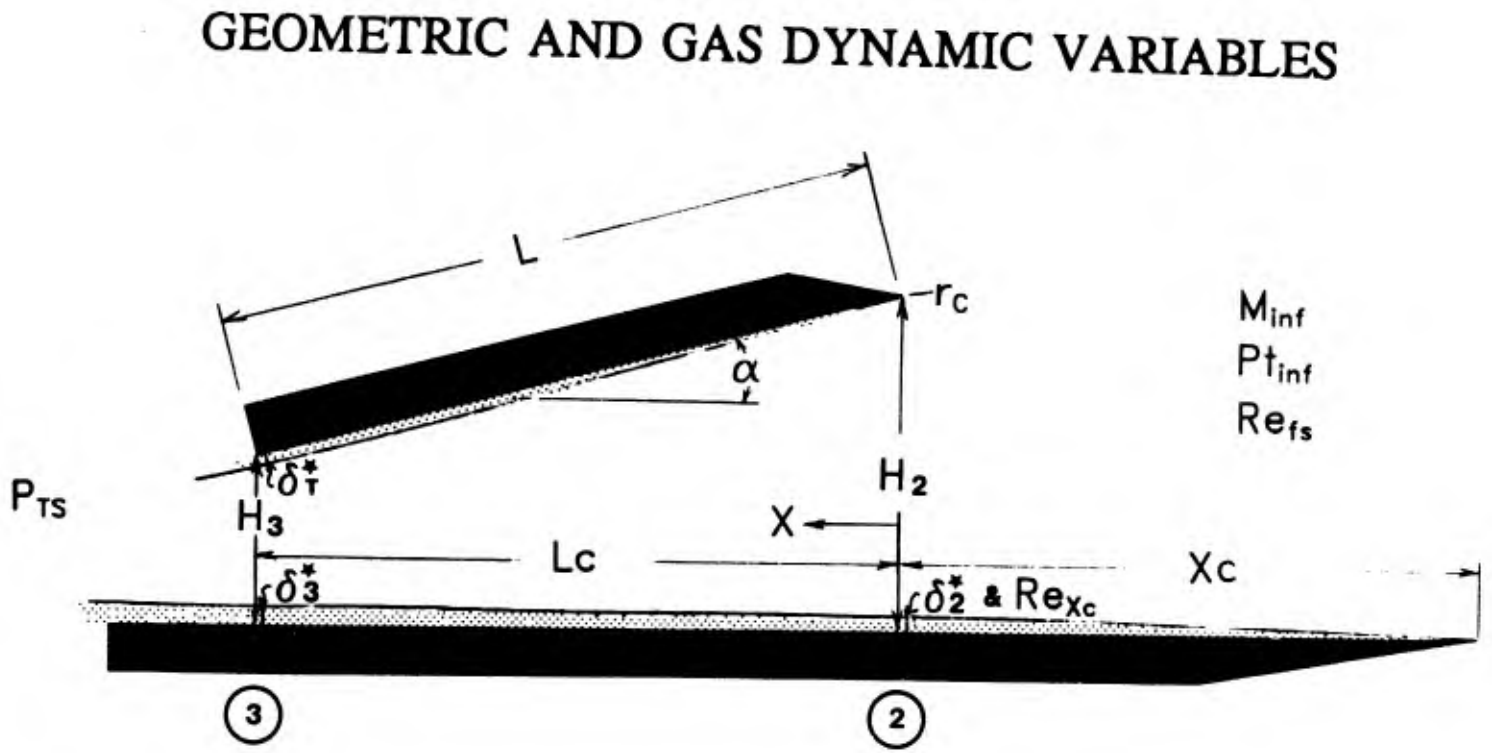

Figure 4.4 Schematic of the 2-dimensional model showing the geometric and gasdynamic parameters.

Pb - initial dump tank pressure

Xc - linear distanced from bottom plate leading edge to cowl

H_2 - cowl entry height

H_3 - cowl exit height

Re_{xc} - surface and momentum thickness Reynolds number

P_2 - inlet entry pressure

P_3 - inlet exit pressure

δ_2^*- entry boundary layer displacement thickness

δ_{3^*}- exit boundary layer displacement thickness

δ_{r^*}- cowl exit boundary layer displacement thickness

4.2.1 Experimental Procedure

4.2.1.1 Model and Instrumentation

The variable cowl inlet model is shown in the diagram of Figure 4.5 and the photograph, Figure 4.6 As a two-dimensional oblique shock type intake it essentially consists of two flat plates between side walls for flow containment. The sidewalls are equipped with optical quality windows to allow schlieren visualization of the flow. The cowl is adjustable to within 0.1 mm of the desired entry and exit height settings over an infinite combination of area ratios between 0 and 30 degrees of inclination. Reynolds number variation (Re_{xc}) is accomplished by positioning the cowl at any one of the four streamwise stations in the sidewalls (Figures 4.5 and 4.6). The cowl length (L), base plate angle of attack, and leading edge bluntness (rc) were fixed for this set of tests at 127 mm, 0 degrees, and .07 mm radius respectively.

The leading edges of the sidewalls (also of .07 mm radius) were even with the bottom plate. The assembly was fixed in the test-section by means of a pivoting support and two threaded bolts in such a way that the inviscid core flow from the nozzle covered the model entry stream tube (see Figure 4.5b).

INLET STARTING ENVELOPE MODEL ASSEMBLY

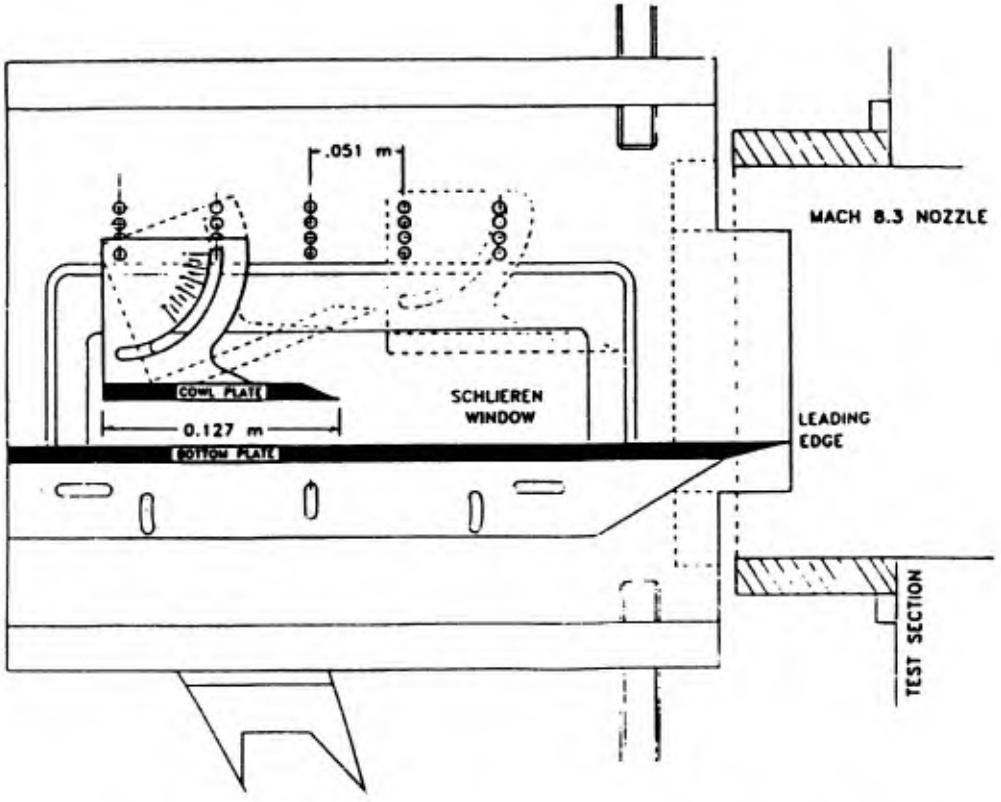

Figure 4.5a Line drawing of the model mechanism showing the lateral and angular adjustability.

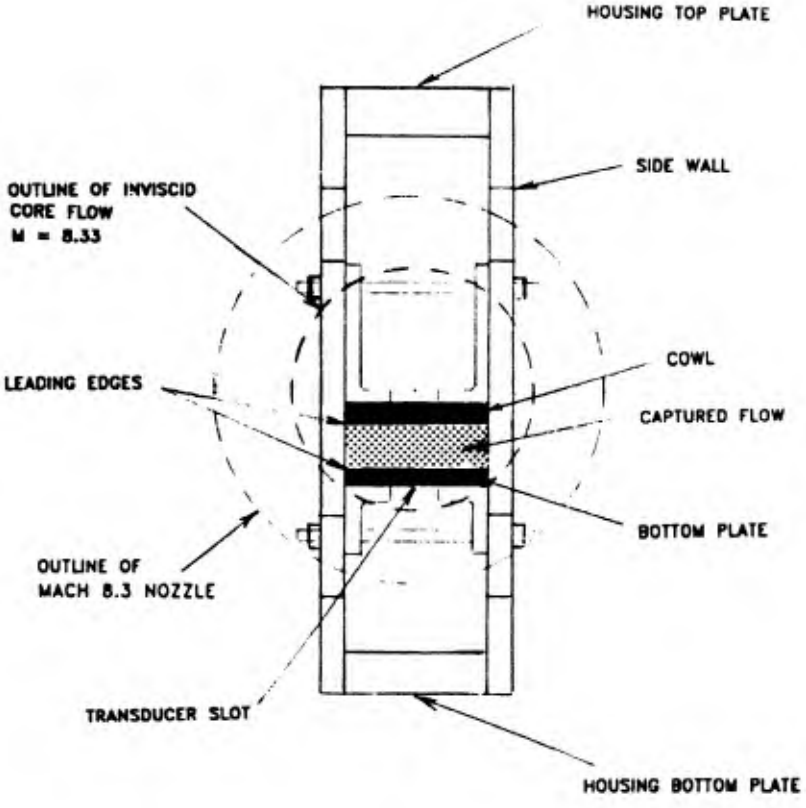

Figure 4.5b Flow view of the model indicating the captured flow within the inviscid core of the nozzle.

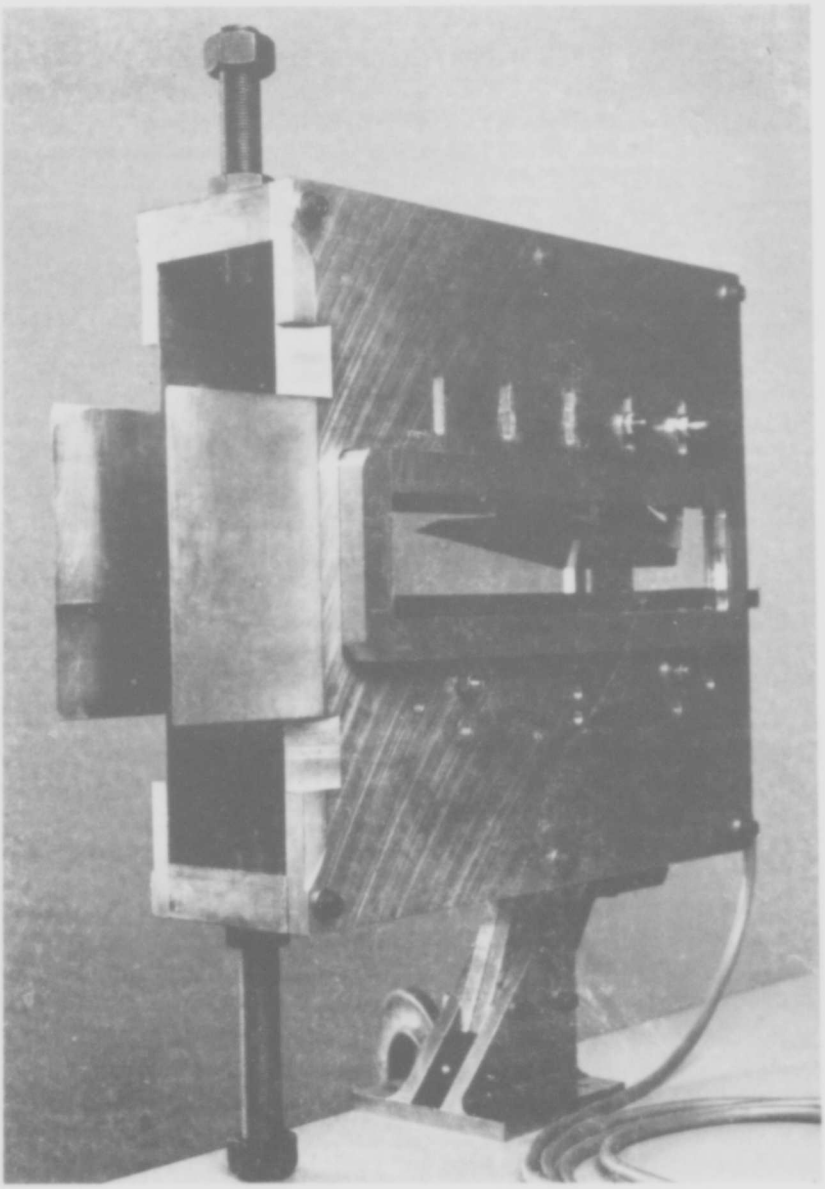

Figure 4.6 Photograph of the gun tunnel model.

The base plate and cowl have been instrumented along the streamwise centerlines with Endevco and Kulite miniature static pressure transducers. These have specific uncertainties that are rated at less than 1% of their maximum pressure.

4.2.1.2 Gun tunnel Conditions

The calibrated specifications of the tunnel have been documented in Reference 4.12. For this series of experiments, gun tunnel driver loading was maintained at approximately 20.8 Mpa. Driven tube pressure was initially changed between 400 and 800 Kpa. Subsequently, the majority of the experiments were run at 800 Kpa giving the following operating conditions for the majority of the program:

Tunnel Mach number	M1 = 8.33
Tunnel total temperature	Tt = 760 K
Tunnel total pressure	Pt = 26.51 Mpa
Test section Reynolds #	Re = 44 * 10^6 m^{-1}

The model was mounted at the centerline of the freestream with the leading edge of the bottom plate at 76 mm downstream of the Mach 8.3 nozzle exit. Initial test section pressure was incremented from the minimum of 40 Pa up to 1500 Pa during the back pressure variation phase of the study.

4.2.1.3 Test Procedure

Between run alterations of the inlet geometry and longitudinal position led to the variation of the independent variables of cowl angle (rate of contraction), area ratio (and therefore capture height), and Reynolds number (and therefore boundary layer influence). The dependent variables - surface static pressure and start condition - were then measured by the instrumentation.

For each of five cowl angles, 2.5, 5, 7.5, 10, and 15 degrees, the area ratio (A_2/A_3) was initially set low (H_2 and H_3 high), at a presumably startable position. Following a successful start, the area ratio was increased (H_2 and H_3 decreased) in order to produce unstart. Successive iterations at each cowl angle

would eventually produce two contraction ratios which bracketed the start/no start condition. A sampling of such a test series is shown in Table 4.1. This type of series was conducted at two longitudinal cowl positions corresponding to Reynolds number of 5.5 million and 9.9 million based on cowl set-back distance from base plate leading edge.

A similar series of runs was performed to investigate the influence of initial plenum pressure (back pressure) on the inlet starting. For these experiments the model area ratio was fixed for a given angle and the initial test section pressure was increased between runs until an inlet unstart was observed. This process was repeated for several different area ratios for each of the cowl angle settings. Gradually increasing the test section pressure to produce unstart rather than varying inlet geometry for a fixed back pressure, reduced model change requirements and significantly reduced run turn-around time.

4.3 Results

4.3.1 Determination of Inlet Starting

Typical results of two inlet starting tests are shown in Figure 4.7 for (a) Run 2-040 and (b) 2-025 ; both runs conducted with an initial gun tunnel barrel pressure of 800 Kpa. This initial barrel pressure gives a barrel end pressure of 26.3 MPa (3800 psi) as shown on the uppermost pressure traces on both Figures 4.7(a) and 4.7(b). A comparison of the two barrel end traces shows the extremely good reproducibility of total pressure from one run to the other. In each case the total width of the trace is 50 ms, each division representing 5 ms. Our testing time is normally taken as the 10 ms interval from 17 to 27 ms. The schlieren pictures are taken at the 20 ms mark for both runs. In Figure 4.7a, the cowl is set at an angle of 2.5 and an area ratio of 10. The flow is unstarted with highly fluctuating static pressures at both entry and exit. Entry pressure is higher than exit pressure which is consistent with sub-sonic flow in a converging channel. The frequency of entry static pressure peaks is about the same as the barrel end pressure peaks thus suggesting that the latter is inducing the fluctuations of pressure in the passage. Unstarted flow is further confirmed by the schlieren picture which shows a lack of a shock wave from the cowl and what appear as multiple waves probably emanating from a region of boundary layer separation

COWL ANGLE	RUN #	A_2/A_3	START COND. 800 kPa BARREL	START COND. 400 kPa BARREL
α = 2.5°	2-040	.250/.030 = 8.30	UNSTART	UNSTART
	2-041	.254/.036 = 7.00	UNSTART	UNSTART
	2-042	.260/.042 = 6.20	START	START
α = 5.0°	2-035	.485/.050 = 9.70	UNSTART	UNSTART
	2-036	.498/.062 = 8.03	START	
	2-037	.492/.056 = 8.79	START	START
α = 10.0°	2-023	1.16/.340 = 3.40	START	START
	2-024	1.12/.250 = 4.37	START	START
	2-025	1.02/.197 = 5.10	START	
	2-026	1.04/.175 = 5.95	START	START
	2-027	.992/.120 = 8.27	UNSTART	UNSTART
	2-031	1.02/.150 = 6.79	START	
	2-032	1.01/.135 = 7.46	START	START
	2-033	.994/.125 = 7.95	UNSTART	UNSTART
α = 15.0°	2-012	1.69/.430 = 4.00	START	START
	2-014	1.45/.140 = 10.0	UNSTART	
	2-015	1.57/.228 = 6.89	UNSTART	
	2-016	1.60/.290 = 5.43	UNSTART	
	2-017	1.68/.350 = 4.80	UNSTART	
	2-021	1.65/.360 = 4.60	UNSTART	UNSTART

REYNOLDS NUMBER = 5.5 MILLION
TUNNEL PLENUM PRESSURE = 40 Pa

Table 4.1 Table showing a sampling of the cowl plate adjustments made and tested in order to determine the limits of starting.

some distance upstream of the cowl. As the subsonic flow is accelerated to sonic velocity, a characteristic normal shock is observed at the exit.

In Fig. 4.7b, the cowl is set at an angle of 10 and an area ratio of 6. The flow is started with static pressures that very closely follow the variation of barrel end pressure with a lag of about 1.5 ms. The lag is due to the time it takes a pressure pulse to travel the length of the gun tunnel nozzle from the barrel end to the model. Note that, with the started flow, the exit static pressure is higher than the entry static pressure which is consistent with supersonic flow in a converging area channel. Shock waves reflecting between the cowl and the lower plate, as seen in the schlieren picture, are further confirmation of started flow. This schlieren picture also shows the shock, emanating from the leading edge of the lower plate, being incident on the bottom surface of the cowl near its leading edge.

The type of experimental results described above were used to judge whether the inlet was or was not started as the cowl angle of attack, the cowl contraction ratio, the longitudinal cowl position and initial plenum pressure were changed.

4.3.2 Effect of Area Ratio and Cowl Angle

Figure 4.8 shows the effect of cowl contraction ratio (A_2/A_3) and cowl angle of attack on the location of the starting line for two different streamwise positions of the cowl. These lines have been determined experimentally on the present model configuration by performing gun tunnel runs at Mach 8.33 with an initial tunnel plenum pressure of 40 Pa. The triangular symbols denote unstarted flow and the square symbols denote started flow. Altogether some 60 runs were made to locate these curves. Only points closest to either side of the starting curve are shown. We note that starting does not occur for high contraction ratios. The curves decline towards higher values of cowl angle of attack, implying that starting is more difficult as the shocks become stronger in the inlet. Also starting is more difficult at low cowl angles and high contraction ratios because the boundary layers on both walls now occupy a significant fraction of the passage. The boundary layer effect is also apparent in considering the two curves. The top curve is for the cowl being closer to the bottom plate leading edge than for the bottom curve. Consequently the boundary layer for the top curve is thinner and a higher geometric contraction ratio inlet

START CONDITION DETERMINATION

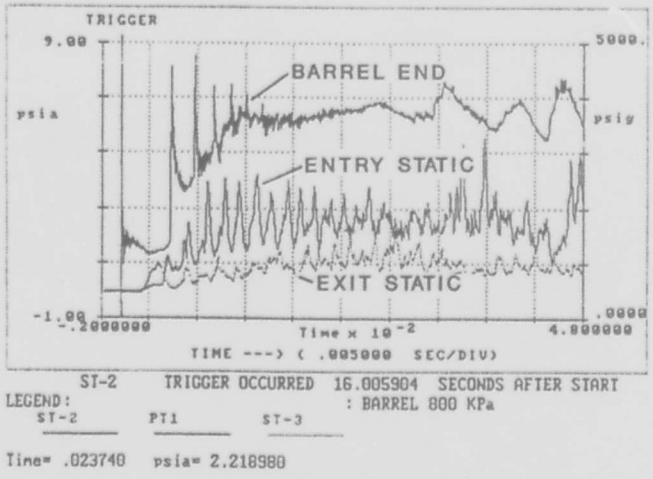

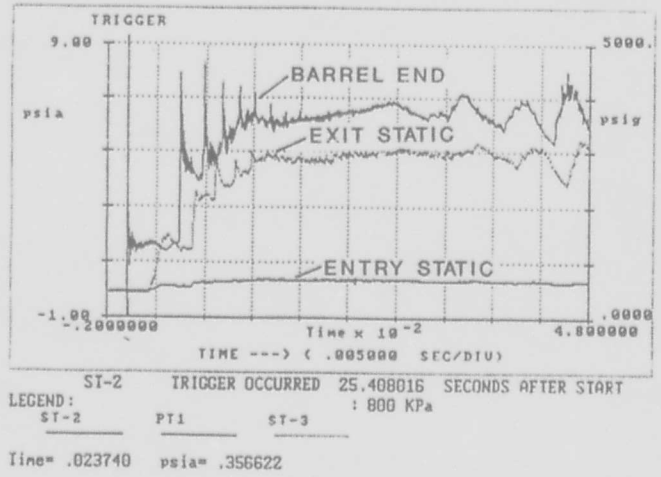

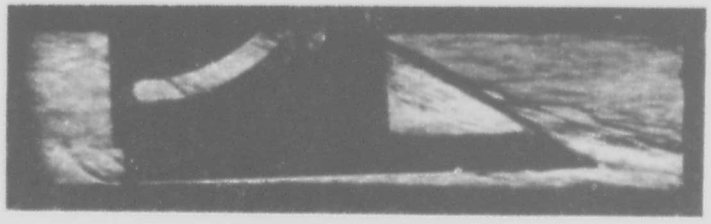

2-040 800 KPa - UNSTARTED

(A)

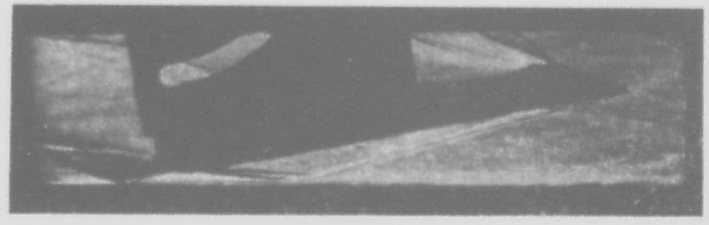

2-025 800 KPa - STARTED

(B)

Figure 4.7 Typical run data showing the characteristics observed for started and unstarted flow.

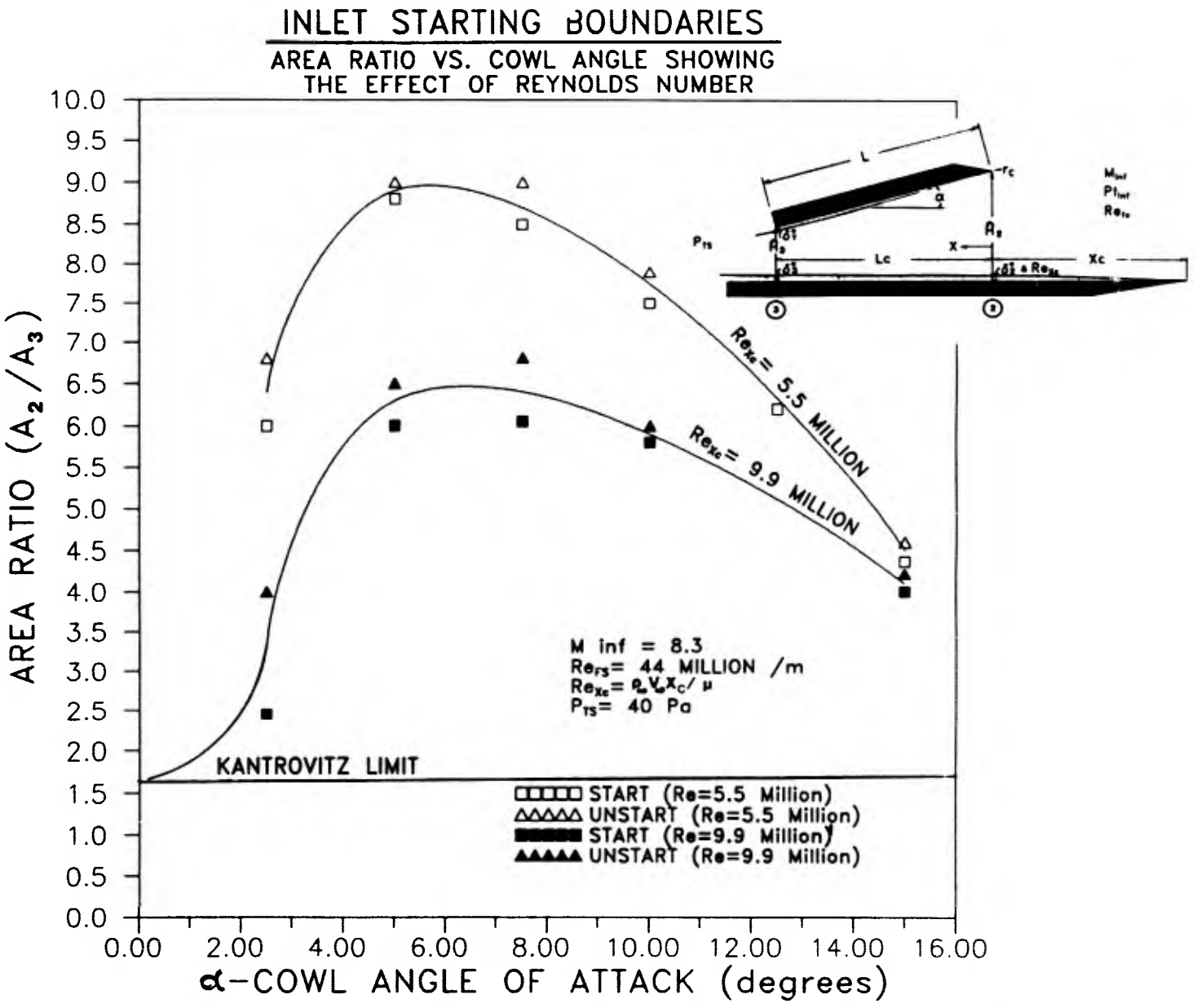

Figure 4.8 The area ratio limits for each of the cowl angle test series are shown at both of the Reynolds number stations.

can be started. This difference becomes more pronounced towards the smaller values of angle of attack where the boundary layer effects are proportionately more significant. Towards larger values of cowl angle of attack the difference due to boundary layer effects becomes smaller as the flow is predominantly inviscid. The Kantrovitz quasi-steady and quasi-one-dimensional starting limit is shown at $A_2/A_3 = 1.666$. The space between our curves and the Kantrovitz limit is attained as a direct result of the non-one-dimensional as well as the impulsive (non quasi-steady) nature of the starting flow. These results are in line with the generalizations that:

a) higher than Kantrovitz-limit area ratio inlets can be started impulsively;

b) this gain in starting contraction ratio deteriorates with inlet performance whether this performance loss is caused by shocks or boundary layers.

For the present inlet geometry and test conditions, it appears that a cowl angle of attack of five degrees will produce the highest contraction ratio inlet that will start impulsively.

4.3.3 Effect of Boundary Layers

Some discussion of viscous effects took place in the previous section in order to reconcile the difference in results for the two longitudinal cowl positions. In this section we present some results of wall pressure measurements together with calculations of inviscid flow and boundary layer behaviour in order to get a better understanding of the effects of viscosity on the starting process.

Figure 4.9 shows the calculated boundary layer thickness on the bottom plate. The Stan6 code has been adapted to perform these calculations. Some discussion of its use and operation can be found in Reference 4.13.

With the cowl in position 1 the boundary layer displacement thickness at cowl leading edge is 1.1 mm, and with cowl in position 2 it is 2.2 mm. The effect of locating the cowl at these two positions, as well as the cowl and sidewall boundary layers are shown by the bottom plate static pressure measurements for a selection of cases involving various ratios in Figure 4.10(a) to (j). Each of these figures shows a

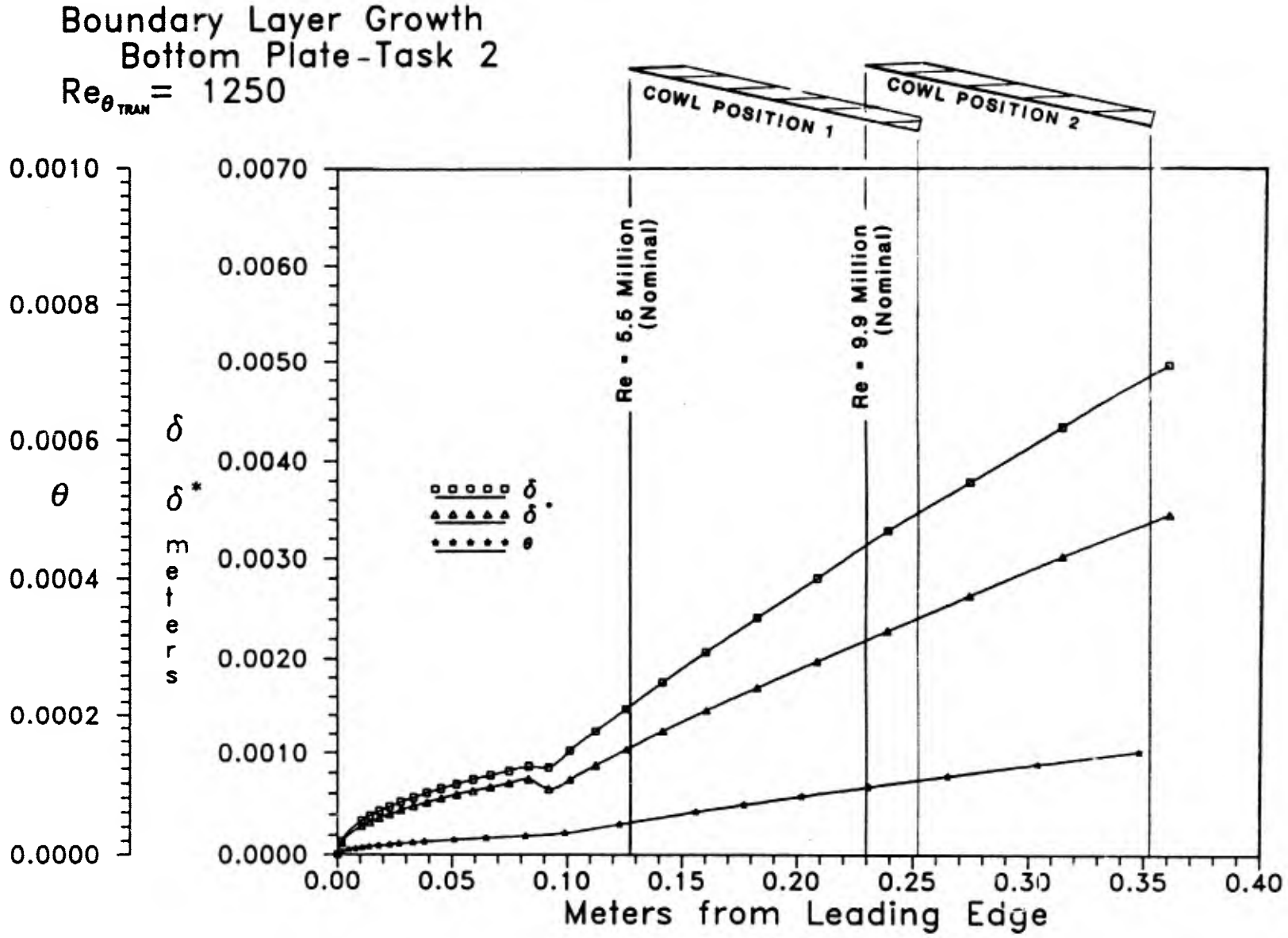

Figure 4.9 Results of the Stan6 base plate boundary layer calculations using a transition Reynolds number corresponding to observed separation.

schlieren picture of the flow in the passage between the cowl and the plate, the calculated inviscid shock structure, the calculated lower wall pressure ratio (INVISCID THEORY), and the measured lower wall pressure ratio (EXPERIMENTAL). In each case the measured shocks lie forward of their predicted positions and the measured wall pressures are higher than those predicted by inviscid theory. Both these results are consistent with the presence of a viscous boundary layer. The effect of the boundary layer is to cause the pressure to rise forward of the place predicted by inviscid theory and to rise higher than predicted by theory. The early rise is particularly noticeable with strong shocks and the higher-than-predicted rise is evident with multiple reflection of weak shocks and high contraction ratios. These results are presented here to confirm started flows in each case for a configuration near unstarting to demonstrate that for the present experimental conditions the boundary layer can have a major influence on inlet flow starting.

Figures 4.10a to 4.10j present the results which were used to confirm started flow. All figures are for a freestream Mach number of 8.33 and a tunnel total pressure of Pt = 26.51 Mpa. The Figures 4.10a to 4.10h are for the cowl plate in the forward position where the Reynolds number, measured along the bottom plate to the cowl leading edge, is $5.5 * 10^6$ and the Figures 4.10i and 4.10j are for the cowl in the downstream position where the cowl leading edge position Reynolds number is $9.9 * 10^6$. Each figure shows a schlieren picture of the flow, the calculated shock location (assuming inviscid flow), and the measured pressure distribution along the bottom plate (assuming inviscid and two-dimensional flow).

Figure 4.10a is for a cowl angle of 15 degrees and a contraction ratio of 2.14. A comparison of the schlieren picture and the calculated shock position shows good correspondence. The schlieren picture also shows a wave emanating form the leading edge of the lower plate (out of view to the right) and compression waves produced by the boundary layer off the bottom plate. Pressure measurements and their comparison with inviscid theory clearly show a region of upstream influence caused by the shock-boundary-layer interaction.

In Figure 4.10b the cowl has been lowered to yield a contraction ratio $A_2/A_3 = 4.0$. The forward influence of the shock-boundary-layer interaction is more pronounced than that in Figure 4.10a. A

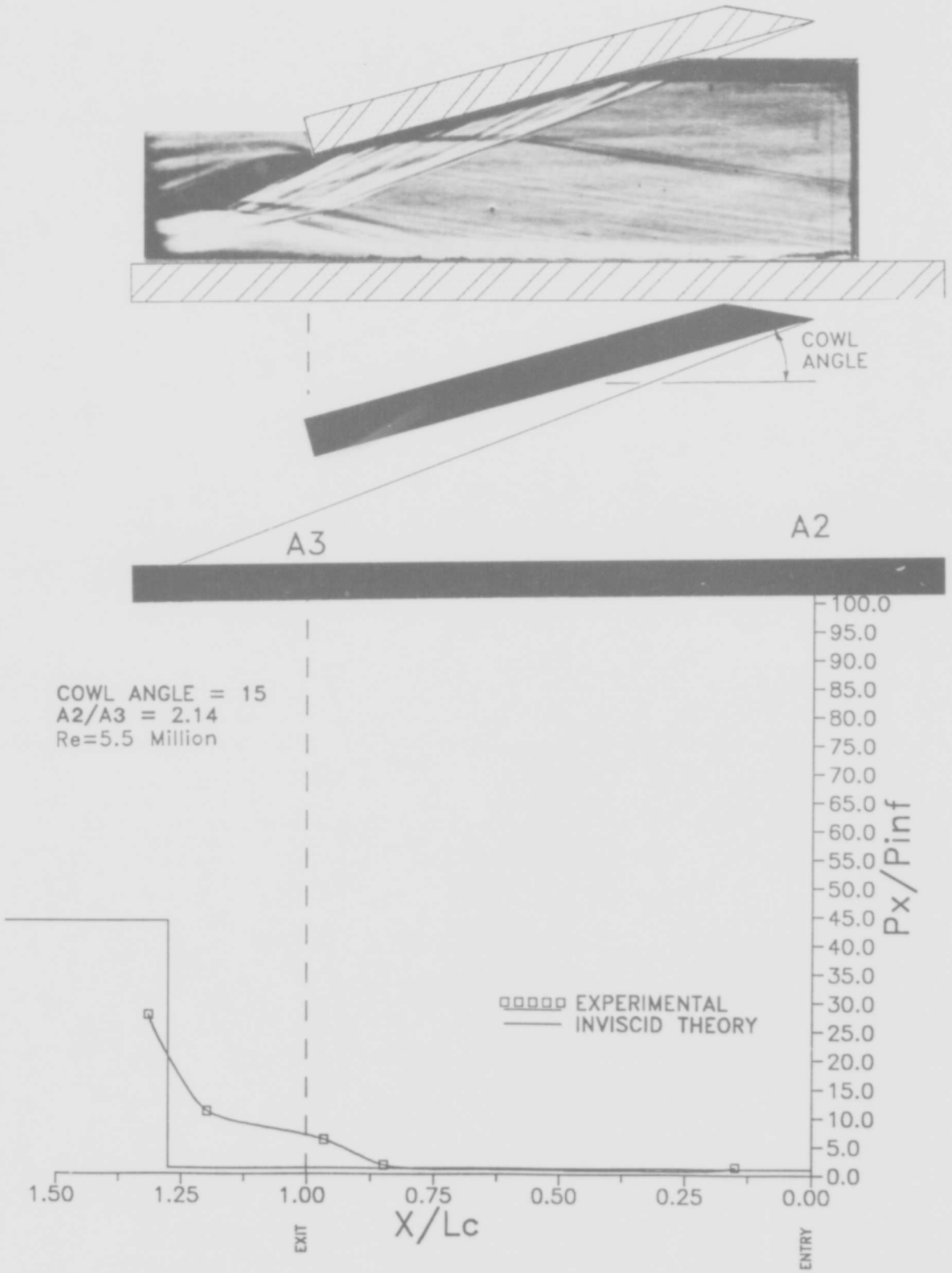

Figure 4.10a-j Experimental and inviscid theoretical pressure and schlieren data are presented for a sampling of tested cowl angles and Reynolds numbers. The effects of shock wave boundary layer interaction on the shock structure and compression can be observed.

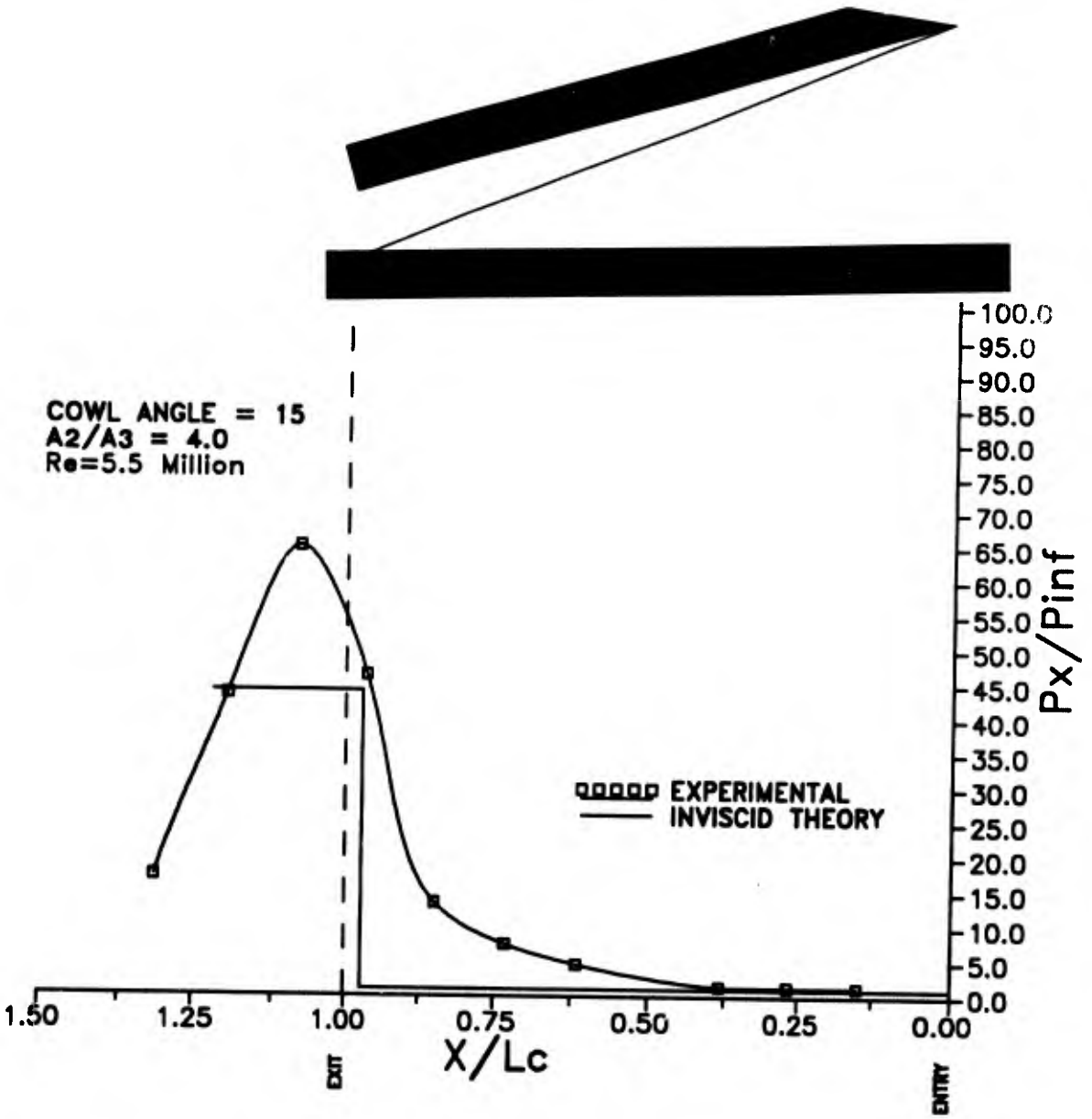
COWL ANGLE = 15
A2/A3 = 4.0
Re=5.5 Million
EXPERIMENTAL
INVISCID THEORY
Px/Pinf
100.0
95.0
90.0
85.0
80.0
75.0
70.0
65.0
60.0
55.0
50.0
45.0
40.0
35.0
30.0
25.0
20.0
15.0
10.0
5.0
0.0
1.50
1.25
1.00
0.75
0.50
0.25
0.00
X/Lc
EXIT
ENTRY

Figure 4.10b

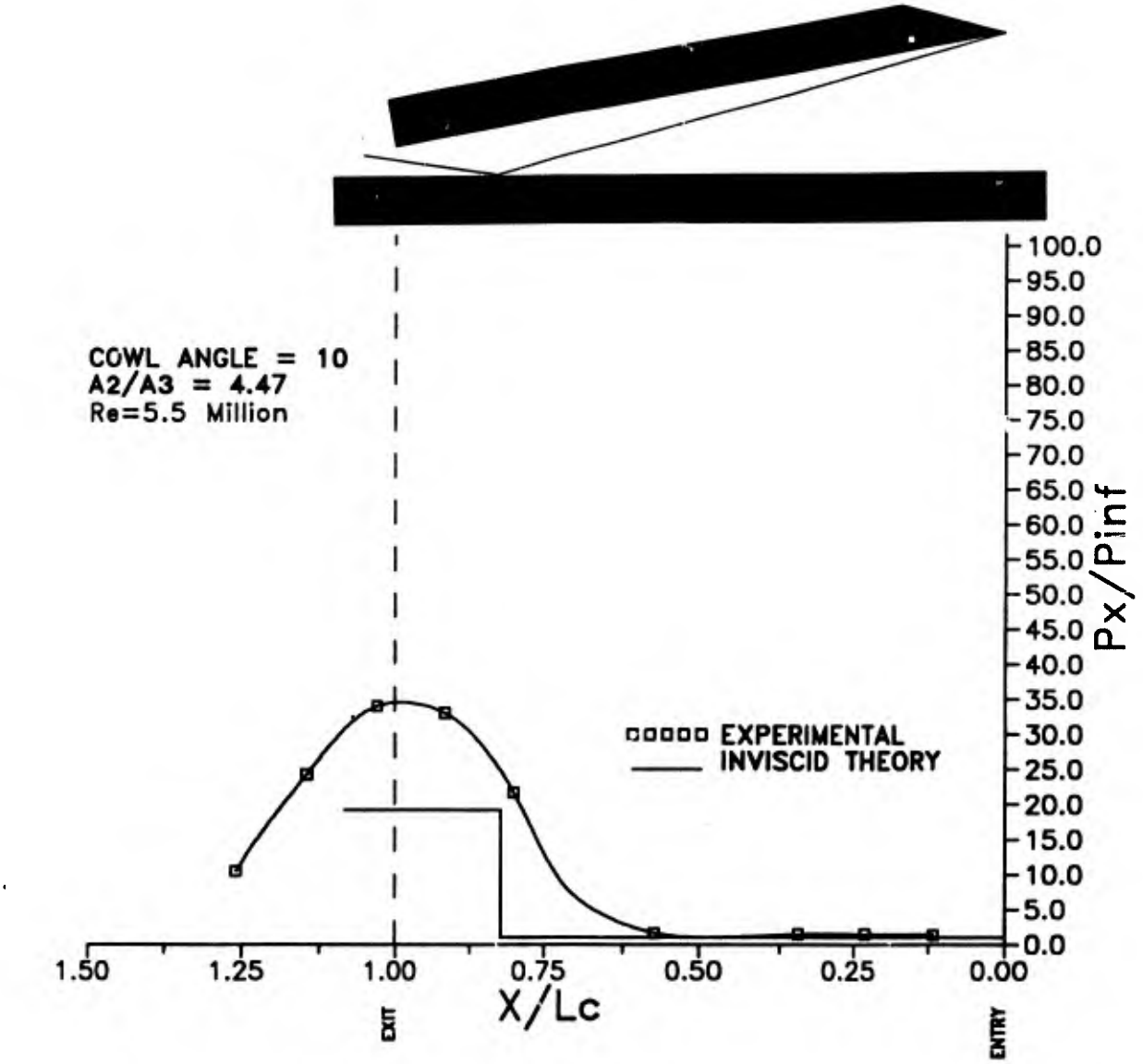
COWL ANGLE = 10
A2/A3 = 4.47
Re=5.5 Million
EXPERIMENTAL
INVISCID THEORY
100.0
95.0
90.0
85.0
80.0
75.0
70.0
65.0
60.0
55.0
50.0
45.0
40.0
35.0
30.0
25.0
20.0
15.0
10.0
5.0
0.0
Px/Pinf
1.50
1.25
1.00
0.75
0.50
0.25
0.00
X/Lc
EXIT
ENTRY

Figure 4.10c

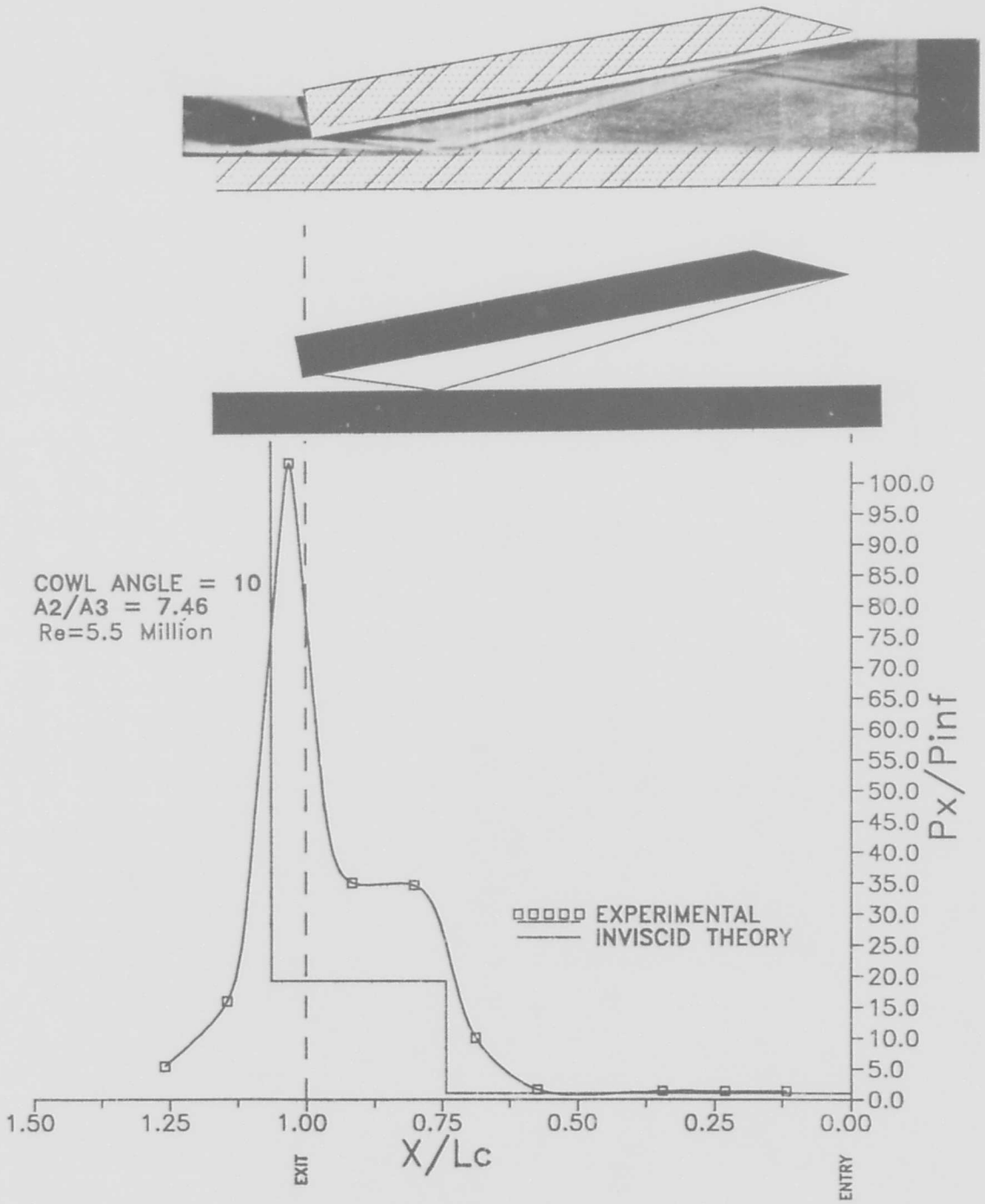
COWL ANGLE = 10
A2/A3 = 7.46
Re=5.5 Million
EXPERIMENTAL
INVISCID THEORY
Px/Pinf
100.0
95.0
90.0
85.0
80.0
75.0
70.0
65.0
60.0
55.0
50.0
45.0
40.0
35.0
30.0
25.0
20.0
15.0
10.0
5.0
0.0
1.50
1.25
1.00
0.75
0.50
0.25
0.00
X/Lc
EXIT
ENTRY

Figure 4.10d

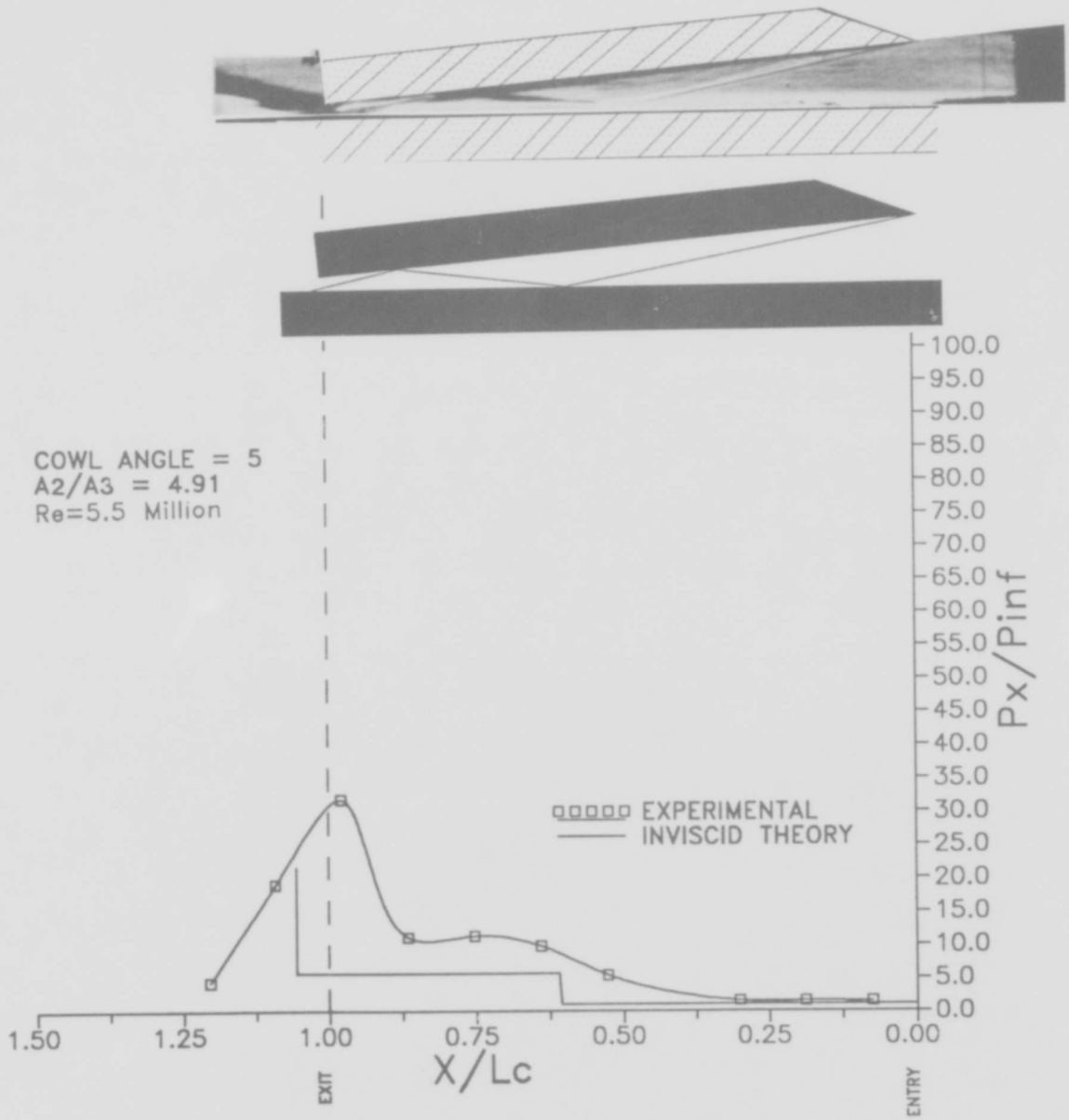
COWL ANGLE = 5
A2/A3 = 4.91
Re=5.5 Million
EXPERIMENTAL
INVISCID THEORY
Px/Pinf
100.0
95.0
90.0
85.0
80.0
75.0
70.0
65.0
60.0
55.0
50.0
45.0
40.0
35.0
30.0
25.0
20.0
15.0
10.0
5.0
0.0
1.50
1.25
1.00
0.75
0.50
0.25
0.00
X/Lc
EXIT
ENTRY

Figure 4.10e

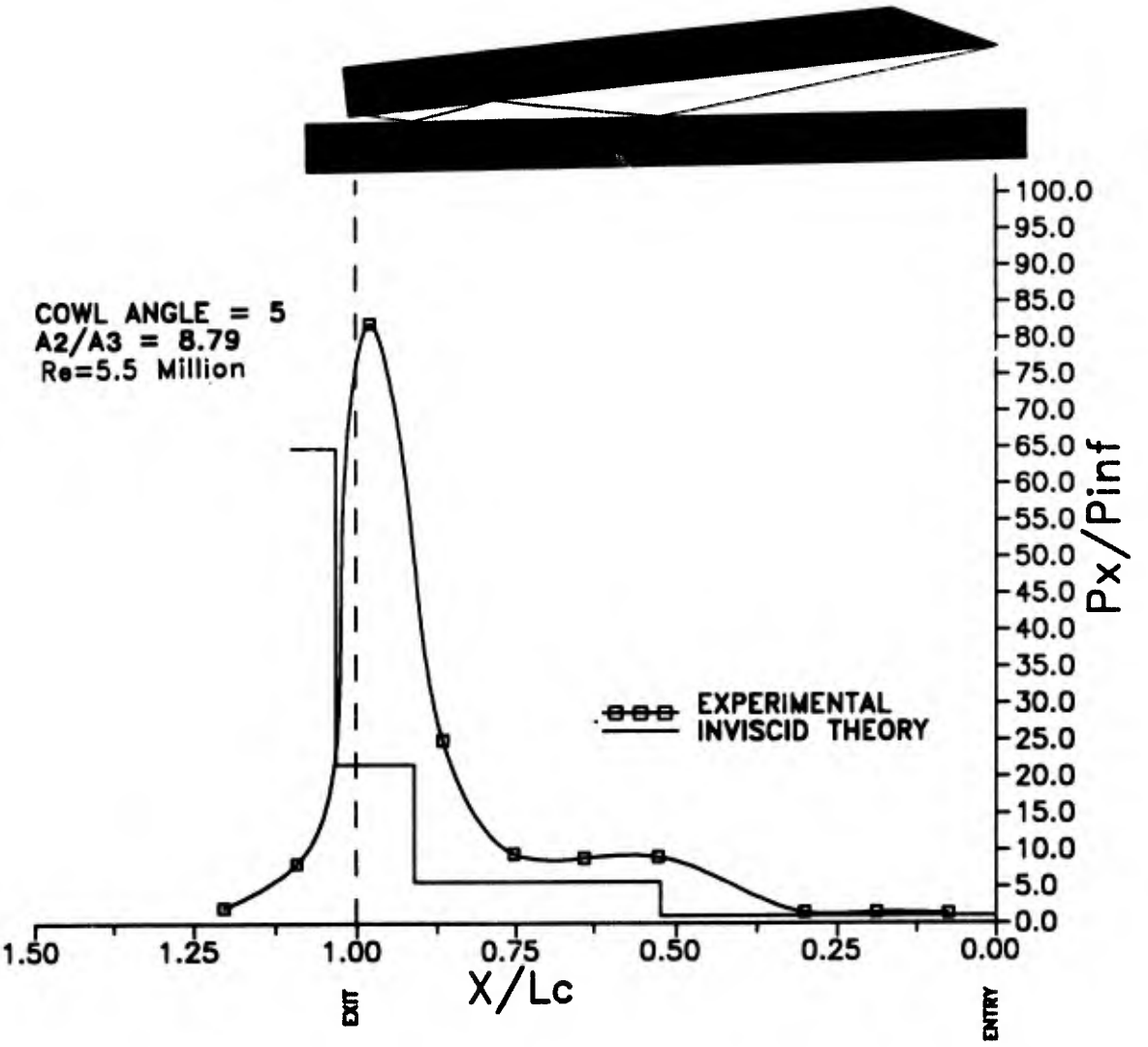
COWL ANGLE = 5
A2/A3 = 8.79
Re=5.5 Million
EXPERIMENTAL
INVISCID THEORY
100.0
95.0
90.0
85.0
80.0
75.0
70.0
65.0
60.0
55.0
50.0
45.0
40.0
35.0
30.0
25.0
20.0
15.0
10.0
5.0
0.0
Px/Pinf
1.50
1.25
1.00
0.75
0.50
0.25
0.00
X/Lc
EXIT
ENTRY

Figure 4.10f

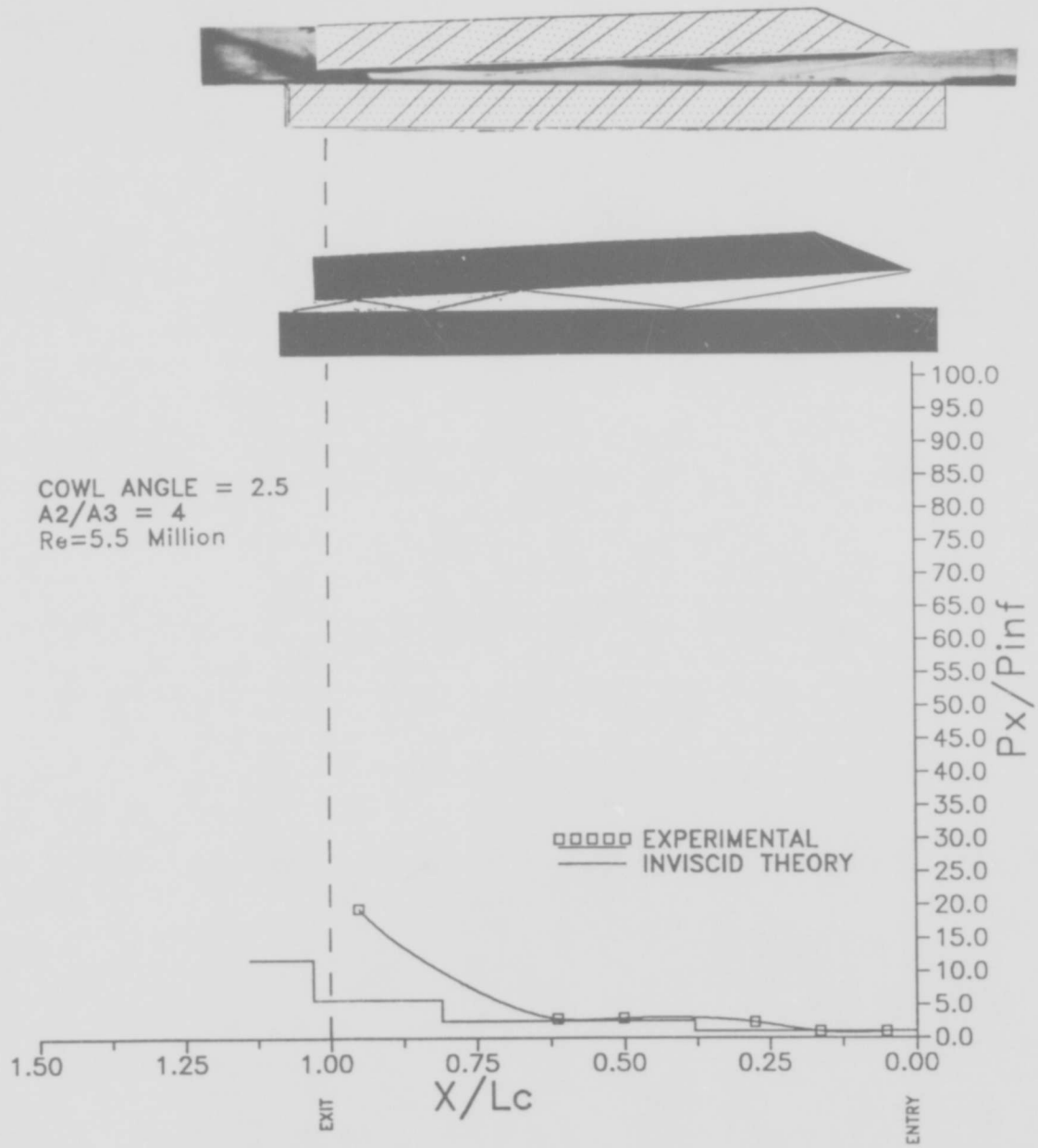
COWL ANGLE = 2.5
A2/A3 = 4
Re=5.5 Million
EXPERIMENTAL
INVISCID THEORY
Px/Pinf
100.0
95.0
90.0
85.0
80.0
75.0
70.0
65.0
60.0
55.0
50.0
45.0
40.0
35.0
30.0
25.0
20.0
15.0
10.0
5.0
0.0
1.50
1.25
1.00
0.75
0.50
0.25
0.00
X/Lc
EXIT
ENTRY

Figure 4.10g

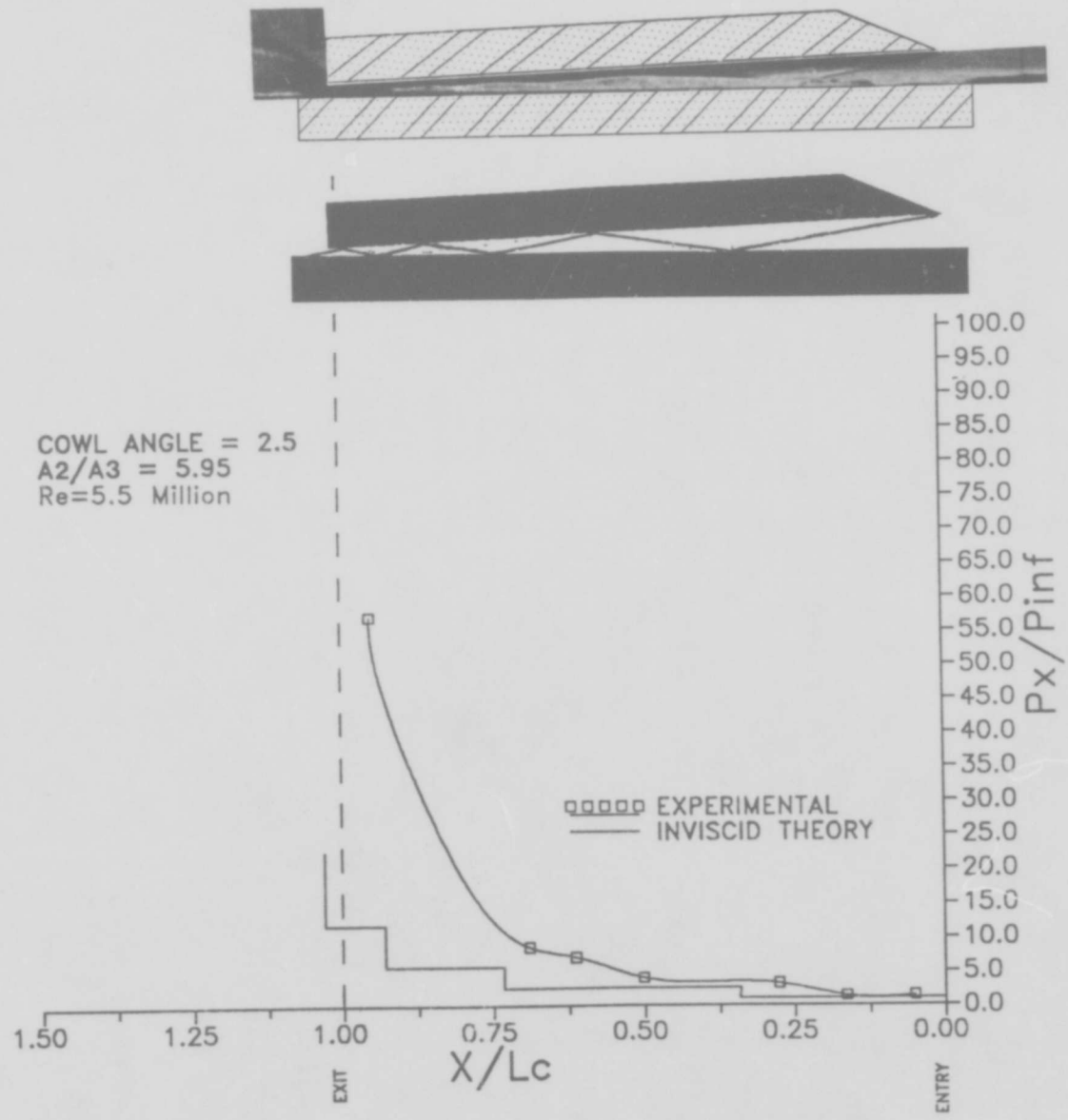
COWL ANGLE = 2.5
A2/A3 = 5.95
Re=5.5 Million
EXPERIMENTAL
INVISCID THEORY
Px/Pinf
100.0
95.0
90.0
85.0
80.0
75.0
70.0
65.0
60.0
55.0
50.0
45.0
40.0
35.0
30.0
25.0
20.0
15.0
10.0
5.0
0.0
1.50
1.25
1.00
0.75
0.50
0.25
0.00
X/Lc
EXIT
ENTRY

Figure 4.10h

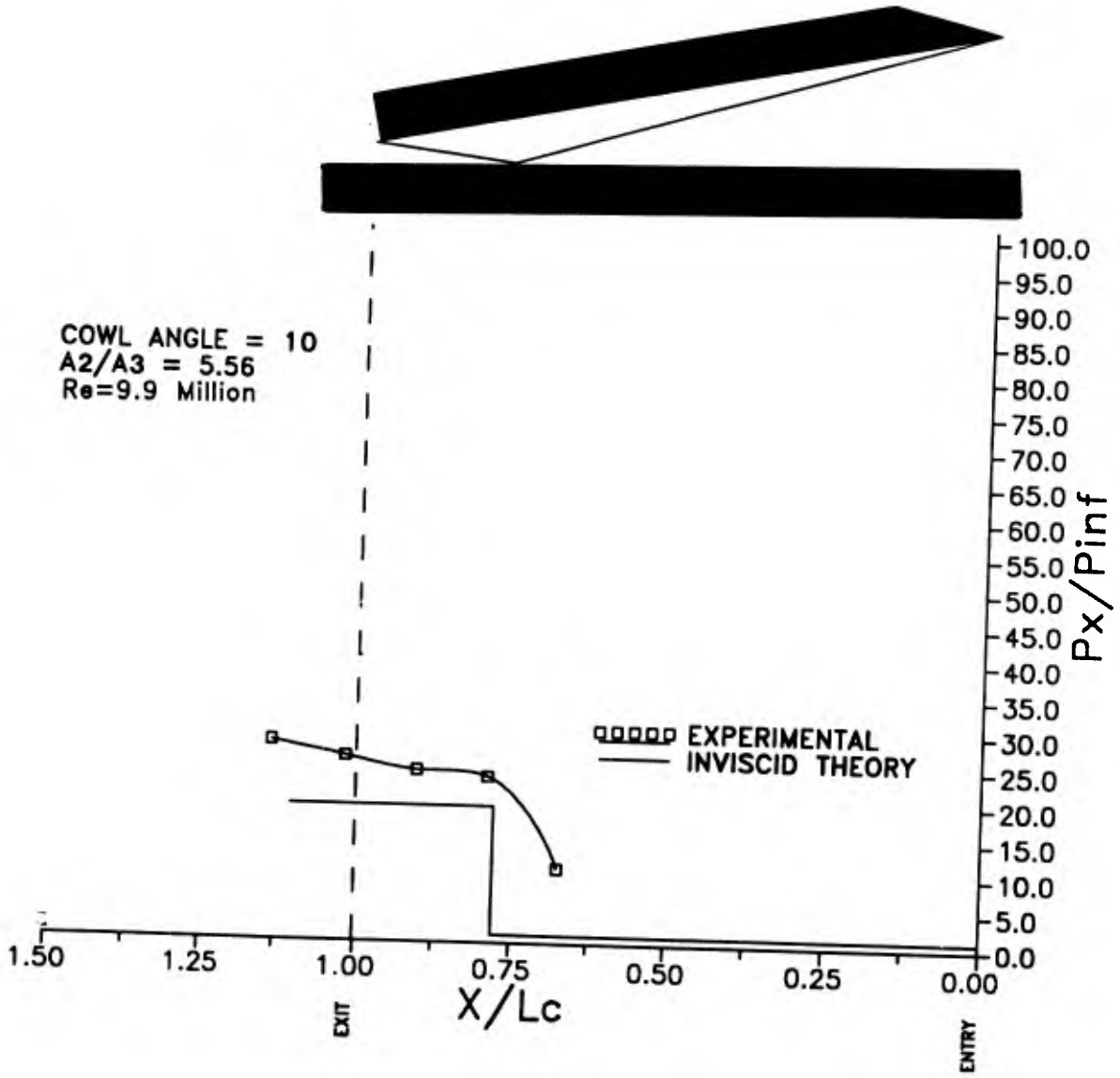
COWL ANGLE = 10
A2/A3 = 5.56
Re=9.9 Million
EXPERIMENTAL
INVISCID THEORY
100.0
95.0
90.0
85.0
80.0
75.0
70.0
65.0
60.0
55.0
50.0
45.0
40.0
35.0
30.0
25.0
20.0
15.0
10.0
5.0
0.0
Px/Pinf
1.50
1.25
1.00
0.75
0.50
0.25
0.00
X/Lc
EXIT
ENTRY

Figure 4.10i

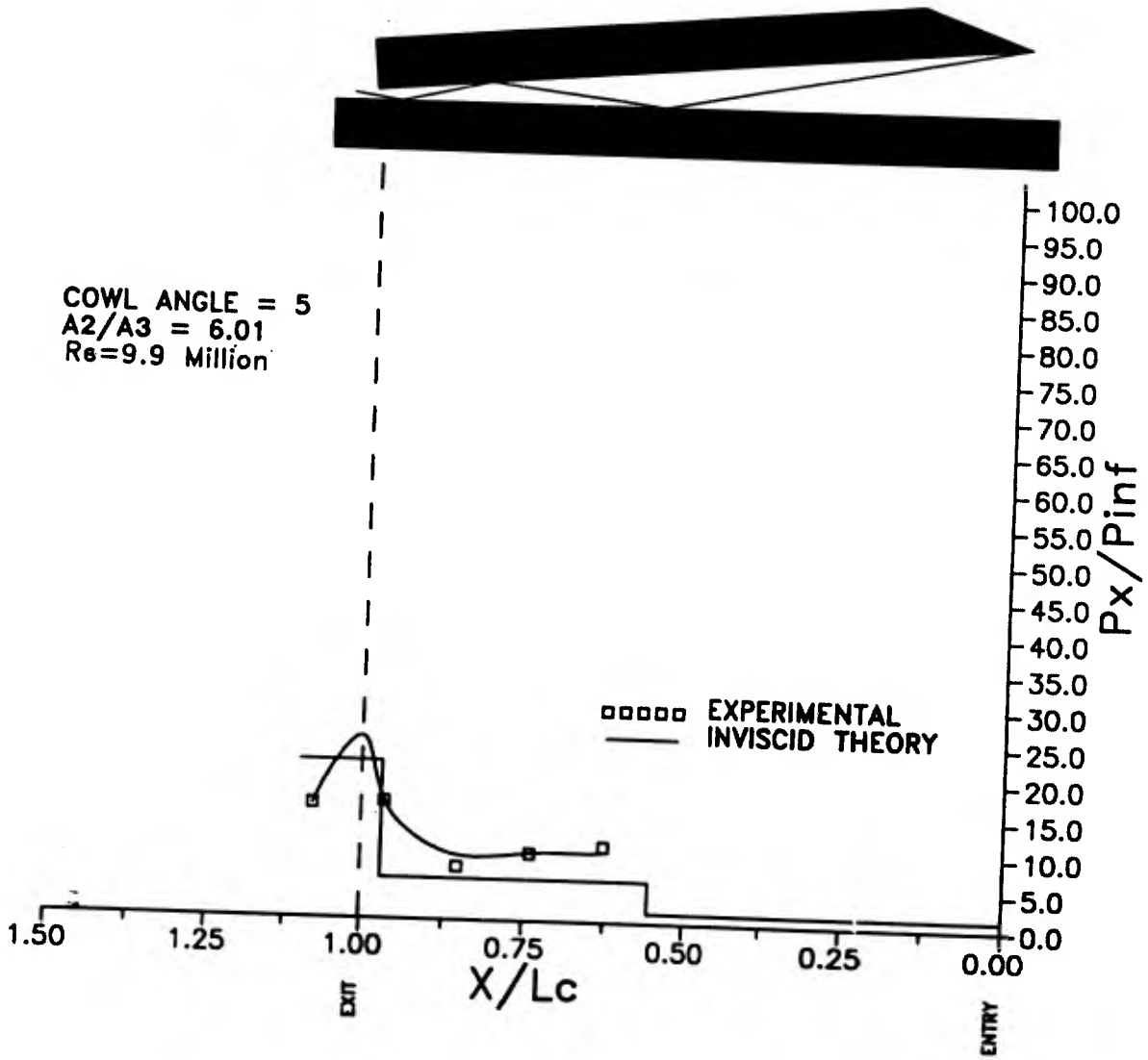
COWL ANGLE = 5
A2/A3 = 6.01
Re=9.9 Million
EXPERIMENTAL
INVISCID THEORY
100.0
95.0
90.0
85.0
80.0
75.0
70.0
65.0
60.0
55.0
50.0
45.0
40.0
35.0
30.0
25.0
20.0
15.0
10.0
5.0
0.0
Px/Pinf
1.50
1.25
1.00
0.75
0.50
0.25
0.00
X/Lc
EXIT
ENTRY

Figure 4.10j

compression ratio of 65 is produced by this cowl configuration. This compares with a theoretically predicted value of 45; the difference being due to viscous effects.

Figures 4.10c and 4.10d are for cowl angles of 10 degrees. Figure 4.10c is for a contraction ratio of 4.47. In this case the first shock reflection is contained in the passage between the cowl and the bottom plate. The measured compression ratio is nearly twice the predicted value. In Figure 4.10d the contraction ratio is 7.46 with a measured compression ratio of 100. This peak pressure is followed by a sharp decrease of pressure due to the expansion waves coming from the trailing edge of the cowl. If the pressure curves of Figures 4.10e and 4.10d are shifted so that the points of impingement of the leading edge shock coincide, then the two pressure curves upstream of the downstream expansion region are quite similar. In Figure 4.10d the schlieren and the theoretical shock positions correlate well.

Figures 4.10e and 4.10f are for a cowl angle of 5 degrees and contraction ratios of 4.91 and 8.79 respectively. The experimental and predicted shock patterns are in good agreement in Figure 4.10e. Pressures are higher than predicted in each case but again the pressure distributions are similar if viewed with respect to distance from the point of shock reflection. It should be noted that the difference in results between figures 4.10e and 4.10f is caused by the change in contraction ratio from A_2/A_3 of 4.91 to 8.79 and that, since the cowl angle is kept constant, the contraction ratio change is due largely to the change in A_3 rather than the change in A_2. The effect of this is that there are marked differences in the pressure results near the exit (cowl trailing edge) whereas changes near the entrance are small. Thus the effects of the forebody boundary layer in the two cases are nearly the same. The flow in Figure 4.10f is meaningful from an inlet designer's viewpoint since it becomes parallel to the freestream after the second shock reflection on the lower plate. This is a desirable feature for flow entering the combustion chamber. For such an inlet, then, we see from Figure 4.10f that the predicted inviscid compression ratio of 21 to 1 is far from the experimentally measured value of 80 to 1. Such are the effects of viscous flow in hypersonic air inlets.

Figures 4.10g and 4.10h are for a cowl angle of 2.5 degrees for contraction ratios of 4 and 5.95, producing four and six shock reflections respectively. Both of these flows are highly viscosity dominated as evidenced from the large differences between calculated inviscid pressures and measured values.

Nevertheless if, as before, the pressure curves are superimposed with the shock reflection points, the pressure curves then become coincident too. This means that the shock-boundary-layer interactions are independent of each other for our experimental conditions.

Figures 4.10i and 4.10j are for the rearward position of the cowl producing a cowl leading edge set-back Reynolds number of 9.9 * 10^6. Predicted (inviscid) compression ratios are again exceeded by the experimental values.

The geometric parameters considered most important to inlet starting are shown again in Figures 4.11 and 12, with consideration now given to the calculated boundary layer displacement thickness.

In Figure 4.11, the cowl angle is plotted against entry height; the latter is non-dimensionalized with respect to the boundary layer displacement thickness. This presents a ratio of inlet capture height to the captured boundary layer displacement thickness.

In the design of an oblique shock inlet under specified cowl angle and boundary layer thickness, a suitable entry height can be found from this curve that will ensure starting.

In an ideal case where there is pure 2-dimensional flow in the diffuser, the expression of the start limits with respect to entry height and displacement thickness (H_2/δ^*) would tend to show a single limit regardless of the Reynolds number. In this study, the 3-dimensional effects inherent in the growth of the side wall boundary layer, cause the start limits to change distinctly with respect to Reynolds number as is indicated by the two limits shown in Figure 4.11.

This circumstance is also apparent in Figure 4.12 where entry height/displacement thickness ratio is plotted against area ratio. Once again the incorporation of entry displacement thickness is not sufficient to uniquely define the starting condition without detailed knowledge of the viscous losses on the inlet sidewalls.

The core flow diameter exiting the Mach 8.33 nozzle restricts the width of the design of oblique shock type intakes to the .076 m width of this model (see Figure 4.5b). Despite the three-dimensional nature of the flow in such a narrow diffuser, Figure 4.12, like Figure 4.11, can be readily applied to the design of startable inlets regardless of the specified forebody length. The line labelled "Segment of 10° cowl operating line" represents design points of all inlet configurations in this model with a 10° cowl and entry

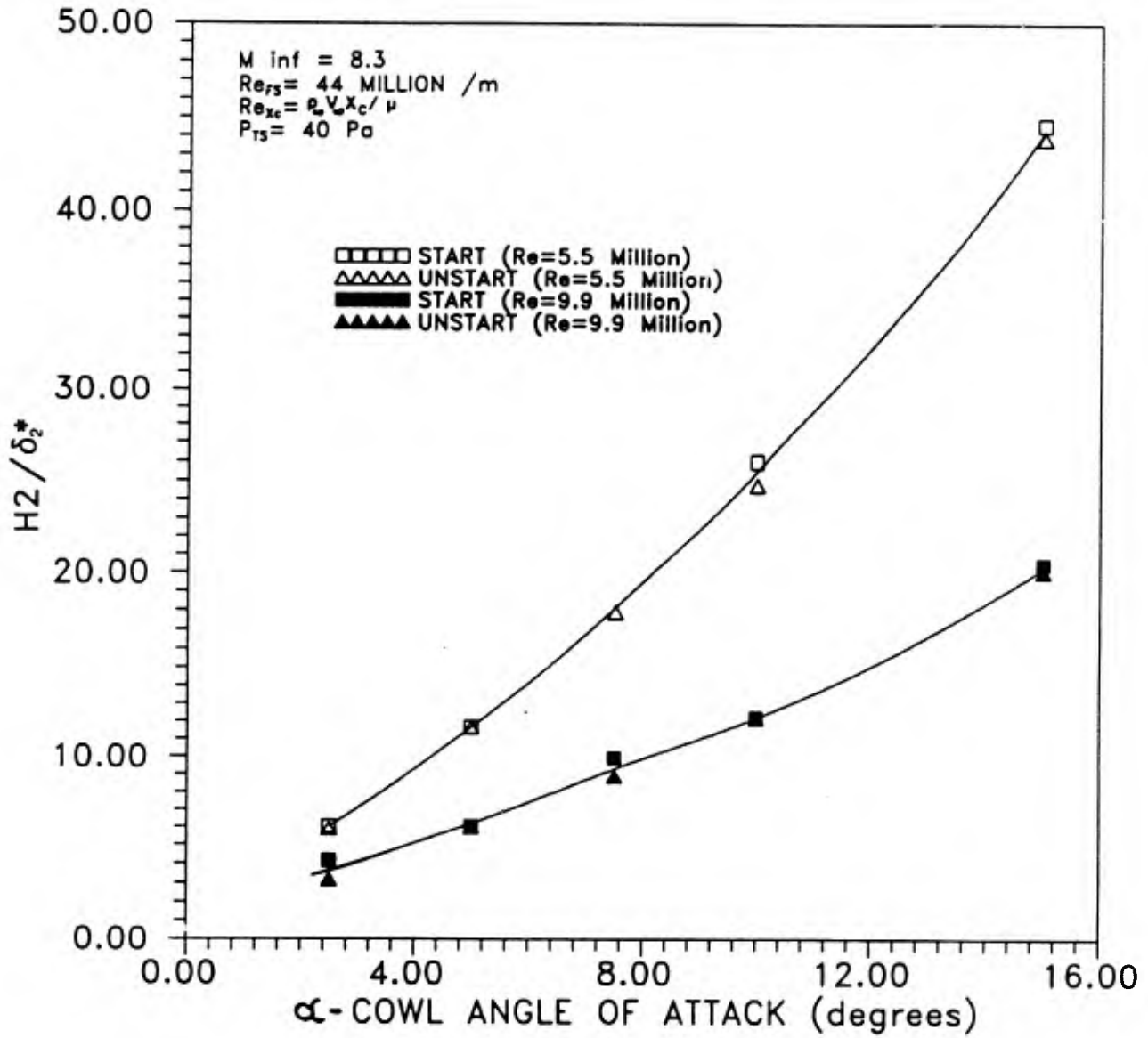

Figure 4.11 The limits of inlet starting for the range of cowl angles are depicted here as a function of entry height/displacement thickness ratio to better assess the viscous influence.

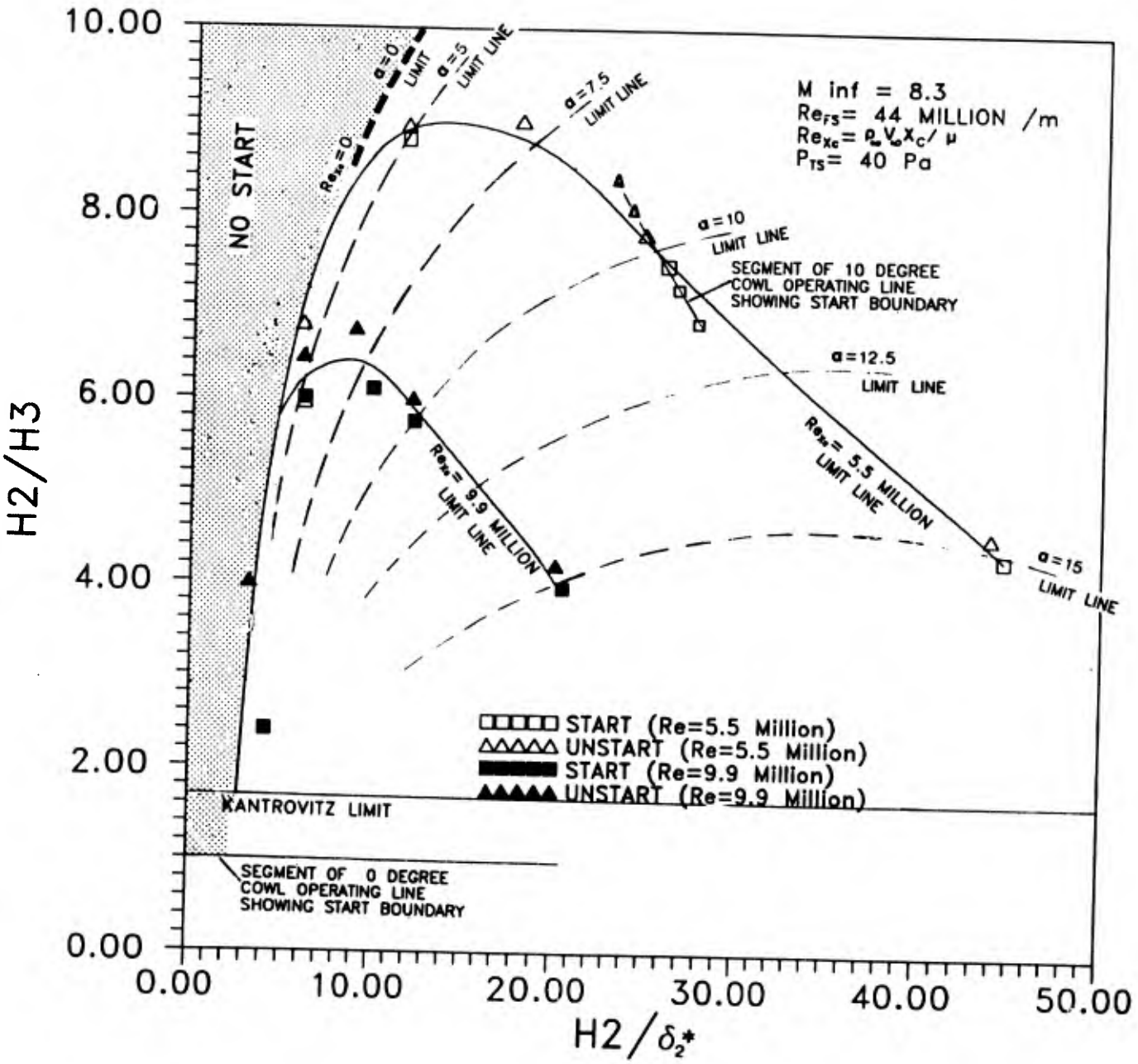

Figure 4.12 All of the geometric and gasdynamic variables are represented in this inlet starting envelope. The trend toward the 0 degree cowl is shown.

Reynolds number of 5.5 million. In fact, these are the just-starting points of the series of inlet configurations tested in the gun tunnel. The solid line labelled "Re = 5.5 Million Limit" joins these starting limits determined for all cowl angles at Re = 5.5 million including, as described here, the 10° cowl family of inlets. All of the experimentally determined START/UNSTART points are not shown for the sake of clarity.

Placing the cowl at a different entry Reynolds number would produce a new entry boundary layer thickness and a new operating line unique to that lateral position. Another 10° cowl operating line, this time at a Reynolds number of 9.9 million, would pass through the 10° cowl start limit point on the line labelled "Re = 9.9 Million Limit". The dashed line between this point and the 5.5 million Reynolds number, 10° cowl starting limit point, represents the limit of starting for all 10° cowl configurations at all Reynolds numbers between 5.5 and 9.9 million.

In other words a solid line is a start limit for one entry Reynolds number but all cowl angles between 2.5° and 15°. A broken line is a start limit at any entry Reynolds number but for a specific set cowl angle.

One interesting extrapolation of these curves is the start boundary at an area ratio of 1. All of the Reynolds number start limits are seen to converge to this point, indicating that the limit is typical regardless of lateral position (and therefore displacement thickness height). For all such rectangular duct diffusers, unstart would appear to be achieved when the cowl plate is lowered to a capture height which is less than 2.5 times the boundary layer displacement thickness.

The region on Figure 4.12 labelled "NO START" is beyond all Reynolds number starting limits. Designs of these specifications will not start, regardless of the lateral location of the cowl.

4.3.4 Static Pressure Measurement

Overall inlet compression ratios can be calculated from the experimentally measured pressure profiles such as those in Figures 4.10a to 4.10h. Some of these compression ratios have been plotted against their design area ratios as the large solid symbols in Figure 4.13. As the cowl at a given angle and entry Reynolds number was successively lowered towards the bottom plate to induce an unstart, higher compression ratios and contraction ratios were observed. These plotted points correspond to maximum

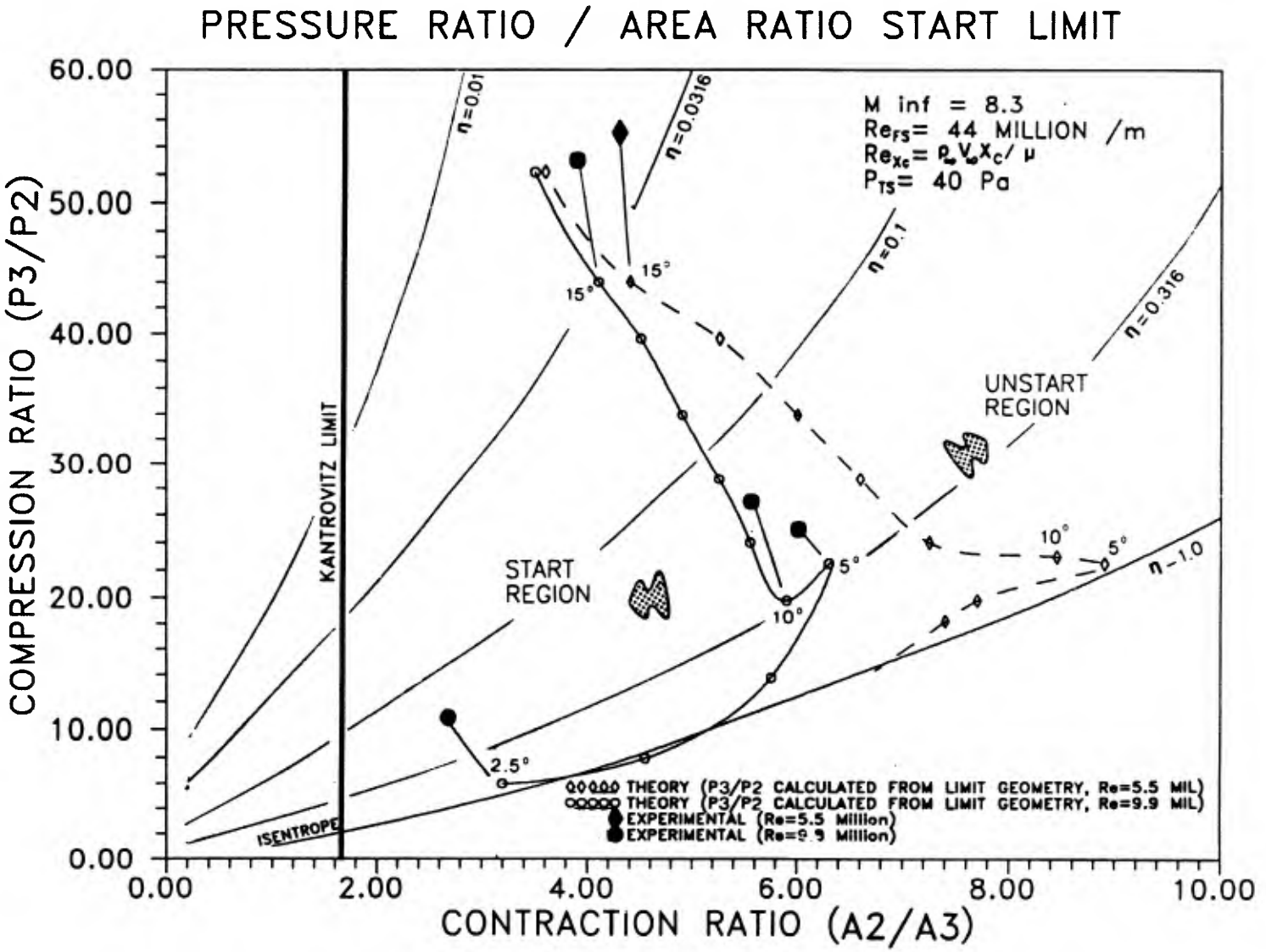

Figure 4.13 Measured and theoretical pressure ratios are shown primarily for the Re=9.9 million cowl station. Higher total pressure recovery efficiency is attained by the maximum compression inlets for cowl angles below 10 degrees.

pressure values achieved before an unstart was induced in the inlet. In the case ot the 9.9 million Reynolds number, the points represent an approximate compression ratio/contraction ratio starting limit.

Referring back to Figure 4.8, the geometric specifications of the inlet at its final started configuration (immediately before the increased area ratio induced an unstart) were used in a 2-dimensional inviscid calculation of pressure ratio. These "theoretical" compressions are at the starting limit as represented by the open symbols, joined by the solid line for Re = 9.9 million and the dotted line for Re = 5.5 million. Particularly for the Re = 9.9 million case, these clearly support the distribution of the experimental measured pressure ratios. For the start limiting theoretical points at 2.5°, 5°, 10°, and 15°, cowl angles, an arrow indicates the proximity of the corresponding experimental design point for that cowl angle. The area ratio for the experimental point is somewhat smaller than that of the theory line since the inlet compression is measured at a final started configuration which is actually not directly on the start limit line. Referring again to Figure 4.8, the Figure 4.13 theoretical inviscid pressure ratios are derived from calculations corresponding to the inlet geometries on the limit lines of Figure 4.8. The experimental pressure measurements, however, are taken from the inlet configurations represented by the square symbols slightly below.

Shown also on this graph are lines of constant total pressure recovery efficiency. Compared with our experimental design points (which each represent the highest possible compression for the given cowl angle), it is clear that these lower cowl angles produce inlets of highest efficiency with a very sharp decline in η_{pt} at cowl angles above 10°.

4.3.5 Effect on Inlet Starting of Initial Plenum Pressure

Results for inlet starting/non-starting as a function of gun tunnel initial plenum pressure are shown in Figure 4.14. This figure gives the cowl angle versus inlet area ratio with the plenum pressure as parameter. The labelled points shown are a small sampling of the experimental results used to generate the contours. Each represents an inlet at a particular cowl angle and area ratio, with the label indicating the initial plenum pressure (+25 Pa) necessary to cause unstart.

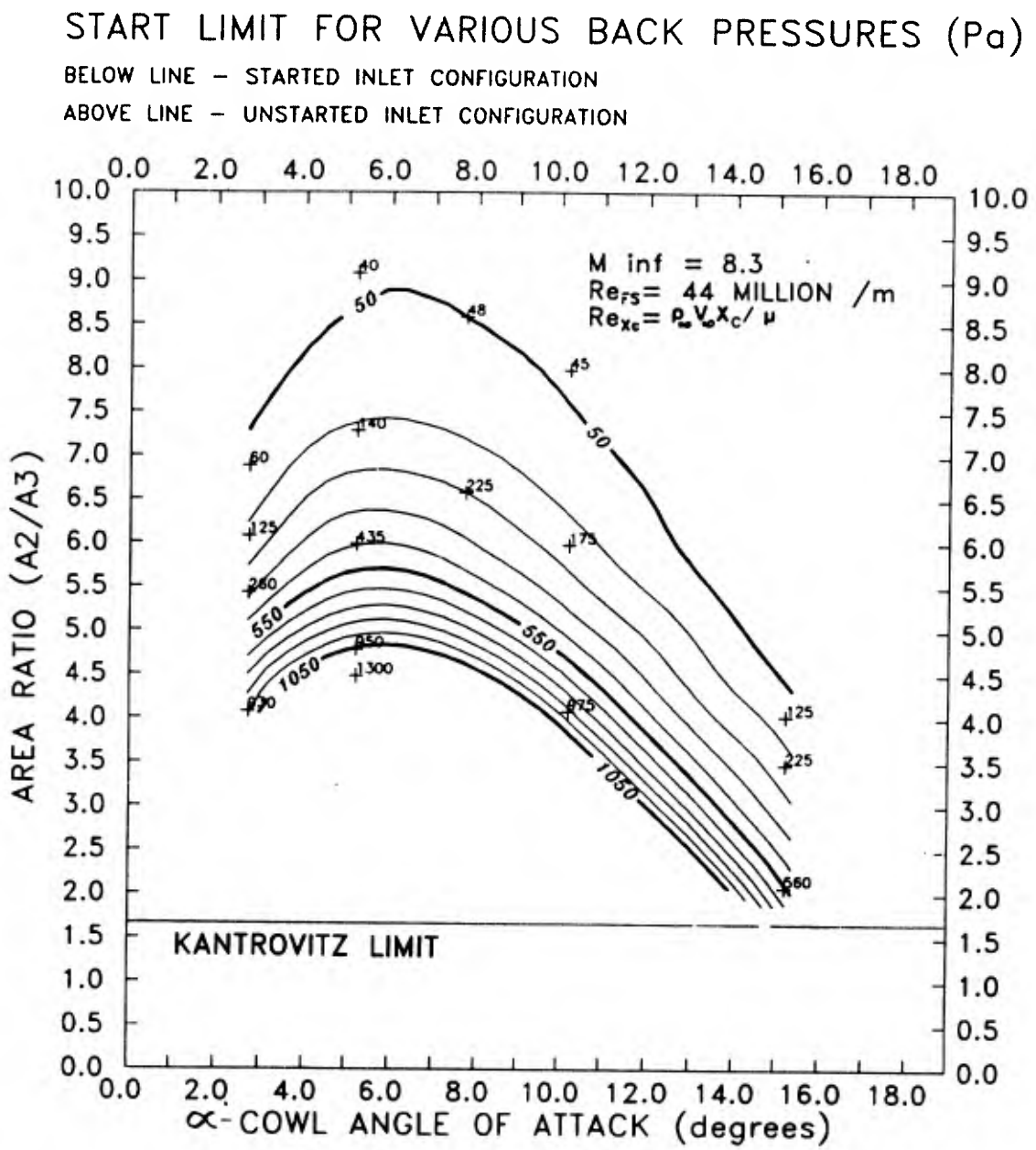

Figure 4.14 The start/unstart limits resulting from incrementally higher initial plenum pressures.

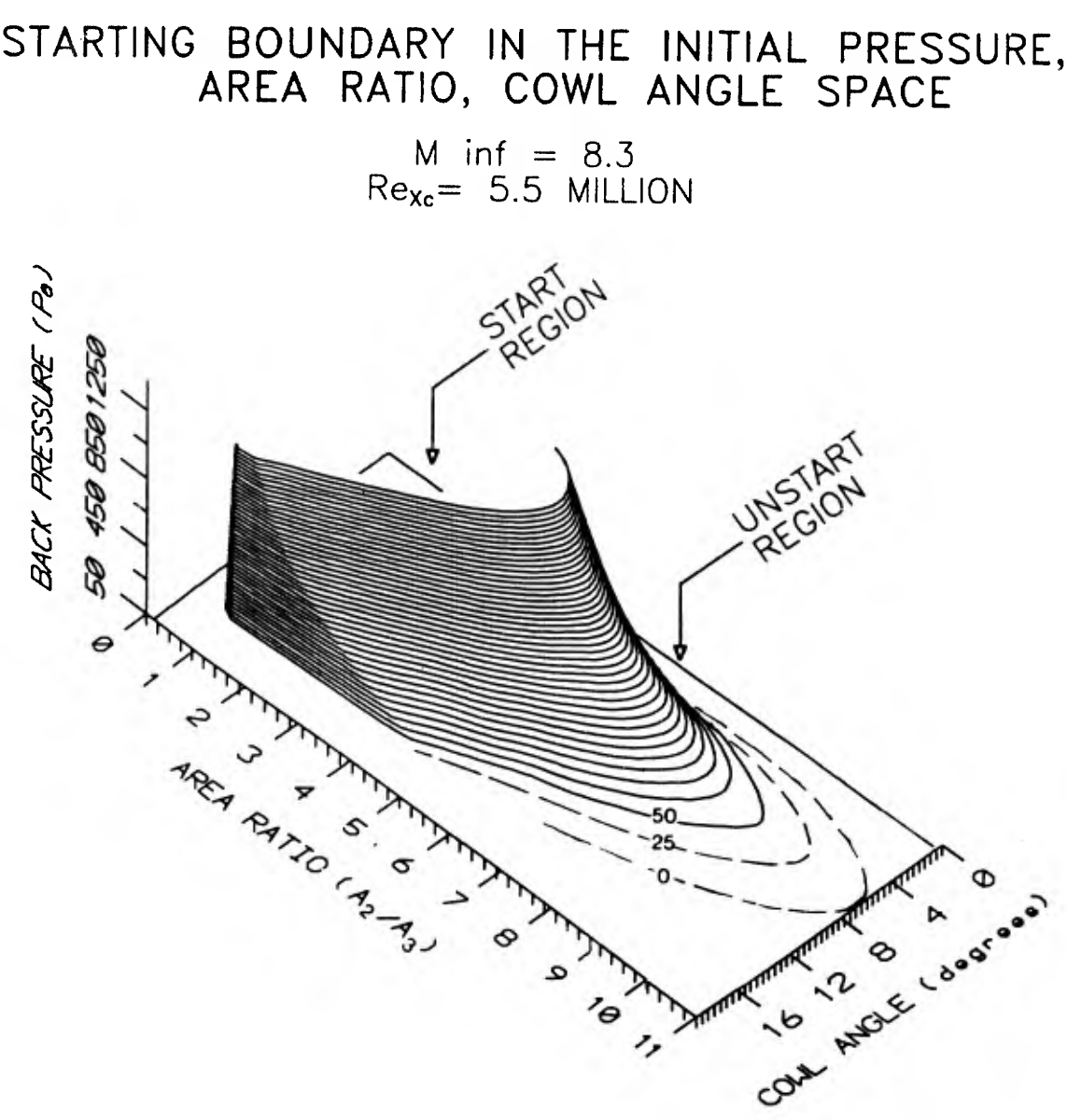

Figure 4.15 A 3-dimensional representation of Figure 4.14 showing the implications towards higher area ratio starting by a computational extrapolation to higher vacuum pressures than the current minimum of 40 Pa.

The resulting contours show the plenum pressures (in Pascals) noted on each line. In the region below that line inlet starting takes place whereas above the line it does not. It is seen that inlet starting is promoted by a decrease in plenum pressure. So that, for example, a six degree cowl angle inlet would not start at an area ratio much higher than 4.5 at a plenum pressure of 1000 Pa (.15 psi) whereas that same inlet could be contracted to an area ratio of 9.0 before it would not start at a plenum pressure of 50 Pa (.074 psi). A factor of two gain in area ratio is obtained by an order of magnitude reduction in plenum pressure and this gain does not vary appreciably with cowl angle.

The start-unstart boundary for our configuration at Re_{FS} = 44 million/m is shown in Figure 4.15 in the back pressure vs. area ratio vs. cowl angle space. The contour labelled 50 Pa represents the highest area ratio starting capability of the gun tunnel in its present form. Extrapolating this 3-dimensional graph to a 0 Pa limit provides some indication of the substantial increase in starting capability possible at very low initial plenum pressures. Starting an oblique shock inlet of area ratio as high as 11 or greater should be possible as absolute vacuum is approached in the plenum prior to the test.

4.4 Conclusions

A discussion has been presented concerning the establishment of steady supersonic/hypersonic flow (starting) in converging passages.

An extensive set of experiments has been conducted on an angled plate in a two-dimensional channel, simulating a hypersonic inlet with a cowl and a forebody, to determine the boundary between started and unstarted flow as determined by Reynolds number, cowl angle of attack, contraction ratio, and initial plenum pressure. Tests were conducted in a hypersonic gun tunnel at a Mach number of 8.33 and a test section Reynolds number of 44 million per meter.

Inlet starting boundaries have been found as a function of all of these geometric and aerodynamic parameters. Results are useful in the design of oblique shock intakes for study in this facility.

It has been found that:

a) Impulsive flow starting in the gun tunnel permits the starting of inlets with contraction ratios far exceeding the limits imposed by the quasi-steady Kantrovitz criterion.

b) Impulsive inlet starting is facilitated by a lower contraction ratio, a lower initial plenum pressure, and a lower Reynolds number based on the boundary layer displacement thickness on the lower plate at the cowl entry station.

c) The amount of gain depends on the flow Reynolds number, the cowl angle and the initial plenum pressure in the gun tunnel's plenum chamber.

d) Inlet starting is facilitated also by a decreasing cowl angle as long as the cowl angle remains above 6 degrees, below which viscous effects cause a reversal in this trend so that a lowering of the cowl angle, while maintaining contraction ratio, causes the inlet not to start.

e) For all Reynolds numbers, a rectangular duct (H2/H3 = 1) will unstart if the boundary layer displacement thickness at entry exceeds 40% of the capture height.

f) Viscous effects cause large variations from the theoretical values of compression.

g) Shock-boundary layer interactions occur independently of each other at the conditions tested.

h) Maximum compression oblique shock inlets are obtained with cowl angles greater than 10 degrees. Although cowl-plate combinations were not specifically designed as inlets some respectable performance was obtained at cowl angles below 10 degrees.

4.5 References

4.1. Fillion, Micheal, "The Shuttle Reborn", *Popular Mechanics*, Aug. 1988.

4.2. McGregor, R.J. and Molder, S, "Analysis and Optimization of Scramjet Inlet Performance", 17th Congress of the International Council of the Aeronautical Sciences. ICAS-90-4.7.3, Sept. 1990.

4.3. Molder, S. and Romeskie, J.M., "Modular Hypersonic Inlets with Conical Flow", AGARD Conference Proceedings No.30., May 1968.

4.4. Shapiro, A.H., "The Dynamics and Thermodynamics of Compressible Fluid Flow", Vol. 1, Ronald Press, 1953.

4.5. Eggink, H., "Strömungsaufbau und Druckrückgevinn in Überschallkanälen Zentrale", f. wiss. Berichtswesen, Berlin-adlershof, F.B.1756 (1943).

4.6. Kantrowitz, A. and Donaldson ,"Preliminary Investigation of Supersonic Diffusers", NACA Wartime Report, ACR l 5 D 20 (1945).

4.7. Molder, S., "Inlets for Hypersonic Ramjets".

4.8. Curran E.T. and Bergsten B.,"Discussion of Inlet Efficiency Parameters", Aeronautical Systems Propulsion Laboratory, ASRPR TM 62-68 (1963).

4.9. Billig, F.S. and Van Wie, D.,"Efficiency Parameters for Inlets Operating at Hypersonic Speeds". JHU/Applied Physics Laboratory.

4.10. Diggins, J.L. and Lange, A.H.,"A Systematic Study of a Variable Area Diffuser for Supersonic Wind Tunnels", NAVORD Rep. 2421, U.S. Naval Ordinance Laboratory (White Oak, Md), Dec.1952.

4.11. Azevedo, D.J., Liu, C.S., Rae, W.J.,"Prediction of Inviscid Stagnation Pressure Losses in Supersonic Inlet Flows", AIAA Journal, Vol.28, No. 10, Oct. 1990.

4.12. Molder, S., McGregor, R.J., Paisley, T.W.,"The Ryerson / U of T Gun tunnel", NASP-WP-1008, NASP Technical Report #NASP-WP-1008, Monterey, May 1989.

4.13. Crawford M.E. and Kays W.M.,"Stan5 - A Program For Numerical Computation of Two-dimensional Internal and External Boundary Layer Flows", NASA CR-2742 , Stanford University, 1976.

4.14. Goldberg, T. and Hefner J.N,"Starting Phenomena for Hypersonic Inlets with Thick Turbulent Boundary Layers at Mach 6", NASA TN D-6280, NASA Langley Research Center, 1971.

4.15. Henry, J.R., Andrews, E.H., Pinkney S., McClinton, C.,"Boundary Layer and Starting Problems on a Short Axisymmetric Scramjet Inlet", NASA SP-216, NASA Langley Research Center.

4.16. Smith, C.E., "The Starting Process in a Hypersonic Nozzle", Journal of Fluid Mechanics", Vol. 24 part 4, pp 625-640, 1966.

5.0 An Experimental Study of Hypersonic Flow Development in a Duct

J. P. Sislian, Z. D. He, R. L. Deschambault, and L.-W. Chen

5.1 Introduction

The structure of a supersonic flow in a duct has important implications in the design and operation of wind tunnel diffusers, inlets and induction systems of hypersonic airbreathing engines. There have been numerous experimental investigations of the viscous-inviscid interactions that occur in such confined flows. These have included the influence of such parameters as: the Mach number M_∞ of the free stream or oncoming flow, pipe diameter D and length L, and the presence or absence of an upstream boundary layer. Depending on the thickness of the boundary layers present, various shock-wave configurations were observed. The boundary layers formed in these flows, as well as their interactions with the shock waves, have also been investigated. The free-stream Mach number M_∞ considered in all of these investigations did not exceed four (see Refs. 5.1-5.11).

Wall pressure distributions in long circular ducts, with length-to-diameter ratio L/D = 42-53 for $1.8 \leq M_\infty \leq 4.2$, were measured in an early paper by Neumann and Lustwerk (Ref. 5.1). The purpose of the study was to determine the optimum length of the throat section of a wind tunnel diffuser. It was found that when shocks were generated in the ducts the pressure rise extended over a length of 8-12 tube diameters. In a subsequent paper (Ref. 5.2) Lustwerk studied the influence of the boundary-layer thickness at the beginning of the shock system formed in a sharp leading edge rectangular duct at $M_\infty = 2.05$. Schlieren pictures of the flow showed that, with no upstream boundary layer, a plane normal shock wave was formed. As the boundary layer thickened, a series of plane or lambda shocks occurred. Further thickening of the boundary layer generated oblique shock waves.

In order to infer friction factor and heat transfer coefficients for a turbulent supersonic channel flow that develops at a nominally constant $M_\infty = 1.5$ without shocks, Richmond and Goldstein (Ref. 5.3) measured streamwise wall static pressure and centerline total pressure distributions in a slowly expanding rectangular duct. The structure of shock waves generated in rectangular ducts at $M_\infty = 1.6$-2.5 was also studied in

Ref. 5.4. It was shown that various shock-wave structures with pressure jumps up nearly to normal shock value could be generated. In Ref. 5.5, shock stabilization in constant-area ducts for Mach numbers of 1.76-2.51, was investigated as applied to the induction system for turbojet inlets.

Test results of supersonic combustion ramjets in hypersonic free jets and in the direct-connect mode showed that combustion in a supersonic flow generates a shock train in the upstream flow. Consequently an isolator duct of prescribed length is required to stabilize the wave train and to prevent combustion-induced disturbances to affect the flow in the engine inlet (see Ref. 5.6) . The flow structure in such isolator ducts was investigated in Refs. 5.7-5.9. Wall static and in-stream pitot pressure distributions, as well as wall shear stress, were measured in a cylindrical duct at $1.13 \leq M_\infty \leq 2.72$ and at a Reynolds numbers Re_θ based on upstream boundary-layer momentum thickness θ of $5\times10^3 \leq Re_\theta \leq 6\times10^4$. Their analysis of these measurements indicated that the shock-wave structure was oblique rather than normal, with the flow remaining supersonic downstream of the shock system. They also investigated the effect of M_∞, D, θ and Re_θ on pressure recovery concluding that, for a given pressure ratio across the disturbance, the distance over which the pressure rise is spread varies approximately directly with the product $\theta^{1/2}D^{1/2}$ and inversely with $(M_\infty^2-1)Re_\theta^{1/4}$.

In a more recent paper Om and Childs (Ref. 5.10) obtained detailed instream pitot, static and wall static pressure measurements for multiple shock wave-turbulent boundary layer interactions in a circular duct at $M_\infty = 1.49$ and at a unit free stream Reynolds number $Re_\infty = 4.90\times10^6$/m. In contrast to the work of Refs. 5.7-5.9, they obtained results consistent with a series of normal shock waves of decreasing strength along the duct and with decreasing distance between the successive shock waves. The overall pressure recovery was much lower than the single normal shock pressure recovery at the same M_∞. In 1987, a detailed experimental study of the supersonic turbulent flow development in a square duct was reported in Ref. 5.11, over a development length $0 \leq L/D \leq 20$ for $M_\infty = 3.9$. Total pressure contours and local skin friction coefficient distributions showed that the flow develops in a manner similar to that observed for the incompressible case.

The objective of the present investigation is to obtain data on the flow developing in a circular duct at $M_\infty = 8.3$. Although a rectangular sectioned duct is perhaps of more immediate interest for scramjet inlets, a circular section was chosen for two reasons. First, the present study is preliminary in nature, and the presence of the shock-boundary layer interactions in the rectangular corners was thought to complicate the task of data interpretation. Second, circular duct data is believed to be particularly useful at this stage for guiding computational code development. The major disadvantage is the lack of schlieren or shadowgraph flow visualization to assist in the interpretation of the results. Described below are the results of technique development and the data obtained thus far.

5.2 Experimental Models

Two models were used in the present tests. The larger had D = 76.2 mm (3.0 ins), and L = 762 mm (30 ins), corresponding to L/D = 10; it was instrumented for wall static pressures, and for in-stream static and pitot pressures. The smaller had D = 50.8 mm (2.0 ins); it incorporated a few wall static pressure taps, and was used mainly to explore the effect of removing sections at the exit on the flow structure in the remaining duct. This was intended to provide insights into the possibilities for development of diagnostic techniques.

The large duct, together with its support system, is depicted in Figure 5.1. In order to minimize leading edge effects on the interior flow, the outer surface was machined to a 3° taper at the entrance to form a leading edge with a tip thickness of 0.127 mm (0.005"). It was made from brass to provide for both material strength and ease in forming the sharp leading edge. The front end was fixed to the test section floor by a support which can rotate around horizontal and vertical axes. The aft end was mounted by a similar support on a traversing mechanism which could move it in both vertical and lateral directions with a positioning accuracy of 0.4 mm (1/64"). This traversing mechanism, together with two pairs of differential pressure transducers for four wall static pressure taps circumferentially located at two axial stations, was used to align the duct axis with the direction of the test section flow. The first alignment station was

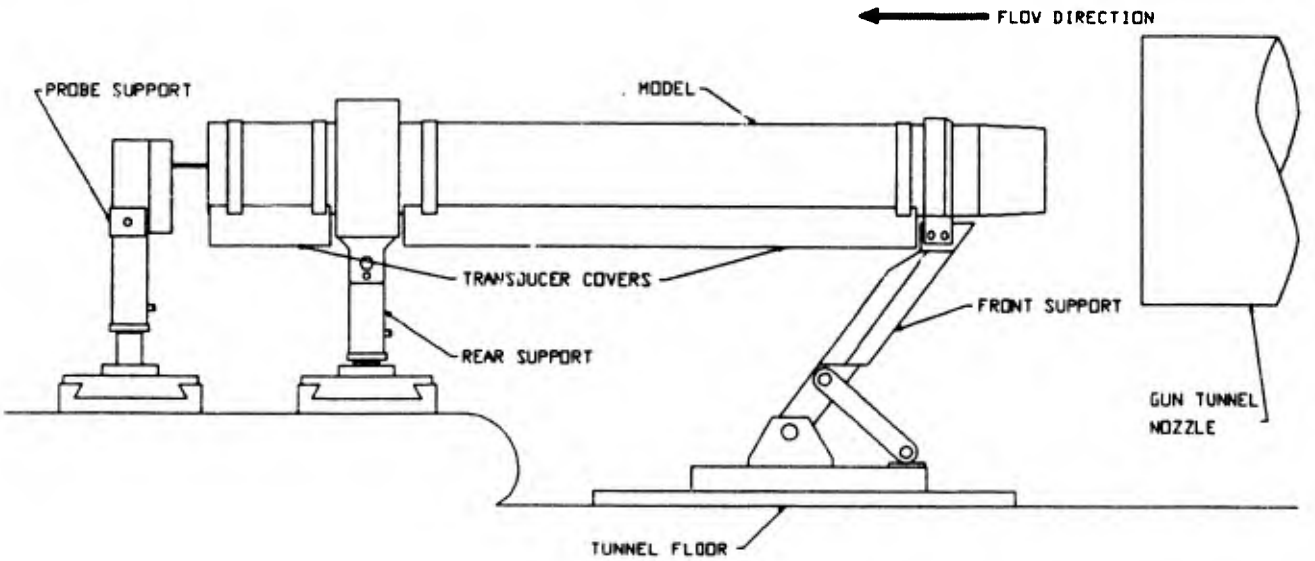

Figure 5.1 Schematic diagram of large duct and support system.

11.4 cm (4.5 ins.) from the entrance, and the second 1.27 cm (0.5 ins.) upstream from the exit. A photograph of the large model mounted in the test section of the tunnel is shown in Figure 5.2.

The smaller duct was manufactured from extruded aluminum tubing; its interior was honed to remove surface irregularities and to obtain a precisely circular section of constant diameter. Owing to the softness of this material the leading edge taper at the entrance was increased to 4.7°. Suitable adaptors were manufactured to allow its installation in the large duct support system. In addition to wall static pressure taps along a generator, this duct was also instrumented for alignment by including four circumferentially located taps 7.62 cm (3 ins.) from its entrance.

5.3 Experimental Procedures and Instrumentation

5.3.1 Tunnel Modifications

Since visualization of the internal flow is impractical, it is necessary to reconstruct the flow from other measurements. However, schlieren flow visualization at the duct entrance and exit is possible,. To achieve the latter for the large duct, the tunnel test section had to be modified to include additional windows. This modification is shown in Figure 5.3.

5.3.2 Static and Pitot Pressure Instrumentation

In the large duct, the wall static pressure measurements were obtained from 22 taps located at 2.54 cm (1 in.) intervals along the bottom generator of the duct as depicted in Figure 5.4. The geometry and dimensions of these taps are depicted in Figure 5.5.

The design and dimensions of the probe used to determine in-stream pitot pressures, including those in the wall boundary layer, is presented in Figure 5.6. A flattened tip was used to reduce the displacement error near the wall. In Figure 5.7 the response of this probe to the freestream flow is compared with that of one of the probes used to calibrate the tunnel; it is significantly slower. It appears that this occurs because the flattening of the tube shown in Figure 5.6 significantly reduces its cross sectional area at the entrance, so that the pressure in volume between tube entrance and transducer port requires longer to equilibrate.

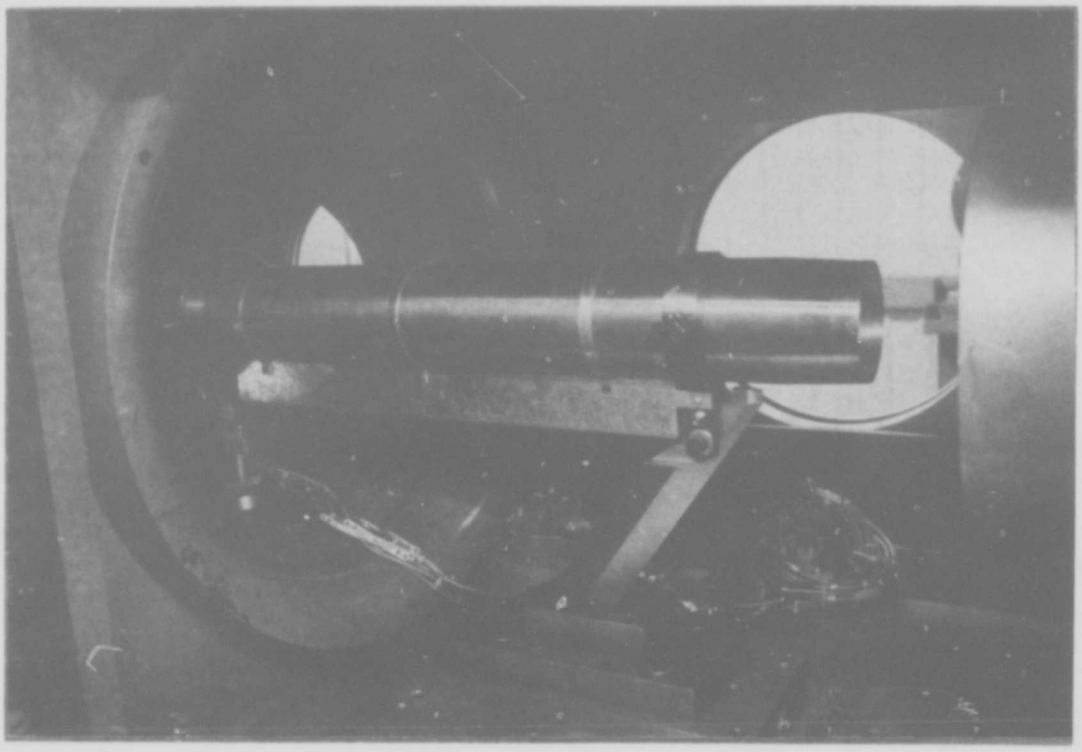

Figure 5.2 Photo of large duct in test section.

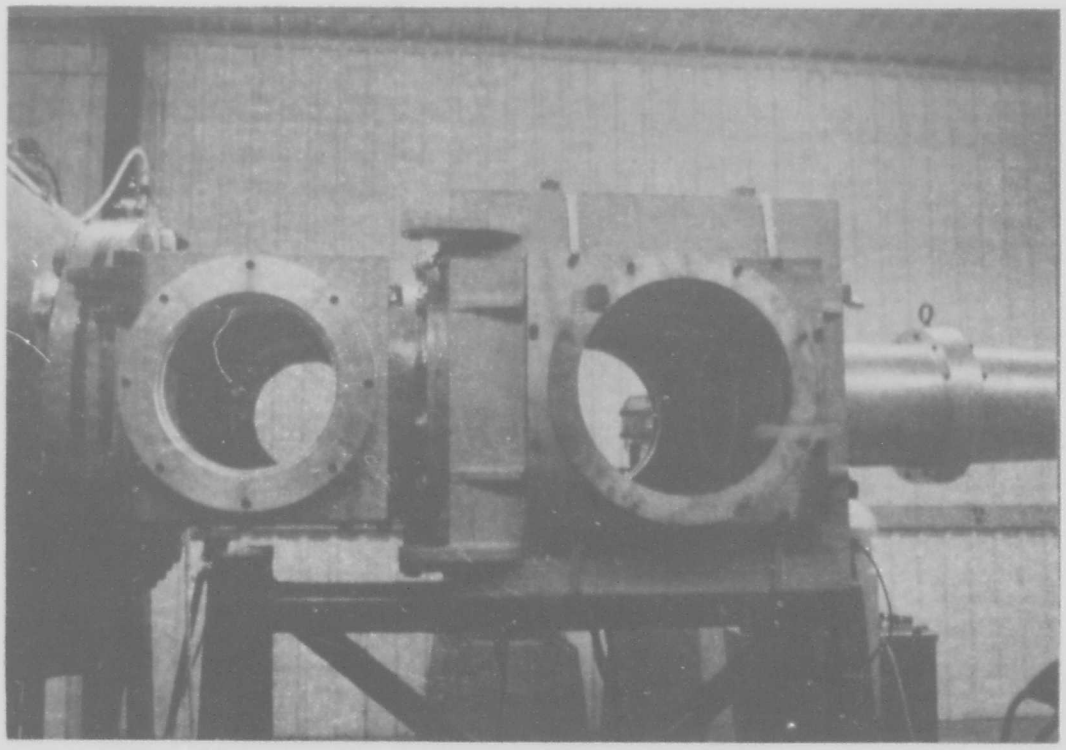

Figure 5.3 Photo of the compound test section.

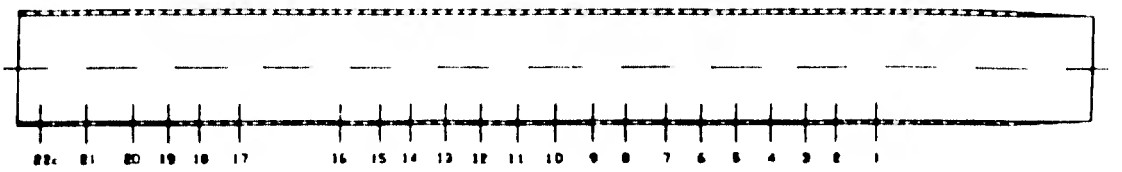

SECTION	POSITION (mm)	POSITION (x/D)
1	152 4	2 00
2	181 0	2 38
3	203 2	2 67
4	228 6	3 00
5	254 0	3 33
6	279 4	3 67
7	304 8	4 00
8	333 4	4 38
9	355 6	4 67
10	381 0	5 00
11	406 4	5 33

SECTION	POSITION (mm)	POSITION (x/D)
12	431 8	5 67
13	457 2	6 00
14	482 6	6 33
15	504 8	6 63
16	533 4	7 00
17	608 0	7 98
18	636 6	8 35
19	658 8	8 65
20	684 2	8 98
21	717 6	9 42
22c	749 3	9 83

34 POSITION RADIAL SURVEY

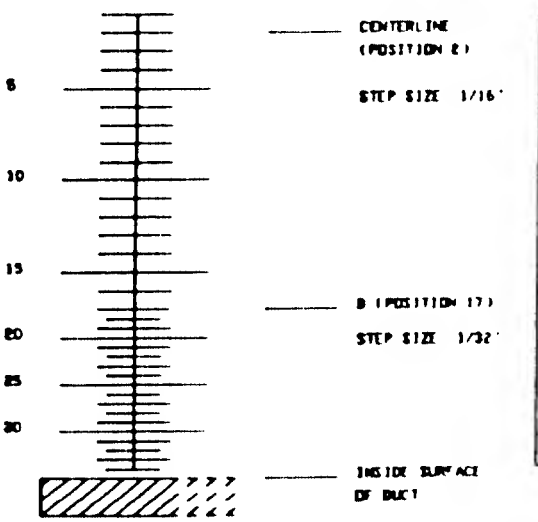

POSITION	(mm)	y/D
1	39 69	0 8208
2	38 10	0 8000
3	36 91	0 4792
4	34 99	0 4583
5	33 34	0 4375
6	31 75	0 4167
7	30 16	0 3958
8	28 58	0 3750
9	26 99	0 3542
10	25 40	0 3333
11	23 81	0 3125
12	22 23	0 2917
13	20 64	0 2708
14	19 05	0 2500
15	17 46	0 2292
16	15 88	0 2083
17	14 29	0 1875

POSITION	(mm)	y/D
18	13 49	0 1771
19	12 70	0 1667
20	11 91	0 1563
21	11 11	0 1458
22	10 32	0 1354
23	9 53	0 1250
24	8 73	0 1146
25	7 94	0 1042
26	7.14	0.0938
27	6 35	0 0833
28	5 56	0 0729
29	4 76	0 0625
30	3 97	0 0521
31	3 18	0 0417
32	2 38	0 0313
33	1 59	0 0208
34	0 79	0 0104

Figure 5.4 Locations of wall static pressure taps and radial positions of in-stream pressure probes at the same location.

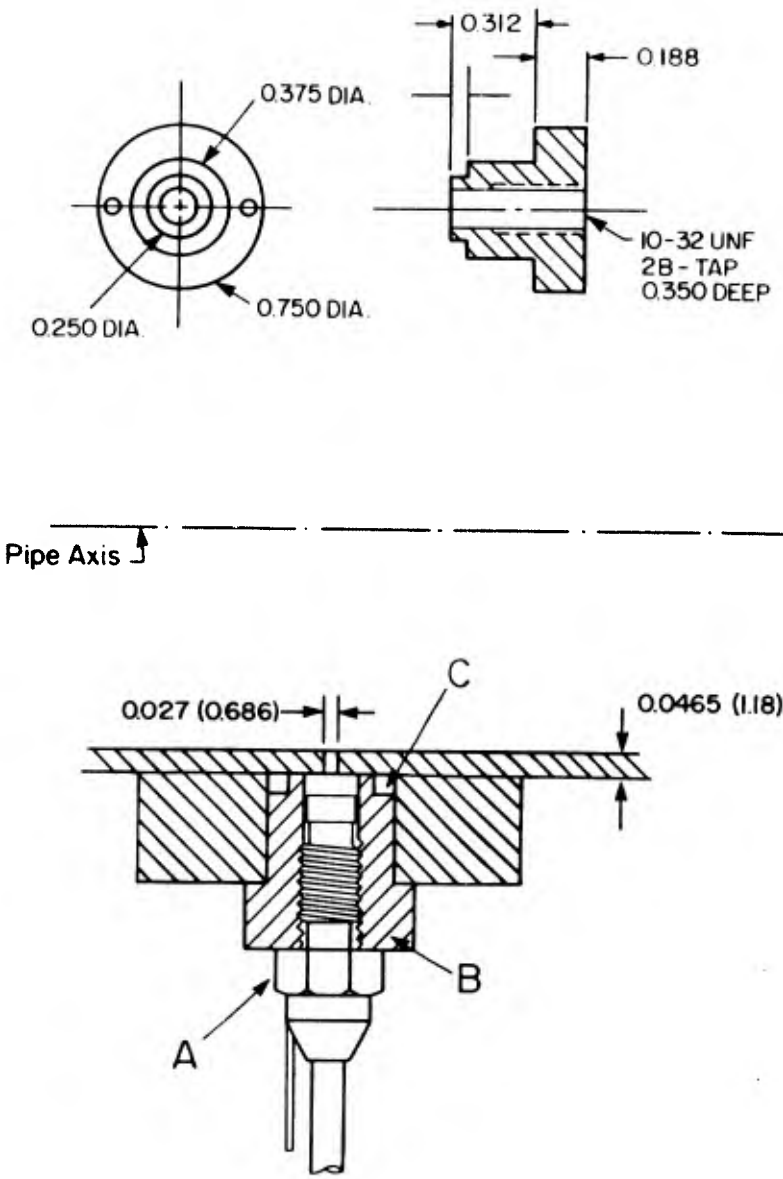

Figure 5.5 Static pressure tap design. The transducer A threads into a mounting block B which in turn is sealed by an O-ring at C.

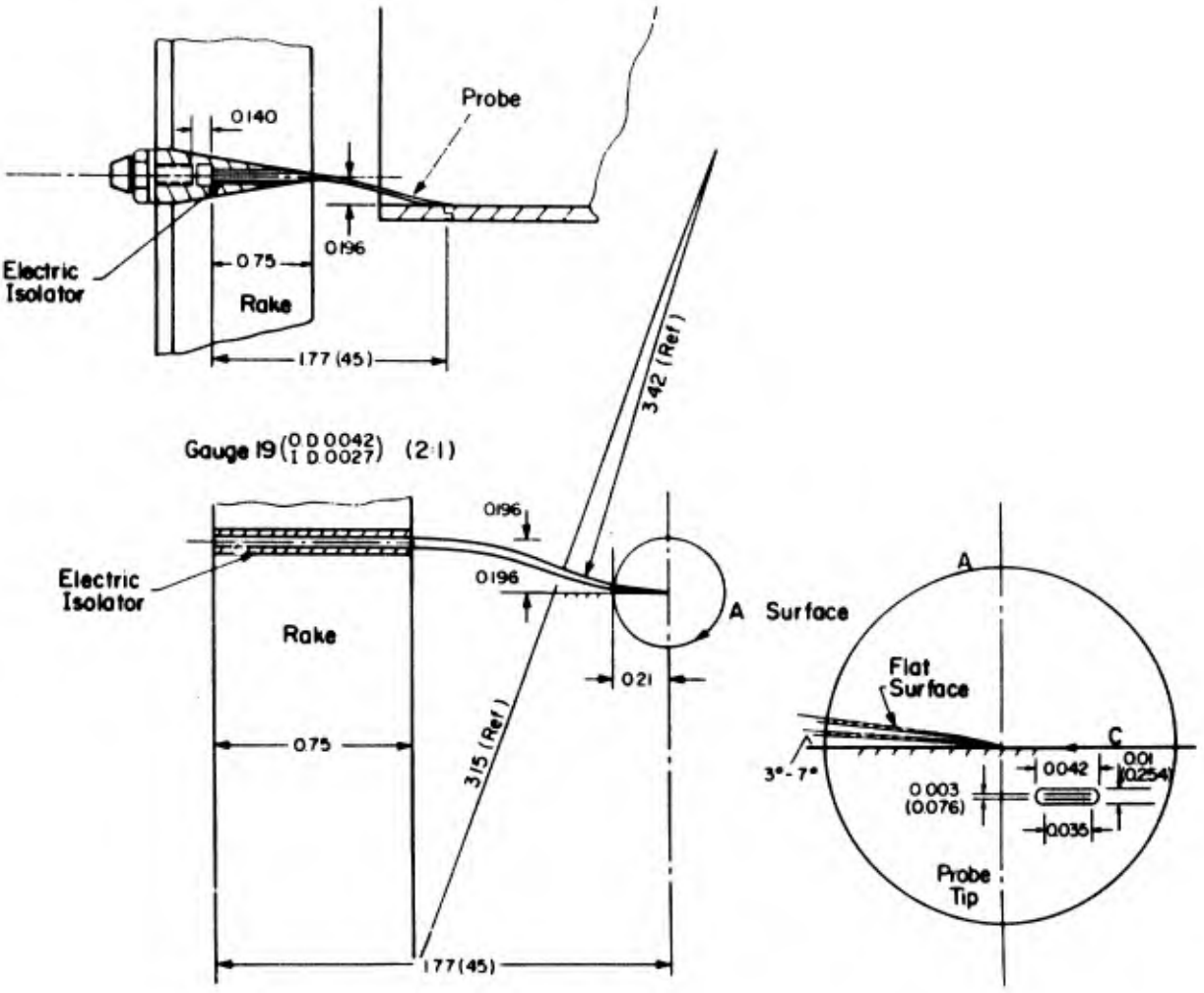

Figure 5.6 Geometry of the pitot pressure probe. The mounting system used at the pipe exit is also shown.

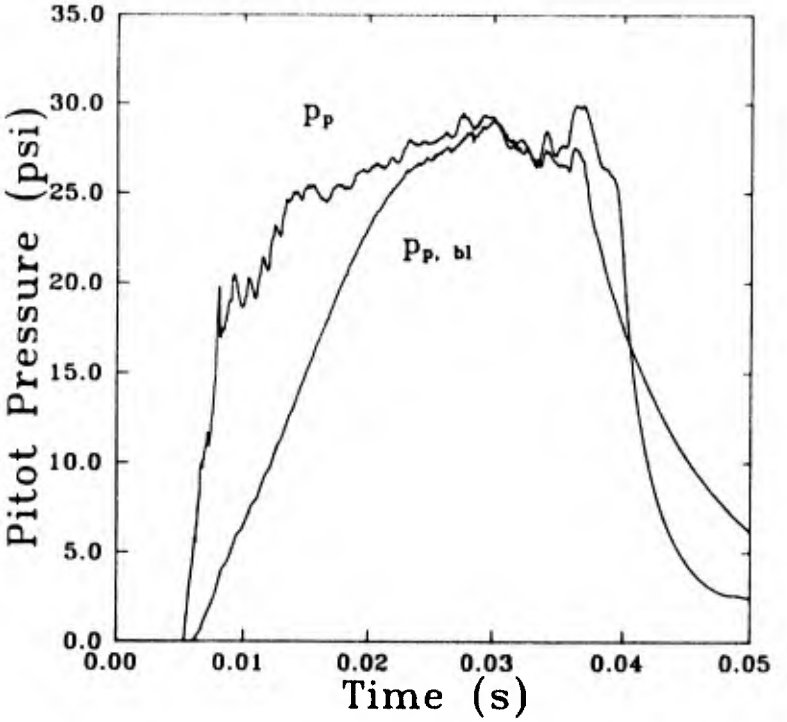

Figure 5.7 Comparison of response of boundary layer in free stream with that of a probe used in calibration.

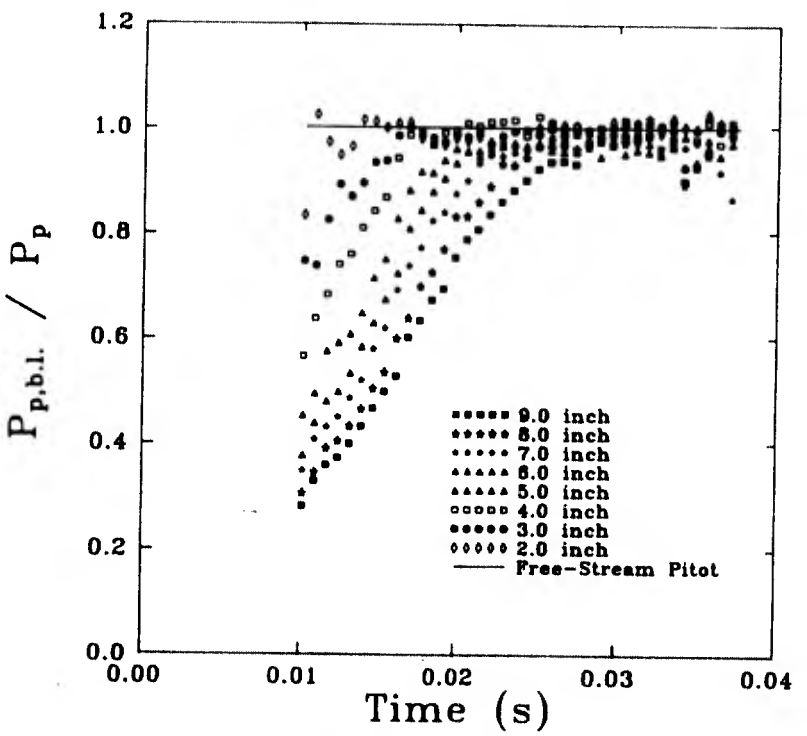

Figure 5.8 Effect of boundary layer pitot probe length on response.

To check this, the effect of the length of the tube on response was determined. The results are shown in Figure 5.8, which is a plot of the ratio of the boundary layer probe pressure history $p_{p,bl}(t)$ to that measured by a probe used to obtain the calibration data in Section 2. As can be seen, this response improves as tube length decreases, with tube lengths of 12.7 cm (5 ins.) or less being adequate.

Various probe geometries have been proposed for in-stream static pressure measurements (Refs. 5.13-5.15). Three different designs having the geometries depicted in Figure 5.9 were evaluated. A total of eight probes were tested; three were based on design (I), two on design (II), and three on design (III). The number and location of the static pressure taps for these probes are given in Table 5.1. They were tested in the tunnel test section, and Figure 5.10 contains the static pressure traces obtained by these probes, as well as the corresponding barrel (reservoir) pressure traces. Table 5.1 also includes estimates of M_∞ obtained from the data in Figure 5.10. It can be seen that case (f) gives both the best steadiness and estimates of M_∞ closest to values predicted from the pitot probe measurements described in Section 2. Therefore this probe was chosen for the in-stream static measurements.

Case (Fig. 5.10)	Design (Fig. 9)	Tube Gage	Number of Taps	Axial Location L/D	Peripheral Location relative to Bottom Generator (degrees)	Measured Free Stream Static Pressure p_∞	Computed Free Stream Mach Number M_∞
a	I	19	4	15	±90±180	2.36	8.18
b	I	19	4	10	±90±180	2.49	8.11
c	I	19	4	20	±90±180	2.15	8.30
d	II	16	2	16	±90	2.59	8.07
e	II	16	2	16	±70	2.33	8.20
f	III	19	3	16	0, ±120	2.15	8.30
g	III	19	2	16	±70	2.27	8.23
h	III	19	2	16	±90	2.22	8.26

Table 5.1 Static Probe Calibration Tests. The computed free stream Mach number assumes a calorically perfect gas with $\gamma = 1.40$ and a mean reservoir pressure $P_0 = 26.7$ MPa.

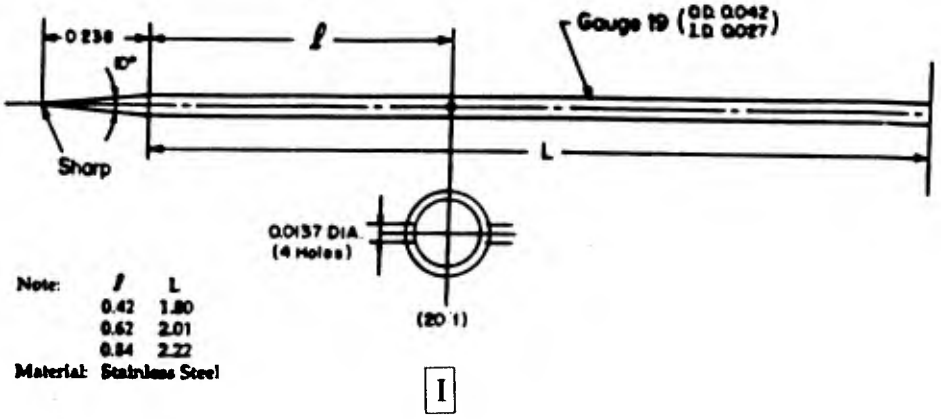

I

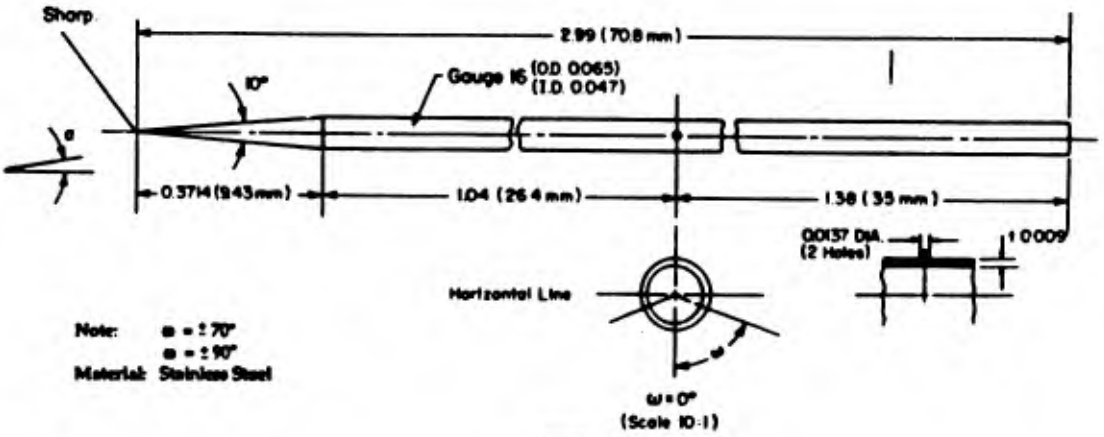

II

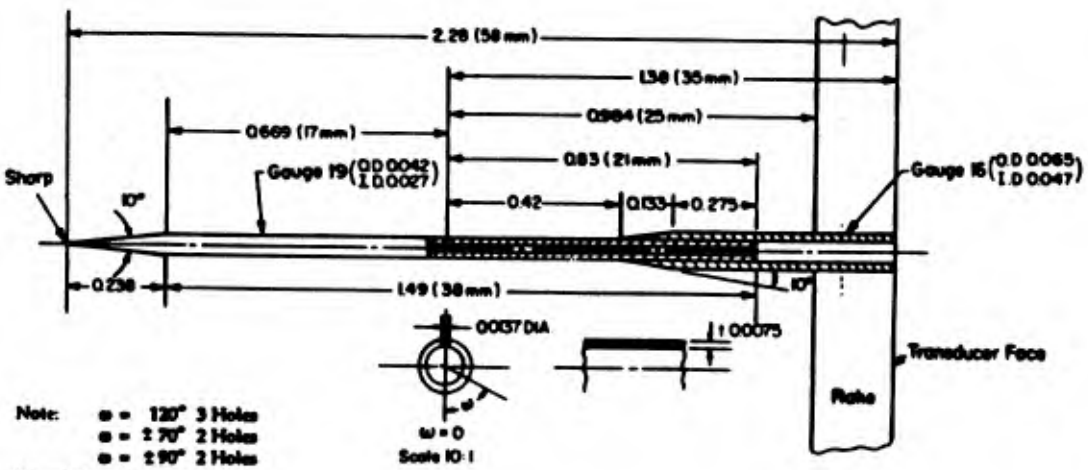

III

Figure 5.9 Static pressure probe designs.

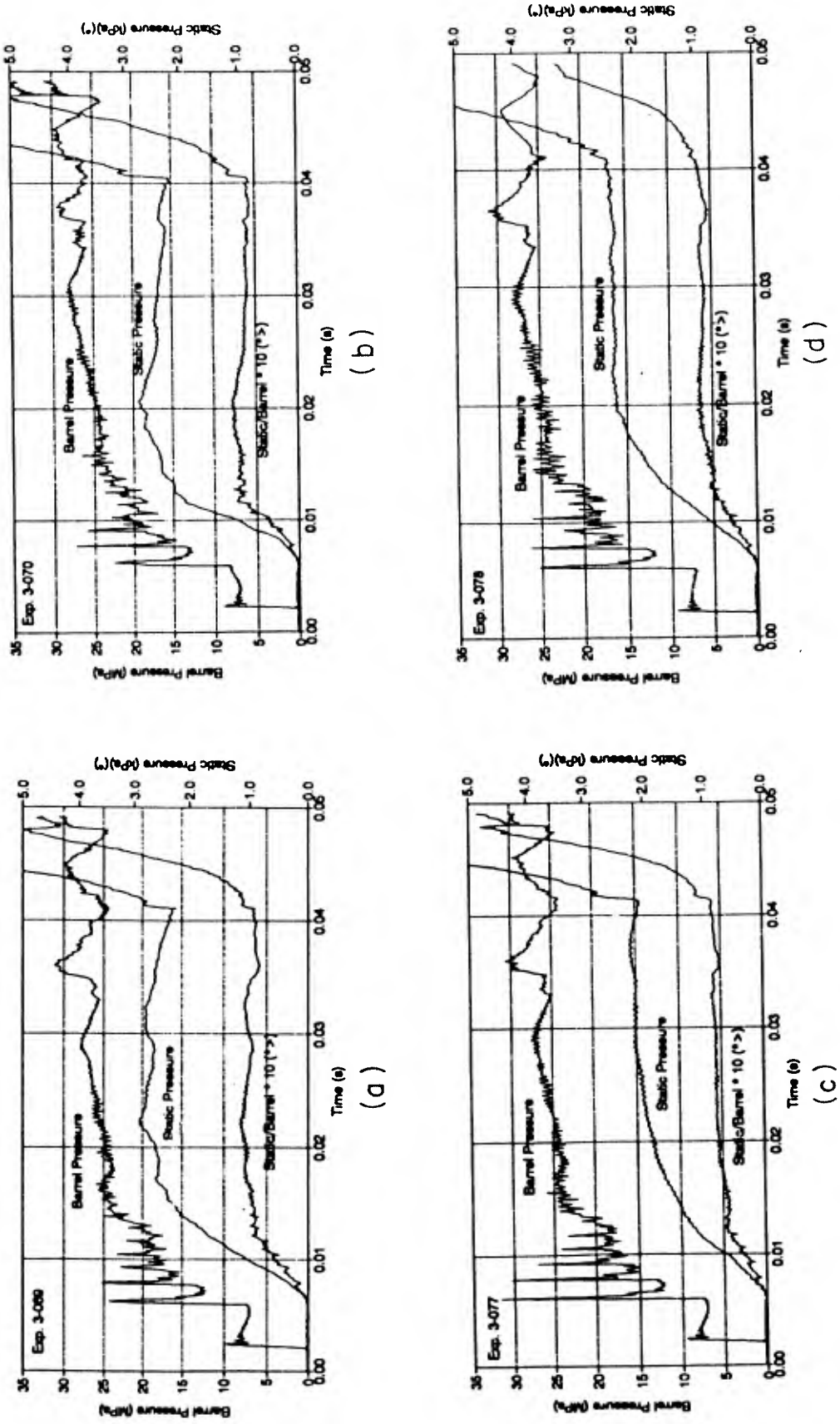

Figure 5.10 Static pressure histories in the tunnel free stream.

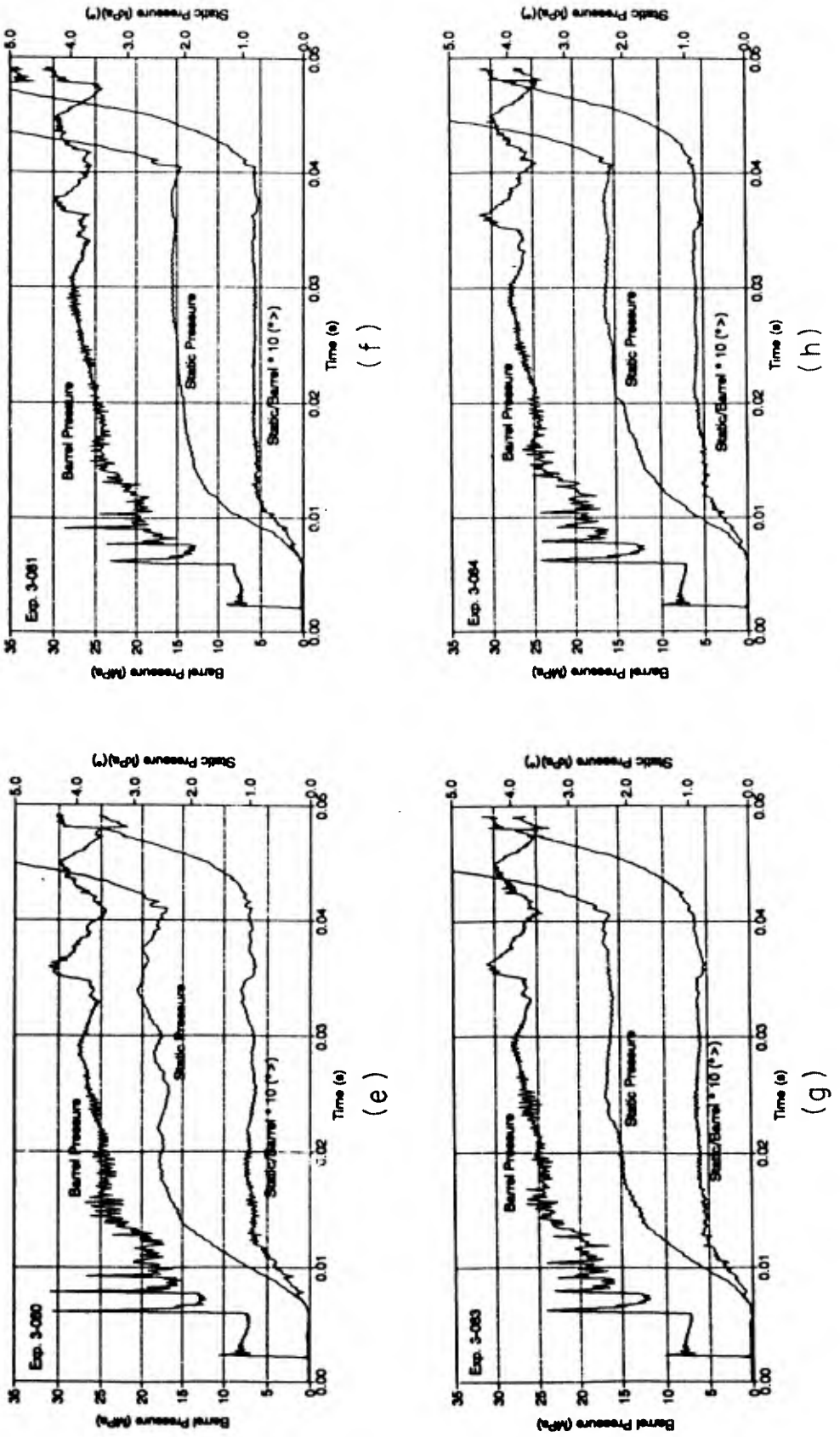

Figure 5.10 continued.

Assuming the flow inside the pipe to be perfectly axisymmetric, in-stream static and pitot pressure measurements were performed by inserting, at each measuring section, two static or two pitot pressure probes into the pipe via two diametrically opposed slots in the vertical symmetry plane of the pipe. The probes were moved radially by a traversing mechanism. Pitot and static pressure probes with distances from the probe stem centerline to the measuring orifices of 63.5 mm (2.5") were constructed (Figure 5.11). Static or pitot pressure measurements were performed simultaneously at two points located in the upper and lower halves of the section. Seventeen such double measurements of static and pitot pressures were taken at each section. For measurements at the duct exit section, the probes were mounted on a probe holder attached to a vertical traverse (see Figure 5.12).

5.3.3 Experimental Procedure

The tunnel was operated and data recorded and digitized as described in Section 2. The raw data files contained approximately 64,000 data points, each consisting of a 12-bit word representing a voltage at a particular time. For the present investigation, the time interval for each point after trigger was 4 μs or 250,000 samples/second. During the experiments, the various pressure histories started approximately 1 ms after trigger and ran for about 40 ms. Hence, over 12,000 data points were obtained during the time of interest. For the purposes of the present experiments, only every 20th point was used (over 600 data points) in the analysis. Averages were taken over a 10 ms span corresponding to the best steadiness in the traces.

For the large duct, all data was taken with tunnel barrel charge pressure p_b = 400 kPa; this corresponds to a test section M_∞ = 8.3 approximately and a unit free stream Reynolds number = 29.5×10^6 m^{-1}. The duct was aligned using the pressure taps described above. Figure 5.13 shows typical pressure histories obtained from the rear end set, and Figure 5.14 shows the effect of pitch angle on the vertical plane static pressures measured at the front set. The alignment of the pipe was further fine-tuned by comparing, at each measuring section, the pitot pressure magnitudes at two symmetrical points, with respect to the axis (along the vertical diameter).

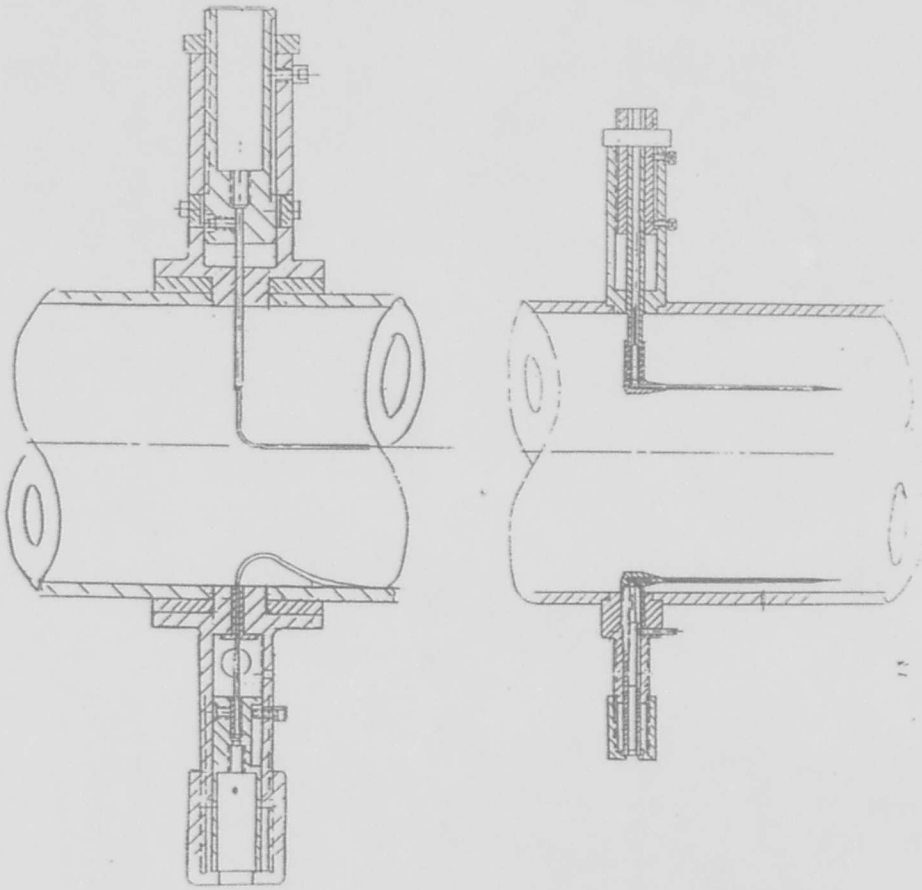

Figure 5.11 Sketch of the inserted pitot and static probes with micropositioner.

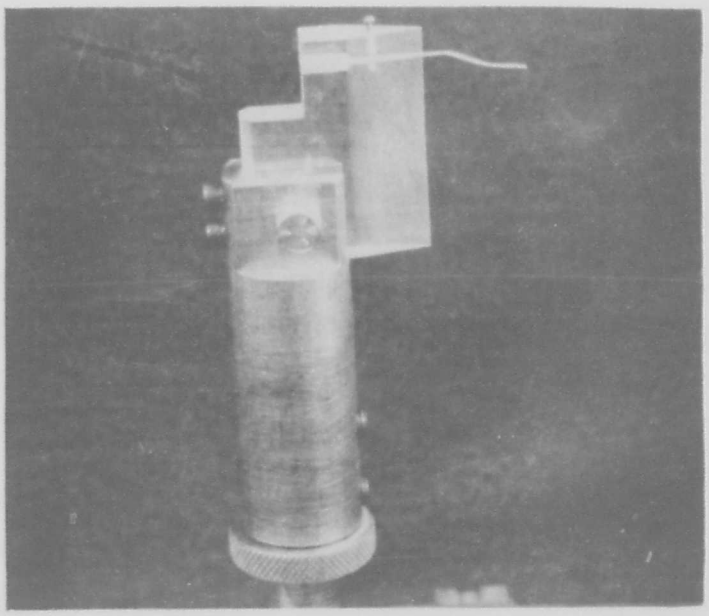

Figure 5.12 Photo of probe holder used in pipe exit measurements.

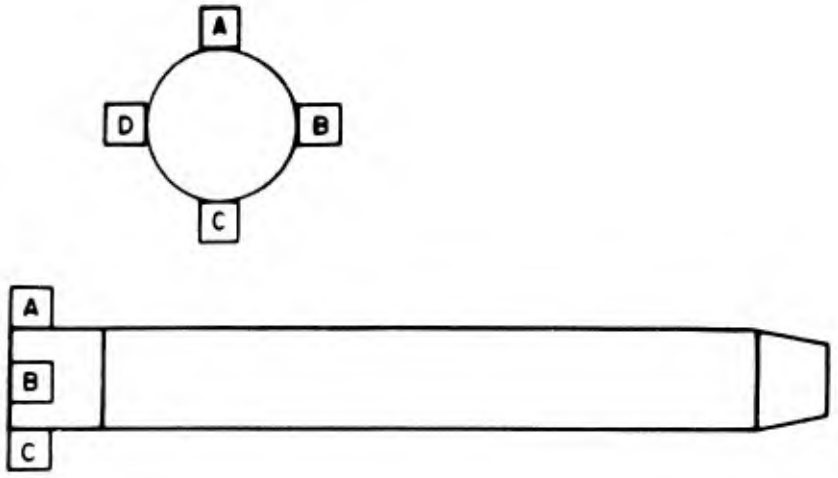

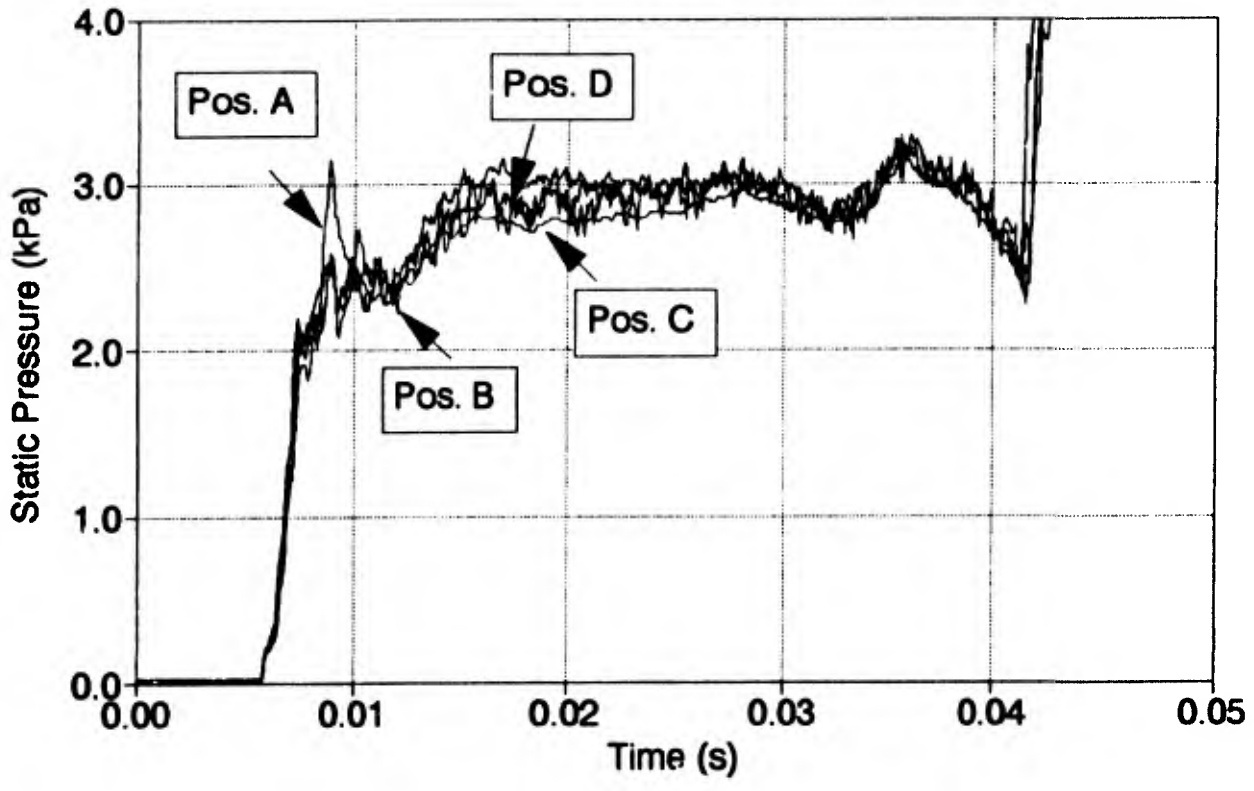

Figure 5.13 Comparison of wall static pressures at the duct exit for preliminary alignment of the axis with the oncoming flow direction.

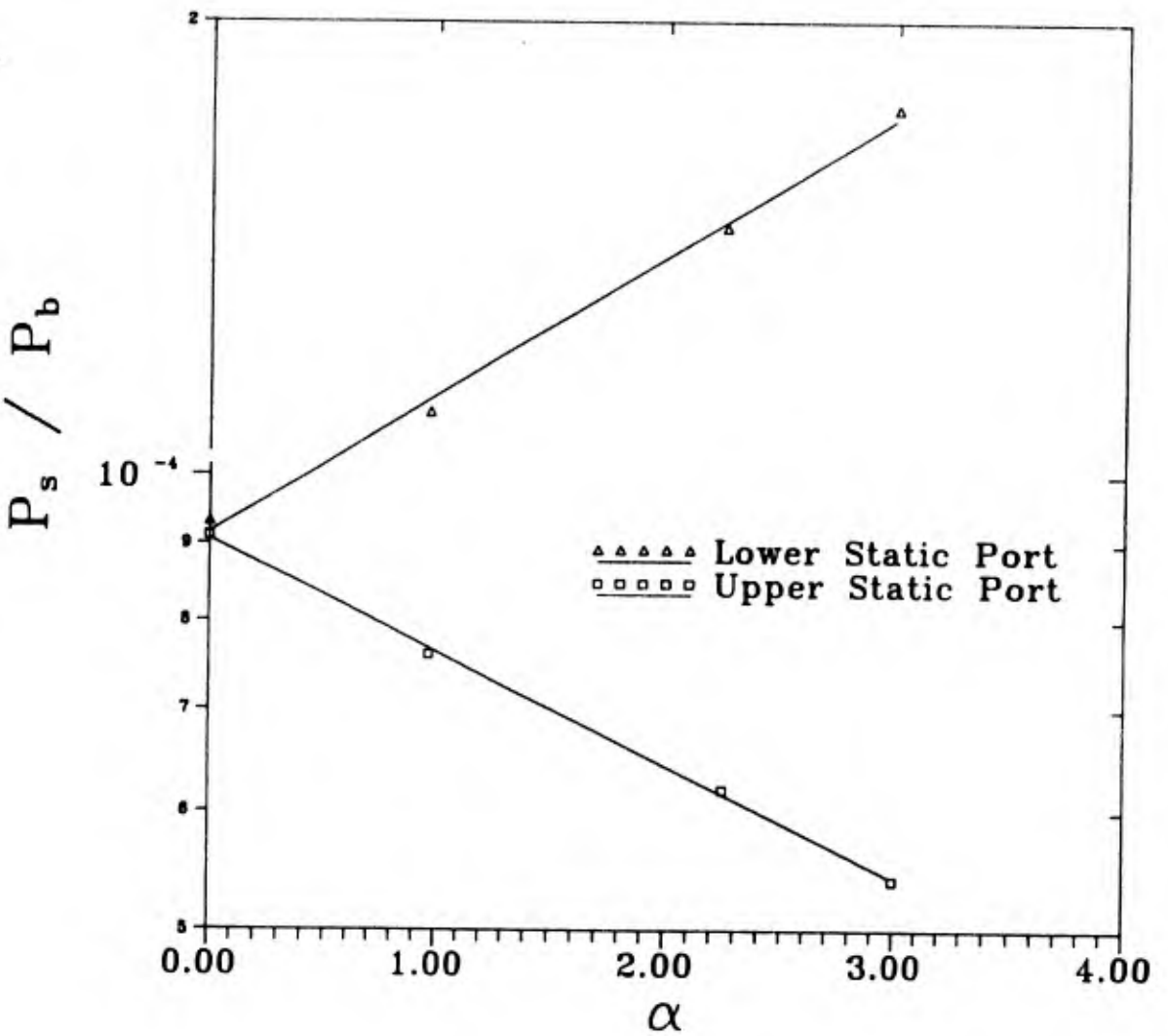

Figure 5.14 Effect of pitch angle α on the static pressure measured at two static ports in the vertical plane.

The small duct was mounted with its entrance (6 ins.) upstream of the nozzle exit plane to allow schlieren visualization of its exit flow in the main test section windows. It was aligned using the procedures for the large duct. Prior to cutting this duct the opportunity was taken to briefly explore Reynolds number effects.

5.4 Experimental Results for the Large Duct

Schlieren photographs of the flow, at both the entrance and the exit of the duct are shown respectively in Figures 5.15 and 5.16. Note that the model has started properly during the run. At the exit, the flow seems to be relatively simple with no waves from the outside of the duct being generated. Only two shock waves and a boundary layer are seen at the exit .

Three gun tunnel runs were required to measure the entire wall static pressure distribution. During each run, pressures at only eight locations were recorded, with measurements at one or two locations being duplicated to check the repeatability of the results. A typical measured distribution of wall pressure distribution p_w is depicted in Figure 5.17. The pressures are nondimensionalized with respect to the free stream static pressure p_∞, and axial distance along the duct x from the entrance is nondimensionalized by the duct diameter D. The wall pressure increases slowly but steadily from the entrance to a peak at x/D = 5.7 of twice p_∞. This seems characteristic of a shock-boundary layer interaction. It then decreases rapidly after the interaction zone, and the flow seems to expand in this region. Thereafter, it slowly decreases to its pre-interaction value. A slight increase in wall pressure occurs for x/D > 8.3.

Instream static and pitot pressures were measured at x/D = 2.38, 3.0, 5.0, 5.67, 6.33, 8.0, 8.65 and 9.83; instream pitot pressures were also measured at x/D = 1.5 and 2.0. The data obtained at each section is presented in Figures 5.18 to 5.27, with the instream static and pitot pressures, p_l and p_p respectively, nondimensionalized by their corresponding freestream values. Whereas the interpretation of the pitot data appears to be straightforward, the static data encountered two difficulties. The first was unsteadiness in the measurements at certain locations, and the second was an interference effect.

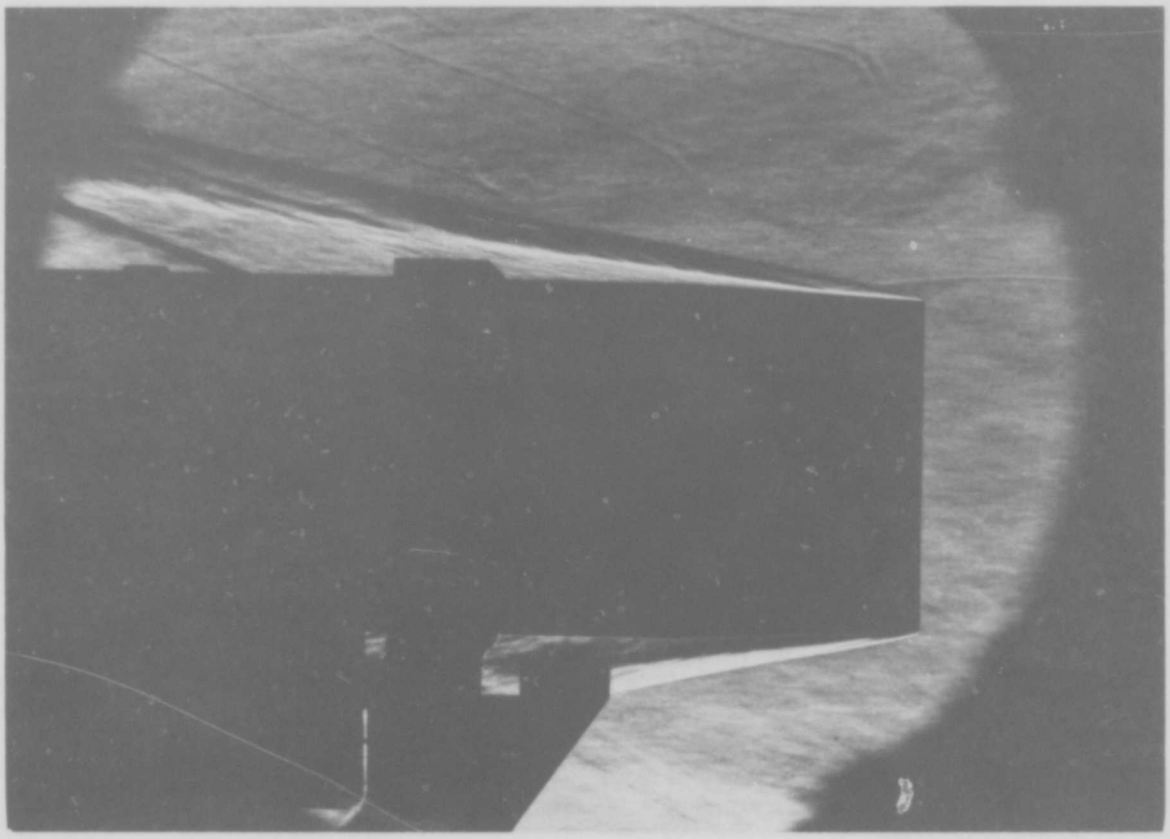

Figure 5.15 Schlieren photo of large duct inlet flow.

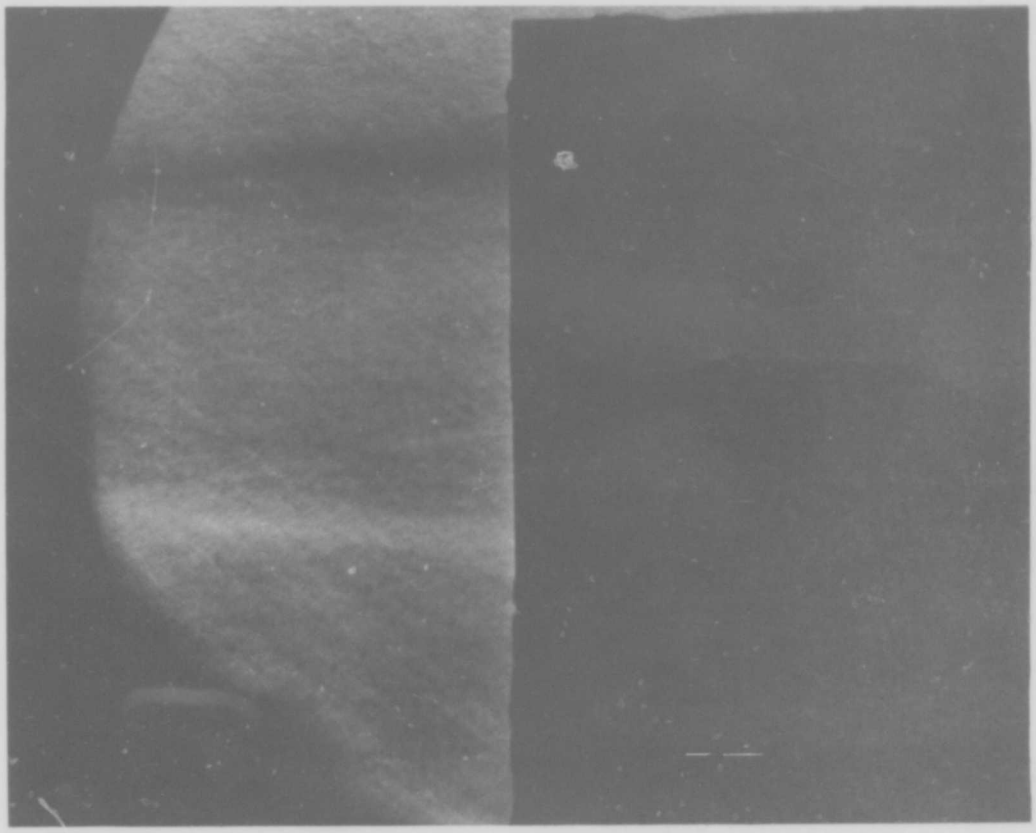

Figure 5.16 Schlieren photo of large duct exit flow.

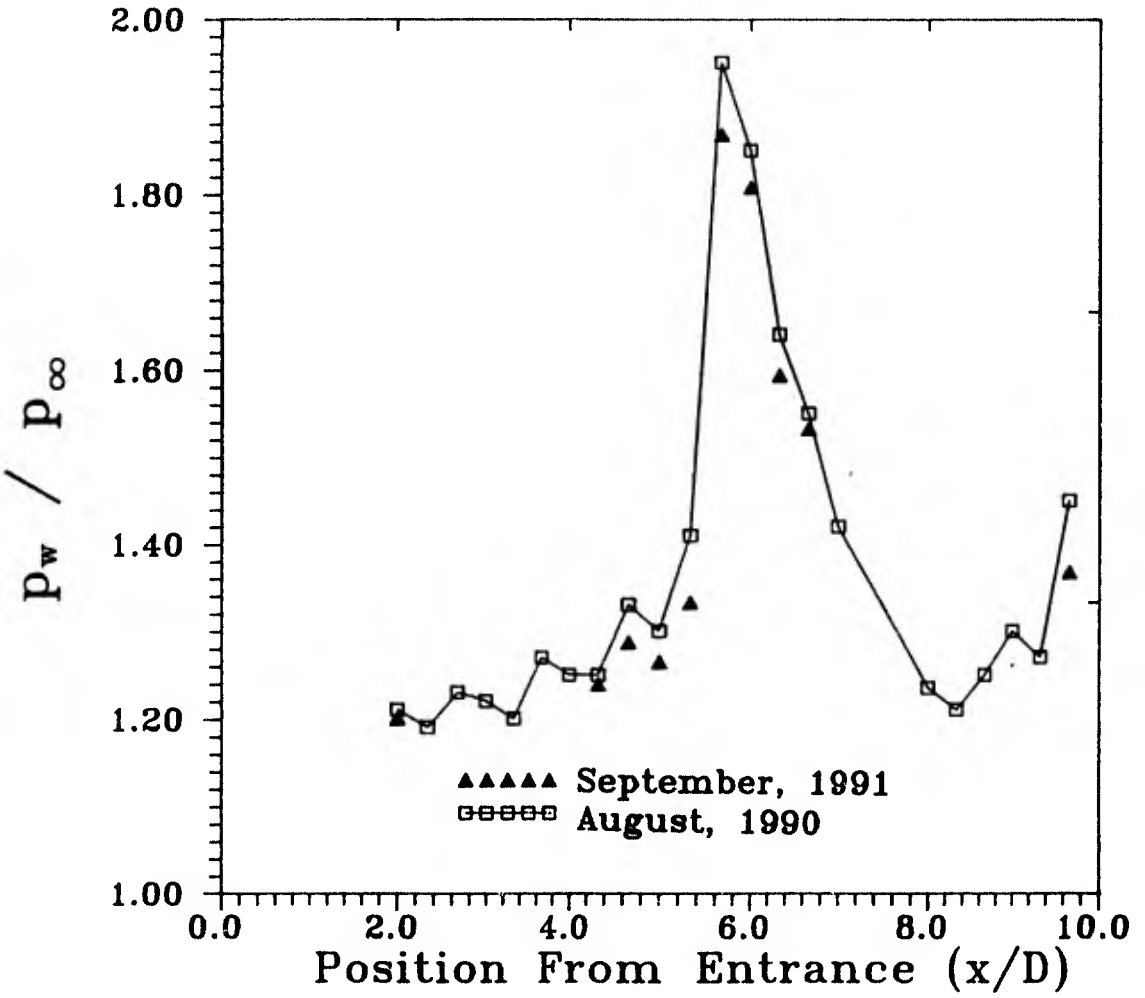

Figure 5.17 Wall static pressure distribution for large duct.

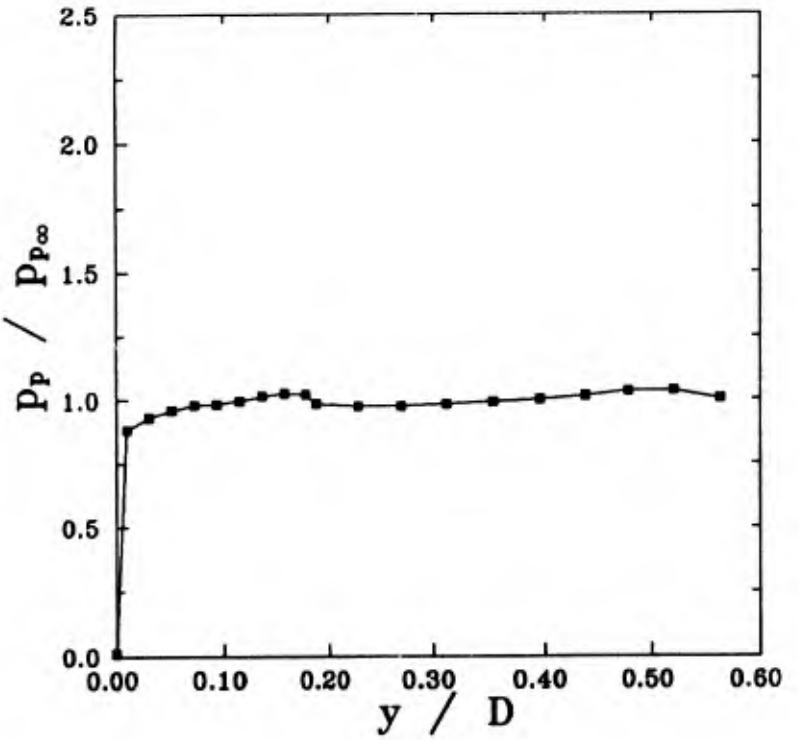

Figure 5.18 Instream pitot profiles at x/D = 1.5. The pressures are normalized by the free stream pitot pressure $p_{p\infty}$; y = 0 and 0.5 correspond, respectively, to the duct wall and centerline.

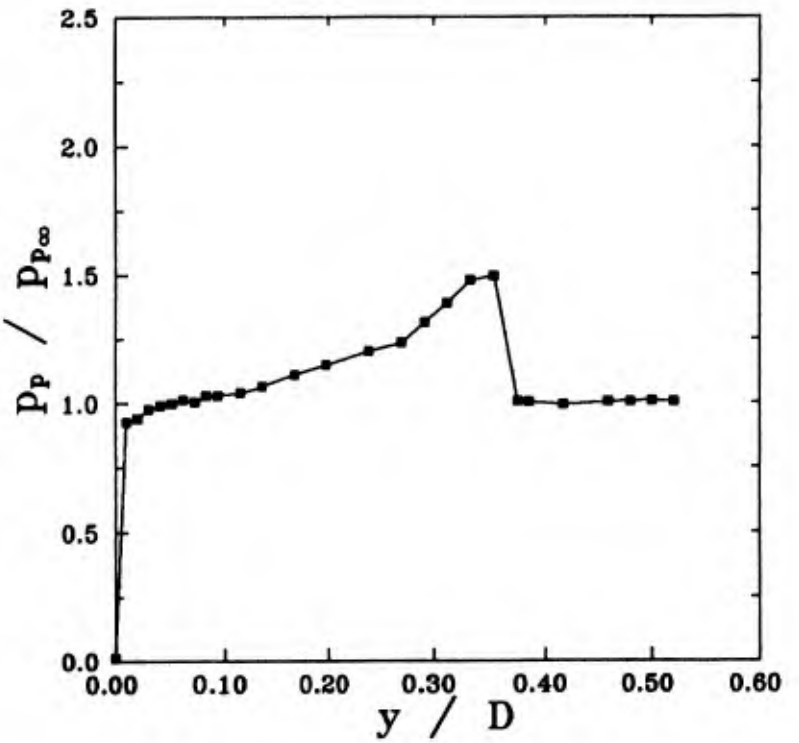

Figure 5.19 Instream pitot profiles at x/D = 2.0.

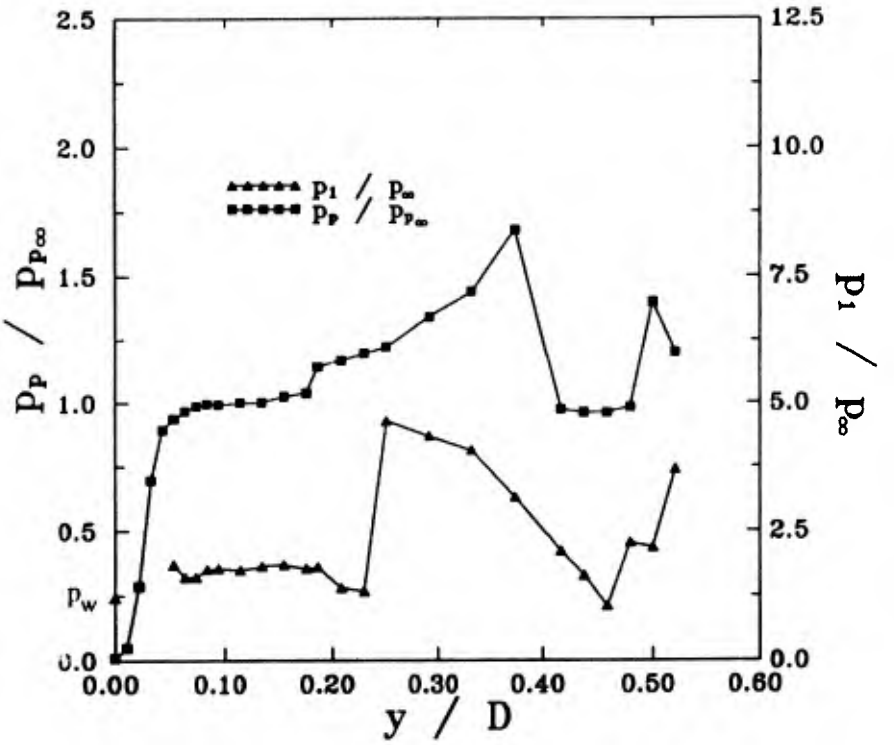

Figure 5.20 Instream pitot and static pressure profiles at x/D = 2.38. The static pressures are normalized with an assumed p_∞ = 2.15 kPa. The value p_w measured at the wall, y = 0, by the wall-static tap is also included.

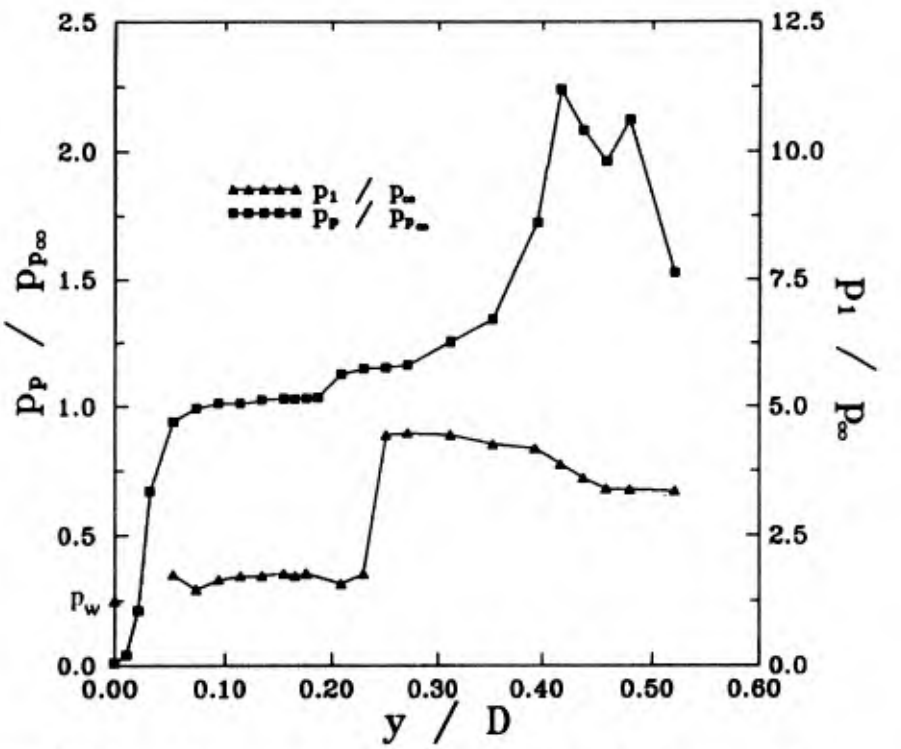

Figure 5.21 Instream pitot and static pressure profiles at x/D = 3.0.

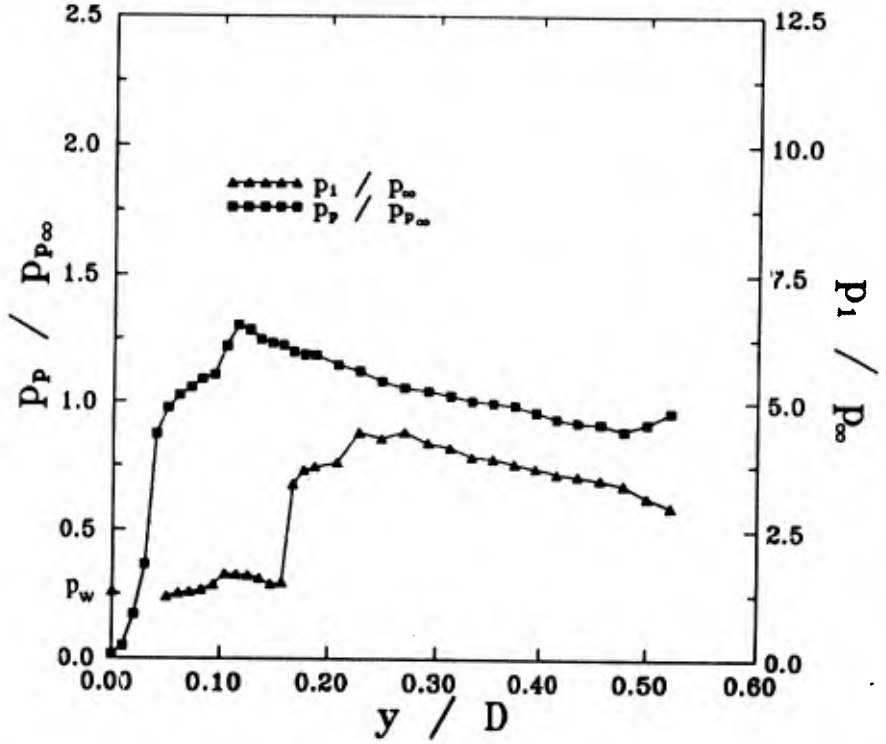

Figure 5.22 Instream pitot and static pressure profiles for x/D = 5.0.

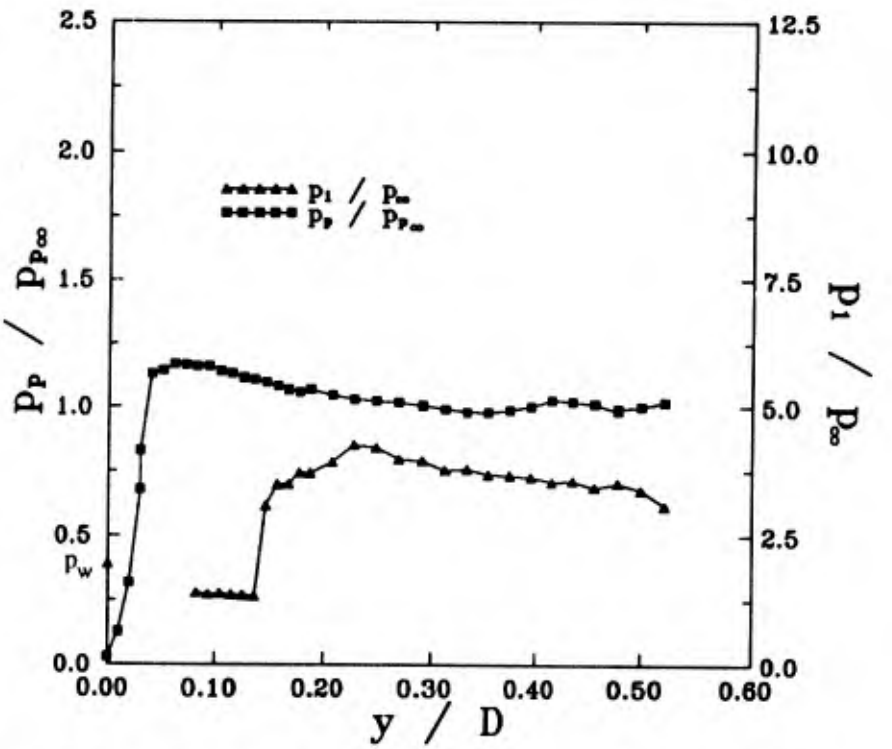

Figure 5.23 Instream pitot and static pressure profiles for x/D = 5.67.

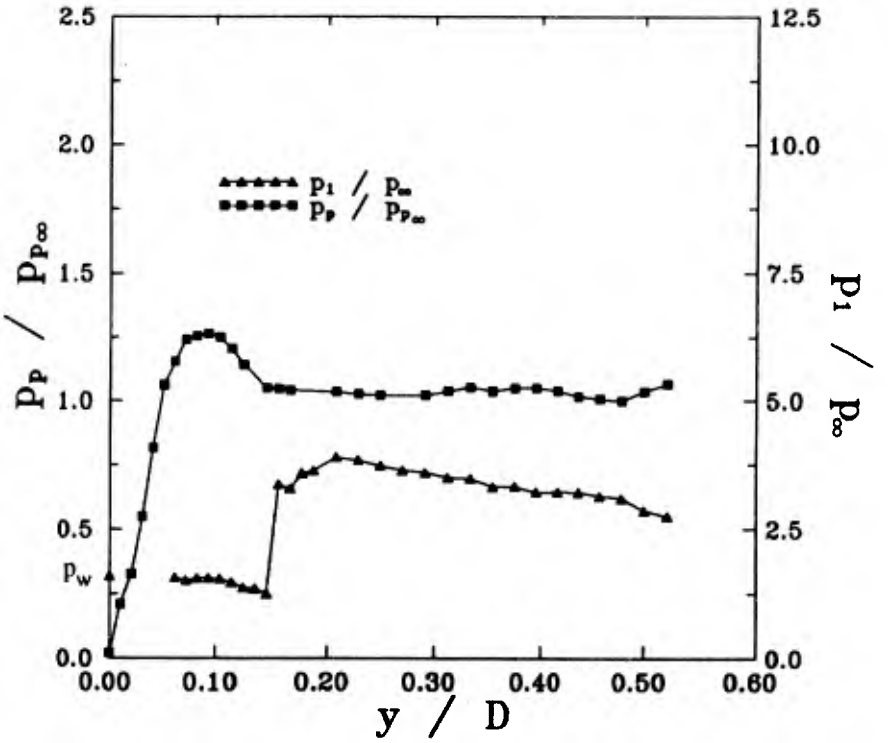

Figure 5.24 Instream pitot and static pressure profiles for x/D = 6.33.

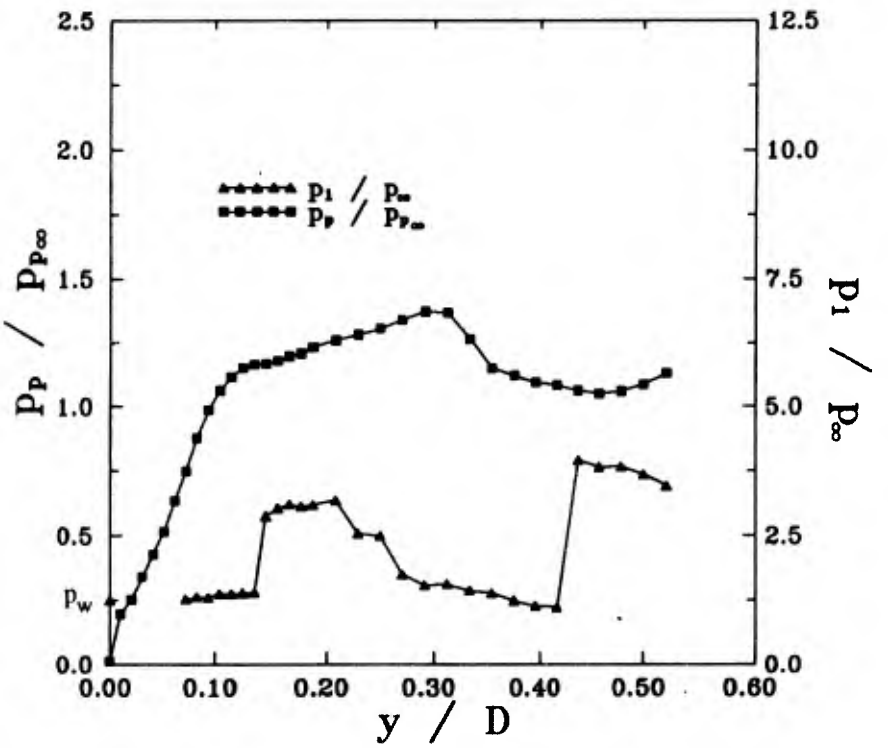

Figure 5.25 Instream pitot and static pressure profiles for x/D = 8.0.

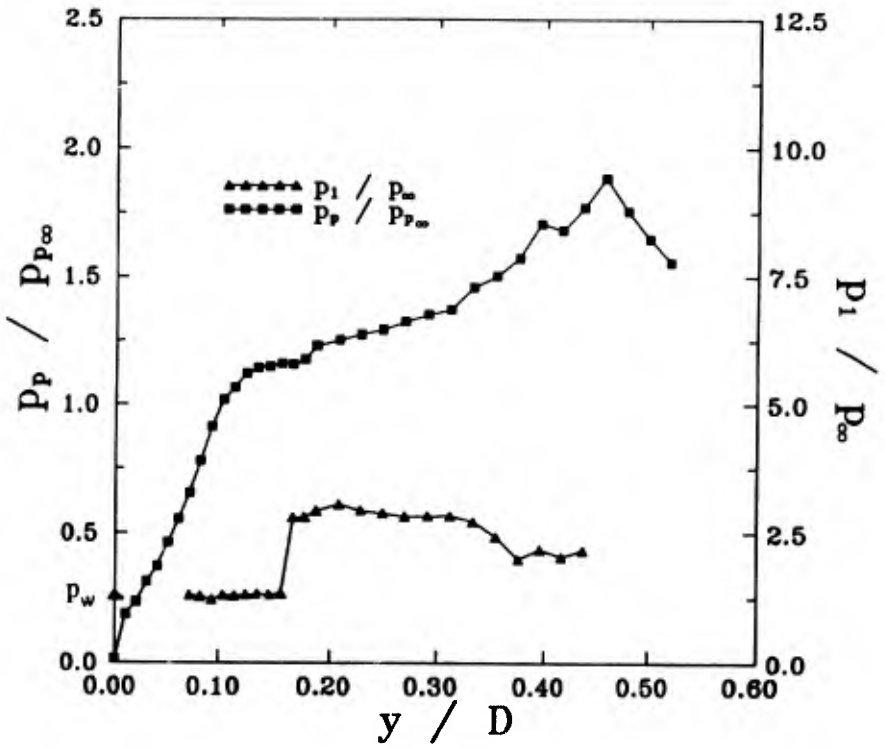

Figure 5.26 Instream pitot and static pressure profiles for x/D = 8.65.

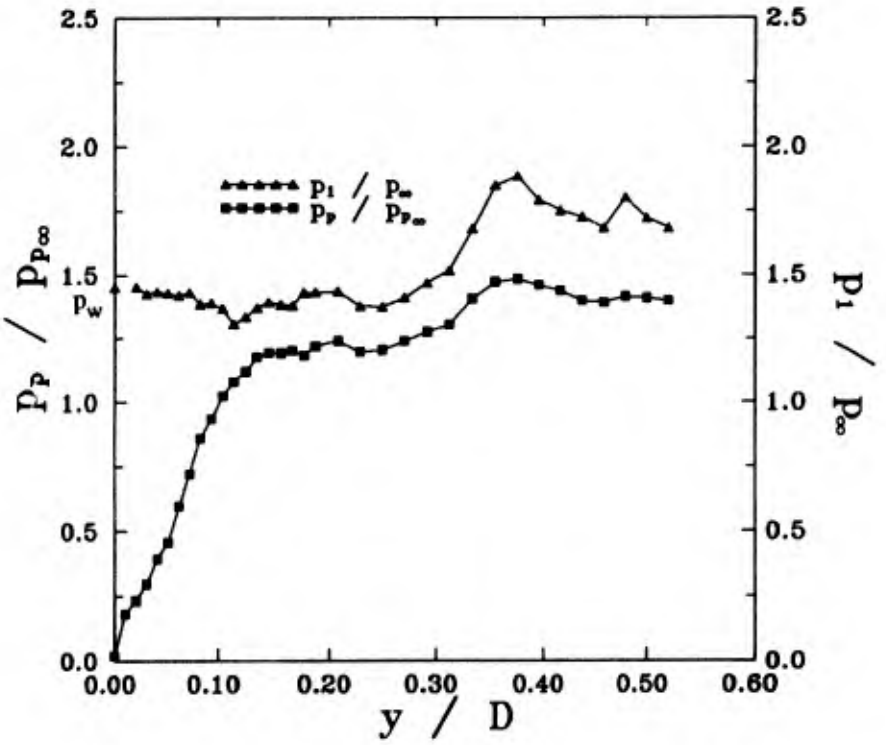

Figure 5.27 Instream pitot and static pressure profiles for x/D = 9.8.

Considering the first difficulty, static probe histories at three locations are shown in Figure 5.28. The probe response in Figure 5.28(a) is representative of most of the measurements. However, in some instances, the probe was probably very close to a wave structure or in the transition region of the wave. A static pressure trace representative of this region is shown in Figure 5.28(b). Moreover, pitot and/or static pressure traces obtained near the axis of symmetry at some sections depicted some flow unsteadiness (see Figure 5.28(c)). Because it was not possible to obtain a meaningful average, values of static pressures in these regions of the flow are not reported.

Considering now the second difficulty, an important consistency check is agreement of the instream static measurements obtained near the duct wall with those obtained from the wall pressure taps. As the data in Figures 5.18 to 5.27 shows, near-wall static pressure measurements at x/D = 5.0, 6.33, 8.0, 8.65 and 9.8 were within ±5% of the values obtained from wall pressure taps at these locations. However, at other sections, the near wall static probe pressure was significantly higher than the value recorded by the wall-mounted transducer. Typically, at x/D = 2.38 the value of p_w/p_∞ is about 1.19, whereas at y/D = 0.0521 the static probe gives $p_1/p_\infty = 1.767$. This discrepancy was traced to a probe interference effect. Figure 5.29 is a plot of pressure histories obtained at a wall static tap with the instream static probe present and removed; clearly the presence of the instream probe has greatly increased the wall-static pressure. The history of the instream probe itself is intermediate between the two. It appears that the bulk of the instream probe mounting system generates a shock-wave boundary layer interaction which propagates upstream to the probe measuring station. Another possibility is an interaction of the wall boundary layer with the shock wave generated by the probe tip. However, as shown in Figure 5.11, the stems of the pitot boundary layer probes present a much smaller cross-section to the oncoming flow, and they do not introduce such an interaction.

Except at x/D = 1.5, distinct pressure jump, characteristic of a shock, is clearly seen in all static and total pressure profiles. At section x/D = 8.0, Figure 5.25, two such jumps are visible. The jump at section x/D = 2.4 is radially located in the vicinity of y/D ~ 0.23. At subsequent sections, it seems to move radially towards the wall up to the section x/D = 5.7, where shock-boundary layer type interaction takes place. Thereafter, it slowly but steadily moves away from the wall and disappears, together with the second shock

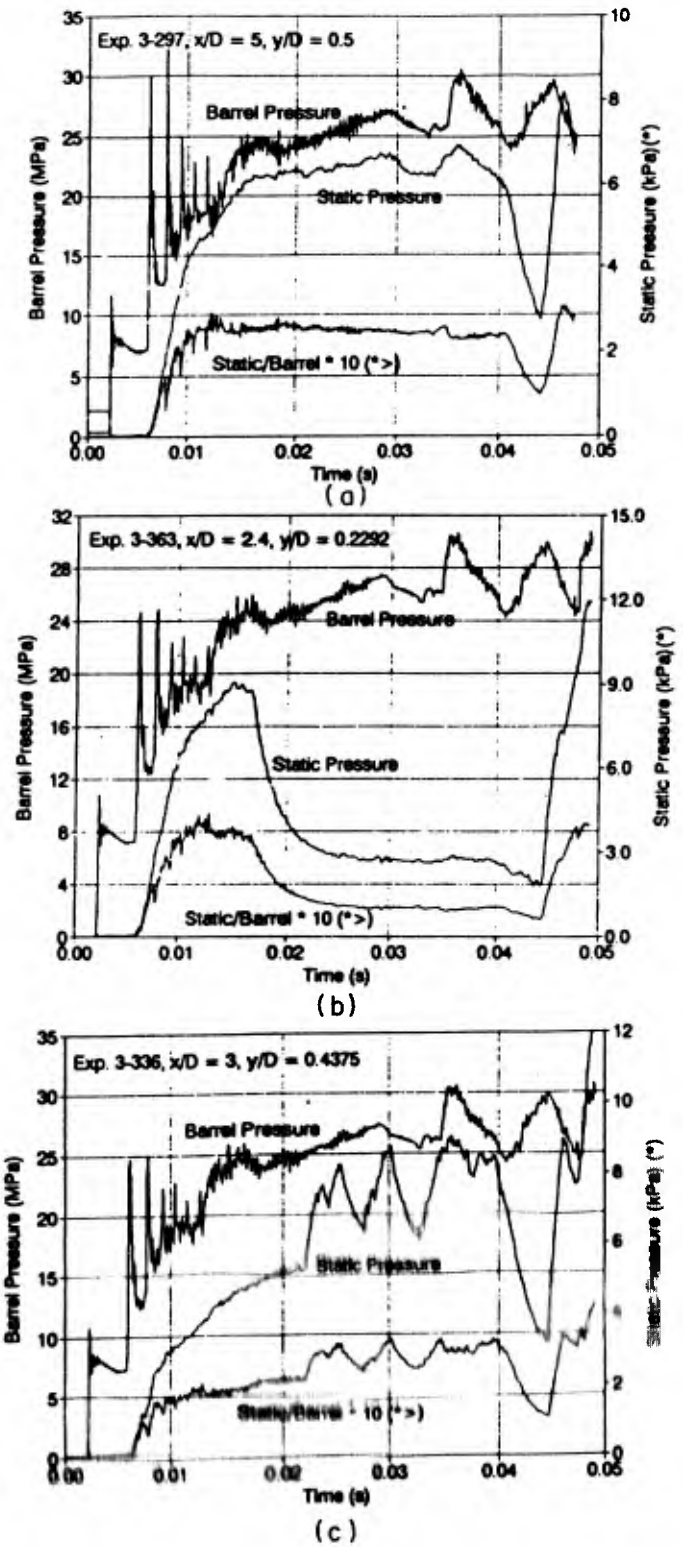

Figure 5.28 Three examples of instream static pressure histories as compared with their corresponding barrel pressure histories.

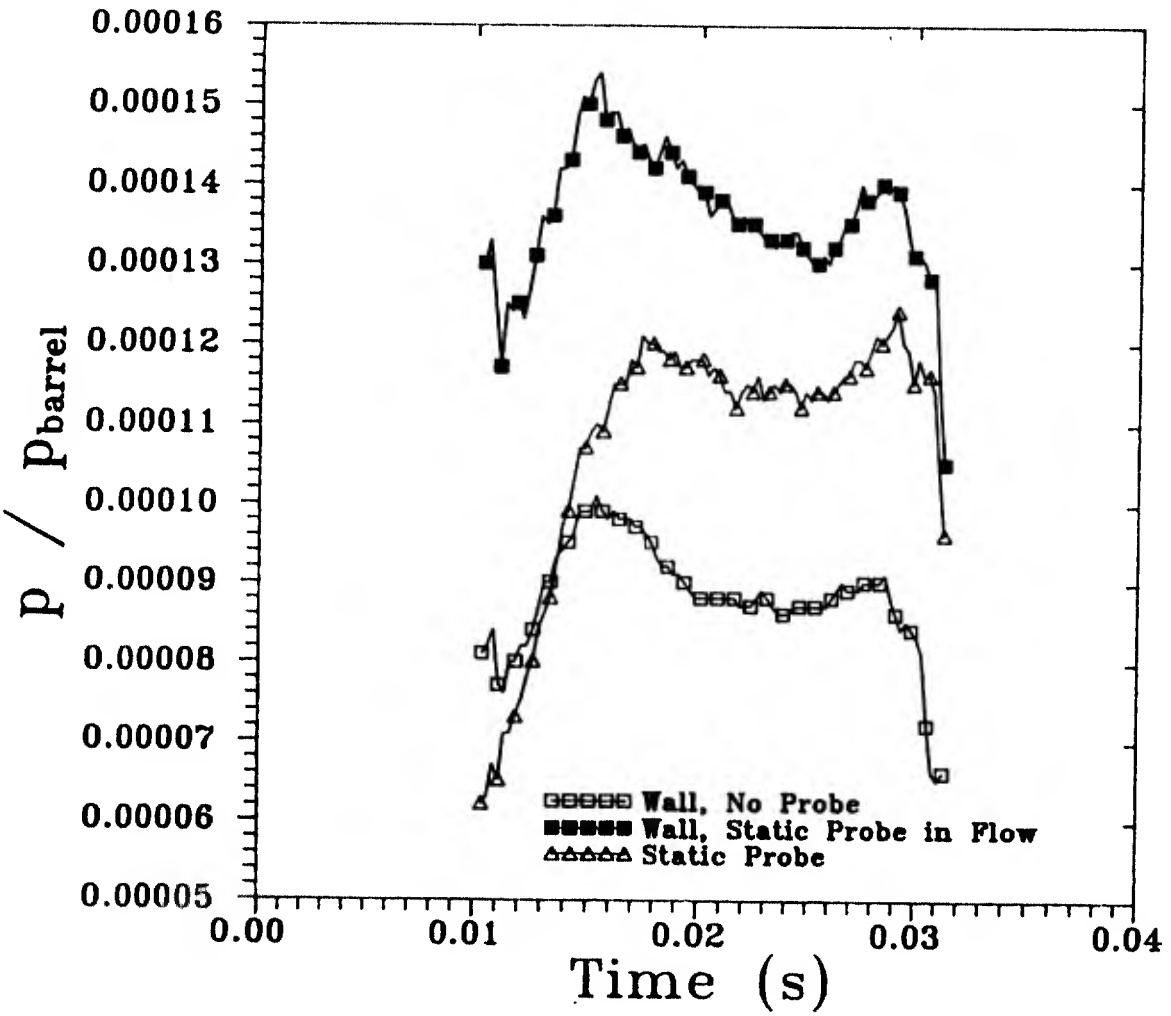

Figure 5.29 Effect of presence of instream static probe on pressure history measured at wall-static taps at x/D = 2.4.

formed near the axis of the pipe, at the exit section of the pipe. The shocks generated in the flow seem to be oblique, with possible normal shocks or Mach discs in central portions of the pipe where these oblique shocks reflect off the axis of symmetry. Also, the pitot pressure profiles near the pipe wall give an insight into the boundary layer thickness, which notably increases in the downstream portion of the pipe flow. The data exhibit some scatter in some regions of the flow which does not exceed 10% approximately (see, for example, Figures 5.21, 5.22 and 5.26).

5.5 Experimental Results for the Small Duct

The difficulties of interpretation arising from lack of internal flow visualization and from the instream static probe interference effects led us to investigate the effect of cutting the duct on the flow upstream. Schlieren flow visualization at the exit is possible, and the static probe could be mounted with its stem outside the pipe, thus eliminating the observed interference effect. If it can be demonstrated that cutting the duct does not significantly affect the flow upstream then the structure of the flow in the uncut duct could be reconstructed from these measurements.

Prior to cutting the small duct, a limited investigation of Reynolds number effects was undertaken, and the results are shown in Figure 5.30, which is a plot of wall static pressure as a function of x/D. It shows a modest effect on the pressure distribution with the pressure at the first tap, corresponding to x/D = 3.0, increasing as Reynolds number decreases. A more complicated trend occurs downstream. Figure 5.31 compares the pressure distributions in the large duct with that obtained from the small duct, at the nearest Re_D: the large differences suggest that phenomena such as the shock structure at the duct axis involve length scales unrelated to D.

Figure 5.32 shows the effect of cutting the duct on the wall static pressure distribution upstream. The continuous curve joins the data for the original length: L/D = 10. The first two cuts, to L/D = 8.75 and 8.0 respectively, cause little effect on the upstream distribution. For L/D = 7.5 significant changes occur but when it is reduced to 6.5, the pressure distribution upstream reverts to that for L/D = 10. It appears that significant effects occur only if the cuts are in the neighborhood of the interactions between shock waves and the wall boundary layer.

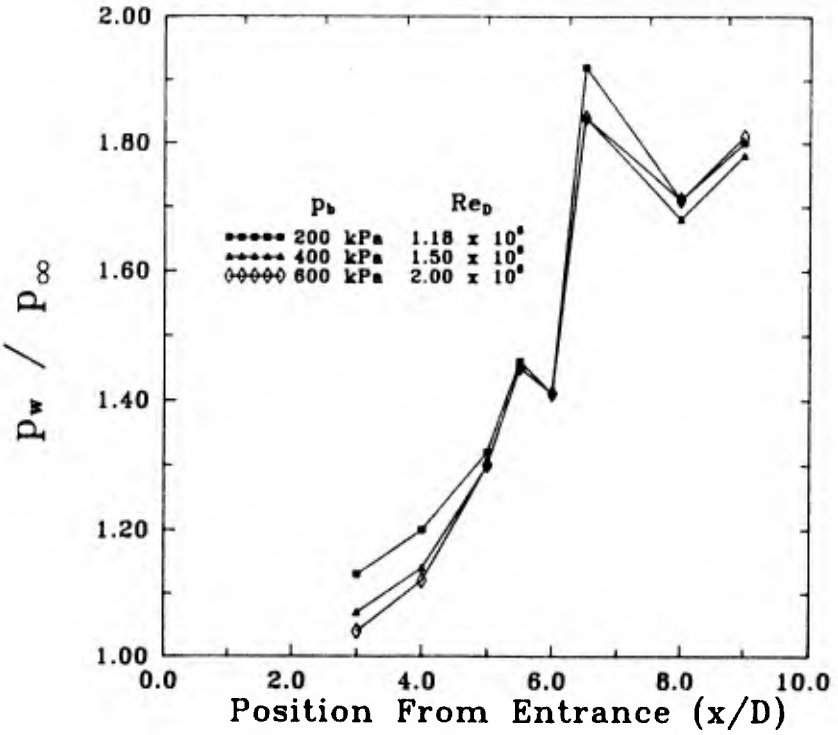

Figure 5.30 Effect of Reynolds number on wall pressure distribution in small duct.

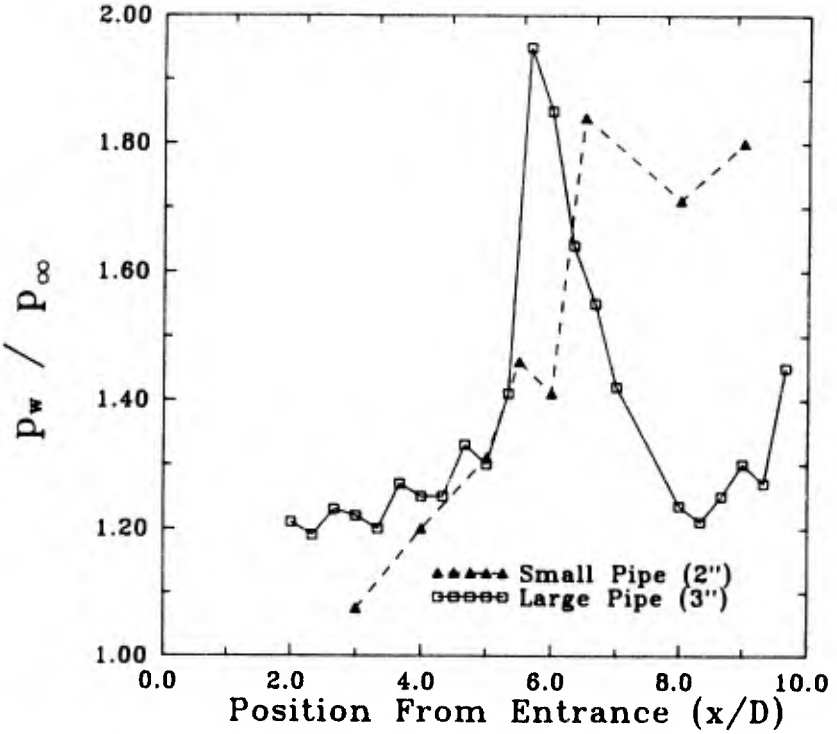

Figure 5.31 Wall static pressure distributions of large and small ducts compared (both with L/D = 10).

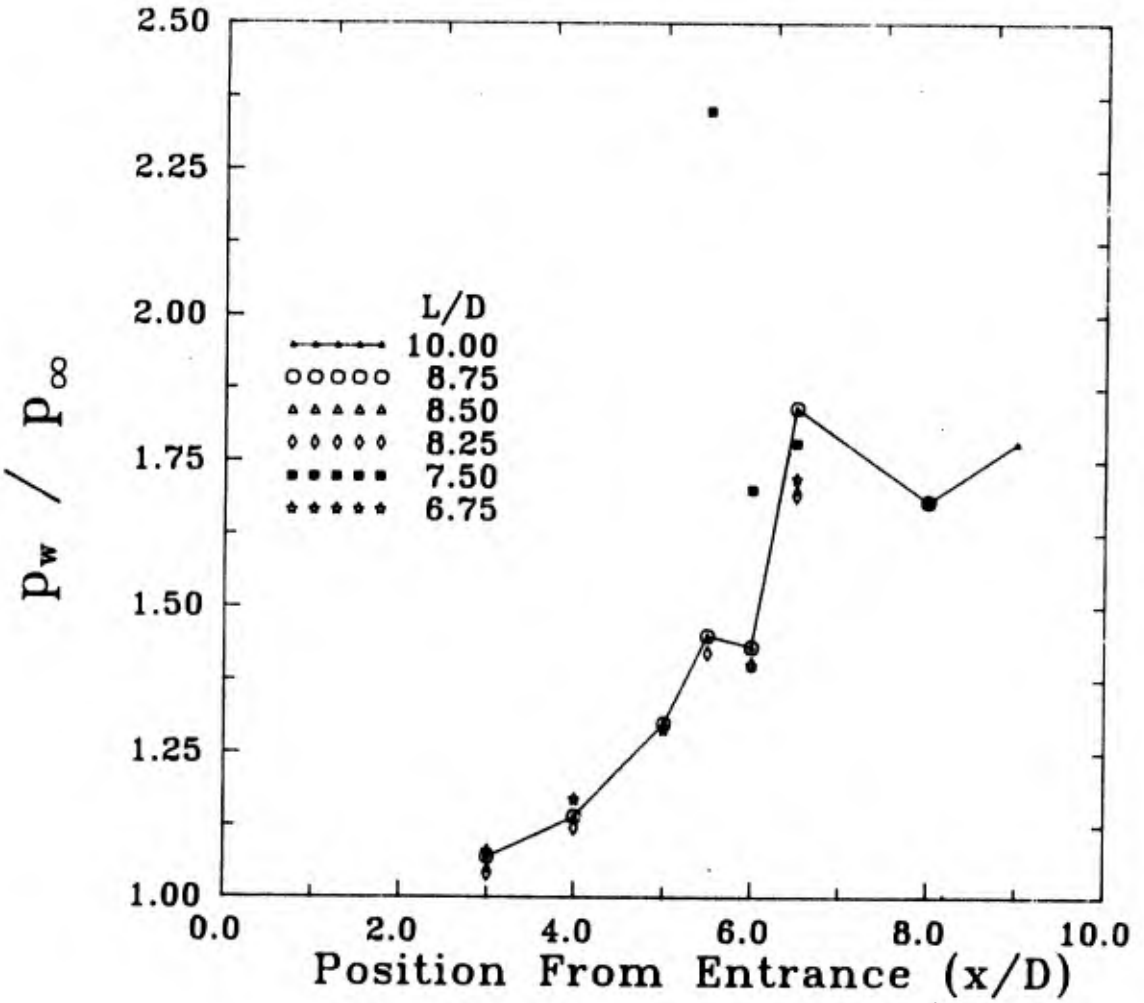

Figure 5.32 Effect of cutting duct on upstream wall static distribution.

5.6 Discussion and Conclusions

In the absence of flow visualization, both instream static and pitot pressure measurements are required to allow a satisfactory reconstruction of the flow field. The boundary layer type pitot tubes are adequate, but the static probes need improvement. A major difficulty is that the slow response of existing designs requires the sensing transducer to be mounted on a relatively bulky stem or support which protrudes into the duct interior, and this creates interference problems. Potential solutions include the use of shorter probes, such as those developed by Pinkney (Ref. 5.15), which would allow the transducer to be mounted outside the duct, and streamlining of the existing supports. In some cases the duct cutting technique could be used to allow insertion of the existing probes at the rear, thus eliminating the interference effect. The duct cutting technique can also be used to provide a limited amount of flow visualization.

With these improvements, a reliable detailed reconstruction of the flow in the duct interior should be possible.

5.7 References

5.1. Neumann, E. P., and Lustwerk, F., Supersonic Diffusers for Wind Tunnels, *Journal of Applied Mechanics*, No. 6, 1949, pp. 195-202.

5.2. Lustwerk, F., "The Influence of Boundary Layer on the Normal Shock Configuration," MIT, Cambridge, Massachusetts, Meteor Report No. 61, Sept. 1950.

5.3. Richmond, J. K., and Goldstein, R., "Fully Developed Turbulent Supersonic Flow in a Rectangular Duct," *AIAA Journal*, No. 8, 1966, pp. 1331-1336.

5.4. Fejer, A. A., et al, "An Investigation of Constant Area Supersonic Flow Diffusion," Aerospace Research Labs., Wright-Patterson Air Force Base, Ohio, Report ARL 64-81, 1965.

5.5. McLafferty, G. H., Krasnoff, E. L., Ranard, E. D., Rose, W. G., and Vergara, R. D., "Investigation of Turbojet Inlet Design Parameters," United Aircraft Corp., East Hartford, Connecticut, Report R-0790-13, Dec. 1955.

5.6. Billig, F. S., Dugger, G. L., and Waltrup, P. J., "Inlet-Combustor Interface Problems in Scramjet Engines," 1st International Symposium on Air Breathing Engines, International Airbreathing Propulsion Committee, Marseilles, France, June 1972.

5.7. Waltrup, P. J., and Billig, F. S., "Precombustion Shock Structure in Scramjet Engines," AIAA/SAE 8th Joint Propulsion Specialist Conference, New Orleans, Louisiana, Dec. 1972, AIAA-72-1181.

5.8. Waltrup, P. J., and Billig, F. S., "Structure of Shock Waves in Cylindrical Ducts," *AIAA Journal*, Vol. 11, No. 10, 1973, pp. 1404-1408.

5.9. Waltrup, P. J., and Cameron, J. M., "Wall Shear and Boundary-Layer Measurements in Shock Separated Flow," *AIAA Journal*, Vol. 12, No. 6, June 1974, pp. 878-880.

5.10. Om, D., and Childs, M. E., "An Experimental Investigation of Multiple Shock Wave/Turbulent Boundary Layer Interactions in a Circular Duct," AIAA 16th Fluid and Plasma Dynamics Conference, Danvers, Massachusetts, July 1983, AIAA-83-1744.

5.11. Gessner, F. B., Ferguson, S. D., and Lo, C. M., "Experiments on Supersonic Turbulent Flow Development in a Square Duct," *AIAA Journal*, Vol. 25, No. 5, 1987, pp. 690-697.

5.12. Chue, S. H., "Pressure Probes for Fluid Measurements," *Prog. Aerospace Sci.*, Vol. 16, No. 2, 1975, pp. 147-223.

5.13 Williams, M. J., "Static Pressure Probes at Mach Number 7.5", Commonwealth of Australia, Aeronautical Research Laboratories, Melbourne, Australia, Note ARL/A 327, 1970.

5.14 Gray, J. D., "Evaluation of Probes for Measuring Static Pressure in Supersonic and Hypersonic Flows", Arnold Engineering Development Center, Arnold Air Force Station, Tennessee, Report AEDC-TR-71-265, 1972.

5.15 Pinckney, S. Z., "A Short Static-Pressure Probe Design for Supersonic Flow", NASA, Washington, D.C., Technical Note D-7978, 1975.

6.0 A Comparison of Three Hypersonic Air Inlets

S. Molder, R.J. McGregor and T.W. Paisley

6.1 Introduction

The growing economic and strategic significance of placing human and material payloads into low earth orbit has guided the technological search for more cost efficient delivery systems. Recent growth of key aerospace technologies has stimulated a renewed interest in air breathing propulsion systems for low earth orbit payload delivery. The U.S. National Aerospace Plane (NASP) project was devised in response to the need for improved cost efficiency over traditional Shuttle and expendable launch capability (Ref. 6.1).

For the NASP project, much attention has been directed to the high specific impulse potential of the scramjet (Ref. 6.2). This engine will power the Aerospace plane through the majority of its trajectory into orbit. The scramjet engine consists of an air inlet, a combustion chamber and an exhaust nozzle. Of vital importance to engine propulsive efficiency, and hence vehicle payload capacity, is the precise optimization of the aerodynamic design of the scramjet engine and its components. In this section, we will deal particularly with one of these components namely the air intake, examining in parti ular the effect of inlet geometry on inlet performance.

In aircraft propulsion systems, the inlet provides the means of channelling freestream air into the engine for the use of its oxygen content for combustion with injected fuel. In so doing it also reduces the Mach number, thus allowing a more efficient heat addition in the combustion chamber. This deceleration brings about inviscid and viscous losses through the boundary layer and shock wave formation. These losses are technically both of a viscous origin caused by the entropy production of viscous dissipation. Several different measures of efficiency, including total pressure recovery, η_{pt} and kinetic energy efficiency, η_{ke}, have been applied to the scramjet inlet, all somehow attempting to measure this entropy production (Refs. 6.3, 6.4).

In searching for an aerodynamically efficient inlet shape, the designer is faced with some opposing requirements. For low inviscid flow losses the inlet tends to be very long; "isentropic" inlet length is

approximately M_∞ times its streamtube capture height. For low viscous flow losses, however, the inlet design tends to be very short so as to minimize the length of the boundary layer and its attendant losses. Also, in the initial phases of design, a decision has to be made on the selection of external or internal compression and axially symmetric flow versus flow with planar symmetry. It is realized that the rationale for some of these decisions stems from overall vehicle design considerations; nevertheless, one of these considerations is the engine and inlet performance and that is why we have chosen to investigate the effect of general inlet geometry on inlet aerodynamic performance.

6.2 Determination of Inlet Performance

In a turbojet or ramjet flying at supersonic speed with a subsonic combustion system, final intake compression is usually accomplished by a normal shock. This characteristically causes subsonic flow and a significant reduction in total pressure. The resulting total pressure determines the static pressures in the combustion chamber and the nozzle. And these in turn govern the engine thrust. The total pressure loss (or recovery) is a useful measure of performance for an inlet whose task is to reduce the supersonic freestream Mach number to a subsonic value. The specification of such an inlet's performance, then, is adequately reflected in this single term called the η_{pt} efficiency (Ref. 6.3).

For a supersonic combustion engine inlet, total pressure recovery is measured after a final deceleration through an oblique shock which results in a supersonic (lower than freestream) Mach number at the combustor entry. The loss of total pressure, as a measure of inlet performance, is less significant. To define the performance of a scramjet inlet, therefore, requires the specification of an *efficiency* term, like total pressure recovery, as well as a *capability* term. The diffuser's capability expresses the amount of diffusion in terms of either contraction (area) ratio, A_1/A_3, compression (static pressure) ratio, p_3/p_1, or entry to exit Mach number. Measures of both capability and efficiency are required in order to define the pressures in the combustor and nozzle so as to obtain engine thrust. Or fundamentally, any two terms such as compression ratio and contraction ratio are sufficient to define the operating conditions, including any one of the efficiency measures, for an inlet operating at a given freestream Mach number if there is

no mass spillage and the flow is adiabatic.

6.2.1 Inlet Performance Measurement - Theoretical Considerations

For the inlet such as shown in Figure 6.1 we consider the quasi-one-dimensional flow between stations (1) and (3) at the entry and exit respectively. Flow behaviour in an inlet is governed by the equations of conservation of mass, momentum and energy and the equation of state of the gas. Furthermore, the change of properties from state (1) to (3) is influenced by the presence of mass flow (spillage), forces acting on the fluid between the two stations and heat transfer to the walls. The efficiency of the process can be evaluated (or specified) from a knowledge of the change of entropy between stations (1) and (3). Thus we are left with five equations in the nine unknowns p_3, ρ_3, T_3, V_3, s_3, A_3, m, f and Q. We can solve for any five of these provided the other four are measured or otherwise specified. A typical practical case is shown in Table 6.1 which lists the nine variables in question. A minimum of four variables have to be known either from measurements or the truth of obvious assumptions. In this case we show the exit pressure, p_3, the exit area, A_3, and the force of the inlet on the fluid to be measured.

We assume, also, that the inlet does not spill or acquire mass. In this case we can calculate the five remaining quantities by solving the following five equations:

$$\rho_1 V_1 A_1 + \dot{m} = \rho_3 V_3 A_3 \tag{6.1a}$$

$$p_1 A_1 - p_3 A_3 - f = \rho_1 V_1 A_1 (V_3 - V_1) \tag{6.1b}$$

$$h_1 + \frac{V_1^2}{2} + Q = h_3 + \frac{V_3^2}{2} \tag{6.1c}$$

$$P_3 = P_3(\rho_3, h_3) \tag{6.1d}$$

$$s_3 = s_3(P_3, h_3) \tag{6.1e}$$

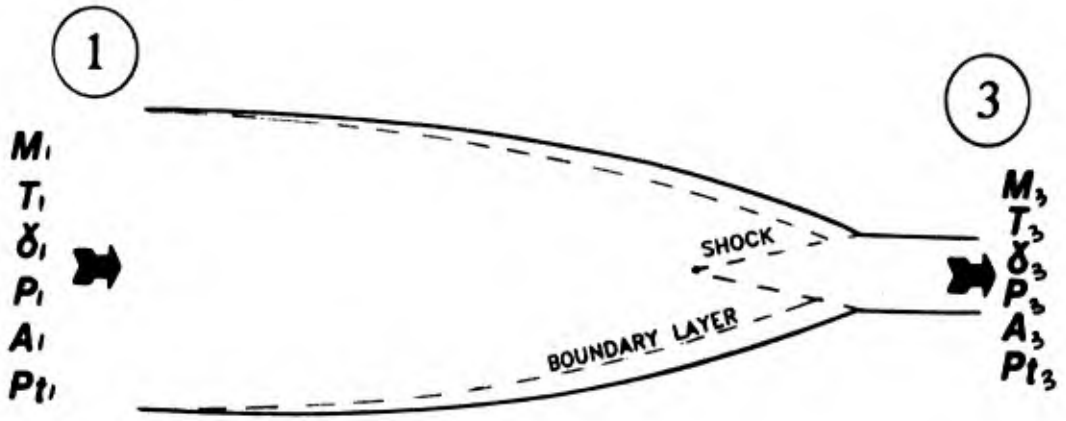

Figure 6.1 Hypersonic inlet flow parameters applied to performance assessment

Quantity	Symbol	Measure (min	Assume 4)	Calculate (max 5)
pressure	P_3	★		
density	ρ_3			★
enthalpy	h_3			★
velocity	V_3			★
entropy	s_3			★
flow area	A_3	★		
mass addition	$\dot{m}$		★(=0)	
force on flow	f	★		
heat addition	Q			★

Table 6.1 The nine principal flow parameters applied to hypersonic inlet performance assessment.

What we normally associate with efficiency is resident in the equations for entropy, $s_3 = s_3(p_3, T_3)$. For example if the inlet is isentropic then $s_3 = s_1$, and we end up with one less variable and one less equation. Or, if we can assume that the flow is adiabatic, Q=0, then we are relieved of having to measure the force exerted on the fluid by the inlet. There is no fundamental difference between the measured/assumed and the calculated variables and we can think of the experimental task being done when we have knowledge of any four of them. The data reduction task is then to solve for the other five. Which variables to measure and which to calculate depends on our ability to readily measure some quantities. For example, in the table shown, the pressure, p_3, can be readily measured; the area, A_3, is found from the physical dimensions of the model; the force, f, is equal and opposite to the force exerted by the fluid on the inlet and can be measured by a load cell; and flow spillage can be convincingly assumed to be zero on a given inlet. We are then in a position to calculate ρ_3, h_3, V_3, s_3 and Q. The above example has shown that from an experimental viewpoint it is convenient to think of pressure and area as the measured values of inlet performance along with a measured inlet drag, f, and mass spillage, m. Consequently we will display inlet performance parameters on graphs with the *contraction ratio* and the *compression ratio* as abscissa and ordinate respectively, keeping in mind that in the most general case a four dimensional plot is really required to represent the four "independent", or measured variables p_3, A_3, m and Q.

6.2.2 Inlet Efficiency and the Pressure-Area Diagram

The operation of an inlet at a given freestream Mach number may be characterized by a point on the graph of contraction ratio (or area ratio) versus compression ratio. These graphs will be called pressure-area, α,π, diagrams. It is desirable to attach a number to a particular inlet operating at some specified conditions represented by a point on this plot, such that when changes are made in the design or operating conditions of the inlet, and the number increases, then the performance of the engine to which the inlet is attached also increases. Total pressure recovery is one such "efficiency" term.

Total Pressure Recovery [η_{pt}]. For a calorically perfect gas, adiabatic flow and no spillage, area ratio can be stated in terms of the total and static pressure ratios:

$$\alpha = \frac{\pi\left(\frac{2}{(\gamma-1)}\tau\left\{\beta\left(\frac{\pi}{\eta_{pt}}\right)^{\frac{1-\gamma}{\gamma}}-1\right\}\right)}{M_1\left(\frac{\pi}{\eta_{pt}}\right)^{\frac{\gamma-1}{2\gamma}}} \tag{6.2}$$

where,

$$\beta = 1 + \frac{\gamma-1}{2}M_1^2 \tag{6.3}$$

The Mach number at the exit can then be found from:

$$M_3^2 = \frac{2}{\gamma-1}\left\{\beta\left(\frac{\eta_{pt}}{\pi}\right)^{\frac{\gamma-1}{\gamma}} - 1\right\} \tag{6.4}$$

Figure 6.2 shows curves of η_{pt} and M_2 in the α,π plane. Negative values of $\log(\alpha)$ represent a diverging duct and are of no interest to inlet designers. It is interesting to note that for every given efficiency, η_{pt}, there is a maximum value of $\log(A_1/A_3)$ and that the duct becomes choked at this condition. Using experimentally measured values of p_1 , p_3 , A_1 , and A_3 ,which define a unique inlet design point, one can use this plot to find the total pressure recovery provided the Mach number is 8.33, there is no flow spillage and the gas is calorically perfect with γ=1.4.

The line joining points having a pressure recovery of 1.0 is labelled the "ISENTROPE". This line represents the highest efficiency attainable. Real inlets, such as those to be discussed in this study, have inviscid design parameters (i.e. isentropic compression, and uniform parallel exit flow) which restrict their

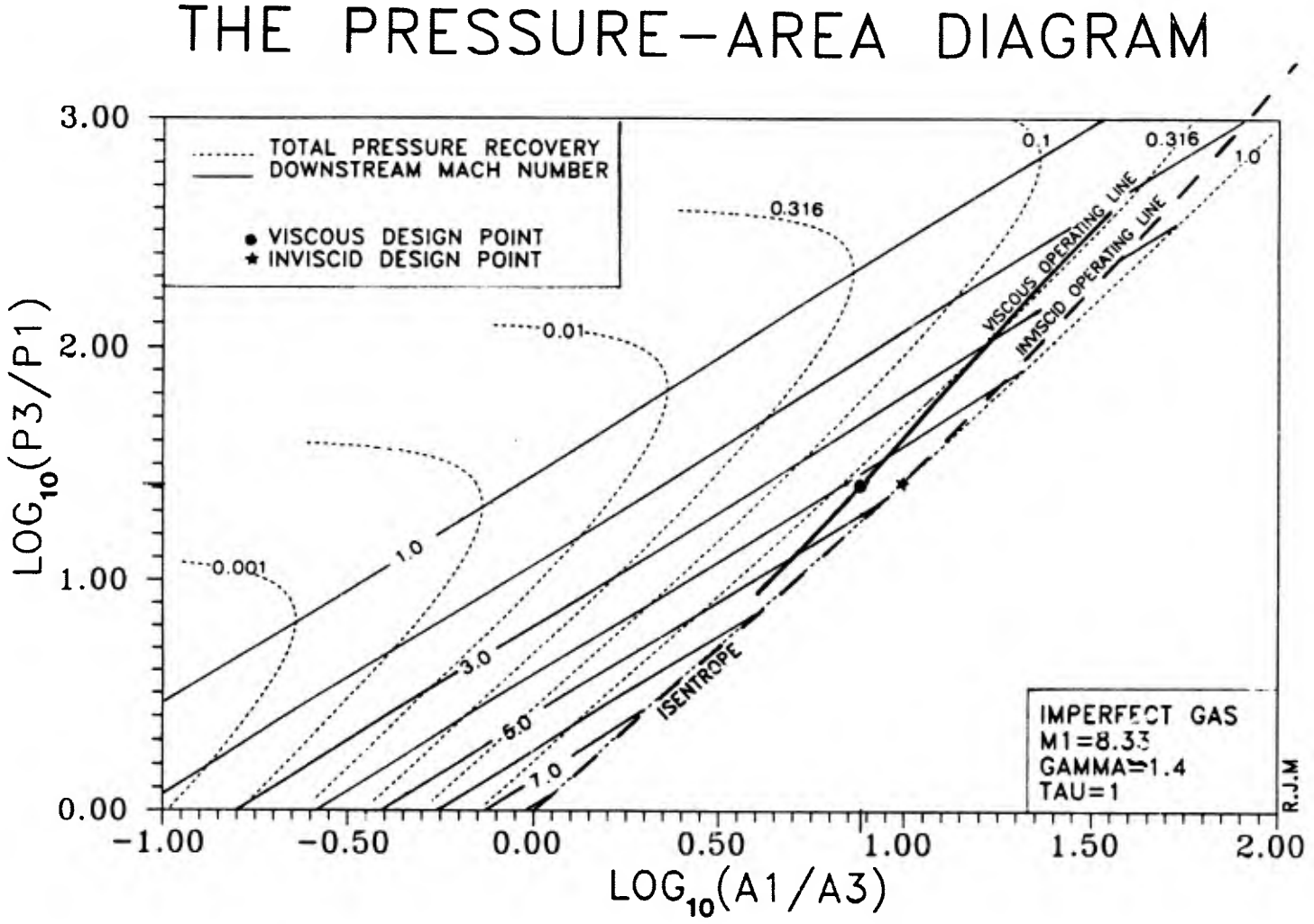

Figure 6.2 Plot of inlet compression vs. contraction ratio with total pressure recovery efficiency as a parameter. This is a convenient and meaningful depiction of inlet design possibilities and performance specifications.

range of design possibilities to an *operating* line shown also in this figure. Each design possibility comprising this line has a unique value of η_{pi} efficiency. These real inlets, because of shock and boundary layer losses, always operate somewhere to the left of the isentrope. The position of a particular intake category operating line will be dependent on its unique shock and compression structure. When losses due to boundary layer are taken into account, a given inlet operating line will be found to the left and above the inviscid representation. The exact location will, in the following sections, be estimated computationally using the Stan6 boundary layer code (Ref. 6.7), and determined experimentally in the gun tunnel.

The usefulness to the designer of plotting efficiency in terms of compression and contraction ratio is apparent when we consider these operating lines. The range of inlet capability is visible at a glance and the efficiency of inlets are readily determined and compared.

6.2.3 Inlet Efficiency From Aerodynamic Drag

Experimental assessment of hypersonic and high compression inlets has posed severe problems in the survey of exit flow profiles. High contraction means small exit areas, this, in turn, requires small pitot probes, which leads to long lag times and consequent incompatibility with the short running times of many facilities. In addition, Mach number gradients may require the measurement of static pressure across the exit flow and high surface heat transfer may require the detailed determination of total temperature profiles.

One is therefore led to ask if there is a method of circumventing the measures of the details of the flow in favour of the measure of some gross or average property which then could be used directly in the calculation of one-dimensional performance parameters.

Using a measurement of inlet internal drag, the one-dimensional inlet efficiency can be determined analytically in a way that is consistent with mass, momentum, and energy considerations. Combined shock wave and boundary layer losses are in this way incorporated. Of the various experimental approaches to efficiency measurement, such as those involving static pressure measurement, pitot pressure measurement, and plenum filling measurement, the forebody force technique results in the least error for

an equal accuracy of facility measurements for each approach (Refs. 6.5, 6.6).

6.3 Task Definition

It is the purpose of the present study to investigate the performance of three hypersonic air inlets both theoretically and experimentally at Mach 8.33 so as to assess their relative merits as manifested in inviscid versus viscous losses, and influenced by external versus internal flow and axisymmetric versus two-dimensional flow. The three types of inlets selected for study are;

a) the Busemann inlet,

b) the Prandtl-Meyer inlet,

c) the Oswatitsch inlet.

Schematics of these inlets are shown in Figure 6.3. Their underlying theory, design and experimental results are described in Sections 6.6, 6.7, and 6.8.

6.4 Rationale For Inlet Selection

In attempting to compare the usefulness of different types of air intakes one is immediately confronted by three questions:

a) What attributes are changed from one inlet to the next; what is really under comparison?

b) More importantly, what attributes should be kept the same;i.e. what is the basis for comparison; how is an "apples to apples" comparison maintained?

c) And finally, by what criteria are the measured differences assessed?

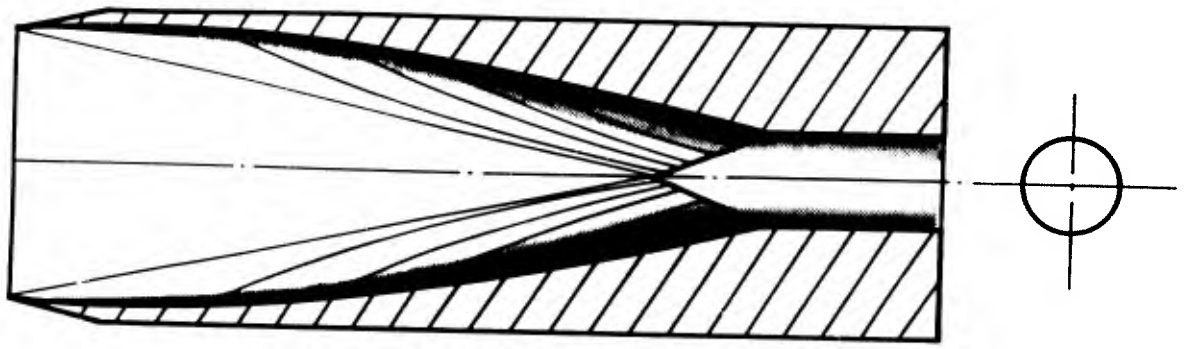

a. BUSEMANN INLET

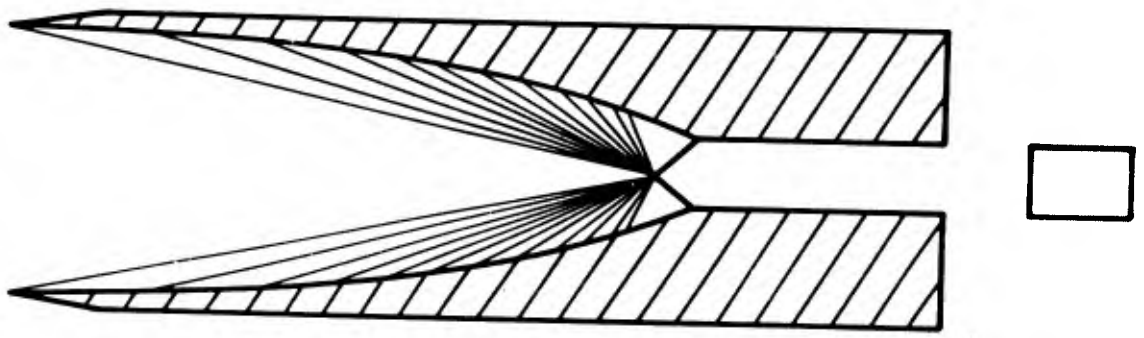

b. PRANDTL–MEYER INLET

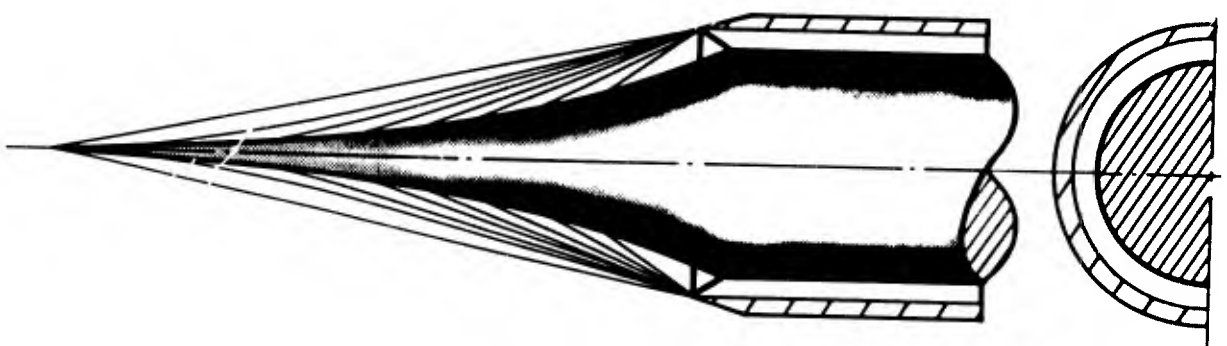

c. OSWATITSCH INLET

Figure 6.3 Schematic representation of three hypersonic air inlet categories.

Careful consideration based on the above questions was given to the technical justifications of several experimental approaches to the comparison.

In order to compare the usefulness of different types of air inlets as influenced by geometry, one must isolate the effects of geometry as they influence the viscous and inviscid losses. Another way of saying the same is to keep other factors constant so that a difference in performance is due to geometric variations alone. Consideration of several experimental approaches were based on the following criteria and arguments.

a) The area ratio will be different from one inlet to the other. This will permit the ready application of a boundary layer correction (using Stan6 described in Ref. 6.7) to the inviscid contour without causing flow spillage (particularly for the Oswatitsch inlet).

b) The compression will be kept constant. This will make it easier to apply boundary layer corrections because the correction would not cause a change in the compression ratio, whereas the contraction ratio would change. Also, since compression ratio is established by the inviscid flow, then it stands to reason that the inviscid flow geometry and properties remains unchanged if a boundary layer correction is applied so as to retain the original compression ratio.

c) In an attempt to answer the question of how inlet efficiency is to be assessed, consider again the pressure-area diagram in Figure 6.2. As stated, every point on this polar has a unique (one-dimensional) value of inlet efficiency. Not only hat, but every point represents a one-dimensional inlet which, when coupled to an engine, produces a calculable value of thrust or specific impulse (s). Thus, every point on a pressure-area diagram has a unique value of engine specific impulse. One of the authors (RJM) has performed extensive scramjet engine cycle analysis to assess engine specific impulse as a function of inlet variation throughout the range of design possibilities on the pressure-

area diagram (Ref. 6.8). Some of the results of this study are reproduced here in Figure 6.4. Two principal conclusions have been drawn and applied to this study. Firstly, from Figures 6.4c and 6.4d one observes an optimum specific impulse region on both the p-a diagram isentrope and the operating line of a real inlet. Throughout a range of freestream Mach numbers, this optimum is consistently found in the region of inlet area ratio 10 and pressure ratio 30. Thus, the inlets have been designed with these findings in mind. Secondly, although η_{pt} and a host of other efficiency terms, η_{ke}, η_{ei}, η_{KE}, η_{th}, and η_x, bore little or no resemblance to the pattern of distribution of engine specific impulse, η_{pp} and η_x, both in pattern and magnitude were found to be reasonable indicators of performance improvement between certain ranges of inlet compression and contraction. Figures 6.4a and 6.4b demonstrate this reasonable correspondence of η_{pt} and η_x with specific impulse between inlet pressure ratios of 10 and 50. On this basis the η_{pt} term has been chosen as the efficiency term and comparison arbiter for this study.

In addition to the compression ratio, a number of other parameters will remain constant for all three intakes.

1) All three inlets will be tested at the same freestream conditions at Mach 8.33 and Reynolds numbers of $44*10^6$/m and $23*10^6$/m.

2) All will capture the same mass flow (same A_1). Spillage will not be allowed.

3) For each inlet, the initial flow turning is isentropic and subsequent turning through the shock re-directs the flow back to the freestream direction. The amount of intermediate

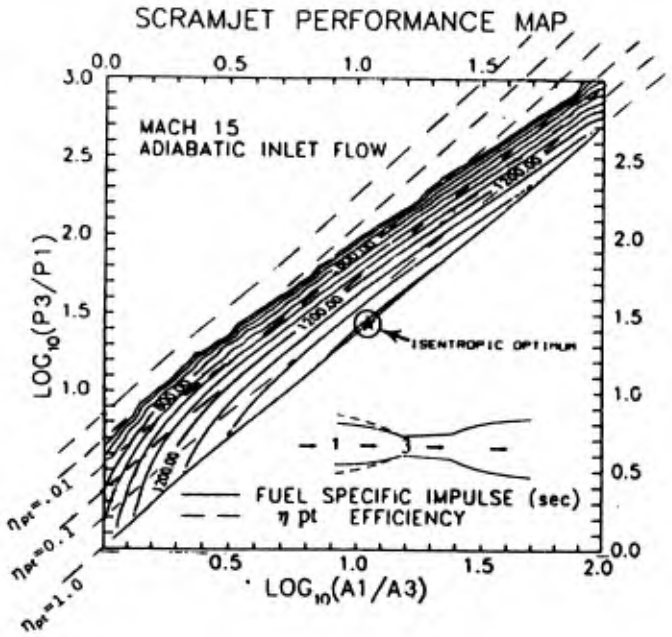

FIG. a)

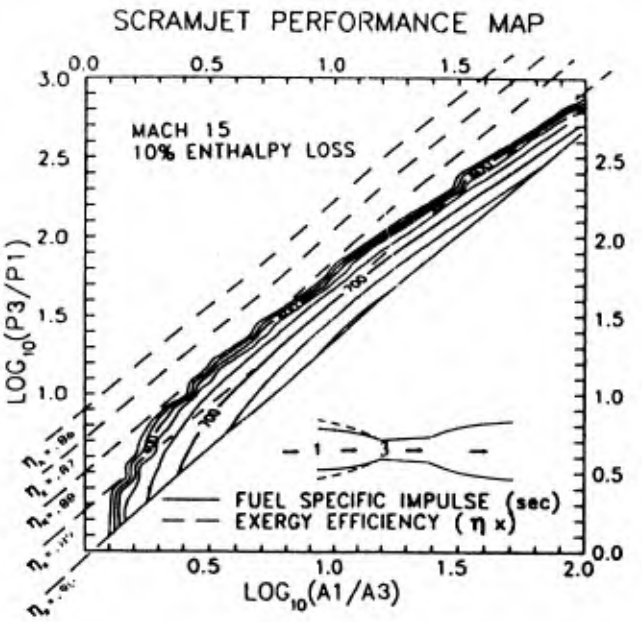

FIG. b)

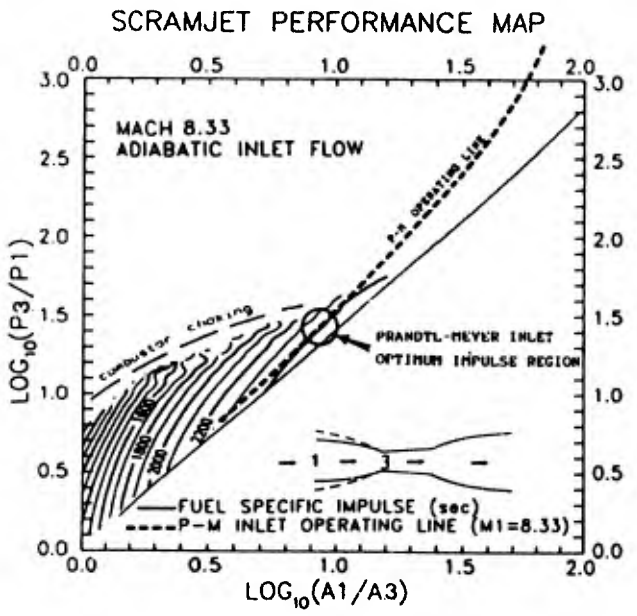

FIG. c)

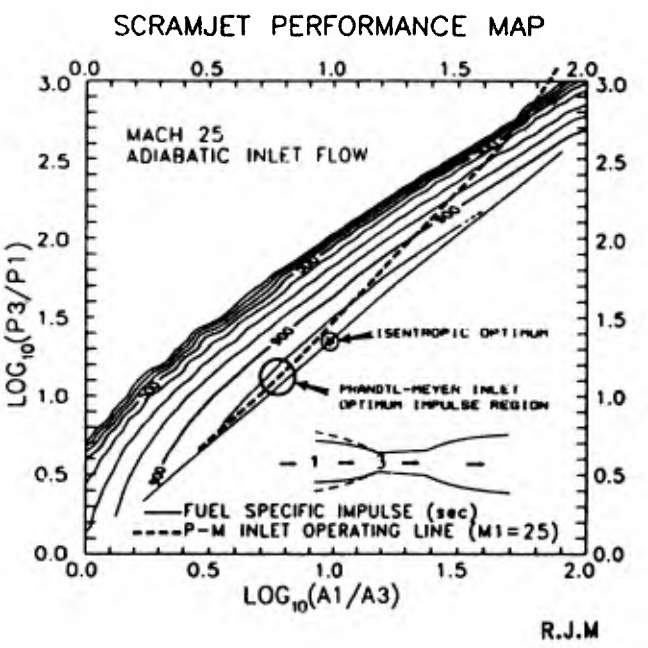

FIG. d)

Figure 6.4 Engine cycle calculations have been performed for a fixed engine design with inlets represented by the complete range of design possibilities on the pressure-area diagram. Regions of optimized inlet design are identified.

turning for each inlet is different.*

4) The length of a high-efficiency inlet is dictated primarily by the flight Mach number; more precisely by the Mach angle, since the leading edge wave in an isentropic compression is inclined at the Mach angle. Since all three inlets start compressing the flow isentropically their lengths are more-or-less the same. A small difference is introduced by the differing lengths of the trailing edge shocks for each inlet. Thus, the three inlets are not only topologically similar from the viewpoint of shock structure but they are also almost geometrically similar in terms of length-to-height proportions. And as a consequence of having the same flow capture area, the three inlets have nearly the same lengths. This is required to enable meaningful comparisons to be made of boundary layer losses as the running lengths of the boundary layers would be nearly the same for the three cases and any differences in boundary layer losses would then be due to the action of the wall and the inviscid flow on the boundary layer.

5) Separated flow regions are generally undesirable because they cause flow unsteadiness and unpredictability. Thus it becomes important to design all models in such a way that boundary layers remain attached. This is particularly important at the point where the shock-wave hits the wall. Thus a common feature of all models is that they all have attached flows everywhere.

---

* In this connection, it is worth while to note that flow turning has been previously used as a measure of compression since it can be uniquely related to pressure ratio for both Prandtl-Meyer and oblique shock flow: however, for more general flows, and in particular for internal flows, where the compression ratio is more closely related to area ratio, the amount of flow turning loses its effectiveness as a measure of inlet performance.

These considerations led to the selection of three geometrically different inlets for study:

1) The Prandtl-Meyer inlet, being two-dimensional, with internal isentropic compression, produces two opposing Prandtl-Meyer compression surfaces followed by plane shocks and uniform exit flow.

2) The Busemann inlet, being axisymmetric, with internal isentropic compression followed by a conical shock and uniform exit flow.

3) The Oswatitsch inlet, being axisymmetric, with external isentropic compression followed by a conical shock and uniform exit flow.

All three inlets are designed for the same freestream Mach number of 8.33. All capture the same mass flow. All inlets have the same compression ratio. All produce an exit flow which is parallel to the flow at the entry and the inviscid portion of which is uniform and irrotational.

In the selection of these models, it is recognized that the Busemann inlet and the Oswatitsch inlet have the "cleanest" boundary conditions. Their axial symmetry introduces no corner or end effects and as a consequence we expect good agreement between experiment and theory. The Prandtl-Meyer inlet, however, cannot be made wide enough to eliminate end effects and end walls will have to be attached, which will introduce sidewall and corner flow boundary layers and their attendant displacements of the internal flow. Despite this, the Prandtl-Meyer inlet will be tested too because;

1) it is an intermediate geometry between the external Oswatitsch inlet and the completely internal flow Busemann inlet,

2) it can be regarded as a more practical inlet because it has a better potential for variable geometry,

3) schlieren visualization is possible with the Prandtl-Meyer inlet,

4) its inviscid aerodynamic performance is identical to the Oswatitsch inlet.

6.5 Experimental Approach

6.5.1 Test Plan

Using the three inviscid compression theories described in Sections 6.6, 6.7, and 6.8, in conjunction with the Stan6 boundary layer code, viscous performance calculations were performed to derive a theoretical viscous operating line for each inlet category. A correction for boundary layer displacement thickness was applied to the design geometries of the three test diffusers.

Experimental measurements were made for each inlet at Mach 8.33 and the results were compared against the calculations. In addition, the following experimental subtasks were identified for each inlet:

1) Confirm flow starting for each inlet. This was done by a combination of schlieren photography and surface static pressure measurements.

2) Confirm other gross features of postulated flows - axial or planar symmetry, shock location and strengths and lack of separation. This was done by schlieren, surface pressures and surface flow visualization.

3) Measure inlet performance by:

a) Determination of contraction and compression ratios.

b) Determination of contraction and total internal drag.

6.5.2 Instrumentation

The instrumentation applied to the test series are briefly detailed here with some discussion of precision specifications. Complete details of these instruments can be found in References 6.9 - 6.11. A thorough discussion of measurement error analysis has been documented in Appendix (A).

6.5.2.1 Pressure

The model surface static pressures were measured with miniature piezoresistive Kulite and Endevco transducers. Transducers rated for pressures of 5, 15, and 50 psi were installed according to the predicted pressures along the surface. After failures of some of the 15 psi Endevco transducers during inlet unstarts, the 50 psi Kulites were used exclusively in the high pressure regions of the model. The Kulites were equipped with RPV thermal shielding. All of these instruments have exceptionally low acceleration and thermal sensitivity and have rated independent linearity of 0.25% of their specified full scale output. These instruments use near flush diaphragms thus eliminating gauge volume pneumatic lag effects on the response. Digital filtering of the signal at 5 kHz proved adequate to remove most noise.

6.5.2.2 Force

The PCB series 208 dynamic force transducers were applied to the measurement of aerodynamic drag. Designed to be mounted in intimate contact with the compressing structures, the cell measures loads of up to +500 lbs with a resolution of .02 lbs. Calibrated linearity is 1% of the full scale reading. This exceptional linearity permits them to be used at smaller incremental ranges within the maximum range.

6.5.2.3 Acceleration

The miniature 2 gram quartz accelerometer (PCB series 303a) was used in conjunction with the PCB force transducers in order to compensate for inertial loads imbedded in the aerodynamic drag measurements. The instrument exhibits high sensitivity (10mV/g), low impedance (100 ohm), and high frequency response with an amplitude linearity of 1% full scale. The range is 500 g's with a resolution of .01g.

6.5.2.4 Flow Visualization

Schlieren photographs were taken for all models using a single pass parallel light system and horizontal knife edge in conjunction with a Pulse Photonics 4 spark argon flash unit and delay generator.

6.5.3 Gun Tunnel Conditions

The pre-fire gun tunnel driver and driven tubes were filled with room-temperature air to 20.80±.15 MPa and 800 kPa respectively. Rupture of the double diaphragms and compression of the driven tube air resulted in a total pressure of 25.5±.1 MPa (measured) and a total temperature of about 800 K. Expansion to Mach 8.33 in the test section produced a static pressure of 2.067 KPa. This gives a flow velocity of 1245 m/s and a Reynolds number of $44*10^6$/m. Tests performed with an initial driven tube pressure of 200 kPa resulted in the same total pressure with stagnation enthalpy of approximately 1.104 MJ/kg and a test section Reynolds number of $23*10^6$/m. Further details on the operation of the gun tunnel are presented in Section 2 and Reference 6.12.

6.5.4 Test Procedure

6.5.4.1 Confirmation of Inlet Starting and Compression Structure

The initial test of each inlet was performed without instrumentation so as to first safely verify starting using the schlieren. The initial run with the Oswatitsch inlet was performed with the cowl removed in order to assess the accuracy of the predicted compression characteristics. Subsequent runs verified starting

with the cowl in place.

The Prandtl-Meyer inlet also started successfully. During the third run of this inlet, one side wall window ruptured requiring a redesign of the glass support structure. Until this modification was completed, starting was confirmed and static pressure profiles were measured using aluminum plates in the existing window frame.

The Busemann inlet model is housed in a large cylindrical enclosure which produces a strong external shock and considerable tunnel blockage. As a consequence, at first testing, neither the tunnel nor the inlet started. The assembly was then moved downstream in the test section so that the external shockwave impinged downstream of the tunnel diffuser entry. This resulted in started flow in both the tunnel and the Busemann Inlet. Thus all three inlets were confirmed to start.

6.5.4.2 Static Pressure Measurement

For the Prandtl-Meyer and Oswatitsch inlets, several runs were performed to determine the maximum transducer pressure lead length which gave adequate pneumatic response in our short run times. Experimentation was then undertaken on the influence of model alignment on flow symmetry which could be readily determined by comparison of pressure measurements from opposing pressure taps. Using the Oswatitsch inlet, it was found that excellent flow symmetry was obtained when the model was inclined at +0.25 degrees from the horizontal. The Prandtl-Meyer inlet and Busemann inlet were less sensitive to the apparent flow inclination in the test section. The annulus pressures in the Oswatitsch inlet were found to be extremely sensitive to the geometric positioning of the cowl. Very accurate assembly was necessary.

Full static pressure surveys were performed on each inlet for 800 kPa barrel (Re= $44*10^6$/m) followed by a repeat series at 200 kPa (Re= $23*10^6$/m).

6.5.4.3 Aerodynamic Drag Measurement

Measurements of compression surface aerodynamic drag were made on the Busemann and Oswatitsch inlets. A PCB load cell was used to measure all force applied to the metric during the run. A simultaneous metric acceleration measurement was recorded by PCB accelerometer to compensate the

force reading for non-aerodynamic loading caused by tunnel vibration.

Spectral analysis of the data signals and experimentation resulted in successful signal filtration at 5 kHz. Several repeated runs were performed so that an average result could be calculated. All drag runs were conducted at a freestream Reynolds number of 23 * 10^6/m.

6.6 The Busemann Inlet

6.6.1 Busemann Inlet - Basic Flow

We postulate the existence of an axially symmetric flow which is compressive in the downstream direction and which is such that all flow properties, on rays drawn from a given origin, are constant. Such flows are called "conical" and a more familiar occurrence of this type of flow is found about a circular cone in a supersonic freestream. It can be shown that the flow, in becoming parallel to the freestream direction at the exit of the inlet, must pass through a conical shock wave. Apart from boundary layer type of viscous losses, this conical shock is the only entropy producing mechanism in the inlet flow. In the isentropic region upstream of the shock, the compression is initiated at the freestream Mach wave. Compressive Mach waves are centered at the origin, as with Prandtl-Meyer flow (see Fig. 6.5).

In the angular region

$$\mu_1 \leq \theta \leq \theta_l \tag{6.5}$$

where,

$$\theta_l = \pi - \delta_2 - \mu_2 \ , \tag{6.6}$$

the δ_2 is the flow deflection through the conical shock and μ_2 is the Mach angle in front of the conical shock. In the angular region $\theta_1 \leq \theta \leq \theta_s$, and the Mach waves from the surface terminate on the front surface of the conical shock. The shock wave, meeting the wall, is cancelled there by the expansive corner, so that the flow downstream of the shock is uniform and parallel to the freestream. This flow may

THE BUSEMANN INLET

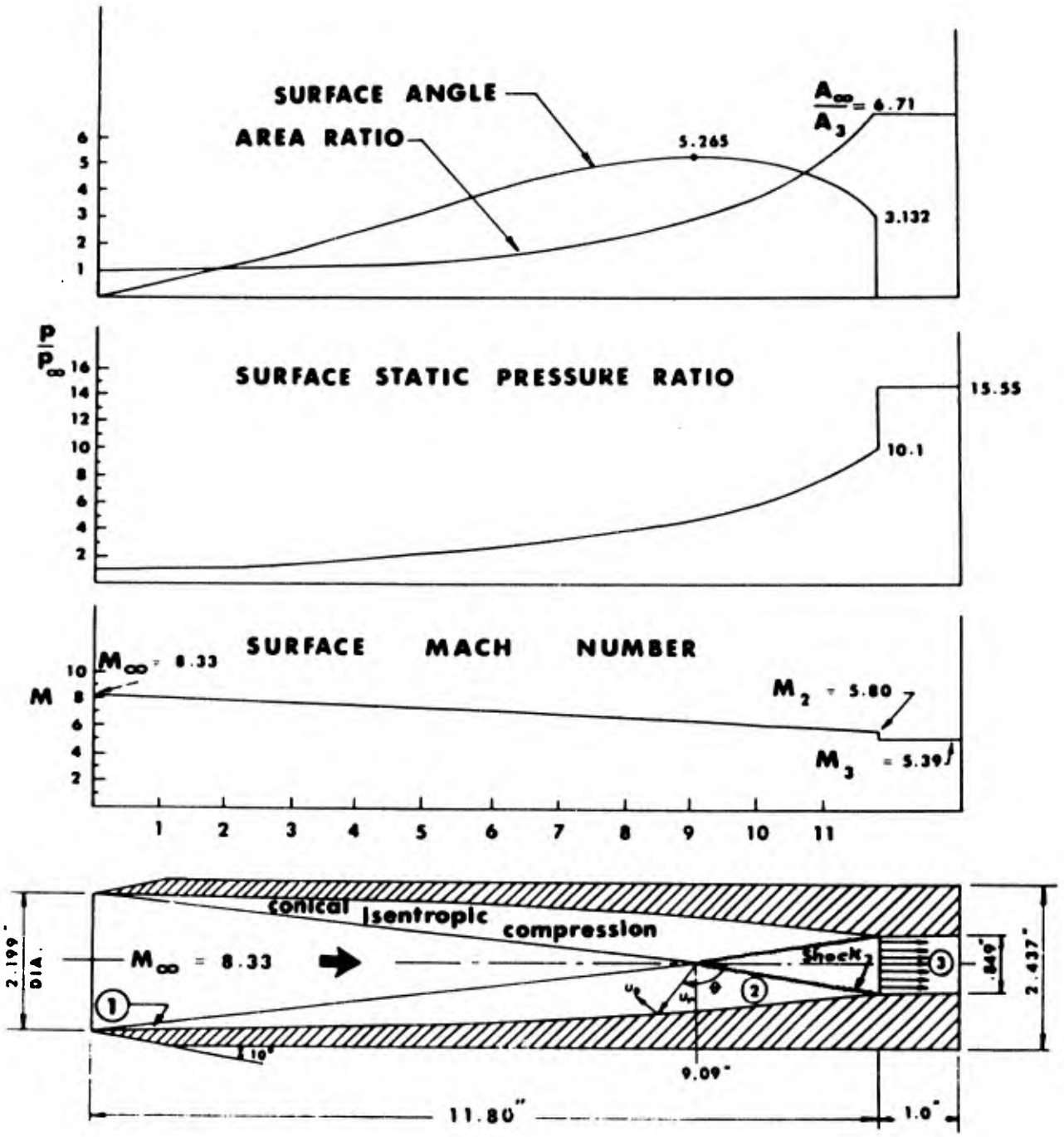

Figure 6.5 Solution of the Taylor-Maccoll equation for inlet entry Mach number of 8.33 and exit Mach number of 5.39.

be subsonic or supersonic depending on the strength of the conical shock.

Flow of this general type obeys the Taylor-Maccoll equation (Ref. 6.13) for axisymmetric conical flow,

$$u'_r{}^2(u_r - u''_r) = (1 - u_r{}^2 - u'_r{}^2)(u''_r + u'_r\cot\theta + 2u_r) \tag{6.7}$$

where u_r represents the velocity component in the radial direction; and u_θ, the velocity in the θ- direction, is given by

$$u_\theta = \frac{du_r}{d\theta} = u'_r \tag{6.8}$$

The Taylor-Maccoll equation is a second order nonlinear equation for u_r in terms of θ and as such requires two boundary conditions. Because of a singularity at the upstream Mach wave (Stn. (1)), the solution is best started at the downstream shock. At this point, the boundary conditions are specified by:

(1) the aerodynamic shock angle, θ_s, and the Mach number upstream of the shock M_2

(2) The condition that the flow downstream of the shock is parallel to the freestream flow:

$$(u_r)_2 = V_2\cos\theta_s \tag{6.9}$$

$$(u_\theta)_2 = (u'_r)_2 = -V\sin\theta_s \tag{6.10}$$

where,

$$V_2 = \sqrt{\frac{(\gamma-1)M_2^2}{2+(\gamma-1)M_2^2}} \tag{6.11}$$

The flow deflection angle through the shock is then δ where

$$\tan\delta_2 = \frac{2\cot\theta_2(M_2^2\sin^2\theta_2 - 1)}{2+M_2^2(\gamma+1-2\sin^2\theta_2)} \tag{6.12}$$

From this and the given θ_s we can then find the physical shock angle, θ, from which to begin the integration

$$\theta = \theta_s - \delta_2 \tag{6.13}$$

Before beginning the integration it is worthwhile to note that :

a) the selection of M_2 is somewhat arbitrary. It should be a value which lies between the desired freestream and exit Mach numbers. Similarly, we are free to select θ_s as long as it lies between μ_2 and $\pi/2$.

b) Having selected M_2 and θ_s we can calculate the normal component of Mach number in front of the shock

$$M_{2N} = M_2\sin\theta_s \tag{6.14}$$

c) Knowing M_{2N} allows the determination of the total pressure ratio across the shock

$$\frac{Pt_3}{Pt_2} = \left[\frac{(\gamma+1)M_{2N}^2}{(\gamma-1)M_{2N}^2+2}\right]^{\frac{\gamma}{\gamma-1}} \left[\frac{\gamma+1}{2\gamma M_{2N}^2-(\gamma-1)}\right]^{\frac{1}{\gamma-1}} \tag{6.15}$$

so that at this early stage of inlet design definition, we already have a figure for the efficiency of this inlet.

d) Also from M_{2N} we can calculate the static pressure ratio across the shock

$$\frac{p_3}{p_2} = \frac{2\gamma M_{2N}^2-(\gamma-1)}{\gamma+1} \tag{6.16}$$

e) The Mach number at the exit is found from

$$M_3^2 = \frac{(\gamma+1)M_2^2M_{2N}^2 - 4(M_{2N}^2-1)(\gamma M_{2N}^2+1)}{\left[2\gamma M_{2N}^2-(\gamma-1)\right]\left[(\gamma-1)M_{2N}^2+2\right]} \tag{6.17}$$

If at this stage of inlet selection, any one of Pt_3/Pt_2, p_3/p_2 or M_3 are unsuitable then we must select new values of M_2 and θ_s before proceeding with the numerical integration. It has been found that selecting a value of θ_s close to μ_2 produces a high efficiency inlet with a weak shock such that M_1, M_2 and M_3 lie close to one another; on the other hand, a value of θ_s close to $\pi/2$ produces a lower efficiency inlet with a stronger shock, a high area ratio, and large differences between M_1, M_2, and M_3.

A numerical solution of the Taylor-Maccoll equation is now performed starting from $\theta = \theta_s - \delta_2$, with θ increasing by some value of $\Delta\theta$ until the freestream is reached as determined by $u_r=0$ or $\delta=0$.

Once the solution has been executed and u_r and u_θ are found in terms of θ, the following additional quantities can be readily determined :

(a) the flow speed

$$V = (u_r^2 + u_\theta^2)^{1/2} \tag{6.18}$$

(b) the speed of sound

$$a = \left[\frac{(\gamma - 1)(1 - u_r^2 - u_\theta^2)}{2}\right]^{1/2} \tag{6.19}$$

(c) the local Mach number

$$M = \frac{V}{a} \tag{6.20}$$

(d) the Cartesian components of velocity

$$u_x = u_r\cos\theta - u_\theta\sin\theta \tag{6.21a}$$

$$u_y = u_r\sin\theta + u_\theta\cos\theta \tag{6.21b}$$

(e) the flow inclination

$$\delta = \tan^{-1}\left(\frac{u_y}{u_x}\right) \tag{6.22}$$

(f) the streamline shape

$$r = \int_{\theta_s}^{\theta} \left(\frac{u_\theta}{u_r}\right)^{-1} d\theta \tag{6.23}$$

where we have set

$$r = r_o = 1 \qquad at \quad \theta = \theta_s - \delta_2 \tag{6.24}$$

(g) the Cartesian coordinates of the $r_o = 1$ streamline

$$x = r\cos\theta \qquad y = r\sin\theta \tag{6.25}$$

Since the calculation begins at the downstream shock and we do not, at the beginning, have any knowledge of the freestream flow, all quantities are left non-dimensionalized with respect to conditions at state (2). Only at the end of the integration, where the freestream is "discovered" by the condition $\delta = 0$ are we able to convert to conditions non-dimensionalized in terms of the freestream quantities.

6.6.1.1 Description of Numerical Integration Technique

For the numerical solution of Equation 6.4 we first write it as two first order simultaneous equations:

$$\frac{du_\theta}{d\theta} = \frac{\dfrac{(\gamma-1)(2u_r + u_\theta\cot\theta)(1-u_r^2-u_\theta^2)}{2} - u_\theta^2 u_r}{u_\theta^2 - \dfrac{(\gamma-1)(1-u_r^2-u_\theta^2)}{2}} \tag{6.26}$$

$$\frac{du_\theta}{d\theta} = u_\theta \tag{6.27}$$

In most cases, we wish to obtain also the streamline shape and it is found convenient to integrate simultaneously for r

$$\frac{d(\log r)}{d\theta} = u_r/u_\theta \tag{6.28}$$

These three equations were solved by a fourth-order Runge-Kutta numerical integration method described in Ref. 6.13. The computer program was verified by comparing results against a) the numerical solutions for a cone presented in Ref. 6.13, b) results previously calculated.

Figure 6.5 shows the results of the solution of the Taylor-Maccoll equation for an inlet entry Mach number of 8.33 and an exit Mach number of 5.39. The Mach number before the conical shock is M_2 = 5.80. The compression ratio is 15.55 and the contraction is 6.71. The pressure ratio across the shock is p_3/p_2 = 15.55/10.1 = 1.54. This pressure ratio is too small to cause separation of either the turbulent or laminar boundary layer at the corner where the shock impinges on the surface.

6.6.2 The Busemann Inlet - Inviscid Design

Solutions of the Taylor-Maccoll flow, described in the previous section, were used to generate a performance map for a wide range of Busemann Inlets (Figure. 6.6). The particular inlet described in the previous section is shown on this map by the symbol X. Work on the Busemann inlet described above was not part of this contract but it is described here because data from this work was used to design the present Busemann inlet. A plot of Busemann inlet performance for a freestream Mach number of 8.33 is shown in Figure 6.7. This plot is based on inviscid flow of calorically imperfect air ($\gamma = \gamma(T)$) and a total temperature of 1845 K. It shows the total pressure recovery, Pt_3/Pt_1, the temperature after diffusion, T_3, the contraction ratio, A_1/A_3, and the compression ratio, p_3/p_1, plotted against the exit Mach number, M_3. From this graph we see that the Busemann inlet described in the previous section, diffusing to M_3 = 5.39 has a total pressure recovery of Pt_3/Pt_1 = .993. For a design which diffuses to M_3 = 2.50 we obtain a compression ratio, p_3/p_1 = 765, a contraction ratio, A_1/A_3 = 92, a static temperature, T_3 = 917 K, and a total pressure recovery of Pt_3/Pt_1 = .867. The comparatively high efficiency figures of the

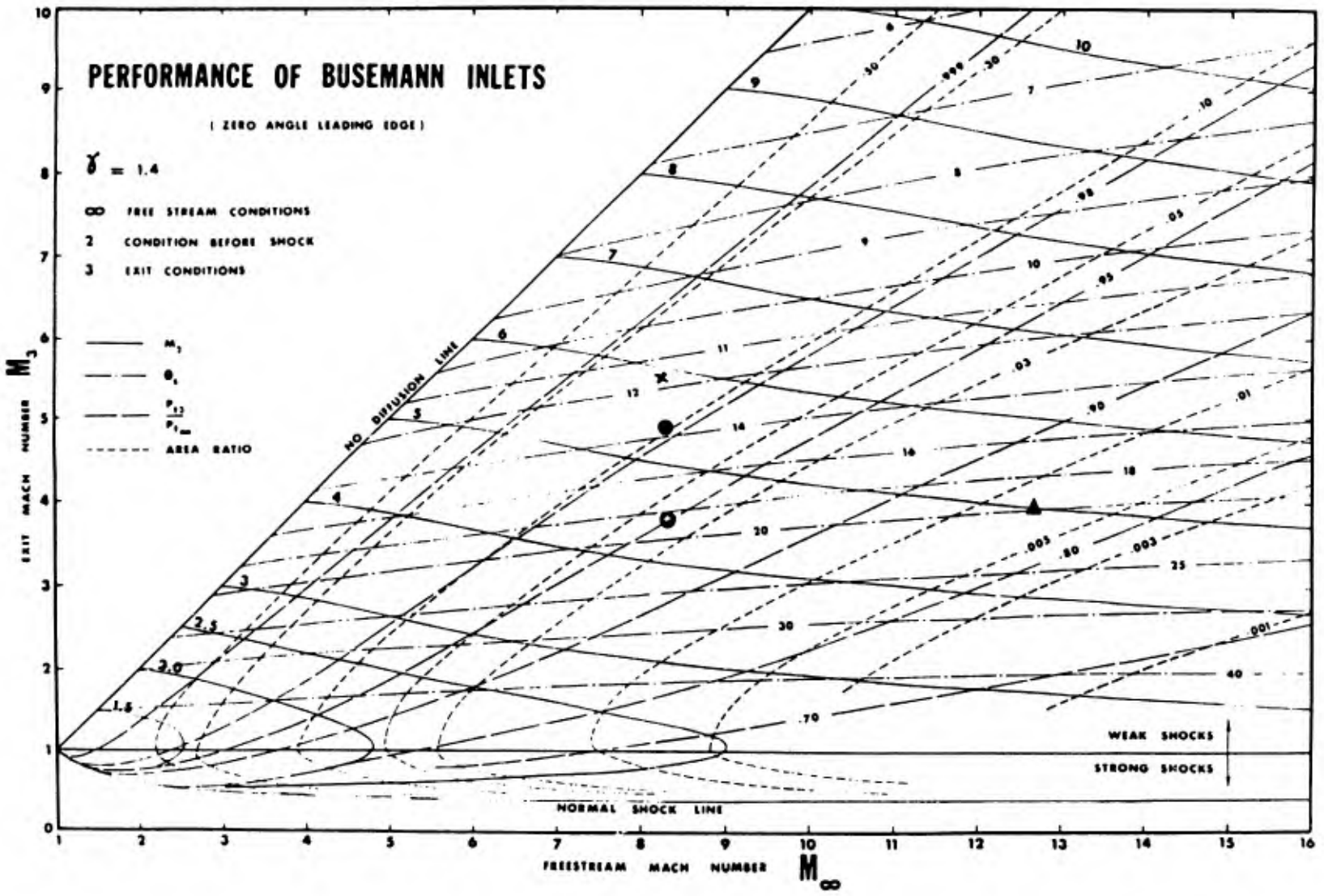

Figure 6.6 Performance diagram for Busemann type hypersonic air inlets.

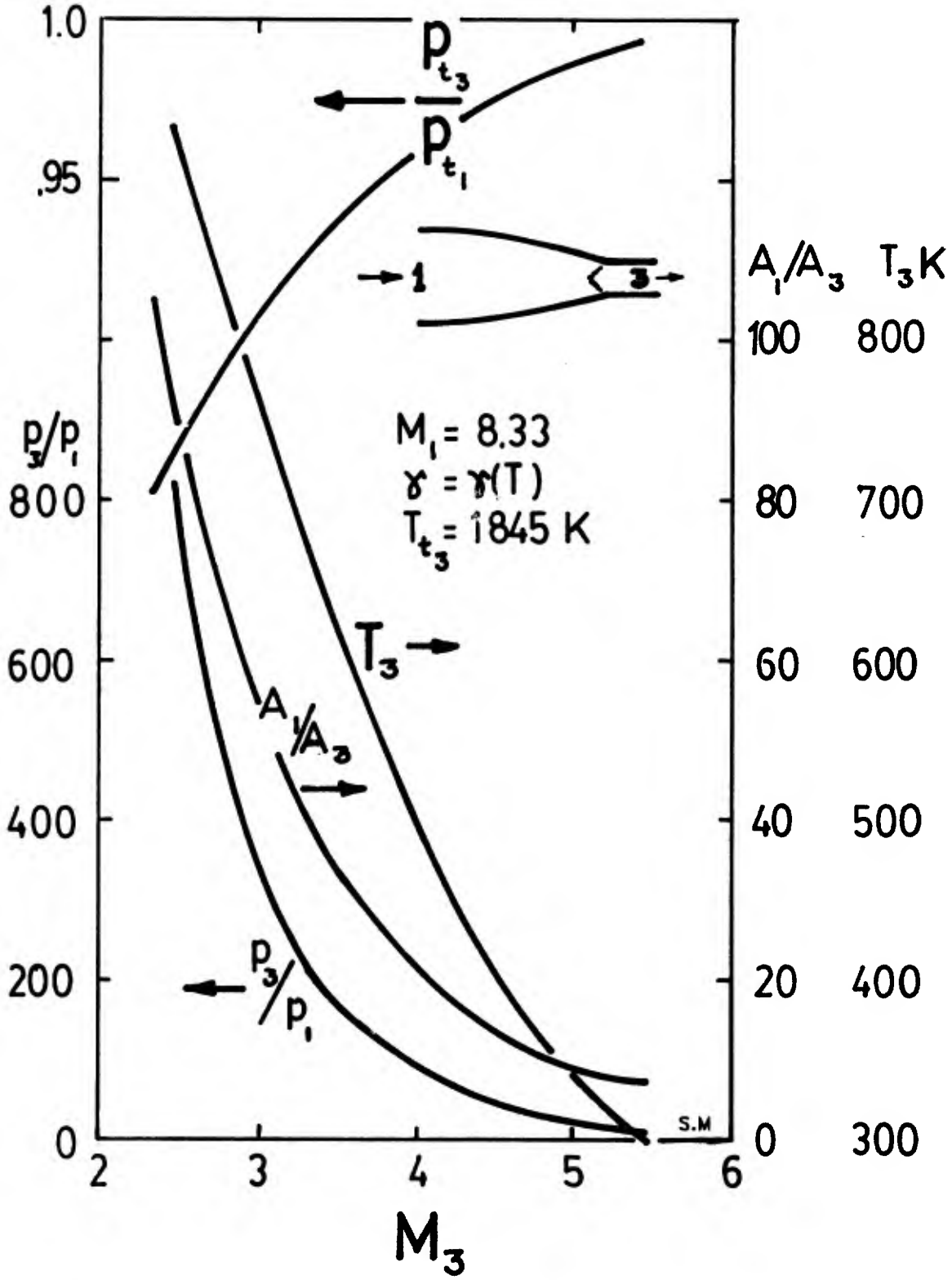

Figure 6.7 Performance range of Busemann inlets with entry Mach numbers of 8.33

Busemann type inlet are due to the fact that most of the required pressure increase and area decrease are brought about isentropically so that very little further compression takes place through the terminal shock and the shock occurs at the very lowest possible Mach number. Another advantage of the weak terminal shock is that it is not so likely to cause separation of the boundary layer.

The Busemann inlet design selected for the present tests is also for a freestream Mach number of 8.33. Its characteristics are listed in Table 6.2. This inlet design was selected so that a) it would start impulsively, b) the trailing shock would not cause boundary layer separation, and c) it would have the same compression ratio as the other two inlets. The Taylor-Maccoll solution for the inviscid surface coordinates was verified by a Parch/Euler simulation which started with the inviscid coordinates as input and calculated the flow in the inlet (Ref. 6.14). The isobars calculated by Parch/Euler are shown in Figure 6.8. It is seen that these are straight and confocal and that there is a crowding of isobars between the focus and the corner, indicating the presence of a shock wave and that this shock is cancelled at the corner, all as predicted by the Taylor-Maccoll solution. Figure 6.9 shows the comparison of pressure distributions between the Parch/Euler simulation and the Taylor-Maccoll solution. Again the overall comparison is very [illegible] especially since the pressure is a very sensitive parameter when used as a basis for comparison.

6.6.3 Busemann Inlet - Viscous Design

The first Busemann inlet described in this section was tested in the NRC Gun Tunnel at Mach 8.33. Initial tests were conducted on the uncorrected (inviscid) contour. Pressure measurements on this contour are shown as the open circles in Figure 6.10. A laminar boundary layer displacement thickness was then calculated and machined out of the inviscid surface. This "viscous design" was then tested and the surface pressure results are shown as the solid circles in Figure 6.10. Correspondence between theory and experiment was excellent. Some scatter at the end of the compression surface may be due to the calculated transitional nature of the boundary layer at this location.

A viscous correction was applied to the present Busemann inlet by calculating the displacement thickness using the Stan6 code (Ref. 6.7). Calculations were performed for a wholly turbulent boundary layer as well as a transitional layer.

	BUSEMANN INLET		OSWATITSCH INLET		PRANDTL-MEYER INLET	
DESIGN PROPERTY	INVISCID DESIGN	VISCOUS DESIGN	INVISCID DESIGN	VISCOUS DESIGN	INVISCID DESIGN	VISCOUS DESIGN
P_3/P_1	26.7420	26.7420	26.8370	26.8370	26.8370	26.8370
A_1/A_3	9.8001	7.6450	9.0672	7.6083	9.0672	7.5178
Pt_3/Pt_1 (ηpt)	0.9831	0.4522	0.7633	0.4423	0.7633	0.4263
M_2	5.3800		6.2000		6.2000	
M_3	4.8990	4.2650	4.6800	4.2450	4.6800	4.2165
P_3/P_2	1.7167	1.7167	4.0839	4.0839	4.0839	4.0839
P_2/P_1	15.5775	15.5775	6.5715	6.5715	6.5715	6.5715
T_3/T_1	2.5687	3.2080	2.7660	3.2310	2.7660	3.2657
T_3/T_2	1.1723		1.6150		1.6150	
T_2/T_1	2.1911		1.7130		1.7130	
RAMP LINEAR DISTANCE	0.44261		0.37748		(5041	
CORNER X	0.44132	0.44141	0.37460	.37469	0.34783	.34792
CORNER Y	0.02933	0.02744	0.04007	.04006	0.03394	.03303
COWL POSITION	.3585,.0430	.3585,.0430	.3555,.0430	.3555,.0430	.3151,.0381	.3151,.0381
ENTRY RADIUS	0.04399	0.04399	0.04399	0.04399		
TOTAL DRAG						

DIMENSIONS IN METERS (m)

R.J.M

Table 6.2 Theoretical design properties of the three inlet models.

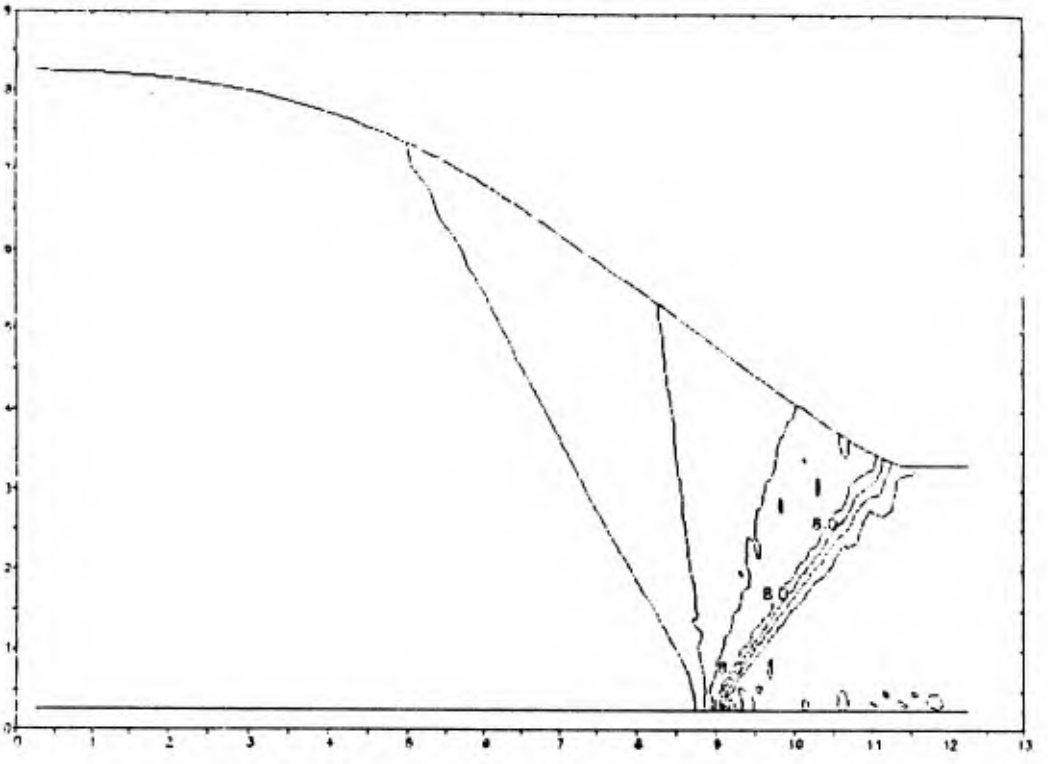

Figure 6.8 Parch/Euler calculation of Busemann inlet isobars.

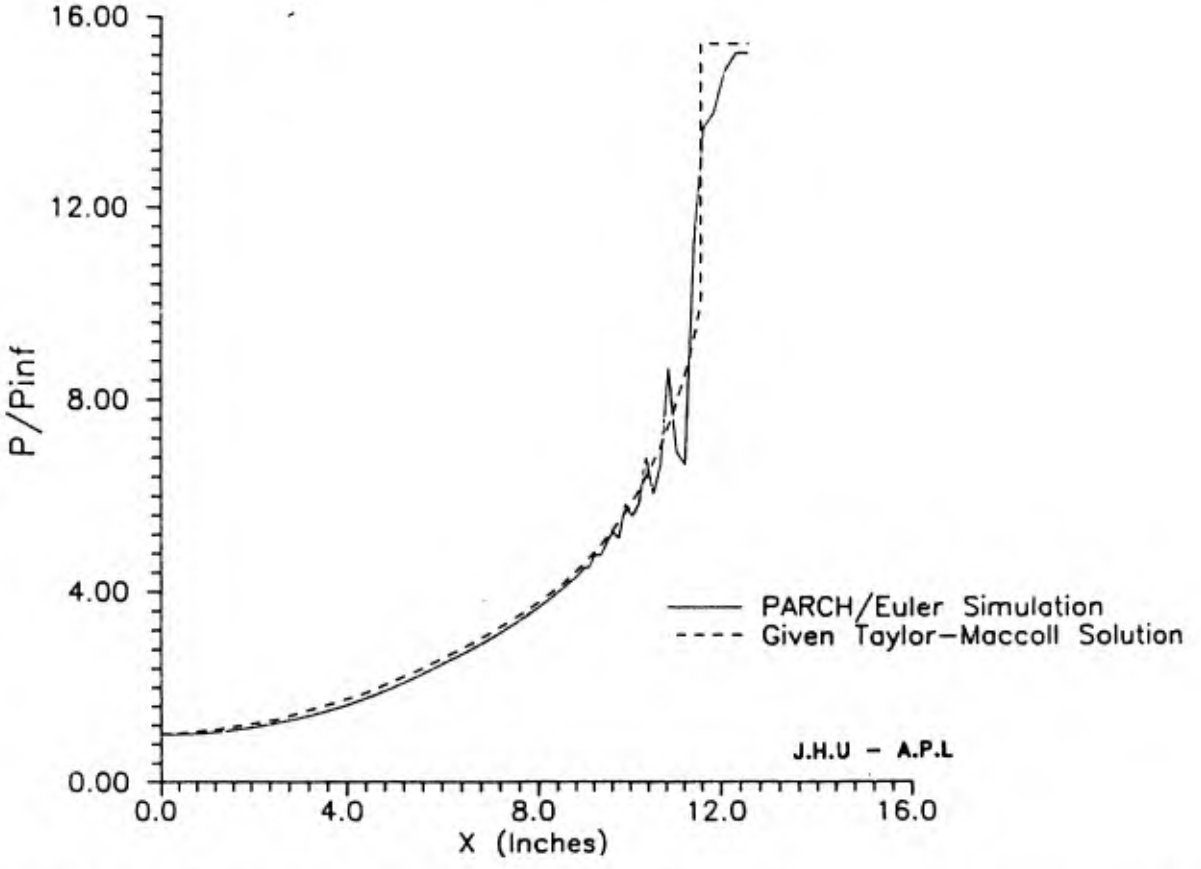

Figure 6.9 Parch/Euler calculation of Busemann inlet compression for comparison to the inviscid Taylor-Maccoll solution.

Calculations done at JHU/APL (Ref. 6.14) are also shown for a SCRINT PNS code. Results are shown in Figure 6.11. The inviscid contour is shown as a solid line. The difference between this and the other lines gives the displacement thickness. We see that the Stan6 transitional line and the PNS solution are in very good agreement, whereas the fully turbulent calculation (not shown) predicts a larger displacement thickness. Previous tests had suggested a transition occurring at about 25 cm and this led us to adopt the transitional/STAN6 displacement thickness for correcting the inviscid contour.

A PNS solution, using SAIC's SCRINT code was also applied by M.V. Thompson and G.W. Corpening at JHU/APL. These calculations show that if the original inviscid Taylor-Maccoll contours were used (Figure 6.12a), there would appear a region of non-conical flow compression. Waves from this compression appear to reflect off the converging surface ahead of the corner, producing a strong compression - perhaps a normal shock - at the centreline. The compression ratio is 24, which is far above the inviscid ratio of 15.57. The same PNS solution, when applied to the corrected contour, Figure 6.12b, shows more-or-less confocal isobars, no obvious wave reflection and a compression ratio of 16 (a value very close to the 15.57 predicted by the Taylor-Maccoll solution). Figures 6.13a and 6.13b show the corresponding surface pressure distributions for the uncorrected and corrected surfaces respectively.

The PNS predicted Mach number at the exit of the inlet and the total pressure recovery of the inviscid core flow are 5.1 and 0.98 which compare well with the Taylor-Maccoll values of 6.9 and 0.9831. The boundary layer correction has been applied in such a way that the viscous design retains the compression ratio of the inviscid design (i.e. p_3/p_1 are identical). As a consequence the contraction ratio A_1/A_3 of the viscous design is lower than that for the inviscid design. Other parameters for the viscous design are calculated on the basis of adiabatic flow.

On the basis of these results, it was felt that the Taylor-Maccoll solution was yielding valid inviscid coordinates and that the STAN6 program was giving the proper boundary layer displacement thickness correction and these were used to generate the model contour and resulting viscous performance parameters that are shown in Table 6.2.

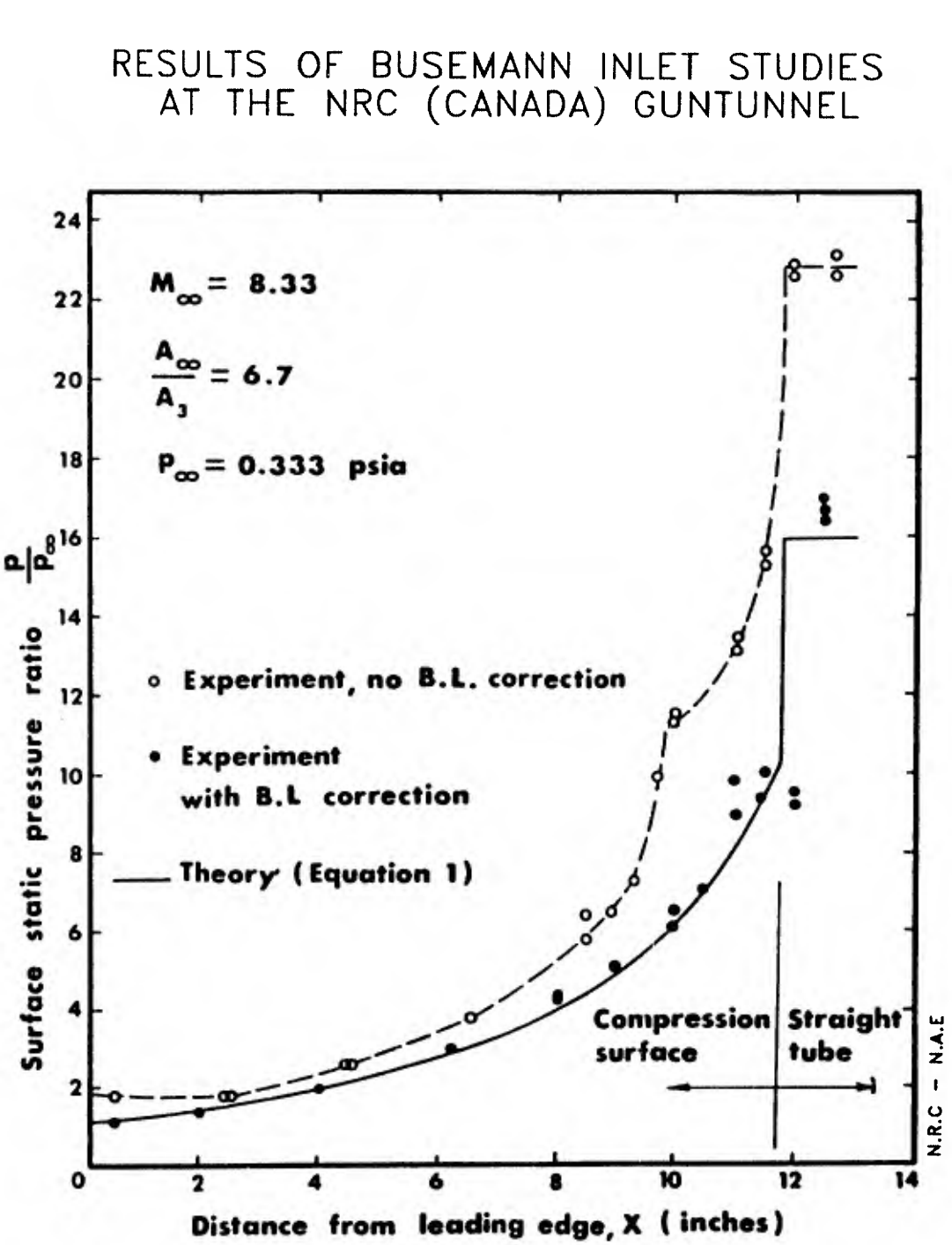

Figure 6.10 NRC Gun Tunnel evaluation of Busemann intakes with and without viscous correction.

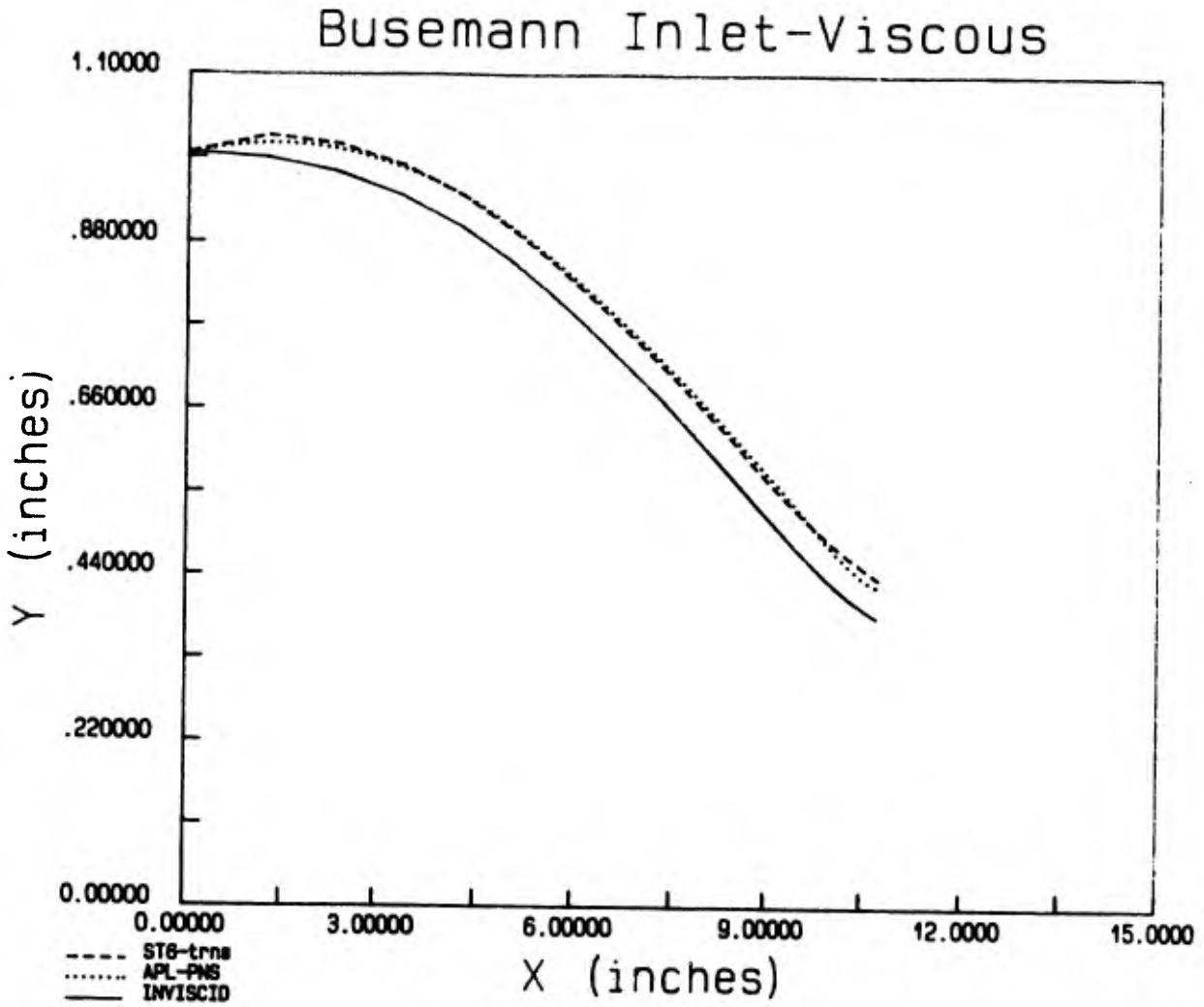

Figure 6.11 Viscous evaluation of Busemann contour using a SCRINT PNS and STAN6 codes.

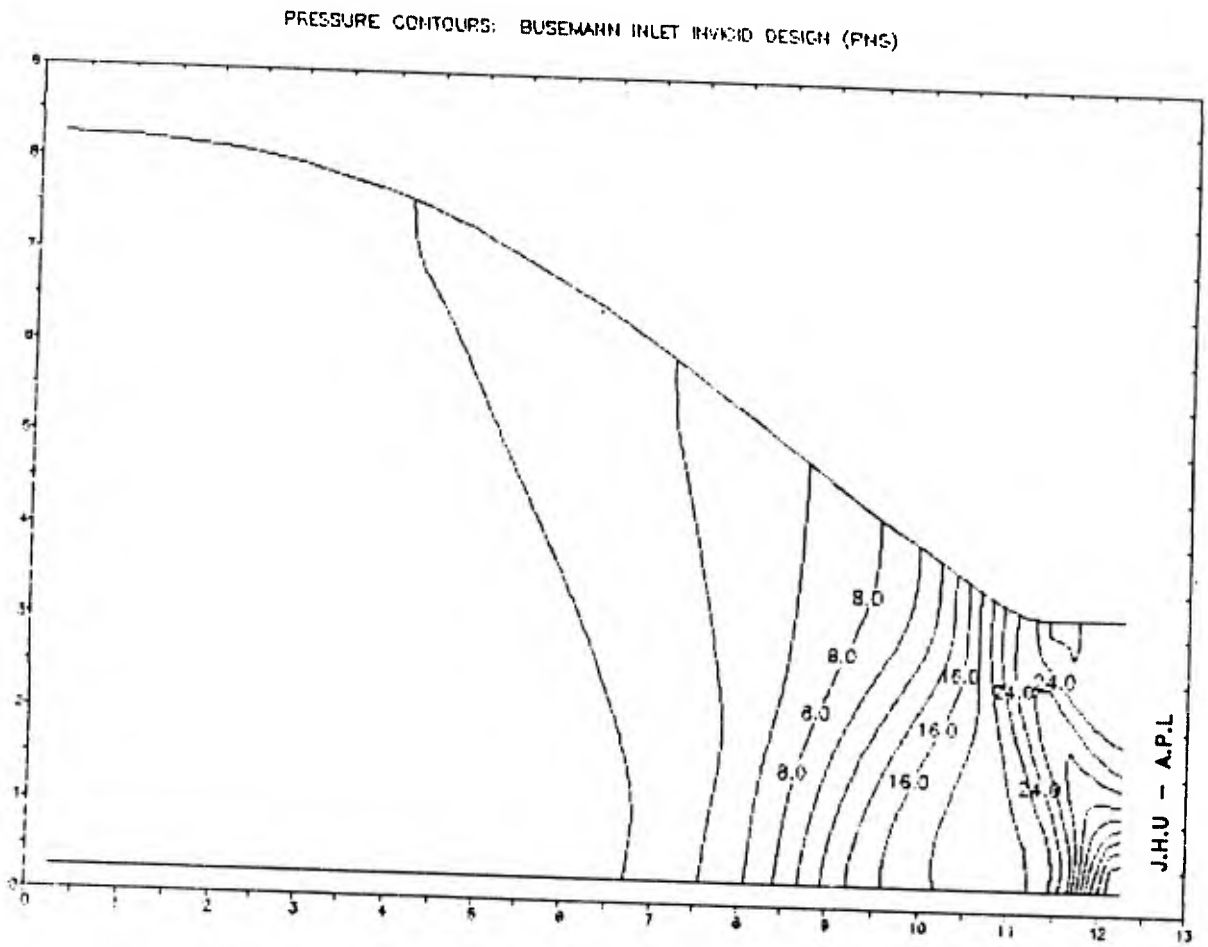

Figure 6.12a PNS evaluation of inviscid Busemann surface.

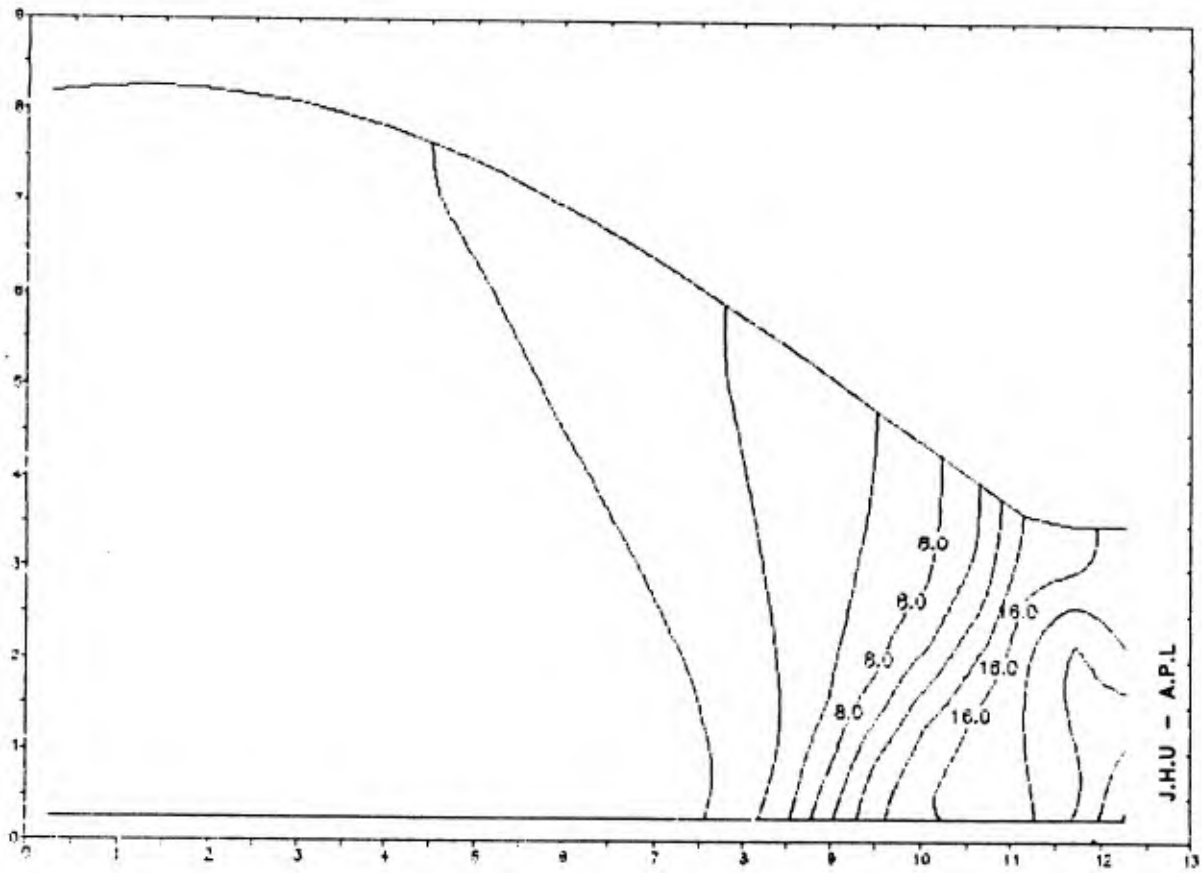

Figure 6.12b Johns Hopkins University Applied Physics Laboratory PNS evaluation of the viscous Busemann inlet surface.

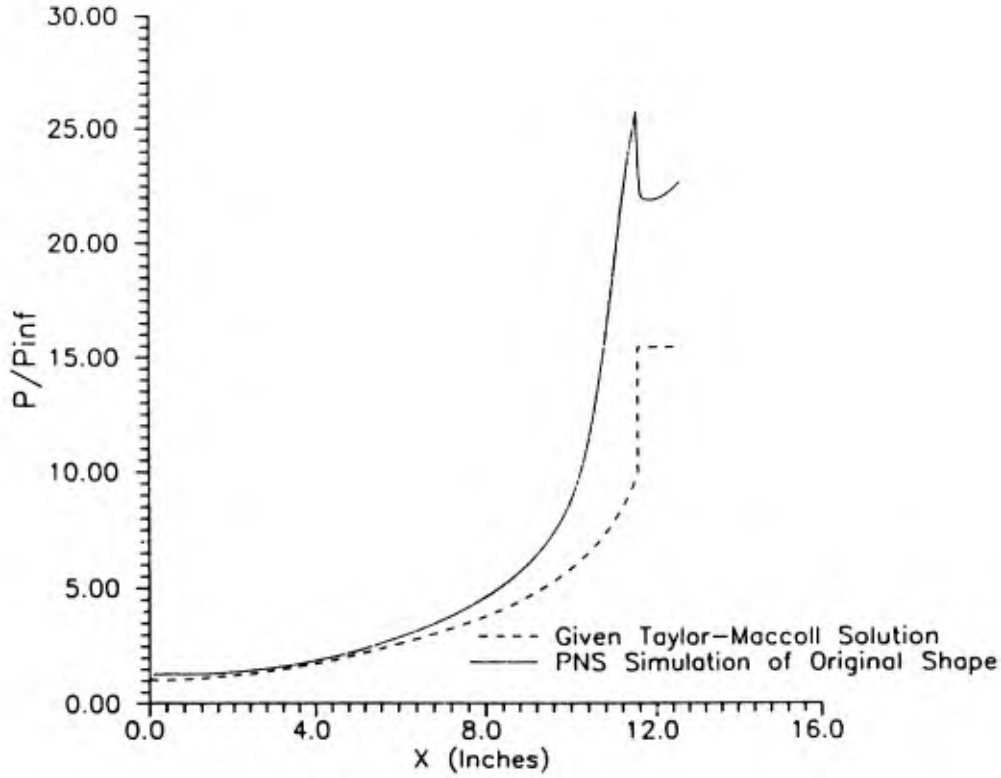

Figure 6.13a PNS prediction of the pressure distribution on an inviscid Busemann surface.

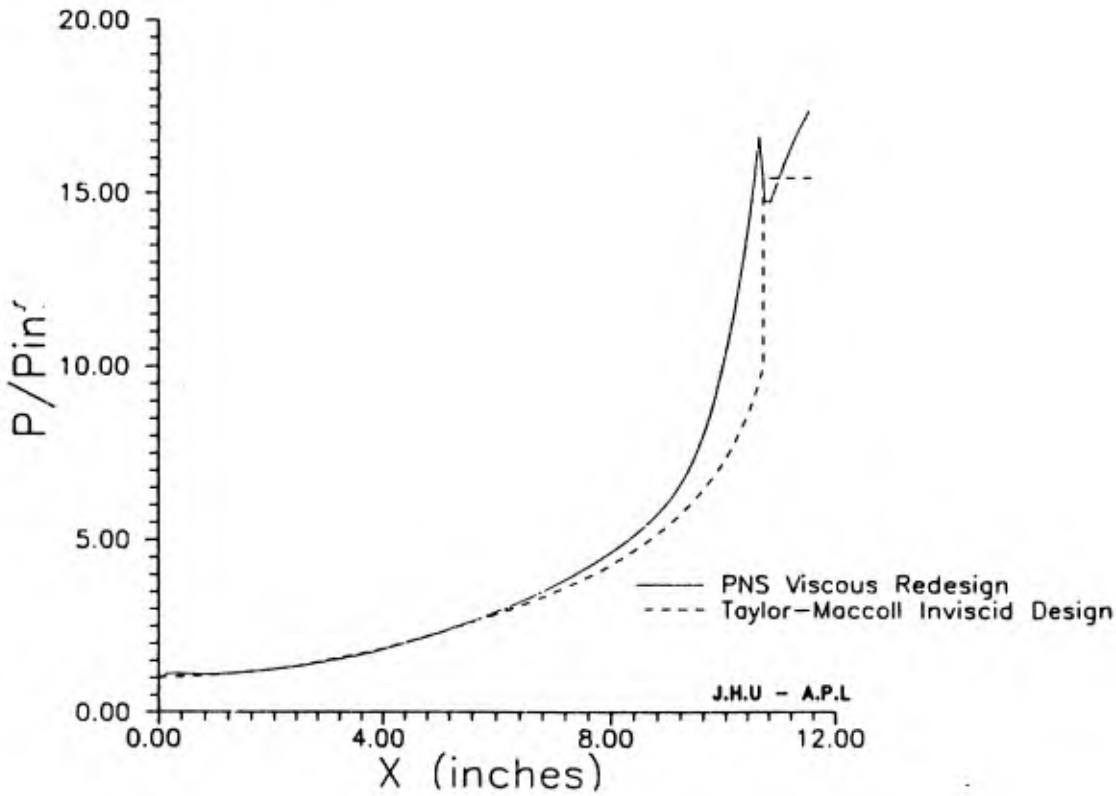

Figure 6.13b PNS prediction of the Busemann inlet pressure distribution after a viscous correction.

6.6.4 Busemann Inlet - Model Construction

The Busemann inlet model has been designed for the measurement of static pressures and aerodynamic drag on the wetted compression surface. The inlet model is shown in Figures 6.14 and 6.15. The internal compression surface, shown lightly shaded in Figure 6.14, is bearing supported within a non-metric housing to eliminate external drag influence on the measurement. The metric and non-metric internal surfaces are separated by a .35 mm gap, located 10 mm downstream of the leading edge. The leading edge drag is in this way removed from the measurement.

As seen in the Figure 6.15 photo, the model is sting mounted with additional strut support possible using less essential bearing mounts on the non-metric. Up to nine bearings support the model centerbody, effectively minimizing friction drag, thus ensuring that virtually all resistance to horizontal aerodynamic force is produced by the load cell. The latter is a PCB force transducer which is intimately joined between the inlet base and the housing base. The accelerometer is positioned diametrically opposite and is used to compensate for the inertial loading induced by the tunnel vibration.

On this model, static pressure transducers are conveniently mounted in the model at the tap location without pneumatic leads. Static pressure taps have been installed in the inlet base to account for the base pressure effect on the load cell reading.

6.6.5 Busemann Inlet - Results

6.6.5.1 Flow Starting

The first tests were performed without instrumentation to ensure that the flow inside the Busemann inlet was started and fully supersonic. The composite Figure 6.16 shows schlierens for entry and exit flows superimposed on the inlet assembly schematic which also depicts the theoretical internal flow characteristics. No bow shock is apparent at entry and shocks appear at the exit, indicating that this flow is supersonic. The exit flow schlieren photo was taken through the secondary windowed model access doors recently installed in the tunnel diffuser.

The 15 cm diameter model housing is the largest ever tested in this tunnel. Unstart of the tunnel was

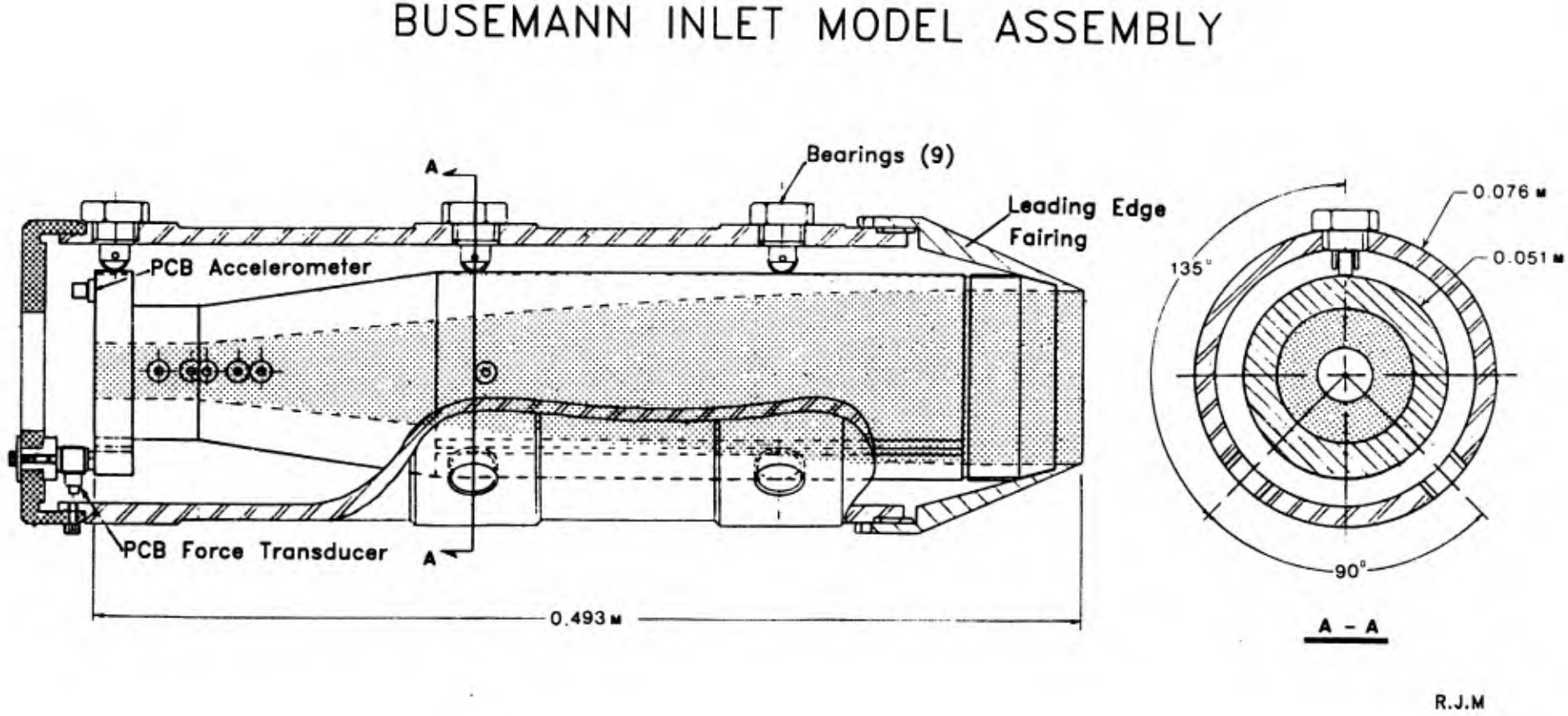

Figure 6.14 Assembly drawing of Busemann inlet model and drag balance.

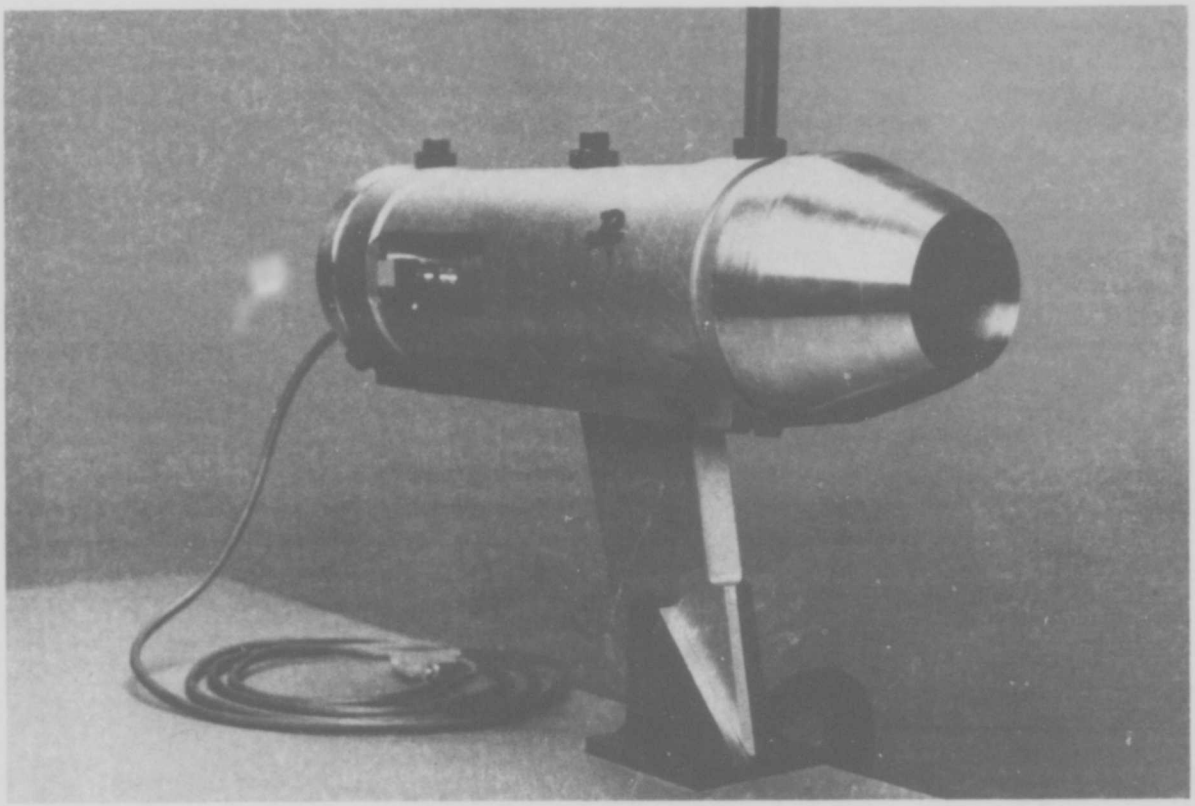

Figure 6.15 Photo of Busemann inlet model assembly.

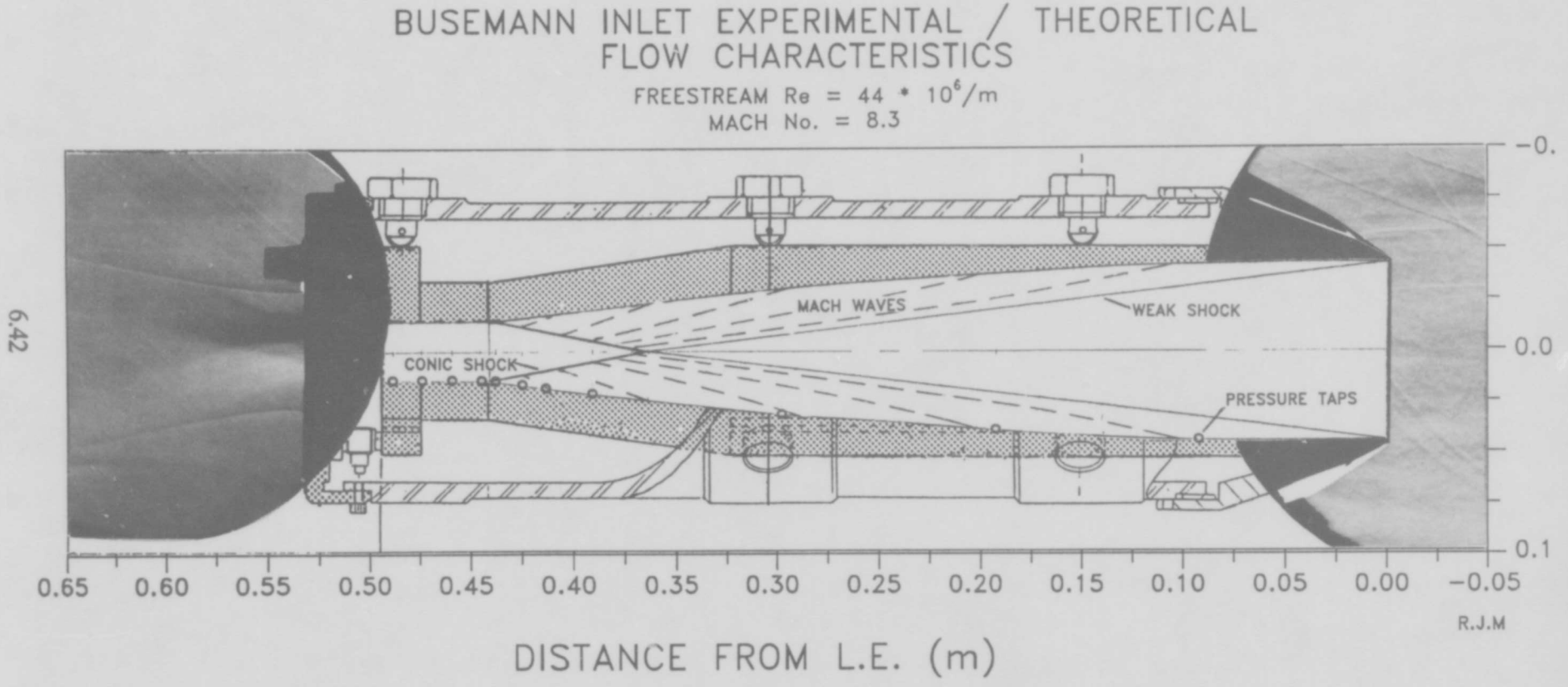

Figure 6.16 Schlieren verification of successful Busemann inlet flow start.

induced if the assembly was mounted in a forward position where the external shocks, seen here to emanate from the leading edge, were positioned upstream and no longer contained in the tunnel diffuser.

Figure 6.17 shows a more detailed view of the inlet exit flow. A measurement of Mach wave slope from this figure gives an exit Mach number of 4.4±.2 which compares well with the predicted viscous value of 4.2650. A relatively large reading error is used in the calculation owing to the uncertainty in the angular measurements from the photo.

6.6.5.2 Pressure Measurements

Surface static pressure measurements are shown in Figure 6.18a and 6.18b for freestream Reynolds numbers of $44*10^6$ m^{-1} and $22*10^6$ m^{-1} respectively. The different symbols and corresponding numbers designate different runs of the gun tunnel. From these results it is seen that measured and theoretical pressures agree well along the first half of the inlet surface. The experimental values are then seen to be consistently higher for both Reynolds numbers up to the predicted shock impingement pressure jump. The location of the jump is in good theoretical/experimental agreement although the magnitude for the Re = $44 * 10^6$ m^{-1} case is underpredicted by theory. A higher than predicted shock pressure jump indicates that the shock is reflecting off the surface ahead of the corner and the generally higher surface pressure in the region of .3 m to .44 m is a possible indication of boundary layer separation in this region. In both cases of Reynolds number, the pressures at the exit are close to predicted values. This indicated that, although flow details are off, the inviscid theory and the boundary layer correction technique yield overall results which are in good agreement with experiment.

The measured pressure ratio, p_3/p_1=25.90 ±.07, and the measured contraction ratio, A_1/A_3=7.645 ±.004, can be used to calculate the efficiency of the inlet. Figure 6.19 has been prepared to aid in the determination of efficiency. It is a plot of pressure ratio vs contraction ratio with lines of constant total pressure recovery, Pt_3/Pt_1, as well as downstream Mach number, M_3, appearing on the figure. The figure is for a freestream Mach number of 8.33, variable γ (however for the tunnel conditions γ varied very little from 1.4), and for adiabatic flow, τ=1. In this figure, the inviscid design is shown at the star, ★, with a contraction of 9.8001 and a pressure ratio of 26.7420. The boundary layer corrected inlet is estimated to

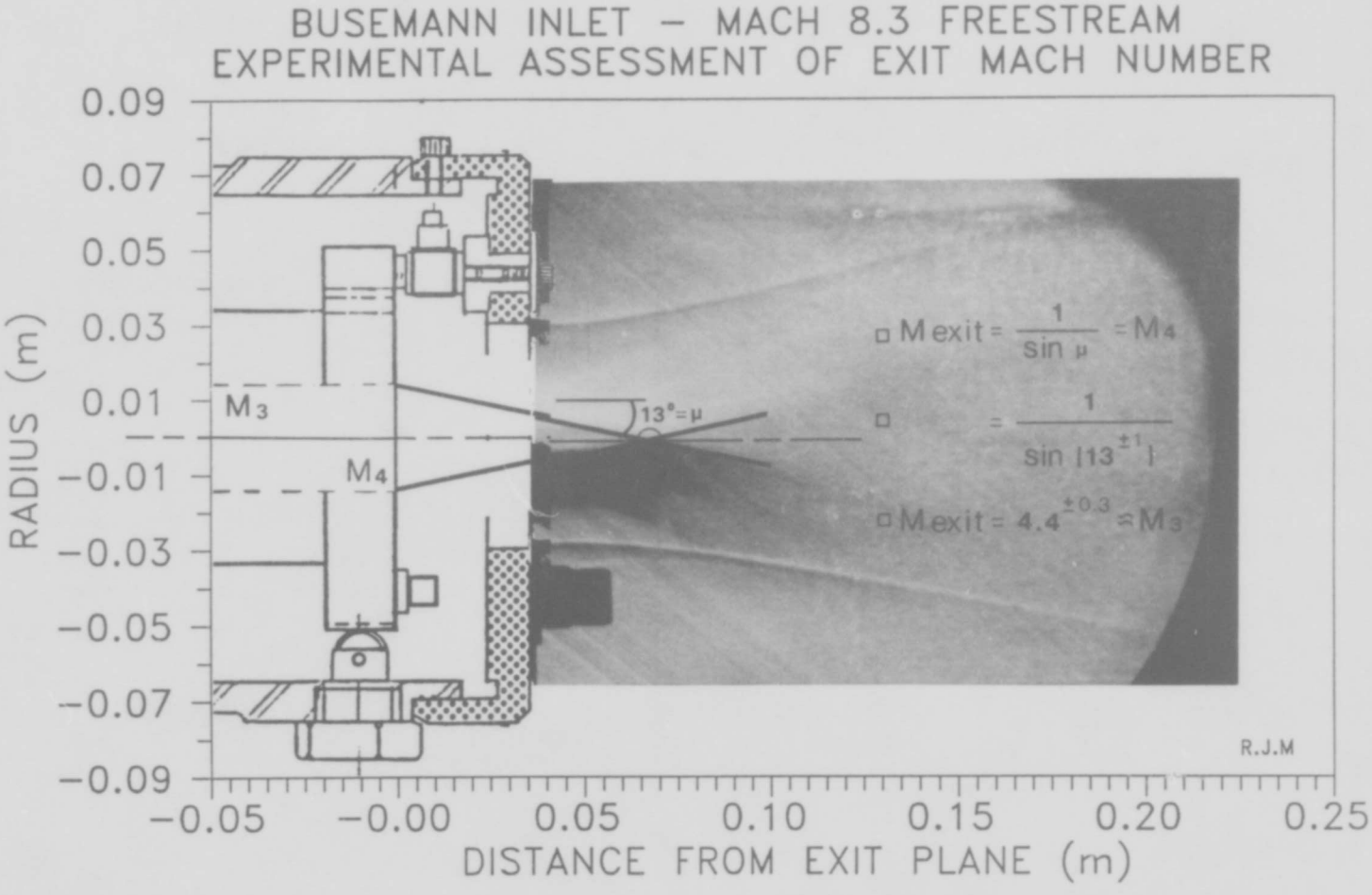

Figure 6.17 Schlieren of Busemann inlet exit flow and calculation of exit Mach number from the Mach wave slope.

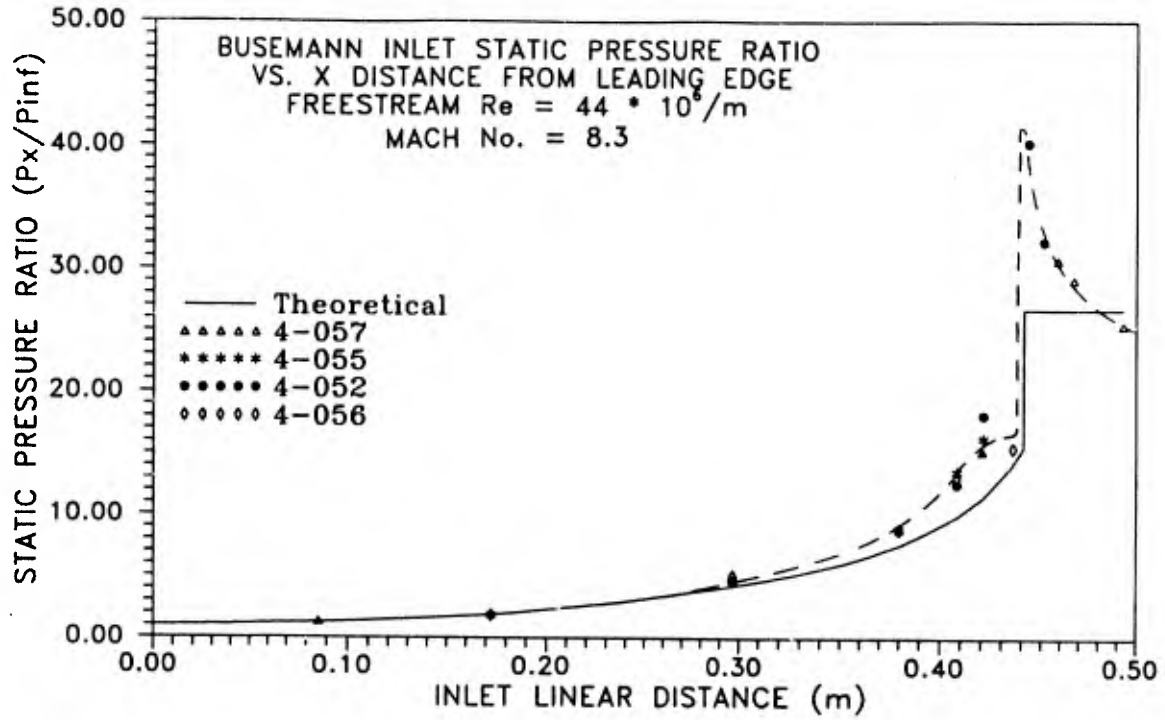

(a)

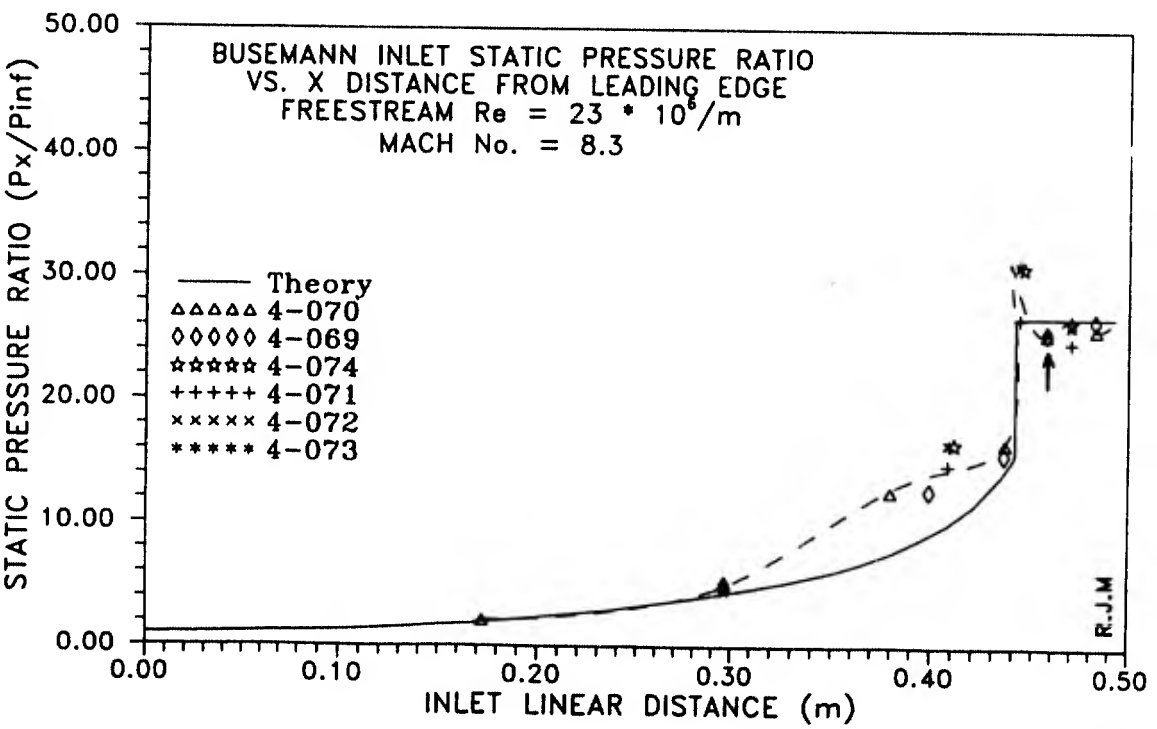

(b)

Figure 6.18a-b Busemann inlet static pressure survey.

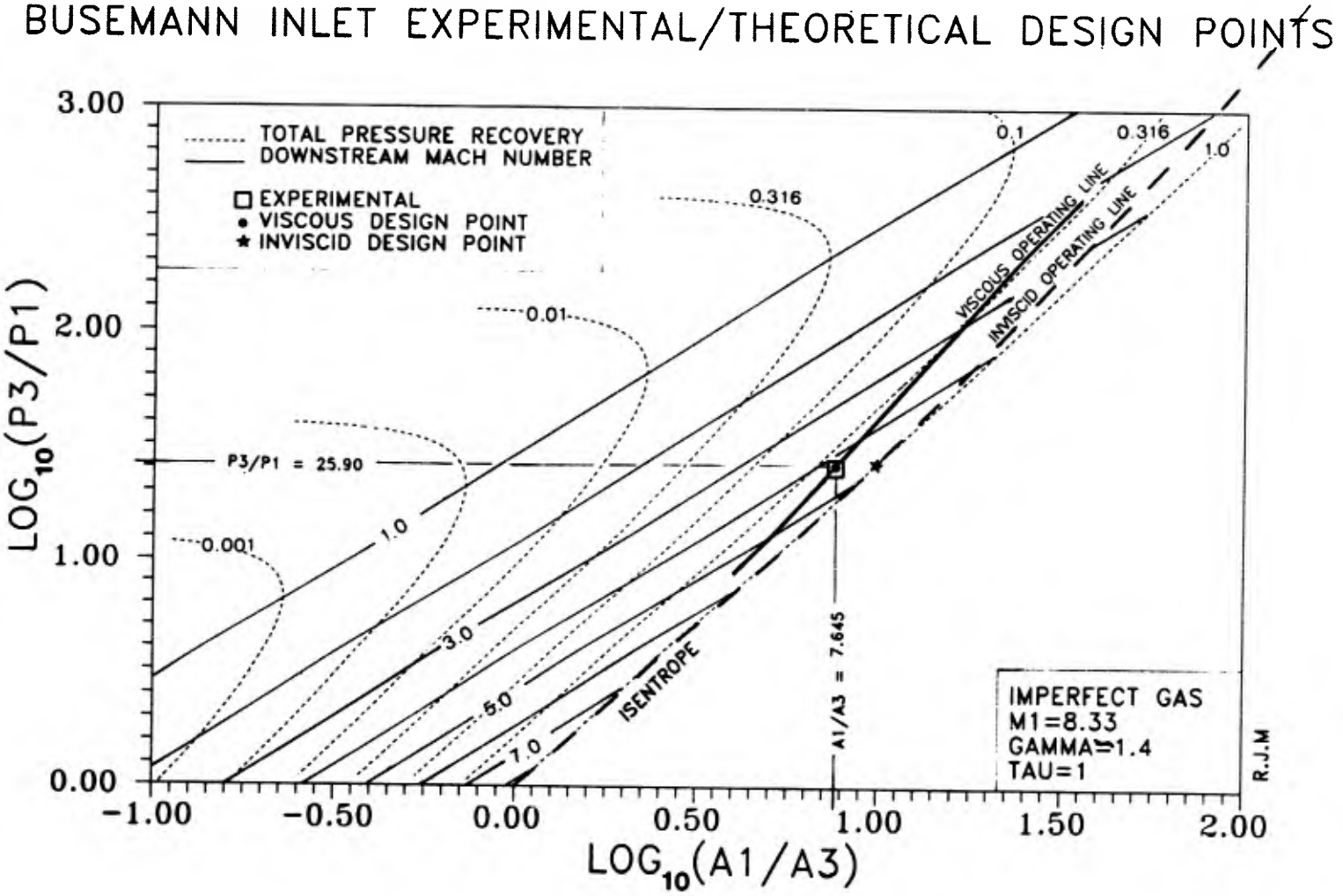

Figure 6.19 Pressure-area diagram showing the predicted and experimental performance of the Busemann intake.

operate at the same pressure ratio but with a smaller contraction ratio of 7.645 giving a total pressure recovery of Pt_3/Pt_1=.4522 at the point denoted by "·". Measured performance is shown by "□" at a contraction of 7.645 and a pressure ratio of 25.9 ±0.7, giving a total pressure recovery of Pt_3/Pt_1=.484 ±.008.

This total pressure recovery efficiency is calculated by equation 6.2 as a function of the measured area ratio and the measured pressure ratio taken at the trough value labelled by the ↑ on Figure 6.18b, just downstream of the turning shock. There are two justifications for the selection of this station in what is obviously not a constant pressure exit duct. Firstly, this through value is assumed closest to throat nominal based on the premise that the pressures have steadied beyond the turning shock and losses due to the throat boundary layer growth and possibly weak reflected shocks are yet to cause a substantial increase in the static pressure. And secondly, it must be recognized that the accuracy of the technique is dependent on the static pressure uniformity throughout the combustor exit plane (Ref. 6.15). Ideally this plane should be at the corner. With the impinging turning shock, however, the static pressure profile (Figure 6.18a) indicates high variation of pressure at this station. It would seem that this would not be a good one-dimensional profile. Once these initial peaks have steadied, a reasonably uniform profile can be assumed in the Busemann inlet. For these reasons, the low pressure station, only a small distance downstream of the shock, was used in the performance calculations.

The Figure 6.19 also shows the performance obtained from the whole family of Busemann inlets operating at a freestream Mach number of 8.33 and various contraction and compression ratios. This performance being shown for both the inviscid flow ("INVISCID OPERATING LINE") and the inlet with viscous correction ("VISCOUS OPERATING LINE"). It is seen that the inviscid Busemann inlet of M_1 = 8.33 operated with high efficiency at Pt_3/Pt_1 >0.5, down to exit flow Mach numbers of 2, and that viscous degradation reduces the total pressure efficiency down to about 0.3. These results and the method of accounting for viscous effects are confirmed by experiment.

6.6.5.3 Drag Measurements

The effectiveness of the inertial compensation is demonstrated in Figures 6.20a and 6.20b. Figure 6.20a shows the filtered raw data of the acceleration of, and force induced by, the inlet centerbody throughout the course of the run. In the region labelled "PRE-FIRE", there is no flow, the tunnel is still, and both instruments show a steady zero reading. At the moment of diaphragm rupture, the tunnel barrel and driver recoil and some vibration is transferred to the test section though the nozzle end seal and the laboratory floor. For 12 ms prior to flow contact with the model, the instruments measure this vibration in terms of the acceleration and force that it induces on the inlet metric. Labelled "PRE-FLOW" in Figure 6.20a, the accelerometer and force readings are sinusoidal and opposite in phase because of the orientation of their installation. As flow contacts the model, aerodynamic loads are added to the still vibrating assembly creating the fluctuating forces and accelerations observed in the "FLOW-DURATION" and "STEADY-FLOW" sections.

When the inertial compensation was performed, the product of the mass and acceleration of the centerbody metric was subtracted from the total force reading to produce the pure aerodynamic drag shown in Figure 6.20b. This is verified by the fact that the compensated drag is now all positive in magnitude and the "PRE-FLOW" region shows a zero force reading. The cancellation to zero of the "PRE-FLOW" data, then, effectively provides us with a "shaker table" calibration which checks the reading of the accelerometer against that of the load cell.

In Figure 6.21, a similar drag trace is plotted after inertial compensation of run 4-077. Also shown above this trace is the measured trace of the tunnel total pressure. In connection with these traces, the following observations are made:

a) There is some correlation between the total pressure and the drag trace. The correlation improves if it is recognized that a pressure pulse takes about .0025 seconds to travel from the total pressure gauge to the drag force transducer. This becomes more apparent if the drag trace is shifted to the left by .0025 seconds.

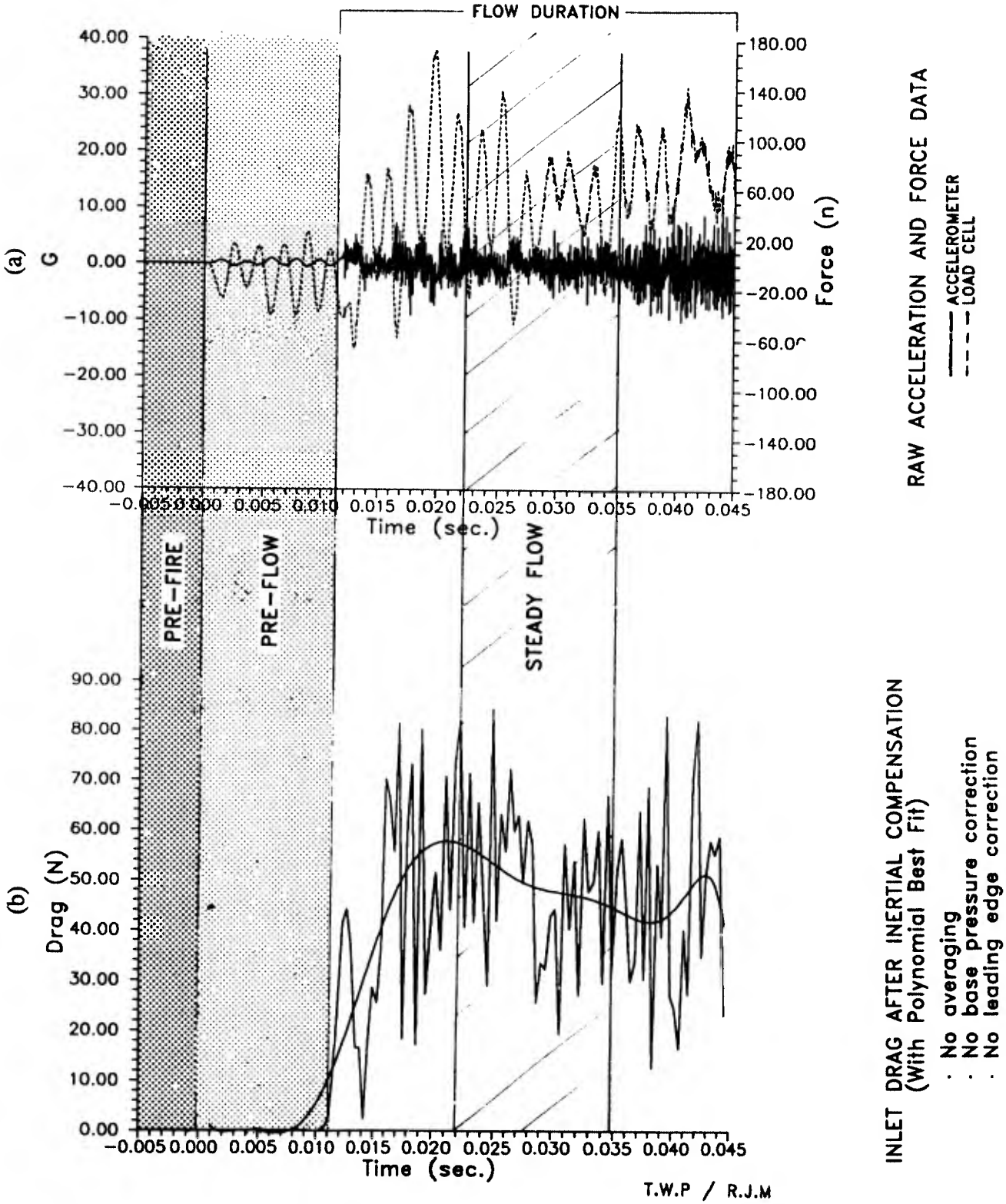

Figure 6.20a-b Inertial compensation of Busemann centerbody force measurement.

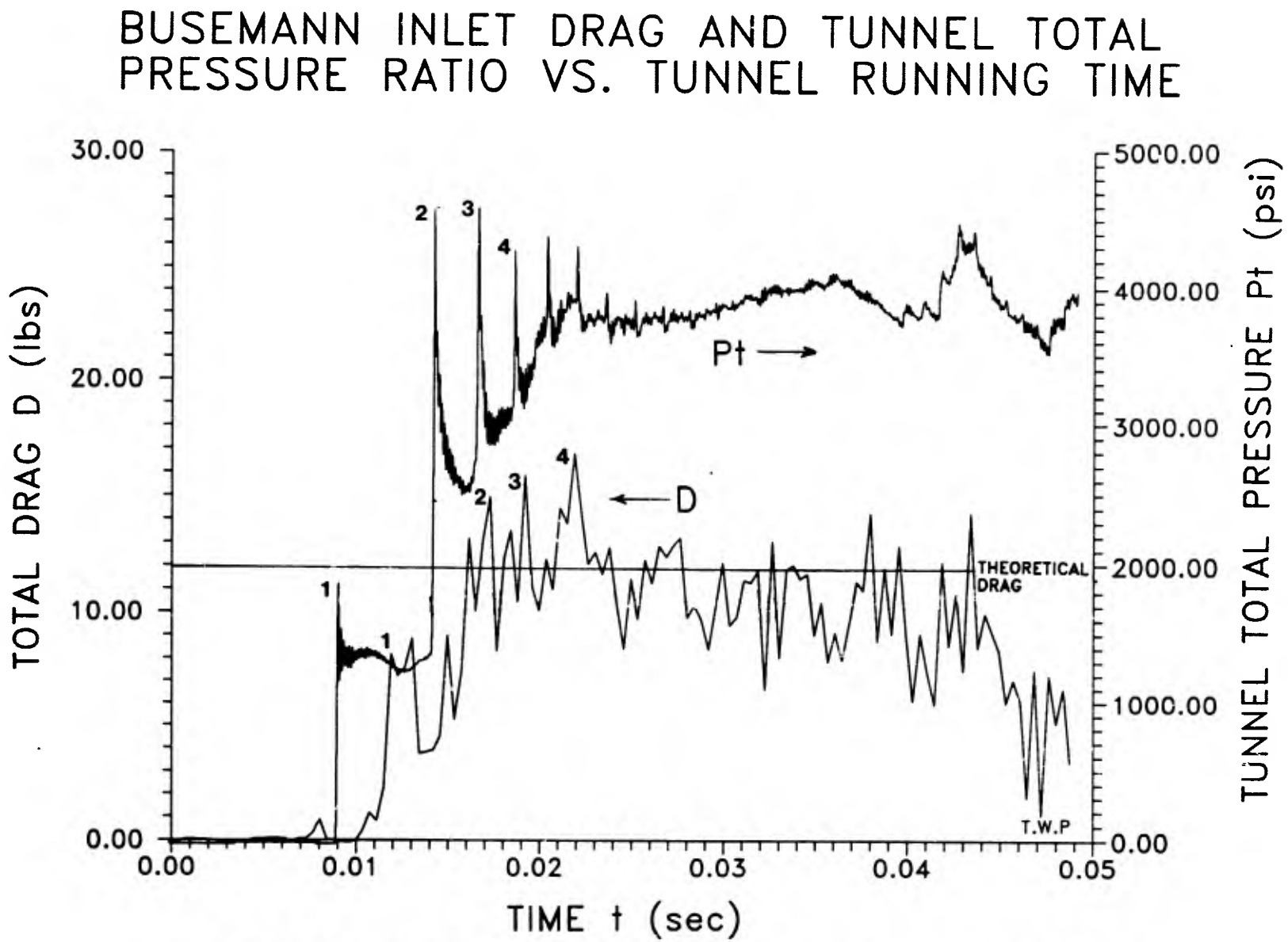

Figure 6.21 Comparison of compensated inlet drag to total pressure history clearly indicates the aerodynamic nature of the drag measurement.

b) The drag trace is more irregular than the total pressure would cause it to be. In particular in the interval of tunnel running time from .025 s to .035 s where the fluctuations in total pressure are of the order of ±5% when the fluctuations in drag are about ±30%.

The line labelled "THEORETICAL DRAG" is calculated by summing the theoretical pressure drag and the theoretical skin friction drag (using STAN6) from the leading edge to the corner on the inlet surface. Heat transfer calculations proved that the inlet flow could be assumed adiabatic with negligible error. The calculated drag value was 52.241 Newtons or 11.97 lbs as shown in Figure 6.21 in imperial units. The experimental trace shown here is not yet corrected for the influence of base pressure thrust shown in Figure 6.22, which will inevitably cause the experimental drag to increase somewhat in magnitude.

The drag traces from six successive runs were corrected for model acceleration and then averaged. This had the effect of reducing the noise from both of these signals. The base thrust shown on Fig. 6.23 was then added which resulted in a drag of 56.8 N at t=.03s. This is within 7% of the calculated value of 53.8 N. The accuracy of the experimental drag measurement could be improved by:

1) Accounting for the leading edge drag.

2) Preventing flow leakage at the forward junction between the model and the housing by the use of labyrinth seals.

3) Increased number of measurements of force acceleration and base pressure.

4) Isolation of the model mount from the tunnel and the laboratory floor to reduce or remove the transfer of driver recoil vibration.

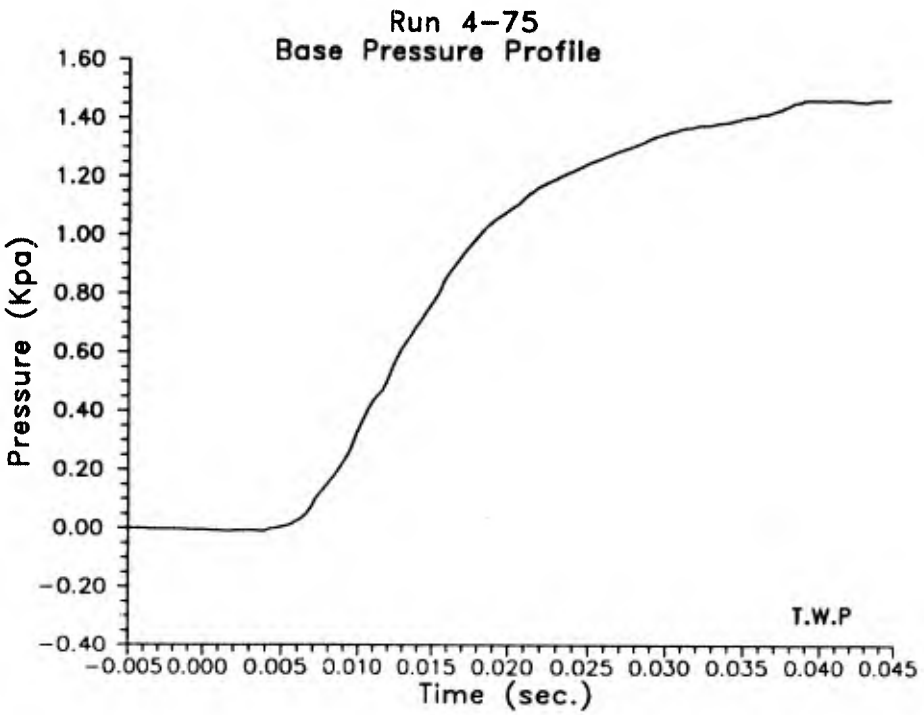

Figure 6.22 Measurement of the static pressure increase on the model base.

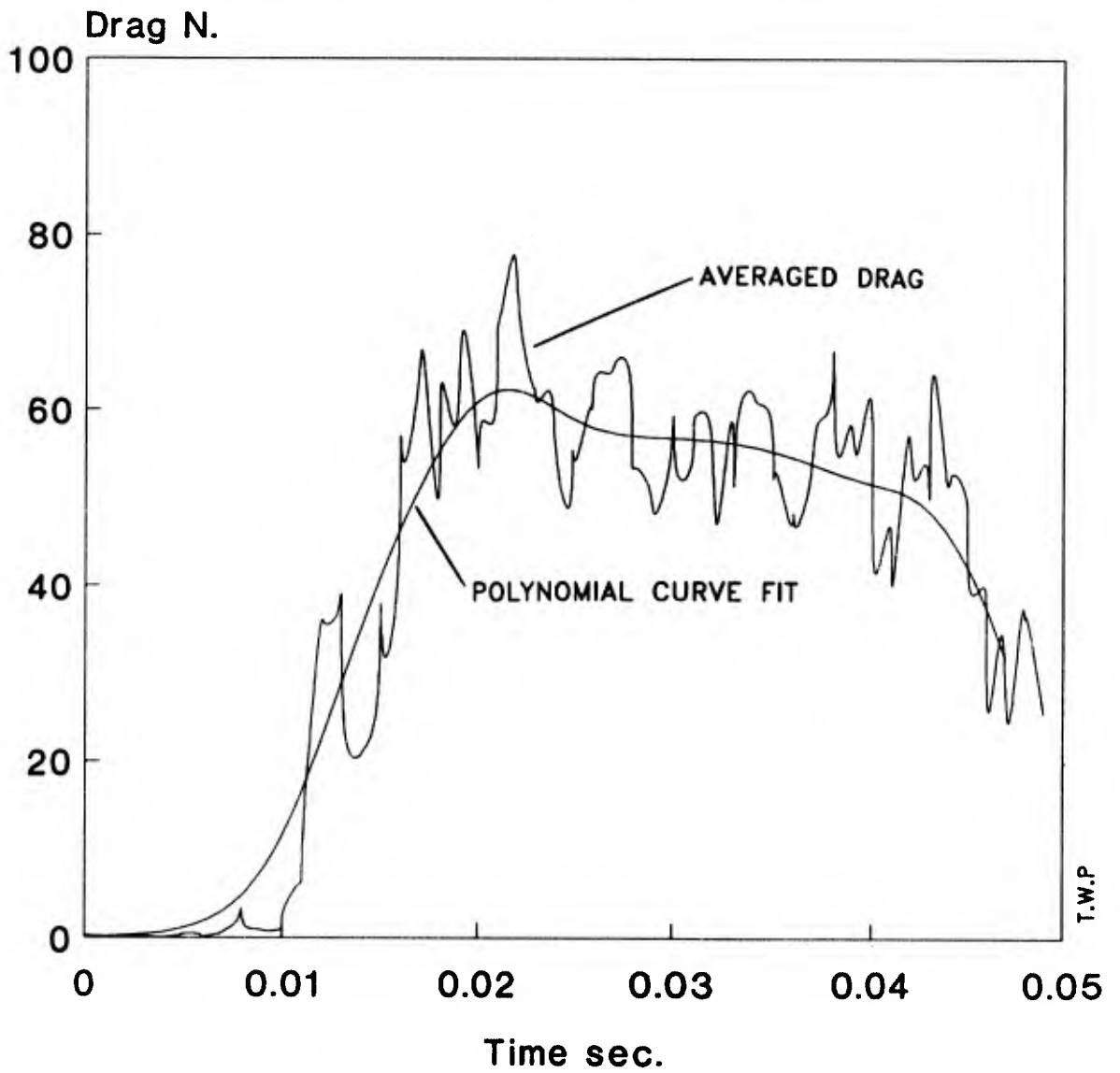

Figure 6.23 Drag history on the Busemann inlet model, inertially compensated, corrected for base pressure, and averaged over six consecutive runs.

6.7 The Prandtl-Meyer Inlet

6.7.1 Prandtl-Meyer Inlet - Basic Flow

In supersonic, planarly symmetric, inviscid flow, one of the few exact solutions is the expansion around a sharp corner. Exactness, in this case, is the result of the self-similarity of the flow in that flow quantities do not vary with respect to the radial distance from the corner. Prandtl (Ref. 6.16) and Meyer (Ref. 6.17), after whom this type of flow is named, derived several relationships relating the flow and geometric parameters of the streamlines. Among these, the most well-known is the Prandtl-Meyer turning angle, giving the angle, ν, through which the flow is turned from Mach 1 to reach a given Mach number, M:

$$\nu = \frac{1}{k}\tan^{-1}k\beta - \tan^{-1}\beta \tag{6.29}$$

where

$$k = \sqrt{\frac{(\gamma-1)}{(\gamma+1)}} \quad \textit{and} \quad \beta = \sqrt{M^2-1} \tag{6.30}$$

If a particular streamline in Prandtl-Meyer flow is selected such that the perpendicular distance from the focal point of the Prandtl-Meyer waves to the streamline, at Mach 1, is 1, then the radial distance from the focal point to any other point on that streamline is

$$r = \left[1 + k^2(M^2-1)\right]^{\frac{1}{2k^2}} \tag{6.31}$$

The angular distance from the Mach 1 radial is:

$$\Phi = \frac{1}{k}\tan^{-1}(k\beta) \tag{6.32}$$

These two equations allow us to find the x and y coordinates of a Prandtl-Meyer streamline and the coordinates of a surface generated by these streamlines. The length of the streamline (measured along the streamline from the sonic point to a point where the Mach number is M) is, for γ=1.4, given by:

$$S = \frac{265}{576}\left[M\beta + \log_e(M+\beta)\right] + \frac{23}{288}M^3\beta + \frac{1}{216}M^3\beta^3 \tag{6.33}$$

and the radius of curvature of the streamline is

$$R_{PM} = -\left[\frac{2}{\gamma+1}\right]^{\frac{3-\gamma}{2(\gamma-1)}}\frac{M^3}{M^2-1}\left[1+\frac{\gamma-1}{2}M^2\right]^{\frac{\gamma+1}{2(\gamma-1)}} \tag{6.34}$$

The last two relations are useful when calculating the boundary layer on the Prandtl-Meyer surface where S becomes the streamwise distance and R_{PM} is used in the evaluation of the pressure gradient parameter and in the Görtler number of transition from laminar to turbulent flow. Equation 6.12 tells us also that if on an arbitrary curved surface where the Mach number is M and the surface curvature is R/R_{PM} then the surface is not a Prandtl-Meyer surface and a centered wave system will not be produced. So it is obvious that Prandtl-Meyer flow depends on both surface shape and local Mach number.

6.7.2 The Prandtl-Meyer Inlet - Inviscid Design

The Prandtl-Meyer inlet is based on a combination of two-dimensional supersonic flows consisting of uniform flow, compression through a Prandtl-Meyer compression and flow through a plane oblique shock wave. Although it is possible to start such an intake surface by a finite angle wedge followed by a

Prandtl-Meyer compression (Ref. 6.18), we have eliminated the starting wedge in order to provide a closer comparison with the Busemann and Oswatitsch inlets. The Prandtl-Meyer inlet was selected for study mainly because, of the three inlets studied, it was the only one that provided a clear view of internal flow for the schlieren system. This would help to confirm both the inviscid and viscous calculations. Also, it is significant to note that it is possible to make the theoretical inviscid performance of the Prandtl-Meyer and Oswatitsch inlets exactly the same, thus providing a comparison of boundary layer losses from a two-dimensional and axisymmetric inlet. The inviscid flow of the Prandtl-Meyer inlet is shown in Figure 6.3b. The flow begins with a freestream Mach number of M_0 which is also the Mach number, M_1, at the beginning of the Prandtl-Meyer compression. For the purpose of calculating surface coordinates, we locate a Cartesian (x,y) coordinate origin at the leading edge and designate the location of the focal point as (X,Y). The direct distance from the origin to the focal point is thus

$$r = \left[1 + k^2(M_1^2 - 1)\right]^{\frac{1}{2k^2}} \tag{6.35}$$

The line joining the origin to the focus is a Mach wave, thus:

$$\sin\mu_1 = \frac{Y}{r_1} = \frac{1}{M_1} \tag{6.36}$$

giving

$$Y = \frac{r_1}{M_1} \tag{6.37}$$

and

$$X = r_1 \frac{\sqrt{M_1^2 - 1}}{M_1} \tag{6.38}$$

as the coordinates of the focus. Since the inviscid flow is scalable we can freely choose one of Y or r_1 and calculate the other in order to obtain an inlet of a desired size and capture area. By using the Mach number, M, as parameter and decreasing its value from M_1 in some suitable small steps we can now calculate the surface coordinates from

$$x = X - r\sin(\Phi - \nu_1) \tag{6.39a}$$

$$y = Y - r\cos(\Phi - \nu_1) \tag{6.39b}$$

where r, Φ, ν_1, X, and Y are given by equations 6.8, 6.9, 6.10, and 6.14.

The distance from the origin along the surface is:

$$\begin{aligned} S = \frac{265}{576}\left[M_1\sqrt{M_1^2-1} + \log_e \frac{M_1+\sqrt{M_1^2-1}}{M+\sqrt{M^2-1}} - M\sqrt{M^2-1}\right] \\ + \frac{23}{288}\left[M_1^3\sqrt{M_1^2-1} - M^3\sqrt{M^2-1}\right] \\ + \frac{1}{216}\left[M_1^3(M_1^2-1)^{\frac{3}{2}} - M^3(M^2-1)^{\frac{3}{2}}\right] \end{aligned} \tag{6.40}$$

The isentropic compression continues until a Mach number, M_2 ,is reached, so that the flow has been turned through an angle ν_1-ν_2. The flow then continues straight and parallel at constant M_2 until it runs into the oblique shock which turns the flow back through the angle, ν_1-ν_2, so as to become parallel to the freestream direction. This is the exit flow designated by the subscript 3. In order to avoid the use of a cowl and thereby incur possible spillage and other losses, two such identical flows were placed back-to-back to give the Prandtl-Meyer inlet shown in Figure 6.3b.

The inviscid design parameters are shown in Table 6.2. The Prandtl-Meyer inviscid design has a compression ratio of 26.8370, a contraction ratio of 9.0672, and a total pressure recovery of 0.7633. Mach

number is reduced from 8.33 to 6.20 by the Prandtl-Meyer compression and further to 4.68 by the oblique shock. The pressure ratio across the Prandtl-Meyer compression is 6.5715 and that across the oblique shock is 4.0839. This letter figure is well below that required to cause separation of a turbulent boundary layer at Mach 6.20. The corner and cowl (focus) positions are given in meters.

6.7.3 Prandtl-Meyer Inlet - Viscous Design

The contoured top and bottom surfaces of the Prandtl-Meyer inlet were enlarged to correct for the displacement effect of a boundary layer. No correction was applied to the sidewalls nor to the exit passage. The sidewalls were not corrected because no credible displacement thickness calculation was available for the type of three-dimensional flow existing on the sidewalls. No correction was applied to the exit passage because no calculation or experiment was available on the nature of the interaction of the shock and the boundary layer of a convex corner. Thus it was expected that the measured pressures at the exit would be somewhat higher than calculated.

To a first approximation, the effect of enlarging the internal passage of the inlet by the displacement thickness is to preserve the inviscid flow (including the wall pressure distribution) and to change the wall geometric contraction ratio. Thus, if we use the compression and contraction ratios as primary measures of inlet performance, then only the contraction ratio is affected by the displacement effect of the boundary layer, and viscous design parameters can be calculated from the unchanged compression ratio and the new geometric area ratio. As shown in Table 6.2, the area, A_3, is enlarged to accommodate the displacement thickness resulting in the contraction ratio, A_1/A_3, decreasing from 9.0672 to 7.5178. This last value together with the compression ratio of 26.8370 can now be used to find the other viscous design parameters. It is seen that the viscous total pressure recovery is 0.4263, the Mach number at the exit is 4.2165, the pressures are unchanged but the temperature at the exit has increased by 18%.

All boundary layer calculations were done using the STAN6 code described in Reference 6.7. Boundary layer transition (Ref. 6.19) was estimated to occur when either the Görtler number

$$G = Re_\theta \cdot \frac{\theta}{R_C} \tag{6.41}$$

exceeded 8, or

$$\frac{Re_\theta}{M} \tag{6.42}$$

exceeded 150, where

$$Re_\theta = \frac{u_e \theta}{\nu_e} \tag{6.43}$$

and;

θ is the momentum thickness;

u_e is the velocity at the edge of the boundary layer;

υ_e is the dynamic viscosity at the edge;

R_c is the radius of curvature of the surface (Eqn. 6.11);

M is the boundary layer edge Mach number

6.7.4 Prandtl-Meyer Inlet - Model Construction

Based on the viscous design, a Prandtl-Meyer Inlet model was designed and constructed for testing at Mach 8.33 in the Ryerson/U of T Gun Tunnel. The capture height of this inlet is 7.62 cm; its width is also 7.62 cm giving a capture area of 58.06 cm^2. The length of each half of the inlet surfaces is 38 cm. The two halves are mounted in a box so that the distance between the two halves can be adjusted (See

Figure 6.24). An oblique-view photograph is shown in Figure 6.25. Up to 5 static pressure taps on each ramp can be instrumented per run. Transducers are connected to the taps by a short length of tygon tubing (.8 mm dia.). The higher surface pressure regions allow tube lengths of up to 18 cms with adequate instrument response. A tube length of less than 4 cm was necessary at the forward tap stations where pressures were as low as 7 KPa and pneumatic lag proved to be a problem with longer lengths.

The side walls are equipped with schlieren quality windows for flow visualization of the internal compression and shock structure. These are 2 cm thick plate glass windows supported in an aluminum frame by a silicone and rubber seat to reduce transfer of vibration from the housing. Some 80% of the flow upstream of the exit is visible to schlieren through the two side windows.

6.7.5 Prandtl-Meyer Inlet - Results

The viscous design contour with its associated wave structure is shown in the bottom of Figure 6.26. A careful study of this figure reveals that in order to preserve the parallel flow at the entry, some undercutting of the contour has been done to correct for the displacement thickness near the entry of the inlet. The middle diagram of Figure 6.26 with the schlieren picture shows the Mach waves emanating from the leading edges; the oblique shocks emanate from a point on the center line about 5 mm ahead of the predicted point. The extent of the compression fan is seen as a bright fan-shaped region originating on the bottom surface and being focused at the intersection of the oblique shocks. Boundary layers are seen on the top and bottom surfaces as light and dark regions respectively. The top diagram of this figure shows the experimental static pressure ratio as compared with that predicted by theory. The pressures agree closely over the first half of the inlet surface. Measured pressures are higher than predicted probably due to the effect of sidewalls and in the straight aft portion of the inlet they are considerably higher (averaging p_3/p_1=35.80) because no boundary layer correction has been applied in this section. All results are for a freestream Reynolds number of $44*10^6$ per metre.

A summary of the Prandtl-Meyer inlet performance is shown in Figure 6.27 on a compression (p_3/p_1) vs contraction (A_1/A_3) ratio plot. This plot has been constructed for an imperfect gas; however the present inlet conditions are such that a plot for γ=1.4 is indistinguishable from the present plot. This plot has

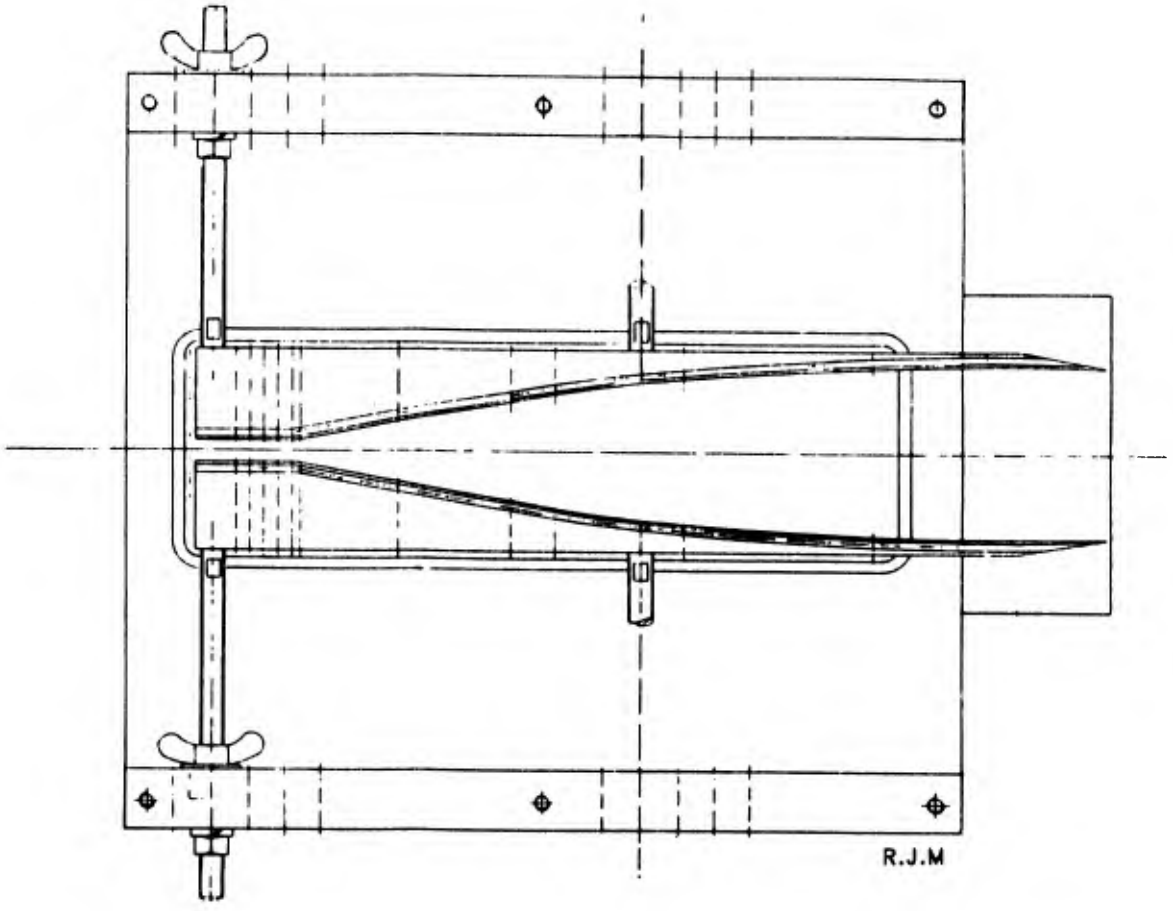

Figure 6.24 Prandtl-Meyer inlet gun tunnel model and mount assembly.

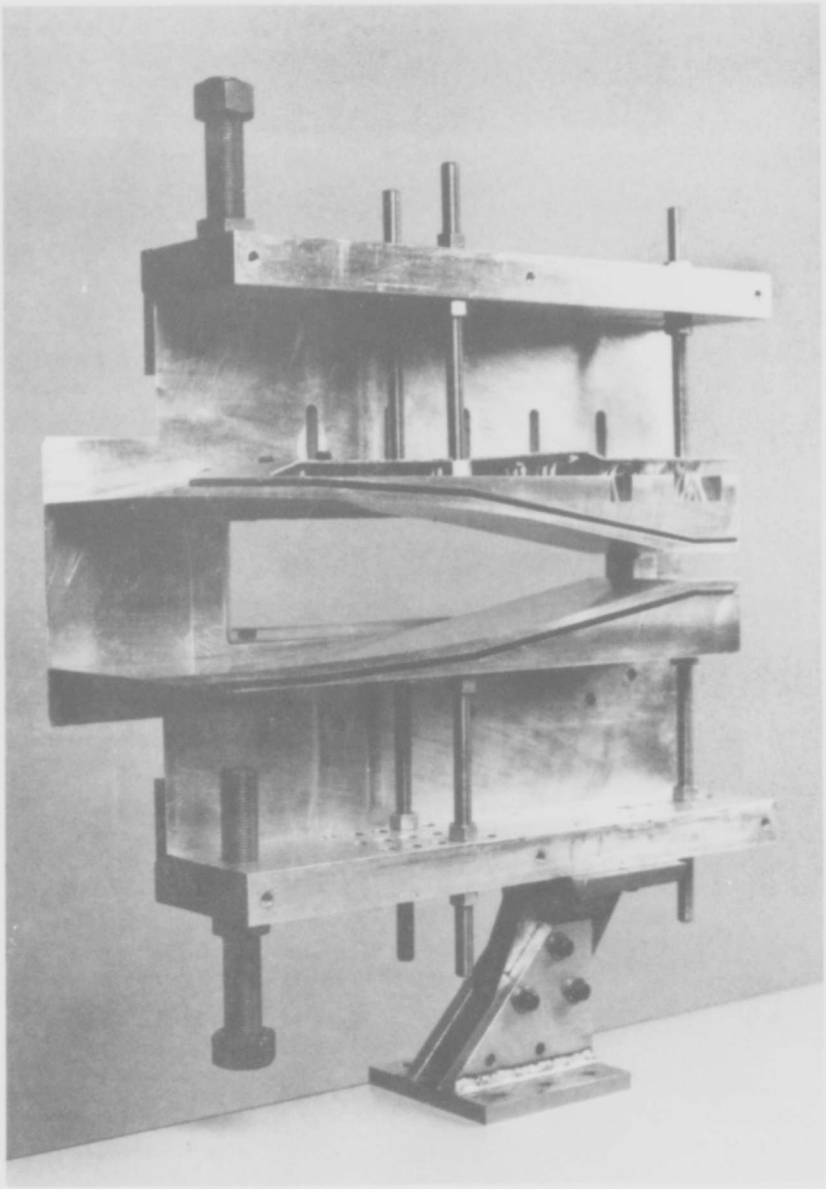

Figure 6.25 Photo of Prandtl-Meyer model and schlieren visualization mount.

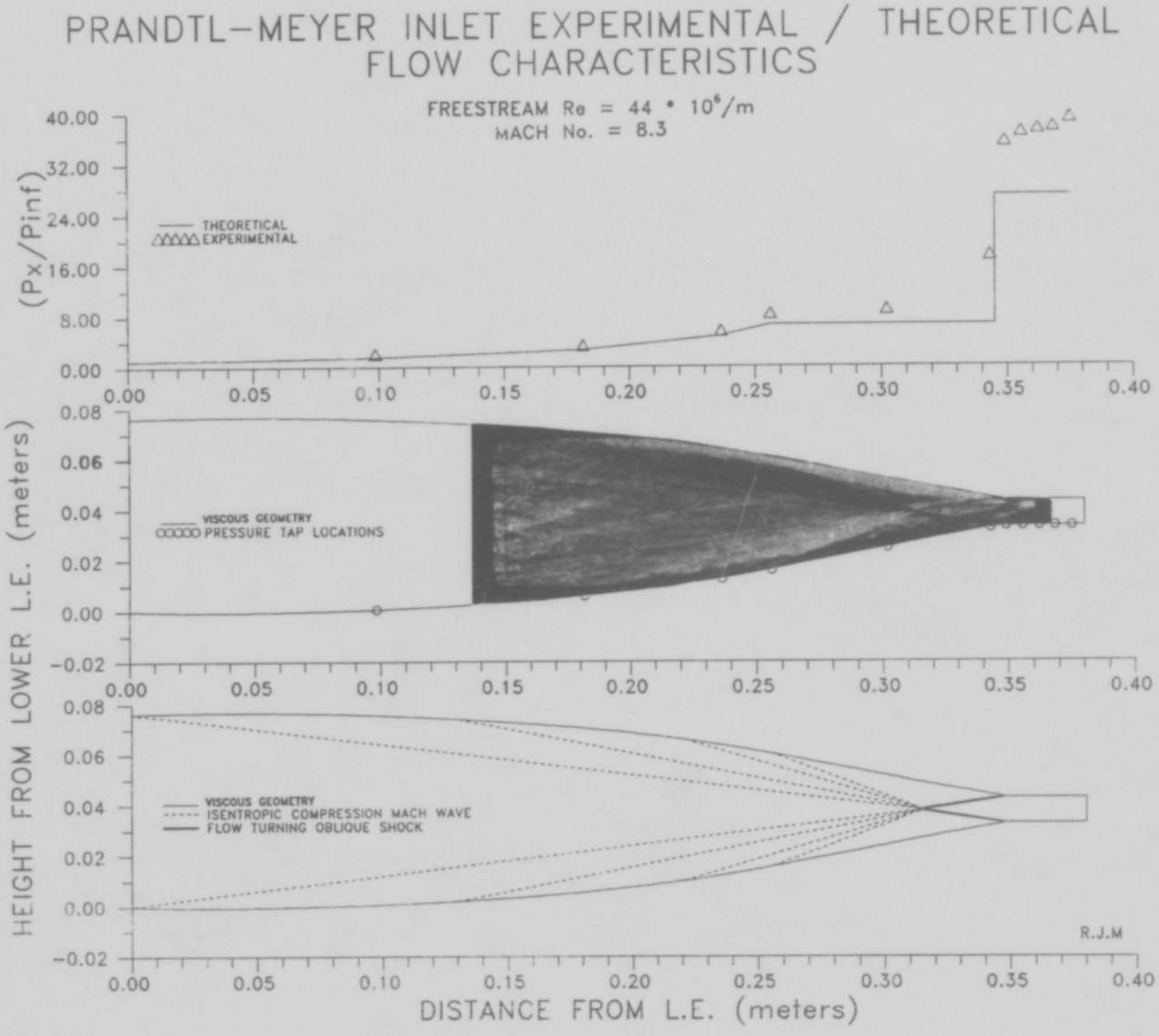

Figure 6.26 Experimental assessment of the Prandtl-Meyer through schlieren flow visualization and static pressure measurement on the compression surface.

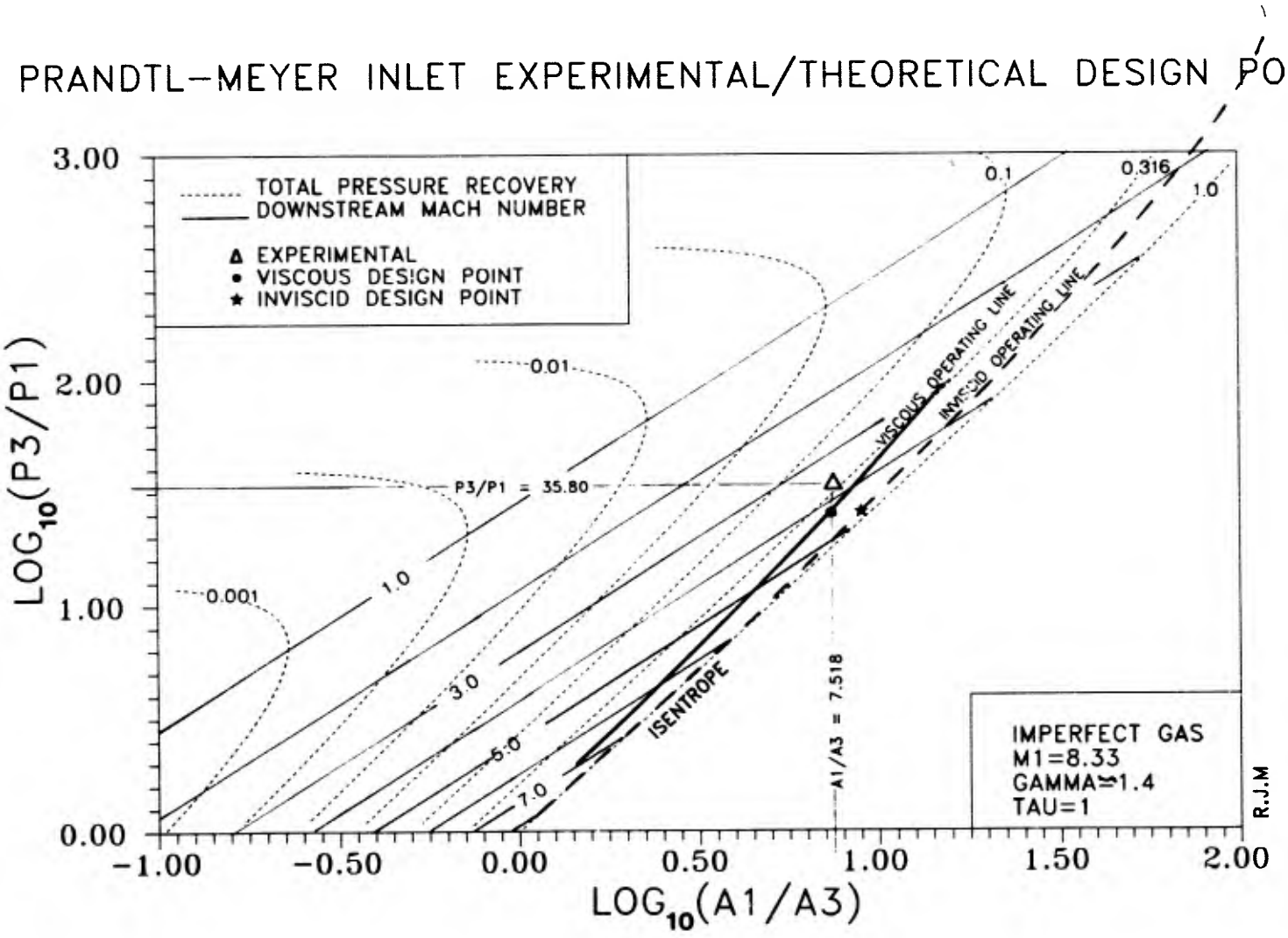

Figure 6.27 Pressure-area diagram indicating theoretical and experimental design points of the Prandtl-Meyer inlet model.

been constructed for a freestream Mach number of 8.33 and adiabatic flow in the inlet. The dashed line labelled the "INVISCID OPERATING LINE" represents the family of Prandtl-Meyer inlets with a freestream Mach number of 8.33. The horizontal distance between this line and the total pressure recovery equals 1.0 line, immediately to the right of it, represents losses caused by the oblique shock wave. The symbol "★" on the inviscid operating line is for the inviscid design at a compression ratio of 26.8370, a contraction ratio of 9.0672, a Mach number, $M_3 = 4.68$, and a total pressure recovery of 0.7633. The solid line labelled the "VISCOUS OPERATING LINE" represents the performance of Prandtl-Meyer inlets which have been boundary layer corrected using the method described above for our gun tunnel conditions. Thus the horizontal distance between the point denoted by "•" on the viscous operating line and "★" on the inviscid operating line represents the viscous losses. Since the boundary layer correction was not applied at the aft end of the inlet a higher experimental compression ratio of 35.80 was obtained. This point is shown as the "▵" and it corresponds to a total pressure recovery of 0.3 and a Mach number of $M_3 = 3.7$.

6.8 The Oswatitsch Inlet

6.8.1 Oswatitsch Inlet - Basic Flow

The Oswatitsch diffuser selected in our study consists of a centerbody and a surrounding cowl, both being axisymmetric so that a cylindrical freestream tube is captured and processed into an annular exit stream tube. The key to understanding and constructing this flow lies in the realization that the flow locally, in the neighbourhood of the cowl, is two-dimensional, exhibiting the gasdynamic features of the Prandtl-Meyer flow described in Section 6.7. With this in mind we will now describe how the air is processed in passing from the entry to the exit of the Oswatitsch inlet. Referring to Figure 6.28, the air, flowing at M_1, enters the inlet through a conical Mach wave, ac. This wave is produced by a very sharp (cusped) tip at a. The surface ab is such as to cause compression waves from ab to focus on the cowl leading edge at c. The last of these compression waves, bc, produces a local Mach number, M_2, at the cowl. Since the flow is locally of the Prandtl-Meyer type at the cowl, we can now find the amount of

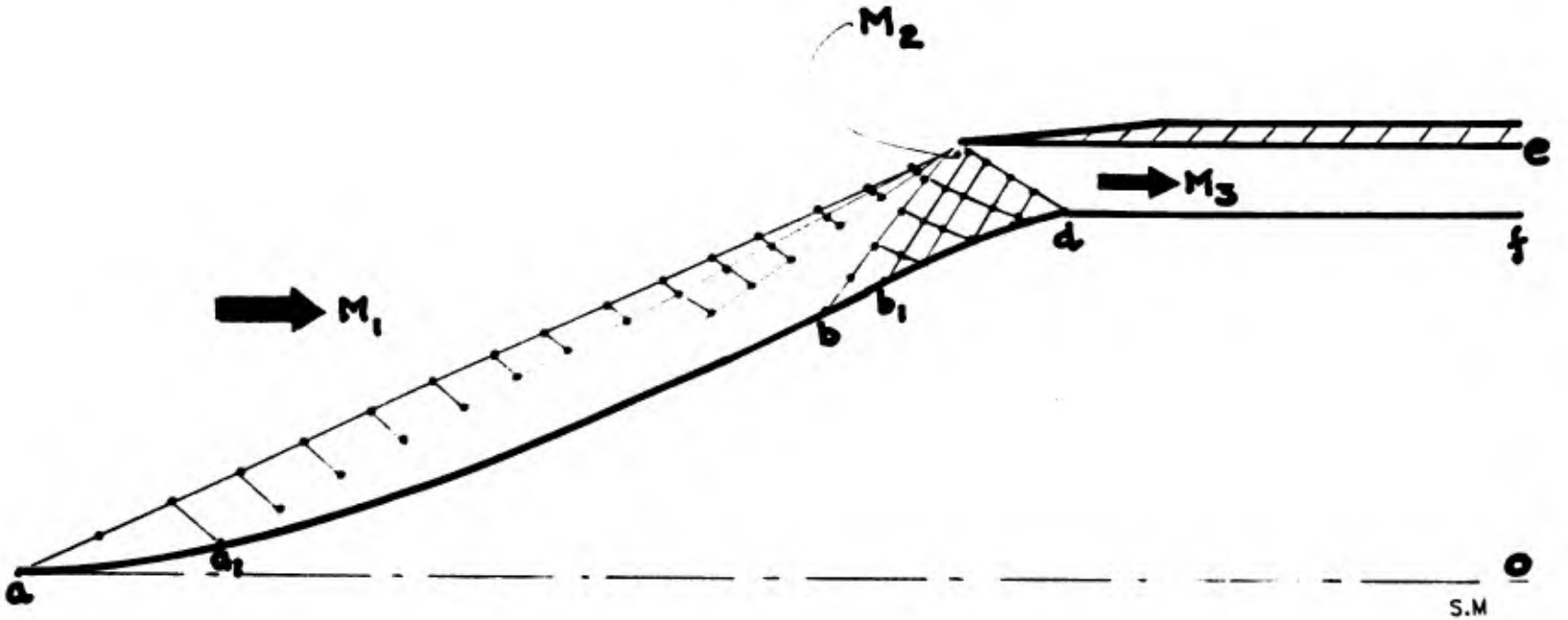

Figure 6.28 Reperesentation of the Method of Characteristics approach to defining the Oswatitsch type of flow geometry.

turning that the flow has experienced in going from M_1 to M_2 from the Prandtl-Meyer turning angle (Equation 6.8). The flow locally, near the cowl, then passes through the oblique shock which is such that the flow turning through the shock is equal, but opposite, to the turning through the immediately preceding Prandtl-Meyer compression. Oblique shock relations are then used to establish M_3 and all other quantities of interest at the exit. Somewhat surprisingly, we have calculated the inviscid performance of the axisymmetric Oswatitsch inlet using simple two-dimensional Prandtl-Meyer and oblique shock relations. The more complicated task is to find the contour, abd, required to produce the locally two-dimensional flow at the cowl and uniform and irrotational flow at the exit. The flow in region abc is calculated by first specifying a Mach number, M_2, and locating a Prandtl-Meyer compression fan in the corner, acb, with the rays of the fan at equal intervals of Mach number between M_1 and M_2. Each ray, being a c+ characteristic, can then be assigned a unique value of Mach number as well as velocity and flow direction at the point c. Thus the point c is multivalued. A series of points is then assigned on the first characteristic, this also being the free-stream Mach wave, so that the conditions at these points are the freestream conditions. The c- characteristics are projected from these points to meet the c+ characteristics coming from c. Thus, a Method of Characteristics solution is performed starting at c and progressing down towards the axis. Characteristic points are thus found on the second c+ characteristic. At every point the total mass flow passing between the point and c is calculated. When this mass flow equals the freestream mass flow (an iteration is usually required) the surface point a_1 is located. In this way, all the characteristics in the region acb and the surface ab are found. In general the characteristics are not straight and the conditions on them are not constant. This distinguishes this type of flow from the usual (planarly symmetric) Prandtl-Meyer flow.

We must now calculate the flow in region bcd, and to do this we note that the flow in region bcd is irrotational. For the flow to be irrotational in region (3) the shock must be straight and for the flow to be axisymmetric the flow must be conical. For a straight shock having a uniform downstream, the upstream conditions must be uniform also. If this is so then these conditions just upstream of the shock are precisely the conditions at the tail end of the compression fan, characterized by M_2. This then allows us to specify the flow variables at an arbitrary number of points on the front surface of the shock, cd.

Progressing form c towards d, from each of these point we construct the c+ characteristics and thereby find the surface, bd, required to produce the uniform flow in front of the shock. There was no apriori assurance that such a surface would exist. In fact there were some opinions that such a flow would not exist. However, in every case calculated, it was found that the last surface point coincided with the previously calculated corner at d, proving at least that mass was being conserved. In every case the surface, bd, turns out to be in the shape of a gentle S-curve with a slight compression near b followed by an equally slight expansion near d. From an inlet designers viewpoint it is not desirable to expand the flow in the inlet. However, this does not worry us greatly in this case because the expansion is very slight and it follows a compression which is isentropic so that no losses are incurred at least not on the inviscid level. The virtue of this particular surface is of course that it produces the straight shock, cd, and the resulting uniform irrotational flow in region (3). Furthermore, it makes it possible to predict the performance of the Oswatitsch inlet being assured that such flow actually exists away from the cowl leading edge.

6.8.1.1 Design Verification by Euler Code

The design method proposed above was checked by space-marching Euler codes at the Applied Physics Laboratory of Johns Hopkins University by D. M. Van Wie, M. W. Thompson and G. P. Corpening (Ref. 6.20). The following four cases were calculated with the Euler codes:

CASE #	M_{inf}	M_2
1	3.00	2.5
2	8.33	6.2
3	8.33	6.0
4	25.0	14.0

All inlets have a radius of 1 so that their lengths are numerically close to their respective freestream Mach numbers. The Euler code required a finite-angle cone for the forebody tip whereas the Oswatitsch geometries had zero slope at the tip. This produced some slight variations between the Method of Characteristics and the Euler solutions. Also some numerical divergence was apparent in the Euler code near the shoulder (at d). Nevertheless, the Euler code did calculate a straight shock projecting towards the corner. Surface pressures and Mach numbers for cases 1, 2, and 4, are presented for the two methods in Figures 6.29a, b, and c. In this figure "Inviscid" means the Euler code and "Molder" stands for the Method of Characteristics design results.

In each case there are small discrepancies at the beginning and end of the inlet due to the effects mentioned above. Overall, however, correspondence between the design and the analysis is very good. In each case the compression and expansion flow calculations agree to within less than 1% accuracy. Figure 6.30 shows details of the Euler isobars in the exit annulus for Case 1. The shock from the cowl appears to be incident on the centerbody at the corner. A reflecting wave structure is predicted with pressure ratios, p_3/p_1, ranging from 3 to 6.5. The Method of Characteristics pressure ratio is 6.5715.

6.8.2 Oswatitsch Inlet - Inviscid Design

The inviscid design parameters are given in Table 6.2. Note that with a matched compression ratio of 26.8730, the thermodynamic variables are exactly the some as those for the Prandtl-Meyer Inlet. Thus, the inviscid performance of these two inlets is the same with a total pressure recovery of 0.7633 for both. The geometric variables of capture area and overall contraction ratio are also the same for both inlets at 58.06 cm^2 and 9.0762 respectively. Mach number is typically reduced from 8.33 to 6.2 by the pseudo-Prandtl-Meyer compression and further to 4.68 by the conical shockwave. The pressure ratio across the pseudo-Prandtl-Meyer compression is 6.5717 and that across the conical shock is 4.0839. This latter figure is well below that required to cause separation of a turbulent boundary layer at Mach 6.2. The geometric variables are given in metres.

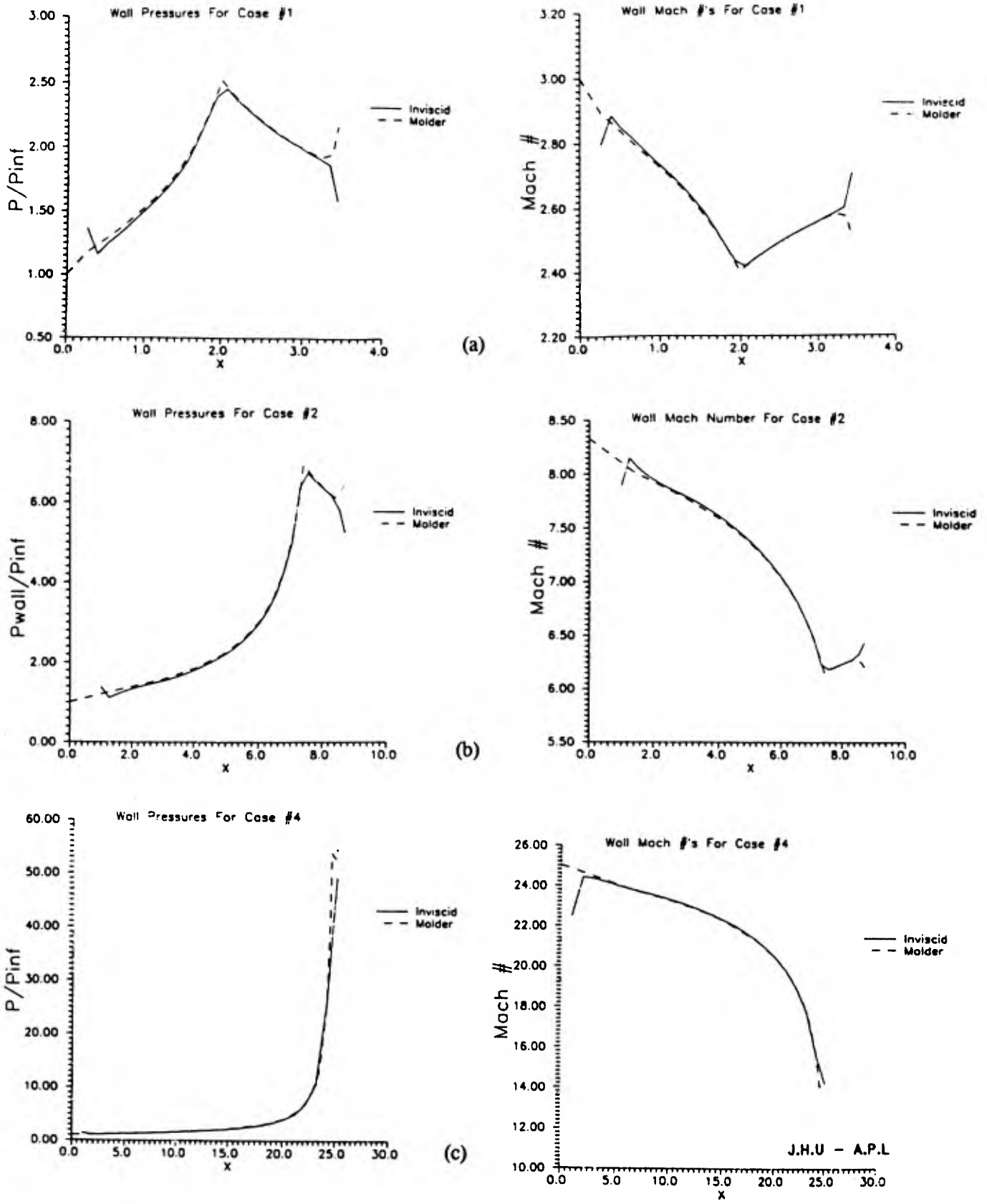

Figure 6.29 Comparison of Oswatitsch surface and flow conditions assessed by space marching Euler code and the Method of Characteristics solution.

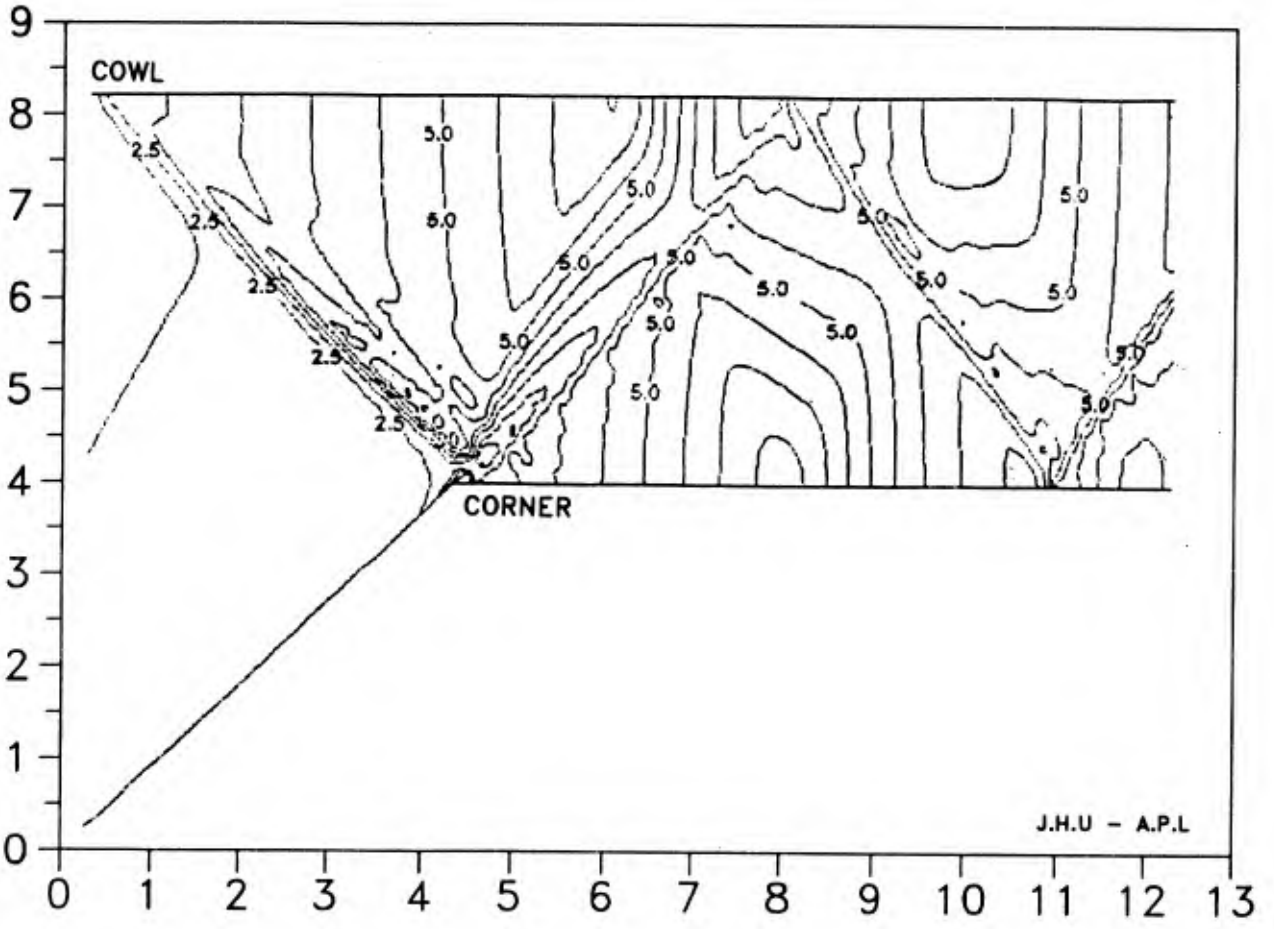

Figure 6.30 Pressure isobars determined by Euler code simulation of an Oswatitsch compression. Reflected shocks in the annulus are indicated.

6.8.3 Oswatitsch Inlet - Viscous Design

The contoured inviscid surface of the axisymmetric centerbody was corrected for the displacement effects of a boundary layer by an appropriate reduction of its diameter. No correction was applied at the tip because this would have resulted in the removal of a considerable (1 to 2 cm) length of the tip entirely and it was felt that the existence of the tip and its effect on the leading wave was more important than the effect of its boundary layer. This assumption may not be justified, especially at higher Mach numbers. The whole question of tip effects deserves further investigation.

No boundary layer correction was applied to the exit passage because no calculation or experiment was available on the nature of the interaction of the shock and the boundary layer at the convex corner. Thus it was expected that measured pressures at the exit would be somewhat higher than predicted by inviscid theory.

To a first approximation, the effect of enlarging the flow passage by the displacement thickness of the boundary layer is to preserve the inviscid flow, including the compression ratio, and to change the wall shape, including the contraction ratio. Using the contraction and compression ratios as primary measures of inlet performance allows us to calculate the performance of the viscous Oswatitsch Inlet. The parameters of this *viscous design* are given in Table 6.2. The compression ratio remains unchanged at 26.8370. The contraction ratio is reduced from the inviscid value of 9.0672 to 7.6083. As a result, the total pressure recovery is reduced from 0.7633 to 0.4423. This reduction in effect represents the boundary layer loss. The Mach number at the exit is 4.2450, the pressures remain unchanged but the average temperature at the exit is 17% higher due to viscous effects. Boundary layer calculations were done by the method described for the Prandtl-Meyer inlet.

It is important to compare the theoretical viscous results for the Prandtl-Meyer and the Oswatitsch inlets because such a comparison, in this case, tells us whether the axisymmetric or two-dimensional inlet has larger boundary layer losses. The theoretical comparison is given in Table 6.2. The major result of this table is that for the Oswatitsch inlet, the boundary layer displacement thickness is less than that for the Prandtl-Meyer inlet. Consequently, the contraction is higher, as is the efficiency. At first sight the margin appears small, being the difference between 0.4263 and 0.4423. This is part of a 0.34 loss in η_{pt} due to

the boundary layer so that we can conclude that boundary layer losses are less on the Oswatitsch inlet by (.4423 - .4263)/.34 = .05 or 5%. This figure would be higher if losses due to the sidewalls on the Prandtl-Meyer inlet were included.

6.8.4 Oswatitsch Inlet - Model Construction

Based on the viscous design, described in the previous section, and Oswatitsch Inlet was constructed for testing in the Ryerson/U of T Gun Tunnel at a Mach number of 8.33 and a Reynolds numbers 23 * 10^6/m and 44 * 10^6/m. The cowl diameter is 8.60 cm giving a streamtube capture area of 58.06 cm^2. The length of the model is 46.2 cm. The model, as shown in Figures 6.31 and 6.32a, has been designed for verification of the inviscid compression profile, newly designed for this study by the method of characteristics solution previously described. Since the flow detail is primarily external, schlieren photographs will also aid in this analysis. Figure 6.32b shows the model mounted in the gun tunnel test section. Some of the schlieren apparatus can be seen in the photograph.

The model centerbody is metric, supported internally on linear bearings for the measurement of aerodynamic drag. Static pressures were measured on the base of the centerbody. The vibration induced internal forces were measured using the accelerometer, also base mounted.

On this external/internal axisymmetric type of model, internal space is in short supply. Transducers are lead mounted from the surface tap to individual transducer housings which are secured in the channel above the bearings or in the load cell chamber. As in the Prandtl-Meyer inlet, it was found that lead lengths of less than 18 cms of 0.8 mm dia. tygon tubing precluded unacceptable pneumatic lag in the readings from the high pressure annulus and downstream compression surface. Significantly shorter leads were necessary towards the leading edge. Only a 2 cm length of tube gave adequate response at the forward tap location.

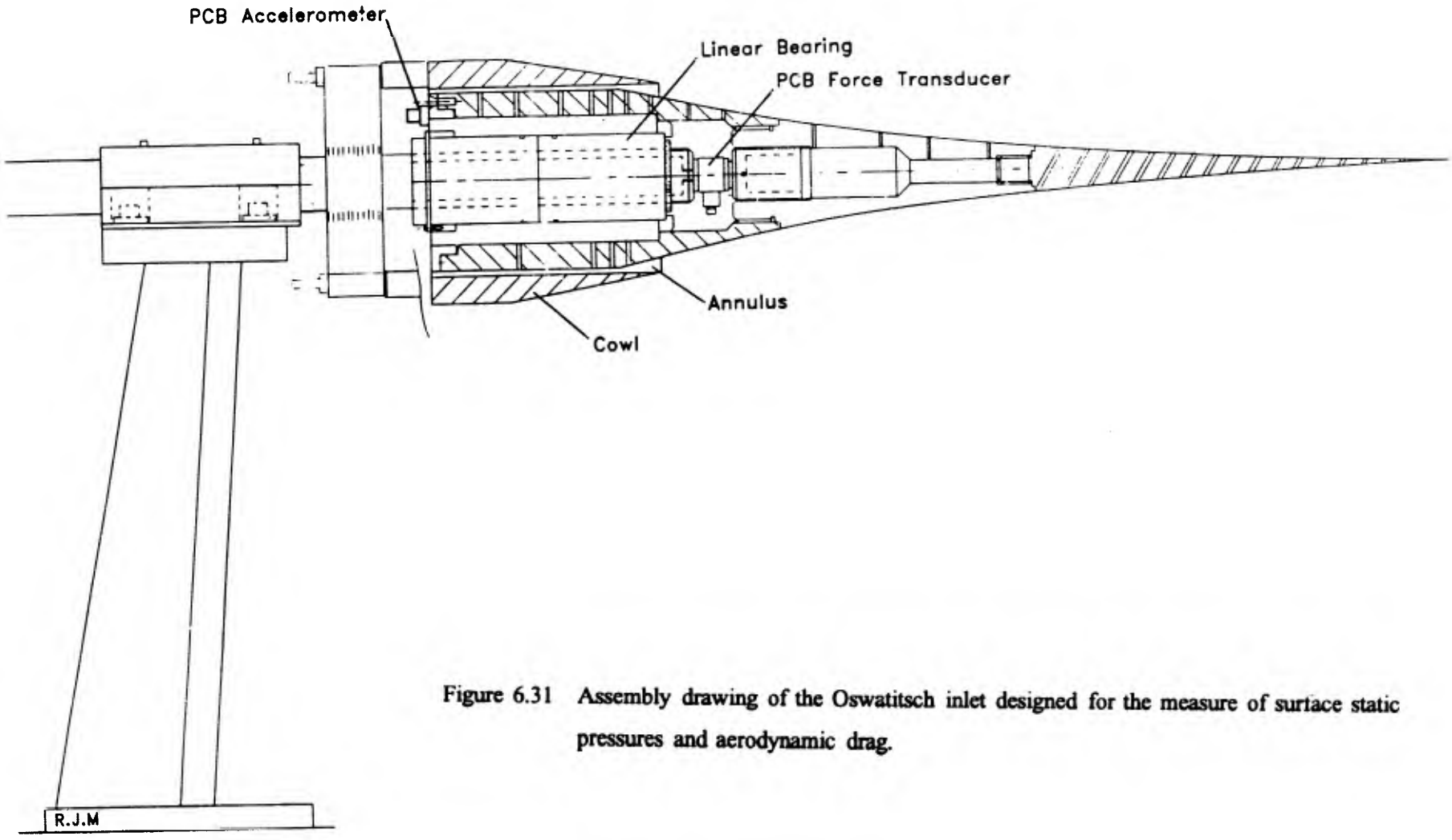

Figure 6.31 Assembly drawing of the Oswatitsch inlet designed for the measure of surface static pressures and aerodynamic drag.

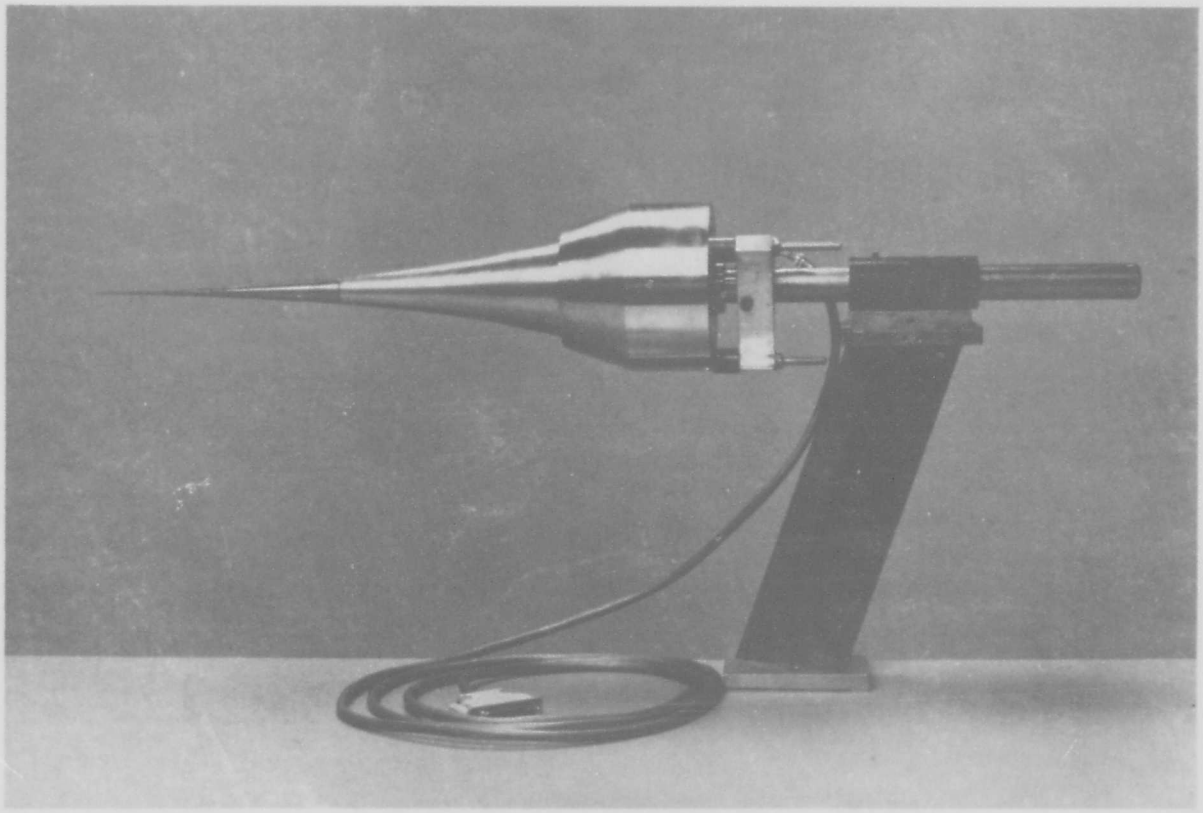

Figure 6.32a Photo of the Oswatitsch inlet model.

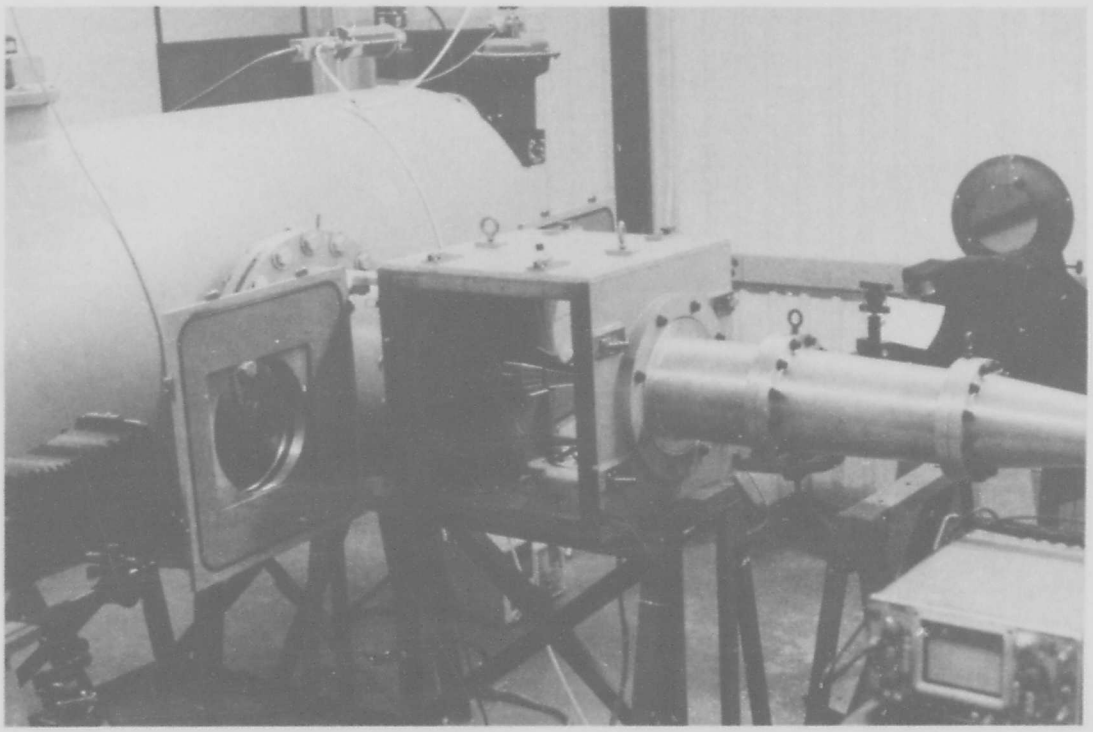

Figure 6.32b Photo of the gun tunnel test section area showing the schlieren apparatus and the Oswatitsch inlet model mounted in the test section.

6.8.5 Oswatitsch Inlet - Results

6.8.5.1 Flow Starting and Wave Structure

Initial experiments with the Oswatitsch inlet began with schlieren visualization of the centerbody with the cowl removed. A precise measurement of the point of experimental coalescence of the isentropic compression Mach waves (i.e. the cowl point) could be in this way obtained. Because of the difficulty with the manufacture of the Oswatitsch centerbody needle-like point, the radii over the first 3 cms of the spike are necessarily oversized to the viscous geometry, with a .5mm radius flat surface on the leading edge. This flat surface produces a weak shock which can be seen in the photo of Figure 6.33 well above the cowl point. The compression waves, including those emanating from the off design geometry of the initial 3 cm, are observed to coalesce at almost precisely at design cowl point. In fact, the point is measured to be about 15% higher than the initially predicted laminar boundary layer displacement thickness at this point. Boundary layer transition, however, is evident in the Figure 6.33 and 6.34 schlieren photos. Subsequent re-assessment of the boundary layer using Stan6 and improved information on transition and freestream Reynolds number has led to a boundary layer prediction which includes transition at Re_m = 1250. At the cowl station of the centerbody the boundary layer thickness was found to be 11% thicker than the purely laminar prediction. The additional 4% of the boundary layer displacement thickness discrepancy could easily be within the reading error. Our inviscid design and viscous correction are clearly well substantiated experimentally. It is important to be aware, however, that this additional displacement thickness calculated under the knowledge of a transitional boundary layer, was not subsequently physically removed from the surface of the centerbody. All experimental results are for a laminar correction only, with a potential small mass flow loss.

6.8.5.2 Pressure Measurements and Flow Verification

The predicted and observed surface pressures are shown in Figure 6.34 with the cowl in place. The accuracy of the predicted isentropic compression is again verified by the evident Mach waves emanating from the centerbody. In this photograph, the blunted point of the centerbody has been filed creating a

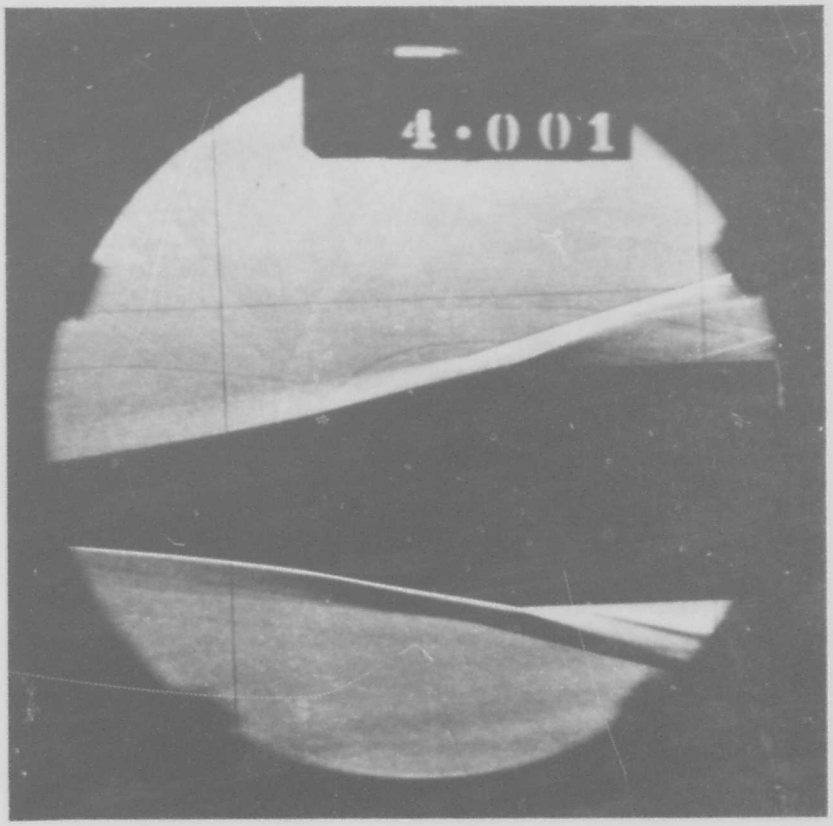

Figure 6.33 Initial schlieren of Oswatitsch centerbody (cowl removed) for verification of predicted Mach wave coalescence at the cowl point.

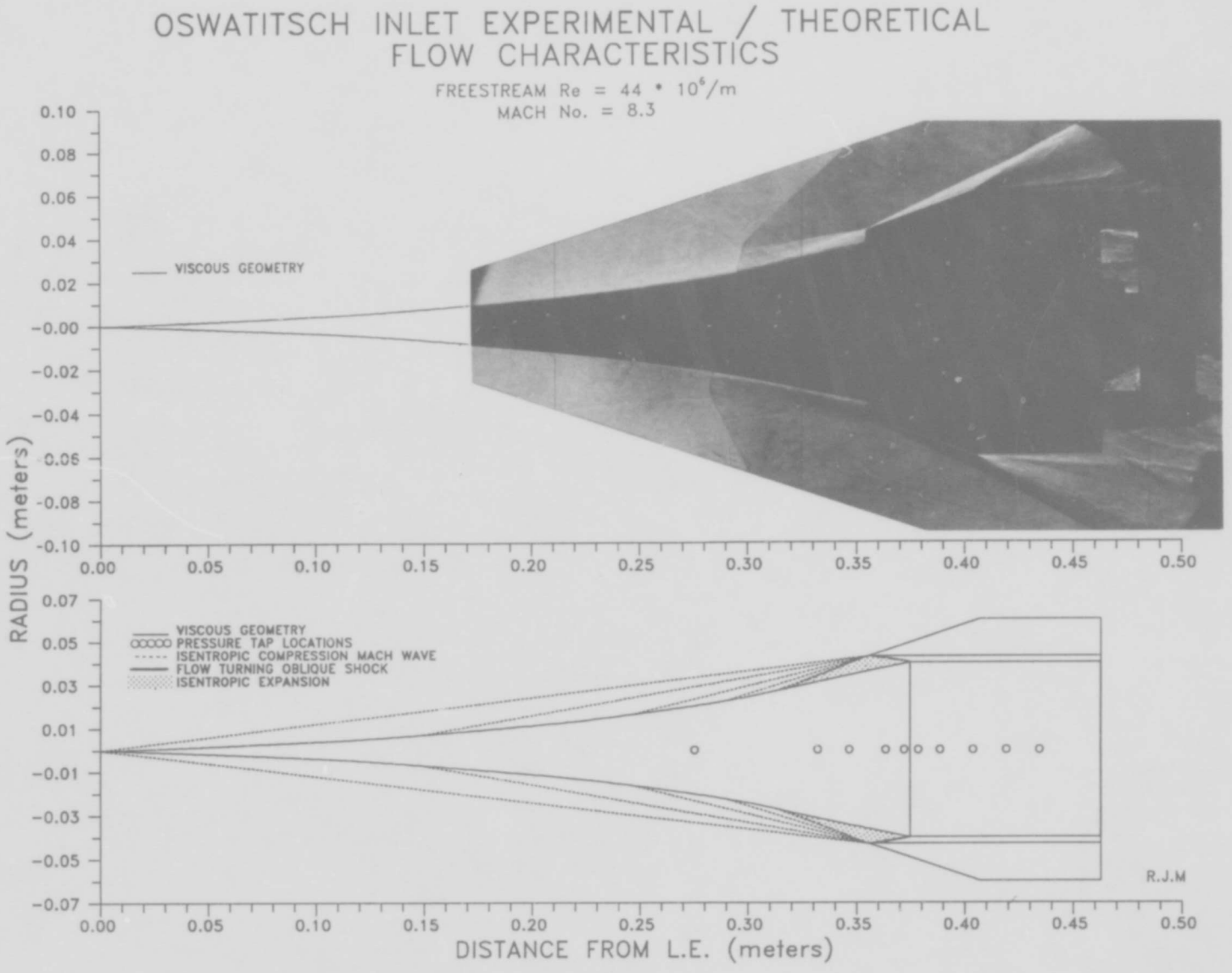

Figure 6.34 Theoretical and experimental compression characteristics are shown for verification of design and demonstration of successful diffuser start.

shallower leading edge shock angle which more closely approaches the cowl point. Supersonic exit flow is also evident in the annulus.

The isentropic compression on the forebody is followed by a re-expansion region prior to the corner shock. The experimental assessment of this region has been detailed in Figure 6.35. The theoretical and measured static pressure profile is shown in the upper figure. The tailored re-expansion begins at the 32 cm station and continues to within 1 cm of the turning shock. This is clearly verified by the surface static pressure measurements shown. The lower figures compare the experimental and predicted Mach wave pattern up to the end of the isentropic compression region. The theoretical compression fan, coalescing at the cowl is clearly evident in the schlieren photo.

The predicted and experimental static pressure ratios along the inlet profile are depicted in Figure 6.36 for both the 44 * 10^6/m and 23 * 10^6/m freestream Reynolds numbers. The experimental values have been averaged from the results of several repeated runs. The scatter of the data at the forbody stations have a standard deviation of ±1.5% to the averaged value shown. The annulus pressures were extremely sensitive to cowl alignment and precise adjustment of the attack angle. A +0.25° model inclination to the tunnel axis resulted in excellent flow symmetry as determined by diametrically opposed station pressure taps. Further discussion of the error analysis can be found in Appendix A.

A sharp pressure rise is observed at the turning shock for the 44 * 10^6/m Reynolds number case. This was also observed in the Busemann inlet under the same flow condition. Pressures a.e then observed to reduce with some fluctuation undoubtably caused by reflected shocks in the narrow annulus. This wavy nature seems to substantiate the waves predicted by the Euler code of Van Wie, Corpening, and Thompson (Ref. 6.20). From these findings, we observe that;

a) the inlet is started,

b) the flow structure appears as predicted,

c) the predicted and measured surface static pressures are in very good agreement.

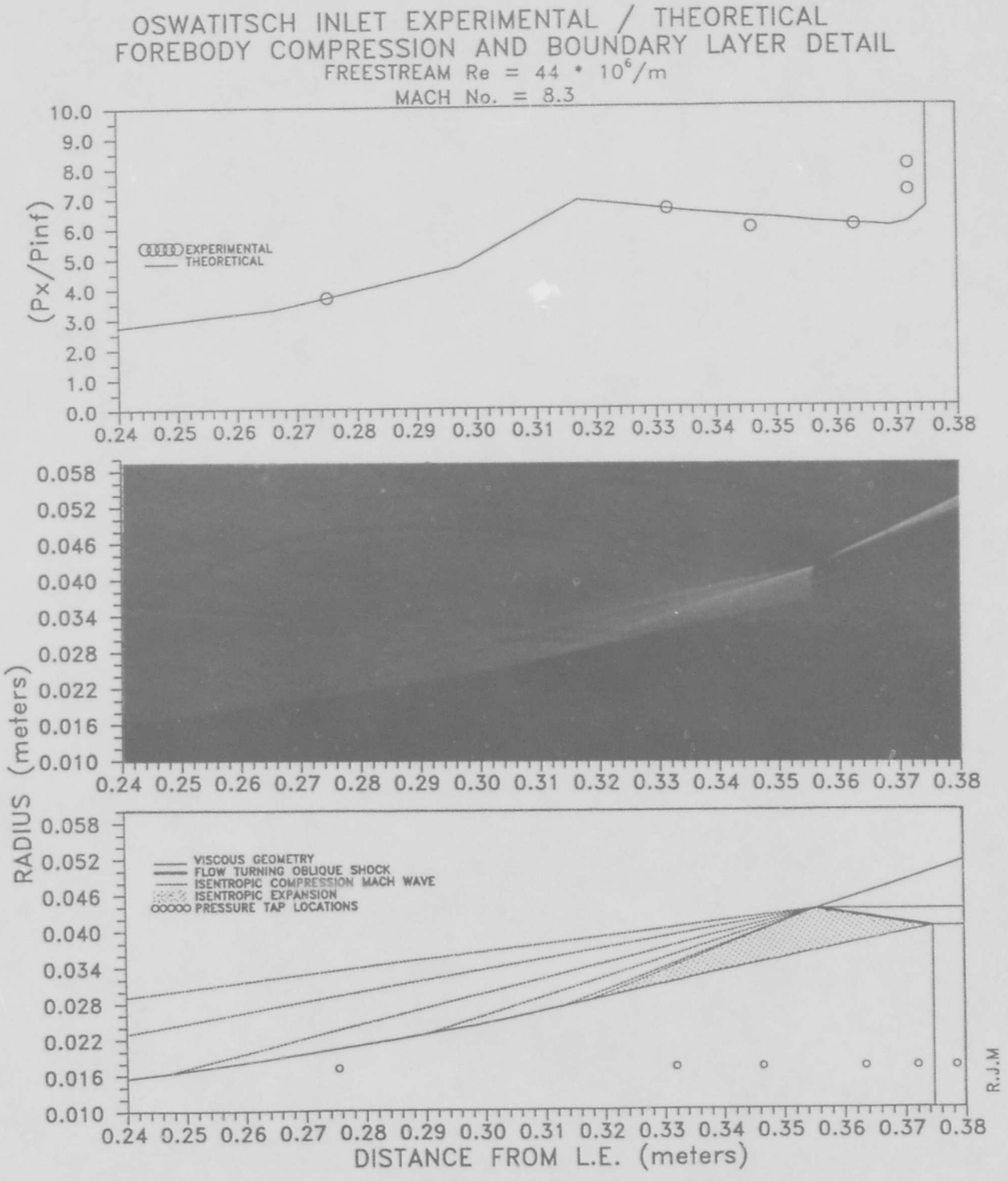

Figure 6.35 Detailed schlieren and pressure assessment of the re-expansion region on the downstream forebody with comparison with the predicted flow characteristics.

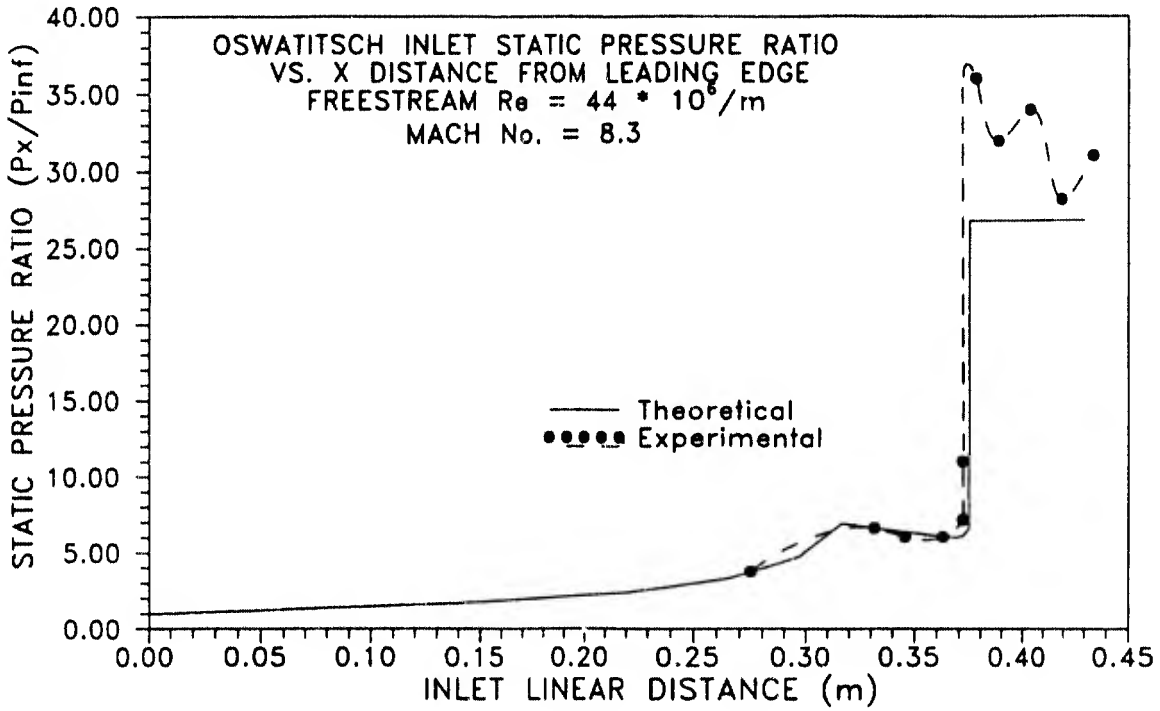

(a)

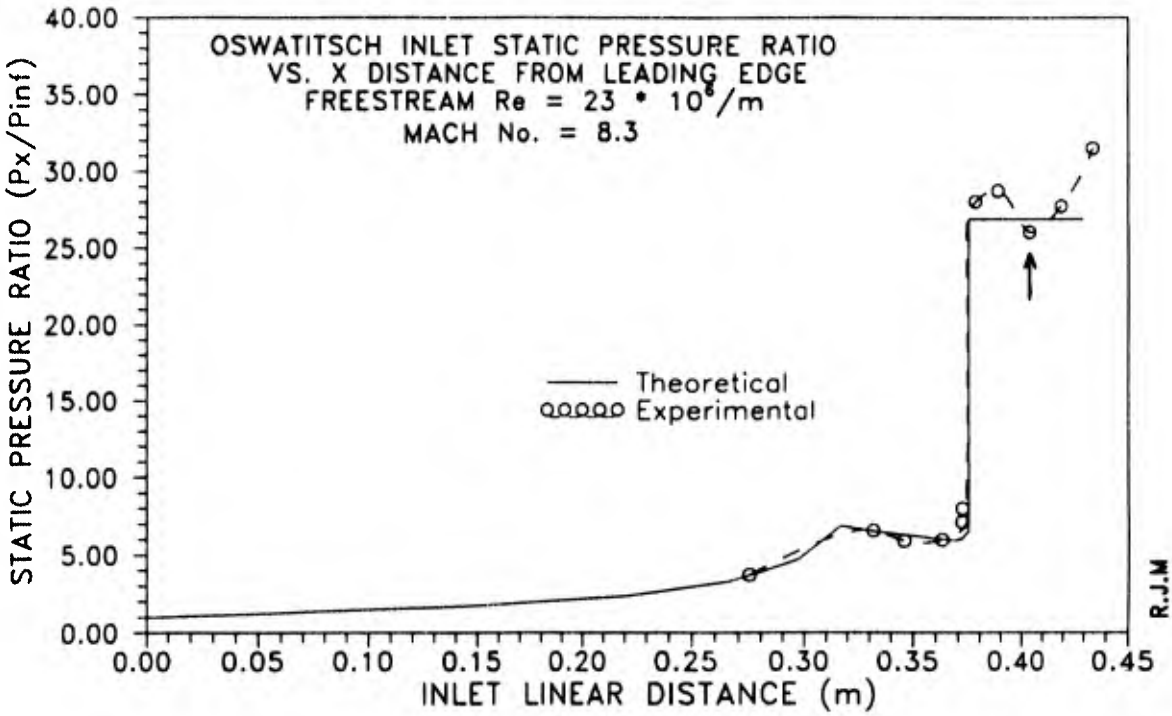

(b)

Figure 6.36a-b Theoretical and experimental static pressure profiles of the Oswatitsch inlet forebody and annulus.

The performance of the Oswatitsch inlet is shown in the contraction/compression ratio plot in Figure 6.37. This plot has been constructed for an imperfect gas, however, the present inlet conditions are such that a plot for γ=1.4 looks exactly as the one here presented for the imperfect gas. This plot is constructed for a freestream Mach number of 8.33 and adiabatic flow in the various inlets. The dashed line labelled "INVISCID OPERATING LINE" represents the whole family of Oswatitsch inlets operating at a freestream Mach number of 8.33 and diffusing to various downstream Mach numbers. The horizontal distance between this line and the total pressure recovery = 1.0 line represents losses caused by the oblique shock wave. The symbol "★" on the "INVISCID OPERATING LINE: is for our inlet of a compression ratio of 26.8370, and a contraction ratio of 9.0672, a Mach number of 4.68, and a total pressure recovery of 0.7633. The "VISCOUS OPERATING LINE" represents the performance of Oswatitsch inlets which have been boundary layer corrected for our gun tunnel conditions. Thus the horizontal distance between the point denoted by "·" on the "VISCOUS OPERATING LINE" and "★" on the "INVISCID OPERATING LINE" represents the viscous losses.

An experimental total pressure recovery of Pt_3/Pt_1= 0.485±0.008 has been calculated using the annulus static pressure marked by the "†" on Figure 6.36b. This is represented by the "o" on Figure 6.37.

6.8.5.3 Drag Measurements

Measurements of centerbody drag on the Oswatitsch inlet produced inordinately high values with high levels of noise. The noise was due to the difficulty of isolating the centerbody from tunnel vibration. High levels of drag are as yet unexplained.

6.9 Comparison of Three Inlets

In this section we will compare the inviscid, viscous and experimental performance of the Busemann, Oswatitsch and Prandtl-Meyer inlets. Since the similarities of these inlets have already been discussed in Section 6.2, we will concentrate on the differences that are of an aerodynamic nature and contribute to the performance of the inlet.

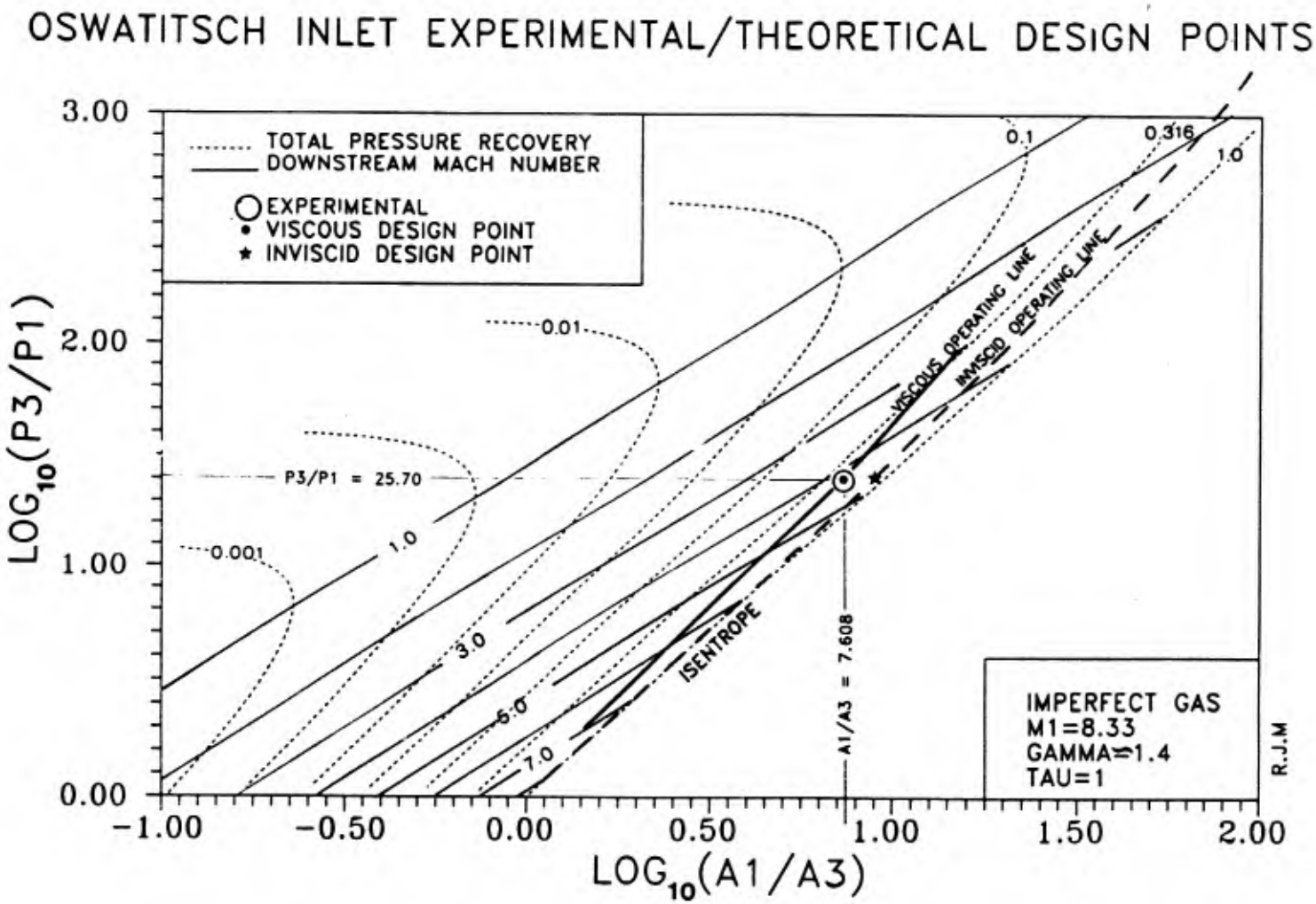

Figure 6.37 Pressure-area diagram showing the experimental and theoretical performance of the Oswatitsch inlet Model.

6.9.1 Inviscid Flow

Busemann type diffuser flow is initially turned *towards* the axis. This turning has the effect of reducing the Mach number and increasing the pressure, and even if no further turning occurs the flow is now converging and further compressing. This feature, being unique to the Busemann diffuser, leads to isentropic compression without flow turning so that when the flow is returned to the freestream direction by the terminal shock, at the exit of the inlet, only a small amount of flow turning is required. As a result, the losses associated with the shock are small and the efficiency of the inlet is high.

For both the Oswatitsch and Prandtl-Meyer inlets, compression is accomplished by Prandtl-Meyer turning only - and consequently, there is no compression by area contraction so that the flow has to be turned through a larger angle to make it parallel to the freestream. Thus, the losses associated with this turning are higher than for the Busemann inlet and the resulting efficiencies are lower. The inviscid total pressure recoveries of the Busemann, Oswatitsch, and Prandtl-Meyer inlets are 0.9831, 0.7633, and 0.7633 respectively. Clearly, on an *inviscid basis*, the Busemann inlet is superior to the other two.

6.9.2 Viscous Flow

The calculated viscous flow efficiencies of the Busemann, Oswatitsch and Prandtl-Meyer inlets are 0.4522, 0.4433, and 0.4263. The Busemann inlet has lost its advantage, possibly due to the large leading edge area being subjected to a high frictional drag. The same degree of loss is not apparent for the Prandtl-Meyer inlet - probably because no account has been taken of the influence of the sidewalls on the viscous flow losses. An accounting for the effect of sidewalls would have led to a lower efficiency value for the Prandtl-Meyer inlet. It is seen that viscosity has a major effect on inlet performance and it is as important as the inviscid flow structure (and inlet geometry) in influencing inlet performance. For our particular inlet designs, there appears no significant performance advantage to one or the other of the three inlets *on purely theoretical grounds.*

6.9.3 Experimental Results

The experimental values for the three inlets are given in Tables 6.3, 6.4, and 6.5. The measured performance of the Busemann and Oswatitsch inlets are identical. It appears that the superior inviscid performance of the Busemann inlet is lost to the higher viscous losses. This suggests a further investigation to see how this situation changes with Mach number, Reynolds number, and amount of diffusion. The performance of the Prandtl-Meyer inlet is lower than the other two presumably because of sidewall and corner flow effects.

6.10 Conclusions

6.10.1 Busemann Inlet

Theory, based on the solution of the Taylor-Maccoll equation, has been presented and used to generate the contour of an internal flow axisymmetric hypersonic air inlet for a freestream Mach number of 8.33 and a uniform irrotational exit flow at Mach number of 5.39. The contour coordinates were corrected for boundary layer displacement and used to machine an axisymmetric model. Independent calculations by Euler and PNS codes were used to verify the inviscid and viscous calculations. Tests conducted at Mach 8.33 produced a compression ratio of 25.90±.07, a total pressure recovery of 0.484±.008, a drag of 56.8 N at a contraction ratio of 7.645±.004, all in good agreement with theoretical predictions.

6.10.2 Prandtl-Meyer Inlet

A planarly symmetric hypersonic air inlet has been designed and constructed on the basis of inviscid flow consisting of Prandtl-Meyer compression followed by plane oblique shock compression and viscous boundary layer theory. Schlieren pictures and pressure measurements on a model inlet tested in a hypersonic gun tunnel at Mach 8.33 are in satisfactory agreement with theory indicating that the postulated flow exists and that it can be calculated using the presented inviscid and viscous theories. Presentation of inlet operating characteristics on the compression/contraction plot clearly illustrates inlet performance and the effect of various losses on this performance.

BUSEMANN INLET

DESIGN PROPERTY	INVISCID DESIGN	VISCOUS DESIGN	EXPERIMENTAL
P_3/P_1	26.7420	26.7420	25.9 ± 0.7
A_1/A_3	9.8001	7.6450	7.645 ± 0.004
Pt_3/Pt_1 (ηpt)	0.9831	0.4522	0.484 ± 0.008 *
M_2	5.3800		
M_3	4.8990	4.2650	4.34 ± 0.05 **
P_3/P_2	1.7167	1.7167	
P_2/P_1	15.5775	15.5775	
T_3/T_1	2.5687	3.2080	
T_3/T_2	1.1723		
T_2/T_1	2.1911		
RAMP LINEAR DISTANCE	0.44261		
CORNER X	0.44132	0.44141	0.441410 ± 0.000005
CORNER Y	0.02933	0.02744	0.027440 ± 0.000005
COWL POSITION	.3585,.0430	.3585,.0430	
ENTRY RADIUS	0.04399	0.04399	0.044399 ± 0.000005
TOTAL DRAG		53.8 N	56.8 N

* CALCULATED FROM PRESSURE DATA
** MEASURE FROM SCHLIEREN PHOTO
DIMENSIONS IN METERS (m)

R.J.M

Table 6.3 The experimentally measured values of the Busemann inlet geometry and flow properties are compared to the theoretical predictions.

OSWATITSCH INLET

DESIGN PROPERTY	INVISCID DESIGN	VISCOUS DESIGN	EXPERIMENTAL
P_3/P_1	26.8370	26.8370	25.7 ± 0.7
A_1/A_3	9.0672	7.6083	7.609 ± 0.004
Pt_3/Pt_1 (ηpt)	0.7633	0.4423	0.485 ± 0.008
M_2	6.2000		
M_3	4.6800	4.2450	4.35 ± 0.05 *
P_3/P_2	4.0839	4.0839	
P_2/P_1	6.5715	6.5715	
T_3/T_1	2.7660	3.2310	
T_3/T_2	1.6150		
T_2/T_1	1.7130		
RAMP LINEAR DISTANCE	0.37748		
CORNER X	0.37460	.37469	0.374690 ± 0.000005
CORNER Y	0.04007	.04006	0.040060 ± 0.000005
COWL POSITION	.3555,.0430	.3555,.0430	(.355,.044) ± 0.001 **
ENTRY RADIUS	0.04399	0.04399	0.04399 $\pm .000005$

R.J.M

* CALCULATED FROM PRESSURE DATA
** MEASURE FROM SCHLIEREN PHOTO
DIMENSIONS IN METERS (m)

Table 6.4 The experimentally measured values of the Oswatitsch inlet geometry and flow properties are compared to the theoretical predictions.

PRANDTL-MEYER INLET

DESIGN PROPERTY	INVISCID DESIGN	VISCOUS DESIGN	EXPERIMENTAL
P_3/P_1	26.8370	26.8370	36^{+1}
A_1/A_3	9.0672	7.5178	7.514 ± 0.004
Pt_3/Pt_1 (η_{pt})	0.7633	0.4263	0.240 ± 0.009
M_2	6.2000		
M_3	4.6800	4.2165	3.57 ± 0.05 *
P_3/P_2	4.0839	4.0839	
P_2/P_1	6.5715	6.5715	
T_3/T_1	2.7660	3.2657	
T_3/T_2	1.6150		
T_2/T_1	1.7130		
RAMP LINEAR DISTANCE	0.35041		
CORNER X	0.34783	.34792	0.347920 ± 0.000005
CORNER Y	0.03394	.03303	0.033030 ± 0.000005
COWL POSITION	.3151,.0381	.3151,.0381	(.313,.0380) ± 0.001 **

R.J.M

* CALCULATED FROM PRESSURE DATA
** MEASURE FROM SCHLIEREN PHOTO
DIMENSIONS IN METERS (m)

Table 6.5 The experimentally measured values of the Prandtl-Meyer inlet geometry and flow properties are compared to the theoretical predictions.

6.10.3 Oswatitsch Inlet

An axisymmetric, centerbody/cowl-type hypersonic air inlet has been designed to have uniform and irrotational flow at the exit and to have the same inviscid performance as a two-dimensional Prandtl-Meyer inlet. As a result the performance of this inlet can be easily calculated from Prandtl-Meyer flow and oblique shock equations. The centerbody contour required to produce this flow is calculated using the Method of Characteristics. This is believed to be the first demonstration of such flow. An independent downstream-marching Euler code and experimental results confirm the existence of the calculated flow. Schlieren photography and surface static pressure measurements agree very well with theoretical predictions. A comparison of viscous losses on the Prandtl-Meyer inlet and the Oswatitsch inlet indicates that viscous losses are smaller on the pointed Oswatitsch inlet than on the leading-edged Prandtl-Meyer inlet.

6.10.4 Inlet Comparisons

Inviscid theory indicates that the Busemann inlet is the most efficient and the Oswatitsch and Prandtl-Meyer inlets are the same. Viscous theory rates the inlets as being equally efficient. Experiment shows that the Busemann and the Oswatitsch inlets have the same performance and the Prandtl-Meyer inlet has the lowest performance.

6.10.5 General Aspects

A gun tunnel is a suitable facility for testing hypersonic air inlets because;

a) high contraction inlets can be impulsively started,

b) at moderate total pressures (~25 MPa) and Mach numbers (8 to 9), the static pressures in the test section are high enough to give adequate pressure transduce response within the ~10 ms useful running time of the tunnel,

c) using the double-diaphragm technique makes data runs repeatable to better than 1%, this makes it possible to average out high frequency noise from data,

d) because of the relatively low total temperatures (800 to 1000 K) tunnel nozzle real gas effects are minimal and hypersonic inlet models can be designed on the basis of a constant value of specific heats, γ=1.4.

6.11 References

6.1. Fillion, M., "The Shuttle Reborn", *Popular Mechanics,* Aug. 1988.

6.2. Pandolfini, P., "Instructions for Using Ramjet Performance Analysis (RJPA) IBM-PC Version 1.0", Nov. 1986.

6.3. Curran, E. T. Sqdn.Ldr, Bergsten, B., "Discussion of Inlet Efficiency Parameters", Air Force Aero Propulsion Laboratory. April, 1963.

6.4. John, J. E., *Gas Dynamics*, Allyn and Bacon Inc., Boston, 1969.

6.5. Kutschenreuter, P. H., and Balent, R. L., "Hypersonic Inlet Performance From Direct Force Measurements", *Journal of Spacecraft*, Vol.2, No.2, March-April, 1965.

6.6. Van Wie, D. M., Thompson, M., Corpening, G. P., Keirsey, J. L. "The Generic Hypersonic Inlet Test Program", JHU/Applied Physics Laboratory. April, 1987.

6.7. Kays, W. M., Crawford, M.E. "STAN5 - A Program for Numerical Computation of Two-Dimensional Internal and External Boundary Layer Flows", NASA Report NASA-CR-2742. Nov., 1976.

6.8. McGregor, R. J., and Molder, S., "Analysis and Optimization of Scramjet Inlet Performance", 17th Congress of the International Council of the Aeronautical Sciences. ICAS-90-4.7.3, Sept. 1990.

6.9. PCB Model, 208 Series ICP Force Transducer Operating Guide.

6.10. PCB Model, 303A Series Miniature Quartz Accelerometer.

6.11. Endevco Corporation, Specifications for the 8506.

6.12. Molder, S., McGregor, R. J., Paisley, T. W., "The Ryerson / U of T Guntunnel", NASP Technical Report #NASP-WP-1008, Monterey, May 1989.

6.13. Molder, S., and Romeskie, J. M.,"Modular Hypersonic Inlets With Conical Flow", AGARD Conference Proceedings No. 30, May 1968.

6.14. Thompson, M. V., Corpening, G. P. The Johns Hopkins University Applied Physics Laboratory. Private Communication (Busemann Assessment), Sept. 6, 1988.

6.15. Van Wie, D., "Techniques for the Measurement of Hypersonic Inlet Performance", The Johns

Hopkins University, Applied Physics Laboratory, Laurel, Maryland. Draft Report.

6.16. Prandtl, l. Phys. Zeitschrift. Vol.8, p. 23, 1970.

6.17. Meyer, T. Uber Zweidimensionale Beweggungsvorgange in einem Gas, das mit Ubershallgeschwindigheit Strömt, Dissertation Gottingen; 1908.

6.18. Paisley, T. W., "An Investigation Into Two-Dimensional Hypersonic Prandtl-Meyer Wedge Inlets", Bachelor of Technology Thesis, Department of Aerospace Engineering, Ryerson Polytechnical Institute, Toronto, 1989.

6.19. Reshoto, E., Bushnell, D. M., Cassidy, M. D., "Report of the Task Force for Boundary Layer Transition", NASP Technical Memorandum 1007, April, 1987.

6.20. Thompson, M.W., Corpening, G. P, The Johns Hopkins University ; Applied Physics Laboratory. Private Communication (Oswatitsch Diffuser), Sept. 1988.

6.21. Binder, R.C., *Fluid Mechanics*, Prentice-Hall, Inc., New York, 1949.

6.22. Ladenburg, R.W., et al., *Physical Measurements in Gas Dynamics and Combustion*, Princetown University Press, 1954.

6.23. Billig, F. S., and Van Wie, D., "Efficiency Parameters For Inlets Operating at Hypersonic Speeds", JHU/Applied Physics Laboratory.

6.24. McGregor, Roderick, J. "Analysis and Optimization of Hypersonic Inlet Performance", Bachelor of Technology thesis, Department of Mechanical Engineering, Ryerson Polytechnical Institute.

6.25. Rizkalla, O., Chinits, W., and Erdos, J.I., "Calculated Chemical and Vibrational Nonequilibrium Effects in Hypersonic Nozzles.", General Applied Science Laboratories, Inc., Ronkonkoma, New York.

6.26. Zucrow, M. J., and Hoffman, J. D., *Gas Dynamics*, Vol. 1, John Wiley and Sons Inc., New York, 1976.

6.27. Martin, J. F., Duryea, G. R., Stevenson, L. M., " Instrumentation For Force and Pressure Measurements in a Hypersonic Shock Tunnel", Cornell Aeronautical Laboratory, 1962.

6.28. Hill, A. F., "Stability and Pressure Measurements in the Naval Surface Weapons Center Hypervelociy Tunnel", Naval Surface Weapons Center, White Oak Laboratory, SilverSpring,

Maryland, 1977.

6.29. Bernstein, I. "Force Measurements In Short Duration Hypersonic Test Facilities". AGARD-AG-214, November, 1975.

7.0 Numerical Predictions of Gun Tunnel Performance

C. P. T. Groth and J. J. Gottlieb

7.1 Introduction

As described in Section 2, the hypersonic gun tunnel of the University of Toronto Institute for Aerospace Studies (UTIAS) and Ryerson Polytechnical Institute (RPI) is a short-duration blow-down experimental wind tunnel capable of producing high Mach number flows ($M \approx 8$). Along with free-piston shock tunnels, gun or impulse tunnels are representative of a class of experimental facilities that have been used successfully to simulate various aspects of hypersonic flight in the laboratory (Refs. 7.1–7.7). In the UTIAS-RPI gun tunnel, a high-pressure driver gas is used to accelerate a piston. This accelerating piston compresses and heats the working gas (air) by means of a multiple-shock nonisentropic process for subsequent expansion through a contoured nozzle to a high Mach number. The use of the piston to separate the driver and working gases is what differentiates the gun tunnel from *shock tunnels* (Refs. 7.1, 7.6, & 7.8–7.10), another related class of hypersonic test facility. Note that gun tunnels offer several advantages. They generally have relatively longer run times than alternate intermittent devices such as shock tunnels and are considerably less costly than continuous or steady-state operating facilities.

The determination of stagnation pressure, stagnation enthalpy or total temperature (a useful measure of the thermodynamic state of the test-section flow), thermodynamic processes in the nozzle of the impulse tunnel, and test-section flow properties are all required for accurate interpretation of experimental data; however, many of these facility characteristics are difficult to measure directly. Furthermore, a thorough understanding of the tunnel operation is required in order to explore various avenues for extending the range of flow conditions that may be simulated.

Previous studies have generally employed simplified analytic techniques to investigate various aspects of hypersonic facility performance (see, for example, Refs. 7.11–7.17). More recently, a simplified quasi-one-dimensional numerical model has been proposed for the starting process in the nozzle of a free-piston shock tunnel (Ref. 7.18). This section of the contract report presents a fairly sophisticated quasi-one-dimensional nonstationary compressible flow analysis and associated total-variation-diminishing (TVD) finite-difference solution schemes,

including approximate Riemann solvers, that have been developed for predicting the complete unsteady performance and operation of the UTIAS-RPI hypersonic gun tunnel. The analysis and related computer program were developed to enhance the understanding of the tunnel operation and capable of predicting barrel stagnation and test-section flow properties, unsteady piston motion, run times, as well as the high-temperature effects associated with the impulse gun flows. The analysis has been used to investigate the operation of the UTIAS-RPI facility and produce performance data that is not always easily determined or available from experimental measurements. In particular, the thermodynamic state of the nozzle-exit flow and high-temperature or real-gas effects have been assessed. Modeling and algorithm details, comparisons with experimental data, and predictions of tunnel performance are all described in this section. Additional information regarding the present impulse tunnel performance analysis is given by Groth, Gottlieb, and Sullivan (Ref. 7.19).

The remainder of this section of the report is divided into seven subsections. Immediately following this introductory subsection is a brief description of the UTIAS-RPI tunnel operation. This is followed by details of the quasi-one-dimensional analysis and thermodynamic models in the next two subsections. The TVD solution algorithm is described in Subsection 7.6 and numerical results given in Subsection 7.7. Concluding remarks and references follow in the last two subsections.

7.2 Review of Gun Tunnel Operation

A schematic of the UTIAS-RPI hypersonic gun tunnel is depicted in Fig. 7.1a. This blow-down or short-duration test facility consists of a 5.6 m long reservoir or driver with an internal radius of 152.4 mm and a 6.4 m long barrel with an internal radius of 38.1 mm that are separated by an isolating ball valve and a double diaphragm. A relatively light aluminum piston weighing approximately 95 g is free to move in the barrel. Various convergent-divergent nozzles may be connected to the barrel at the nozzle breech. A 1.54 m long nozzle with throat and exit radii of 6.35 and 108.87 mm, respectively, is currently employed. This nozzle has a design Mach number of 8.33. The nozzle projects into a 0.61 m long test section with a rectangular cross section of 0.61 m × 0.64 m which is in turn connected by a diffuser to a relatively large dump tank with a volume of approximately 2.85 m^3. The initial pressure of the driver gas (currently air) in the reservoir is normally maintained at 20.5 MPa and initial barrel pressure for the working gas (again this is usually air) ranges between 200 and 800 kPa. A

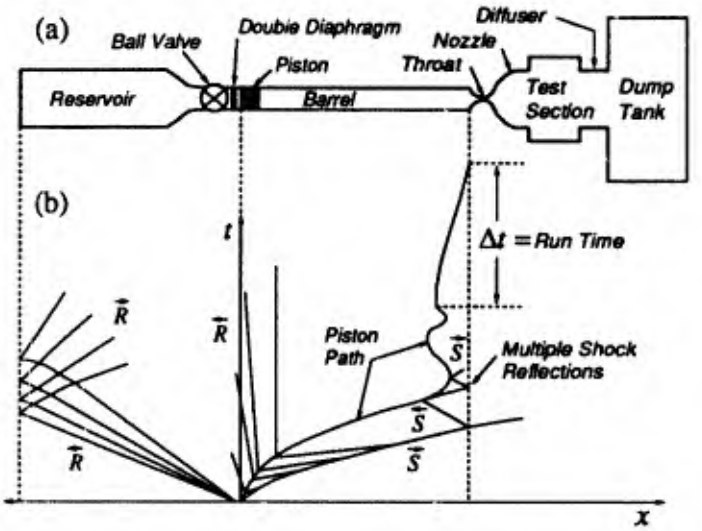

Figure 7.1: UTIAS-RPI hypersonic impulse tunnel.
(a) Schematic diagram of facility,
(b) x-t diagram of tunnel operation.

small Lexan plug is placed in the throat of the nozzle so that the test section can be evacuated down to pressures nearing 50 Pa.

During tunnel operation, the double diaphragm is burst and the high-pressure driver gas rapidly accelerates the piston along the barrel. The accelerating piston creates a series of multiple shock reflections in the barrel that heat and compress the working gas. The nozzle throat plug is expelled by the first reflected shock and the working gas then flows through the convergent-divergent nozzle and on through the test section. The piston eventually comes to rest at the end of the barrel when the working gas is depleted. Typical run times for this facility are between 10–30 ms. The impulse tunnel operation is illustrated in the x-t wave diagram of Fig. 7.1b. The primary shock and rarefaction wave patterns characterizing the nonstationary wave interaction processes occurring in the tunnel, indicated by $\vec{S}$ and $\vec{R}$ respectively, are shown in this figure. Note that a more complete description of the UTIAS-RPI hypersonic gun tunnel, which includes details of tunnel instrumentation and calibration, is given in Section 2. Additional information may be found in Ref. 7.7.

It should be clear from the preceding description that the operation cylce of the UTIAS-RPI hypersonics gun tunnel is an inherently unsteady process involving complicated nonstationary compressible flow, strong shocks, and large piston acceleration and deceleration forces. The modeling of the gaseous flow and piston motion used in the present tunnel analysis now follows.

7.3 Equations of Motion

The complex unsteady flow of the driver and working gases in the reservoir, barrel, and nozzle behind and in front of the accelerating piston are modeled by solving the equations of motion (continuity, momentum, and energy) for generalized one-dimensional nonstationary compressible flows in ducts. The equations include inhomogeneous source terms associated with the flow driving potentials of area change, friction, heat transfer, and head loss and are well documented in many textbooks (see, for example, Ref. 7.20). They have been used successfully in previous studies to predict nonstationary flows in other experimental facilities such as blast-wave simulators and two-stage light-gas hypervelocity launchers (Refs. 7.21–7.23). The weakly conservative forms of these partial differential equations may be expressed as

$$\frac{\partial}{\partial t}(\mathbf{U}) + \frac{\partial}{\partial x}[\mathbf{F}(\mathbf{U})] = \mathbf{A}(\mathbf{U}) + \mathbf{S}(\mathbf{U}), \tag{7.1}$$

where the multi-component solution and flux column vectors **U** and **F** are given by

$$\mathbf{U} = \begin{bmatrix} \rho \\ \rho u \\ \rho(e + \frac{1}{2}u^2) \end{bmatrix}, \quad \mathbf{F} = \begin{bmatrix} \rho u \\ \rho u^2 + p \\ \rho u \left(e + \frac{p}{\rho} + \frac{1}{2}u^2\right) \end{bmatrix}, \tag{7.2}$$

the source column vectors **A** and **S** are defined by

$$\mathbf{A} = \begin{bmatrix} -\rho u \frac{1}{A}\frac{dA}{dx} \\ -\rho u^2 \frac{1}{A}\frac{dA}{dx} \\ -\rho u \left(e + \frac{p}{\rho} + \frac{1}{2}u^2\right) \frac{1}{A}\frac{dA}{dx} \end{bmatrix}, \quad \mathbf{S} = \begin{bmatrix} 0 \\ F_{wall} + F_{loss} \\ Q_{wall} + Q_{zero} \end{bmatrix}, \tag{7.3}$$

and the symbols ρ, u, p, and e denote the gas density, velocity, pressure, and total specific internal energy, and x and t are position and time. The variable A is the local cross-sectional area of the duct which is taken to be a known function of x. The other terms appearing in column vectors **A** and **S** represent the effects of area change, boundary-layer friction, wall heat transfer, and other flow pressure or head losses. F_{wall} is an equivalent body force per unit

volume to account for viscous or frictional losses in the boundary layer near the wall of the duct flow. F_{loss} is a similar body force per unit volume that includes additional pressure losses for flows through area changes and over diaphragm remnants. The variable Q_{wall} denotes the heat transfer rate per unit volume from the duct walls to the gas and the variable Q_{zero} represents the time rate of change in the zero-point energy of the gas resulting from chemical reactions. This latter term is required when modeling finite-rate reaction processes.

The body force due to boundary layer friction can be expressed in the form

$$F_{wall} = -\frac{f}{D_h}\frac{\rho u|u|}{2}, \tag{7.4}$$

where f is the Darcy-Weisbach friction factor and D_h is the local hydraulic diameter of the duct ($D_h = 2\pi r$ for pipes where r is the radius). In this study, the friction factor is obtained by using

$$f = \begin{cases} \dfrac{64}{\mathrm{R}\Lambda} & 0 < \mathrm{R} < 2000\,, \\ \dfrac{0.032}{\Lambda}\left[\dfrac{\mathrm{R}}{2000}\right]^{0.3187} & 2000 \le \mathrm{R} \le 4000\,, \\ \left[1.14 - 2\log_{10}(21.25\mathrm{R}^{-0.9} + \dfrac{\varepsilon}{D_h})\right]^{-2}\Lambda^{-1} & \mathrm{R} > 4000\,, \end{cases} \tag{7.5}$$

for which $\mathrm{R} = \rho|u|D_h/\mu$ is the local Reynolds number, μ is the gas viscosity, and ε denotes the absolute roughness of the wall surface. The previous relationships are taken from steady pipe flow theory. The first expression is the well-known theoretical result from Hagen-Poiseuille flow which describes the friction factor in the laminar regime ($0 < \mathrm{R} < 2000$), the third is an explicit empirical expression developed by Jain (Ref. 7.24) valid in the fully turbulent regime ($\mathrm{R} > 4000$), and the other expression provides estimates for the friction factor in the transitional regime ($2000 \le \mathrm{R} \le 4000$). Note that Λ is a compressibility correction factor. It is calculated from the semi-empirical relation $\Lambda = 1 + (\gamma - 1)\Omega\mathrm{M}^2/2$ as suggested by Liepmann and Goddard (Ref. 7.25), where γ is the specific heat ratio of the gas, M is the local flow Mach number, and Ω is the recovery factor. This last parameter can be approximated by $\mathrm{Pr}^{1/2}$ for laminar flows and $\mathrm{Pr}^{1/3}$ for turbulent flows where Pr is the Prandtl number for the gas.

Similarly, the body forces due to pressure or head losses in the flow can be written as

$$F_{loss} = -\frac{K}{L}\frac{\rho u|u|}{2}, \tag{7.6}$$

where K is the head-loss coefficient and L is the finite duct length over which the losses are distributed ($L = 2D_h$ in the present study). Although these losses are usually small, values for K can range between 0–10 depending on the flow obstructions.

The rate of heat transfer to the gas from the wall per unit volume of the flow Q_{wall} is prescribed by employing the semi-empirical form of Reynolds' analogy for compressible pipe flow suggested by Colburn (Ref. 7.26). The heat transfer rate is thus given by

$$Q_{wall} = \frac{4k\mathrm{Nu}}{D_h^2}[T_w - T_{aw}] = \frac{fC_p\rho|u|}{2\mathrm{Pr}^{2/3}D_h}[T_w - \Lambda T], \tag{7.7}$$

where Nu, k, and C_p, T, and T_{aw} are the gas Nusselt number, thermal conductivity, specific heat at constant pressure, temperature, and adiabatic wall temperature, respectively, and T_w is the local duct wall temperature. Note that the Prandtl number is defined by $\mathrm{Pr} = \mu C_p/k$ and the effects of compressibility appear in Eq.(7.7) via the friction factor f and correction factor Λ.

The piston of the UTIAS-RPI hypersonic impulse tunnel is basically a thick aluminum disc with a trailing tapered skirt that provides stability during motion. Holes are machined through the skirt to reduce weight. In order to model the piston motion in the barrel, it is assumed that the piston is a rigid cylinder of length L_p and radius r_p. Newton's law is then applied with pressure, inertial, and viscous drag forces all taken into account. This results in a differential equation for the piston motion which can be written as

$$m_p\frac{dV_p}{dt} = \pi r_p^2(p_f - p_b) + F_p, \tag{7.8}$$

where V_p is the piston velocity, p_f and p_b are the front and back face pressures exerted on the piston by the high-pressure gases, F_p is the frictional force acting on the piston, and m_p is the piston mass. The friction force is determined by assuming that a quasi-steady Couette flow exists between the exterior surface of the piston and the tunnel walls and a Reynolds number

correlation similar to those for fully developed pipe flow is used to determine the frictional shear stress at the piston surface. F_p can then be approximated by

$$F_p = -2\pi r_p L_p (1-\sigma) f_p \left[\frac{\mu V_p}{r - r_p}\right], \tag{7.9}$$

where f_p is the piston friction factor having the form $f_p = c\mathrm{R}_p^n$ and $\mathrm{R}_p = \rho V_p (r - r_p)/\mu$ is the piston Reynolds number; c and n are constants. The variable σ $(0 \leq \sigma < 1)$ is the porosity of the piston skirt.

7.4 Thermodynamic Models for Air

At the present time, air is used almost exclusively as the driver and working gas in the UTIAS-RPI hypersonic gun tunnel. Thermodynamic and caloric models are required to interrelate the various intensive properties of air, such as pressure, temperature, and internal energy, and thereby complete or close the governing set of equations given by Eqs.(7.1)–(7.7). In this study, three different models are employed to describe the thermodynamic and transport properties of air. They are the perfect-gas model (polytropic or thermally and calorically perfect gas), an equilibrium real-gas model, and a nonequilibrium (vibrationally relaxing and chemically reacting) high-temperature model. The three different thermodynamic models are very helpful in assessing the magnitude of the high-temperature effects in the impulse tunnel flows and the departure of the working gas behaviour from the ideal.

7.4.1 Polytropic Model

For polytropic gases, the pressure and temperature can be related to the density and total specific internal energy using the well-known ideal-gas equation of state

$$p = \rho RT = (\gamma - 1)\rho e\,, \tag{7.10}$$

where γ is the specific heat ratio, R is the gas constant, and $C_p = \gamma R/(\gamma - 1)$. In the case of air, the values of γ and R are taken to be 1.40 and 287.06 Pa-m^3/kg-K, respectively. The

sound speed a can also be related to the other intensive properties by the expressions

$$a^2 = \gamma RT = \gamma \frac{p}{\rho} = \gamma(\gamma - 1)e\,. \tag{7.11}$$

The polytropic model is completed by employing semi-empirical expressions for the dynamic viscosity and Prandtl number. An empirical extension of Sutherland's law of the form

$$\mu = \frac{c_1 T^{3/2}}{c_2 + T^{c_3} + c_4/T}\,, \tag{7.12}$$

is used, where c_1, c_2, c_3, and c_4 are constants and equal to 5.2192×10^{-7}, -3.31132, 0.865351, and 2365.27, respectively, for air. The Prandtl number for air depends primarily on the specific heat ratio. A modified form of Euken's formula is used herein to prescribe the Prandtl number. The formula is based on some ideas of Chapman and Cowling (Ref. 7.27) and given by

$$\mathrm{Pr} = \frac{20\gamma}{39\gamma - 15}\,, \tag{7.13}$$

which is in good agreement with experimental data.

7.4.2 Equilibrium Model

The curve fits of Srinivasan, Tannehill, and Weilmuenster (Ref. 7.28) and Srinivasan and Tannehill (Ref. 7.29) are used to represent the equilibrium thermodynamic and transport properties of air. These curve fits are constructed from bicubic polynomials and Grabau-type transition functions to model the thermodynamic properties in a piecewise manner. They are valid for temperatures up to 25,000 K. The correlations for the pressure p, temperature T, sound speed a, viscosity μ, Prandtl number Pr, and thermal conductivity $k = \mu C_p/\mathrm{Pr}$ in the form $p = p(\rho, e)$, $T = T(\rho, e)$, $a = a(\rho, e)$, $\mu = \mu(\rho, T)$, $\mathrm{Pr} = \mathrm{Pr}(\rho, T)$, and $k = k(\rho, e)$ are all employed. Note that if the equation of state has the form $p = p(\rho, e)$, then the sound speed can be related to the pressure, density, and internal energy by the relationship

$$a^2 = \left.\frac{\partial p}{\partial \rho}\right|_s = \left.\frac{\partial p}{\partial \rho}\right|_e + \frac{p}{\rho^2}\left.\frac{\partial p}{\partial e}\right|_\rho\,, \tag{7.14}$$

where s is the entropy.

7.4.3 Nonequilibrium Model

The thermodynamics of the nonequilibrium air is modeled by treating it as a chemically reactive mixture of thermally perfect gases for which the thermal state can be described by the following separate and independent temperatures (or internal energies): a translational-rotational temperature and the vibrational temperatures of the polyatomic species. The translational-rotational temperature represents the contribution to the internal energy by the translational and rotational modes of all molecules and atoms in the mixture. These modes are assumed to be in equilibrium, which is a reasonable approximation for most continuum flow studies. Each vibrational temperature represents the contribution to the internal energy by the vibrational modes of the corresponding polyatomic species. Intermolecular forces, electronic excitation, and ionization effects are all neglected.

Additional equations for species mass and vibrational energy are necessary for describing the one-dimensional flow of a nonequilibrium mixture. They may be written as (Ref. 7.30)

$$\frac{\partial \mathbf{W}}{\partial t} + u\frac{\partial \mathbf{W}}{\partial x} = \mathbf{Q}(\mathbf{W}), \tag{7.15}$$

where the column vectors $\mathbf{W}$ and $\mathbf{Q}$ are defined by

$$\mathbf{W} = \begin{bmatrix} c_1 \\ \vdots \\ c_N \\ c_1 e_{v_1} \\ \vdots \\ c_N e_{v_N} \end{bmatrix}, \quad \mathbf{Q} = \begin{bmatrix} w_1 \\ \vdots \\ w_N \\ c_1 q_1 + \beta_1 w_1 e_{v_1} \\ \vdots \\ c_N q_N + \beta_N w_N e_{v_N} \end{bmatrix}, \tag{7.16}$$

and where $c_s = \rho_s/\rho$ is the mass fraction of species s with $\sum_s c_s = 1$, ρ_s is the density of species s, e_{v_s} is the specific vibrational energy of species s, $e_v = \sum_s c_s e_{v_s}$ is the total specific vibrational energy of the mixture, and N is total number of species in the mixture. The variable

w_s represents the time rate of change of the concentration of the species s brought about by the chemical reactions. The variable q_s represents the time rate of change of the vibrational energy of the species s brought about by relaxation to its equilibrium value. Finally, the term $\beta_s w_s e_{v_s}$ appearing in Eqs. (7.15) and (7.16) is related to the change in the vibrational energy of species s per unit volume of the mixture due to the chemical reactions. The quantity β_s is an empirical value greater than or equal to unity. It is introduced to reflect the observed preference of *higher-than-average* vibrationally excited molecules to dissociate and the tendency of atoms to combine and form higher-than-average vibrationally excited molecules (Ref. 7.30).

The total specific internal energy of the thermally perfect gaseous mixture is the sum of translational-rotational and vibrational energies and given by

$$e = e_{tr} + e_v = e_{tr} + \sum_{s=1}^{N} c_s e_{v_s} , \tag{7.17}$$

where e_{tr} is the translational-rotational energy. The mixture pressure may then be expressed in terms of the translational-rotational temperature T and (or) energy e_{tr} and the various mixture properties by employing the ideal equation of state for each thermally perfect species and applying Dalton's law of partial pressure. The resulting equation of state for the mixture is

$$p = \rho R T = (\gamma - 1)\rho e_{tr} , \tag{7.18}$$

where $R = \mathcal{R}(\sum_s c_s/\mathcal{M}_s) = \sum_s c_s R_s$ is the specific gas constant of the mixture, $\mathcal{R}$ is the universal gas constant, $\mathcal{M}_s$ is the molecular weight of species s, $R_s = \mathcal{R}/\mathcal{M}_s$ is the specific gas constant of species s, and $\gamma = 1 + [\sum_s c_s R_s]/[\sum_s c_s R_s/(\gamma_s - 1)]$ is defined to be the *frozen* specific heat ratio of the mixture. The variable γ_s represents the frozen specific heat ratio of species s (i.e., the specific heat ratio of the species in the absence of vibrational excitation). It is also possible to define a frozen sound speed for the mixture. This intensive property may be related to the other mixture properties by the expression

$$a^2 = \gamma R T = \gamma \frac{p}{\rho} = \gamma(\gamma - 1) e_{tr} , \tag{7.19}$$

where a is the frozen sound speed.

In the present work, a five-species (N_2, O_2, NO, N, and O) four-temperature (i.e., translational-rotational temperature T, and vibrational temperatures $T_{v_{N_2}}$, $T_{v_{O_2}}$, and $T_{v_{NO}}$) nonequilibrium thermodynamic model of air is employed. The model is valid for temperatures up to 8000 K and pressures above 1 kPa. In this model, the dissociation-recombination reaction mechanism of air is represented by the elementary reactions

$$\begin{aligned} &N_2 + M \rightleftharpoons 2N + M, \\ &O_2 + M \rightleftharpoons 2O + M, \\ &NO + M \rightleftharpoons NO + M, \\ &NO + O \rightleftharpoons N + O_2, \\ &N_2 + O \rightleftharpoons NO + N, \end{aligned} \tag{7.20}$$

where M is a collision partner; it can be any of the five species. Collision theory is used to describe the finite-rate reaction processes from which empirical expressions for the time rate of change of the species concentrations may be obtained. These expressions have the form

$$w_s = \mathcal{M}_s \sum_{r=1}^{N_R} (\sigma_{s,r}^b - \sigma_{s,r}^f) \left\{ k_r^f \prod_{s'=1}^{N} \left(\frac{c_{s'}}{\mathcal{M}_{s'}}\right)^{\sigma_{s',r}^f} - k_r^b \prod_{s'=1}^{N} \left(\frac{c_{s'}}{\mathcal{M}_{s'}}\right)^{\sigma_{s',r}^b} \right\}, \tag{7.21}$$

where $\sigma_{s,r}^f$ and $\sigma_{s,r}^b$ are the stoichiometric coefficients of the reactant and product species s for the reaction r, and k_r^f and k_r^b are the forward and backward reaction rates of reaction r. The variable N_R represents the total number of elementary reactions. The reaction rates are assumed to be functions of the rotational-translational temperature and are described by modified forms of the Arrhenius equation. They are given by

$$k_r^f = C_r^f \, T^{n_r^f} \exp\left(\frac{-E_r^f}{KT}\right), \quad k_r^b = C_r^b \, T^{n_r^b} \exp\left(\frac{-E_r^b}{KT}\right). \tag{7.22}$$

The reaction rate coefficients C_r^f, C_r^b, n_r^f, n_f^b, E_r^f, and E_r^b of Eq. (7.22) are taken from the data set compiled by Dunn and Kang (Ref. 7.31).

The finite-rate vibrational relaxation of the diatomic molecules is represented in the five-species four-temperature nonequilibrium model of air by assuming that the vibrationally excited molecules behave as ideal harmonic oscillators. It is further assumed that the relaxation process from an excited nonequilibrium state to a state of thermodynamic equilibrium (i.e., $T = T_{v_{N_2}} = T_{v_{O_2}} = T_{v_{NO}}$) occurs only through translational-vibrational collisions. Under these assumptions, it is possible to prescribe the time rate of change of the vibrational energy of the species s by

$$q_s = \frac{e_{v_s}^* - e_{v_s}}{\tau_s}, \tag{7.23}$$

where e_v^* is the local equilibrium temperature given by

$$e_{v_s}^* = \frac{\Theta_{v_s} R_s}{\exp(\Theta_{v_s}/T) - 1}, \tag{7.24}$$

and τ_s is the characteristic relaxation time. The characteristic vibrational temperatures $\Theta_{v_{N_2}}$, $\Theta_{v_{O_2}}$, and $\Theta_{v_{NO}}$ are taken to be 3353, 2239, and 2699 K, respectively. The semi-empirical correlations of Millikan and White (Ref. 7.32) based on modifications to the Landau-Teller equation are used to determine τ_s. These correlations have the form

$$\tau_s = \frac{\sum_{s'} \frac{c_{s'}}{\mathcal{M}_{s'}} \exp[\mathcal{A}_s(T^{-1/3} - 0.015(\frac{\mathcal{M}_s \mathcal{M}_{s'}}{\mathcal{M}_s + \mathcal{M}_{s'}})^{1/4}) - 18.42]}{p \sum_{s'} \frac{c_{s'}}{\mathcal{M}_{s'}}}, \tag{7.25}$$

and $\mathcal{A}_{N_2}$, $\mathcal{A}_{O_2}$, and $\mathcal{A}_{NO}$ are assumed to have values of 220, 129, and 168, respectively.

Using the preceding relations, it is possible to prescribe the source term Q_{zero} of Eq. (7.1) that represents the total change in the zero-point energy of the mixture resulting from the chemical reactions by the expression

$$Q_{zero} = -\rho \sum_{s=1}^{N} w_s \Delta h_{f_s}^0, \tag{7.26}$$

where $\Delta h_{f_s}^0$ is the heat of formation of species s evaluated at a temperature of 0 K. The heats of

formation for the five species were taken to be $\Delta h^0_{f_{N_2}} = 0$, $\Delta h^0_{f_{O_2}} = 0$, $\Delta h^0_{f_{NO}} = 2991.89$ kJ/kg, $\Delta h^0_{f_N} = 33613.91$ kJ/kg, and $\Delta h^0_{f_O} = 15424.95$ kJ/kg. Note that Q_{zero} is identically zero for the polytropic and equilibrium models. Note additionally that the effect of the preferential dissociation of vibrationally excited diatomic molecules is not included herein and β_s is taken to be unity in the present work.

Finally, transport properties of nonequilibrium air required for the determination of the boundary-layer friction F_{wall} and heat transfer Q_{wall} in Eq. (7.1)–(7.3) are computed as follows. The mixture specific heat and Prandtl number are approximated by the frozen flow (i.e., polytropic-gas equivalent) relations $C_p = \gamma R/(\gamma - 1)$ and $\mathrm{Pr} = 20\gamma/(39\gamma - 15)$, respectively. The viscosity of each species μ_s is defined in terms of the translational-rotational temperature T by using the semi-empirical correlations of Blottner, Johnson, and Ellis (Ref. 7.33) given by

$$\mu_s = 0.10 \exp\left[(b_{1_s} \ln T + b_{2_s}) \ln T + b_{3_s}\right] , \tag{7.27}$$

and the mixture or total viscosity is calculated by employing the semi-empirical mixing rule of Wilke (Ref. 7.34) as follows:

$$\mu = \sum_{s=1}^{N} \frac{c_s \mu_s}{\mathcal{M}_s \phi_s} , \tag{7.28}$$

where

$$\phi_s = \sum_{s'=1}^{N} \frac{c_{s'}}{\mathcal{M}_{s'}} \left[1 + \left(\frac{\mu_s}{\mu_{s'}}\right)^{1/2} \left(\frac{\mathcal{M}_{s'}}{\mathcal{M}_s}\right)^{1/4}\right]^2 \left[8\left(1 + \frac{\mathcal{M}_s}{\mathcal{M}_{s'}}\right)\right]^{-1/2} . \tag{7.29}$$

The curve fits of Eq. (7.27) are appropriate for temperatures up to 10,000 K and the constant coefficients b_{1_s}, b_{2_s}, and b_{3_s} for each species are taken from Ref. 7.33.

7.5 Numerical Solution Procedure

General solutions to the preceding equations prescribing the flow of the gun tunnel driver and working gases and the motion of the piston in the barrel and must be obtained numerically. The differential equation for the piston motion given by Eq. (7.8) can be integrated by decoupling

it from the gas dynamic equations and employing the most recent flow field solution in a forward Euler time-stepping procedure. This simple approach is sufficiently accurate and robust as the characteristic time scales associated with the piston motion are very much larger than the gas dynamic time scales. The gas dynamic equations given by Eqs. (7.1)–(7.3) may then be solved in a separate integration procedure where, at each level or time step, the corresponding updated solution for the piston motion is employed. However, the numerical solution of this inhomogeneous system of hyperbolic conservation laws is made difficult by the presence of large solution gradients and strong shocks. It is further complicated if source terms are stiff. Classical first-order shock-capturing finite-difference schemes can require excessive grid refinement to resolve the complicated shock structure, and second-order schemes can lead to spurious Gibb's oscillations or nonlinear instabilities near discontinuities. In the last 5-10 years, solution-dependent nonlinear higher-order methods have been developed, such as the total-variation-diminishing (TVD) finite-difference schemes of Harten (Refs. 7.35 & 7.36), Roe (Refs. 7.37–7.39), Davis (Ref. 7.40), Yee (Ref. 7.41), and Chakravarthy and Osher (Refs. 7.42 & 7.43). They are very appropriate for the hyperbolic system considered here. These schemes effectively eliminate oscillations near extrema, limit numerical diffusion, maintain higher-order accuracy wherever possible, and thereby permit the efficient resolution of weak solutions.

In this study, the explicit higher-order TVD upwind difference scheme of Roe (Refs. 7.37, 7.38, & 7.44) is used to solve the governing partial differential equations of the gaseous flows when supplemented by the ancillary equations of the polytropic and equilibrium thermodynamic models. Roe's approximate Riemann solver is used in the evaluation of the numerical fluxes for the polytropic case and an extension of this approximate solver proposed by Glaister (Ref. 7.45) is employed for the equilibrium case.

When supplemented with nonequilibrium thermodynamic model equations, the solution of Eq. (7.1) is complicated by the additional species mass and vibrational energy conservation equations Eq. (7.15), as well as the presence of inhomogeneous source terms representing the finite-rate vibrational relaxation and chemical reaction processes. The additional source terms are often large and can make the solution algorithms stiff (i.e., the time stepping of a marching procedure is drastically constrained by stability considerations rather than by the usual accuracy concerns). In this case, the gas dynamic and thermodynamic equation sets are partially decoupled by employing a *frozen flow* approximation. Both sets of decoupled equations are then integrated alternately in a lagged manner within a time marching procedure. A semi-implicit

version of the Roe's scheme is applied to each equation set. The inhomogeneous source terms associated with the finite-rate processes are treated implicitly in the time-stepping scheme and an extension of Roe's approximate Riemann solver is used to evaluate the numerical flux functions. The extended Riemann solver provides the eigenvalues and eigenvectors of the fully coupled system.

Further details of these TVD shock-capturing schemes are given in the following subsections. The various algorithm extensions particular to the present application are discussed. This includes the approximate Riemann solvers, partial-decoupling procedure, implicit treatment of stiff source terms, and boundary conditions.

7.5.1 Solution Algorithm for Polytropic and Equilibrium Gas Flows

TVD schemes were originally developed for solving linear and nonlinear scalar homogeneous hyperbolic conservation laws in one space dimension. Algorithm extensions are necessary to deal with the vector nature and source terms of inhomogeneous systems of differential equations. In Roe's flux-differencing method, a local characteristic approach is adopted in which the properties of the inviscid flux Jacobians are utilized in conjunction with approximate Riemann solvers to represent the solution and flux vector jumps in terms of characteristic variables. A TVD algorithm is then applied to each characteristic field in a *scalar* fashion. Source terms may be treated either explicitly or implicitly depending on the nature of the equations.

In the case of the polytropic and equilibrium thermodynamic models, Roe method solutions of the one-dimensional three-component system given by Eq. (7.1) can be formulated as follows. Let $\mathbf{U}_i^n$ be the numerical approximation of the solution at discrete locations $x = x_i$ and time $t = t^n$. The solution at subsequent time levels is obtained by means of the time-stepping procedure

$$\mathbf{U}_i^{n+1} = \mathcal{L}_{\mathbf{U}}^{\Delta t} \mathbf{U}_i^n \,, \tag{7.30}$$

where the solution operator $\mathcal{L}_{\mathbf{U}}^{\Delta t}$ advances the solution $\mathbf{U}$ through a time interval Δt^n with $\Delta t^n = t^{n+1} - t^n$ and is defined by the two-stage difference scheme

$$\mathbf{U}_i^{\overline{n+1}} = \mathbf{U}_i^n + \Delta\mathbf{U}_i^{\overline{n}} = \mathbf{U}_i^n + \Delta t^n\left(\mathbf{A}_i^n + \mathbf{S}_i^n\right) -$$

$$\frac{1}{2}\sum_{k=1}^{3}\left\{\left[\left(\nu_{i+1/2,k}^n - |\nu_{i+1/2,k}^n|\right) + \phi_{i+1/2,k}^n|\nu_{i+1/2,k}^n|\left(1 - |\nu_{i+1/2,k}^n|\right)\right]\Delta\mathbf{U}_{i+1/2,k}^n +\right.$$

$$\left.\left[\left(\nu_{i-1/2,k}^n + |\nu_{i-1/2,k}^n|\right) - \phi_{i-1/2,k}^n|\nu_{i-1/2,k}^n|\left(1 - |\nu_{i-1/2,k}^n|\right)\right]\Delta\mathbf{U}_{i-1/2,k}^n\right\}, \tag{7.31}$$

$$\mathbf{U}_i^{n+1} = \mathbf{U}_i^n + \Delta\mathbf{U}_i^n = \mathbf{U}_i^{\overline{n+1}} + \frac{1}{2}\Delta t^n\left(\mathbf{A}_i^{\overline{n+1}} - \mathbf{A}_i^n + \mathbf{S}_i^{\overline{n+1}} - \mathbf{S}_i^n\right), \tag{7.32}$$

and where $\Delta\mathbf{U}_i^n = \mathbf{U}_i^{n+1} - \mathbf{U}_i^n$, $\Delta\mathbf{U}_i^{\overline{n}} = \mathbf{U}_i^{\overline{n+1}} - \mathbf{U}_i^n$, and $\mathbf{U}_i^{\overline{n+1}}$ denotes an intermediate solution state. The quantities $\nu_{i+1/2,k}^n$ and $\Delta\mathbf{U}_{i+1/2,k}^n$ appearing in Eq. (7.31) are the local average Courant-Friedrichs-Lewy (CFL) number and solution jump vector associated with the k^{th} elemental wave of the i^{th} approximate Riemann problem posed between the i^{th} and $i^{\text{th}} + 1$ nodes of the spatial grid. They may be related to the eigenvalues and eigenvectors of the Jacobian of the homogeneous flux vector $\mathbf{J} = \partial\mathbf{F}/\partial\mathbf{U}$ by employing Roe's approximate Riemann solver. The CFL numbers and solution jump vectors can be defined by

$$\nu_{i+1/2,k}^n = \frac{\Delta t^n \lambda_{i+1/2,k}^n}{\Delta x_{i+1/2}}, \tag{7.33}$$

$$\Delta\mathbf{U}_{i+1/2,k}^n = \alpha_{i+1/2,k}^n \mathbf{e}_{i+1/2,k}^n, \tag{7.34}$$

with $\Delta x_{i+1/2} = x_{i+1} - x_i$, and where $\lambda_{i+1/2,k}^n$ and $\mathbf{e}_{i+1/2,k}^n$ are the k^{th} eigenvalue and eigenvector of the flux Jacobian evaluated at an appropriate average state $\mathbf{U}_{i+1/2}^n$ The variable $\alpha_{i+1/2,k}^n$ is the strength of the k^{th} elemental wave. The eigenvalues of the Jacobian $\mathbf{J} = \partial\mathbf{F}/\partial\mathbf{U}$ are given by

$$\lambda_{i+1/2,1}^n = u_{i+1/2}^n - a_{i+1/2}^n, \quad \lambda_{i+1/2,2}^n = u_{i+1/2}^n, \quad \lambda_{i+1/2,3}^n = u_{i+1/2}^n + a_{i+1/2}^n, \tag{7.35}$$

and the eigenvectors can be written as

$$e^n_{i+1/2,1} = \begin{bmatrix} 1 \\ u^n_{i+1/2} - a^n_{i+1/2} \\ h^n_{i+1/2} - u^n_{i+1/2}a^n_{i+1/2} \end{bmatrix}, \quad e^n_{i+1/2,3} = \begin{bmatrix} 1 \\ u^n_{i+1/2} + a^n_{i+1/2} \\ h^n_{i+1/2} + u^n_{i+1/2}a^n_{i+1/2} \end{bmatrix}, \tag{7.36}$$

$$e^n_{i+1/2,2} = \begin{bmatrix} 1 \\ u^n_{i+1/2} \\ h^n_{i+1/2} - \dfrac{\rho^n_{i+1/2}(a^n_{i+1/2})^2}{\left(\dfrac{\partial p}{\partial e}\right)^n_{i+1/2}} \end{bmatrix}, \tag{7.37}$$

where $a^n_{i+1/2}$ is the local average state sound speed and $h = e + p/\rho + u^2/2$ is the specific enthalpy. Note that for polytropic gases, $\partial p/\partial e = (\gamma - 1)\rho$ and, therefore, $h - \rho a^2/(\partial p/\partial e) = u^2/2$. Using the condition $\Delta \mathbf{U}^n_{i+1/2} = \mathbf{U}^n_{i+1} - \mathbf{U}^n_i = \sum_k \alpha^n_{i+1/2,k} e^n_{i+1/2,k}$, it is possible to relate the elemental wave strengths to the average state values of the primitive variables $\rho^n_{i+1/2}$ $u^n_{i+1/2}$, $e^n_{i+1/2}$, $p^n_{i+1/2}$, $a^n_{i+1/2}$, and $h^n_{i+1/2}$, and the solution jumps $\Delta\rho^n_{i+1/2} = \rho^n_{i+1} - \rho^n_i$, $\Delta u^n_{i+1/2} = u^n_{i+1} - u^n_i$, and $\Delta p^n_{i+1/2} = p^n_{i+1} - p^n_i$. The resulting expressions are

$$\alpha^n_{i+1/2,1} = \frac{1}{2(a^n_{i+1/2})^2}\left[\Delta p^n_{i+1/2} - \rho^n_{i+1/2}a^n_{i+1/2}\Delta u^n_{i+1/2}\right], \tag{7.38}$$

$$\alpha^n_{i+1/2,2} = \Delta\rho^n_{i+1/2} - \frac{\Delta p^n_{i+1/2}}{(a^n_{i+1/2})^2}, \tag{7.39}$$

$$\alpha^n_{i+1/2,3} = \frac{1}{2(a^n_{i+1/2})^2}\left[\Delta p^n_{i+1/2} + \rho^n_{i+1/2}a^n_{i+1/2}\Delta u^n_{i+1/2}\right]. \tag{7.40}$$

In deriving these wave strengths, it has been assumed that linearized approximations such as $\Delta(\rho u)^n_{i+1/2} = \rho^n_{i+1/2}\Delta u^n_{i+1/2} + u^n_{i+1/2}\Delta\rho^n_{i+1/2}$ apply in the more general case where the solution jumps are large.

For polytropic gases obeying the ideal equation of state, Roe (Ref. 7.37) has constructed approximate Riemann problem solutions and shown that the appropriate average state $\mathbf{U}^n_{i+1/2}$ should be defined as follows:

$$\rho^n_{i+1/2} = \sqrt{\rho^n_{i+1}\rho^n_i}, \tag{7.41}$$

$$Z^n_{i+1/2} = \frac{\sqrt{\rho^n_{i+1}}Z^n_{i+1} + \sqrt{\rho^n_i}Z^n_i}{\sqrt{\rho^n_{i+1}} + \sqrt{\rho^n_i}}, \quad Z = u, e, \text{ and } h, \tag{7.42}$$

$$p^n_{i+1/2} = \rho^n_{i+1/2}\left[h^n_{i+1/2} - e^n_{i+1/2} - \frac{1}{2}\left(u^n_{i+1/2}\right)^2\right], \tag{7.43}$$

$$a^n_{i+1/2} = \left\{(\gamma - 1)\left[h^n_{i+1/2} - \frac{1}{2}\left(u^n_{i+1/2}\right)^2\right]\right\}^{1/2}. \tag{7.44}$$

These averages guarantee conservation and afford the difference scheme excellent shock-capturing attributes (using the preceding definition of the average state, the approximate Riemann solution is exact for the case of a single discontinuity). Glaister (Ref. 7.45) has since extended Roe's approximate solution to the more general case of equilibrium real-gas equations of state that have the form $p = p(\rho, e)$. In this case, the preceding averages for ρ, u, e, h, and p given by Eqs. (7.41)–(7.43) are still applicable, but additional relations are required for determining local average-state values of the partial derivatives of the pressure with respect to the density and internal energy and for evaluating the average-state sound speed. Glaister's proposed averages for $\partial p/\partial\rho$ and $\partial p/\partial e$ are

$$\left(\frac{\partial p}{\partial \rho}\right)^n_{i+1/2} = \begin{cases} \dfrac{1}{2\Delta\rho^n_{i+1/2}}\left([p(\rho^n_{i+1}, e^n_{i+1}) + p(\rho^n_{i+1}, e^n_i)] - [p(\rho^n_i, e^n_{i+1}) + p(\rho^n_i, e^n_i)]\right) & \\ & \Delta\rho^n_{i+1/2} \neq 0, \\ \dfrac{1}{2}\left[\left(\dfrac{\partial p}{\partial \rho}\right)^n_{i+1} + \left(\dfrac{\partial p}{\partial \rho}\right)^n_i\right] & \Delta\rho^n_{i+1/2} = 0, \end{cases} \tag{7.45}$$

$$\left(\frac{\partial p}{\partial e}\right)^n_{i+1/2} = \begin{cases} \dfrac{1}{2\Delta e^n_{i+1/2}}\left([p(\rho^n_{i+1}, e^n_{i+1}) + p(\rho^n_{i+1}, e^n_i)] - [p(\rho^n_{i+1}, e^n_i) + p(\rho^n_i, e^n_i]\right)\right) & \\ & \Delta e^n_{i+1/2} \neq 0, \\ \dfrac{1}{2}\left[\left(\dfrac{\partial p}{\partial e}\right)^n_{i+1} + \left(\dfrac{\partial p}{\partial e}\right)^n_i\right] & \Delta e^n_{i+1/2} = 0, \end{cases} \tag{7.46}$$

and a is then specified using Eq. (7.14) by the expression

$$a^n_{i+1/2} = \left[\left(\frac{\partial p}{\partial \rho}\right)^n_{i+1/2} + \frac{p^n_{i+1/2}}{(\rho^n_{i+1/2})^2}\left(\frac{\partial p}{\partial e}\right)^n_{i+1/2}\right]^{1/2}. \tag{7.47}$$

Although other averages have been proposed, see for example Liou, van Leer, and Shuen (Ref. 7.46), this choice of averaging has been demonstrated to provide accurate solutions in a relatively efficient manner.

The higher-order flux-differencing scheme of Roe is a *smart* solution adaptive method that provides improved numerical accuracy and monotonic or oscillation-free solutions by having difference coefficients that depend on the local solution at each time step. The underlying constant-coefficient or *unlimited* scheme is a combination of the second-order schemes of Lax and Wendroff (Ref. 7.47) (central differences) and Warming and Beam (Ref. 7.48) (upwind differences). Flux limiters are employed to limit the magnitude of the second-order antidiffusive fluxes and reduce the scheme to the first-order fully-upwind method of Cole and Murman (Ref. 7.49) at local extrema of the solution. In the case of linear and nonlinear scalar homogeneous hyperbolic conservation laws and linear systems of homogeneous conservation laws, the resulting *nonlinear* scheme is TVD (Refs. 7.35 & 7.36), which guarantees that the scheme is monotonicity preserving. In the more general case of nonlinear inhomogeneous systems as given by Eq. (7.1), numerical experiments provide evidence that Roe's flux-limited scheme has good shock-capturing capabilities. The term 'higher-order' is applied to Roe's method to indicate that the formal accuracy of the scheme with uniform computational domain is second order for regions where the solution is smooth (i.e., almost everywhere), but reduces to first order at extrema. Note that in the difference scheme of Eqs. (7.30)–(7.32), the source terms of Eq. (7.1) are integrated by using a second-order Runge-Kutta or predictor corrector explicit time-stepping procedure. This provides second-order accuracy and makes the integration of the inhomogeneous terms consistent with the Roe-method time differencing of the homogeneous terms.

Following Sweby (Ref. 7.44) the flux limiters $\phi^n_{i+1/2,k}$ of Eq. (7.31) are defined to be functions of the local antidiffusive flux ratios. van Leer's flux limiter

$$\phi^n_{i+1/2,k} = \begin{cases} 0 & \nu^n_{i+1/2,k} > 0,\ b^n_{i,k} \le 0, \\ \dfrac{2b^n_{i,k}}{1+b^n_{i,k}} & \nu^n_{i+1/2,k} > 0,\ b^n_{i,k} > 0, \\ 0 & \nu^n_{i+1/2,k} < 0,\ b^n_{i+1,k} \le 0, \\ \dfrac{2}{1+b^n_{i+1,k}} & \nu^n_{i+1/2,k} < 0,\ b^n_{i+1,k} > 0, \end{cases} \tag{7.48}$$

is used for the $k = 1$ and 3 characteristic fields, and the *superbee* limiter of Roe

$$\phi^n_{i+1/2,k} = \begin{cases} 0 & \nu^n_{i+1/2,k} > 0,\ b^n_{i,k} \le 0\,, \\ \max(\min(1, 2b^n_{i,k}), \min(2, b^n_{i,k})) & \nu^n_{i+1/2,k} > 0,\ b^n_{i,k} > 0\,, \\ 0 & \nu^n_{i+1/2,k} < 0,\ b^n_{i+1,k} \le 0\,, \\ \max(\min(1, \dfrac{2}{b^n_{i+1,k}}), \min(2, \dfrac{1}{b^n_{i+1,k}})) & \nu^n_{i+1/2,k} < 0,\ b^n_{i+1,k} > 0\,, \end{cases} \tag{7.49}$$

is used for the $k = 2$ characteristic field. The latter more compressive limiter improves the sharpness of contact surfaces. The flux ratio $b^n_{i,k}$ is given by the ratio of the antidiffusive fluxes

$$b^n_{i,k} = \frac{|\nu^n_{i-1/2,k}|(1 - |\nu^n_{i-1/2,k}|)(\Delta \mathbf{U}^n_{i-1/2,k} \cdot \mathbf{N}_{\mathbf{U}_k})}{|\nu^n_{i+1/2,k}|(1 - |\nu^n_{i+1/2,k}|)(\Delta \mathbf{U}^n_{i+1/2,k} \cdot \mathbf{N}_{\mathbf{U}_k})}\,, \tag{7.50}$$

where $\mathbf{N}_{\mathbf{U}_k}$ are normalization row vectors. In the present algorithm, $\mathbf{N}_{\mathbf{U}_k} = [1, 0, 0]$ for $k = 1$, 2, and 3.

The time-marching procedure represented by Eqs. (7.30)–(7.32) is conditionally stable. The CFL criterion

$$\Delta t^n < \min_i \frac{\Delta x_{i+1/2}}{|u^n_i| + a^n_i}\,, \tag{7.51}$$

is used to restrict the magnitude of the time increment and thereby ensure stability and convergence of the numerical solutions.

It is also necessary to modify the finite-difference scheme near sonic points in order that the scheme be entropy satisfying and converge to the correct physical solution. In particular, the inviscid flux functions associated with nonlinear characteristic fields 1 and 3 must be augmented to prevent the formation of *expansion* shocks. A variant of the entropy fix suggested by Roe and Pike (Ref. 7.38) is employed. Consider elemental wave 1. A wave spreading parameter for this wave is defined to be

$$\delta^n_{i+1/2,1} = 2[\lambda^n_{i+1/2,1} - (u^n_i - a^n_i)]\,. \tag{7.52}$$

If $\lambda^n_{i+1/2,1} - 1/2\delta^n_{i+1/2,1} < 0$ and $\lambda^n_{i+1/2,1} + 1/2\delta^n_{i+1/2,1} > 0$, then the flux limiter $\phi^n_{i+1/2,1}$ is set to zero and the first-order flux jump is split into two components; that is,

$$\frac{1}{2}(\nu^n_{i+1/2,1} - |\nu^n_{i+1/2,1}|)\Delta \mathbf{U}^n_{i+1/2,1}\,, \tag{7.53}$$

is replaced by

$$\frac{f}{2}(\nu^{n+}_{i+1/2,1} - |\nu^{n+}_{i+1/2,1}|)\Delta \mathbf{U}^n_{i+1/2,1} + \frac{(1-f)}{2}(\nu^{n-}_{i+1/2,1} - |\nu^{n-}_{i+1/2,1}|)\Delta \mathbf{U}^n_{i+1/2,1}\,, \tag{7.54}$$

where

$$\nu^{n+}_{i+1/2,1} = \frac{1}{2}(\lambda^n_{i+1/2,1} + \frac{1}{2}\delta^n_{i+1/2,1})\,, \quad \nu^{n-}_{i+1/2,1} = \frac{1}{2}(\lambda^n_{i+1/2,1} - \frac{1}{2}\delta^n_{i+1/2,1})\,, \tag{7.55}$$

and

$$f = \frac{1}{2} + \frac{\lambda^n_{i+1/2,1}}{\delta^n_{i+1/2,1}}\,. \tag{7.56}$$

A similar procedure is required for the $k = 3$ nonlinear characteristic field.

7.5.2 Solution Algorithm for Nonequilibrium Gas Flows

For the case of the nonequilibrium thermodynamic model, Roe method solutions of Eq. (7.1) coupled with the additional species concentration and vibrational energy conservation equations of Eq. (7.15) are required. In the present work, these two subsystems defining the complete solution $\mathcal{U}(x,t) = \mathcal{U}(\mathbf{U}(x,t), \mathbf{W}(x,t))$ are not integrated in a directly coupled simultaneous fashion. Instead, two alternate gas dynamic and thermodynamic subsystems are defined and the resulting subsystems are then integrated in a time-lagged decoupled manner. This marching algorithm may be defined as follows. Given a solution $\mathcal{U}(x,t_0)$ of Eqs. (7.1) and (7.15) at

time t_0, an approximate solution at some later time $t_o+\Delta t$, where Δt is a small time increment, is obtained by first solving a frozen flow or gas dynamic initial value problem defined by

$$\frac{\partial}{\partial t}(\hat{\mathbf{U}}) + \frac{\partial}{\partial x}[\hat{\mathbf{F}}(\hat{\mathbf{U}})] = \hat{\mathbf{A}}(\hat{\mathbf{U}}) + \hat{\mathbf{S}}(\hat{\mathbf{U}}), \quad t_0 < t \le t_0 + \Delta t, \tag{7.57}$$

$$\hat{\mathbf{U}}(x, t_0) = \hat{\mathbf{U}}(\boldsymbol{\mathcal{U}}(x, t_0)) = \hat{\mathbf{U}}(\mathbf{U}(x, t_0), \mathbf{W}(x, t_0)), \tag{7.58}$$

and then solving a nonequilibrium thermodynamic initial value problem defined by

$$\frac{\partial \hat{\mathbf{W}}}{\partial t} + u\frac{\partial}{\partial x}[\mathbf{H}(\hat{\mathbf{W}})] = \hat{\mathbf{Q}}(\hat{\mathbf{W}}), \quad t_0 < t \le t_0 + \Delta t, \tag{7.59}$$

$$\hat{\mathbf{W}}(x, t_0) = \hat{\mathbf{W}}(\hat{\mathbf{U}}(x, t_0 + \Delta t), \mathbf{W}(x, t_0)), \tag{7.60}$$

where

$$\hat{\mathbf{U}} = \begin{bmatrix} \rho \\ \rho u \\ \rho\left(\frac{p}{\gamma - 1} + e_v + \frac{1}{2}u^2\right) \\ \rho\gamma \\ \rho R \\ \rho e_v \end{bmatrix}, \quad \hat{\mathbf{W}} = \begin{bmatrix} c_1 \\ \vdots \\ c_N \\ c_1 e_{v_1} \\ \vdots \\ c_N e_{v_N} \\ \sum_{s=1}^{N}\left[\frac{c_s R_s}{(\gamma_s - 1)}T + c_s e_{v_s}\right] + \frac{1}{2}u^2 \end{bmatrix}, \tag{7.61}$$

$$\hat{\mathbf{F}} = \begin{bmatrix} \rho u \\ \rho u^2 + p \\ \rho u\left(\frac{\gamma p}{(\gamma - 1)\rho} + e_v + \frac{1}{2}u^2\right) \\ \rho u\gamma \\ \rho u R \\ \rho u e_v \end{bmatrix}, \quad \hat{\mathbf{A}} = \begin{bmatrix} -\rho u\frac{1}{A}\frac{dA}{dx} \\ -\rho u^2\frac{1}{A}\frac{dA}{dx} \\ -\rho u\left(\frac{\gamma p}{(\gamma - 1)\rho} + e_v + \frac{1}{2}u^2\right)\frac{1}{A}\frac{dA}{dx} \\ -\rho u\gamma\frac{1}{A}\frac{dA}{dx} \\ -\rho u R\frac{1}{A}\frac{dA}{dx} \\ -\rho u e_v\frac{1}{A}\frac{dA}{dx} \end{bmatrix}, \tag{7.62}$$

$$\hat{\mathbf{S}} = \begin{bmatrix} 0 \\ F_{wall} + F_{loss} \\ Q_{wall} \\ 0 \\ 0 \\ 0 \end{bmatrix}, \quad \mathbf{H} = \begin{bmatrix} c_1 \\ \vdots \\ c_N \\ c_1 e_{v_1} \\ \vdots \\ c_N e_{v_N} \\ 0 \end{bmatrix}, \quad \hat{\mathbf{Q}} = \begin{bmatrix} w_1 \\ \vdots \\ w_N \\ c_1 q_1 + \beta_1 w_1 e_{v_1} \\ \vdots \\ c_N q_N + \beta_N w_N e_{v_N} \\ -\sum_{s=1}^{N} w_s \Delta h^0_{f_s} \end{bmatrix}. \tag{7.63}$$

The approximate solution at $t_0 + \Delta t$ is then given by

$$\mathcal{U}(x, t_0 + \Delta t) \approx \mathcal{U}(\hat{\mathbf{U}}(x, t_0 + \Delta t), \hat{\mathbf{W}}(x, t_0 + \Delta t)). \tag{7.64}$$

A solution for all time $t > t_0$ may be obtained by repeating the preceding two-step algorithm and, in the limit of vanishing Δt, this solution should converge to the exact solution of Eqs. (7.1) and (7.15).

The six-component subsystem of Eq. (7.57) has been derived by employing a *frozen flow* assumption and setting the finite-rate thermodynamic source terms of Eq. (7.1) to zero. Under this assumption, the behaviour of the gaseous mixture is essentially that of a polytropic (thermally and calorically perfect) gas, except that the specific heat ratio and gas constant may vary throughout the flow field and a portion of the internal energy is locked in the vibrational modes. The last three equations of the gas dynamic subsystem are introduced to include these effects and describe changes in the quantities γ, R, and e_v, which, in the frozen flow limit, are merely convected with the flow. Note that the solution of Eq. (7.57) updates the mixture gas dynamic flow properties (e.g., ρ, u, e, e_v, p, etc..) but does not alter the individual species mass fractions or vibrational energies.

The multi-component N-species nonequilibrium thermodynamic subsystem represented by Eq. (7.59) has been derived by assuming that the velocity and density distributions are known and fixed. This set describes the time rate of change of the species mass fractions and vibrational energies and the total internal energy of the mixture. It includes the source terms neglected in the derivation of Eq. (7.57). The primitive variables c_s, e_{v_s}, and T, and con-

sequently e, e_v, p, and the other thermodynamic properties, are all updated by solving the thermodynamic subsystem. However, ρ and u remain unchanged.

The preceding decoupled solution procedure is similar in spirit to the techniques put forward by Glaz, Colella, Collins and Ferguson (Ref. 7.50) and Ben-Artzi (Ref. 7.51), and the resulting subsystems resemble the decoupled equation sets that may be obtained by using the equation-partitioning procedure suggested by Yee and Shinn (Ref. 7.52). The term 'partially decoupled' is applied herein to distinguish the current method from fully-coupled algorithms, which at each level in a marching procedure solve all of the conservation equations together in a single step, and loosely-coupled or chemistry-split techniques, which at each level decouple the gas dynamic and finite-rate thermodynamic equations and solve the two sets separately in a two-stage process (Ref. 7.52).

Unlike fully-coupled methods, the present alternative provides a distinct separation of the gas dynamic and finite-rate models. As a consequence, one solver can be developed for Eq. (7.57) and used to predict the flow of many different nonequilibrium gaseous mixtures. Mixture-specific solvers are only required for Eq. (7.59). This simplifies computer program development and can make the solution algorithm more versatile than many fully-coupled techniques.

The partial-decoupling approach differs from loosely-coupled or chemistry-split methods because the decoupling procedure readily permits the use of the eigenvalues and eigenvectors of the complete system in the evaluation of the numerical fluxes of each subsystem. Loosely-coupled methods usually employ the eigenvalues and eigenvectors of each decoupled subsystem. It is believed that the use of the eigenvalues and eigenvectors of the full equations enhances the coupling between the decoupled equation sets and thereby improves numerical solution quality (Ref. 7.52).

Letting $\mathcal{U}_i^n$ be the numerical approximation of the solution to Eqs. (7.1) and (7.15) at $x = x_i$ and $t = t^n$, the solution at subsequent time levels is obtained by employing the partial-decoupling procedure described above and applying explicit and semi-implicit versions of Roe's method to the gas dynamic and thermodynamic subsystems, respectively. The complete algorithm can be defined by

$$\mathcal{U}_i^{n+2} = \mathcal{L}_{\hat{\mathrm{U}}}^{\Delta t} \mathcal{L}_{\hat{\mathrm{W}}}^{2\Delta t} \mathcal{L}_{\hat{\mathrm{U}}}^{\Delta t} \mathcal{U}_i^n \,, \tag{7.65}$$

where the solution operator $\mathcal{L}^{\Delta t}_{\hat{\mathbf{U}}}\mathcal{U}^n_i = \mathcal{U}(\hat{\mathbf{U}}_i^{\widetilde{n+1}}, \hat{\mathbf{W}}_i^n)$ is represented by

$$\hat{\mathbf{U}}_i^{\overline{n+1}} = \hat{\mathbf{U}}_i^n + \Delta\hat{\mathbf{U}}_i^{\overline{n}} = \hat{\mathbf{U}}_i^n + \Delta t^n \left(\hat{\mathbf{A}}_i^n + \hat{\mathbf{S}}_i^n\right) -$$

$$\frac{1}{2}\sum_{k=1}^{6}\left\{[(\nu^n_{i+1/2,k} - |\nu^n_{i+1/2,k}|) + \phi^n_{i+1/2,k}|\nu^n_{i+1/2,k}|(1 - |\nu^n_{i+1/2,k}|)]\Delta\hat{\mathbf{U}}^n_{i+1/2,k} + \right.$$

$$\left.[(\nu^n_{i-1/2,k} + |\nu^n_{i-1/2,k}|) - \phi^n_{i-1/2,k}|\nu^n_{i-1/2,k}|(1 - |\nu^n_{i-1/2,k}|)]\Delta\hat{\mathbf{U}}^n_{i-1/2,k}\right\}, \tag{7.66}$$

$$\hat{\mathbf{U}}_i^{\widetilde{n+1}} = \hat{\mathbf{U}}_i^n + \Delta\hat{\mathbf{U}}_i^{\widetilde{n}} = \hat{\mathbf{U}}_i^{\overline{n+1}} + \frac{1}{2}\Delta t^n \left(\hat{\mathbf{A}}_i^{\overline{n+1}} - \hat{\mathbf{A}}_i^n + \hat{\mathbf{S}}_i^{\overline{n+1}} - \hat{\mathbf{S}}_i^n\right), \tag{7.67}$$

and the solution operator $\mathcal{L}^{\Delta t}_{\hat{\mathbf{W}}}\mathcal{U}^n_i = \mathcal{U}(\hat{\mathbf{U}}_i^n, \hat{\mathbf{W}}_i^{\widetilde{n+1}})$ is given by

$$\left[\mathbf{I} - \theta\Delta t^n \frac{\partial\hat{\mathbf{Q}}}{\partial\hat{\mathbf{W}}})^n_i\right]\left(\hat{\mathbf{W}}_i^{\widetilde{n+1}} - \hat{\mathbf{W}}_i^n\right) = \left[\mathbf{I} - \theta\Delta t^n \frac{\partial\hat{\mathbf{Q}}}{\partial\hat{\mathbf{W}}})^n_i\right]\Delta\hat{\mathbf{W}}_i^{\widetilde{n}} = \Delta t^n\hat{\mathbf{Q}}_i^n -$$

$$\frac{1}{2}\sum_{k=1}^{2N+1}\left\{[(\omega^n_{i+1/2} - |\omega^n_{i+1/2}|) + \psi^n_{i+1/2,k}|\omega^n_{i+1/2}|(1 - |\omega^n_{i+1/2,k}|)]\Delta\mathbf{H}^n_{i+1/2,k} + \right.$$

$$\left.[(\omega^n_{i-1/2} + |\omega^n_{i-1/2}|) - \psi^n_{i-1/2,k}|\omega^n_{i-1/2}|(1 - |\omega^n_{i-1/2}|)]\Delta\mathbf{H}^n_{i-1/2,k}\right\}, \tag{7.68}$$

and where $\Delta\hat{\mathbf{U}}_i^{\widetilde{n}} = \hat{\mathbf{U}}_i^{\widetilde{n+1}} - \hat{\mathbf{U}}_i^n$, $\Delta\hat{\mathbf{U}}_i^{\overline{n}} = \hat{\mathbf{U}}_i^{\overline{n+1}} - \hat{\mathbf{U}}_i^n$, $\Delta\hat{\mathbf{W}}_i^{\widetilde{n}} = \hat{\mathbf{W}}_i^{\widetilde{n+1}} - \hat{\mathbf{W}}_i^n$, and $\hat{\mathbf{U}}_i^{\widetilde{n+1}}$, $\hat{\mathbf{U}}_i^{\overline{n+1}}$, and $\hat{\mathbf{W}}_i^{\widetilde{n+1}}$ denote intermediate solution states.

The solution of the frozen-flow gas dynamic subsystem Eq. (7.57) is provided by the difference scheme of Eqs. (7.66) and (7.67). As was the case for the solution of the hyperbolic conservation laws of gases obeying the ideal and equilibrium *real-gas* equations of state, the quantities $\nu^n_{i+1/2,k}$ and $\Delta\mathbf{U}^n_{i+1/2,k}$ appearing in these equations are again the local average CFL numbers and solution jump vectors. They are defined in terms of the eigenvalues and eigenvectors $\lambda^n_{i+1/2,k}$ and $\mathbf{e}^n_{i+1/2,k}$ of the Jacobian matrix $\hat{\mathbf{J}} = \partial\hat{\mathbf{F}}/\partial\hat{\mathbf{U}}$ evaluated at some average state and are given by

$$\nu^n_{i+1/2,k} = \frac{\Delta t^n \lambda^n_{i+1/2,k}}{\Delta x_{i+1/2}}, \tag{7.69}$$

$$\Delta\hat{\mathbf{U}}^n_{i+1/2,k} = \alpha^n_{i+1/2,k}\mathbf{e}^n_{i+1/2,k}\,, \tag{7.70}$$

where $\alpha^n_{i+1/2,k}$ are the wave strengths. It can be shown that the eigenvalues and eigenvectors of the flux Jacobian $\hat{\mathbf{J}}$ of the six-component subsystem represented by Eq. (7.57) are

$$\lambda^n_{i+1/2,1} = u^n_{i+1/2} - a^n_{i+1/2}\,, \quad \lambda^n_{i+1/2,6} = u^n_{i+1/2} + a^n_{i+1/2}\,, \tag{7.71}$$

$$\lambda^n_{i+1/2,2} = \lambda^n_{i+1/2,3} = \lambda^n_{i+1/2,4} = \lambda^n_{i+1/2,5} = u^n_{i+1/2}\,, \tag{7.72}$$

$$\mathbf{e}^n_{i+1/2,1} = \begin{bmatrix} 1 \\ u^n_{i+1/2} - a^n_{i+1/2} \\ h^n_{i+1/2} - u^n_{i+1/2}a^n_{i+1/2} \\ \gamma^n_{i+1/2} \\ R^n_{i+1/2} \\ e^n_{v_{i+1/2}} \end{bmatrix}, \quad \mathbf{e}^n_{i+1/2,6} = \begin{bmatrix} 1 \\ u^n_{i+1/2} + a^n_{i+1/2} \\ h^n_{i+1/2} + u^n_{i+1/2}a^n_{i+1/2} \\ \gamma^n_{i+1/2} \\ R^n_{i+1/2} \\ e^n_{v_{i+1/2}} \end{bmatrix}, \tag{7.73}$$

$$\mathbf{e}^n_{i+1/2,2} = \begin{bmatrix} 1 \\ u^n_{i+1/2} \\ \frac{1}{2}(u^n_{i+1/2})^2 + e^n_{v_{i+1/2}} \\ \gamma^n_{i+1/2} \\ R^n_{i+1/2} \\ e^n_{v_{i+1/2}} \end{bmatrix}, \quad \mathbf{e}^n_{i+1/2,3} = \begin{bmatrix} 0 \\ 0 \\ -\dfrac{(a^n_{i+1/2})^2}{(\gamma^n_{i+1/2}-1)^2} \\ \gamma^n_{i+1/2} \\ 0 \\ 0 \end{bmatrix}, \tag{7.74}$$

$$e^n_{i+1/2,4} = \begin{bmatrix} 0 \\ 0 \\ 0 \\ 0 \\ R^n_{i+1/2} \\ 0 \end{bmatrix}, \quad e^n_{i+1/2,5} = \begin{bmatrix} 0 \\ 0 \\ e^n_{v_{i+1/2}} \\ 0 \\ 0 \\ e^n_{v_{i+1/2}} \end{bmatrix}, \tag{7.75}$$

with $h = [\gamma p/(\gamma - 1)\rho] + e_v + u^2/2$. An extension of Roe's approximate Riemann solver has been developed herein to specify the appropriate average state primitive variables and wave strengths used in the preceding equations. This extension of the approximate Riemann problem solution for the subsystem of Eq. (7.57) yields the following averages:

$$\rho^n_{i+1/2} = \sqrt{\rho^n_{i+1}\rho^n_i}, \tag{7.76}$$

$$Z^n_{i+1/2} = \frac{\sqrt{\rho^n_{i+1}}Z^n_{i+1} + \sqrt{\rho^n_i}Z^n_i}{\sqrt{\rho^n_{i+1}} + \sqrt{\rho^n_i}}, \quad Z = u, \gamma, R, e_v, \text{ and } h, \tag{7.77}$$

$$a^n_{i+1/2} = \left\{(\gamma^n_{i+1/2} - 1)\left[h^n_{i+1/2} - e^n_{v_{i+1/2}} - \frac{1}{2}\left(u^n_{i+1/2}\right)^2\right]\right\}^{1/2}, \tag{7.78}$$

and wave strengths

$$\alpha^n_{i+1/2,1} = \frac{1}{2(a^n_{i+1/2})^2}\left[\Delta p^n_{i+1/2} - \rho^n_{i+1/2}a^n_{i+1/2}\Delta u^n_{i+1/2}\right], \tag{7.79}$$

$$\alpha^n_{i+1/2,2} = \Delta\rho^n_{i+1/2} - \frac{\Delta p^n_{i+1/2}}{(a^n_{i+1/2})^2}, \tag{7.80}$$

$$\alpha^n_{i+1/2,3} = \frac{\rho^n_{i+1/2}}{\gamma^n_{i+1/2}}\Delta\gamma^n_{i+1/2}, \quad \alpha^n_{i+1/2,4} = \frac{\rho^n_{i+1/2}}{R^n_{i+1/2}}\Delta R^n_{i+1/2}, \quad \alpha^n_{i+1/2,5} = \frac{\rho^n_{i+1/2}}{e^n_{v_{i+1/2}}}\Delta e^n_{v_{i+1/2}}, \tag{7.81}$$

$$\alpha^n_{i+1/2,6} = \frac{1}{2(a^n_{i+1/2})^2}\left[\Delta p^n_{i+1/2} + \rho^n_{i+1/2}a^n_{i+1/2}\Delta u^n_{i+1/2}\right]. \tag{7.82}$$

Note that the flux limiters $\phi^n_{i+1/2,k}$, which provide the difference scheme of Eqs. (7.66) and (7.67) with the desirable TVD property, are evaluated similarly to the limiters used in the solution for the polytropic and equilibrium cases. The flux limiter of van Leer defined by Eq. (7.48) is used for the $k = 1$ and 6 characteristic fields and the superbee flux limiter of Eq. (7.49) is used for the $k = 2$, 3, 4, and 5 characteristic fields. Appropriate values for the flux ratios and normalization row vectors are used. Finally, note also that the flux functions of the $k = 1$ and 6 nonlinear characteristic fields are modified by employing entropy fixes of the form given by Eqs. (7.52)–(7.56).

The integration of the thermodynamic subsystem Eq. (7.59) is provided by the TVD semi-implicit scheme of Eq. (7.68). In Eq. (7.68), $\mathbf{I}$ is the identity matrix, $\partial\hat{\mathbf{Q}}/\partial\hat{\mathbf{W}}$ is the source Jacobian matrix, $\omega^n_{i+1/2}$ and $\Delta\mathbf{H}^n_{i+1/2,k}$ are the local average CFL number and solution jump vectors used in evaluating the flux functions for the species concentration and vibrational energy equations, and $\psi^n_{i+1/2,k}$ are the flux limiters. The homogeneous form of the subsystem given by Eq. (7.59) is essentially a system of independent convection equations and, therefore, the numerical flux functions can be evaluated quite simply. The CFL number $\omega^n_{i+1/2}$ is given by

$$\omega^n_{i+1/2} = \frac{\Delta\iota^n u^n_{i+1/2}}{\Delta x_{i+1/2}}, \tag{7.83}$$

where $u^n_{i+1/2}$ is evaluated by using Eqs. (7.76) and (7.77) resulting from the extended approximate Riemann solver. This ensures that the eigenvalues and eigenvectors of the fully-coupled system are used in the computation of the flux functions of both the gas dynamic and thermodynamic subsystems. The solution jump column vectors for the $N_D = 2N + 1$ component thermodynamic subsystem are given by

$$\Delta\mathbf{H}^n_{i+1/2,k} = \mathbf{D}_k\Delta\mathbf{H}^n_{i+1/2}, \tag{7.84}$$

where $\Delta\mathbf{H}^n_{i+1/2} = \mathbf{H}^n_{i+1} - \mathbf{H}^n_i$, $\mathbf{D}_k$ is a diagonal matrix for which the elements of the diagonal are $(\delta_{1k}, \ldots, \delta_{kk}, \ldots, \delta_{N_Dk})$, and δ is the usual Kronecker delta function. Finally, the flux limiters $\psi^n_{i+1/2,k}$ for each component of the solution vector, which limit the magnitude of

the antidiffusive flux in Eq.(7.68), are evaluated by employing the superbee formulation of Eq.(7.49). The flux ratio is again defined in terms of the ratio and the antidiffusive fluxes and the normalization row vector is chosen to recover the component of the antidiffusive flux vector associated with the k^{th} component of the solution vector $\hat{\mathbf{W}}$. Note that entropy corrections are not required in the solution of the thermodynamic subsystem.

The stiffness of the source terms associated with the finite-rate reaction and relaxation processes of Eq.(7.68) force the time step sizes of explicit schemes to be excessively small and the corresponding computer times to be prohibitively large. For this reason, the source terms of the operator $\mathcal{L}^{\Delta t}_{\hat{\mathbf{W}}}$ are integrated by using an implicit time-stepping procedure that is similar to the semi-implicit algorithms proposed by Bussing and Murman (Ref. 7.53), Yee and Shinn (Ref. 7.52), and Ben-Artzi (Ref. 7.51) for the computation of chemically reacting flows. These schemes treat only the source terms implicitly. This effectively alleviates the stiffness associated with the finite-rate relaxation and reaction time scales while avoiding large matrix inversions. The quantity $[\mathbf{I} - \theta\Delta t^n(\partial\hat{\mathbf{Q}}/\partial\hat{\mathbf{W}})^n_i]$ is similar to the preconditioning matrices used by Bussing and Murman (Ref. 7.53). The parameter θ controls the implicit time stepping. For $\theta = 0$, the time differencing is Euler explicit. For $\theta = 1$, the time differencing is Euler implicit. This value produces the most stable scheme and is appropriate for problems with extremely stiff source terms. A value of $\theta = 1/2$ produces a trapezoidal implicit time differencing that is best suited and consistent with the explicit time-differencing of the homogeneous terms. Note that the time-marching procedure represented by Eqs.(7.66)–(7.68) is conditionally stable. For $\theta \geq 1/2$, the CFL condition of Eq.(7.51) ensures stability and convergence.

7.5.3 Boundary Conditions

Boundary conditions are necessary for the prescription of the numerical solutions at the extremities of the computational domains. There are two types of boundary conditions required for the hypersonic gun tunnel simulations. Firstly, a solid-surface reflecting boundary condition is needed for the flow properties at the closed end of the reservoir and the front and back faces of the moving piston. Secondly, an outflow boundary condition is needed for the flow properties at the exit of the contoured nozzle.

Reflecting boundary conditions are applied by forcing the flow to have the velocity of the solid boundary or piston and then employing Rankine-Hugoniot and Riemann invariant relations across shocks and rarefaction waves to determine the other solution properties. For

the outflow boundary condition at the nozzle exit, it is recognized that, except for very early in the tunnel operation cycle, the flow is almost always supersonic at this point and disturbances from the test section cannot propagate upstream. Simple constant extrapolation boundary conditions (Ref. 7.54) at the nozzle exit are therefore quite appropriate and are used here.

7.6 Discussion of Numerical Results and Performance Data

This section presents numerical predictions of the UTIAS-RPI hypersonic gun tunnel performance obtained by solving the one-dimensional flow and thermodynamic model equations of Subsections 7.3 and 7.4 using the TVD numerical integration schemes described in Subsection 7.5. The performance of the facility is first assessed by considering its operation under two firing states that are commonly used for much of the ongoing experimental hypersonic research at UTIAS. Additional numerical results are then presented to establish more thoroughly the tunnel performance envelope and operating range.

The UTIAS-RPI gun tunnel is generally operated with initial reservoir pressure $p_{res} = 20.5$ MPa, initial reservoir and barrel temperatures $T_{res} = T_{brl} = 293$ K, and piston mass $m_p = 96$ g. Different operating conditions are achieved by varying the initial barrel pressure p_{brl}. Two firing modes are employed in the majority of experiments. In one mode, $p_{brl} = 400$ kPa and in the other, $p_{brl} = 200$ kPa. Note that the firing state with the lower initial barrel pressure produces a higher stagnation enthalpy flow in the test section.

For the computations of the tunnel operation in these two modes, and indeed for all of the predictions presented in this subsection, the unsteady motion of the driver and working gases is solved for the entire facility between the closed end of the reservoir and the nozzle exit. The cross-sectional area function $A(x)$ used in the numerical simulations is illustrated in Fig. 7.2 in terms of the axial position x and local tunnel radius $r(x)$ where $A = \pi r^2$. A total of 570 spatial nodes are used to represent the discretized computational domain. Convergence tests suggest that this nodal density is sufficient as numerical errors appear to be nominally less than 3–5% when 500–600 nodes are used. Boundary-layer frictional losses and heat transfer are included with $\varepsilon = 0.025$ mm. These loss effects are, however, not included in the computation of the flow in the nozzle section. This is a reasonable approximation because the flow in this section of the tunnel is definitely not fully developed. The nozzle has been specifically designed to produce a relatively large inviscid core flow with a boundary layer that is confined, for the most part, to the near wall region. A value of 0.25 is assumed for the head-

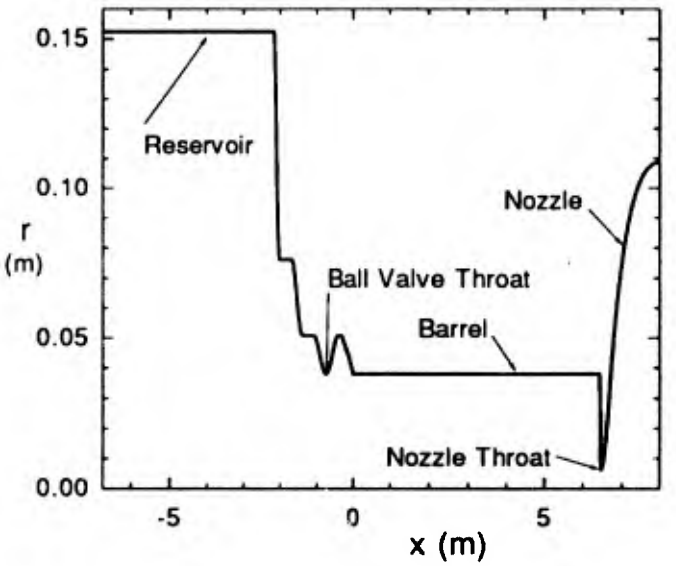

Figure 7.2: UTIAS-RPI hypersonic impulse tunnel geometry used in numerical simulations.

loss coefficients K of the two diaphragms located just downstream of the ball valve section. Note that the diaphragm head losses are phased in during the first 5 ms after diaphragm rupture using a linear-ramping function in order to more accurately simulate the developing flow situation occurring in the initial stages of tunnel startup. All of the computations were performed on a Hewlett-Packard/Apollo 400s workstation. The simulations of the ideal and equilibrium gas cases required approximately 4–5 central-processing-unit (CPU) hours, whereas the nonequilibrium gas cases required about 13–14 CPU hours.

The predictions of the tunnel operation with initial barrel pressures of 400 and 200 kPa are presented in Figs. 7.3–7.14. The first set of results for a barrel pressure of 400 kPa is given in Figs. 7.3–7.7, whereas the other set for a barrel pressure of 200 kPa is in Figs. 7.8–7.14. Note that the calculations were performed with the ideal, real equilibrium, and five-species four-temperature nonequilibrium gas models, and the results for these three different thermodynamic models are compared in these figures.

Consider first the results with $p_{brl} = 400$ kPa. The piston velocity V_p and acceleration a_p as a function of piston position in the barrel x_p are given in Fig. 7.3. From the figure, it is clear that the piston rapidly accelerates during the first meter of travel and then is subjected to very little acceleration until the first reflected shock from the barrel end causes it to decelerate.

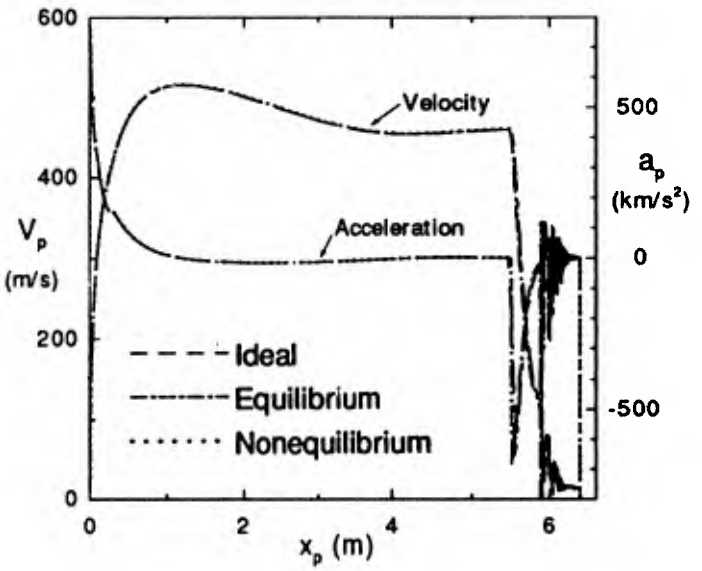

Figure 7.3: Piston velocity V_p and acceleration a_p,
$p_{res} = 20.5$ MPa, $p_{brl} = 400$ kPa,
$T_{res} = T_{brl} = 293$ K, $m_p = 96$ g.

Subsequent reflections cause further deceleration and the piston eventually comes to rest at the end of the barrel ($x_p \approx 6.7$ m). A maximum velocity of somewhere near 515 m/s and a peak acceleration approaching 760 km/s^2 are predicted. The figure also clearly illustrates that high-temperature and (or) real-gas effects have very little effect on the predicted piston motion. The piston trajectories determined using the real equilibrium and nonequilibrium gas thermodynamic models are virtually identical to the trajectory obtained using the polytropic model.

The predicted temporal variations of the stagnation pressure p_o and temperature T_o at the end of the barrel as the flow in the nozzle relaxes towards a steady state condition are illustrated in Figs. 7.4 and 7.5. The time $t = 0$, in these and other temporal distributions to follow, corresponds to the time when the first of the two diaphragms ruptures. The multiple shock reflections associated with the nonisentropic compression of the working gas is clearly illustrated by the successive pressure and temperature jumps in the time histories. These jumps indicate the passage of the reflected shocks between the piston front face and end of the barrel. The two sets of curves in the figures indicate that high-temperature phenomena are important in determining the nozzle flow stagnation conditions. Although there are only minor differences between the ideal, equilibrium, and nonequilibrium results for the stagnation pressures, the stagnation temperatures obtained with each thermodynamic model are quite different. It can

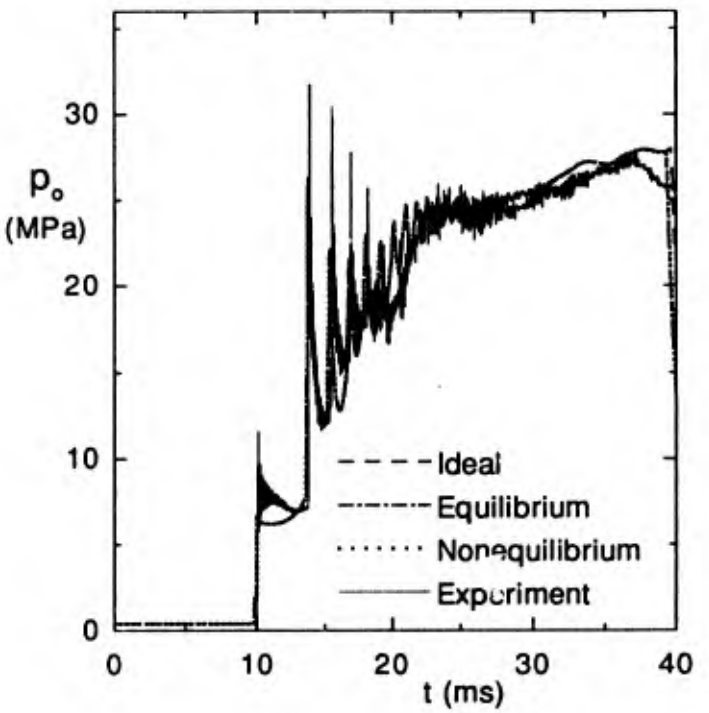

Figure 7.4: Barrel end stagnation pressure p_o,
$p_{res} = 20.5$ MPa, $p_{brl} = 400$ kPa,
$T_{res} = T_{brl} = 293$ K, $m_p = 96$ g.

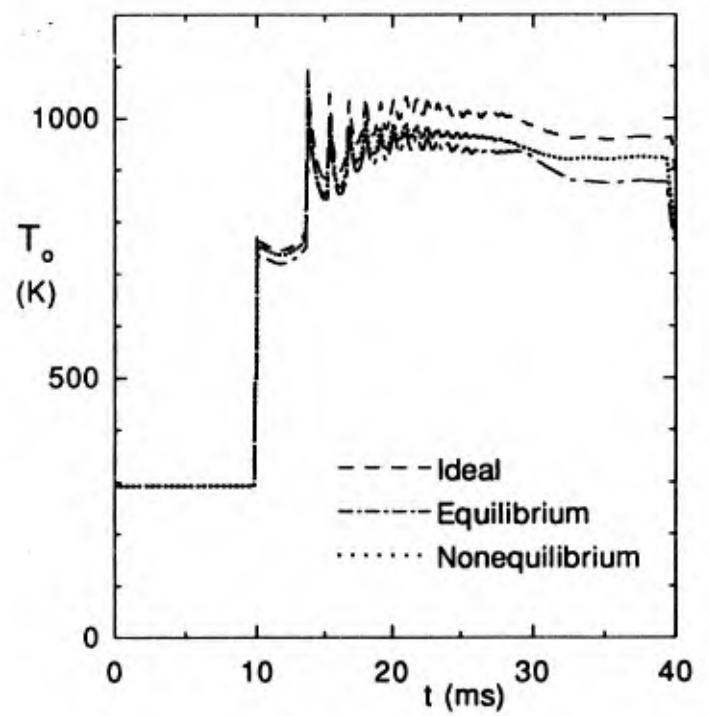

Figure 7.5: Barrel end stagnation temperature T_o,
$p_{res} = 20.5$ MPa, $p_{brl} = 400$ kPa,
$T_{res} = T_{brl} = 293$ K, $m_p = 96$ g.

be seen that the predicted stagnation pressure during the period of relatively steady-state nozzle flow is between 24–27 MPa for all three thermodynamic models. This pressure begins to drop rapidly around $t = 39$ ms when the working gas is depleted and the piston comes to rest at the end of the barrel. The polytropic model provides a higher stagnation temperature than the temperatures predicted by the two real-gas models, as should be expected. The predicted ideal stagnation temperature appears to be around 980–1000 K whereas the equilibrium and nonequilibrium values are around 910–920 and 940–950 K, respectively. Note that at these stagnation temperatures, vibrational excitation of the nitrogen (N_2) and oxygen (O_2) diatomic molecules is significant, but dissociation of these species is small. The differences in the curves of Fig. 7.5 indicate that nonequilibrium relaxation must be considered in order to determine the stagnation temperature accurately.

As an additional comparison, an experimental stagnation pressure trace measured during a firing of the UTIAS-RPI facility with an initial barrel pressure of 400 kPa is also presented in Fig. 7.4. It is evident from the figure that many of the detailed features and complicated wave structure of the nonstationary flow in the tunnel, such as shock strengths and times of

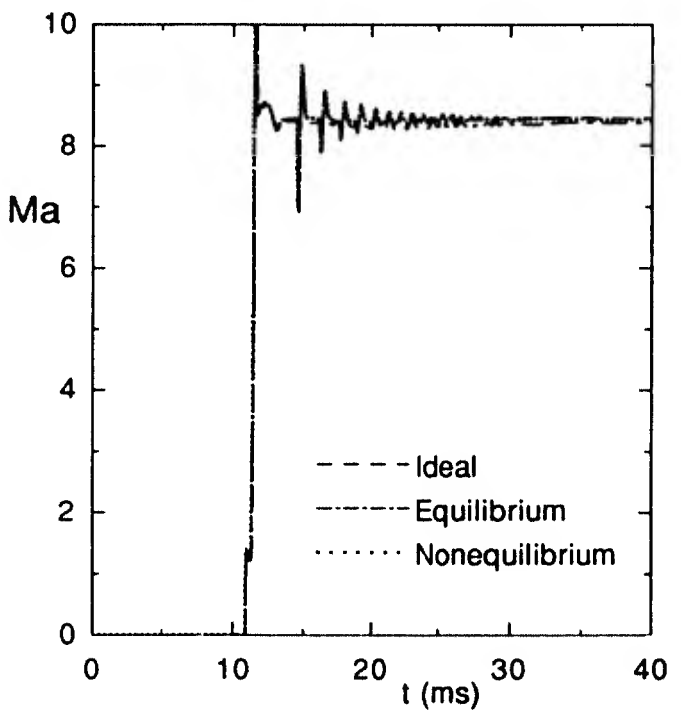

Figure 7.6: Nozzle exit Mach number M,
$p_{res} = 20.5$ MPa, $p_{brl} = 400$ kPa,
$T_{res} = T_{brl} = 293$ K, $m_p = 96$ g.

arrival, are correctly reproduced by the one-dimensional nonstationary flow model calculations and that the numerical predictions are in good agreement with the experimental time-history data, both qualitatively and quantitatively.

Figure 7.6 depicts the temporal variation of the flow Mach number M at the exit of the contoured nozzle. The figure clearly demonstrates the establishment of steady flow in the nozzle. The exit Mach number initially oscillates about a mean value. These oscillations indicate the passage of transmitted shock waves through the nozzle and test section. A relatively steady-state nozzle flow is then achieved at about 25 ms after the first diaphragm has burst and is maintained until sometime just after the $t = 40$ ms mark. At this time, the piston has come to rest and the stagnation pressure and temperature at the nozzle entrance have dropped dramatically. This suggests a run time of somewhere between 15 and 17 ms for this particular mode of tunnel operation. It is interesting to note that, as mentioned in Subsection 7.2, the contoured nozzle employed in the present impulse tunnel configuration was built with an exit flow Mach number of 8.33 as one of the design specifications and that, for all thermodynamic models, the predicted steady-state nozzle exit Mach number is about 8.35–8.45. Note also that the numerical results show that the pressure p, temperature T, and specific heat ratio γ of the

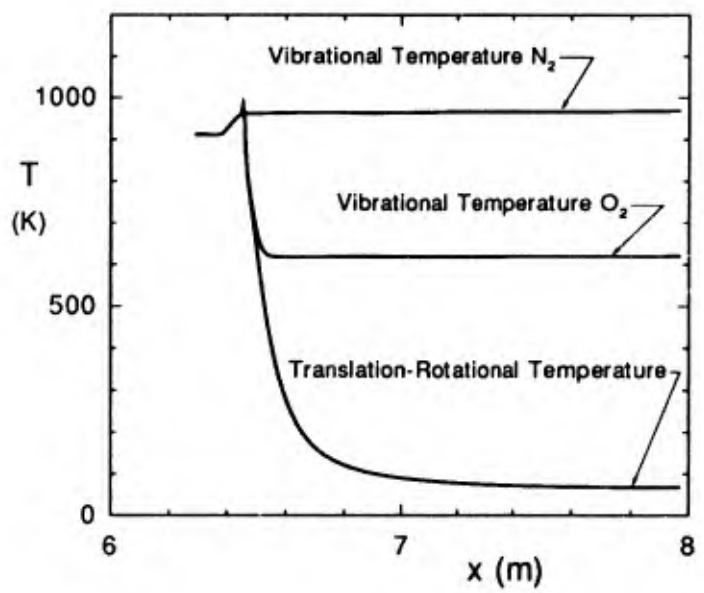

Figure 7.7: Temperature distributions in nozzle, $t = 30$ ms,
$p_{res} = 20.5$ MPa, $p_{brl} = 400$ kPa,
$T_{res} = T_{brl} = 293$ K, $m_p = 96$ g.

air flow at the nozzle exit are approximately 1.6–1.7 kPa, 65–75 K, and 1.4, respectively.

Plots of the spatial distributions of the vibrational temperatures of the two excited diatomic species (N_2 and O_2) and the equilibrium translational and rotational temperature at time t = 30 ms in the UTIAS-RPI tunnel from the piston front face to nozzle exit are also shown in Fig. 7.7. These numerical results were obtained with the nonequilibrium thermodynamic model. Note that the calculations performed show that in this operation mode dissociation/recombination effects are negligible and the principal nonequilibrium phenomenon that occurs at stagnation in the barrel is vibrational relaxation. This is as expected for these stagnation temperatures. It has long been known that typically vibrationally excited air *freezes* when it becomes moderately supersonic (Refs. 7.15 & 7.17) and this seems to be the case here. The distributions of Fig. 7.7 demonstrate that the air in the nozzle freezes somewhere close to the nozzle throat, with the nitrogen freezing first near 965 K and the oxygen following at a temperature of about 620 K. This produces a test-section flow of air with excited vibrational states and vibrational temperatures much higher than the equilibrium translational-rotational temperature of 67 K.

Figures 7.8–7.12 show the numerical predictions of the UTIAS-RPI hypersonic gun tunnel operation with an initial barrel pressure of 200 kPa. The results are similar to those of the

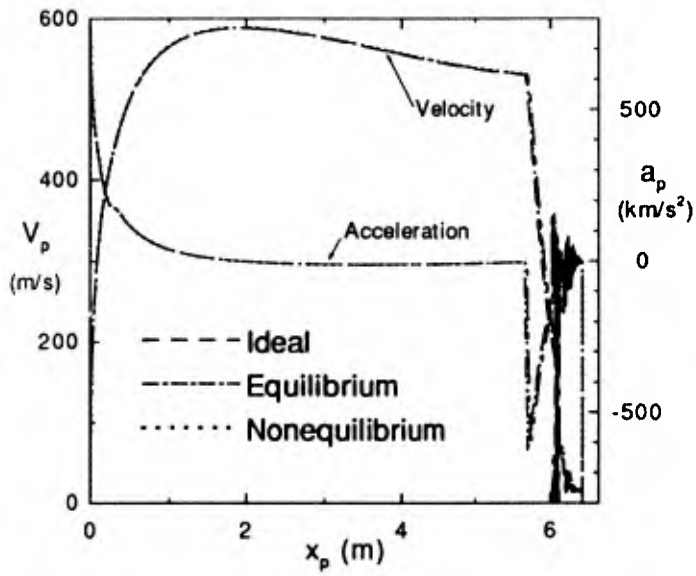

Figure 7.8: Piston velocity V_p and acceleration a_p,
p_{res} = 20.5 MPa, p_{brl} = 200 kPa,
$T_{res} = T_{brl}$ = 293 K, m_p = 96 g.

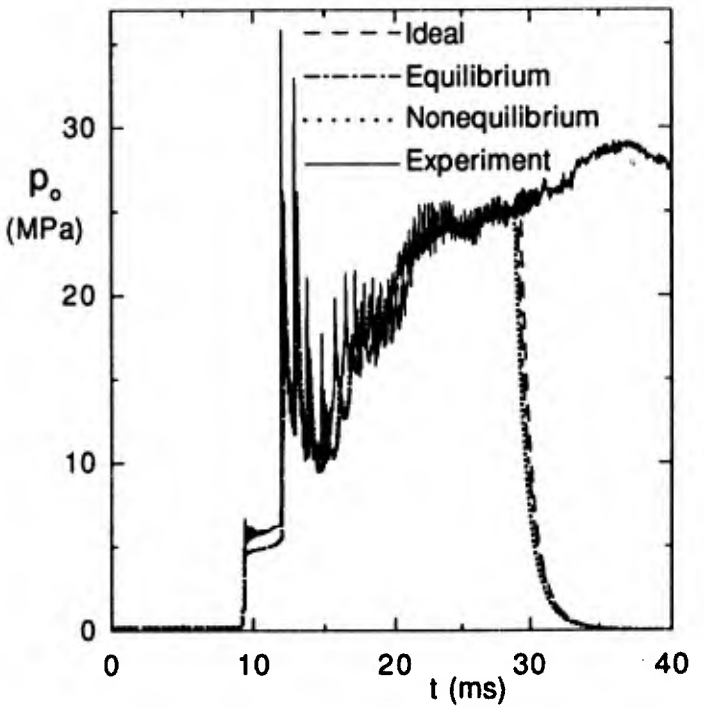

Figure 7.9: Barrel end stagnation pressure p_o,
$p_{res} = 20.5$ MPa, $p_{brl} = 200$ kPa,
$T_{res} = T_{brl} = 293$ K, $m_p = 96$ g.

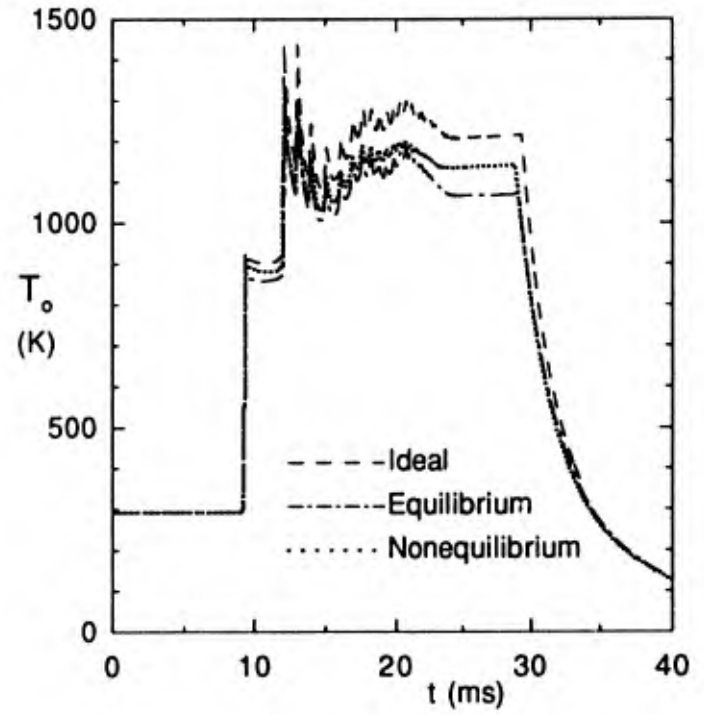

Figure 7.10: Barrel end stagnation temperature T_o,
$p_{res} = 20.5$ MPa, $p_{brl} = 200$ kPa,
$T_{res} = T_{brl} = 293$ K, $m_p = 96$ g.

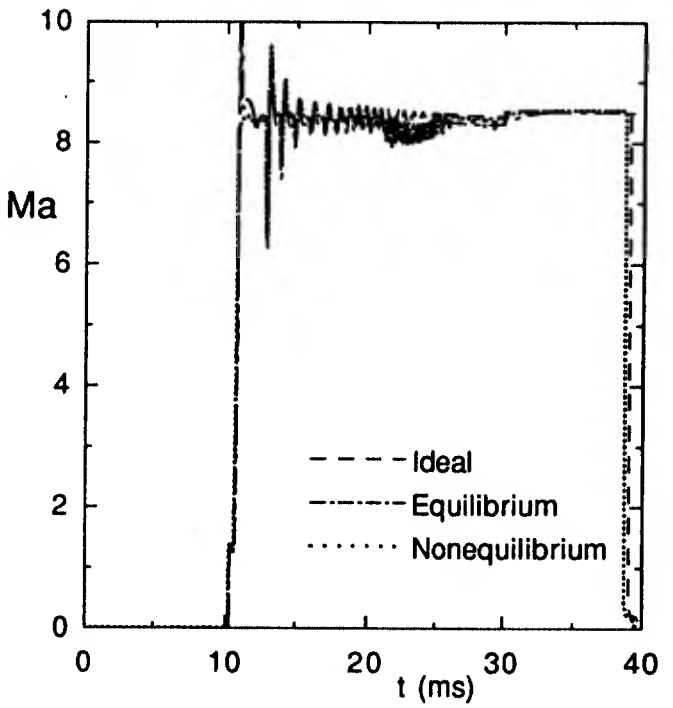

Figure 7.11: Nozzle exit Mach number M,
p_{res} = 20.5 MPa, p_{brl} = 200 kPa,
$T_{res} = T_{brl}$ = 293 K, m_p = 96 g.

400 kPa simulations, except that the maximum piston velocity is now higher and approaches 600 m/s, the stagnation pressure is around 24–25 MPa, the simulated stagnation temperatures are considerably higher ranging from 1070–1210 K, and the duration of steady nozzle flow is now reduced to about 9.5 ms. Figure 7.9 illustrates that, except for some differences in the later stages of the tunnel operation cycle ($t > 30$ ms), the agreement between numerical predictions and experimental measurements of the stagnation pressure is again good. The differences after $t = 30$ ms can be explained as follows. The stagnation pressure ahead of the piston drops in the numerical predictions. However, this characteristic pressure drop is not observed in the experimental signature because, in this particular firing, the piston has passed by the transducer and sealed the entrance to the nozzle. Figure 7.12 provides further evidence that the air flow at the nozzle exit, and thus the air flow in the test section, of the UTIAS-RPI facility has considerable energy locked in the excited vibrational modes of the nitrogen and oxygen gas molecules. Vibrational temperatures at the nozzle exit of 1180 and 830 K are predicted for N_2 and O_2, respectively. Note that the low-amplitude oscillatory nature of the N_2 temperature distribution of Fig. 7.12 in the region downstream of the throat is a consequence of

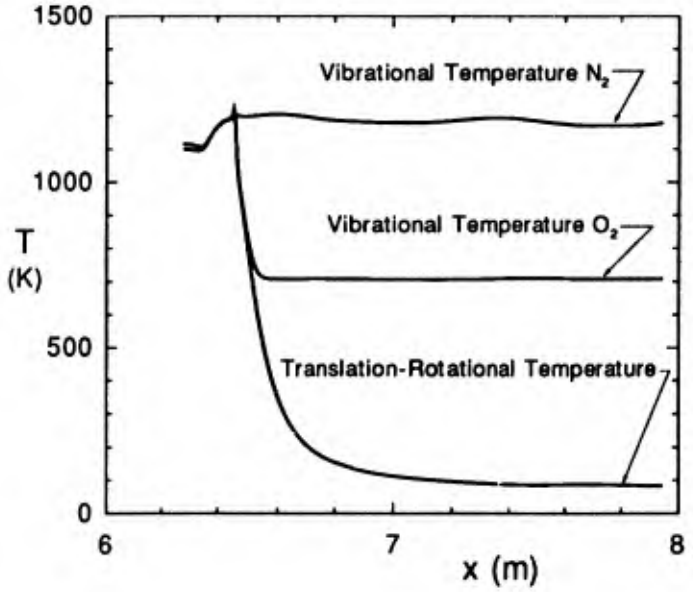

Figure 7.12: Temperature distributions in nozzle, $t = 30$ ms,
$p_{res} = 20.5$ MPa, $p_{brl} = 200$ kPa,
$T_{res} = T_{brl} = 293$ K, $m_p = 96$ g.

the temporal variations in the stagnation conditions created by the nonisentropic compression process occurring in the barrel.

Two additional results are given for this second set of predictions with an initial barrel pressure of 200 kPa. Shown in Figs. 7.13 and 7.14 are the temporal variation of the static pressure and temperature at the nozzle exit as calculated using the three thermodynamic models (ideal, real equilibrium, and five-species four-temperature nonequilibrium gas models). These two figures clearly depict the rather unsteady nature of the flow that is present at the nozzle exit (and thus in the test section) during gun tunnel operation.

Before continuing, it is worth mentioning that the influence of boundary-layer friction and heat-transfer, included in the present analysis, are important and cannot be neglected if accurate predictions of stagnation, nozzle, and test-section flow properties are desired. This is illustrated in Fig. 7.15, where two predictions of the ideal-gas stagnation pressure p_o are depicted. In one case the stagnation pressure is computed with the boundary-layer losses included and in the other these effects have been omitted. It is apparent that the times of arrival and strengths of nonstationary shocks, as well as the resulting steady-state stagnation pressure, are very different for these two cases. In order to obtain the level of quantitative

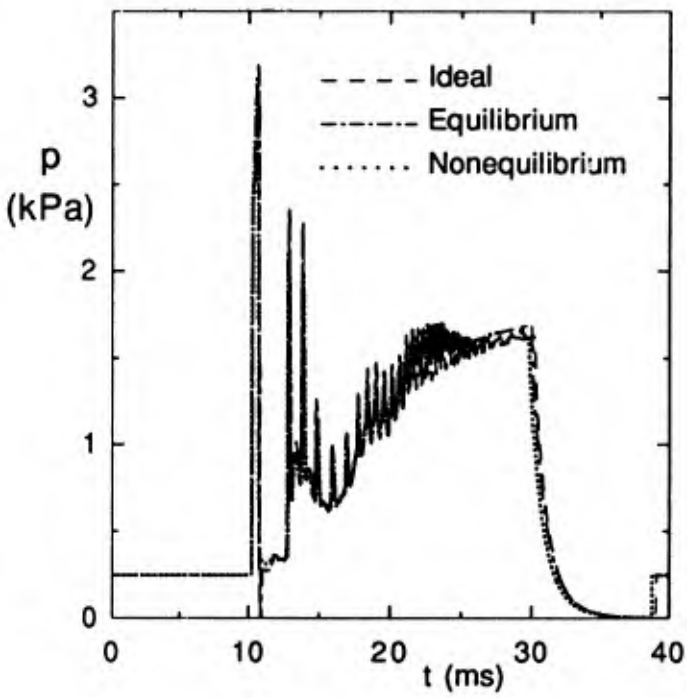

Figure 7.13: Nozzle exit static pressure p,
$p_{res} = 20.5$ MPa, $p_{brl} = 200$ kPa,
$T_{res} = T_{brl} = 293$ K, $m_p = 96$ g.

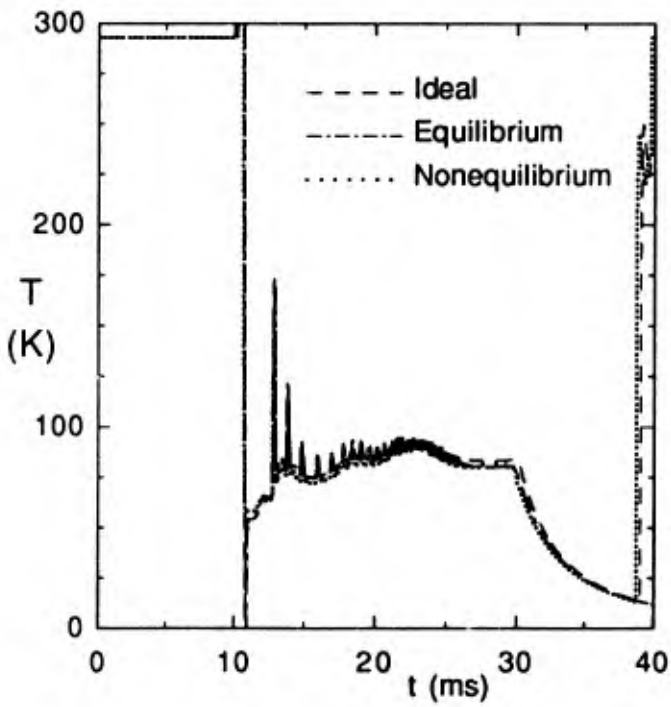

Figure 7.14: Nozzle exit static temperature T,
$p_{res} = 20.5$ MPa, $p_{brl} = 200$ kPa,
$T_{res} = T_{brl} = 293$ K, $m_p = 96$ g.

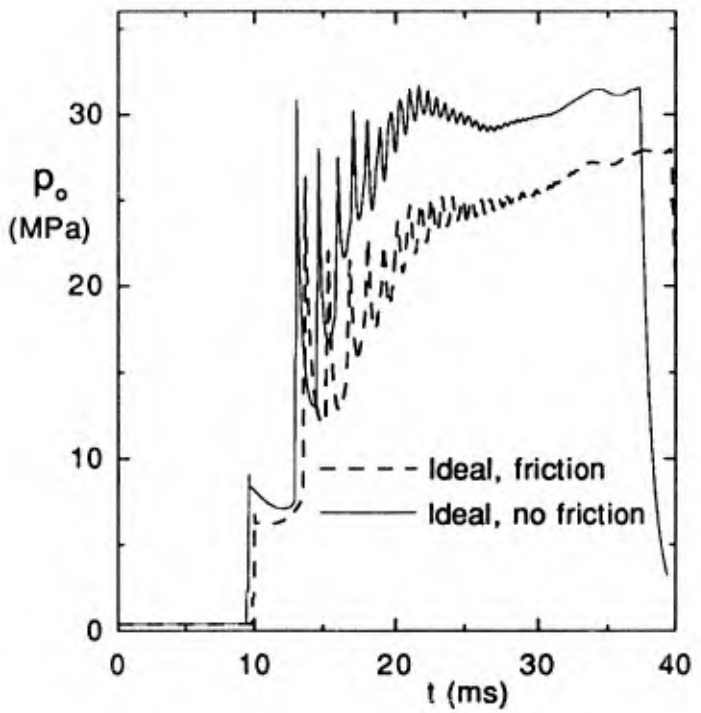

Figure 7.15: Barrel end stagnation pressure p_o,
$p_{res} = 20.5$ MPa, $p_{brl} = 400$ kPa,
$T_{res} = T_{brl} = 293$ K, $m_p = 96$ g.

agreement between numerical predictions and experimental measurements found in Figs. 7.4 and 7.9, the incorporation of boundary-layer effects into the analysis seems to be required.

It should also be noted that the time scales associated with the finite-rate source terms in the preceding nonequilibrium computations were approximately 500–10,000 times smaller than the gas dynamic time scales. The semi-implicit solver of Eqs. (7.65)–(7.68) effectively removed the stability constraints imposed by the finite-rate times scales and permitted the computations to be performed with the numerical time steps controlled only by the gas dynamic time scales.

The performance characteristics of the UTIAS-RPI hypersonic gun tunnel are further illustrated by the numerical results depicted in Figs. 7.16–7.21. In these figures, the computed barrel end stagnation pressure T_o, facility run time Δt, nozzle exit flow Mach number M, and nozzle exit flow Reynolds number per unit length R/L are given as functions of the initial barrel pressure p_{brl}, piston mass m_p, and initial barrel temperature T_{brl}. The results are again given for all three thermodynamic models.

In Figs. 7.16–7.19, the effects of varying the initial barrel pressure from 100 to 800 kPa with $p_{res} = 20.5$ MPa, $T_{res} = T_{brl} = 293$ K, and $m_p = 96$ g all fixed are explored. Figure 7.16

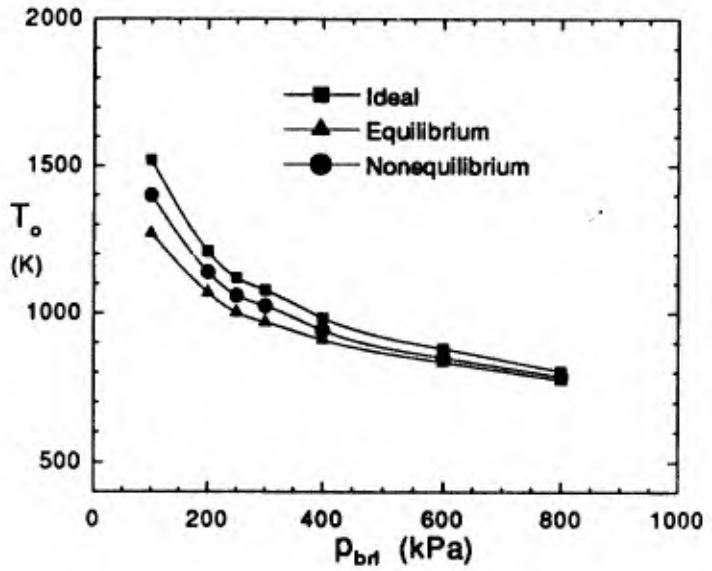

Figure 7.16: Barrel end stagnation temperature T_o as a function of initial barrel pressure p_{brl}, $p_{res} = 20.5$ MPa, $T_{res} = T_{brl} = 293$ K, $m_p = 96$ g.

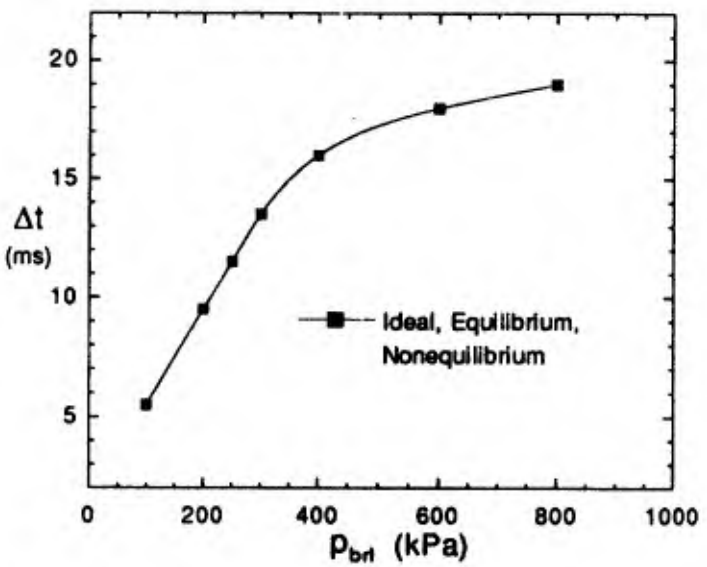

Figure 7.17: Run time Δt as a function of the initial barrel pressure p_{brl}, $p_{res} = 20.5$ MPa, $T_{res} = T_{brl} = 293$ K, $m_p = 96$ g.

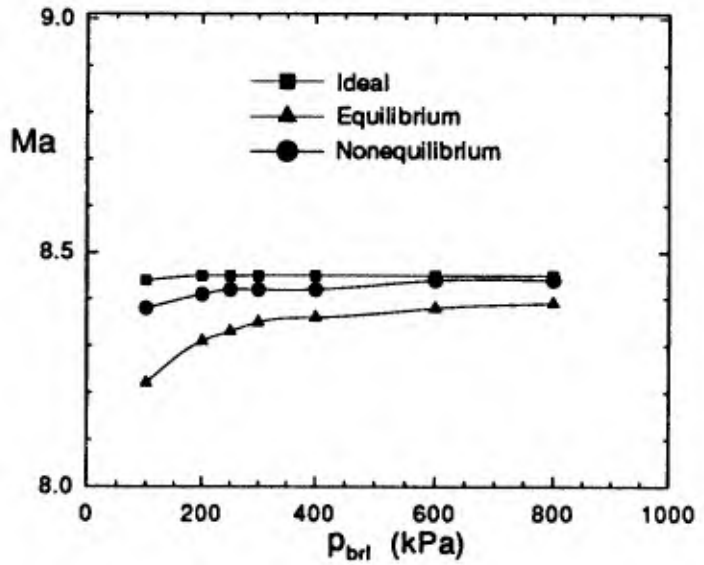

Figure 7.18: Nozzle exit Mach number M as a function of initial barrel pressure p_{brl}, p_{res} = 20.5 MPa, $T_{res} = T_{brl}$ = 293 K, m_p = 96 g.

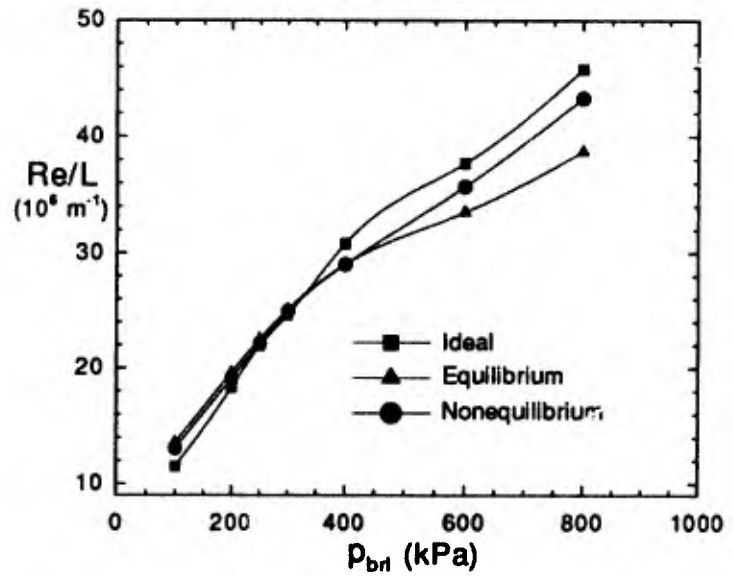

Figure 7.19: Nozzle exit Reynolds number per unit length R/L as a function of the initial barrel pressure p_{brl}, p_{res} = 20.5 MPa, $T_{res} = T_{brl}$ = 293 K, m_p = 96 g.

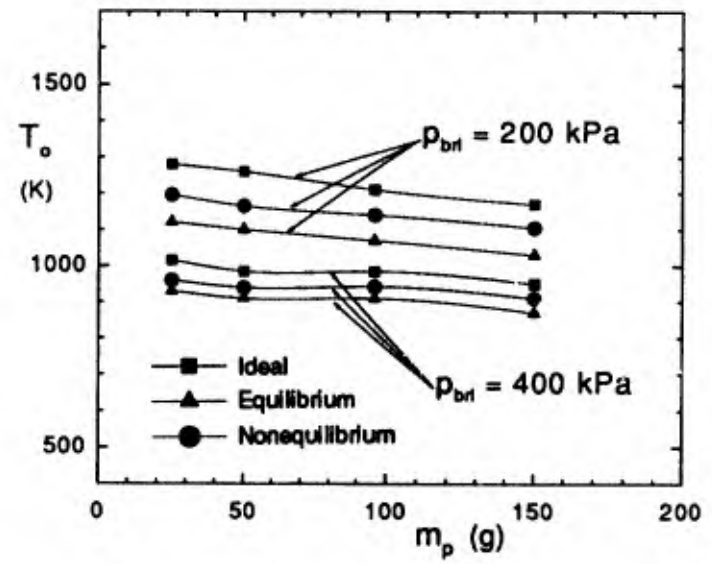

Figure 7.20: Barrel end stagnation temperature T_o as a function of the piston mass m_p, p_{res} = 20.5 MPa, p_{brl} = 200 & 400 kPa, $T_{res} = T_{brl}$ = 293 K.

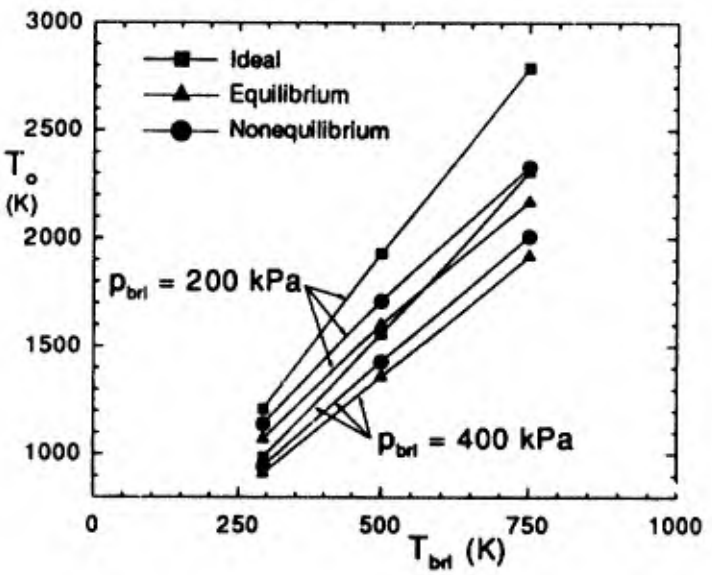

Figure 7.21: Barrel end stagnation temperature T_o as a function of initial barrel temperature T_{brl}, p_{res} = 20.5 MPa, p_{brl} = 200 & 400 kPa, T_{res} = 293 K, m_p = 96 g.

shows that by reducing the barrel pressure higher stagnation temperatures approaching 1500 K are possible. However, Fig. 7.17 shows that these moderate increases in stagnation enthalpy are offset by a corresponding decrease in the facility run time, which may be detrimental to experiments in many cases. Note that the run times are virtually the same for all three thermodynamic models. Figure 7.18 illustrates that the test-section flow Mach number is rather insensitive to the initial barrel pressure. This should be expected for it depends primarily on the exit to throat area ratio. Although not shown, the stagnation pressure was also found to be insensitive to initial barrel pressure. Values for p_o were found to be around 24–27 MPa for all of the operating conditions considered. Finally, Fig. 7.19 presents the range of nozzle-exit or test-section flow Reynolds number per unit length that may be achieved with the UTIAS-RPI tunnel. The Reynolds number varies from 10^7 to 5×10^7 m^{-1}, which suggests that, depending on the model size and orientation in the test section, fully laminar, transitional, and even fully turbulent boundary-layers may be obtained.

For many experimental programs, higher test-section stagnation temperatures are desired. Two of the possible and more practical avenues for achieving higher temperatures are to redesign and reduce the piston mass by employing lightweight high strength materials or to preheat the working gas in the barrel before diaphragm rupture. The effects of varying the piston weight and initial barrel temperature with p_{res} = 20.5 MPa, T_{res} = 293 K, and p_{brl} = 200 and 400 kPa are shown in Figs. 7.20 and 7.21. It should be obvious from Fig. 7.20 that changing the piston mass has little effect. Even the reduction of the piston mass by as much as 75% provides a corresponding increase in the predicted stagnation temperatures of only 40 K. On the other hand, Fig. 7.21 shows that preheating the barrel gases is more worthwhile. An increase in the initial barrel temperature of 200 K can provide a corresponding increase in the stagnation pressure of up to 400 K. It should, however, be noted that preheating the working gas does reduce the run time. With p_{brl} = 200 kPa, the run time Δt was found to decrease almost linearly with temperature from 10 ms at T_{brl} = 293 K down to 5 ms at T_{brl} = 750 K.

7.7 Concluding Remarks

A quasi-one-dimensional unsteady flow analysis and TVD finite-difference solution algorithm with new numerical features have been presented for the prediction of the UTIAS-RPI hypersonic impulse tunnel operation and performance. Unlike previous studies which have generally employed quasi-steady and mostly analytic techniques, modern CFD methods are used to pre-

dict for the first time the complete unsteady behaviour of the gun tunnel from initial startup to blow down. Furthermore, the use of polytropic gas, real equilibrium gas, and four-temperature five-species nonequilibrium gas thermodynamic models in the analysis has permitted the evaluation of high temperature effects for this experimental facility. Numerical results and comparisons to available experimental data have demonstrated the capabilities and usefulness of these modeling techniques.

Under typical operating conditions, the numerical predictions have shown that the run time for the UTIAS-RPI gun tunnel is about 15–20 ms and that the stagnation pressure and temperature are 24–27 MPa and 1000–1200 K, respectively. Test section flow Mach and Reynolds numbers of 8.35–8.45 and 10^7 to 5×10^7 m^{-1} were found. In addition, the static pressure and temperature in the test section were determined to be about 1.6–1.7 kPa and 65–75 K, respectively. For the predicted stagnation enthalpies, it was shown that in most cases the primary high-temperature phenomenon occurring in the tunnel was vibrational excitation. The degrees of dissociation of N_2 and O_2 were found not to exceed 1/2 and 2%, respectively, even in the extreme cases considered where stagnation temperatures neared 2000 K. It was also demonstrated that vibrational excitation must be treated as a finite-rate process to obtain accurate predictions of the tunnel stagnation conditions.

Vibrational relaxation effects were also found to be of importance in the hypersonic nozzle flows of the UTIAS-RPI facility. It was shown that the air typically freezes downstream but very close to the nozzle throat and results in test-section flows with considerable energy bound in the vibrational modes of the nitrogen and oxygen molecules. The N_2 and O_2 species can have vibrational temperatures of 960–1200 K and 620–830 K, respectively. This means that the vibrational modes of N_2 are only marginally less than barrel-end stagnation temperatures and the vibrational temperatures of O_2, although lower than stagnation temperatures, are still much higher than the predicted test-section translational-rotational temperatures. This level of vibrational excitation may be important in the assessment of tunnel experimental data.

One of the limitations of the UTIAS-RPI facility seems to be the rather low stagnation enthalpies that can be obtained. The present performance assessment of the impulse tunnel indicates a possible technique for extending the range of flow conditions that can be achieved in the test section. Reducing the piston weight proves to be fruitless; however, preheating of the working gas can lead to substantially higher stagnation temperatures and feasible preheating mechanisms could be examined in the future.

7.8 References

7.1 Lukasiewicz, J., "Experimental Methods of Hypersonics", Marcel Dekker Inc., NY, 1973.

7.2 Hornung, H.G., "28th Lanchester Memorial Lecture — Experimental Real-Gas Hypersonics", The Aeronautical Journal, Vol. 92, pp. 379–389, 1988.

7.3 Stollery, J.L., Maull, D.J., and Belcher, B.J., "The Imperial College Hypersonic Gun Tunnel, August 1958–July 1959", Journal of the Royal Aeronautical Society, Vol. 64, pp. 24–32, 1960.

7.4 Stalker, R.J., "Preliminary Results with a Free Piston Shock Tunnel", AIAA Journal, Vol. 3, pp. 1170–1171, 1965.

7.5 Stalker, R.J., "A Study of the Free-Piston Shock Tunnel", AIAA Journal, Vol. 5, pp. 2160–2165, 1967.

7.6 Stalker, R.J., "Hypervelocity Aerodynamics with Chemical Nonequilibrium", Annual Review of Fluid Mechanics, Vol. 21, pp. 37–60, 1989.

7.7 Deschambault, R.L., Hawboldt, R.J., Sullivan, P.A., and Molder, S., "The University of Toronto–Ryerson Polytechnical Institute Hypersonic Gun Tunnel", Proceedings of the First Canandian Symposium on Aerodynamics, Ottawa, Canada, December 4–5, 1989. Canadian Aeronautics and Space Institute, Ottawa, 1989.

7.8 Hertzberg, A., "A Shock Tube Method of Generating Hypersonic Flows", Journal of the Aeronautical Sciences, Vol. 18, pp. 803–804, 1951.

7.9 Hertzberg, A., "The Shock Tunnel and its Applications to Hypersonic Flight", NATO AGARD Report 144, July 1957.

7.10 Wittliff, C.E., Wilson, M.R., and Hertzberg, A., "The Tailored-Interface Hypersonic Shock Tunnel" Journal of the Aero/Space Sciences, Vol. 26, pp. 219–228, 1959.

7.11 Evans, C. and Evans, F., "Shock Compression of a Perfect Gas", Journal of Fluid Mechanics, Vol. 1, pp. 399–408, 1956.

7.12 Stollery, J.L. and Maull, D.J., "A Note on the Compression of Air Through Repeated Shock Waves", Journal of Fluid Mechanics, Vol. 4, pp. 650–654, 1958.

7.13 Winter, D.F.T., "Multiple Shock Compression Using a Piston of Finite Weight", Journal of Fluid Mechanics, Vol. 8, pp. 264–272, 1960.

7.14 Stalker, R.J., "Rebound of a High Speed Piston By Gas Compression in a Closed Tube", National Research Council of Canada Mechanical Engineering Report MT–42, March 1961.

7.15 Stollery, J.L. and Smith, J.E., "A Note on the Variation of Vibrational Temperature Along a Nozzle", Journal of Fluid Mechanics, Vol. 13, pp. 225–236, 1962.

7.16 Lemcke, B., "An Investigation of the Stagnation Conditions in the Shock-Compression Heater of a Gun Tunnel", Aeronautical Research Institute of Sweden Report 90, February 1962.

7.17 Stollery, J.L. and Park, C., "Computer Solutions to the Problem of Vibrational Relaxation in Hypersonic Nozzle Flows", Imperial College of Science and Technology, Aeronautics Department Report No. 115, January 1963.

7.18 Jacobs, P.A., "Transient, Hypervelocity Flow in an Axisymmetric Nozzle", ICASE Report No. 91-1, January 1991.

7.19 Groth, C.P.T., Gottlieb, J.J., and Sullivan, P.A., "Numerical Investigation of High-Temperature Effects in the UTIAS-RPI Hypersonic Impulse Tunnel", Canadian Journal of Physics, Vol. 69, pp. 897–918, 1991.

7.20 Zucrow, M.J. and Hoffman, J.D., "Gas Dynamics, Vol. 1", John Wiley and Sons, Toronto, 1976.

7.21 Zhang, K.Y. and Gottlieb, J.J., "Simulation of a Blast Wave in a Shock Tube by Using Perforated Plates in the Driver", University of Toronto Institute for Aerospace Studies Report No. 304, March 1986.

7.22 Groth, C.P.T. and Gottlieb, J.J., "Numerical Study of Two-Stage Light-Gas Hypervelocity Projectile Launchers", University of Toronto Institute for Aerospace Studies Report No. 327, October 1988.

7.23 Gottlieb, J.J., Groth, C.P.T., Lesage, F., and Maillette, J., "Numerical Model for Prediction of Two-Stage Light-Gas Gun Performance", Proceedings of the 11th International

Symposium on Ballistics, Brussels, Belgium, May 9–11, 1989. Departments of Armament and Ballistics and Applied Chemistry, Royal Military Academy, Brussels, Belgium, 1989, Vol. I, pp. 445–455.

7.24 Jain, A.K., "Accurate Explicit Expression for Friction Factor", ASCE Journal, Vol. 102, pp. 674-677, 1976.

7.25 Liepmann, H.W. and Goddard, F.E., "Note on the Mach Number Effect Upon the Skin Friction of Rough Surfaces", Journal of the Aeronautical Sciences, Vol. 24, pp. 784, 1957.

7.26 Kreith, F., "Principles of Heat Transfer", International Textbook Co., Scranton, Pa., 1967.

7.27 Chapman, S. and Cowling, T.G., "The Mathematical Theory of Non-Uniform Gases", Cambridge University Press, London, 1970.

7.28 Srinivasan, S., Tannehill, J.C., and Weilmuenster, K.J., "Simplified Curve Fits for the Thermodynamic Properties of Equilibrium Air", NASA Reference Publication 1181, August 1987.

7.29 Srinivasan, S. and Tannehill, J.C., "Simplified Curve Fits for the Transport Properties of Equilibrium Air", NASA Contractor Report 178411, December 1987.

7.30 Gnoffo, P.A., Gupta, R.N., and Shinn, J.L., "Conservation Equations and Physical Models for Hypersonic Air Flows in Thermal and Chemical Nonequilibrium", NASA Technical Paper 2867, February 1989.

7.31 Dunn, M.G. and Kang, S.W., "Theoretical and Experimental Studies of Reentry Plasmas", NASA Contractor Report 2232, April 1973.

7.32 Millikan, R.C. and White, D.R., "Systematics of Vibrational Relaxation", Journal of Chemical Physics, Vol. 39, pp. 3209–3213, 1963.

7.33 Blottner, F.G., Johnson, M., and Ellis, M., "Chemically Reacting Viscous Flow Program for Multicomponent Gas Mixtures", Sandia Laboratories Report No. SC-RR-70-754, 1971.

7.34 Wilke, C.R., "A Viscosity Equation for Gas Mixtures", Journal of Chemical Physics, Vol. 18, pp. 517–519, 1950.

7.35 Harten, A., "High Resolution Schemes for Hyperbolic Conservation Laws", Journal of Computational Physics, Vol. 49, pp. 357–393, 1983.

7.36 Harten, A., "On a Class of High Resolution Total-Variation-Stable Finite-Difference Schemes", SIAM Journal on Numerical Analysis, Vol. 21, pp. 1–23, 1984.

7.37 Roe, P.L., "Approximate Riemann Solvers, Parameter Vectors, and Difference Schemes", Journal of Computational Physics, Vol. 43, pp. 357–372, 1981.

7.38 Roe, P.L. and Pike, J., "Efficient Construction and Utilisation of Approximate Riemann Solutions", Computing Methods in Applied Science and Engineering VI, Edited by R. Glowinski and J.L. Lions, North-Holland Publishing Co., Amsterdam, pp. 499–518, 1984.

7.39 Roe, P.L., "Generalized Formulation of TVD Lax-Wendroff Schemes", ICASE Report No. 84-53, 1984.

7.40 Davis, S.F., "TVD Finite Difference Schemes and Artificial Viscosity", ICASE Report No. 84-20, 1984.

7.41 Yee, H.C., "Construction of Explicit and Implicit Symmetric TVD Schemes and Their Applications", Journal of Computational Physics, Vol. 68, pp. 151–179, 1987.

7.42 Chakravarthy, S.R. and Osher, S., "A New Class of High Accuracy TVD Schemes for Hyperbolic Conservation Laws", AIAA Paper No. 85-0363, 1985.

7.43 Chakravarthy, S.R. and Osher, S., "Computing with High-Resolution Upwind Schemes for Hyperbolic Equations", Large Scale Computations in Fluid Mechanics, Lectures in Applied Mathematics, Vol. 22, American Mathematical Society, 1985, pp. 57–86.

7.44 Sweby, P.K., "High Resolution Schemes Using Flux Limiters for Hyperbolic Conservation Laws", SIAM Journal on Numerical Analysis, Vol. 21, pp. 995–1011, 1984.

7.45 Glaister, P., "An Approximate Linearized Riemann Solver for the Euler Equations for Real Gases", Journal of Computational Physics, Vol. 74, pp. 382–408, 1988.

7.46 Liou, M.-S., van Leer, B., and Shuen, J.-S., "Splitting of Inviscid Fluxes for Real Gases", Journal of Computational Physics, Vol. 87, pp. 1–24, 1990.

7.47 Lax, P.D. and Wendroff, B., "Systems of Conservation Laws", Communications in Pure and Applied Mathematics, Vol. 13, pp. 217–237, 1960.

7.48 Warming, R.F. and Beam, R.M., "Upwind Second-Order Difference Schemes and Application in Aerodynamic Flows", AIAA Journal, Vol. 14, pp. 1241–1249, 1976.

7.49 Murman, E.M., "Analysis of Embedded Shock Waves Calculated by Relaxation Methods", AIAA Journal, Vol. 12, pp. 626–633, 1974.

7.50 Glaz, H.M., Colella, P., Collins, J.P., and Ferguson, R.E., "Nonequilibrium Effects in Oblique Shock-Wave Reflections", AIAA Journal, Vol. 26, pp. 698–705, 1988.

7.51 Ben-Artzi, M., "The Generalized Riemann Problem for Reactive Flows", Journal of Computational Physics, Vol. 81, pp. 70–101, 1989.

7.52 Yee, H.C. and Shinn, J.L., "Semi-Implicit and Fully Implicit Shock-Capturing Methods for Nonequilibrium Flows", AIAA Journal, Vol. 27, pp. 299–307, 1989.

7.53 Bussing, T.R.A. and Murman, E.M., "Finite-Volume Method for the Calculation of Compressible Chemically Reacting Flows", AIAA Journal, Vol. 26, pp. 1070–1078, 1988.

7.54 Kamowitz, D., "Some Observations of Boundary Conditions for Numerical Conservation Laws", ICASE Report No. 88-67, 1988.

8.0 Two-Dimensional Unsteady Hypersonic Flow Predictions

D. F. Hawken and J. J. Gottlieb

8.1 Introduction

The aim of this computational fluid dynamics (CFD) project, which is intended to complement the ongoing experimental research, is to eventually develop a code that will have the capability of computing nonstationary viscous gas flow through or around the models of space-plane inlets that are being tested in the UTIAS-RPI hypersonic impulse tunnel. As a preliminary stage, a code has been developed that will compute two-dimensional planar and axisymmetric inviscid flows. Future work will involve extending the code to include the viscous effects.

This section of the contract report summarizes the finite-difference techniques and total variation diminishing (TVD) schemes utilizing Roe's approximate Riemann solver, which are incorporated into an efficient and accurate computer code, in order to predict nonstationary planar and axisymmetric flows with steep shocks and thin slip streams on two-dimensional grids having multiple connected domains. Work on the development of this computer code for the prediction of hypersonic flows within model hypersonic inlets is reported, and numerical results for some test problems are presented.

8.2 Current Status of CFD Computer Program

The present code solves the Euler equations for calorically and thermally perfect gas flow, transformed from a physical domain having curved boundaries to a computational domain subdivided into square cells. Algebraic stretching functions control the physical distribution of the grid lines. Both explicit and implicit total-variation-diminishing (TVD) algorithms may be used to solve the transformed conservation equations. The code computes the approximate solution of a Riemann problem as one stage in the solution procedure. The algorithm of Roe (Ref. 8.1) is used as the Riemann problem solver and is implemented so as to compute first-order-accurate fluxes on a rectangular grid. A second-order-accurate flux-limited correction is added to the first-order-accurate flux. Use of the flux limiter to reduce the accuracy towards first order near steep transitions prevents development of oscillations typical of conventional second-order-accurate calculations. Our early work was modelled after the TVD scheme of Chakravarthy (Ref. 8.2) and use was made of the work of Yee (Ref. 8.3) during the later stages

of code development. This section of the report is not intended to be a comprehensive survey of TVD methods, so emphasis will be placed on schemes which have proven useful during development of the CFD code. Additional descriptions of the present solution algorithm are given by Hawken and Gottlieb (Refs 8.4 & 8.5).

The TVD code has been constructed so that the grid may be divided into several subgrids or multiply-connected domains. Time-stepping is executed on each subgrid in turn. The highly vectorized algorithm is applied to an entire column of cells at a time. At present, it is possible to specify four types of boundary conditions at the edges of a subgrid. The boundary condition types are as follows: (1) symmetry of energy, density, and parallel gas flow, and antisymmetry of perpendicular gas flow (i.e., at the walls of an inlet); (2) reflectionless transmission of disturbances at the edge of the computed flow field; (3) supersonic inflow; and (4) continuation of the solution from an adjacent subgrid.

The code has been implemented on the CRAY X-MP/24 at the Ontario Centre for Large Scale Computation, at the University of Toronto. A number of test problems have been solved using both explicit and implicit time-stepping and good results have been obtained. A detailed description of the construction and behaviour of the various versions of the code is contained in Subsections 8.5 through 8.10. As it stands now, the TVD code forms an excellent basis for extension to the solution of viscid flows through domains of complex configuration using a real-gas equation of state.

8.3 Some Classical Finite-Difference Techniques

TVD techniques are most simply introduced when applied to a one-dimensional scalar partial differential equation (PDE). Extension to a system of partial differential equations (the Euler equations) on a two-dimensional domain will be discussed in Subsection 8.5. It is illuminating to consider the application on a one-dimensional domain of a number of classical finite-difference techniques to a scalar partial difference equation of the form

$$\frac{\partial U}{\partial t} + \frac{\partial f}{\partial X} = 0, \tag{8.1}$$

where U is the solution, t is time, X is the spatial coordinate, and the flux $f = f(U)$ is a function, possibly nonlinear, of U. If the PDE contains viscous terms then f is also a function

of spatial derivatives of U. This PDE is in conservation-law form. The general definition of conservation-law form, applicable to systems of PDE's, is that coefficients external to the derivatives are constant, or, if they are variable, their derivatives appear nowhere in the system of PDE's. This conservation-law form is, in fact, an expression, in differential format, of the conservation of some quantity (i.e., mass, momentum, energy). In many cases (see the discussion on shock capturing in Ref. 8.6) it has been shown that conservation-law form will cause the solution of an inviscid equation, that was obtained by removing the second order derivatives from a (physically more accurate) viscid equation, to converge to the solution of the original viscid equation.

It is often desirable to use the conservation-law form when applying a finite-difference algorithm. Assume that the domain has been subdivided into N equal intervals of size ΔX. The intervals (or cells) are centered at $X = i\Delta X - \frac{1}{2}\Delta X$ where i varies from 1 to N. A conservation-law finite-difference algorithm can be constructed by obtaining an approximation to f at the interface between each cell; that is, at $X = i\Delta X$ where i varies from 0 to N. The interface between cell i and cell $i+1$ will be labeled as interface $i+\frac{1}{2}$ in what follows. The boundary interfaces at the left-hand and right-hand sides of the domain will be designated as interface $\frac{1}{2}$ and $N+\frac{1}{2}$, respectively. A difference equation for the solution in the centre of cell i may be written as

$$U_i^{n+1} = U_i^n - \beta\left[F_{i+\frac{1}{2}}^n - F_{i-\frac{1}{2}}^n\right], \tag{8.2}$$

where $\beta = \Delta t/\Delta X$ is the ratio of the time-step size to the cell width, U_i^n is the numerical solution at node i after the n^{th} time-step, and $F_{i+\frac{1}{2}}^n$ is an approximation to f at the interface between cell i and cell $i+1$ after the n^{th} time-step. $F_{i+\frac{1}{2}}^n$ is an estimate of the flux of U across the interface. Because of the construction of the difference equation, the sum of the fluxes between all the cells is zero. Only the boundary-interface fluxes can contribute to the total flux. That is

$$\sum_{i=1}^{N}\left(F_{i+\frac{1}{2}}^n - F_{i-\frac{1}{2}}^n\right) = F_{N+\frac{1}{2}}^n - F_{\frac{1}{2}}^n, \tag{8.3}$$

In what follows, Eq. (8.2) will be said to be in conservative-difference form.

Application of the explicit central-difference method to an inviscid PDE yields an interface flux of the form

$$F^n_{i+\frac{1}{2}} = \frac{f(U^n_{i+1}) + f(U^n_i)}{2}. \tag{8.4}$$

The boundary-interface fluxes may be handled by placing an extra (or image) cell at each end of the domain and assigning a value to U within the extra cell. In some cases known behaviour of the solution outside the domain will supply the value. If this information is not available, imposition of symmetry or antisymmetry about the boundary may supply a suitable value of U or $f(U)$ in the image cell. Extrapolation from the interior of the domain with the application of analytical relationships is also used, but it can lead to instabilities. Implementation of boundary conditions will be discussed in greater detail at the end of this subsection and at the end of Subsection 8.5.

The spatial-truncation error of the explicit central-difference method is second-order while the time-truncation error is first-order. If the linear wave equation

$$\frac{\partial U}{\partial t} = -C\frac{\partial U}{\partial X}, \tag{8.5}$$

where C is a characteristic velocity of propagation, is to be solved, then f is equal to CU. It can be shown that the explicit central-difference method is unconditionally unstable when applied to the linear wave equation. That is, any error in the numerical estimate of U will grow from time-step to time-step. In general, the explicit central-difference method is unconditionally unstable when applied to a PDE that does not contain viscous terms. It does however form a useful basis for methods that add an artificial or numerical viscosity term to the explicit central-difference term. These methods include the TVD algorithms to be discussed later. An algorithm that is conditionally stable, when applied to the linear wave equation, is the first-order upwind scheme. This method applied to an inviscid PDE results in an interface flux of the form

$$F^n_{i+\frac{1}{2}} = \frac{f(U^n_{i+1}) + f(U^n_i)}{2} - \frac{\sigma_{i+\frac{1}{2}}}{2}\left[f(U^n_{i+1}) - f(U^n_i)\right], \tag{8.6}$$

where $\sigma_{i+\frac{1}{2}}$ is the sign of the (scalar valued) Jacobian of the interface flux (i.e., derivative of

f with respect to U) evaluated at interface $i+\frac{1}{2}$. The Jacobian of the interface flux will be designated by $\lambda_{i+\frac{1}{2}}$ in what follows. $\sigma_{i+\frac{1}{2}}$ is equal to $+1$ if $\lambda_{i+\frac{1}{2}}$ is positive, and it equals -1 otherwise. In order to keep in mind the scalar nature of the present equations and to be consistent with the use of vector-valued fluxes in work to be described in Subsection 8.5, $\lambda_{i+\frac{1}{2}}$ will also be called the interface-flux eigenvalue.

In the case of the linear wave equation, the interface flux reduces to the form

$$F^n_{i+\frac{1}{2}} = \frac{C-|C|}{2}U^n_{i+1} + \frac{C+|C|}{2}U^n_i \,. \tag{8.7}$$

In other words, backward differences are used if the "wind," C, is positive, and forward differences otherwise. The error will not grow with time if the CFL condition condition $|C\beta| \leq 1$ is satisfied. Unfortunately, the spatial truncation error is only first order. A method in which the truncation error is second order in both space and time, is the explicit algorithm of MacCormack (Ref. 8.7). This method consists of the predictor step

$$\check{U}^n_i = U^n_i - \beta[f(U^n_i) - f(U^n_{i-1})] \,, \tag{8.8}$$

followed by the corrector step

$$U^{n+1}_i = U^n_i + \frac{1}{2}\Big[\,\check{U}^n_i - U^n_i - \beta[f(\check{U}^n_{i+1}) - f(\check{U}^n_i)]\,\Big] \,. \tag{8.9}$$

If the solution contains a shock wave, a slightly better result occurs if the predictor differencing is in the upwind direction followed by downwind differencing in the corrector. Thus, in some cases there is an advantage to using forward differences in the predictor followed by backward differences in the corrector. In more complex cases, the direction of differencing is alternated from time-step to time-step in order to eliminate any bias. An xamination of the corrector equation reveals that

$$F^n_{i+\frac{1}{2}} = \frac{f(\check{U}^n_{i+1}) + f(U^n_i)}{2} \tag{8.10}$$

is the resulting interface flux.

A method closely related to MacCormack's scheme is that of Lax and Wendroff (Ref. 8.8). The methods have the same truncation error in time and space. The methods are identical when applied to the linear wave equation; the solution is stable if the CFL condition $|C\beta| \leq 1$ is satisfied. The Lax-Wendroff method may be written in the form

$$U_i^{n+1} = U_i^n - \frac{\beta}{2}[f(U_{i+1}^n) - f(U_{i-1}^n)] + \frac{\beta^2}{2}\left[\lambda_{i+\frac{1}{2}}[f(U_{i+1}^n) - f(U_i^n)] + \lambda_{i-\frac{1}{2}}[f(U_i^n) - f(U_{i-1}^n)]\right]. \quad (8.11)$$

The last term is a thinly disguised central-difference approximation to a second-order spatial derivative and amounts to the inclusion of an artificial viscosity term.

The interface flux for the Lax-Wendroff method may be written

$$F_{i+\frac{1}{2}}^n = \frac{f(U_{i+1}^n) + f(U_i^n)}{2} - \beta\frac{\lambda_{i+\frac{1}{2}}}{2}\left[f(U_{i+1}^n) - f(U_i^n)\right]. \quad (8.12)$$

In fact, this is just a first-order Taylor expansion about U_{i+1}^n of the MacCormack interface flux.

In the case of the linear wave equation, the interface flux reduces to the form

$$F_{i+\frac{1}{2}}^n = \frac{C - \beta C^2}{2}U_{i+1}^n + \frac{C + \beta C^2}{2}U_i^n. \quad (8.13)$$

For this linear equation, it is evident that the Lax-Wendroff interface flux reduces to the first-order upwind interface flux when $|C\beta|$ is unity. If $|C\beta|$ is close to zero, the interface flux of the (unconditionally unstable) explicit central-difference method is approximated. Intermediate values of $|C\beta|$ yield a mixture of central and first-order upwind differences. For nonlinear problems, the Lax-Wendroff and MacCormack methods give the most accurate results when β is chosen so that the CFL limit of one is approached; the leading coefficient of the truncation error approaches zero as $|C\beta|$ approaches unity.

Examination of the interface fluxes for the first-order upwind, MacCormack, and Lax-Wendroff methods reveals that they consist of the interface flux for the explicit central-difference method plus some extra terms. These extra terms amount to the addition of artificial or numerical viscosity to the difference equations. There are many other difference methods

which can also be written in the form of the explicit central-difference method with additional artificial viscosity terms.

The first-order upwind method is the most effective in eliminating oscillations near shocks; the solution of the linear wave equation is always monotone near a shock. However, the shock thickness is much larger than that obtained if a higher order method is used. Unfortunately, as proven by Harten, Hyman and Lax (Ref. 8.9), no higher-order classical finite-difference method can produce monotone shocks.

Many of the methods use extra information about the solution, obtained by examining the interface-flux Jacobian, to modify the interface fluxes. In the case of systems of PDE's, the solution characteristics (or eigenvalues of the Jacobian vector of the fluxes) are examined. Note that, if f is nonlinear, the Jacobian and therefore the coefficients of f in the expressions for the interface fluxes may vary from interface to interface. In one sense, the conservation-law form of Eq. (8.1) has been compromised. However, the closely related property of satisfying Eq. (8.3) has been retained.

A commonly used spatially zero-order accurate means of imposing a transmission boundary condition is applied by requiring that the value of U in the image cell be set to the value of U in the real cell directly adjacent to the boundary (i.e., the first derivative of U is set to zero at the boundary). This is denoted as "constant extrapolation" by Kamowitz (Ref. 8.10). Kamowitz has investigated the passage of a shock-like solution structures through transmissive boundaries. He computed the solution of a number of one-dimensional scalar test equations problems (in which U denotes a velocity of propagation) using the MacCormack, Lax-Wendroff and similar schemes. Kamowitz showed that if constant extrapolation is used the shocks exit through the boundary without disturbing the solution within the domain of calculation.

Since the Lax-Wendroff and MacCormack schemes are spatially second-order accurate, it is desirable to also use a transmission boundary condition with greater than zero-order accuracy. If higher order extrapolation of U is used (i.e., second or third derivative of U is set to zero at the boundary) then the shock is properly transmitted if f is a linear function of U, but a nonlinear f created boundary layers or reflected shocks. The combination of nonlinear f and higher-order extrapolation caused the value of U at the real cell adjacent to the boundary to remain zero or have an inappropriate sign during the outward propagation of the shock.

Kamowitz recommended the use of characteristic extrapolation as a means of obtaining both a first-order accurate boundary condition and acceptable transmission of shock waves. In

the context of this report, the scheme involves the storage of image-cell values U_0 and U_{N+1} which are updated before the start of each time-step using the relations

$$U_0^{n+1} = U_0^n - \beta[f(U_1^n) - f(U_0^n)] \tag{8.14}$$

and

$$U_{N+1}^{n+1} = U_{N+1}^n - \beta[f(U_{N+1}^n) - f(U_N^n)]\,, \tag{8.15}$$

respectively.

8.4 TVD Methods Applied to a Scalar Equation

Use of the solution characteristics has proven to be a desirable ingredient in improving solution quality. The TVD methods examine additional solution properties in order to modify the interface flux so that it reduces to the first-order upwind interface flux in regions of rapid solution variation but is of higher order accuracy elsewhere. A very simple TVD interface flux may be written in the form

$$\begin{aligned} F_{i+\frac{1}{2}}^n = {} & \frac{f(U_{i+1}^n) + f(U_i^n)}{2} - \frac{\sigma_{i+\frac{1}{2}}}{2}\left[f(U_{i+1}^n) - f(U_i^n)\right] \\ & + \frac{\sigma_{i+\frac{1}{2}}}{2}\text{minmod}(\Delta f_{i+\frac{3}{2}}^-, \Delta f_{i+\frac{1}{2}}^-) + \frac{\sigma_{i+\frac{1}{2}}}{2}\text{minmod}(\Delta f_{i+\frac{1}{2}}^+, \Delta f_{i-\frac{1}{2}}^+)\,. \end{aligned} \tag{8.16}$$

Using the notation $\sigma_{i+\frac{1}{2}}^{\pm} = \frac{1}{2}[\sigma_{i+\frac{1}{2}} \pm 1]$, the quantity

$$\Delta f_{i+\frac{1}{2}}^+ = \sigma_{i+\frac{1}{2}}^+\left[f(U_{i+1}^n) - f(U_i^n)\right] \tag{8.17}$$

is equal to the flux difference at interface $i+\frac{1}{2}$, if the interface-flux eigenvalue is positive, and it is equal to zero otherwise. The closely related quantity

$$\Delta f_{i+\frac{1}{2}}^- = -\sigma_{i+\frac{1}{2}}^-\left[f(U_{i+1}^n) - f(U_i^n)\right] \tag{8.18}$$

is the flux difference at interface $i+\frac{1}{2}$ if the interface-flux eigenvalue is negative, and it is zero

otherwise. The function 'minmod', which was originated by Roe and well described by Sweby (Ref. 8.11) is defined as

$$\text{minmod(a,b)} = \begin{cases} 0 & \text{if } ab < 0, \\ a & \text{if } |a| \leq |b|, \\ b & \text{if } |b| \leq |a|. \end{cases} \tag{8.19}$$

In other words, 'minmod' returns the argument of least magnitude unless the arguments are of different sign, in which case it is zero.

The first two terms in Eq. (8.16) comprise the first-order accurate upwind interface flux at interface $i + \frac{1}{2}$. The last two terms will cancel the second term to yield the spatially second-order accurate explicit central-difference interface flux under the following condition: the flux difference at interface $i + \frac{1}{2}$ does not exceed the flux difference at the interface in the upwind direction from interface $i + \frac{1}{2}$ and is of the same sign. If this condition is violated and the flux differences are of the same sign there is only a partial cancellation of the second term in Eq. (8.16). The first-order upwind interface flux is retained if the flux differences are of opposite sign. Only the upwind interface has an influence because of the design of the last two terms in Eq. (8.16). Many other "flux limiters" besides minmod have been designed and are discussed, for example, by Yee (Ref. 8.3).

If the last three terms in Eq. (8.16) are linearized with respect to U and a few simplifying approximations are made, a nearly equivalent formulation may be written in terms of the differences of U across an interface. The result is

$$\begin{aligned} F^n_{i+\frac{1}{2}} = {} & \frac{f(U^n_{i+1}) + f(U^n_i)}{2} - \frac{|\lambda_{i+\frac{1}{2}}|}{2}\Delta U^n_{i+\frac{1}{2}} \\ & - \frac{\lambda^-_{i+\frac{1}{2}}}{2}\text{minmod}(\Delta U^n_{i+\frac{3}{2}}, \Delta U^n_{i+\frac{1}{2}}) + \frac{\lambda^+_{i+\frac{1}{2}}}{2}\text{minmod}(\Delta U^n_{i+\frac{1}{2}}, \Delta U^n_{i-\frac{1}{2}}), \end{aligned} \tag{8.20}$$

where

$$\Delta U^n_{i+\frac{1}{2}} = U^n_{i+1} - U^n_i \qquad \text{and} \qquad \lambda^{\pm}_{i+\frac{1}{2}} = \frac{\lambda_{i+\frac{1}{2}} \pm |\lambda_{i+\frac{1}{2}}|}{2}. \tag{8.21}$$

Use of Eq. (8.20) instead of Eq. (8.16) results in a smaller operation count since fewer flux functions need be evaluated. In this case, the degree of cancellation of the second term by the

last two terms depends on the relative sizes of the difference of U across interface $i+\frac{1}{2}$ and the difference of U across the upwind interface.

Chakravarthy (Ref. 8.2) has evolved a more flexible, but more complex, scheme in which the interface flux may be written in the form

$$F^n_{i+\frac{1}{2}} = \frac{f(U^n_{i+1}) + f(U^n_i)}{2} - \frac{|\lambda_{i+\frac{1}{2}}|}{2}\Delta U^n_{i+\frac{1}{2}}$$
$$- \lambda^-_{i+\frac{1}{2}}\left(\frac{1-\theta}{4}\text{minmod}(\Delta U^n_{i+\frac{3}{2}}, \omega\Delta U^n_{i+\frac{1}{2}}) + \frac{1+\theta}{4}\text{minmod}(\omega\Delta U^n_{i+\frac{3}{2}}, \Delta U^n_{i+\frac{1}{2}})\right)$$
$$+ \lambda^+_{i+\frac{1}{2}}\left(\frac{1+\theta}{4}\text{minmod}(\Delta U^n_{i+\frac{1}{2}}, \omega\Delta U^n_{i-\frac{1}{2}}) + \frac{1-\theta}{4}\text{minmod}(\omega\Delta U^n_{i+\frac{1}{2}}, \Delta U^n_{i-\frac{1}{2}})\right) . \quad (8.22)$$

Equation (8.22) is identical to Eq. (8.20) if the compression parameter, ω, is set equal to unity, regardless of the value of θ.

Steeper shocks are obtained if ω is set to a value larger than unity. In sufficiently smooth regions, the last two terms cancel the second term so as to produce a higher-order interface flux. The specific difference scheme that results is determined by the value of θ, and it is stable if ω is within the limits given by

$$0 < \omega \leq \frac{3-\theta}{1-\theta}, \quad (8.23)$$

and if the time-step size is controlled such that the Courant number is less than

$$\frac{4}{5-\theta+\omega(1+\theta)} . \quad (8.24)$$

A number of special cases have been analyzed by Chakravarthy (Ref. 8.2). If θ equals +1, the scheme is central differences and ω has no limit. If the value of θ is -1 the scheme is fully upwind and ω must be less than 2. A value of $-\frac{1}{3}$ for θ yields the requirement that ω be less than $\frac{5}{2}$, while a limit for ω of 3 results if θ equals 0. The smallest truncation error occurs if θ is set to $\frac{1}{2}$, in which case ω must be smaller than 5 for stability. All the previously listed values of θ result in formally second-order accurate schemes. If θ is given the value of $\frac{1}{3}$ a third-order accurate steady-state solution scheme is obtained, in which ω is constrained to be less than four. It is usually better to use a value of ω that is less than the permitted value,

partly because the resultant allowed Courant number is larger and partly because the limits on ω were obtained by means of a linear analysis.

The case $\theta = 1$ warrants further study. The resultant interface flux is identical to that in Eq. (8.20) except for the presence of ω. The condition for cancellation of the second term in Eq. (8.22) becomes: ΔU at interface $i + \frac{1}{2}$ does not exceed the product of ω and ΔU at the interface in the upwind direction from interface $i + \frac{1}{2}$ and is of the same sign. If ω exceeds 1, the result is greater compression of transitions. Conversely, if ω is less than one, the result is reduced compression of transitions and ultimately the first-order upwind method is reproduced for ω equal to zero.

A somewhat different TVD method based on the Lax-Wendroff differencing scheme was employed by Roe, described more clearly by Roe and Pike (Ref. 8.12) and most clearly by Sweby (Ref. 8.11). It may be written as

$$U_i^{n+1} = U_i^n - \beta\lambda^-_{i+\frac{1}{2}}\Delta U^n_{i+\frac{1}{2}} - \beta\lambda^+_{i-\frac{1}{2}}\Delta U^n_{i-\frac{1}{2}} - \beta\left[\Phi^n_{i+\frac{1}{2}} - \Phi^n_{i-\frac{1}{r}2}\right], \tag{8.25}$$

where $\Phi^n_{i+\frac{1}{2}}$ is defined by

$$\Phi^n_{i+\frac{1}{2}} = \sigma^-_{i+\frac{1}{2}}\text{minmod}(\Delta h^n_{i+\frac{3}{2}}, \Delta h^n_{i+\frac{1}{2}}) + \sigma^+_{i+\frac{1}{2}}\text{minmod}(\Delta h^n_{i+\frac{1}{2}}, \Delta h^n_{i-\frac{1}{2}}), \tag{8.26}$$

where in turn

$$\Delta h^n_{i+\frac{1}{2}} = \frac{1 - \beta|\lambda_{i+\frac{1}{2}}|}{2}\lambda_{i+\frac{1}{2}}[U^n_{i+1} - U^n_i]. \tag{8.27}$$

If the solution is sufficiently smooth the $\Phi^n_{i\pm\frac{1}{2}}$ terms are nonzero and convert, to some extent, the interface flux to that of the spatially and temporally second-order accurate Lax-Wendroff method in linearized form. Otherwise, the first-order upwind interface flux is obtained.

Inspection of the first line of Eq. (8.25) reveals that it is not in conservative-difference form. A closely related TVD method which is in conservative-difference form may be written if the interface flux is defined by

$$F^n_{i+\frac{1}{2}} = \frac{f(U^n_{i+1}) + f(U^n_i)}{2} - \frac{|\lambda_{i+\frac{1}{2}}|}{2}\Delta U^n_{i+\frac{1}{2}} + \Phi^n_{i+\frac{1}{2}}. \tag{8.28}$$

In this equation, $\Phi^n_{i+\frac{1}{2}}$ may be defined as above, or it may be simplified to yield the nearly equivalent expression

$$\Phi^n_{i+\frac{1}{2}} = \frac{|\lambda_{i+\frac{1}{2}}| - \beta(\lambda_{i+\frac{1}{2}})^2}{2} Q^n_{i+\frac{1}{2}} \tag{8.29}$$

by using the limiter term

$$Q^n_{i+\frac{1}{2}} = -\sigma^-_{i+\frac{1}{2}} \text{minmod}(\Delta U^n_{i+\frac{3}{2}}, \Delta U^n_{i+\frac{1}{2}}) + \sigma^+_{i+\frac{1}{2}} \text{minmod}(\Delta U^n_{i+\frac{1}{2}}, \Delta U^n_{i-\frac{1}{2}}) . \tag{8.30}$$

Yee (Ref. 8.3) advocates an operator splitting approach that uses TVD differencing as a post-processor after application of the MacCormack scheme. She recommends the use of the MacCormack scheme as an efficient means of including source terms ($S_i = S(U_i, X_i)$), especially when the method is extended to the solution of multidimensional problems. The equations may be expressed as a predictor step

$$\check{U}^n_i = U^n_i - \beta[f(U^n_i) - f(U^n_{i-1})] - \Delta t\, S_i . \tag{8.31}$$

followed by the MacCormack corrector step

$$\check{U}^{n+1}_i = U^n_i + \frac{1}{2}\left[\check{U}^n_i - U^n_i - \beta\left[f(\check{U}^n_{i+1}) - f(\check{U}^n_i)\right] \right] - \Delta t\, \hat{S}_i , \tag{8.32}$$

which in turn is followed by the TVD post-processor

$$U^{n+1}_i = \tilde{U}^n_i - \beta\left[\tilde{\Phi}^n_{i+\frac{1}{2}} - \tilde{\Phi}^n_{i-\frac{1}{2}}\right] . \tag{8.33}$$

where

$$\tilde{\Phi}^n_{i+\frac{1}{2}} = \frac{|\tilde{\lambda}_{i+\frac{1}{2}}| - \beta(\tilde{\lambda}_{i+\frac{1}{2}})^2}{2}\left[\tilde{Q}^n_{i+\frac{1}{2}} - \Delta\tilde{U}^n_{i+\frac{1}{2}}\right] . \tag{8.34}$$

The quantity within the final set of brackets is zero in regions where the solution is sufficiently smooth, owing to the action of the limiter term, $\tilde{Q}^n_{i+\frac{1}{2}}$ which, to be consistent with the upwind

weighting of previous equations may be defined as in Eq. (8.30). In regions where the solution is insufficiently smooth, $\tilde{\Phi}^n_{i+\frac{1}{2}}$ tends to replace the Lax-Wendroff-like interface flux of the MacCormack method with the interface flux of the first-order upwind method. Yee (Ref. 8.3) advocates the use of a symmetric, or nonupwind weighted, limiter term in Eq. (8.33), which in this case might take such forms as

$$\tilde{Q}^n_{i+\frac{1}{2}} = \text{minmod}(\Delta\tilde{U}^n_{i+\frac{3}{2}}, \Delta\tilde{U}^n_{i+\frac{1}{2}}) + \text{minmod}(\Delta\tilde{U}^n_{i+\frac{1}{2}}, \Delta\tilde{U}^n_{i-\frac{1}{2}}) - \Delta\tilde{U}^n_{i+\frac{1}{2}} \tag{8.35}$$

or

$$\tilde{Q}^n_{i+\frac{1}{2}} = \text{minmod}\left(\Delta\tilde{U}^n_{i+\frac{1}{2}}, \text{minmod}(\Delta\tilde{U}^n_{i+\frac{3}{2}}, \Delta\tilde{U}^n_{i-\frac{1}{2}})\right) . \tag{8.36}$$

Use of symmetric limiter terms results in a lower operations count at the cost of a slight degeneration in quality.

There are a large number of additional TVD formulations which cannot be discussed here, owing to lack of space. However, many are treated in detail by Yee (Ref. 8.3) along with various forms of limiter terms.

8.5 Application of TVD Method to Euler Equations

It is convenient to write the inviscid equations of gasdynamics in terms of the time derivatives of four conserved quantities E, ρ, ρU, and ρV on a two-dimensional spatial domain with coordinates X and Y. E is the total energy of the gas per unit volume, ρ is the gas density, and U and V are the gas velocities in the X and Y directions, respectively. The spatial domain is essentially rectangular in shape but may have curved or sloping boundaries. The inviscid gasdynamical equations in planar or axisymmetric form may be expressed in vector form as

$$\frac{\partial \underline{U}}{\partial t} + \frac{\partial \underline{f}}{\partial X} + \frac{\partial \underline{h}}{\partial Y} + \underline{S} = 0 . \tag{8.37}$$

$\underline{U}$ is a column vector which contains the four components of the solution and is defined by

$$\underline{U} = [E \quad \rho \quad \rho U \quad \rho V]^T, \tag{8.38}$$

where T is the transpose operator. $\underline{f}$ and $\underline{h}$ are the vector valued fluxes along the X and Y

directions, respectively. They are defined as

$$\underline{f} = \left[EU + PU \quad \rho U \quad \rho U^2 + P \quad \rho UV\right]^T, \tag{8.39}$$

$$\underline{h} = \left[EV + PV \quad \rho V \quad \rho UV \quad \rho V^2 + P\right]^T, \tag{8.40}$$

where the pressure, P, may be computed from the components of $\underline{U}$ using the formula

$$P = (\gamma - 1)\left[E - \frac{(\rho U)^2 + (\rho V)^2}{2\rho}\right], \tag{8.41}$$

for the case of a perfect gas, where γ is the specific heat ratio. $\underline{S}$ is a source term which is zero if the problem to be solved uses Cartesian coordinates. If an axisymmetric problem is to be solved, $\underline{S}$ is given by

$$\underline{S} = \left[\frac{E + P}{Y}V \quad \frac{\rho V}{Y} \quad \frac{\rho UV}{Y} \quad \frac{\rho V^2}{Y}\right]^T. \tag{8.42}$$

In the above column vector, it is assumed that the X axis is the axis of symmetry and that Y is the radius about the X axis.

It is convenient to transform these equations from the spatial domain with coordinates X and Y, to a rectangular computational domain with coordinates ξ and η. The Jacobian of the transformation, J, which is a scalar function of the first-order partial derivatives of X and Y with respect ξ and η, is defined by

$$\frac{1}{J} = X_\xi Y_\eta - X_\eta Y_\xi \,. \tag{8.43}$$

It is also useful to introduce a notation where X_ξ is the partial derivative of X with respect to ξ at constant η and t, and X_η is the partial derivative of X with respect to η at constant ξ and t. The partial derivatives Y_ξ and Y_η have analogous definitions.

The transformed Euler equations may be written as

$$\frac{\partial \bar{U}}{\partial t} + \frac{\partial \bar{f}}{\partial \xi} + \frac{\partial \bar{h}}{\partial \eta} + \bar{S} = 0\,, \tag{8.44}$$

where any quantity with an overhead bar is a column vector that has the factor J in its denominator. More specifically, $\bar{U} = \underline{U}/J$, $\bar{f} = \underline{f}\xi_x/J + \underline{h}\xi_y/J$, $\bar{h} = \underline{f}\eta_x/J + \underline{h}\eta_y/J$, and $\bar{S} = \underline{S}/J$. The quantities ξ_x, ξ_y, η_x, and η_y are the partial derivatives of ξ and η with respect to X or Y. The identities $\xi_x/J = Y_\eta$, $\xi_y/J = -X_\eta$, $\eta_x/J = -Y_\xi$, and $\eta_y/J = X_\xi$ facilitate calculation of metrics in the computational frame. The transformed vector-valued equation originally contains the additional terms $\underline{f}[Y_{\xi\eta} - Y_{\eta\xi}]$ and $\underline{h}[X_{\eta\xi} - X_{\xi\eta}]$ but the extra terms are identically zero because the second-order derivatives satisfy the identities $Y_{\xi\eta} = Y_{\eta\xi}$ and $X_{\xi\eta} = X_{\eta\xi}$. As discussed in detail by Thomas and Lombard (Ref. 8.13), it is crucial to select the differencing method so that the two identities still hold when the metrics are approximated by finite differences. Violation of the two identities results in the effective introduction of an extra source term and would cause nonconservation of the free stream.

The scalar TVD formulation must be modified to deal with the vector nature of the PDE's. Equation (8.44) without the source term may be linearized to obtain

$$\frac{\partial \bar{U}}{\partial t} + \left[\frac{\partial \bar{f}}{\partial \bar{U}}\right]\frac{\partial \bar{U}}{\partial \xi} + \left[\frac{\partial \bar{h}}{\partial \bar{U}}\right]\frac{\partial \bar{U}}{\partial \eta} = 0 . \tag{8.45}$$

$[\partial \bar{f}/\partial \bar{U}]$ is a four by four matrix whose components are the derivatives of the components of $\bar{f}$ with respect to the components of $\bar{U}$ and will be called the Jacobian of $\bar{f}$. Similarly, $[\partial \bar{h}/\partial U]$ will be denoted the Jacobian of $\bar{h}$. The TVD fluxes are are expressed as weighted sums of the eigenvectors of the Jacobians. The size and sign of the weights depend on the smoothness of the solution and the four eigenvalues of each Jacobian matrix, in a manner that will be detailed later.

In order to discretize the transformed equations, the rectangular computational domain is divided into square cells by vertical and horizontal lines with unit spacing. It is convenient to label the cells with the index pair i,k such that i equals one along the left-most column of cells and increases to the right, whereas k equals one along the bottom row of cells and increases upwards. The values of ξ and η at the centre of cell i,k are $\xi_{i,k} = i$ and $\eta_{i,k} = k$, respectively. The four corners of cell i,k have numerical coordinates $i \pm \frac{1}{2}$, $k \pm \frac{1}{2}$. The square cells are mapped onto, possibly deformed, rectangles in the spatial coordinate system. Using the above definition of ξ and η the transformed equations are discretized at each cell i,k to

obtain the difference equation

$$\underline{U}_{i,k}^{n+1} - \underline{U}_{i,k}^{n} = -\beta_{i,k}\left[\bar{F}_{i+\frac{1}{2},k}^{n} - \bar{F}_{i-\frac{1}{2},k}^{n}\right] - \beta_{i,k}\left[\bar{H}_{i,k+\frac{1}{2}}^{n} - \bar{H}_{i,k-\frac{1}{2}}^{n}\right] - \beta_{i,k}\bar{S}_{i,k}^{n}, \qquad (8.46)$$

where $\beta_{i,k}$ is the value of $J\Delta t$ evaluated at the centre of cell i,k and $\bar{F}_{i+\frac{1}{2},k}^{n}$ is a numerical estimate of the flux through the right-hand interface of cell i,k evaluated at time level n and has the form

$$\bar{F}_{i+\frac{1}{2},k}^{n} = \frac{\underline{f}(\underline{U}_{i+1,k}^{n}) + \underline{f}(\underline{U}_{i,k}^{n})}{2}\hat{\Omega}_x + \frac{\underline{h}(\underline{U}_{i+1,k}^{n}) + \underline{h}(\underline{U}_{i,k}^{n})}{2}\hat{\Omega}_y - \sum_{m=1}^{4} W_{i+\frac{1}{2},k}^{m}\underline{R}_{i+\frac{1}{2},k}^{m}. \qquad (8.47)$$

$\hat{\Omega}_x = \xi_x/J$ and $\hat{\Omega}_y = \xi_y/J$ evaluated at $i+\frac{1}{2},k$ (i.e., $\hat{\Omega}_x = Y_{i+\frac{1}{2},k+\frac{1}{2}} - Y_{i+\frac{1}{2},k-\frac{1}{2}}$ and $\hat{\Omega}_y = X_{i+\frac{1}{2},k-\frac{1}{2}} - X_{i+\frac{1}{2},k+\frac{1}{2}}$) incorporate the effect of the length and orientation of the right-hand interface of cell i,k on the flux.

If only the first two terms in the expression for the interface flux were present, the explicit central-difference method would be obtained. The last term adds numerical viscosity to the first two terms to produce the first-order upwind method except when the solution is sufficiently smooth. The last term is the weighted summation the four eigenvectors of the Jacobian of $\underline{f}\xi_x/J + \underline{h}\xi_y/J$ evaluated at the right-hand interface of cell i,k. After Chakravarthy (Ref. 8.2), it is convenient to define a four by four matrix [R] whose columns are the eigenvectors. In this manner,

$$[R] = \begin{bmatrix} \frac{Q^2}{2C} - U_c + \frac{C}{\gamma-1} & \frac{Q^2}{2C} + V_c & \frac{Q^2}{2C} - V_c & \frac{Q^2}{2C} + U_c + \frac{C}{\gamma-1} \\ \frac{1}{C} & \frac{1}{C} & \frac{1}{C} & \frac{1}{C} \\ \frac{U}{C} - \Omega_x & \frac{U}{C} - \Omega_y & \frac{U}{C} + \Omega_y & \frac{U}{C} + \Omega_x \\ \frac{V}{C} - \Omega_y & \frac{V}{C} + \Omega_x & \frac{V}{C} - \Omega_x & \frac{V}{C} + \Omega_y \end{bmatrix}. \qquad (8.48)$$

where $\Omega_x = \hat{\Omega}_x/\sqrt{\hat{\Omega}_x\hat{\Omega}_x + \hat{\Omega}_y\hat{\Omega}_y}$, $\Omega_y = \hat{\Omega}_y/\sqrt{\hat{\Omega}_x\hat{\Omega}_x + \hat{\Omega}_y\hat{\Omega}_y}$, C is the speed of sound, and $Q^2 = U^2 + V^2$, all evaluated at the right-hand interface of cell i,k. $U_c = U\Omega_x + V\Omega_y$ is the flow speed perpendicular to the interface and $V_c = V\Omega_x - U\Omega_y$ is the flow speed parallel to the interface. $\underline{R}_{j+\frac{1}{2},k}^{m}$ has components given by the m^{th} column of $[R]$.

The weights in the summation of Eq. (8.47) have the form

$$W^m_{i+\frac{1}{2},k} = \frac{|\lambda^m_{i+\frac{1}{2},k}|}{2}\alpha^m_{i+\frac{1}{2},k}$$
$$+ \lambda^{m-}_{i+\frac{1}{2},k}\left(\frac{1-\theta}{4}\text{minmod}(\alpha'^m_{i+\frac{3}{2},k}, \omega\alpha^m_{i+\frac{1}{2},k}) + \frac{1+\theta}{4}\text{minmod}(\omega\alpha'^m_{i+\frac{3}{2},k}, \alpha^m_{i+\frac{1}{2},k})\right)$$
$$- \lambda^{m+}_{i+\frac{1}{2},k}\left(\frac{1+\theta}{4}\text{minmod}(\alpha^m_{i+\frac{1}{2},k}, \omega\alpha'^m_{i-\frac{1}{2},k}) + \frac{1-\theta}{4}\text{minmod}(\omega\alpha^m_{i+\frac{1}{2},k}, \alpha'^m_{i-\frac{1}{2},k})\right), \quad (8.49)$$

where $\alpha^m_{i+\frac{1}{2},k}$ is the projection of the difference in $\underline{U}$ across interface $i+\frac{1}{2},k$ onto the m^{th} eigenvector. The projection is calculated using

$$\alpha^m_{i+\frac{1}{2},k} = \underline{L}^m_{i+\frac{1}{2},k} \bullet \left[\underline{U}_{i+1,k} - \underline{U}_{i,k}\right]. \quad (8.50)$$

The projections of the difference in $\underline{U}$ at the interfaces to each side of interface $i+\frac{1}{2},k$ are given by

$$\alpha'^m_{i+\frac{3}{2},k} = \underline{L}^m_{i+\frac{1}{2},k} \bullet \left[\underline{U}_{i+2,k} - \underline{U}_{i+1,k}\right] \quad \text{and} \quad \alpha'^m_{i-\frac{1}{2},k} = \underline{L}^m_{i+\frac{1}{2},k} \bullet \left[\underline{U}_{i,k} - \underline{U}_{i-1,k}\right]. \quad (8.51)$$

The vector $\underline{L}^m_{i+\frac{1}{2},k}$ is given by the m^{th} row of the four by four matrix

$$[L] = \frac{1}{2}\begin{bmatrix} +\frac{\gamma-1}{C} & +\frac{\gamma-1}{2C}Q^2 + U_c & -\frac{\gamma-1}{C}U - \Omega_x & -\frac{\gamma-1}{C}V - \Omega_y \\ -\frac{\gamma-1}{C} & -\frac{\gamma-1}{2C}Q^2 - V_c + C & +\frac{\gamma-1}{C}U - \Omega_y & +\frac{\gamma-1}{C}V + \Omega_x \\ -\frac{\gamma-1}{C} & -\frac{\gamma-1}{2C}Q^2 + V_c + C & +\frac{\gamma-1}{C}U + \Omega_y & +\frac{\gamma-1}{C}V - \Omega_x \\ +\frac{\gamma-1}{C} & +\frac{\gamma-1}{2C}Q^2 - U_c & -\frac{\gamma-1}{C}U + \Omega_x & -\frac{\gamma-1}{C}V + \Omega_y \end{bmatrix}, \quad (8.52)$$

which is the inverse of $[R]$. Strictly speaking, $\underline{U}_{i+1,k} - \underline{U}_{i,k}$ in Eq. (8.50) should be $\bar{U}_{i+1,k} - \bar{U}_{i,k}$, but the missing factor $1/J$ is included in $\lambda^m_{i+\frac{1}{2},k}$, which is the m^{th} eigenvalue of $[\partial\bar{f}/\partial\bar{U}]$ divided

by J evaluated at the right-hand interface of cell i,k. The values of $\lambda^m_{i+\frac{1}{2},k}$ that correspond to $\underline{R}^m_{i+\frac{1}{2},k}$ and $\underline{L}^m_{i+\frac{1}{2},k}$ are given by

$$\begin{aligned}
\lambda^1_{i+\frac{1}{2},k} &= [U_c - C]\sqrt{\hat{\Omega}_x\hat{\Omega}_x + \hat{\Omega}_y\hat{\Omega}_y}\,, \\
\lambda^2_{i+\frac{1}{2},k} &= \lambda^3_{i+\frac{1}{2},k} = U_c\sqrt{\hat{\Omega}_x\hat{\Omega}_x + \hat{\Omega}_y\hat{\Omega}_y}\,, \\
\lambda^4_{i+\frac{1}{2},k} &= [U_c + C]\sqrt{\hat{\Omega}_x\hat{\Omega}_x + \hat{\Omega}_y\hat{\Omega}_y}\,.
\end{aligned} \tag{8.53}$$

The eigenvalues correspond to characteristics of the system of PDE's. The signs of the eigenvalues at an interface determine the influence of the solution at one cell on the solution at adjacent cells. In what follows the "eigenvalues" will always contain a factor of J in the denominator.

The first and fourth eigenvalues must be adjusted to prevent the development of aphysical shock-like structures in rarefaction waves ("rarefaction shocks") in regions where the flow velocity changes from subsonic to supersonic. A number of "sonic correction" techniques have been used. One of the simplest. described by Yee (Ref. 8.3), has been used in this work. Let $|\lambda^{max}|$ be the absolute value of the eigenvalue with maximum magnitude at interface $i+\frac{1}{2},k$ (that is, $|\lambda^{max}| = [|U_c| + C]\sqrt{\hat{\Omega}_x\hat{\Omega}_x + \hat{\Omega}_y\hat{\Omega}_y}$). Then the first and fourth eigenvalues are adjusted using the formula

$$\lambda = \begin{cases} \lambda & \text{if } |\lambda| \geq |\lambda^{max}|\,\delta \\ \dfrac{\lambda^2 + |\lambda^{max}|^2\,\delta^2}{2|\lambda^{max}|\,\delta}\,\text{sign}(\lambda) & \text{if } |\lambda| < |\lambda^{max}|\,\delta \end{cases}, \tag{8.54}$$

where δ is a small number ranging from 0.01 to 0.15.

In order to evaluate the eigenvectors and eigenvalues at the interface, an approximation to $\underline{U}$ must be obtained. A very simple approximation is to take the arithmetic average of $\underline{U}$ in the cells to each side. A number of more complex approximations have been used. The approach taken by Chakravarthy (Ref. 8.2) and retained herein is to use the averages of Roe (Ref. 8.1), which lead to particularly thin shocks. The average density, velocities, enthalpy, and speed of sound are expressed as

$$\rho_{i+\frac{1}{2},k} = \sqrt{\rho_{i+1,k}}\sqrt{\rho_{i,k}}\,, \tag{8.55}$$

$$U_{i+\frac{1}{2},k} = \frac{U_{i+1,k}\sqrt{\rho_{i+1,k}} + U_{i,k}\sqrt{\rho_{i,k}}}{\sqrt{\rho_{i+1,k}} + \sqrt{\rho_{i,k}}}\,, \tag{8.56}$$

$$V_{i+\frac{1}{2},k} = \frac{V_{i+1,k}\sqrt{\rho_{i+1,k}} + V_{i,k}\sqrt{\rho_{i,k}}}{\sqrt{\rho_{i+1,k}} + \sqrt{\rho_{i,k}}}, \tag{8.57}$$

$$\varepsilon_{i+\frac{1}{2},k} = \frac{\varepsilon_{i+1,k}\sqrt{\rho_{i+1,k}} + \varepsilon_{i,k}\sqrt{\rho_{i,k}}}{\sqrt{\rho_{i+1,k}} + \sqrt{\rho_{i,k}}}, \tag{8.58}$$

$$C_{i+\frac{1}{2},k} = \sqrt{\gamma - 1}\sqrt{\varepsilon_{i+\frac{1}{2},k} - \frac{U_{i+\frac{1}{2},k}U_{i+\frac{1}{2},k} + V_{i+\frac{1}{2},k}V_{i+\frac{1}{2},k}}{2}}, \tag{8.59}$$

where $\varepsilon_{i,k} = [E_{i,k} + P_{i,k}]/\rho_{i,k}$.

$\bar{H}^n_{i,k+\frac{1}{2}}$ is a numerical estimate of the flux through the top interface of cell i,k evaluated at time level n. It may be calculated using Eqs. (8.47)–(8.59) with $i+1,k$ replaced by $i,k+1$, $i+\frac{1}{2},k$ replaced by $i,k+\frac{1}{2}$, $\hat{\Omega}_x$ equal to $Y_{i-\frac{1}{2},k+\frac{1}{2}} - Y_{i+\frac{1}{2},k+\frac{1}{2}}$, ($\eta_x/J$ evaluated at $i,k+\frac{1}{2}$) and $\hat{\Omega}_y$ equal to $X_{i+\frac{1}{2},k+\frac{1}{2}} - X_{i-\frac{1}{2},k+\frac{1}{2}}$ (η_y/J evaluated at $i,k+\frac{1}{2}$).

After Chakravarthy (Ref. 8.2), the value of $1/J$ at the centre of each cell is taken to be the area of the cell. Thus the value of $1/J$ in the centre of cell j,k is given by

$$\begin{aligned}\frac{1}{J_{i,k}} &= \frac{1}{2}\left[X_{i-\frac{1}{2},k-\frac{1}{2}} - X_{i+\frac{1}{2},k+\frac{1}{2}}\right]\left[Y_{i+\frac{1}{2},k-\frac{1}{2}} - Y_{i-\frac{1}{2},k+\frac{1}{2}}\right] \\ &+ \frac{1}{2}\left[X_{i+\frac{1}{2},k-\frac{1}{2}} - X_{i-\frac{1}{2},k+\frac{1}{2}}\right]\left[Y_{i+\frac{1}{2},k+\frac{1}{2}} - Y_{i-\frac{1}{2},k-\frac{1}{2}}\right].\end{aligned} \tag{8.60}$$

Note that it is the components of $\bar{U}$ that are conserved. That is, the average of each component of $\underline{U}$ times the area of the cell is conserved. The flux through an interface between two adjacent cells increases the value of $\bar{U}$ in one cell by the same amount by which it decreases the value of $\underline{U}$ in the adjacent cell. However, if the area of the adjacent cells is different, then the values of the change in $\underline{U}$ in each cell will not be of equal size. Degradation of the solution will not occur if the cell sizes and shapes vary smoothly across the physical domain. That is, the most accurate numerical solutions are obtained when $1/J$ varies smoothly across the domain. The explicit time-step size is either held constant or is set equal to the maximum allowed explicit time-step size (based on the maximum allowed Courant number) decreased by a problem-dependent multiplicative factor. The Courant number for cell i,k is taken to be the sum, over the four sides of the cell, of $\frac{|\lambda^{max}|}{2}\beta_{i,k}$.

The grid may consist of several rectangular subgrids. Reflection or transmission boundary conditions may be specified at the left, right, bottom or top edge of a subgrid. Two additional boundary conditions may be specified at the left and right edge of a subgrid: supersonic inflow

and continuation of the solution from an adjacent subgrid. It is convenient, in what follows, to discuss the implementation of boundary conditions at the left edge of a grid. The discussion and results are easily generalized to describe boundary conditions at the right, bottom, or top edge of a grid.

A reflection boundary condition is implemented by adding two columns of virtual cells (designated outer- and inner-column) to the left of the boundary. The values of the components of $\underline{U}$ in the virtual cells are assigned so that E, ρ, and parallel gas velocity are symmetric about the boundary while the gas velocity perpendicular to the boundary is antisymmetric. Since the Euler equations are inviscid, slippage is allowed along walls. In other words, it is assumed that the flow near the boundary approximates that which would occur if a stream of gas meets a parallel flowing stream in such a way that no matter crosses the boundary. Two rows of virtual cells are required to compute the interface flux at the boundary because of the method of construction of the flux-limiters. As a seldom used option, the compression parameter may be set to zero when computing the interface flux at a reflective boundary so that the data in the outer column of virtual cells does not effect the solution.

Transmission boundary conditions were initially also implemented by simply adding two columns of virtual cells to the left of the boundary. The value of $\underline{U}$ in the virtual cells was assigned so that $\underline{U}$ would be symmetric about the boundary. This simple scheme resulted in unsatisfactory transmission of rarefaction waves in a one-dimensional Euler problem solved using the TVD scheme. It was soon determined that rarefaction waves were transmitted without extraneous reflections if the first-order upwind method was employed instead. A great deal of further numerical experimentation showed that much smaller extraneous reflections could be obtained for the TVD scheme if the compression parameter was set to zero when computing the interface flux at the boundary and at the interface just to the right of the boundary. The zero values of compression parameter at the two interfaces caused the value of the solution in the (real) cell just to the right of the boundary to be, in effect, computed using the first-order upwind method. The extraneous reflections were due to an unwitting attempt to use higher-order accuracy at a boundary and are related to the difficulties experienced by Kamowitz (Ref. 8.10) when using greater than zero-order extrapolation of flow velocities for a transmission boundary condition.

An alternative approach to transmission boundary conditions has been developed by extending the characteristic extrapolation scheme of Kamowitz for use in two-dimensional do-

mains. The alternative approach gives equivalent quality in one-dimensional problems and reduces extraneous reflections in two-dimensional problems. An extra column of image cells is used along the left edge of the domain to store boundary data. (An extra column or row of image cells is placed along the right, top, and bottom edge of the domain to deal with transmissive left, upper, and lower boundaries.) The data in the column of image cells is used instead of an inner column of virtual cells. Before the TVD scheme is applied the value of $\underline{U}_{0,k}$ for the image cells are updated by using

$$\underline{U}_{0,k}^{n+1} = \underline{U}_{0,k}^{n} - \beta_{1,k}\left[\frac{\underline{f}(\underline{U}_{1,k}^{n}) - \underline{f}(\underline{U}_{0,k}^{n})}{2}\hat{\Omega}_x + \frac{\underline{h}(\underline{U}_{1,k}^{n}) - \underline{h}(\underline{U}_{0,k}^{n})}{2}\hat{\Omega}_y\right], \qquad (8.61)$$

where $\hat{\Omega}_x = Y_{\frac{1}{2},k+\frac{1}{2}} - Y_{\frac{1}{2},k-\frac{1}{2}}$ and $\hat{\Omega}_y = X_{\frac{1}{2},k-\frac{1}{2}} - X_{\frac{1}{2},k+\frac{1}{2}}$ incorporate the effect of the length and orientation of the boundary interface on the row-wise flux into cell 0,k. It is convenient to evaluate $\beta = J\Delta t$ at the center of (real) cell $1,k$ rather than (image) cell $0,k$. The procedure amounts to application of characteristic extrapolation in the row-wise direction. Best results are produced when the solution in the outer column of virtual cells is set to the updated solution in the column of image cells.

Characteristic extrapolation is also performed at the right edge of the domain if there is a transmission boundary there. The TVD scheme is then applied to the entire grid including image columns but the row-wise TVD fluxes are set to zero when computing the TVD flux into an image-column cell owing to the prior addition of the row-wise flux using characteristic extrapolation.

A similar procedure is used to apply transmission boundary conditions at the top and bottom of the domain. Since the TVD fluxes are computed one cell-column at a time, it is convenient compute the row-wise TVD fluxes within a cell-column, then apply column-wise characteristic extrapolation to update the solution in an image cell at the top or bottom of the cell-column, finally followed by computation of column-wise TVD fluxes within the cell-column. Column-wise TVD fluxes are set to zero when computing the TVD flux into an image cell at the top or bottom of the cell-column, owing to the prior addition of the column-wise flux using characteristic extrapolation.

Note that a cell which is at the intersection of a row and column of image cells is only updated using characteristic extrapolation. The difference in the order of application of TVD fluxes and of characteristic extrapolation in the row-wise and column-wise directions does not result in detectable degradation of the solution.

Cell-columns are updated from left to right within a subgrid. Continuation boundary conditions are handled automatically as long as the solution in a subgrid is not computed until the solution in all the subgrids to its left have been computed. A supersonic inflow left-boundary condition is handled by leaving two columns of cells at the left side of the domain whose values are never updated but are simply used to compute row-wise fluxes into the left boundary.

The TVD time-stepping is applied one cell-column at a time by calling a highly vectorized subroutine. The subroutine is supplied with the old values of the solution at the centers and the spatial coordinates at the corners of the cells in the column that is to be updated (designated column b). The old values of the solution within the cell-column to the left (column a) and within the two cell-columns to the right of column b (columns c and d) are also supplied. Cell columns a, b, c, or d may be given virtual values to aid in specifying reflection or transmission left or right boundary conditions. Two extra cells are appended to the top and bottom of all four cell columns and may be given virtual values to aid in the specification of transmission or reflection upper or lower boundary conditions. The values of row-wise interface flux into the left-hand sides of the cells in column b form part of the input into the subroutine. The subroutine returns the updated values of the solution within cell-column b along with the values of row-wise flux out of the right-hand sides of the cells.

The flux limiter 'minmod' was used exclusively during the early stages of code development. As discussed by Yee (Ref. 8.2), there are a number of alternative flux limiters that have been used by various authors. The very compressive limiter of Roe, 'superbee', as modified by Sweby (Ref. 8.11), was introduced in the later stages of code development. This limiter results in particularly thin contact surfaces. The function 'superbee(a,b)' is the maximum of 'minmod(a,ωb)' and 'minmod(ωa,b)'.

Expressions of the form $\frac{1}{2}[1 \pm \theta]\text{minmod}(a, \omega b) + \frac{1}{2}[1 \mp \theta]\text{minmod}(\omega a, b)$ in Eq. (8.49) are replaced by superbee(a, b) to yield

$$W^m_{i+\frac{1}{2},k} = \frac{|\lambda^m_{i+\frac{1}{2},k}|}{2}\alpha^m_{i+\frac{1}{2},k} + \frac{\lambda^{m-}_{i+\frac{1}{2},k}}{2}\text{superbee}(\alpha'^m_{i+\frac{3}{2},k}, \alpha^m_{i+\frac{1}{2},k}) - \frac{\lambda^{m+}_{i+\frac{1}{2},k}}{2}\text{superbee}(\alpha^m_{i+\frac{1}{2},k}, \alpha'^m_{i-\frac{1}{2},k}). \quad (8.62)$$

The altered expressions are larger near transitions and hence cancel out a greater portion of the

first term in $W^m_{i+\frac{1}{2},k}$. For a given value of ω, the differencing has a smaller first-order upwind component when 'superbee' is used instead of 'minmod'. The maximum Courant number must not exceed $2/[2+\omega]$, and ω must not exceed 2. As recommended in Yee (Ref. 8.3) and Sweby (Ref. 8.11), 'superbee' is only employed in computing the second and third weights (associated with characteristic velocity U_c) in the sum of Eq. (8.47). If 'superbee' is used to compute the first and fourth weights (associated with characteristic velocities $U_c \mp C$), oscillations occur in smooth regions for large Mach numbers.

8.6 Results of Explicit TVD Calculations

The TVD code was initially developed to run on a Perkin-Elmer 3250 computer at UTIAS. The initial installation of the TVD code on the Cray X-MP/24 at the Ontario Centre for Large Scale Computation at the University of Toronto resulted in a 100-fold increase in execution speed. Subsequent tailoring of the TVD code to include increased vectorization and a more efficient output yielded an additional increase in execution speed by a factor of four. Additional vectorization is possible.

It is of interest to discuss a one-dimensional problem solved on a 200-cell grid. Figures 8.1a and 8.1b illustrate density profiles at various times for a fairly conventional type planar shock tube which initially has three regions with zero gas velocity and the same temperature, but with the central region has one-tenth of the pressure of the two outer regions. These three regions are separated by two bursting diaphragms. On diaphragm rupture, two shock waves proceed into the low-pressure region and reflect at the centre of the shock tube. Rarefaction waves propagate outwards into the high-pressure regions and reflect off the closed ends of the shock tube. Two contact surfaces between the gas cooled by a rarefaction wave and the gas heated by a shock wave move with the flow towards the centre.

Use of flux limiters to reduce the calculation to first order near steep transitions has prevented development of the oscillations near shocks typical of conventional second-order accurate calculations. The compression parameter of 'minmod' was set to 1 and that of 'superbee' was set to 1.25. Slightly larger values of the compression parameters resulted in shocks that were not flat at the top. Somewhat larger values of the compression parameters could be used if the initial pressure ratio across the diaphragms was reduced to two. The value of θ was set to $\frac{1}{2}$ since that gave the thinnest transitions. The above computation will be designated calculation ST1 (Shock Tube 1) in what follows.

If the compression parameters are set to zero, then the first-order upwind method is obtained. The profiles in Fig. 8.2 were generated by such an upwind calculation, and they display much broader density transitions than occur in the previous Figs. 8.1a and 8.1b, especially for the contact surface.

It will have been noticed that there are small moving bumps in the reflecting rarefaction waves in Figs. 8.1a and 8.1b. The bumps quickly disappear after the rarefaction waves have

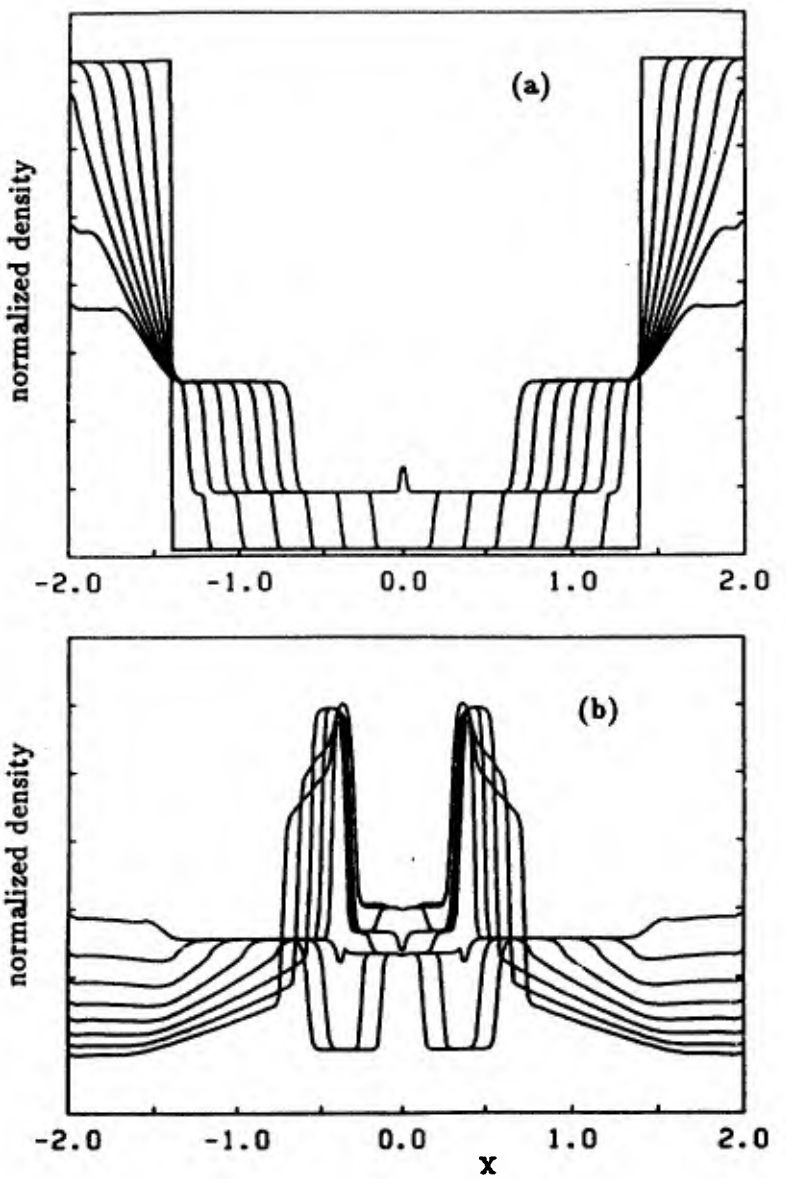

Fig. 8.1 ST1: Density profiles from $t = 0$ to $t = 0.875$ (a) and from $t = 1$ to $t = 1.875$ (b) for a one-dimensional shock-tube problem, obtained with 'minmod' and 'superbee' compression parameters set to 1 and 1.25, respectively. Approximate time intervals between profiles is $\Delta t = 0.125$. Calculations were performed on a 200-cell grid.

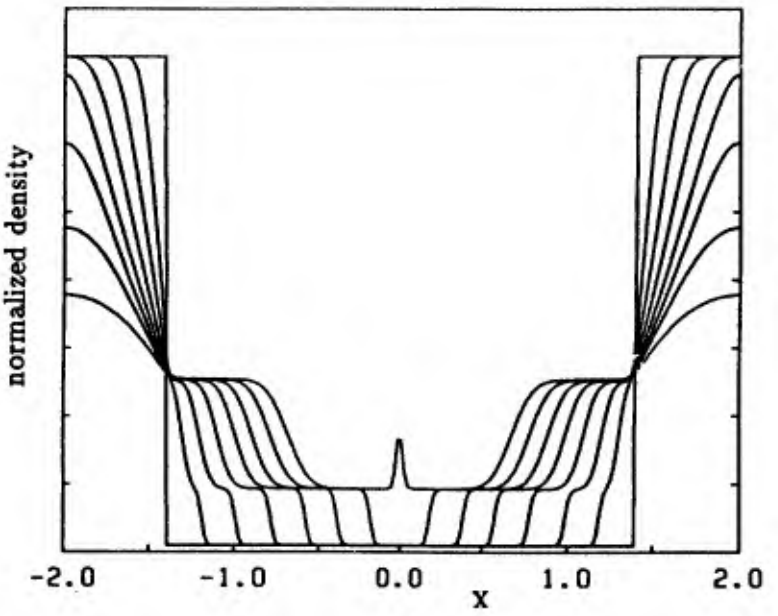

Fig. 8.2 Density profiles from $t = 0$ to $t = 0.875$ for the one-dimensional shock-tube problem, obtained with 'minmod' and 'superbee' compression parameters both set to zero. Approximate time interval between profiles is $\Delta t = 0.125$. Calculations were done on a 200-cell grid.

been completely reflected. The bumps do not appear if smaller compression parameters are used, but the transitions become thicker. The small fixed bumps that remain attached to each end of the shock tube do not disturb the rest of the flow field and may not be present depending on how the reflection boundary condition is enforced. The bumps do not appear if the initial pressure ratio across the bursting diaphragms is reduced to two.

The TVD code was used to solve a two-dimensional test problem on a four-unit by four-unit square domain on which a three-unit by three-unit centrally located square region initially had one-tenth the density of the surrounding region. This was the so-called 'shock-box' problem due to Aki, an extension of the previous one-dimensional shock-tube problem to two dimensions. The gas flow over one-quarter of the domain was modelled on a 200-cell by 200-cell grid with perpendicular reflection boundary conditions imposed on the both the bottom and right-hand sides of the grid, and transmission boundary conditions were imposed on the other two sides or boundaries.

Figures 8.3a and 8.3b illustrate the resulting lines of constant density at times $t = 0.375$ and $t = 0.5625$ if only the limiter 'minmod', with $\theta = \frac{1}{2}$, is used. A shock wave proceeds inwards, trailed by a contact surface, and a rarefaction wave moves outwards towards the boundaries. The two legs of the rarefaction wave reflect at the corner to produce a very steep expansion thereat. Note that the entire computation took 5 CPU minutes and is designated calculation

SQR1 in the discussion which follows.

The compression parameter had to be set to 0.75 to suppress oscillations where the two legs of the rarefaction wave reflected. This adjustment resulted in a thickening of the shock wave

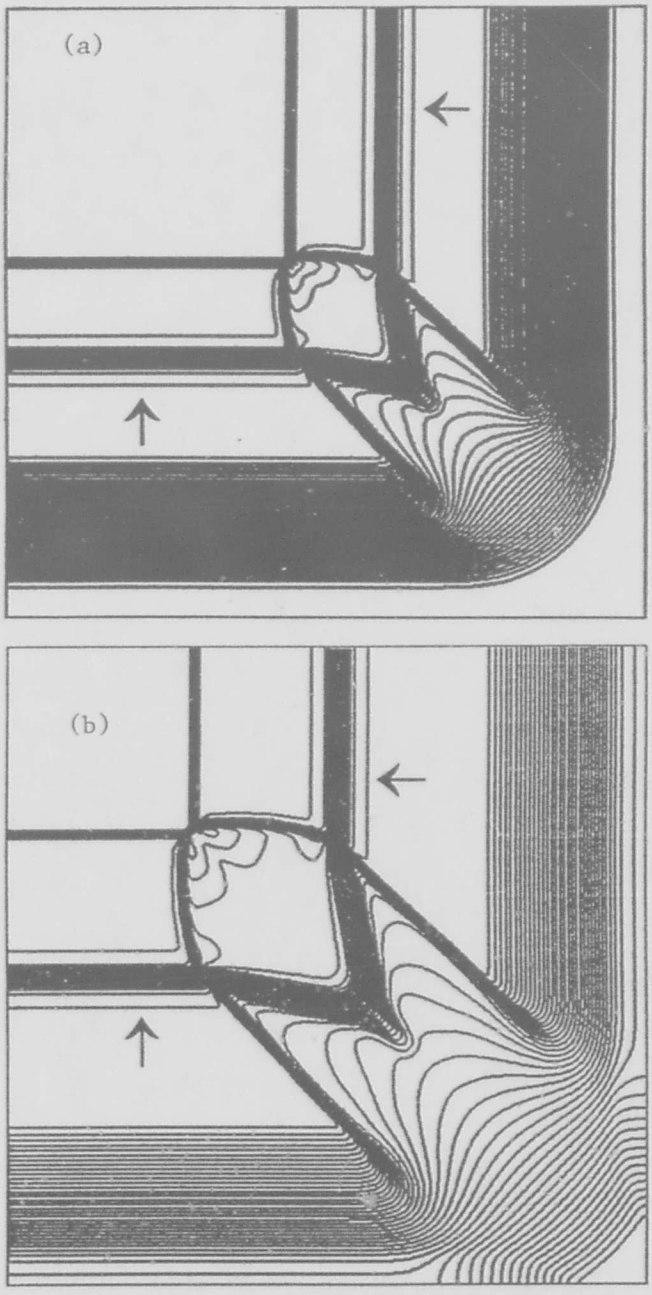

Fig. 8.3 Contours of constant density for the 'shock-box' problem at $t = 0.375$ before the rarefaction wave reaches the outer grid boundary (a) and at $t = 0.5625$ when the rarefaction wave begins to reflect off the solid wall (b). The 'minmod' compression parameter was set to 0.75, and computations were done with a 200-cell by 200-cell grid.

and contact surface. Note that reduction of the compression parameter to a value between zero and one is equivalent to maintaining a first-order upwind component of difference, over the entire flow field.

Figure 8.4 illustrates the resulting lines of constant density for the shock-box problem at $t = 0.5625$ if 'superbee' is used for m equal to two and three in a computation that will be designated as calculation SQR2. The compression parameter of 'minmod' is set to 0.75 and that of 'superbee' is set to 1.25. The shock wave is slightly thinner and the contact surface is considerably reduced in thickness. There are a few small wiggles visible. Use of smaller compression parameters will suppress these wiggles but result in thicker transitions. It is clear that use of a TVD code involves selection of priorities that depend on the use to which the solution will be applied.

The use of 'superbee' increases the execution time to about 6 minutes because of a reduction in the permitted Courant number. If 'minmod' is retained with a compression parameter set equal to 1.25 for m equal to two and three, the execution time, thickness of the transitions, and abundance of wiggles are intermediate between results for the calculation for SQR1 and

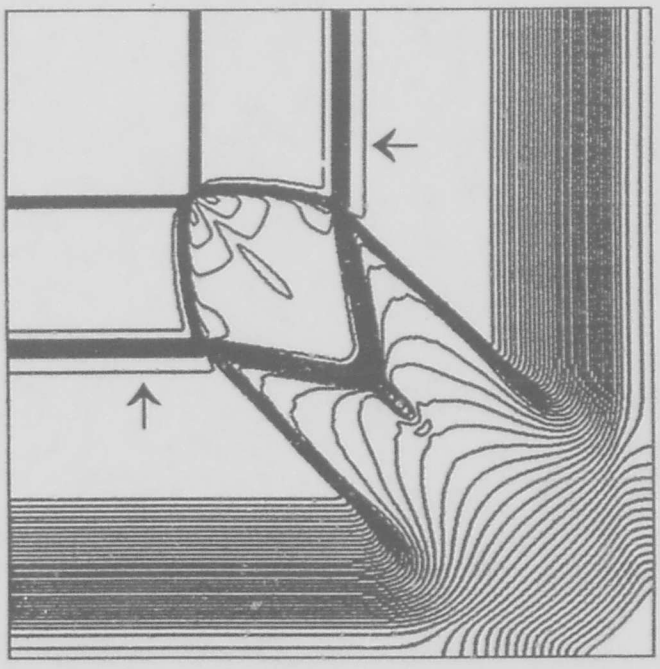

Fig. 8.4 SQR2: Contours of constant density for Aki's 'shock-box' problem at $t = 0.5625$, just after the rarefaction wave has reflected off the solid walls of the box, obtained with 'minmod' and 'superbee' compression parameters set to 0.75 and 1.25, respectively. Computations were done with a 200-cell by 200-cell grid.

those of the calculation for SQR2.

The accuracy of the code was tested by computing flows resulting from a planar shock with a Mach number of 3.72 incident from the right on a 40-degree wedge. The compression parameter of 'minmod' was set equal to 0.75, that of 'superbee' was set to 1.25, and θ was set to one. The calculation required about 27 CPU minutes.

The 500-cell by 110-cell grid grid and contours of constant density obtained by calculation 'WEDGE1' are illustrated in Figs. 8.5a and 8.5b. The upper surface of the wedge lies along the bottom edge of the grid. Hence, perpendicular reflection boundary conditions were imposed at the bottom edge. Transmission boundary conditions were imposed on the other three edges of the grid. The leftmost contour lines consist of a Mach stem (moving perpendicular to the surface of the wedge) and the remaining portion of the (vertical) incident shock that meet the reflected shock at a sharp angle. The reflected shock consists of a straight contour joined to a curved contour at a point of inflection. A second Mach stem is attached at the point of inflection and extends towards the wedge surface. A slip stream is seen to extend from the top of the first Mach stem to near the base of the second Mach stem. This particular oblique shock reflection pattern has been called double-Mach reflection by Glaz, Colella, Glass, and Deschambault (Ref. 8.14).

All flow structures are well resolved. The contours of constant density are a good match to contours computed by Glaz and Colella (Ref. 8.14), and they are in very good agreement with Deschambault's experimental data (Ref. 8.14).

Calculation 'WEDGE2', in which the compression parameter for 'minmod' is increased to one, develops supersonic flow near the surface of the wedge that deforms the base of the leading Mach stem, as shown in Fig. 8.6. The amount of deformation increases with the strength of the incident shock and the size of compression parameter or time-step. Because the deformation decreases as the values of the compression parameters are increased, it is conjectured that the deformation is a consequence of the absence of viscosity in a region that is experiencing large pressure changes due to shock reflection but which would be inside a boundary layer if the full Navier-Stokes equations were being solved. Similar behaviour has occurred for θ equal to $\frac{1}{2}$, zero, or minus one. An alternate explanation is that the 'toeing-out' of the Mach stem is due partly to the grid (that is, the nonuniformity in the widths of cells along the wedge surface), and partly due to a low Courant number based on the smallest cell size of the computational grid.

The code has been tested on its ability to solve problems on multiply-connected domains having curved boundaries. Supersonic flow resulting from the impingement from the right of a shock with a Mach number of 6 on an inlet of more or less arbitrary shape has been modelled

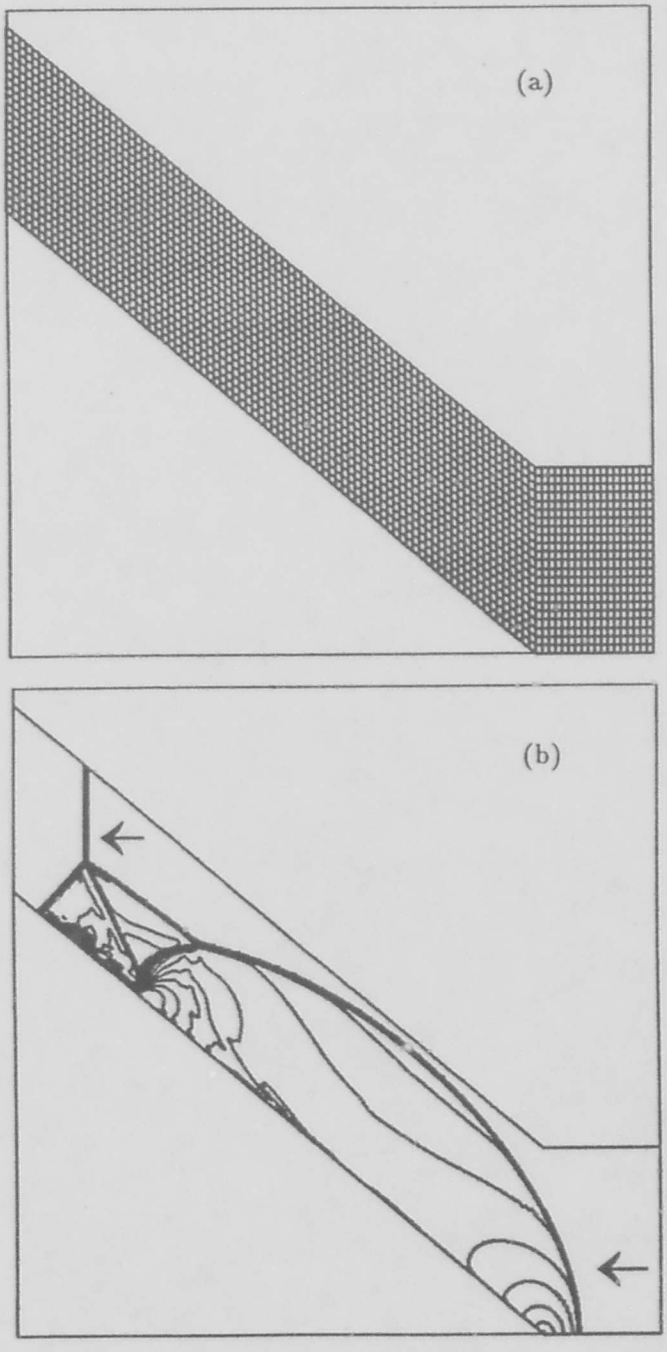

Fig. 8.5 WEDGE1: Grid for Mach-3.72 shock incident from the right on a 40 degree wedge (a) and computed contours of constant density (b), obtained with 'minmod' and 'superbee' compression parameters set to 0.75 and 1.25, respectively. Only every fifth grid line is shown to maintain clarity.

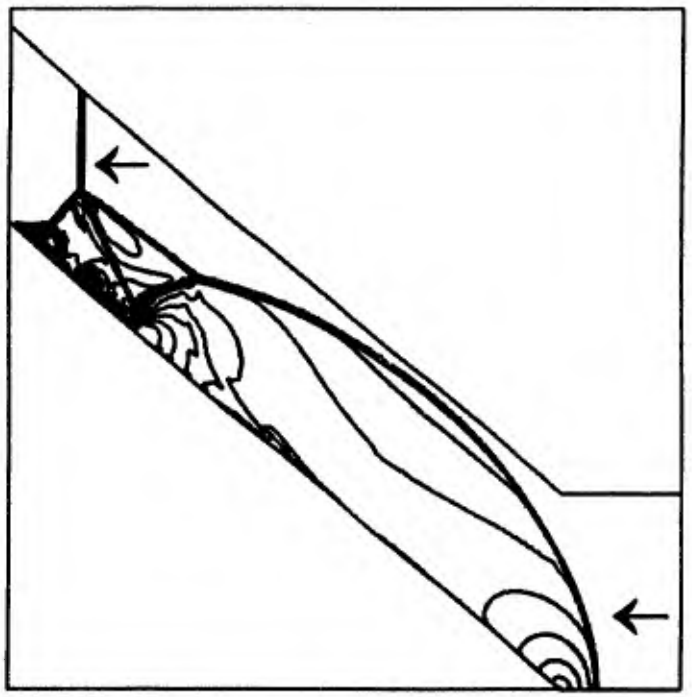

Fig. 8.6 WEDGE2: Contours of constant density for Mach-3.72 shock incident from the right on the wedge, obtained with 'minmod' compression parameter increased to 1.0.

using a 388-cell by 80-cell grid.

The grid and contours of constant density are illustrated in Figs. 8.7a and 8.7b. Planar geometry is assumed; hence, the non-gridded regions with curved outlines at the bottom and interior of the grid represent a cowl and underbody of uniform cross section in the direction perpendicular to the plane of the figures. The width of the cell columns was varied so that the cell height would be approximately equal to the cell width within the inlet. Transmission boundary conditions were imposed on the left, right, and top sides of the grid. Perpendicular reflection boundary conditions are imposed at the surfaces of the cowl and underbody. The domain was broken into four subgrids, with continuation boundary conditions imposed at the interfaces. The compression parameters for 'minmod' and 'superbee' were both set to one, and θ was set to $\frac{1}{2}$. This calculation took about 36 CPU minutes.

In Fig. 8.7b, the solution has approached a near-steady state flow. The small horizontal gap in the contouring occurs because the contours on the top 40 and bottom 40 rows of cells are computed separately and are based on density values at the centres of the cells. A bow shock remains attached to the leading edge of the underbody. A second shock remains detached from the leading edge of the cowl but merges with the bow shock to reinforce it. The incident shock passes through the inlet and the left-hand boundary, leaving shocks attached to the

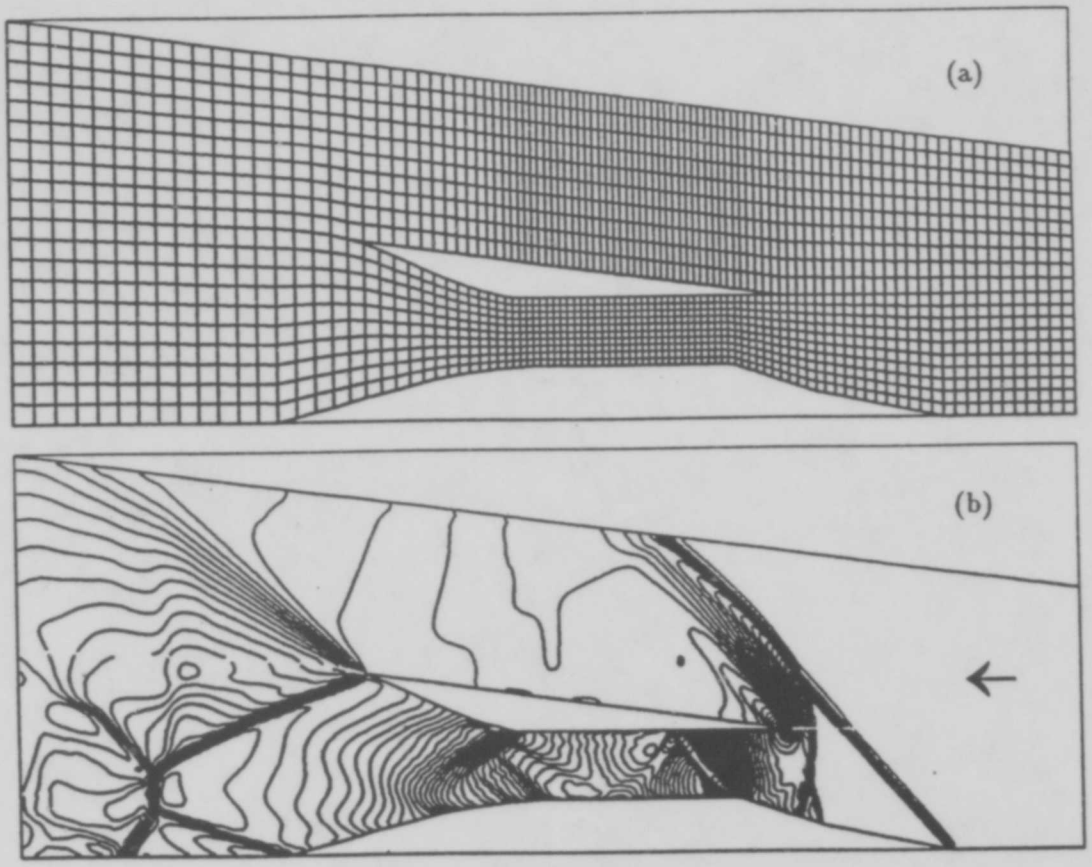

Fig. 8.7 Grid for Mach-6 shock incident from the right on an inlet (a), and contours of constant density (b), obtained with 'minmod' and 'superbee' compression parameters both set one. Only every fourth grid line is shown.

trailing edges of the inlet. The flow through the inlet undergoes compression and expansion as it proceeds towards the trailing shocks. The flow over the top of the cowl encounters a rarefaction wave attached to the cowl's trailing edge.

The code has been tested in its ability to solve flows through the inlet models placed in the hypersonic impulse tunnel located at UTIAS. Figures 8.8a–8.8d illustrate the 476-cell by 40-cell grid used to to compute the upper half of the flow field for a Prandtl-Meyer inlet and the resulting contours of constant density at $t = 1.2$, $t = 4.2$, and $t = 4.8$. The widths of the cells decrease from left to right in a linear manner. The leading edge of the inlet is four cell-columns from the left-hand side of the grid. Reflection boundary conditions are imposed along the walls of the inlet and along the bottom of the grid. Transmission boundary conditions are imposed on all other edges of the grid. The area ratio of the inlet was about 9.1 to one. The compression parameters for 'minmod' and 'superbee' were set to one and 1.15, respectively,

and θ was set to $\frac{1}{2}$. Calculation 'PM1' took about 46 CPU minutes.

At the start of the calculation the first two cell-columns in the grid contain gas flowing to the right at a Mach number of 8.4 towards the inlet in which the gas is stationary. The ratios of the temperature and density of the gas in the first two cell-columns to temperature and density of the gas in the rest of the domain are $\frac{2}{7}$ and seventy, respectively. The ratios of the gasdynamical variables are loosely based on the one-dimensional predictions of conditions in

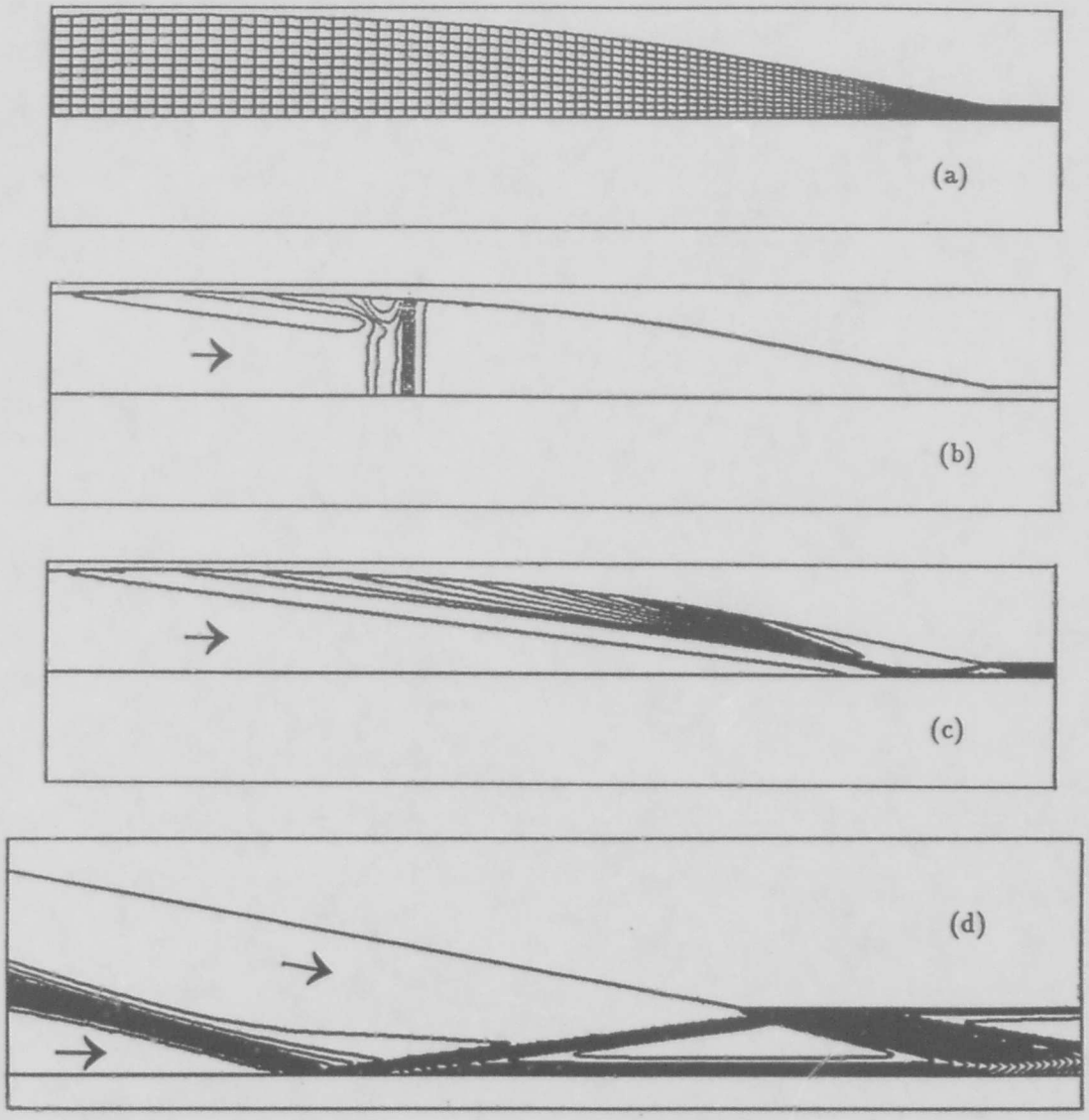

Fig. 8.8 PM1: Grid for Mach-8.4 flow from the right into a Prandtl-Meyer inlet (a), and contours of constant density at $t = 1.2$ (b), at $t = 4.2$ (c), and at $t = 4.8$ with increased resolution (d), obtained with 'minmod' and 'superbee' compression parameters set to 1.0 and 1.15, respectively. Only every fourth grid line is shown.

the test section of the impulse tunnel that were performed by Groth, Gottlieb, and Sullivan (Ref. 8.15) and are described in Section 7 of this contract report. As illustrated in Fig. 8.8b, this initial discontinuity in the flow variables separates into a right-ward moving shock wave trailed by a contact surface and an upstream-facing rarefaction wave.

The region in the vicinity of the throat of the Prandtl-Meyer inlet has been enlarged by a factor of five in Fig. 8.8d to display the time-asymptotic contours of constant density. The flow encounters a compression fan produced by the curved wall of the leading portion of the inlet and eventually reaches a region of increased constant pressure adjacent to a portion of wall that is straight. The compression characteristics coalesce into a shock which is reflected off the centre of symmetry along the bottom of the grid and strikes the wall of the inlet just downstream of the corner where the walls of the inlet become horizontal. The gas near the wall in the region of increased constant pressure encounters the corner before reaching the reflected shock and produces a rarefaction fan which crosses the reflected shock to produce an expansion in the throat of the inlet.

The Courant number increased by a factor of three during one time-step. This did not lead to visible deterioration of the solution because the size of the next time-step was reduced by a factor of three to satisfy the limitation on Courant number. However, a more sophisticated time-step strategy, still based on the size of Courant number but allowing repetition of a time-step under certain conditions, would increase the reliability of the calculation.

It is desirable to use as large an initial density ratio as is possible to match experimental conditions for which the inlet is initially at vacuum pressures. The trailing contact surface and rarefaction wave in the numerical solution decrease in strength and eventually cease to be present as the density ratio is increased. Variant density ratios result in the same steady state solution since the rarefaction wave and contact surface are eventually swept out of the domain but small density ratios do result in less realistic unsteady flows. If a density ratio of 140 is used in the numerical calculations the solution proceeds,unfortunately, only to the time $t = 2.4$ before anomolous negative densities occur. This is presumably due to a sudden increase in the Courant number.

8.7 Implicit Solution of TVD Equations

An implicit predictor-corrector method has been developed that is first-order accurate in time and requires the storage of $\dot{\underline{U}}$ (the first-order time-derivatives of $\underline{U}$) for each cell. The time

derivatives at time-level n, $\dot{\underline{U}}^n_{i,k}$, are used in the predictor equation

$$\underline{U}^{n+1(0)}_{i,k} = \underline{U}^n_{i,k} + \Delta t \dot{\underline{U}}^n_{i,k}\,, \tag{8.63}$$

to extrapolate the solution at time-level n to obtain $\underline{U}^{n+1(0)}_{i,k}$, an initial approximation to the solution at time-level $n+1$. Newton's method with simplifications is applied to a modified form of Eq. (8.46) to obtain a corrector equation. Development of the corrector equation is described in detail below.

The interface flux, $\bar{F}^n_{i+\frac{1}{2},k}$, may be be written in the alternative forms

$$\begin{aligned}\bar{F}^n_{i+\frac{1}{2},k} &= \frac{\underline{f}(\underline{U}^n_{i+1,k}) - \underline{f}(\underline{U}^n_{i,k})}{2}\hat{\Omega}_x + \frac{\underline{h}(\underline{U}^n_{i+1,k}) - \underline{h}(\underline{U}^n_{i,k})}{2}\hat{\Omega}_y - \sum_{m=1}^{4} W^m_{i+\frac{1}{2},k}\underline{R}^m_{i+\frac{1}{2},k} \\ &\quad + \underline{f}(\underline{U}^n_{i,k})[Y_{i+\frac{1}{2},k+\frac{1}{2}} - Y_{i+\frac{1}{2},k-\frac{1}{2}}] + \underline{h}(\underline{U}^n_{i,k})[X_{i+\frac{1}{2},k-\frac{1}{2}} - X_{i+\frac{1}{2},k+\frac{1}{2}}]\,.\end{aligned} \tag{8.64}$$

and

$$\begin{aligned}\bar{F}^n_{i+\frac{1}{2},k} &= -\frac{\underline{f}(\underline{U}^n_{i+1,k}) - \underline{f}(\underline{U}^n_{i,k})}{2}\hat{\Omega}_x - \frac{\underline{h}(\underline{U}^n_{i+1,k}) - \underline{h}(\underline{U}^n_{i,k})}{2}\hat{\Omega}_y - \sum_{m=1}^{4} W^m_{i+\frac{1}{2},k}\underline{R}^m_{i+\frac{1}{2},k} \\ &\quad + \underline{f}(\underline{U}^n_{i+1,k})[Y_{i+\frac{1}{2},k+\frac{1}{2}} - Y_{i+\frac{1}{2},k-\frac{1}{2}}] + \underline{h}(\underline{U}^n_{i+:,k})[X_{i+\frac{1}{2},k-\frac{1}{2}} - X_{i+\frac{1}{2},k+\frac{1}{2}}]\,.\end{aligned} \tag{8.65}$$

If $\beta_{i,k}[\bar{F}^n_{i+\frac{1}{2},k} - \bar{F}^n_{i-\frac{1}{2},k}]$ is evaluted by using Eqs. (8.64) and (8.65), the second lines in these equations result in the expression $\beta_{i,k}\underline{f}(\underline{U}^n_{i,k})\tilde{Y}_{\eta\xi} - \beta_{i,k}\underline{h}(\underline{U}^n_{i,k})\tilde{X}_{\eta\xi}$, where $\tilde{Y}_{\eta\xi}$ and $\tilde{X}_{\eta\xi}$ are approximations to $Y_{\eta\xi}$ and $X_{\eta\xi}$, evaluated by using central differences in cell i,k. In a similar manner, if $\beta_{i,k}[\bar{H}^n_{i,k+\frac{1}{2}} - \bar{H}^n_{i,k-\frac{1}{2}}]$ is evaluated by using equations analogous to Eqs. (8.64) and (8.65), the expression $-\beta_{i,k}\underline{f}(\underline{U}^n_{i,k})\tilde{Y}_{\xi\eta} + \beta_{i,k}\underline{h}(\underline{U}^n_{i,k})\tilde{X}_{\xi\eta}$ is then obtained. These two expressions cancel because the differencing method has been chosen such that $\tilde{Y}_{\xi\eta} = \tilde{Y}_{\eta\xi}$ and $\tilde{X}_{\xi\eta} = \tilde{X}_{\eta\xi}$. Therefore, for cell i,k, all terms proportional to $\underline{f}(\underline{U}^n_{i,k})$ and $\underline{h}(\underline{U}^n_{i,k})$ within the expressions for the interface fluxes $\bar{F}^n_{i+\frac{1}{2},k}$, $\bar{F}^n_{i-\frac{1}{2},k}$, $\bar{H}^n_{i,k+\frac{1}{2}}$, and $\bar{H}^n_{i,k-\frac{1}{2}}$ may be made to cancel exactly. As a consequence, the right-hand side of Eq. (8.46) can be reformulated in terms of differences of $\underline{f}$, $\underline{h}$, and $\underline{U}$ across cell interfaces.

If the differences in $\underline{f}$ and $\underline{h}$ are linearized in terms of the differences in $\underline{U}$, the homogeneous part of Eq. (8.46) (without the source term) may be approximated by

$$\underline{U}_{i,k}^{n+1} - \underline{U}_{i,k}^{n} = -\beta_{i,k} \sum_{m=1}^{4} \lambda_{i+\frac{1}{2},k}^{m-} \alpha_{i+\frac{1}{2},k}^{m} \underline{R}_{i+\frac{1}{2},k}^{m} + \lambda_{i-\frac{1}{2},k}^{m+} \alpha_{i-\frac{1}{2},k}^{m} \underline{R}_{i-\frac{1}{2},k}^{m}$$

$$-\beta_{i,k} \sum_{m=1}^{4} \lambda_{i,k+\frac{1}{2}}^{m-} \alpha_{i,k+\frac{1}{2}}^{m} \underline{R}_{i,k+\frac{1}{2}}^{m} + \lambda_{i,k-\frac{1}{2}}^{m+} \alpha_{i,k-\frac{1}{2}}^{m} \underline{R}_{i,k-\frac{1}{2}}^{m}$$

$$-\beta_{i,k} \sum_{m=1}^{4} \Phi_{i+\frac{1}{2},k}^{m} \underline{R}_{i+\frac{1}{2},k}^{m} - \Phi_{i-\frac{1}{2},k}^{m} \underline{R}_{i-\frac{1}{2},k}^{m}$$

$$-\beta_{i,k} \sum_{m=1}^{4} \Phi_{i,k+\frac{1}{2}}^{m} \underline{R}_{i,k+\frac{1}{2}}^{m} - \Phi_{i,k-\frac{1}{2}}^{m} \underline{R}_{i,k-\frac{1}{2}}^{m} , \qquad (8.66)$$

where $\Phi_{i+\frac{1}{2},k}^{m}$ is simply $-W_{i+\frac{1}{2},k}^{m}$ with the first term removed because of its incorporation in $\lambda_{i+\frac{1}{2},k}^{m-}$ used in the first row of Eq. (8.66). The quantities $\underline{R}_{i,k+\frac{1}{2}}^{m}$, $\alpha_{i,k+\frac{1}{2}}^{m}$, and $\Phi_{i,k+\frac{1}{2}}^{m}$ are computed at the upper interface of cell i,k using formulae analogous to those used for the right-hand interface. The relationship between Eq. (8.46) and Eq. (8.66) is similar to the relationship between Eq. (8.25) and Eq. (8.2) using the interface flux of Eq. (8.28).

Equation (8.66) has the disadvantage that it is not in conservative-difference form but has the advantage that it is simple to linearize for implicit calculations. The right-hand side of Eq. (8.66) is essentially a linear function of the cell-interface differences in $\underline{U}$ that are contained within the factors $\alpha_{i\pm\frac{1}{2},k}^{m}$ and $\alpha_{i,k\pm\frac{1}{2}}^{m}$; the quantities $\lambda_{i\pm\frac{1}{2},k}^{m}$, $\underline{L}_{i\pm\frac{1}{2},k}^{m}$, $\underline{R}_{i\pm\frac{1}{2},k}^{m}$, $\lambda_{i,k\pm\frac{1}{2}}^{m}$, $\underline{L}_{i,k\pm\frac{1}{2}}^{m}$, and $\underline{R}_{i,k\pm\frac{1}{2}}^{m}$ are relatively slowly changing functions of the components of $\underline{U}$.

Chakravarthy (Ref. 8.2) has derived the corrector equation

$$-[A^{+}]_{i-\frac{1}{2},k} \delta\underline{U}_{i-1,k}^{n+1(Q)} + \left(\frac{[I]}{2\beta_{i,k}} + [A^{+}]_{i-\frac{1}{2},k} - [A^{-}]_{i+\frac{1}{2},k}\right) \delta\underline{U}_{i,k}^{n+1(Q)} + [A^{-}]_{i+\frac{1}{2},k} \delta\underline{U}_{i+1,k}^{n+1(Q)}$$

$$-[A^{+}]_{i,k-\frac{1}{2}} \delta\underline{U}_{i,k-1}^{n+1(Q)} + \left(\frac{[I]}{2\beta_{i,k}} + [A^{+}]_{i,k-\frac{1}{2}} - [A^{-}]_{i,k+\frac{1}{2}}\right) \delta\underline{U}_{i,k}^{n+1(Q)} + [A^{-}]_{i,k+\frac{1}{2}} \delta\underline{U}_{i,k+1}^{n+1(Q)}$$

$$= -\frac{1}{\beta_{i,k}} \left[\underline{U}_{i,k}^{n+1(Q-1)} - \underline{U}_{i,k}^{n}\right] - \bar{S}_{i,k}^{n+1(Q-1)}$$

$$- \left[\bar{F}_{i+\frac{1}{2},k}^{n+1(Q-1)} - \bar{F}_{i-\frac{1}{2},k}^{n+1(Q-1)}\right] - \left[\bar{H}_{i,k+\frac{1}{2}}^{n+1(Q-1)} - \bar{H}_{i,k-\frac{1}{2}}^{n+1(Q-1)}\right] , \qquad (8.67)$$

where $[I]$ is a 4×4 identity matrix, $[A^{\pm}]_{i,k\mp\frac{1}{2}}$ is a 4×4 matrix giving the influence of a difference in components of $\underline{U}$ across interface $i,k\mp\frac{1}{2}$ on the value of components of $\underline{U}_{i,k}$, $\underline{U}_{i,k}^{n+1(Q)}$ is the

result of the Q^{th} correction of the solution, $\bar{F}^{n+1(Q-1)}_{i+\frac{1}{2},k}$ and $\bar{H}^{n+1(Q-1)}_{i,k+\frac{1}{2}}$ are interface fluxes computed using the previous estimate of the solution, and $\delta\underline{U}^{n+1(Q)}_{i,k} = \underline{U}^{n+1(Q)}_{i,k} - \underline{U}^{n+1(Q-1)}_{i,k}$ is the residual of the solution (departure from the previous estimate of the solution) in each cell. The left-hand side of Eq. (8.67) may be obtained by applying Newton's method to Eq. (8.66) with the last two lines discarded so as to retain only first-order accuracy and by treating the first two lines as linear functions of the cell-interface differences in $\underline{U}$. The right-hand side of Eq. (8.67) uses the right-hand side of Eq. (8.46) so as to obtain the advantages of the conservative-difference form. Equation (8.67) for all i,k is assembled into a sparse matrix system which may be solved for all $\delta\underline{U}^{n+1(Q)}_{i,k}$.

The influence matrix, $[A^{\pm}]_{i,k\mp\frac{1}{2}}$, is computed using

$$[A^{\pm}]_{i,k\mp\frac{1}{2}} = \sum_{m=1}^{4} \underline{R}^{m}_{i,k\mp\frac{1}{2}} \lambda^{m\pm}_{i,k\mp\frac{1}{2}} \underline{L}^{m}_{i,k\mp\frac{1}{2}} = [R]_{i,k\mp\frac{1}{2}} [\lambda^{\pm}]_{i,k\mp\frac{1}{2}} [L]_{i,k\mp\frac{1}{2}} , \tag{8.68}$$

where $[\lambda^{\pm}]_{i,k\mp\frac{1}{2}}$ is a diagonal matrix whose diagonal elements are $\lambda^{m\pm}_{i,k\mp\frac{1}{2}}$. It is usually convenient to evaluate $[A^{\pm}]_{i,k\mp\frac{1}{2}}$ in terms of the previous estimate of the solution, $\underline{U}^{n+1(Q-1)}$, in the appropriate cells. The matrix $[A^{\pm}]_{i\mp\frac{1}{2},k}$ is computed in an analogous manner.

An early version of the implicit algorithm which was developed for simplified problems in which one spatial dimension was suppressed by using only one column of cells and computing column-wise fluxes only, will now be described. Time-step control was closely modelled after that of the predictor-corrector method of Gear (Ref. 8.16). The predictor equation is the same as given above. The corrector consists of a block-tridiagonal equation with rows given by

$$\begin{aligned} &-[A^{+}]_{i,k-\frac{1}{2}} \delta\underline{U}^{n+1(Q)}_{i,k-1} + \left(\frac{[I]}{\beta_{i,k}} + [A^{+}]_{i,k-\frac{1}{2}} - [A^{-}]_{i,k+\frac{1}{2}} \right) \delta\underline{U}^{n+1(Q)}_{i,k} + [A^{-}]_{i,k+\frac{1}{2}} \delta\underline{U}^{n+1(Q)}_{i,k+1} \\ &= -\frac{1}{\beta_{i,k}} \left[\underline{U}^{n+1(Q-1)}_{i,k} - \underline{U}^{n}_{i,k} \right] - \left[\bar{H}^{n+1(Q-1)}_{i,k+\frac{1}{2}} - \bar{H}^{n+1(Q-1)}_{i,k-\frac{1}{2}} \right] - \bar{S}^{n+1(Q-1)}_{i,k} , \end{aligned} \tag{8.69}$$

obtained by suppressing the terms with indices $i \pm \frac{1}{2}, k$ in Eq. (8.67).

The residuals of density and total energy per unit volume are used to compute the quantity

$$\frac{3}{2N} \sum_{k=1}^{N} \left| \frac{E^{n+1(Q)}_{i,k} - E^{n+1(Q-1)}_{i,k}}{E^{n}_{i,k}} \right| + \left| \frac{\rho^{n+1(Q)}_{i,k} - \rho^{n+1(Q-1)}_{i,k}}{\rho^{n}_{i,k}} \right| , \tag{8.70}$$

which is compared to a specified tolerance (denoted TOL in what follows) as a test for convergence after each application of the corrector. The time-step size is quartered if TOL is still exceeded after a specified number of corrections (usually 3) are performed. The accumulated residuals constitute the 'correction' to the solution at each cell.

If the convergence test is passed within the specified number of applications of the corrector, the corrections to E and ρ are used to compute the error estimate,

$$EST = \frac{1}{4N} \sum_{k=1}^{N} \left| \frac{E_{i,k}^{n+1(Q)} - E_{i,k}^{n+1(0)}}{E_{i,k}^{n}} \right| + \left| \frac{\rho_{i,k}^{n+1(Q)} - \rho_{i,k}^{n+1(0)}}{\rho_{i,k}^{n}} \right| . \tag{8.71}$$

The step fails if $EST > TOL$. Regardless of success or failure of the error test, the maximum allowed size of time-step is estimated by multiplying the current size of time-step by the ratio

$$\frac{1}{1.2\left[\sqrt{\frac{EST}{TOL}} + 10^{-6}\right]} , \tag{8.72}$$

but the size of time-step is only allowed to increase on every second time-step if the ratio has exceeded 1.2 on the last ten time-steps.

On the event of a successful step the corrections are also used to update stored values of $\Delta t\dot{\underline{U}}$ for each cell. If the convergence or error tests are not passed, the step is retried with the indicated reduction of time-step size. The values of $\Delta t\dot{\underline{U}}$ are adjusted for changes in the size of time-step. The explicit algorithm is used to compute the values of $\Delta t\dot{\underline{U}}$ at the start of execution of the code and whenever the error test has failed three times in a row.

It was soon determined that larger time-steps could be achieved if certain off-diagonal coefficients of $[A^{\pm}]_{i,k\mp\frac{1}{2}}$ were set to zero so as to make the matrix equation more diagonally dominant. In a later development, inspired by the work of Yee (Ref. 8.3), $[\lambda^{\pm}]_{i,k\mp\frac{1}{2}}$ was replaced by a diagonal matrix whose diagonals were all equal to $\lambda_{i,k\mp\frac{1}{2}}^{max\pm}$ where $\lambda_{i,k\mp\frac{1}{2}}^{max}$ was chosen to be the value of λ^m at interface $i, k \mp \frac{1}{2}$ with maximum magnitude. Despite the use of the less accurate influence matrices time-step size was typically doubled because diagonal dominance was enhanced. The execution time devoted to computation of matrix coefficients was greatly reduced because $[A^{\pm}]_{i,k\mp\frac{1}{2}}$ was simplified to $\lambda_{i,k\mp\frac{1}{2}}^{max\pm}[I]$. The execution time devoted to matrix inversion was also greatly reduced because the block-tridiagonal system was replaced by four

tridiagonal systems, one for each component of $\underline{U}$.

The implicit time-stepping strategy, described above, exhibits an excellent ability to predict optimum time-step size and demonstrates a robust recovery from failure of corrector-convergence or error-size tests when applied to a number of one-dimensional problems. Owing to the fact that the left-hand side of Eq. (8.69) is only of first-order accuracy, shock waves and contact surfaces tend to be thicker for the implicit method than for the explicit method if the same values of compression parameters are used. Increasing the size of the compression parameters for implicit calculations reduces the increase in thickness and gives more satisfactory results in some cases.

Time-step size control based on the magnitude of *EST* gives good results for one-dimensional problems but is inconvenient to use in two dimensional problems because of the necessity of storing the corrections to $\underline{U}$ over the entire domain. The strategy that has been developed for two-dimensional problems is to set the implicit time-step size to the maximum allowed explicit time-step size enlarged by a problem-dependent multiplicative factor.

Direct solution of Eq. (8.67) involves the inversion of a matrix that can have a very large bandwidth. After Chakravarthy (Ref. 8.2) the off-diagonal terms in the row-wise direction are discarded. The equations are further simplified by use of $\lambda^{max\pm}$ in the influence matrices. The resultant tridiagonal-matrix equation, with rows given by

$$
\begin{aligned}
&-\lambda^{max+}_{i,k-\frac{1}{2}}\delta\underline{U}^{n+1(Q)}_{i,k-1} + \left(\frac{1}{\beta_{i,k}} + \lambda^{max+}_{i,k-\frac{1}{2}} - \lambda^{max-}_{i,k+\frac{1}{2}}\right)\delta\underline{U}^{n+1(Q)}_{i,k} + \lambda^{max-}_{i,k+\frac{1}{2}}\delta\underline{U}^{n+1(Q)}_{i,k+1} \\
&+ \left(\lambda^{max+}_{i-\frac{1}{2},k} - \lambda^{max-}_{i+\frac{1}{2},k}\right)\delta\underline{U}^{n+1(Q)}_{i,k} = -\frac{1}{\beta_{i,k}}\left[\underline{U}^{n+1(Q-1)}_{i,k} - \underline{U}^{n}_{i,k}\right] - \bar{S}^{n+1(Q-1)}_{i,k} \\
&\qquad - \left[\bar{F}^{n+1(Q-1)}_{i+\frac{1}{2},k} - \bar{F}^{n+1(Q-1)}_{i-\frac{1}{2},k}\right] - \left[\bar{H}^{n+1(Q-1)}_{i,k+\frac{1}{2}} - \bar{H}^{n+1(Q-1)}_{i,k-\frac{1}{2}}\right], \qquad (8.73)
\end{aligned}
$$

is solved cell-column by cell-column to provide quick relaxation of the residuals along the column-wise direction. Note that the coefficients of $\delta\underline{U}^{n+1(Q)}_{i,k}$ are all positive and exceed the sum of the coefficients of the off-diagonal residuals so that the system of equations is diagonally dominant. The tridiagonal matrices associated with each of the components of $\underline{U}$ are identical if reflection or transmission boundary conditions at the top or bottom of the cell-column are handled appropriately. Relaxation of the residuals along the row-wise direction is induced by application of the corrector in left to right sweeps across the domain as described below.

At the start of each time-step the solution over the entire domain is predicted using Eq.(8.63). The tridiagonal corrector equation is then applied once within each cell-column in a preliminary sweep through the entire domain. On subsequent sweeps the corrector is only applied within cell-columns that are adjacent to a continuation boundary, that failed the convergence test on a previous sweep, or that are within a margin of eight columns of a cell-column which failed the convergence test. Sweeping is discontinued when all cell-columns have passed the convergence test. The number of sweeps required is typically less than ten.

Attempts to allow use of more than one application of the corrector in each cell-column during a sweep increase the number of sweeps to more than 25 before all cell-columns pass the convergence test on the first application of the corrector. Use of only one application of the corrector in each cell-column gives a more nearly equal propagation of information in the column-wise and row-wise directions.

8.8 Results of Implicit TVD Calculations

The thickness of a moving shock-wave is doubled if calculation PM1 is repeated with implicit time-stepping; despite this, the implicit and explicit calculations converge to the same steady-state solution. A larger initial density ratio may be used than in the explicit calculations. Figures 8.9a and 8.9b display contours of constant density at $t = 1.2$ and $t = 4.2$, respectively,

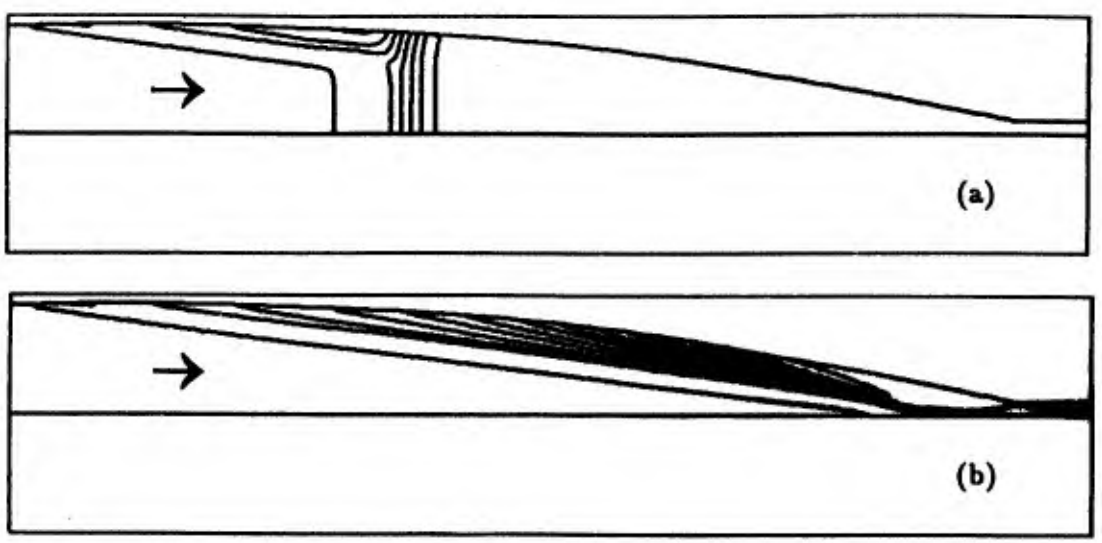

Fig. 8.9 PM2: Contours of constant density for Mach-8.4 flow from the right into the Prandtl-Meyer inlet at $t = 1.2$ (a) and at $t = 4.2$ (b), obtained using implicit time-stepping with 'minmod' and 'superbee' compression parameters set to 1.0 and 1.15, respectively.

obtained by repeating calculation PM1 with an initial density ratio of 140 and with the compression parameters for 'minmod' and 'superbee' set to one and 1.25, respectively. As shown in Fig. 8.9a, the strengths of the trailing contact surface and rarefaction wave are considerably reduced. Execution time was only increased by fifteen per cent because multiple application of the corrector was only required in the vicinity of the moving waves and because the specified limit on size of Courant number was 43 per cent larger than in the explicit calculation.

Figure 8.10 illustrates the 500-cell by 48-cell grid for a spike inlet with the same area ratio as was used for the Prandtl-Meyer inlet. The bottom of the grid conforms to the shape of the cylindrically symmetrical spike whose point is located four cell-columns from the left-hand side of the grid. There is a narrow slit in the right-hand side of the grid to accommodate a cowl. Reflection boundary condition are imposed along the bottom of the grid and on the surface of the cowl. Transmission boundary conditions are imposed on all other edges of the grid. The domain is broken up into three subgrids, with continuation boundary conditions imposed at the interfaces. The widths of the cells decrease from left to right in a linear manner and linear stretching of the cell heights was applied in the upper 24 rows of cells. The same initial ratios of gasdynamical variables were used as in calculation PM1. The compression parameters for 'minmod' and 'superbee' were set to 0.75 and one, respectively, and θ was set to one. The implicit calculation took about 88 CPU minutes.

Contours of constant density at $t = 1.2$ and at $t = 4.8$ and contours of constant pressure in the vicinity of the cowl with five times the resolution at $t = 4.8$ are shown in Figs. 8.11a–8.11c. Gas flowing at a Mach number of 8.4 approaches the inlet from the left and is compressed by

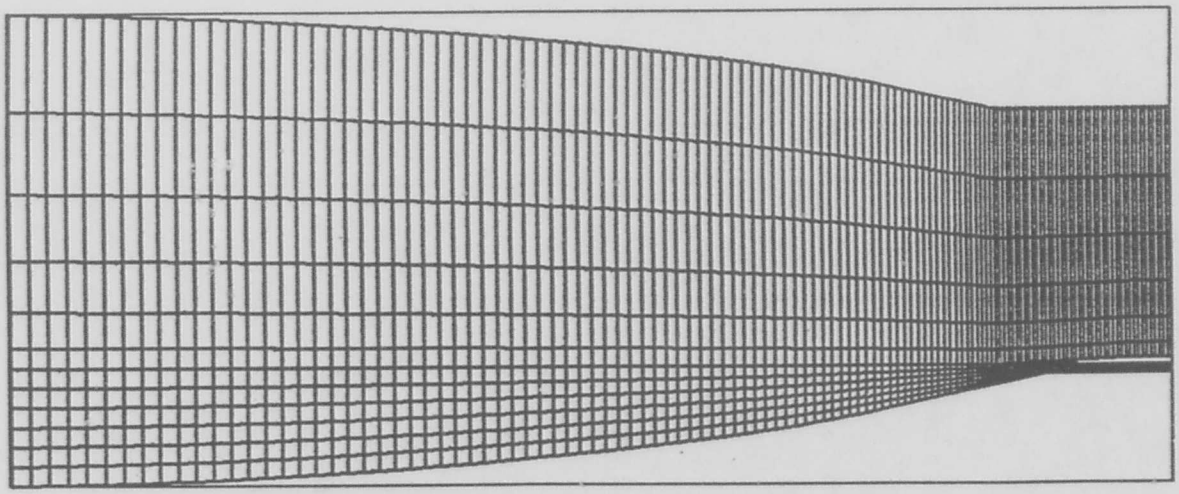

Fig. 8.10 Grid for Mach-8.4 flow from right into a spike inlet. Only every fourth grid line is shown.

the spike before entry into the annular space between the spike and cowl. The flow encounters a compression fan produced by the curved surface of the spike and eventually reaches a region of increased constant pressure near the (conical) base of the spike. The point of focus of the compression fan is not clearly illustrated in Fig. 8.11c because the pressure contours in the top 24 and bottom 24 cell-rows are computed separately, leaving a gap in the contour lines.

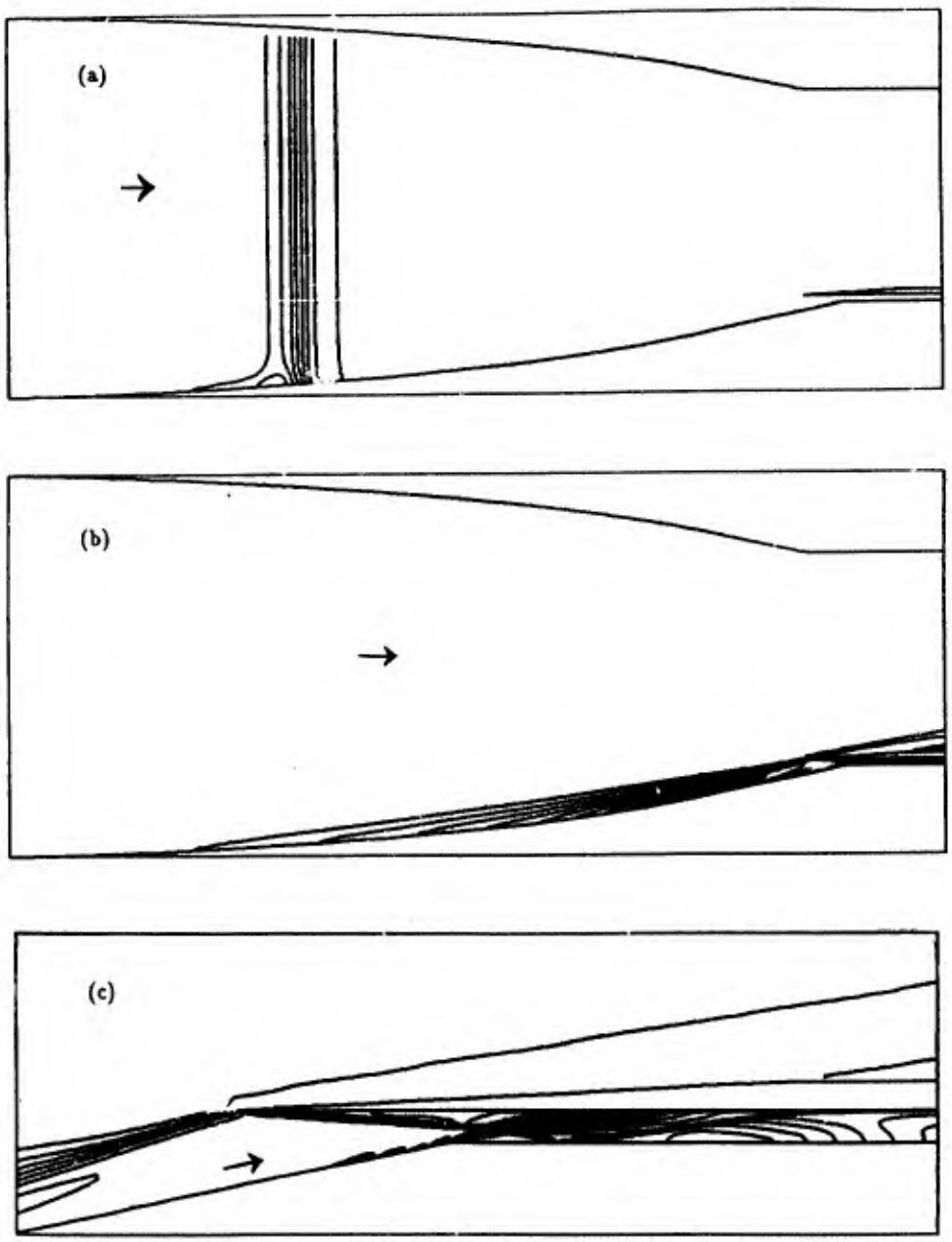

Fig. 8.11 Contours of constant density at $t = 1.2$ (a), at $t = 4.8$ (b), and at $t = 4.8$ with increased resolution (c), for Mach-8.4 flow from right into a spike inlet obtained using implicit time-stepping with 'minmod' and 'superbee' compression parameters set to 0.75 and one, respectively.

However, the fact that there are only two contour lines over the top of the cowl indicates that there is little spillage of the flow. The compression fan reflects off the underside of the leading edge of the cowl as a shock. The shock crosses the expansion fan produced by flow about the corner at the base of the spike and is reflected back towards the cowl at a position downstream of the corner. The separate structures of the expansion fan and shock wave downstream of their point of intersection were not resolved in a plot of the contours of constant density.

Attempts to use a larger initial density ratio have failed thus far owing to the evolution of negative densities. If explicit time-stepping is employed, the solution only proceeds to $t = 2.4$ before the calculation fails owing to the evolution of negative densities.

8.9 TVD Explicit MacCormack Based Method

An alternate form of explicit TVD code, based on the work of Yee (Ref. 8.3), has been developed in which the method of MacCormack is applied as the first half of a time-step. The two-stage MacCormack algorithm may be expressed as

$$\underline{\check{U}}^n_{i,k} = \underline{U}^n_{i,k} - \beta_{i,k}\Delta F(\underline{U}^n)_{i-\frac{1}{2},k} - \beta_{i,k}\Delta \bar{H}(\underline{U}^n)_{i,k+\frac{1}{2}} - \beta_{i,k}\bar{S}(\underline{U}^n)_{i,k} \tag{8.74}$$

followed by

$$\underline{\bar{U}}^{n+1}_{i,k} = \underline{U}^n_{i,k} + \frac{1}{2}\left[\underline{\check{U}}^n_{i,k} - \underline{U}^n_{i,k} - \beta_{i,k}\Delta \bar{F}(\underline{\check{U}}^n)_{i+\frac{1}{2},k} - \beta_{i,k}\Delta H(\underline{\check{U}}^n)_{i,k-\frac{1}{2}}\right] - \beta_{i,k}S(\underline{\check{U}}^n)_{i,k}. \tag{8.75}$$

In these expressions,

$$\Delta \bar{H}(\underline{\check{U}}^n)_{i,k-\frac{1}{2}} = \left[\underline{f}(\underline{\check{U}}^n_{i,k}) - \underline{f}(\underline{\check{U}}^n_{i,k-1})\right]\hat{\Omega}_x + \left[\underline{h}(\underline{\check{U}}^n_{i,k}) - \underline{h}(\underline{\check{U}}^n_{i,k-1})\right]\hat{\Omega}_y \tag{8.76}$$

is the flux difference across interface $i, k-\frac{1}{2}$ where $\hat{\Omega}_x$ and $\hat{\Omega}_y$ are η_x/J and η_y/J, respectively, evaluated at interface $i, k-\frac{1}{2}$. The flux-differences $\Delta \bar{F}(\underline{\check{U}}^n)_{i+\frac{1}{2},k}$, $\Delta \bar{H}(\underline{U}^n)_{i,k+\frac{1}{2}}$, and $\Delta \bar{F}(\underline{U}^n)_{i-\frac{1}{2},k}$ are computed using similar formulae. The resulting solution is spatially and temporally of second-order accuracy if the grid is uniform. The MacCormack equations can be applied cell-column by cell-column from left to right across the domain in one sweep if $\underline{\check{U}}^n_{i,k-1}$, the value of the intermediate solution in cell $i, k-1$ in the previous cell-column, is retained for use in computing the second-stage fluxes into cell i, k.

The post-processor

$$\underline{U}_{i,k}^{n+1} = \underline{\tilde{U}}_{i,k}^{n} - \beta_{i,k} \sum_{m=1}^{4} \tilde{\Phi}_{i+\frac{1}{2},k}^{m} \underline{\tilde{R}}_{i+\frac{1}{2},k}^{m} - \tilde{\Phi}_{i-\frac{1}{2},k}^{m} \underline{\tilde{R}}_{i-\frac{1}{2},k}^{m}$$

$$- \beta_{i,k} \sum_{m=1}^{4} \tilde{\Phi}_{i,k+\frac{1}{2}}^{m} \underline{\tilde{R}}_{i,k+\frac{1}{2}}^{m} - \tilde{\Phi}_{i,k-\frac{1}{2}}^{m} \underline{\tilde{R}}_{i,k-\frac{1}{2}}^{m} , \tag{8.77}$$

is then applied to obtain a TVD solution. Here

$$\tilde{\Phi}_{i+\frac{1}{2},k}^{m} = \frac{|\tilde{\lambda}_{i+\frac{1}{2},k}^{m}| - \beta_{i+\frac{1}{2},k}(\tilde{\lambda}_{i+\frac{1}{2},k}^{m})^2}{2} \left[\tilde{Q}_{i+\frac{1}{2},k}^{m} - \tilde{\alpha}_{i+\frac{1}{2},k}^{m} \right], \tag{8.78}$$

where $\beta_{i+\frac{1}{2},k} = [\beta_{i+1,k} + \beta_{i,k}]/2$ and $\tilde{Q}_{i+\frac{1}{2},k}^{m}$ is a limiter term which for m equal to 1 or 4 is given by

$$\tilde{Q}_{i+\frac{1}{2},k}^{m} = - \tilde{\sigma}_{i+\frac{1}{2},k}^{m-} \left(\frac{1-\theta}{4} \text{minmod}(\tilde{\alpha}_{i+\frac{3}{2},k}^{'m}, \omega \tilde{\alpha}_{i+\frac{1}{2},k}^{m}) + \frac{1+\theta}{4} \text{minmod}(\omega \tilde{\alpha}_{i+\frac{3}{2},k}^{'m}, \tilde{\alpha}_{i+\frac{1}{2},k}^{m}) \right)$$

$$+ \tilde{\sigma}_{i+\frac{1}{2},k}^{m+} \left(\frac{1+\theta}{4} \text{minmod}(\tilde{\alpha}_{i+\frac{1}{2},k}^{m}, \omega \tilde{\alpha}_{i-\frac{1}{2},k}^{'m}) + \frac{1-\theta}{4} \text{minmod}(\omega \tilde{\alpha}_{i+\frac{1}{2},k}^{m}, \tilde{\alpha}_{i-\frac{1}{2},k}^{'m}) \right) \tag{8.79}$$

and for m equal to 2 or 3 is given by

$$\tilde{Q}_{i+\frac{1}{2},k}^{m} = - \frac{\tilde{\sigma}_{i+\frac{1}{2},k}^{m-}}{2} \text{superbee}(\tilde{\alpha}_{i+\frac{3}{2},k}^{'m}, \tilde{\alpha}_{i+\frac{1}{2},k}^{m}) + \frac{\tilde{\sigma}_{i+\frac{1}{2},k}^{m+}}{2} \text{superbee}(\tilde{\alpha}_{i+\frac{1}{2},k}^{m}, \tilde{\alpha}_{i-\frac{1}{2},k}^{'m}) . \tag{8.80}$$

Note that the quantity $\beta_{i+\frac{1}{2},k}(\tilde{\lambda}_{i+\frac{1}{2},k}^{m})^2$ is computed before the sonic correction is applied to $\tilde{\lambda}_{i+\frac{1}{2},k}^{m}$ since the post-processor must replace the Lax-Wendroff-like interface-flux of the MacCormack method with first-order upwind differences in regions of rapid change in the solution. $\tilde{\Phi}_{i,k+\frac{1}{2}}^{m}$ is calculated in a similar manner.

Owing to the action of the post-processor, there is little need to alternate between backward and forward flux differences in Eqs. (8.74) and (8.75) from time-step to time-step as would be required if the MacCormack method was used by itself. However, such alternation is left as an option in the code for the column-wise flux differences, $\Delta \tilde{H}_{i,k\pm\frac{1}{2}}$.

8.10 Results of Explicit TVD-MacCormack Calculations

Figures 8.12a and 8.12b illustrate the results of repeating the calculation for shock-tube problem ST1 with identical parameters but using the TVD-MacCormack scheme. The density transitions are slightly thicker and there is a small bump at the top of the shocks. Note the absence of the previous bumps in the reflected rarefaction wave. The positions of the various

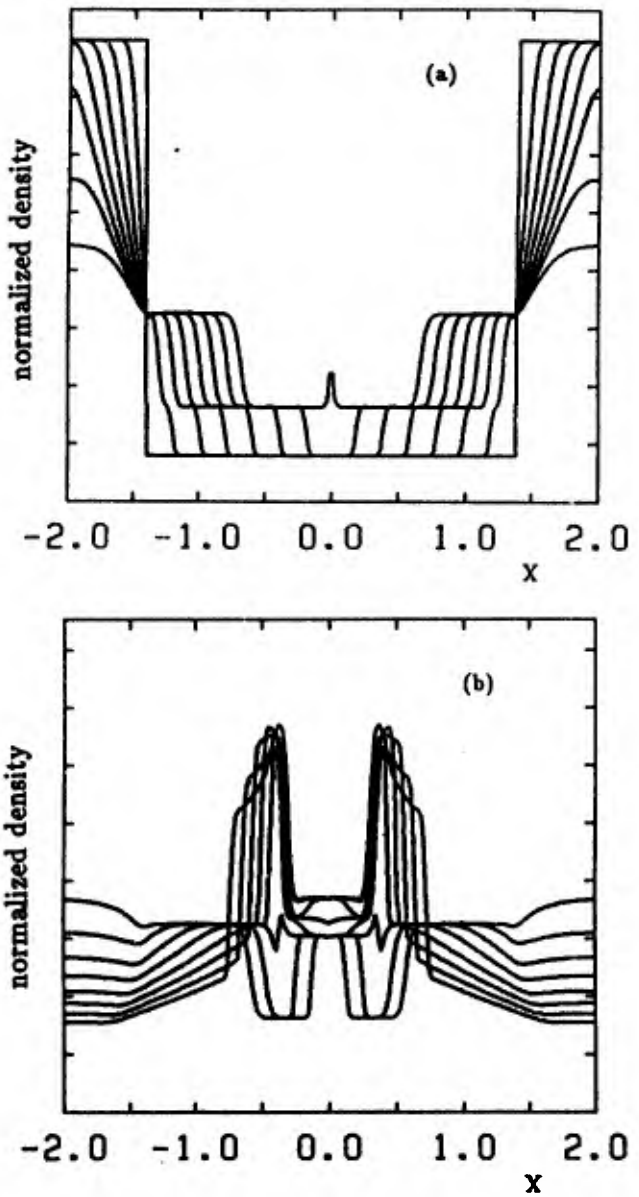

Fig. 8.12 ST2: Density profiles from $t = 0$ to $t = 0.875$ (a) and from $t = 1$ to $t = 1.875$ (b) for the one-dimensional shock-tube problem, using the TVD-MacCormack scheme with 'minmod' and 'superbee' compression parameters set to 1.00 and 1.25, respectively. Approximate time intervals between profiles is $\Delta t = 0.125$. Calculations were performed on a 200-cell grid.

wave fronts corresponds to those obtained in calculation ST1 but there is a small difference in some of the wave forms.

Calculation SQ2 for the shock-box of Aki was repeated using the TVD-MacCormack scheme. As shown in Fig. 8.13, the density transitions resulting from calculation SQR3 are only slightly thicker than those from calculation SQR2. Execution time was increased by about 14 per cent, despite the use of an identical number of time-steps, because of the two-stage nature of the MacCormack scheme.

The WEDGE1 calculation for the case of the double-Mach oblique-reflection problem has also been repeated by using the TVD-MacCormack scheme. As shown in Fig. 8.14 there is a reasonably good correspondence in the previously computed and these contours of constant density, except near the base of the leading Mach stem where the 'toe-out' deformation is again evident.

Execution time was increased by about 26 per cent partly because of the two-stage nature of the MacCormack scheme and partly because of a slight increase in the number of time-steps. Experimentation with the sizes of the compression parameters or time-step would reduce the

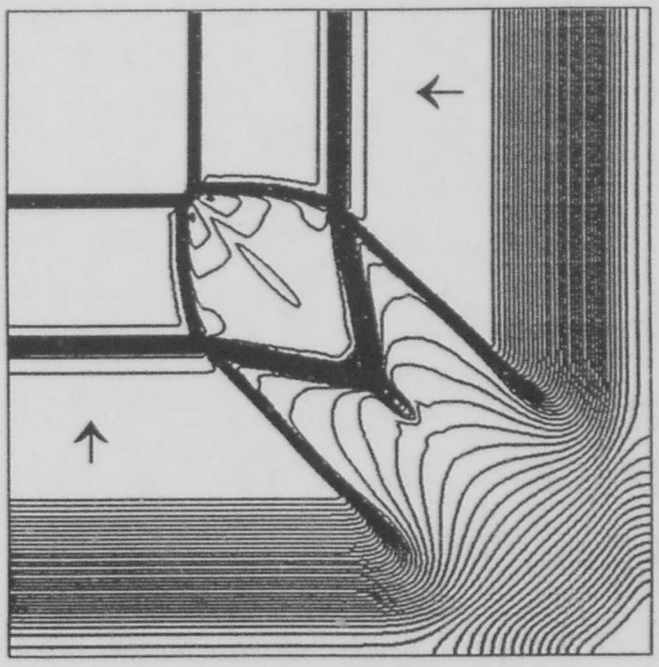

Fig. 8.13 SQR3: Contours of constant density for the 'shock-box' problem at $t = 0.5625$, just after the rarefaction wave has reflected off the solid walls of the box, obtained with 'minmod' and 'superbee' compression parameters set to 0.75 and 1.25, respectively. Computations were done with a 200-cell by 200-cell grid using the explicit TVD-MacCormack scheme.

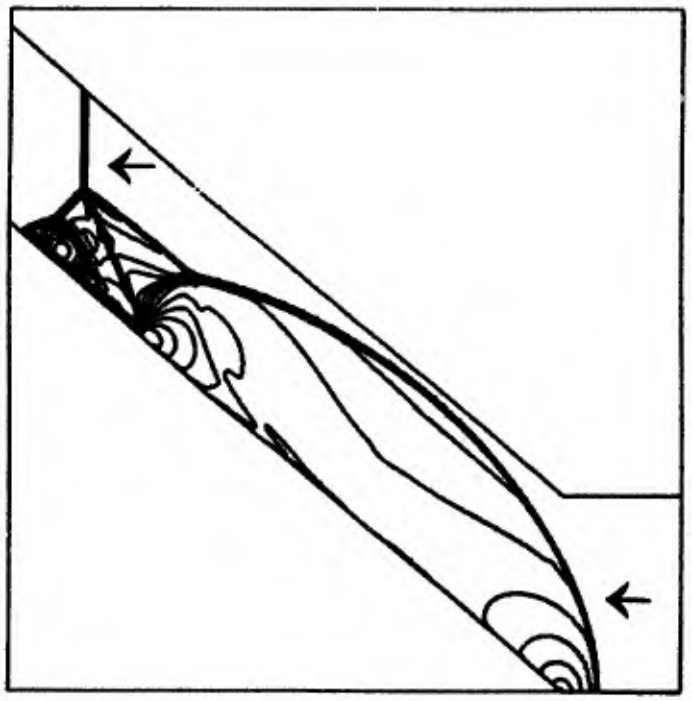

Fig. 8.14 SQR3: Contours of constant density for the 'shock-box' problem at time $t = 0.5625$, just after the rarefaction wave has reflected off the solid walls of the box, obtained with 'minmod' and 'superbee' compression parameters set to 0.75 and 1.25, respectively. Computations were done with a 200-cell by 200-cell grid using the explicit TVD-MacCormack scheme.

deformation but not the execution time. Figures 8.15a–8.15c illustrate the 424-cell by 40-cell grid and the contours of constant density at $t = 1.2$ and $t = 4.2$, for the Prandtl-Meyer inlet obtained by using the TVD-MacCormack scheme with the compression parameters for 'minmod' and 'superbee' both set one and with θ set to $\frac{1}{2}$. The contours of constant density at $t = 4.2$ obtained by calculation PM3 are in reasonable agreement with those obtained by calculation PM1 even though a different grid was used. At $t = 1.2$ the trailing rarefaction wave and contact surface are weaker than in calculation PM1 (the same strength as in calculation PM2) because it was possible to use a density ratio of 140 without encountering numerical difficulties.

8.11 Conclusions

The quality of the calculations is sensitive to the time-step size, the method of flux limiting, and the value of compression parameter. Nonetheless, with a little attention to selection of parameters, it is currently possible to obtain excellent results with the TVD code on domains of complex configuration using explicit time-stepping. Some improvement could be made in

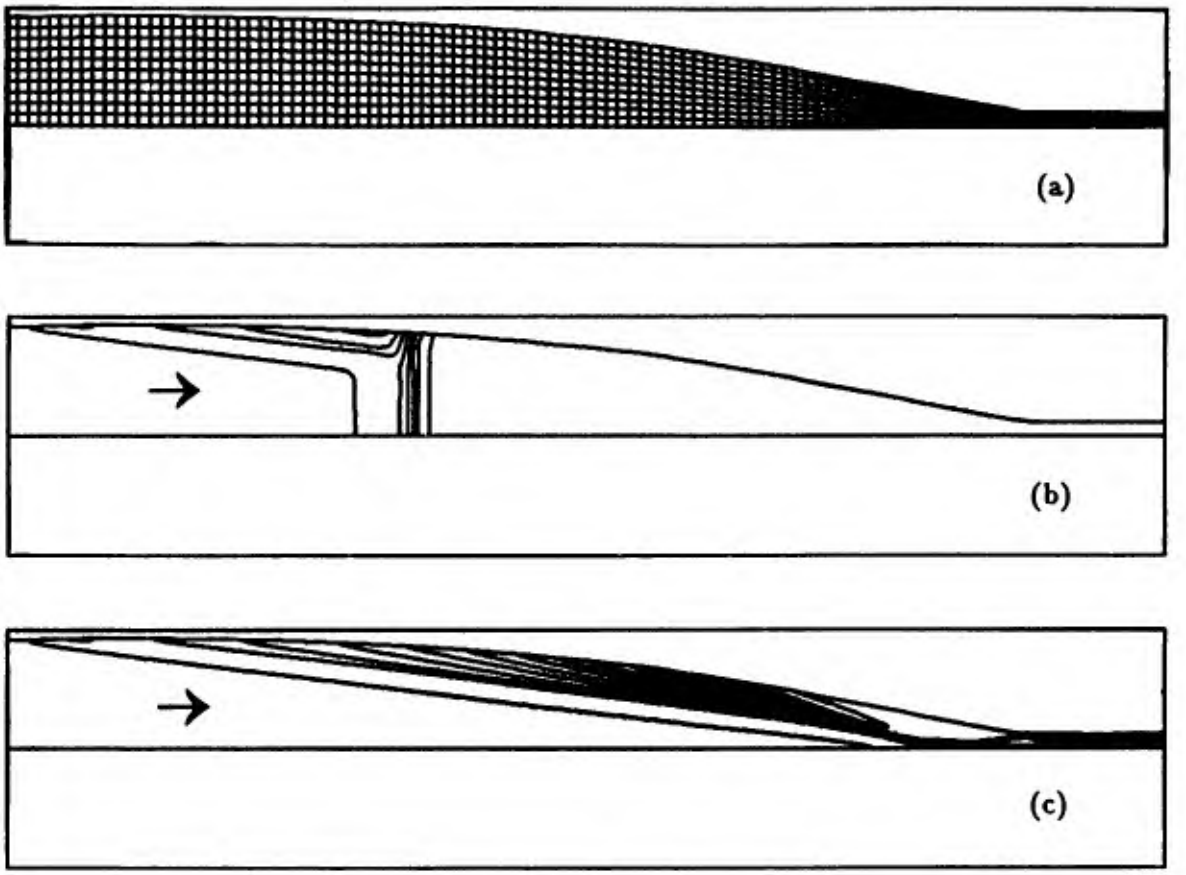

Fig. 8.15 PM3: Grid for Mach-8.4 flow from the right side into the Prandtl-Meyer inlet (a), and contours of constant density at $t = 1.2$ (b), at $t = 4.2$ (c), obtained using the explicit TVD-MacCormack scheme with 'minmod' and 'superbee' compression parameters both set to unity. Only every fourth grid line is shown.

the strategy for selection of size of time-step based on Courant number.

Owing to the use of selective solution predictor-corrector procedures, the execution times for inviscid two-dimensional problems using implicit time-stepping are only slightly greater than the execution times required for explicit time-steps. Both implicit and explicit time-stepping converge to the same steady-state solution. The relative efficiency of implicit time-stepping would be much greater for viscid flows. In some cases an implicit calculation will run to completion for conditions that cause the failure of an explicit calculation.

The TVD-MacCormack code requires greater execution times than the originally implemented explicit method and has not yet given better quality solutions in most cases. It may prove to have increased value if converted to use implicit time-stepping.

As it stands now, the present TVD code in its various versions forms an excellent basis for extension to the solution of viscid flows through domains of complex configuration using

the real gas-equation of state. Extension to the use of three-dimensional domains is straightforward although computationally expensive.

8.12 References

8.1 Roe, P.L., "Approximate Riemann Solvers, Parameter Vectors, and Difference Schemes", Journal of Computational Physics, Vol. 43, pp. 357–372, 1981.

8.2 Chakravarthy, S.R., "Development of Upwind Schemes for the Euler Equations", NASA Contractor Report 4043, 1987.

8.3 Yee, H.C., "Upwind and Symmetric Shock-Capturing Schemes", NASA Technical Memorandum 89464, May 1987.

8.4 Hawken, D.F., and Gottlieb, J.J., "Numerical Solution of Two-Dimensional Time-Dependent Gasdynamic Flows for Hypersonic Studies", Proceedings of the Supercomputing Symposium '89, pp. 475–492, Toronto, Canada, June 19–21, 1989.

8.5 Hawken, D.F., and Gottlieb, J.J., "Prediction of Two-Dimensional Time-Dependent Gasdynamic flows for Hypersonic Studies", University of Toronto Institute for Aerospace Studies Rept. No. 335, March 1990.

8.6 Anderson, D.A., Tannehill, J.C., and Pletcher, R.H., "Computational Fluid Mechanics and Heat Transfer", McGraw-Hill, New York, 1984.

8.7 MacCormack, R.W., "The Effect of Viscosity in Hypervelocity Impact Cratering", AIAA Paper No. 69–354, 1969.

8.8 Lax, P.D., and Wendroff, B., "Systems of Conservation Laws", Communications in Pure and Applied Mathematics, Vol. 13, pp. 217–237, 1960.

8.9 Harten, A., Hyman, J.M., and Lax, P.D., "On Finite-Difference Approximations and Entropy Conditions for Shocks", Communications in Pure and Applied Mathematics, Vol. 29, pp. 297–322, 1976.

8.10 Kamowitz, D., "Some Observations of Boundary Conditions for Numerical Conservation Laws", ICASE Report No. 88–67, 1988.

8.11 Sweby, P.K., "High Resolution Schemes Using Flux Limiters for Hyperbolic Conservation Laws", SIAM Journal on Numerical Analysis, Vol. 21, pp. 995–1011, 1984.

8.12 Roe, P.L., and Pike. J., "Efficient Construction and Utilisation of Approximate Riemann Solutions", Computing Methods in Applied Science and Engineering VI, Edited by R. Glowinski and J.L. Lions, North-Holland, Amsterdam, pp. 499–518, 1984.

8.13 Thomas, P.D., and Lombard, C.K., "Geometric Conservation Law and its Application to Flow Computations on Moving Grids", AIAA Journal, Vol. 17, pp. 1030–1037, 1979.

8.14 Glaz, H.M., Colella, P., Glass, I.I., and Deschambault, R.L., "A Detailed Numerical, Graphical, and Experimental Study of Oblique Shock Wave Reflections", University of Toronto Institute for Aerospace Studies Rept. No. 285, August 1986.

8.15 Groth, C.P.T., Gottlieb, J.J., and Sullivan, P.A., "Numerical Investigation of High-Temperature Effects in the UTIAS-RPI Hypersonic Impulse Tunnel", accepted for publication in Canadian Journal of Physics, April 1991.

8.16 Gear, C.W., "Numerical Initial Value Problems in Ordinary Differential Equations", Prentice Hall, New Jersey, 1971.

9.0 Dynamic Finite Element Analysis and Optimization of a Hypersonic Gun Tunnel Piston

S. C. Weston and R. J. Rogers

9.1 Introduction

Recent plans to develop aircraft and air breathing missiles capable of flying at very high Mach numbers and altitudes have renewed interest in hypersonic fluid mechanics. Experiments with high enthalpy and high Mach number fluid flows have required the development of hypersonic test facilities, such as the hypersonic gun tunnel described in this report. A hypersonic gun tunnel is a very short duration blow-down wind tunnel which generates high Mach number flows by driving a piston down a barrel to compress and heat the working fluid. A piston made from 7075-T6 aluminum alloy acts like a bullet in a gun's barrel being shot down the tunnel using compressed air from a driver. As the piston reaches the barrel end it rapidly compresses and heats the air in front of it and shock waves are generated. The heated air flows through a hypersonic convergent-divergent nozzle into the test section to create the desired flow conditions.

The main components of the tunnel are described in Section 2. The piston experiences dynamic loads on both front and rear faces requiring high strength in both the accelerating and decelerating stages of its motion. Weight must be kept as low as possible to allow for high Mach numbers and reduced inertial forces. Upon firing the pressure on the piston's rear face is a step load with an estimated 0.5 ms rise time. The next significant pressure loading is on the front face when the piston is approaching the barrel end. The reflecting shock waves return pressure to the piston's face from the barrel end, referred to as the Barrel End Pressure (BEP). Initially frequent piston failures were experienced after a few firings. The piston being used was the original cup-shaped design from 1965 which was developed by trial and error. It had a diameter of 76.2 mm (3.0 in.) and a 30.48 mm (1.2 in.) skirt, with two rows of holes for weight reduction. A modification to this design was implemented by decreasing the leading edge holes from 11.11 mm (7/16 in.) to 9.53 mm (3/8 in.) diameter; see figure 9.1. Except at the highest ratio of driver to barrel pressure currently used, this modified piston design has worked satisfactorily.

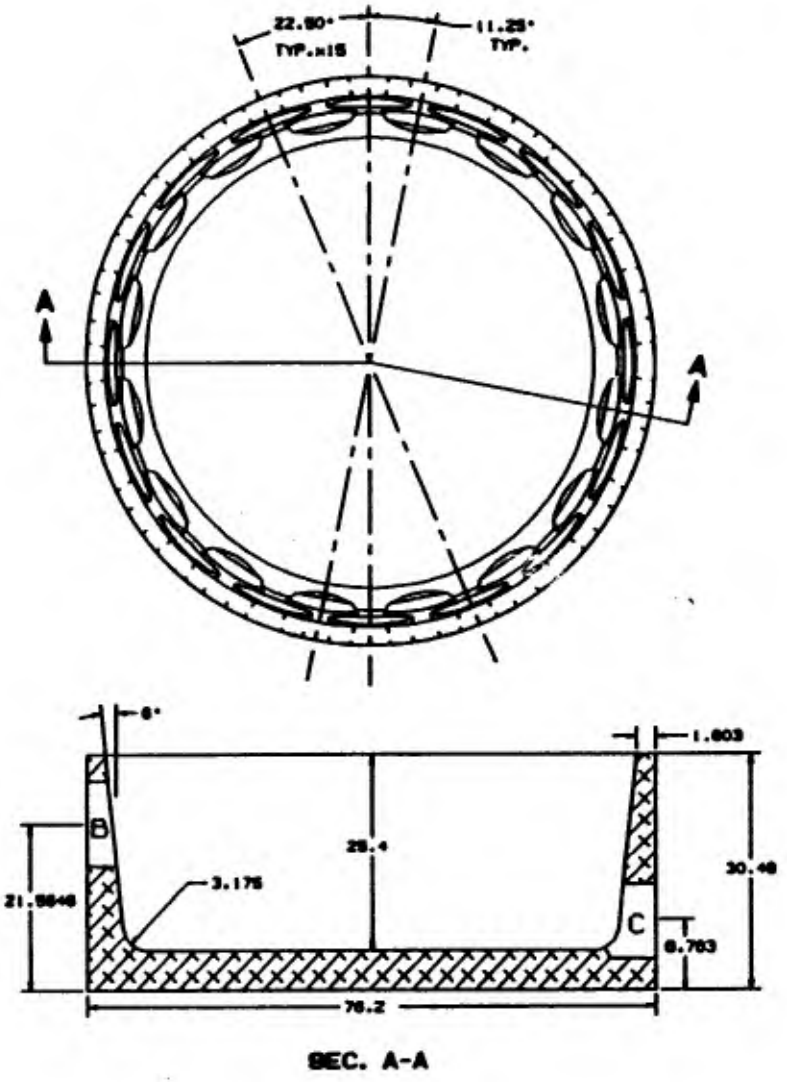

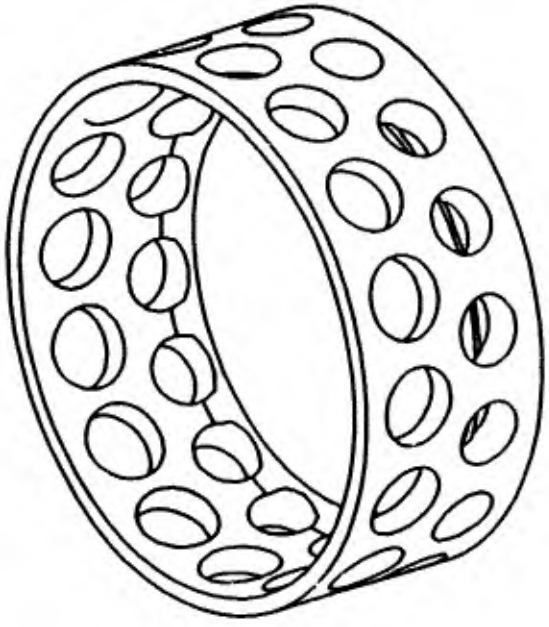

Figure 9.1 Modified piston design.

9.2 Application of Dynamic Finite Element Analysis

An analysis and redesign of the piston using finite element analysis (FEA) was undertaken using the ANSYS code (Ref. 9.1). The analysis uses the modified piston as a design that succeeds in order to determine the peak stresses and their locations. Using these stresses a redesign is performed to decrease the weight of the piston while providing the equivalent strength. A 1/32 sector of the piston is used as the smallest domain for the FEA. Figure 9.2 shows the FE mesh used. A dynamic analysis is necessary in order to calculate the stresses resulting from the pressure which accelerates and decelerates the piston.

Two types of linear analysis could be performed to simulate the loads on the piston, namely mode superposition and direct integration. Mode superposition is a linear method which first extracts the eigenvalues and eigenvectors of modes in a specified frequency range and then uses these modes to calculate the stresses from the dynamic load. Direct integration directly solves the simultaneous equations representing the model in order to determine the stresses for linear or nonlinear materials. Direct integration is generally slower than mode superposition because it solves equations representing all natural frequencies available from the number of degrees of freedom (DOF) in the FE model. Mode superposition is used for this project as the primary solver since only a few modes are used, making the calculation time shorter. The eigenvalue analysis uses a reduced type solution which extracted all available modes for a reduced number of degrees of freedom which are user defined Master DOF (MDOF).

The three main steps in the analysis are: the eigenvalue analysis, which obtains the natural frequencies and the reduced mode shapes in terms of MDOF's; the displacement pass, to acquire the reduced displacement solution; and the stress pass which transforms the reduced displacement solution into a stress solution at all DOF's (Ref. 9.1). The mode superposition method utilizes the Newmark time integration scheme which solves the equations of motion for transient dynamic analysis (Ref. 9.1). Ten time steps are used for the highest mode included in the analysis. A convergence study was done in order to determine the number of flexible modes required to provide sufficient accuracy in the stress analysis. The transient analysis also requires the rigid body mode of a free piston.

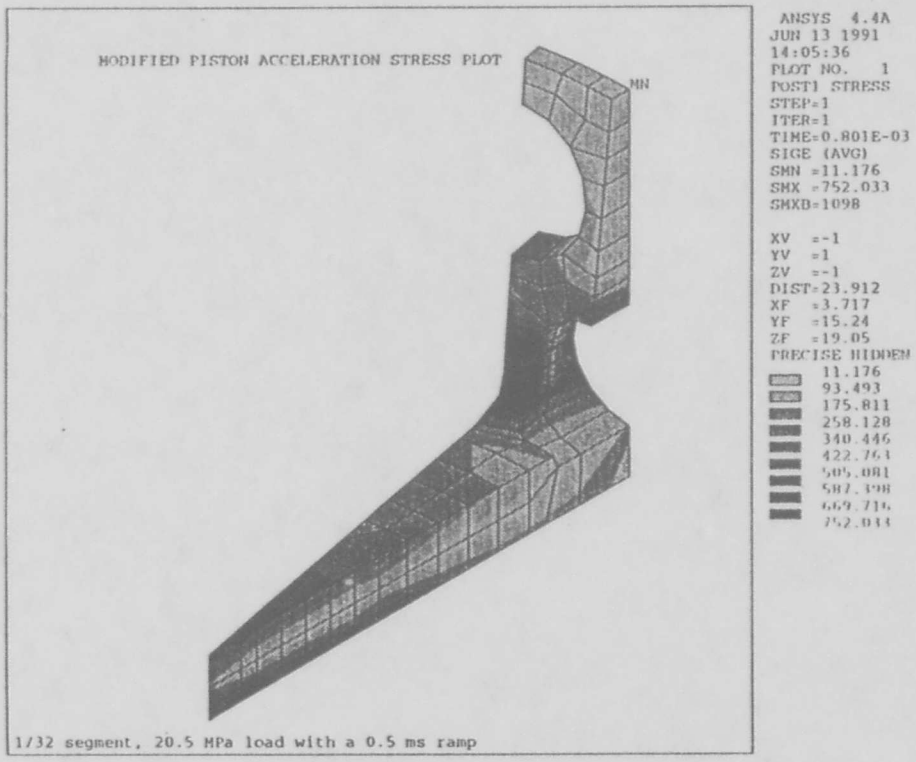

Figure 9.2 Modified piston acceleration stress contour plot.

The stress analysis of a dynamic problem requires a stress history in order to determine the time when the stresses are maximum. A critical stress zone must first be determined by performing a stress pass at some time in the analysis to create a stress contour plot. This is used to help isolate the nodes in the highest stress region for investigation in the stress history. A second stress pass is then performed for the stress history over the entire analysis time on these nodes in order to show their peak stress time. This time is then specified in the final stress pass to create a plot showing the maximum stress contours. The stress history shows the nodal stress for a particular element, and the stress contour plot displays the element stresses based on averaged nodal stresses. For this reason differences may be seen between a stress history and the peak stresses of its corresponding contour plot.

9.3 Present Piston Loads and Stresses

Due to the piston geometry, a pressure load applied on the front face produces different stresses than a similar load applied on the rear face. The two main loading cases that the piston experiences are an acceleration load on the rear face to drive the piston down the barrel and a deceleration load on the front face as the piston reaches the barrel end. These cases required separate FE loadings and analyses. The loads are assumed to be axisymmetric and uniformly distributed across the faces. The acceleration or driving load is a 20.5 MPa step with a 0.5 ms ramp applied to the back face of the piston. The 20.5 MPa is based on the static pressure of the driver prior to tunnel firing. The ramp of 0.5 ms is based on estimates from diaphragm rupture tests. The expanding gas forces are assumed to act primarily on the back face and not on the skirt so that radial loads on the skirt are not considered. The deceleration load is based on the measured BEP, having a time history similar to figure 9.3(b) with pressure spikes up to 26 MPa. Friction forces on the outside of the skirt are assumed negligible.

The boundary conditions allow for free flying in the axial direction in keeping with actual piston motion. Although the predicted temperature at the nozzle end of the barrel, and subsequently the piston's face during tests reached 1300K, the duration is very short (approximately 30 ms). For this reason it is assumed that the heat penetration into the piston is negligible and would have little effect on stresses. No

deflection limits are considered since the tolerance between the piston and the barrel wall is greater than any expected radial deflections.

Typical acceleration and deceleration stress histories are shown in figures 9.3(a), (b). The stress histories show cycling stresses close to the first mode natural frequencies, which suggest this mode is predominant in the stress analysis. For example, figure 9.3(a) has a stress cycling at 2 cycles/0.24 ms = 8333 Hz. This is within 2% of the FEA calculations of the piston's first natural mode frequency.

The modified piston Von Mises stress maxima are 752 MPa in acceleration (figure 9.2) and 612 MPa in deceleration. Since the calculated stress maxima exceed the 480 MPa yield strength of the 7075-T6 aluminum alloy, it appears that the applied loadings tend to exaggerate the actual conditions experienced by the piston. This is acceptable since the stress maxima are used as design stresses for the redesign with the same boundary conditions. Further mesh refinement would likely show even higher peak stresses. This is not done since the design stresses determined to this point are deemed sufficient to provide an ample stress margin for the piston redesign. A fine mesh in the piston redesign ensures that these stresses are conservative.

9.4 Optimization with Dynamic Analysis

"Design optimization is a programmed technique that integrates the design cycle into an automated process" (Ref. 9.1). This automated design approach controls the FEA in conjunction with the optimizer's evaluation and modification techniques, generating design variations until specified criteria are met. The FE problem is parametrically defined with design variables, limited by state variables and optimized until an objective function is reached. An FE optimization problem involves five basic steps (Ref. 9.2): (1) Initial conditions of design variable parameters, (2) parametric FE model definition, (3) solution, (4) postprocessing, and (5) optimization looping. Steps (1) through (4) are much like a typical FEA. The optimization procedure envelopes the parametric FEA and manipulates the design variables to achieve a minimum objective function.

Design variables are independent parameters such as thickness which are varied to obtain the objective function. State variables are dependent functions of one or more design variables and represent the response of the design to loadings, boundary conditions or changes in design variables. These are most commonly design stresses, but could also be displacements. The objective function is a dependent variable consisting of one or more design variables, which is minimized during optimization. It is most commonly defined as volume. In this project piston face and skirt thicknesses are the design variables, limited by the design stresses which are calculated during the acceleration and deceleration load case analyses. The objective function is defined by the piston's total volume in order to minimize its mass.

A brief summary of the design optimization procedure is as follows: The optimizer creates several random trial configurations within the user specified limits. The sets of data points are curve fitted by the method of least squares in order to represent approximations of the objective function and the state variables. Penalty functions which account for the constraints imposed on the design and state variables are combined with the unconstrained objective function. In the ANSYS program,minimization uses the sequential unconstrained minimization technique (Ref. 9.1), to search for the minimum of the current approximation. From this a new trial design is determined and then analyzed to create a new design set. Evaluation between this design and the best design yet encountered determines if termination will result. The solution is terminated if: convergence to a feasible solution appears to have occurred, the maximum number of specified loops is reached, or if too many sequential infeasible solutions develop (Ref. 9.1).

It was decided that the currently used 7075-T6 aluminum alloy is a suitable material for the piston redesign due to its linear properties, low mass density compared to its high strength, cost effectiveness over other more elaborate alloys or materials, as well as its machinability. Temperature, wear resistance, and life cycle endurance have also proven effective. The redesigned piston requires a diameter of 76.2 mm to match the tunnel's bore, a length of at least 30.48 mm and the front face needs to be flat in order to match the barrel end surface. The specified length is 40% of the diameter as recommended from work by others (Ref. 9.2).

Geometric assumptions to limit the redesign possibilities are also required. Although the holes in the skirt of the existing pistons are intended to decrease mass, they also cause stress concentrations which lead

to failure. By utilizing an axisymmetric design three geometric considerations are employed: (1) the critical stress zones between skirt holes would be avoided through an axisymmetric geometry, (2) the use of axisymmetric elements and loadings would greatly simplify the modelling, file space and solver time requirements, and (3) a better mass distribution along the skirt would reduce inertial stresses.

The acceleration load case tends to cause significant stress oscillations. This created difficulties in specifying a single point in time for postprocessing to determine the peak stresses during the optimization loop. With these oscillations it is possible that stresses could be considered at either extreme of the stress history which would impede the convergence of the analysis. Increasing the ramp time decreases these stress oscillations while allowing the mean stress magnitude to stay the same. Preliminary piston redesigns showed stress oscillations in the order of 50 MPa with a 0.5 ms ramp, yet only a few MPa for a 1 ms ramp. Therefore a 700 MPa state variable could allow a solution with maximum stresses of approximately 750 MPa with a 0.5 ms ramp, but stresses just over 700 MPa with a 1 ms ramp. By analyzing with a 1 ms ramp and a state variable (ASE) of 700 MPa, the optimization could converge. Once a design converged a final solution with a 0.5 ms ramp was performed to ensure that the 752 MPa design stress is not exceeded. For deceleration the stress state variable (DSE) is set at 600 MPa.

From the design constraints a parametric model for optimization is devised for the piston redesign, and is shown in figure 9.4. The axisymmetric parametric piston was defined using four areas; two for the face, and one each for the face-to-skirt transition and the skirt: Area 1 (front face) is defined by fixed parameter F1 = 1 mm, Area 2 (rear face) is defined by variable parameter s F2 through F7 (a spline provided a smooth rear face), Area 3 (transition) is defined by variable parameter RAD, a fillet radius, and Area 4 (skirt) is defined by parameters S1 and S2.

In the early optimization solutions it was found that the skirt thickness always converged to the minimum defined limits. This occurred since the main load experienced by the skirt is inertial in both loading cases. As the skirt thickness tended to decrease so would the stresses, yet the skirt needed some practical strength to resist the tipping of the piston in the barrel. A skirt thickness investigation was made to determine a geometry with adequate strength. The original skirt geometry without the holes was compared to other solid skirt thicknesses. A FE cylinder similar to Area 4 was investigated with full constraints at S1

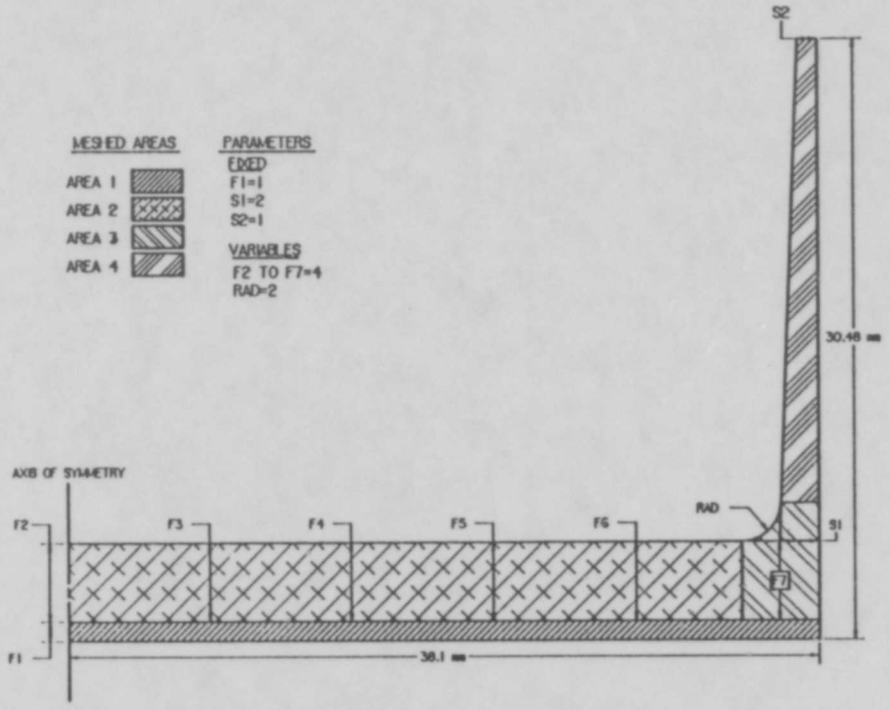

Figure 9.4 Parametric piston model for optimization.

and a radial inward point load at S2. Based on the original geometry and several trial thicknesses, an assumed radial jamming load of 100 N showed stresses and deflections within a reasonable range. It is felt that a fixed thickness limit for S2 = 1 mm would provide a safety factor while still remaining machinable and S1 = 2 mm would give a taper to reduce bending stresses.

Typical initial and limiting values for the design parameters, state variables and the objective function DVOL (Design Volume) were:

Variable	Initial Value	Limits	Tolerance	Units
F2 to F7	4	0.5 to 7	0.1	mm
RAD	2	0.5 to 5	0.1	mm
ASE	—	0 to 700	1	MPa
DSE	—	0 to 600	1	MPa
DVOL	—	—	10	mm^3

9.5 Results

Several optimizations were performed on the model with various design variable limits and tolerances. Two basic solution forms were obtained. From these solutions OPT1 and OPT2, the best two, are reviewed. The only difference between OPT1 and OPT2 is that the upper limit of the design variables F2 to F7 for OPT1 is 7 mm and for OPT2 it is 10 mm. Both solutions had ten random trials. OPT1 converged after five more trials and OPT2 took nine more trials. Figures 9.5(a), (b) show the different geometries of the two solutions,OPT1 and OPT2, which have volumes of 26168.1 mm^3 and 26614.5 mm^3, respectively. Although it was decided by virtue of the lower volume that OPT1 is the better solution, it is significant to note that various solutions can occur with different design limits or types of parametric models.

A final stress analysis was performed for the acceleration (0.5 ms ramp) and deceleration load cases based on the OPT1 geometry, to ensure that the optimized piston is within the design stress limits. The peak Von Mises stresses for the optimized design are 749 MPa in acceleration and 598 MPa in deceleration. See figure 9.6 for acceleration stress plot.

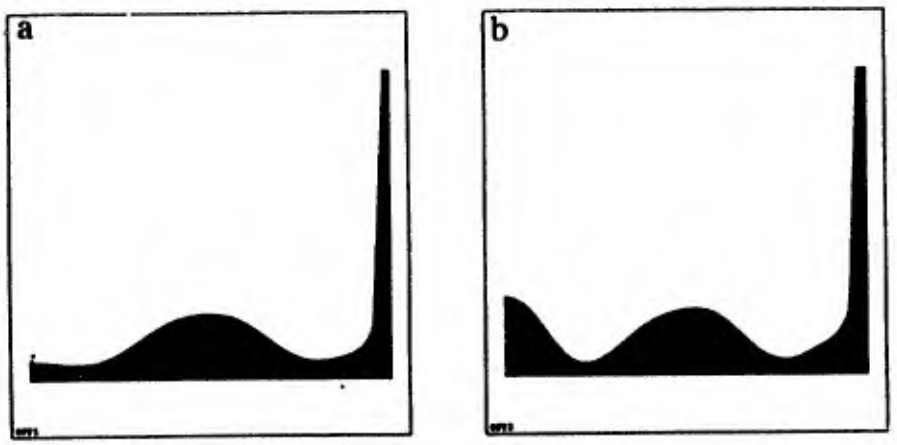

Figure 9.5 Optimization geometry plots, (a) OPT1, (b) OPT2.

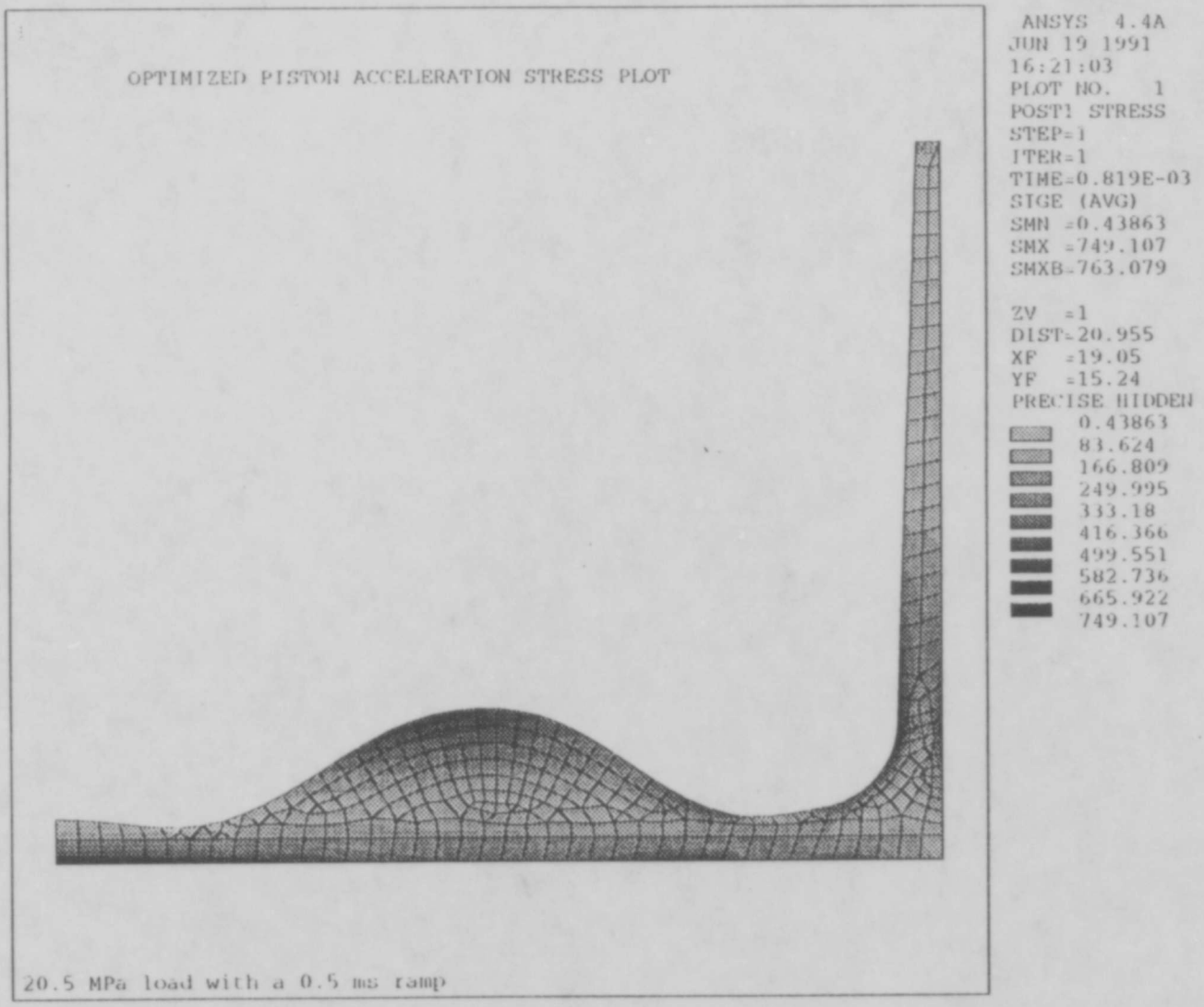

Figure 9.6 OPT1 acceleration stress contour plot.

The optimized piston's peak stresses are slightly lower than the peak stresses of the modified piston, based on the loading and boundary conditions applied. The following is a list of assumptions which provide additional factors of safety for the optimized redesign: (1) the acceleration load assumes that the full driver pressure is experienced by the piston's rear face, which is conservative, (2) the deceleration load assumes full BEP is applied to the piston's front face, not fully accounting for the pressure equalization of the driver pressure, which could decrease some of this load, (3) a relatively coarse mesh is used in the modified piston analysis to ensure that the interpreted design stresses are conservative, (4) the state variables, ASE and DSE, are rounded down, and (5) a fine mesh, shown in figure 9.6, is used for the optimized piston to ensure that the design stress limits are not exceeded.

9.6 Conclusions and Future Work

The investigation of an aluminum alloy hypersonic gun tunnel piston using transient dynamic finite element analysis and the subsequent redesign using optimization has yielded a marginal stress reduction by being conservative and a 25% mass reduction, 71.3 grams compared to 95.9 grams. Actual test firing of the optimized piston is required in order to verify it as a successful design.

The use of nonlinear materials, which is the next logical step in future piston redesigns, would increase analysis requirements. For example, modelling a composite disc with similar dimensions to the existing pistons could be investigated. Honeycomb composite aligned for strength in the direction of the applied forces, in layer combinations with fibre reinforcement, could be employed. This "puck" design may prove to have a more desirable shape and mass distribution.

9.7 References

9.1 "ANSYS Revision 4.4 User's, Mode Superposition and Optimization Manuals and Tutorials," Swanson Analysis Systems Inc., Houston, PA.

9.2 Lemcke, B., "An Investigation of the Stagnation Conditions in the Shock-Compression Heater of a Gun Tunnel," The Aeronautical Research Institute of Sweden, Stockholm, Sweden, FFA Report 90, February 1962.

Appendix A: Error Analysis and Data Precision for Section 6

The calculation of inlet efficiency is based on the experimental measurement of compression ratio and contraction ratio given the calibrated independent variables of freestream Mach number and specific heat ratio, γ. The γ value is considered to be 1.4 with negligible error. The freestream Mach number has been determined to $8.30 \pm .05$. The uncertainty in this value has been considered in all of the calculations.

Since area is a geometric parameter, its measured accuracy is obviously dependent on valid inviscid design and viscous correction followed by high precision manufacture. Inspection on all inlets has verified the specified tolerance of $\pm 1.27 \times 10^{-5}$ m ($\pm .0005$ in.). The subsequent calculation of area ratio shows a negligible error of $\pm 0.05\%$.

Efficiency uncertainty, however, is highly dependent on accurate measurement of the throat static pressure. The piezoresistive pressure transducers used (both Kulite and Endevco) demonstrate excellent linearity with very low hysteresis, low thermal and acceleration sensitivity. Specific uncertainty is less than 1% of the maximum rated pressure. Initial pressure results, however, indicate a relatively high degree of data scatter in the initial runs on the Prandtl-Meyer and Oswatitsch inlets. This was alleviated by an increase in the number of directly repeated runs with careful reproduction of tunnel initial conditions. Highly repeatable pressure data has been obtained on all of the inlets with a standard deviation that is roughly 2.7% of the nominal pressure value at each tap station of the throat. A 1.5% standard deviation was observed for the stations on the isentropic compression surfaces for both the 23 million and 44 million freestream Reynolds numbers. These stations were significantly less sensitive to imprecision of angle of attack setting and cowl alignment.

The uncertainty in the area and pressure measurements combined with the uncertainty in the freestream Mach number produce a $\pm 3\%$ error in the value of total pressure recovery, η_{pt}', calculated for each inlet.

It is important to recognize that there remains an undetermined precision uncertainty associated with any variation from flow one-dimensionality in the plane of the measured static pressure. The pressure data and schlieren photographs from the Prandtl-Meyer flow, for instance, are shown in Figures 6.26. They clearly

indicate that the turning shock is forming just upstream of the corner causing stronger reflected shocks and significant disruption to the flow uniformity along with static pressure increase in the annulus.

The Oswatitsch inlet, with its narrow annular exit may be experiencing multiple weak reflected shocks as well, along with a detrimental boundary layer development. Both factors would conspire to rapidly increase the static pressure as is seen in the Figure 6.36 profile. Although the reflected shock activity is not verifiable by schlieren it has been predicted by the PNS simulation shown in Figure 6.30. Furthermore, experimental studies have shown large deviations from one-dimensional predictions of flow properties, particularly where there are large boundary-layer thickness to duct passage ratios such as those occurring in small scale models like the Oswatitsch and Prandtl-Meyer inlets (Ref. 6.5).

Considering the Busemann inlet, on the other hand, the static pressure profile along the surface length of the throat section is seen to be very steady (Figure 6.18b). In addition, what little boundary layer growth has taken place up to this pressure station represents only a small fraction of the core flow area. It has had, therefore, minimal effect on the core pressure. Any flow disruption caused by reflected shocks would be absent or extremely weak given the apparent exactness of the shock location on the corner indicated by the pressure profile of Figure 6.18b and oil dot visualization. In addition, the schlieren evaluation of the Busemann exit Mach number of $4.4 \pm .3$, although a less precise measurement, has provided a verification of the theoretical and static pressure based figure ($4.34 \pm .05$). Any substantial reflecting shock activity in the throat would have significantly reduced the Mach number between corner and exit. For these reasons it can be expected that the validity of the efficiency measurement is undoubtedly best demonstrated by the clean exit flow properties of this intake.